AGARD-CP-529

AGARD

ADVISORY GROUP FOR AEROSPACE RESEARCH & DEVELOPMENT
7 RUE ANCELLE 92200 NEUILLY SUR SEINE FRANCE

AGARD CONFERENCE PROCEEDINGS 529

ELF/VLF/LF Radio Propagation and Systems Aspects

(La Propagation des Ondes Radio ELF/VLF/LF et les Aspects Systèmes)

Papers presented at the Electromagnetic Wave Propagation Panel Symposium, held at the Quartier Reine Elisabeth, Brussels, Belgium, 28th September—2nd October 1992.

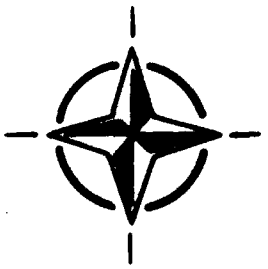

NORTH ATLANTIC TREATY ORGANIZATION

Published May 1993

Distribution and Availability on Back Cover

AGARD-CP-529

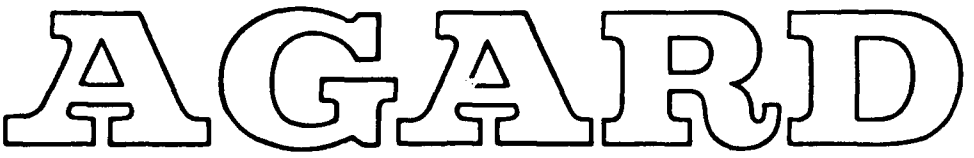

ADVISORY GROUP FOR AEROSPACE RESEARCH & DEVELOPMENT
7 RUE ANCELLE 92200 NEUILLY SUR SEINE FRANCE

AGARD CONFERENCE PROCEEDINGS 529

ELF/VLF/LF Radio Propagation and Systems Aspects

(La Propagation des Ondes Radio ELF/VLF/LF
et les Aspects Systèmes)

Papers presented at the Electromagnetic Wave Propagation Panel Symposium, held at the Quartier Reine Elisabeth, Brussels, Belgium, 28th September—2nd October 1992.

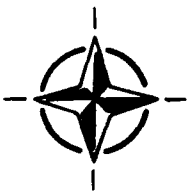

North Atlantic Treaty Organization
Organisation du Traité de l'Atlantique Nord

The Mission of AGARD

According to its Charter, the mission of AGARD is to bring together the leading personalities of the NATO nations in the fields of science and technology relating to aerospace for the following purposes:

- Recommending effective ways for the member nations to use their research and development capabilities for the common benefit of the NATO community;
- Providing scientific and technical advice and assistance to the Military Committee in the field of aerospace research and development (with particular regard to its military application);
- Continuously stimulating advances in the aerospace sciences relevant to strengthening the common defence posture;
- Improving the co-operation among member nations in aerospace research and development;
- Exchange of scientific and technical information;
- Providing assistance to member nations for the purpose of increasing their scientific and technical potential;
- Rendering scientific and technical assistance, as requested, to other NATO bodies and to member nations in connection with research and development problems in the aerospace field.

The highest authority within AGARD is the National Delegates Board consisting of officially appointed senior representatives from each member nation. The mission of AGARD is carried out through the Panels which are composed of experts appointed by the National Delegates, the Consultant and Exchange Programme and the Aerospace Applications Studies Programme. The results of AGARD work are reported to the member nations and the NATO Authorities through the AGARD series of publications of which this is one.

Participation in AGARD activities is by invitation only and is normally limited to citizens of the NATO nations.

Published May 1993

ISBN 92-835-0712-6

Printed by Specialised Printing Services Limited
40 Chigwell Lane, Loughton, Essex IG10 3TZ

Theme

There is currently a renewed interest in NATO in ELF/VLF/LF communications, particularly with respect to communications to locations in the Arctic and to points under the sea and beneath sea ice; and the concern about VLF transmitting antenna performance for 4-channel MSK transmission, which requires an antenna band-width of 200 Hz. This band-width exceeds that available for the major VLF stations in the world. Also, recent developments in the application of VLF/LF computer codes to predict propagation in the earth's ionospheric waveguide have exemplified the need to predict circuit performance, rather than field strength only, and for this one requires a world wide model for ELF/VLF/LF radio noise, and detail on the performance of MSK modems in a non-gaussian radio noise environment.

During the past decade, since propagation, communications and systems aspects were considered by the AGARD/EPP for this frequency band, there have been new developments in antenna design, for fixed stations (changes to existing stations and commissioning of new stations); for transportable application; and for deployment from space platforms. Performance prediction for space based systems requires a detailed knowledge of the complex interaction between long wire antennas with the earth's magnetic field and ionospheric plasma, and associated problems with respect to generation and radiation of ELF/VLF/LF radio waves from antennas in space, particularly with regard to propagation through the ionosphere, and with coupling into the earth ionosphere waveguide mode.

Thème

Les télécommunications ELF/VLF/LF connaissent un renouveau d'intérêt au sein de la communauté OTAN, en particulier en ce qui concerne les transmissions destinées à l'océan arctique et à des points situés au-dessous de la surface de la mer et de la glace marine. Cet intérêt porte également sur les performances des antennes d'émission VLF pour la transmission tétraphonique à modulation par déplacement minimal (MSK), qui demande une bande passante d'antenne de 200 Hz. Or, aucune des stations VLF dans le monde ne peut satisfaire à cette exigence. Aussi, les développements récents en ce qui concerne la mise en œuvre des codes de calcul VLF/LF pour la prévision de la propagation dans le guide d'ondes Terre-ionosphère ont démontré qu'il est nécessaire de prévoir les performances des circuits, plutôt que la seule intensité du champ, et que pour le faire, il faut disposer d'un modèle mondial du bruit radioélectrique ELF/VLF/LF et d'informations détaillées sur la performance des modems MSK en environnement non-gaussien.

Au cours de la dernière décennie, et depuis la dernière fois que la commission EPP de l'AGARD a examiné les aspects propagation, télécommunications et systèmes pour cette bande de fréquences, la conception des antennes a évoluée considérablement; qu'il s'agisse d'antennes destinées à des stations fixes (modifications de stations existantes et mise en service de nouvelles stations), des antennes pour applications transportables ou des antennes déployées à partir de plateformes spatiales. La prévision des performances des systèmes basés dans l'espace demande des connaissances approfondies de l'interaction complexe entre les antennes à long fil, le champ magnétique terrestre et le plasma ionosphérique, ainsi que des problèmes qui y sont associés et notamment l'élaboration et le rayonnement d'ondes hertziennes ELF/VLF/LF à partir d'antennes basées dans l'espace, en particulier en ce qui concerne la propagation à travers l'ionosphère avec couplage au guide d'ondes Terre-ionosphère.

Electromagnetic Wave Propagation Panel

Chairman: Dr J.H. Richter
Naval Command, Control and Ocean
Surveillance Center
RDT&E Division, Code 54
San Diego, CA 92152-5000
United States

Deputy Chairman: Dr D.H. Höhn, apl. Prof.
FGAN
Forschungsinstitut für Optik
Schloss Kressbach
D-7400 Tübingen
Germany

TECHNICAL PROGRAMME COMMITTEE

Co-Chairmen

Dr John S. Belrose
PO Box 11490
Communications Research Center
Station H
Ottawa, ON K2H 8S2
Canada

Prof. Giorgio Tacconi
Universita' di Genova
Dipartimento Ingegneria Biofisica
via all'Opera Pia 11/A
16145 Genova
Italy

Members

Prof. L. Bossy
174, Avenue Winston Churchill
UCCLE
B-1180 Bruxelles
Belgium

Dr J.A. Ferguson
Code 544
Naval Ocean Systems Center
San Diego, CA 92152-5000
United States

Prof. Marino Dobrowolny
Institute for the Physics of
Interplanetary Space
Italian Research Council
Frascati (Rome)
Italy

Mr George H. Hagn
SRI International
1611 N. Kent Street
Arlington, VA 22209-2173
United States

PANEL EXECUTIVE

Mail from Europe:
AGARD—OTAN
Attn: EPP Executive
7, rue Ancelle
92200 Neuilly-sur-Seine
France

Mail from US and Canada:
AGARD—NATO
Attn: EPP Executive
Unit 21551
APO AE 09777

Tel: 33(1)47 48 57 68
Telex: 610176 (France)
Telefax: 33(1) 47 38 57 99

Contents

INTRODUCTION

John S. Belrose
Communications Research Centre
PO Box 11490, Station H
Ottawa ON Canada K2H 8S2

Introduction

Good morning Ladies and Gentlemen. I am pleased to welcome you to this Specialists' Meeting on "ELF/VLF/LF Radio Propagation and System Aspects".

VLF/LF radio propagation and communications is a research area that brings back nostalgic remembrances for me. I started my research career in September 1951 as a young engineer in the field of LF communications engineering, see Belrose et. al. [1959]. In 1953 I joined the Radio Group, Cavendish Laboratories, Cambridge University, then headed by the late Jack Ratcliffe, where I carried out studies on the propagation of long waves. The results of my studies conducted at Cambridge, and further studies made subsequently on return to my home Laboratory in 1958, were written up as an AGARD Lecture, see Belrose [1968]. This lecture was one of several on radio propagation presented at Leicester, UK in 1968, and subsequently repeated at Ottawa, CA in 1970.

The last time the AGARD/EPP panel addressed the subject of long/very long wave propagation in a full conference forum was in 1981, a conference which was held in Brussels, BE, 21-25 September 1981. It is coincidental but appropriate that this specialists' meeting a decade later is being held in the same city.

The published proceedings of this earlier meeting provided a good overview on the propagation medium, Belrose [1981a]. This subject will not be addressed in this meeting. A good overview on ELF propagation was presented by Bannister [1981], who will present paper(s) later at this meeting. VLF propagation was in my view not well overviewed. Concerning LF the title of the paper by Belrose [1981b] was "LF Propagation: An Overview", however the paper was not really an overview, since emphasis was given to some of the peculiarities of LF propagation. The subject of numerical modeling of the propagation medium at ELF/VLF and LF was overviewed by Morfitt, Ferguson and Snyder [1981]. This subject will be re-visited at this meeting.

In my introduction to this specialists' meeting I will briefly overview some of the early history of radio communications, since it is frequently said that long distance radio communications began at VLF. I will make comment on the need to revisit the subject of ELF/VLF/LF propagation and systems aspects. And, with the hope of stimulating discussion I will address a few topics that are of special interest to me.

Long Distance Radio Communications Began at LF

Heinrich Hertz's classical experiments were conducted in his Laboratory using a small end-loaded dipole driven by an induction coil and a spark gap for his transmitter, and since the frequency transmitted was determined by the resonant frequency of his antenna system, his experiments in 1887 were conducted at VHF/UHF (60 to 500 MHz)----this being a practical dimensional wavelength for indoor antennas.

Marconi's initial experiments, following the lead of Hertz, were also conducted at UHF. But for his transatlantic experiment in December 1901, he employed a much larger antenna system, which radiated on a frequency of about 820 kHz. Recall that the frequency of a spark gap transmitter is determined by the resonant frequency of the antenna. The transmitting station at Poldhu, Cornwall, station call sign PN, was designed and supervised by Fleming. While the fundamental frequency of his transmitting system was about 820 kHz, there is no way that this signal could have been heard during daytime at Signal Hill, Newfoundland, a distance of 3500 kilometers, c.f. Ratcliffe [1974] -- even though it was winter, in a sunspot minimum period, and there were no magnetic storms on days before or on the day when he claimed to have successfully received the signal (on 12 December 1901). His receiver was untuned, and he used a kite supported long wire antenna. Unbeknownst to him he must have been listening to a harmonic, perhaps the third harmonic (2460 kHz), of his spark gap transmitter. Even this frequency is rather low. We have experimentally modeled the antenna system used by the sender at Poldhu in Cornwall. Our antenna was resonant at 943 kHz and 3660 kHz. It was anti resonant at 2390 kHz. Marconi's kite supported receiving antenna was a wire 152.4 metres long. At a possible receive frequency of 2460 kHz this wire antenna would be 1.25-wavelengths

long--which corresponds to the $5\lambda/4$ resonance (λ is the wavelength). Recall that a wire monopole antenna fed against ground is resonant on odd multiples of a quarter wavelength. Marconi's receiver was untuned. The bobbing of the kite which supported his antenna was probably in part responsible for the erratic nature of the received signal---this bobbing action would in effect "tune-and-detune" the antenna of his receiving system---the antenna being the only "tuned element" of his receiver.

Reginald Aubrey Fessenden, perhaps some of you will say who was Fessenden, a Canadian working in the USA, began his experiments at VLF. His belief was that radio transmission should be by way of continuous waves, see Fessenden [1908], not the damped-wave whip-and-lash type of transmission provided by spark transmitters. Marconi, Fleming and others ridiculed Fessenden's suggestion that a wireless signal could be transmitted by applying an alternating current to an antenna. All were unanimous in their view that a spark was essential to wireless. Some "antenna authorities" even claimed that the gap, which initially was between the antenna input terminal and ground, was an essential element of the radiating system.

The not wanted 'gap' was eliminated by Braun, a German physicist who in 1898 patented a circuit in which the spark gap was in a separate primary circuit in series with an appropriate coil and condenser. But the contribution of the Braun patent is about as controversial as is the subject of who was the first to devise electromagnetic antennas. The German patent has been criticized, since nothing original was said about tuning. On the contrary, Braun seems to have had no clear understanding of spark transmission, since the oscillating circuit was said to be much 'slower (tuned to a lower frequency) than the antenna circuit.' While a double humped amplitude-frequency response is possible if the tuned primary and secondary circuits are over-coupled, this is an undesirable feature. Notwithstanding, his "tank circuit" was coupled inductively to a secondary consisting of the antenna in series with a coupling coil in which the driving electromotive force was induced and which provided a continuous conducting path from the antenna to ground. Except for the later insertion of a transmission line between the antenna and the coupling coil the Braun antenna arrangement provided the complete electrical equivalent of the present day base driven monopole antenna.

Fessenden was the inventor of continuous waves. The idea came to him during discussions with his uncle Cortez Fessenden, while visiting with him at his cottage on Chemong Lake, near Peterborough in 1897. He discussed his concept of wave transmission by dropping pebbles into a quiet lake, and noting how waves traveled radially out from the point source of the disturbance. His theory of continuous waves is described in his US patent No. 706,737, August 12, 1902, but it was not before the fall of 1906, when he developed the HF alternator to a point where it could be used to generate frequencies up to 100 kHz, that continuous wave transmission over long distances was practical and feasible. Early versions of HF alternators developed by Tesla [Quinby, 1984] provided a capability to generate frequencies in the 10-20 kHz range, and there is no fundamental reason that long distance communications could not have used frequencies in this band---but there was a practical reason. The physical practical size of antenna's used by the early radio experimenters was too small to radiate efficiently at VLF, hence long distance radio communications began with Fessenden at LF in January 1906.

To illustrate the reaction of Fessenden's colleagues to this departure from conventional transmission methods, from spark or whip-and-lash transmissions to continuous waves, we should note that J.A. Fleming in his book "Electromagnetic Waves" published in 1906 said, in reference to Pat. No. 706,737, that "there was no HF alternator of the kind described by Fessenden, and it is doubtful if any appreciable radiation would result if such a machine were available and were used as Fessenden proposes." History, and present knowledge, showed that Fleming was totally wrong, since 1906 was the year of Fessenden's greatest achievement, using continuous waves generated by a HF alternator (the only means of generating CW at that time). The HF alternator was connected between the antenna's input terminal and ground. For the first time the transmit frequency was not determined by antenna tuning. Antenna tuning affected the transfer of power from the generator to the antenna system. Certainly that statement did not appear in subsequent editions of Fleming's book. Judge Mayer, in his opinion upholding Fessenden's patent on this invention, said, in effect it has been established that the prior art practiced, spark or damped wave transmission, from which Fessenden departed and introduced a new or continuous-wave transmission for the practice of which he provided a suitable mechanism -- which has since come into extensive use, cf. Kintner [1932].

Fessenden had built and tried arc transmitters but without much success. The only known way to generate continuous waves at a sufficient power level and having the required spectral purity was to use a HF alternator. But in the late 1800/early 1900s, 10 KHz was the highest frequency achieved

using an HF alternator. But the efficiency of practical antenna systems was very poor at such a low VLF frequency. So he strove to increase the frequency generated by his HF alternator.

In the meantime he made significant improvements to spark gap transmitters. In 1900, he devised an interrupter that would operate at an unheard of rate of 5000 to 10,000 breaks/second. The reason for this was because he wanted to transmit voice without wires. Using this interrupter, with a spark gap transmitter, see Fig. 1, and inserting a carbon microphone directly in the antenna lead, he successfully transmitted his voice over a distance of 1-mile, between 50-foot antennas. The voice was said to be perfectly intelligible, but it was accompanied by an extremely loud disagreeable noise due to the irregularity of the spark. The frequency used was probably in the 3-5 MHz band, judged by the physical size of the antenna masts used.

Fessenden's early radio telegraphy experiments had to make due with spark transmitters, the only known means at that time to develop appreciable power, and so he set his mind to make this type of transmission more CW like. This lead to his development of the synchronous rotary spark-gap transmitter, Fig. 2. The AC generator providing the power was directly coupled to the rotary spark-gap. If the rotary gaps were phased to fire on both positive and negative excursions of a 3-phase 125 Hz waveform, this would generate a spark rate of 750 sparks/second. This provided pseudo-MCW, certainly a more continuous transmission than existing spark-gap transmitters, and the musical tone heard in the headphones of Fessenden receivers was more easily distinguishable against the atmospheric noise and interference compared with the buzz-buzz of the spark gap transmitter of that day. Using 420-foot umbrella top loaded antennas (Fig. 3), tuned to about 88 kHz, he successfully communicated two-ways across the Atlantic in January 1906, between Brant Rock, MA and Machrihamish, Scotland. Marconi in the meantime had not succeeded in transmitting a complete message, even one way across the Atlantic. Marconi was however building bigger antenna systems, and hence moving down in frequency. By 1904 his English antenna had become a pyramidal monopole with umbrella wires, and the frequency was 70 kHz. In 1905 his Canadian antenna, installed at Glace Bay, NS was a capacitive top loaded structure, with 200 horizontal radial wires each 1000 feet long, at a height of 180 feet, and the frequency was 82 kHz.

In the September 1906 the GE Company delivered a HF alternator built for Fessenden under the supervision of Alexanderson. This in Fessenden's words was a "useless machine" capable only of generating frequencies as high as 10 kHz. So Fessenden rebuilt it. Finally he succeeded in November 1906 in developing a machine capable of running at speeds that would generate frequencies as high as 100 kHz. His first HF alternator was a small machine of the Mordey type, having a fixed armature in the form of a fixed disk, or ring, and a revolving field magnet with 360 teeth, or projections. At a speed of 222 revolutions per second, an alternating current of 80,000 Hz was generated. The maximum output of this alternator at the above speed was about 300 watts. Very little difficulty seems to have obtained in running the machine at so high a speed, a simple flat belt drive was used, driven by a steam engine, and a thin self-centering shaft which entirely obliviated excessive vibration and pressure on the bearings.

Again, using a carbon microphone inserted directly in the lead to the antenna, but this time modulating a true CW wave, he began experimenting in November 1906 with voice transmission, using for the first time a continuous wave at a frequency well above voice band frequencies. Let me recount the first transmission of voice across the Atlantic. Fessenden and colleagues were conducting experimental transmissions using his newly developed HF alternator, between stations at Brant Rock and Plymouth, MA. About midnight, on an evening early in November, 1906 Mr. Stein was telling the operator at Plymouth how to run the dynamo. His voice was heard by Mr. Armour at the Machrihamish, Scotland station with such clarity that there was no doubt about the speaker---and the station log book confirmed the report.

Reginald Fessenden's greatest success was still to come---the first radio telephony broadcast to ships in the Caribbean and North Atlantic on Christmas eve in December 1906. The broadcast was repeated on New Year's eve.

So much for the early history of radio communications.

NATO Interest in ELF/VLF/LF

There is currently a renewed interest in NATO in ELF/VLF/LF communications, particularly with respect to communications to locations in the Arctic and to points under the sea and beneath sea ice; and there is at present a concern about VLF transmitting antenna performance for 4-channel MSK transmission, which requires an antenna band-width of 200 Hz. This band-width exceeds that available for all but one of the major VLF stations in the world. Also, recent developments in the application of VLF/LF

computer codes to predict propagation in the earth-ionosphere wave guide have exemplified the need to predict circuit performance, rather than field strength only, and for this one requires a world wide model for ELF/VLF/LF radio noise, and detailed knowledge on the performance of MSK modems in a non-gaussian radio noise environment.

During the past decade, since propagation, communications and systems aspects were considered by the AGARD/EPP for this frequency band, there have been new developments in antenna design for fixed stations [Belrose, 1991], changes to existing stations and commissioning of new stations; and progress has been made wrt antennas for transportable application; and for deployment from space platforms. Performance prediction for space based systems requires a detailed knowledge of the complex interaction between long wire antennas with the earth's magnetic field and ionospheric plasma, and associated problems with respect to generation and radiation of ELF/VLF/LF radio waves from antennas in space, particularly with regard to propagation through the ionosphere, and with coupling into the earth ionosphere wave guide.

Aspects of these topics will be covered by papers to be presented at this meeting.

Finally
A few Topics of Interest to Me

On Propagation Mode

VLF waves steeply incident on the ionosphere, and low frequency waves more obliquely incident on the ionosphere, penetrate to heights within the D-region, and the phase of a received signal exhibits a diurnal variation that changes continuously with the altitude of the sun -- a cosinusoidal diurnal variation. VLF waves and LF waves more obliquely incident on the ionosphere, particularly for north-south paths, exhibit a trapezoidal diurnal variation in the phase height of reflection. There is a marked difference with respect to the frequency-distance range where the change over from a cosinusoidal to a trapezoidal pattern occurs, between Europe and North America. This difference is attributed to the higher geomagnetic latitudes for paths at similar geographic latitudes in North America. This difference has long been known, since the fifties. These differing phase-height variation patterns were first pointed out by Bracewell and Bain and colleagues while working at Cambridge, UK. The differences are attributed the formation and decay of two "layers" in the D-region---a D-layer and a lower ledge or C-layer.

The D-layer is dominantly due to solar ionization of a trace constituent NO. The ionization source for the C-layer is cosmic radiation. Since the electron production by cosmic rays is the same during the daytime as during nighttime, the sudden appearance of a low ledge (the C-layer) at dawn is due to the photo detachment of electrons from a bank of negative ions; and the disappearance of this ledge at night is due to disappearance of electrons to form negative ions.

VLF propagation as noted above provides some insight on the way ionization builds up and decays, and provides a routine monitor for the detection and time change of solar-geophysical disturbances. VLF waves steeply incident on the ionosphere are reflected from heights within the D-layer, and exhibit a cosinusoidal diurnal variation. For example the classic pattern for the GBR, Rugby 16 kHz path to Cambridge, Fig. 4. Such a phase change can be interpreted as giving a measure of the scale height in the D-region, and scale height is related to temperature. The regular decrease in phase height during the hours before dawn is clearly indicative of a nocturnal electron production. The winter/summer difference is due to a seasonal change in pressure. The electron density profile is closely tied to a pressure isopleth.

VLF waves very obliquely incident on the ionosphere are reflected from the base of the D-region, and, particularly for north-south paths, exhibit a trapezoidal diurnal phase variation (c.f. Fig. 5 the Balboa - Ottawa path). The phase height decreases rapidly at dawn, increases somewhat less rapidly at sunset, and is fairly constant during the daytime. The phase variation for these very oblique incidence paths give information on the appearance and disappearance of the low lying ledge (the C-layer).

For long east-west paths the diurnal change of phase exhibits a step-like perturbation of a basic pattern, see Fig. 6, as if the sun rose over each ionospheric reflection point, thinking of propagation in terms of a multi-hop wave-hop mode, followed by another step change of phase later, and etc. This in spite of the fact that many of the properties of long distance VLF propagation are best described, and better numerically modeled, in terms of a wave guide mode propagation model.

I have discussed these features in some detail for two reasons. First, because there seems to some misunderstanding of the physics behind the observed phase changes on long VLF paths. The daytime phase height does not change for a long north-south path, whereas phase does change throughout the morning (and afternoon) on a long east-west path. But such a phase change has nothing to do with the regular

build up and decay of a D-layer due to ionization of NO, as inferred by the author of a manuscript I recently reviewed, since reflection takes place below this height. The continuous phase change is because the sun does not rise abruptly along a long EW path.

Also, it interesting to note that while VLF/LF propagation over long paths is best described by a wave-guide mode propagation model, there is evidence, the stepped phase changes, to suggest a multi-hop wave-hop mode of propagation. Perhaps some one may wish to address this topic at this meeting.

Effect of the Finite Conductivity of the Ground

It is well known that an extensive radial wire ground screen must be used to reduce the ground resistance loss for VLF/LF antennas, particularly so for VLF frequencies, since practical monopoles are electrically short, and the radiation resistance of practical antennas is very small. Less well known is how the ground in front of a VLF/LF antenna effects the performance of the antenna, that is the ability of the antenna to launch skywaves or to couple into and excite a wave guide propagation mode. Belrose [1983] has argued, describing LF/MF propagation as multi-hop wave-hop propagation medium that for long distance propagation the ground in front of the antenna fifty or more wavelengths is important for low angle skywave. At 3.75 MHz this corresponds to a distance of 4 kilometers, and I have evidence that this is a realistic distance. But at 25 kHz this distance amounts to 200-kilometers. Should one be concerned with the ground conductivity in front of an antenna to such a distance?

At my home I operate a HF radio amateur station. Let me tell you about my experience in long distance nighttime propagation using a frequency in the 75/80M band (3750 kHz), an observational experience extending over more than 5-years. During nighttime hours it possible to communicate over very long distances using such frequencies. I am control station on Saturday nights for a group of fellow amateurs, the Pow Wow Club, with station locations from coast to coast in Canada, and in the UK. I have regularly used two antennas, a grounded half-wave loop, and a dipole at 15 metres. Both antennas are oriented NS and should have bi-directional patterns in the EW directions. For the loop, the polarization is vertical. Recall that finite ground conductivity affects the vertical radiation pattern for vertical polarization much more than for horizontal polarization. The ground in front of a vertical antenna very much affects the antenna's ability to launch a low angle skywave.

Distant stations, toward the west, beyond about 1000 kilometers, are typically received up to 15 dB stronger on the vertically polarized loop compared with the dipole. The dipole is too low to the ground to form a good low angle lobe. The variability in signal differences between the two antennas depends on distance and propagation conditions. However stations to the east, whatever distance, are always received better on the dipole. What is the reason for this apparent unidirectional pattern of my NS oriented half-loop? Its pattern should be bi-directional in the EW directions.

On figure. seven I have drawn a circle centered on my house with a radius of 4 kilometers (50 wavelengths at 3750 kHz). Toward the east, for distances less than 50 wavelengths, there are two golf-courses, so the ground conductivity should be good, yet this is the direction in which my vertically polarized antenna apparently does not launch a good low angle skywave. Toward the east, beyond 50 wavelengths, we have the cities of Hull/Ottawa. Toward the west to distances less than 50 wavelengths and beyond this distance we have fields, a river and fields again.

Clearly the ground conductivity to 50 wavelengths and beyond must influence the ability of a vertically polarized antenna to launch a low angle skywave. The effective conductivity of cities is poor compared with fields and rivers.

Now let us look at the situation for long range VLF propagation. A northern hemisphere coverage pattern for a hypothetical VLF transmitter located in central Canada, predicted by the NOSC Wave Guide Propagation Prediction Program, this program will be addressed later, is shown in Fig. 8, calculated for 1 kW radiated power, summer day conditions, at a frequency of 24 kHz. The field strengths are in dB relative to 1 μV/m. Notice that in general the contours agree with expectation. Propagation from east-to-west is better than west-to-east; and notice the interesting anomaly in the field strength contours which results from the very low ground conductivity of Greenland. But the point I wish to make is the increased field strengths due to the good conductivity of the sea water of Hudson Bay, compared with the surrounding low conductivity of Arctic terrain. The terrain in front of the antenna is characterized by high conductivity (σ = 10-20 mS/m), see Fig. 9, and so if the surroundings to a distance of a hundred or more kilometers about the antenna is important, this should be a good location for a VLF transmitter.

We have tried to make a detailed study of the effect of finite conductivity, and relate this to criteria for antenna siting---but without too much success. The finite ground conductivity along the whole of the path is important, e.g. notice the effect of the Greenland icecap. Another example follows. We show in Fig. 10 a similar field strength contour map for a hypothetical 24 kHz transmitter located at Halifax, NS. We will next examine in more detail field-strength vs. distance for a particular path, but let us refer again to Fig. 9. Note the poor conductivity for a path from Halifax across the Laurentian Shield and over the Ungava Peninsula. On Fig. 10 this path is marked, and notice that even on this scale of mapping, there is a minor "tightening" of the 40 dB μ/m contour and a suggested anomaly in the field-strength as the path passes over the Ungava Peninsula. In Fig. 11 we show field strength calculations vs. distance for this path, at three frequencies 15, 25 and 35 kHz, for daytime propagation conditions. The poor ground conductivity for this propagation path, across the Laurentian shield in Canada, affects the frequencies differently. A transmit frequency of 25 kHz is the best frequency for this path. The frequency differences are less marked at night. see Fig. 12.

Coincidentally a frequency of 25 kHz is the middle of the VLF band currently in use for maritime fleet broadcast---but the move to higher frequencies (to the band 20-30 kHz) was prompted by the need to improve antenna radiation efficiencies and bandwidths compared with the band previously used (15-20 kHz). It was not made to improve propagation in the Canadian Arctic!

VLF Antennas

The search for a better VLF antenna continues: an antenna that provides improved radiation characteristics, particularly high radiation efficiency and wide bandwidth, and having less wire in the air, from the point of view icing and wind. The radiation coupled VLF antenna system used by the German Navy, at Rhauderfehn, GE intrigued me. We have modeled this antenna numerically and experimentally, or at least an antenna of this type, and I had the opportunity to visit the transmitter site, even to take an elevator to the top of one of the eight towers. This study, and other studies conducted at my Laboratory will be addressed later, in the antenna session of this meeting.

Final Remarks

Perhaps some of these random thoughts will provide food for thought and stimulate discussion in the pertinent sessions. So, let us get on with the technical program, by introducing the first speaker.

References

AGARD Conference Proceedings No. 305, "Medium, Long and Very Long Wave Propagation (At frequencies less than 3000 kHz)," September 1981. Available from CFSTI, Springfield, VI, Reference NASA Accession No. N82-

Belrose, J.S., Hatton, W.L. Hatton, C.A. McKerrow and R.S. Thain, 1959, "The engineering of communications systems for low frequencies," Proc. IRE, 47, 661.

Belrose, J.S., 1968, "Low and Very Low Frequency Radio Wave Propagation," In Radio Propagation, AGARD LS XXIX. Available from CFSTI, Springfield, VA, Reference NASA Accession No. N68-37825.

Belrose, J.S., 1981a, "The Propagation Medium: An Overview," AGARD Conf. Proc. No. 305, Medium, Long and Very Long Wave Propagation (at frequencies less than 3000 kHz)," pp. 1-1 to 1-18.

Belrose, J.S., 1981b, "LF Propagation: an Overview," Ibid, pp 22-1-22-10.

Belrose, J.S., "VLF, LF and MF Antennas," in The Handbook of Antenna Design, Volume 2 (editors Rudge, Milne, Olver and Knight), pp. 553-662, IEE Electromagnetic Series, 1983.

Belrose, J.S., April 1991, "VLF Transmitting Antennas: Multiple-Tuning vs. Single-Tuning," Seventh International Conference on Antennas and Propagation, IEE Conf. Pub. No. 333, 640-644.

Fessenden, R.A., 20 June 1908, 'Wireless Telephony,' paper presented at 25th annual convention of the American Institute of Electrical Engineers, Atlantic City, NJ.

Geddes, L.A., "A Century of Progress: The History of Electrical Engineering at Purdue (1888-1988)", 1989, School of Electrical Engineering, Purdue University.

Kintner, S.M., July 1932, "Some Recollections of Early Radio Days," QST, 31-35, 90.

Ratcliffe, J.A., September 1974, "Scientists' reactions to Marconi's transatlantic radio experiment, Proc. of IEE, 121, 1033-1038.

"Wireless Telegraphy," Fessenden's Patent Application 706,737 filed 29 May 1901

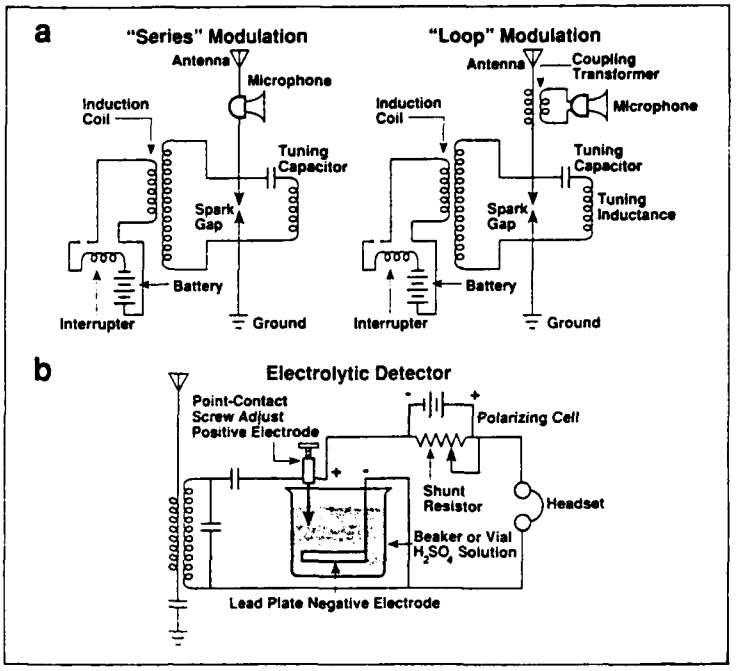

Fig. 1 Prof. Fessenden's spark gap transmitter and receiver for wireless telephony, used to transmit voice without wires in December 1900 [after Geddes, 1989].

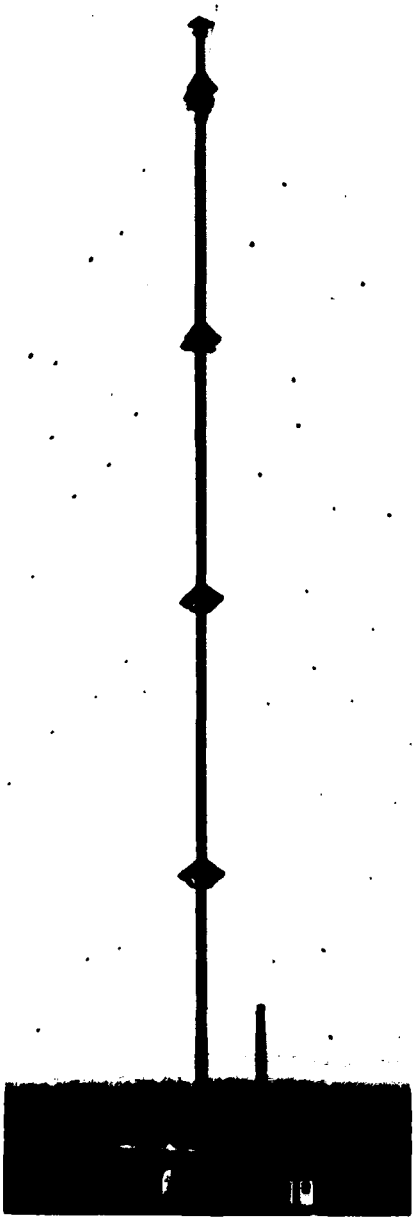

Fig. 3 Umbrella top loaded antenna at Brant Rock, MA, 1905.

Fig. 2 Fessenden's rotary spark gap transmitter.

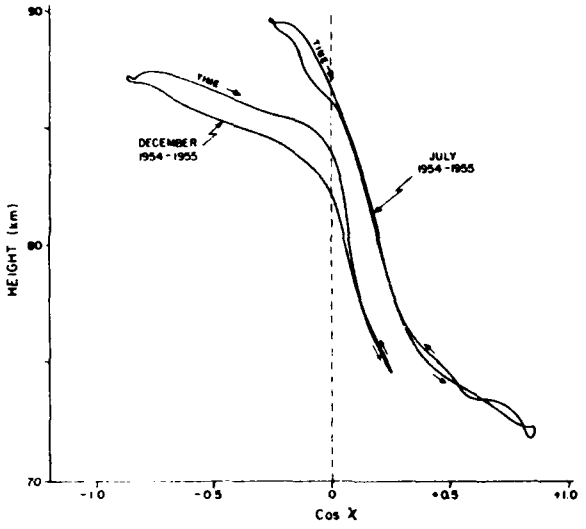

Fig. 4 Diurnal variation of VLF (16 kHz) phase height of reflection for the Rugby-Cambridge transmission path in December and July 1954-55 (sunspot minimum years) [after Belrose, 1981a].

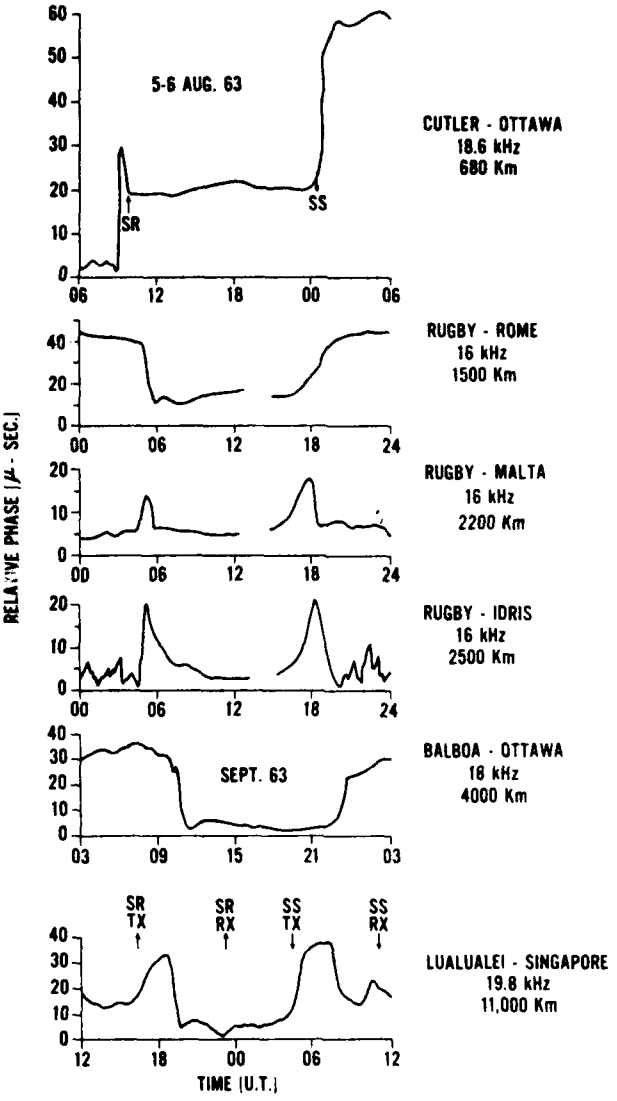

Fig. 5 Diurnal variation in the phase of VLF waves observed at various places for paths of different length [after Belrose, 1968].

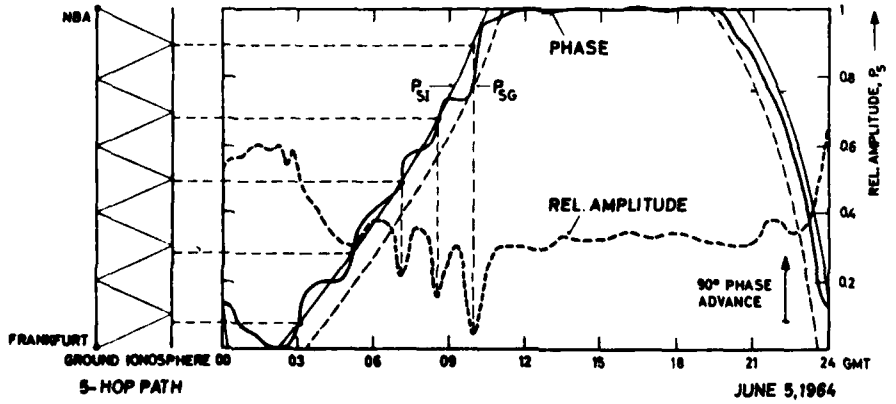

Fig. 6 Diurnal variation of the phase of VLF waves observed on a long east-west path, Balboa, CZ to Frankfurt, FRG.

Fig. 7 Map of the Ottawa/Hull/Aylmer, ON/QC. The circle has a radius of 4-km centered on the author house.

Fig. 8 Field strength contours (dB μV/m) for 1 kW radiated power, for a hypothetical transmitter located in central Canada. Frequency 24 kHz, for summer day.

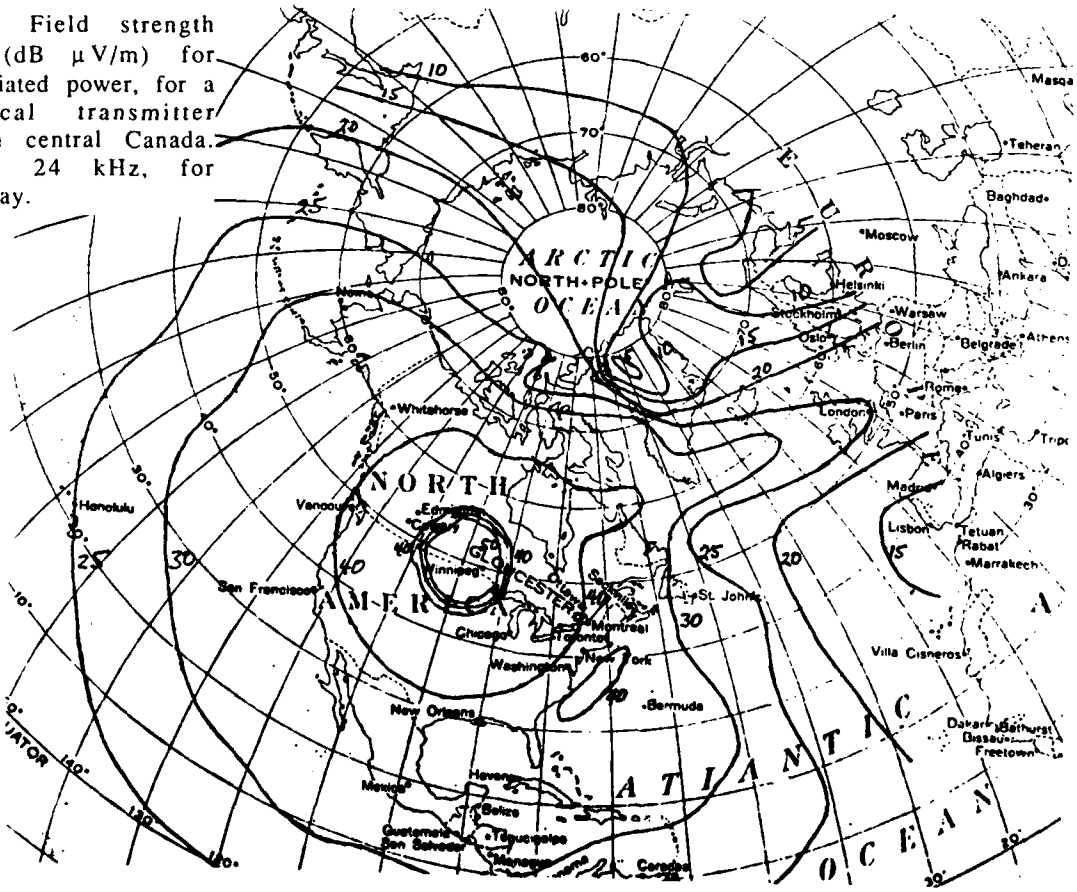

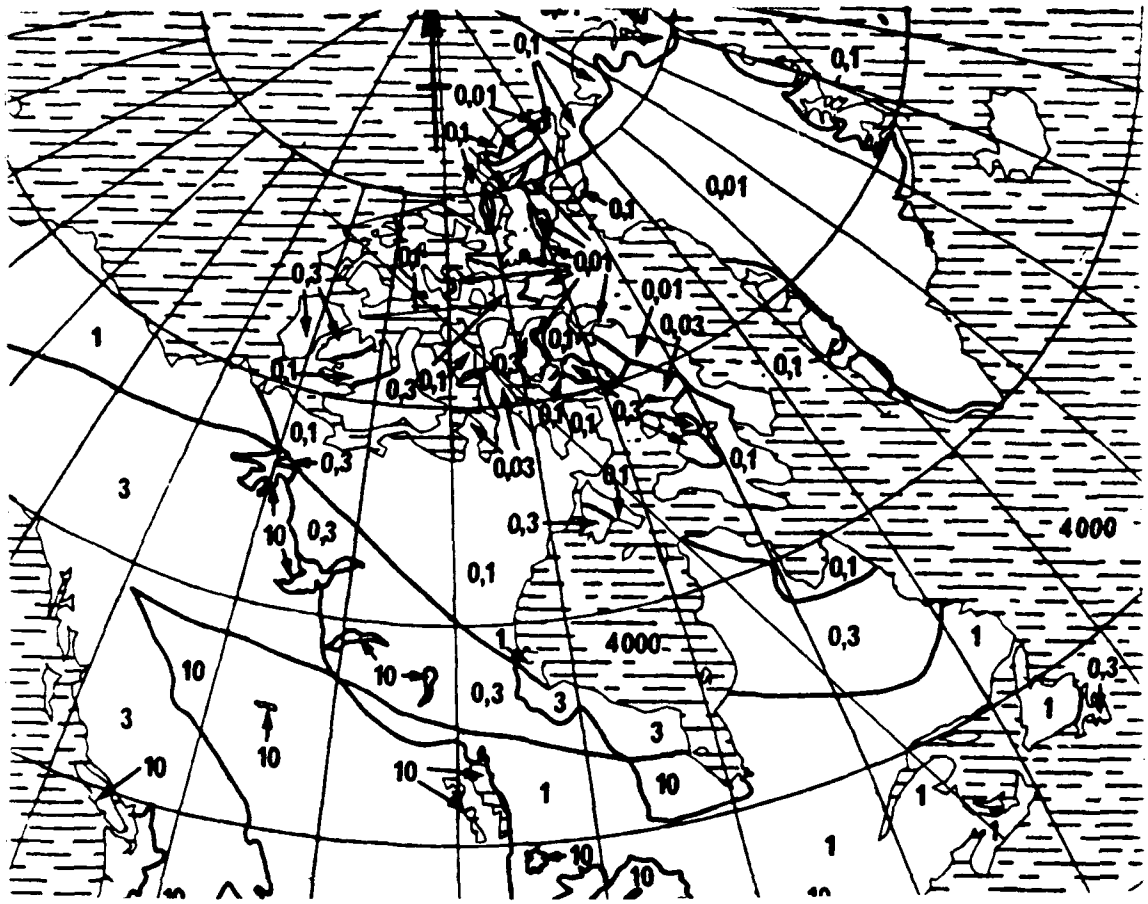

Fig. 9 VLF ground conductivity map for Canada and the Arctic (milli S/m).

Fig. 10 Field strength contours (dB μV/m) for 1 kW radiated power from a hypothetical transmitter located at Halifax, NS. Frequency 24 kHz, summer day.

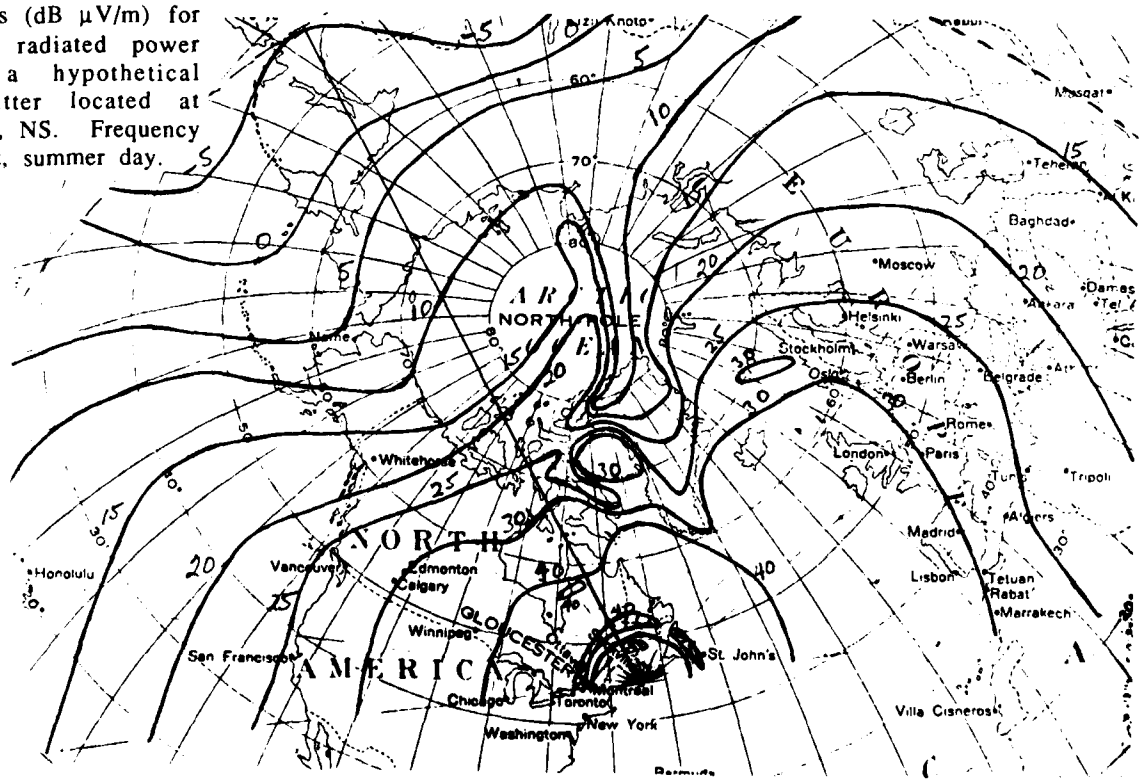

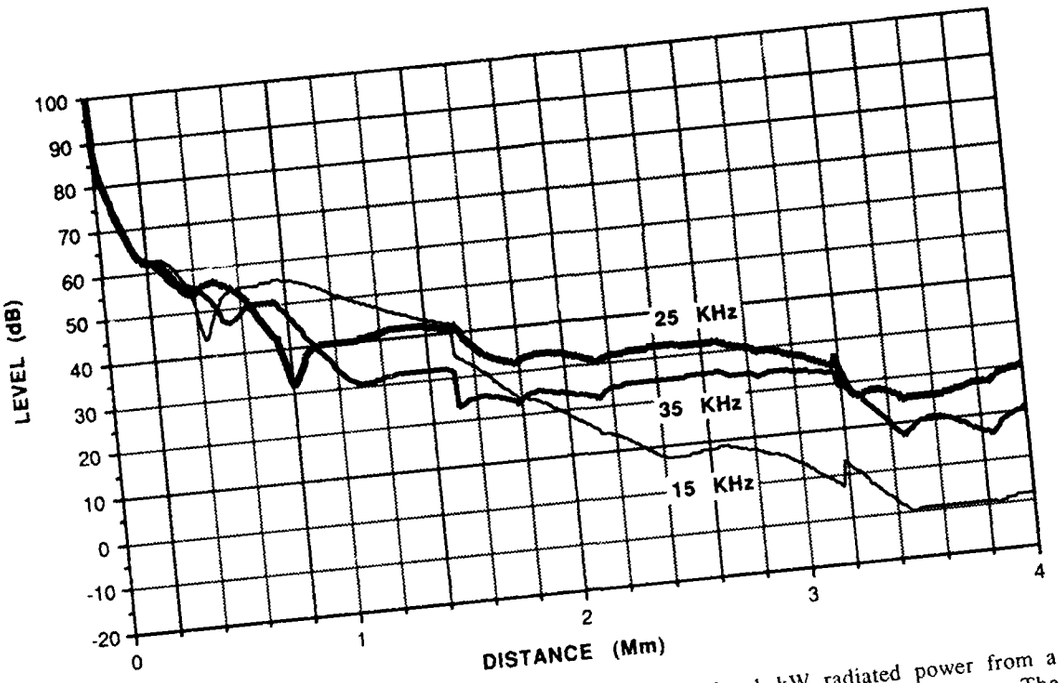

Fig. 11 Field strength vs distance at a bearing of 340° N for 1 kW radiated power from a hypothetical transmitter located at Halifax, for 3 frequencies, for summer day. The transmission path is drawn on Fig. 10.

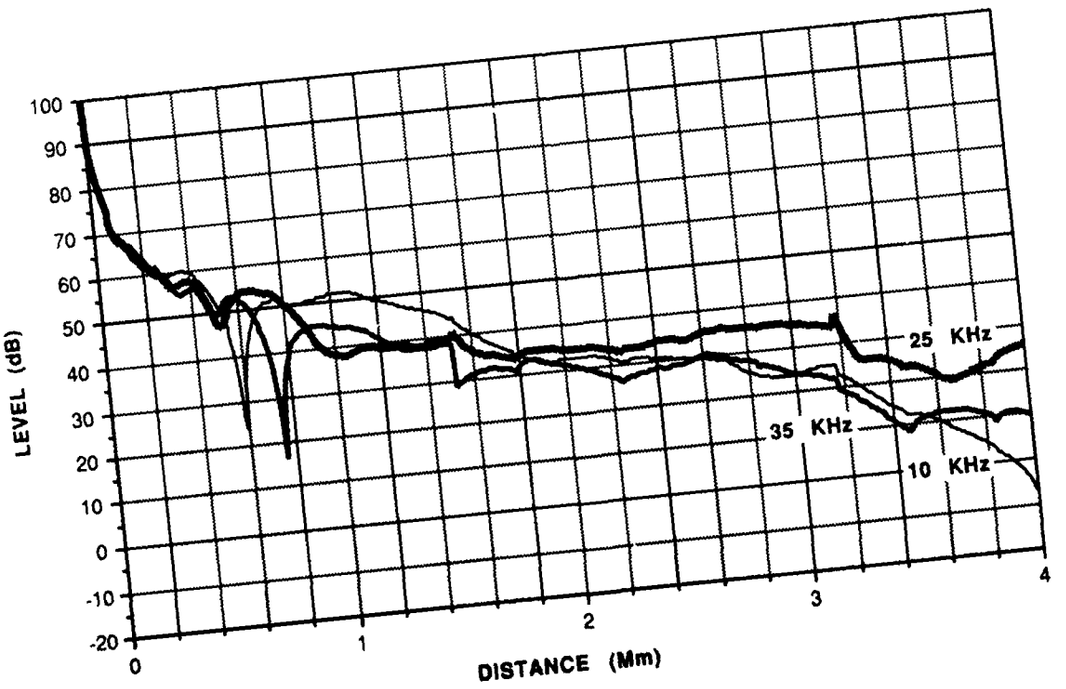

Fig. 12 As for Fig. 11, but for nighttime.

NUMERICAL MODELING OF THE PROPAGATION MEDIUM AT VLF/LF

J. A. Ferguson
Ocean and Atmospheric Sciences Division
Naval Command, Control and Ocean Surveillance Center
Research, Development, Test and Evaluation Division
San Diego, CA 92152-5000, USA

SUMMARY

A reliable knowledge of radio signal amplitude and phase characteristics is required to design and maintain communications and navigational circuits at vlf and lf. The ability to accurately calculate signal levels as a function of frequency, position and time is of considerable importance in achieving reliable assessment of communication and navigation coverage. Detailed computer models based on multiple mode waveguide theory have been developed. These models have been found to produce good comparisons between measurements and calculations of signal variations as a function of propagation distance. However, results can be very sensitive to the ionospheric inputs to these computer models. This paper presents an overview of the computer model and results of empirical modeling of the propagation medium.

INTRODUCTION

The propagation of long wavelength radio waves is of considerable practical importance for communications, navigation systems, and worldwide frequency and time comparisons. The propagation of these signals is characterized by high stability in both phase and amplitude. Little attenuation of the waves occurs so they propagate to great distances. The signals are not greatly affected by most naturally occurring ionospheric disturbances apart from high latitude disturbances, and radio communications can usually be maintained under conditions that make communication very difficult at higher frequencies. Because of these characteristics, vlf and lf systems are prime components in emergency communications networks. Marine communicators are highly dependent upon the vlf radio frequency band for broadcast communications to ships at sea. Other communicators have interests in propagation at frequencies at the lower end of the lf range for transmission between inflight aircraft. These frequencies are used for navigation at the low end of the vlf range (OMEGA) and in the middle of the lf range (LORAN).

The emphasis of this paper is on selection of representative ionospheric conductivity profiles for use in propagation predictions. Morfitt *et al.* (1981) compared measured data with calculations using several different models of the ionosphere. This paper reviews more recent results of similar comparisons. In this endeavor, we prefer data recorded as a function of distance from the transmitter, such as aboard inflight aircraft, because it gives us a number of visual clues to guide our selection of the optimum ionospheric profile. We have recently collected valuable data aboard merchant ships making repeated crossings of the ocean along a number of similar tracks.

Few approaches to find ionospheric profiles are available. The most natural approach is to survey the literature for published profiles of ionospheric density, notably Deeks (1966), Piggott and Thrane (1966), Thomas and Harrison (1970), Bain and Harrison (1972), Bain (1974), Bain (1981), Belrose and Segal (1974), Bjontegaard (1974), Mowforth and Jones (1983), McNamara (1979), Barr (1982), Orlov *et al.* (1983), Campbell *et al.* (1988) and Liande (1988). The profiles presented by these authors derive from a common approach, namely, fitting observations of the signal strength of radio waves to calculations on relatively short propagation paths. In our cases, we use a similar approach using much longer paths. In the approach used in both cases, the ionospheric profile is used to compute signal strength variation as a function of distance from the transmitter and perform some sort of comparison with measurements. The strength of this approach is in the increase in the number of fitting factors, which we will discuss later.

With enough different profiles and signal measurements, regression analysis could be performed in terms of temporal and geophysical variations to determine the required profiles. Unfortunately, the number of propagation paths for which we have many sets of measurements is very low. In addition to this shortcoming in the data base, we have rarely found profiles from short path observations, as are commonly found in the literature, to give us calculations which match the measured long path measurements of signal strength, especially at night. Consequently, we have resorted to using exponential conductivity profiles because these simple two parameter models are easy to modify.

PROPAGATION MODEL

The propagation of long wavelength terrestrial radio waves is conveniently represented in terms of waveguide mode theory (Budden, 1961). The waveguide model developed at the Naval Command, Control and Ocean Surveillance Center (NCCOSC), formerly the Naval Ocean Systems Center (NOSC), is used in the analysis presented in this paper. In general, this model obtains the full wave solution for a waveguide that has arbitrary electron and ion density distributions and collision frequency (with height) and a lower boundary which is a smooth homogeneous earth characterized by an adjustable surface conductivity and dielectric constant. The model allows for earth curvature, ionospheric inhomogeneity, and anisotropy resulting from the earth's magnetic field. It also allows for the calculation of both horizontal and vertical components of the electric field at an arbitrary height in the waveguide. The NCCOSC waveguide model is described in a series of papers by Pappert (1968, 1970, 1981) and Pappert *et al.* (1967, 1970, 1972, 1975).

The simplest form of the waveguide is horizontally homogeneous and is applied to most daytime propagation paths which have unvarying ground conductivity. Generally, the parameters of the waveguide must be varied to realistically describe propagation paths. Obviously, some of these paths cross land-sea and day-night boundaries and, not so obviously, regions through which the geomagnetic field variations are significant (Bickel *et al.*, 1970). The modeling of such paths is accomplished by dividing them into horizontally homogeneous segments. As an example, a land-sea boundary might mark the

end of one segment and the beginning of the next.

The simplest method used for computing fields over these segmented paths is mode conversion (Pappert and Snyder, 1972). The so-called WKB (Wait, 1964) has been used when changes in the modal parameters are sufficiently gradual along the path. This method has been used successfully (Bickel *et al.*, 1970). However, we have found that this method is not as generally useful as the mode conversion model. In this latter model, conversion coefficients from each incoming mode to each out-going mode are calculated at each boundary of the path. The mode conversion model allows for an arbitrary number and order of modes on each side of each segment boundary. Furthermore, the mode conversion model can be applied even in the event that the propagation path has only slowly varying waveguide parameters, in place of the WKB model.

MODELING OF LONG PATH VLF/LF MEASUREMENTS

As stated earlier, we prefer using data collected as a function of distance from the transmitter. Such data provide an indirect but useful description of the ionosphere for propagation prediction. The important ionospheric parameter needed to simulate actual propagation data is the ionospheric conductivity profile through which the radio waves must pass. This parameter is the principal unknown and most variable input to the propagation models and is a function of the height variation of electron and ion density distributions and collision frequencies. The procedure for determining the effective conductivity profile using long path propagation measurements works indirectly by comparison of fields calculated with the waveguide computer program to the measured fields. The ionospheric profile input to the waveguide calculations is varied until acceptable agreement with measurement is reached. In the past, this approach required some sort of systematic trial and error procedure. The degree of fit was generally limited by the cost of computer time.

For propagation during ambient conditions, only the electron density distribution need be considered in calculations. The ion distributions may be neglected. The ionospheric conductivity, ω_r, becomes just a function of the electron density divided by the electron-neutral particle collision frequency. One of the simplest ionospheric profiles is an exponential variation of conductivity with height. It can be specified by only two parameters: a scale height, β, and a reference height, h'. Following Wait and Spies (1964), we write the conductivity at height, h, as

$$\omega_r(h) = 2.5 \times 10^5 \exp(\beta(h-h')).$$

In general, for daytime conditions, we find β in the range 0.3 to 0.5 km^{-1} while h' is in the range 70 to 75 km. For night conditions, we find β in the range 0.3 to 2.0 km^{-1} and h' from 84 to 90 km at middle geomagnetic latitudes. At high geomagnetic latitudes at night, we find that h' tends to be in the range 75 to 80 km. These lower values of h' at high latitudes have also been reported by Egeland and Riedler (1964), Muraoka (1983) and Westerlund and Reder (1973). Furthermore, working with 10 frequency sounder data, we find that β varies with frequency. The exact nature of this variation is not well known due to a wide variation in the measurements from one sampling period to the next (Morfitt, 1977; Ferguson, 1980).

In general, the ionospheric models determined from the above procedure must be considered to represent an averaged ionosphere since the modeling assumes that the ionosphere was static during any aircraft flight period. The data fitting procedure attempts to find a calculated pattern of amplitude as a function of distance which agrees with the large scale pattern of the measured data. Thus, many small amplitude variations are averaged. It is possible that profiles of more complex forms than the exponential could be found to produce a better fit to measured data in some instances, but since the propagation paths considered are quite long, any profile determined to produce a good fit to the data is still an average profile for the total path.

AIRBORNE MEASUREMENTS

Part of the problem in generating ionospheric models is illustrated in Figure 1. These data represent the single most frequently sampled path at one frequency found in our data base: 6 measurements only! The path is from Jim Creek in the northwest corner of the state of Washington towards the east coast; 4 measurements while flying towards Annapolis, Maryland and two while flying towards Cutler, Maine. The data are for nighttime propagation. This plot shows a vertical scale with dB above one microvolt per meter, normalized to one kilowatt of radiated power (dB/1μV/m/kW). The horizontal axis represents distance from the transmitter. If we focus on the location of the deep signal minimum between 2000 and 3000 km, we see 4 cases with the minimum near 2000 km and two with it near 2300 km. Furthermore, we see that this minimum can move 300 km from one night to the next (the middle pair of curves).

To illustrate the observations made earlier, Figure 2 shows one sample of data from Figure 1 together with a calculations using a best fit ionospheric profile. We claim that the data (dashed line) are well fit by the calculations (solid line). This is about as good as we expect to fit any data. However, we note the value of h'. Observe that typical values of h' are expected to be in the range 70 to 75 km in the day and 85 to 90 km at night. Here we have a nighttime measurement giving us an h' of 76 km. Such a low value of h' is consistent with our expectations at high geomagnetic latitudes. In fact, we consider this path to be in what might be called the transition between middle and high latitudes.

Another example of night time complication is illustrated in Figure 3. The data were collected on a flight from Jim Creek to Hawaii. The solid line represents the measurement and the dashed and dotted lines are for two different exponential profiles. Note that neither theoretical curve fits the deep signal minimum near 3000 km. However, we found that satellite data of particle precipitation showed a clear enhancement where the magnetic dip angle was 70° (Larsen *et al.*, 1976). So, just for modeling purposes, we defined an arbitrary boundary several degrees wide and varied h' linearly across that boundary. The result of this spatially varying h' is shown in Figure 4, with some improvement in the degree of fit between the measurements and the calculations. The satellite data suggest a width of 4° to 6°, consistent with our results. Although the fit to the data is not extremely good, it is clear that a spatially varying ionosphere is required for such paths. The missing factor at this time is establishment of the location of the boundary and its variability with solar or geomagnetic activity.

Now, as part of our ongoing validation effort, we have digitized all of our aircraft data and developed procedures for automatically generating comparisons between models and data. During the process of digitizing the data, I reviewed the reports from which the data were taken. Generally, these reports contained comparisons between calculations and measurements and if I liked the fit, I recorded the β and h' reported. For example, I like the fit shown in Figure 3, so an entry was made in my data base for that set of data. One of the reasons for doing this was to help resolve the disparity between daytime models observed by other workers, primarily the split between β equal to 0.5 km^{-1} and 0.3^{-1}. For instance,

Morfitt (1977) suggested β of 0.5 km^{-1} for the Pacific Ocean in the summer but 0.3 km^{-1} at other latitudes and seasons. The results of this analysis are shown in Figure 5. This figure shows β and h' organized according to the date of the aircraft flight. This figure includes all frequencies and paths. Data for a single date are further sorted by frequency, mostly 10 sounder data. The open squares are for β. As expected, h' ranges from 70 to 75 km with the bulk of the data suggesting 73 km. However, there are only 7 cases calling for β of 0.5 km^{-1}. Furthermore, the combination of 0.5 km^{-1} and 70 km occurs only 6 times out of the 24 cases shown. We expect that the day time data should be sensibly organized according to solar zenith angle. Those flights for which we have take off and landing times, we have calculated the midpath solar zenith angle and organized the data accordingly in Figure 6. Sad to say, but we only have 4 samples of data outside the range 42° to 45°. More importantly, the difference between β of 0.5 km^{-1} and 0.3 km^{-1} is not resolved by this comparison. Recent measurements by Bickel (Private communication) still strongly support β of 0.5 km^{-1} for summer conditions at near the equator.

We now consider β and h' organized by date for the night time cases in Figure 7. The two samples of data from the 10 frequency sounder are seen in the middle of the figure and we see the two different ranges of β for those data. Other than that, there is not much to say about this figure. The night time data do not show a pattern when organized this way. However, we might expect the night time data to be organized in some way by the magnetic latitude. Again, for those flights for which we have the necessary information, the corrected geomagnetic latitude of midpath was computed. We see that at least the values of h' show some stability below 40° and much variability above 40°, as expected.

SHIPBOARD MEASUREMENTS

The data from the Callaghan measurements were signal strength as a function of distance from the US transmitters at Annapolis, MD, radiating at 21.4 and 51.6 kHz, at Cutler, ME, radiating at 24 kHz, and the English transmitters at Rugby, radiating at 16 kHz, and at Anthorn, radiating at 16.4 kHz. Data were recorded aboard the Military Sealift Command ship, Callaghan, from March 29, 1985 through April 18, 1986. During this period the ship made 50 crossings of the North Atlantic, each crossing taking about a week. The data recorded during these crossings are unique in the large number of measurements repeated at various distances from the transmitter over a long time, thus permitting examination of the variability of the signal in space and time. The track of the ship varied with the tides and the weather, but a lot of the data were recorded along a corridor from the eastern coast of the United States and from the area around England southwest into the middle of the North Atlantic Ocean. These data were analyzed using a new, computer aided technique which determined the most frequently occurring profile over a distance range from the transmitter to 4000 km from each transmitter (Ferguson, 1992). This technique is summarized below.

The data available from the repeated ship crossings allows us to determine an ionospheric profile which fits most of the available data and to deduce something of the spatial and temporal variability of the environment. The approach taken here is to fit small segments of the measured signal strength with calculations generated from a number of profiles from a predetermined set. We accumulate the number of occurrences in which calculations from each profile matches the data. We then plot contours of occurrence in the β-h' plane to pick the most commonly occurring profile. The application of this technique assumes that the ionosphere is homogeneous over the path defined by the transmitter and the segment of data. Furthermore, generation of the model data is simplified by using a single propagation path from each transmitter. Furthermore, since the data were collected during a period of low solar activity, we ignored the possible effects of the polar cap. Daytime propagation is taken to occur when the solar zenith angle at both the transmitter and the ship is less than 90°. For daytime propagation conditions, we set up a 9 x 9 matrix of profiles with β ranging from 0.2 to 0.4 km^{-1} (increment of 0.025 km^{-1}) and h' ranging from 72 to 80 km (increment of 1 km). Similarly, we define all nighttime propagation when the solar zenith angle at both the transmitter and the ship is greater than 99°. For nighttime propagation conditions, we set up another matrix of profiles with β ranging from 0.3 to 0.7 km^{-1} (increment of 0.05 km^{-1}) and h' ranging from 82 to 90 km (increment of 1 km). Calculations of signal strength along the fixed propagation path were made for each of the 81 profiles in each of the matrices.

Figure 9 shows measurements of signal strength recorded during a single crossing of the Atlantic Ocean when the path from the transmitter to the ship was all daylight. The vertical scale is dB above 1 μVm^{-1} and the horizontal scale is kilometers. This figure illustrates the first step in the process of profile selection. A single curve of calculated signal strength, using a β of 0.3 km^{-1} and an h' of 74 km, is shown with the segments of data. In this figure we see the expected general pattern of signal strength minima and maxima as a function of distance. The average of the absolute value of the difference between the measured and calculated signal strength over each segment is found. If this average is less than 3 dB, then a counter for the profile is incremented by 1. In this figure, the calculations for the sample profile fit the segments of data at 1800, 4200 and 5000 km so the counter for this profile would be incremented by 3. We have tried different values of the measure of fit and found 3 dB to give the most unambiguous results.

After all data segments have been compared to calculations for all profiles in the matrix, we make a plot of contours of equal occurrence in the β-h' plane using the accumulated counts. The combination of β and h' which occur most often is selected from the maximum in the contour plot. The contour plot for the daytime data at 21.4 kHz is shown in Figure 10. This figure shows the best fit profile is for β equal to 0.284 km^{-1} and h' equal to 74.25 km.

Figure 11 shows a plot of all of the daytime portions of data collected over the entire measurement period. It can be seen that the best fit profile gives calculations which run through the middle of the measurements while basically ignoring very low and very high values. The analysis technique gives us the most frequently occurring horizontally homogeneous profile. However, it is clearly evident that the calculations using the resultant profile do not fit every sample of data. In fact, an otherwise unbiased observer might just as reasonably chose the upper envelope. Indeed, a modified criterion for incrementing the profile counter based on fit to the data should give a different best fit profile. In any case, the procedure is automatic and objective. We also note that this sort of data collection shows the inherent day to day variation of the signal strength far better than the small sampling seen in Figure 1. Such data also help us with the engineering questions concerning reliability and time availability.

Figure 12 shows a summary of the values of β and h' obtained with the above analysis for both day and night propagation. In each panel, the solid straight line represents parameter variations suggested by Morfitt (1977) and Ferguson (1981). In the daytime, β shows 3 of the 5 values along the dashed line which crosses β = 0.3 km^{-1} at 10 kHz and 0.26

km^{-1} at 60 kHz. The values at 16 and 19 kHz are below and above this line, respectively. The results for h' are less scattered with 4 of the 5 values close to 73.5 km. The variation of β at night show some scatter about the linear fit but the values of h' are quite close to the linear fit. It is speculated that part of the difference between the parameter variations shown in the solid versus the dashed lines will be found to be in the difference in solar activity during the data collection periods.

CONCLUSION

Propagation of VLF is sensitive to the D region of the ionosphere. Many of us have taken advantage of this sensitivity to infer information about the ionosphere using VLF measurements. Much of the earlier work was based on short paths, hence, steep incidence. The profiles of electron density variation with altitude which were derived in this early work depended a great deal on preconcieved notions of the structure of the ionosphere. Morfitt *et al.* (1981) has shown that these structured ionospheric models do not reproduce long path measurements. Our work has consistently relied on simple exponential models of ionospheric conductivity which have been very successful in reproducing long path measurements, i.e., Bickel *et al.* (1970), Morfitt (1977) and Ferguson (1981). Recent collections of data provide even more detailed insight into the variation of signal strength and, consequently, into ionospheric variability. Evolving automation of the propagation calculations makes analysis of these data more straightforward. More complicated analyses of these data are limited only by the available computer time.

REFERENCES

Bain, W. C. (1974), The use of vlf propagation results in ionospheric modelling, in ELF-VLF Radio wave Propagation, J.A. Holtet (Ed.), 151-163, D. Reidel Publishing Co., Dordrecht, Holland.

Bain, W. C. (1981), Models of the ionospheric D region at noon, IEE Conf. Proc. 169, 203-206.

Bain, W. C. and Harrison, M. D. (1972), Model ionosphere for D-region at summer noon during sunspot maximum, Proc. IEEE, *119*, 790-796.

Barr, R. (1982), The nocturnal D-region as seen by VLF radio waves, J. Atmos. Terr. Phys., *44*, 407-413.

Belrose, J. S. and Segal, B. (1974), On interpretation of CW propagation data for long radio waves, in Methods of Measurements and Results of Lower Ionosphere Structure, Akademic-Verlag, Berlin.

Bickel, J. E., Ferguson, J. A. and Stanley, G. V. (1970), Experimental observations of magnetic field effects on VLF propagation at night, Radio Sci., *5*, 19-25.

Bjetegaard, G. (1974), Deductions of daytime electron density profiles from VLF measurements over a middle latitude path during quiet conditions, J. Atmos. Terr, Phys., *36*, 693-698.

Budden, K. G. (1961), The waveguide-mode theory of wave propagation, Prentice Hall.

Campbell, P. H. M., Jones, T. B., and Burgess, B. (1988), Experimental studies of daytime LF radio propagation and their implications for D-region electron densities, J. Atmos. Terr. Phys., *50*, 725-737.

Deeks, D. G. (1966), D-region electron density distributions in middle latitudes deduced from the reflection of long radio waves, Proc. Roy. Soc. A 2, *91*, 413-437.

Egeland, A., and Riedler, W. (1964), Long-term variation of ionospheric reflection heights for v.l.f. radio waves, J. Atmos. Terr. Phys., *26*, 351-365.

Ferguson, J. A. (1980), Ionospheric profiles for predicting nighttime vlf/lf propagation, Naval Ocean Systems Center Technical Report 530, NTIS, ADA 085399.

Ferguson, J. A. (1992), A technique for determining operationally useful models of the ionospheric conductivity at very low frequencies, Submitted to Radio Sci.

Larsen, T. R., Reagan, J. B., Imhof, W. L., Montbriand, L. E. and Belrose, J.S. (1976), A coordinated study of energetic electron precipitation and D-region electron concentrations over Ottawa during disturbed conditions, J. Geophys. Res., *81*, 2200-2211.

Liande, P. (1988), Propagation path of low-frequency sky-wave signals, Scientia Sinica (Series A), *31*, 987-995.

McNamara, L. F. (1979), Statistical model at the D-region, Radio Sci., *14*, 1165-1173.

Morfitt, D. G. (1977), Effective electron density distributions describing vlf/lf propagation data, Naval Ocean Systems Center Technical Report 141, NTIS, ADA 047508.

Morfitt, D. G., Ferguson, J. A., and Snyder, F. P. (1981), Numerical modeling of the propagation medium at ELF, VLF, LF, AGARD CP-305.

Mowforth, K. E., and Jones, T. B. (1983), The determination of the propagation characteristics of very low frequency radio waves, IEE Conf. Proc. 219, 199-203, 199-203.

Muraoka, Y. (1985), The D-region winter anomaly and dynamical effects of atmospheric planetary-scale waves, J. Geomag. Geoelect., *37*, 509-530.

Orlov, A. B., Azarnin, G. V., and Ivanov, V. I. (1983), A model of the midday lower ionosphere for the prediction of VLF fields at solar minimum, Geomag. and Aeron., *23*, 626-630.

Pappert, R. A. (1968), A numerical study of vlf mode structure and polarization below and anisotropic ionosphere. Radio Sci., *3* (New Series), 219-233.

Pappert, R. A. (1970), Effects of Elevation and Ground Conductivity on Horizontal Dipole Excitation of the Earth-Ionosphere Waveguide, Radio Sci., *5*, 579-590.

Pappert, R. A. and Bickel, J. E. (1970), Vertical and Horizontal VLF Fields Excited by Dipoles of Arbitrary Orientation and Elevation, Radio Sci., *5*, 1445-1452.

Pappert, R. A., Gossard, E. E. and Rothmuller, I. J. (1967), A Numerical Investigation of Classical Approximations Used in VLF Propagation, Radio Sci., *2*, 387-400, Apr 1967.

Pappert, R. A. and Morfitt, D. G. (1975), Theoretical and experimental sunrise mode conversion results at vlf, Radio Sci., *10*, 537-546.

Pappert, R. A. and Snyder, F. P. (1972), Some results of a mode-conversion program for vlf, Radio Sci., *7*, 913-923.

Piggott, W. R., and Thrane, E. V. (1966), The electron densities

in the E- and D-regions above Kjeller, J. Atmos. Terr. Phys., *28*, 467-479.

Thomas, L. and Harrison, M.D. (1970), The electron density distributions in the D-region during the night and presunrise period, J. Atmos. and Terr. Phys., *32*, 1-4.

Wait, J. R. (1964), Two dimensional treatment of mode theory of the propagation of vlf radio waves, Radio Sci., *68D*, 81-93.

Wait, J. R. and Spies, K. P. (1964), Characteristics of the earth-ionosphere waveguide for vlf radiowaves, NBS Technical Note 300.

Westerlund, S. and Reder, F. H. (1973), Vlf radio signals propagating over the Greenland ice-sheet, J. Atmos. Terr. Phys., *35*, 1475-1491.

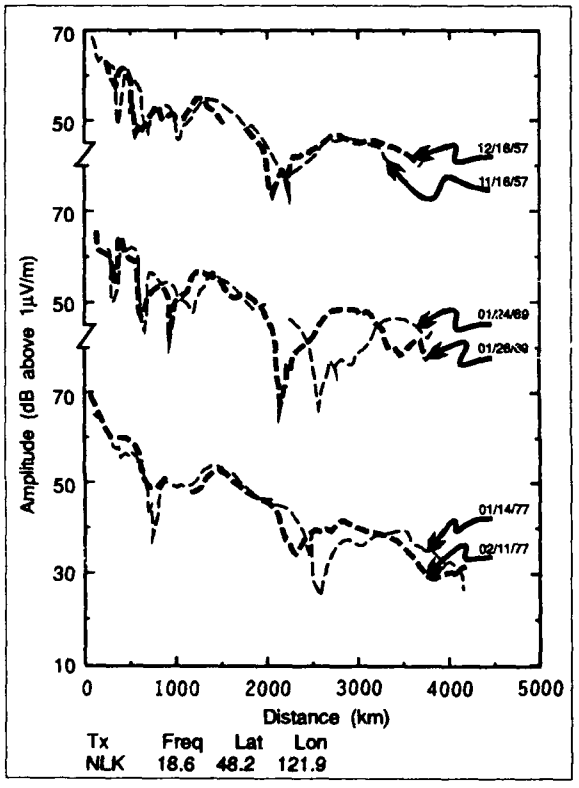

Figure 1: Jim Creek towards the east; night.

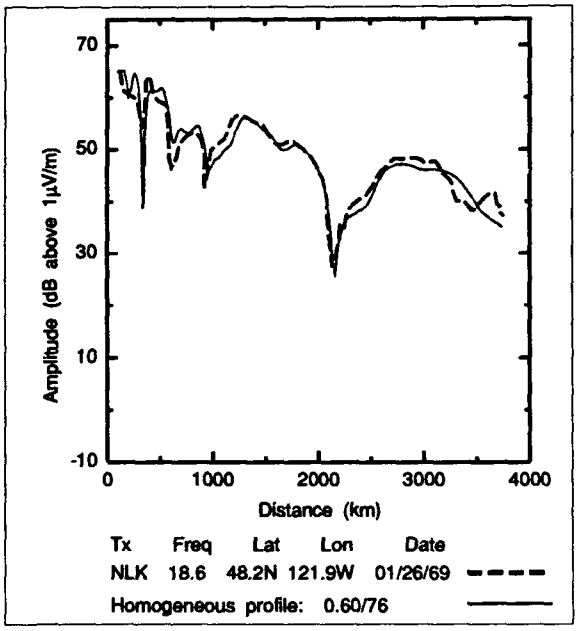

Figure 2: Jim Creek to Annapolis; h' = 76 km.

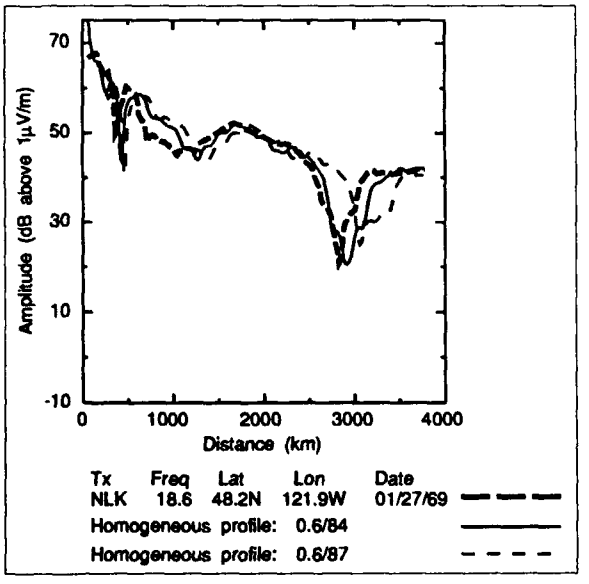

Figure 3: Jim Creek to Hawaii; homogeneous h'.

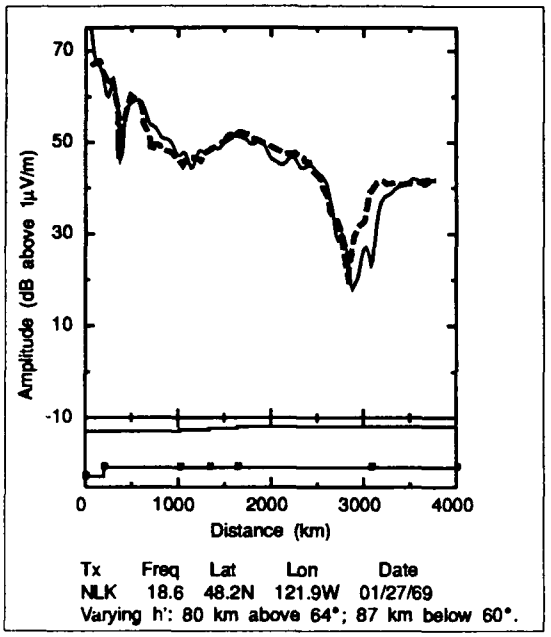

Figure 4: Jim Creek to Hawaii; h' varies with dip.

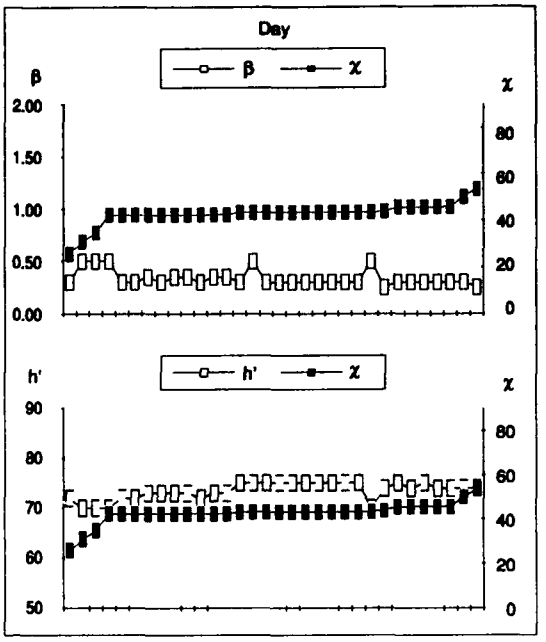

Figure 6: β and h' vs. solar zenith angle; day.

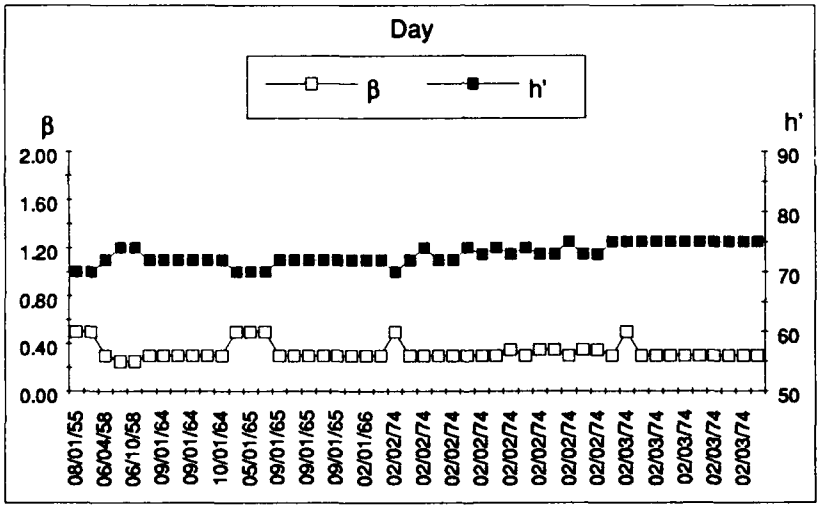

Figure 5: β and h' vs. date; day.

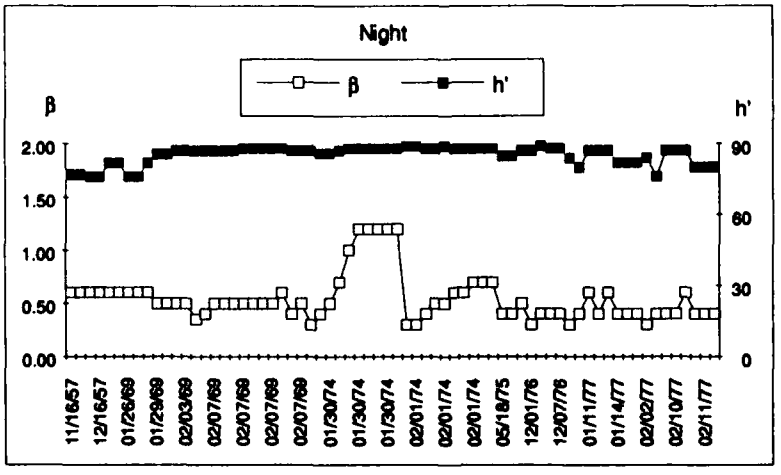

Figure 7: β and h' vs. date; night.

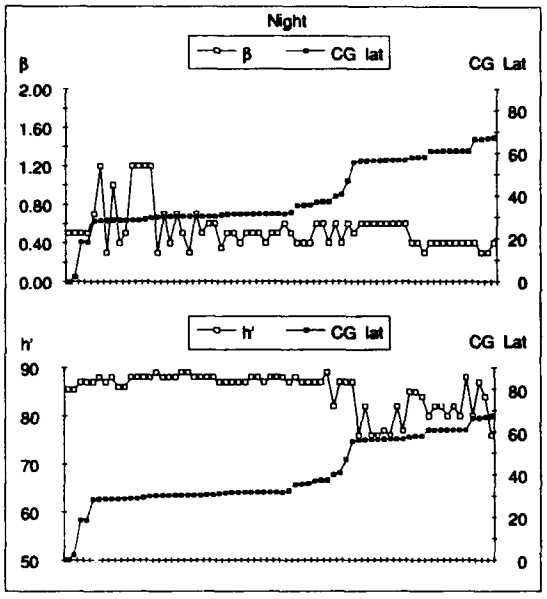

Figure 8: β and h' vs. corrected geomagnetic latitude; night.

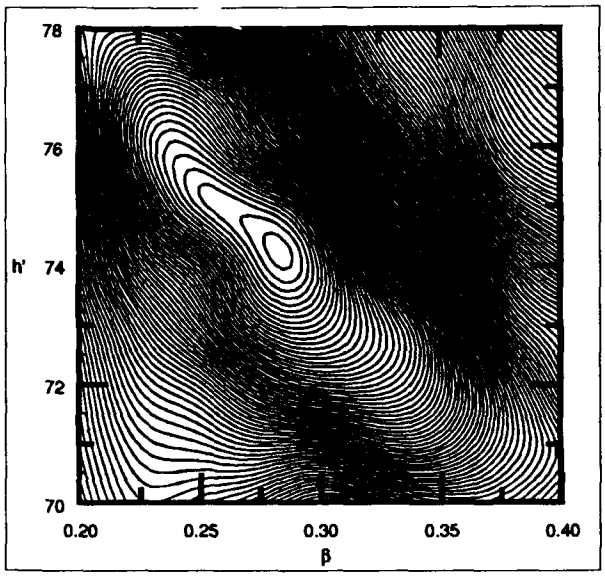

Figure 10: Contour plot of profile matches.

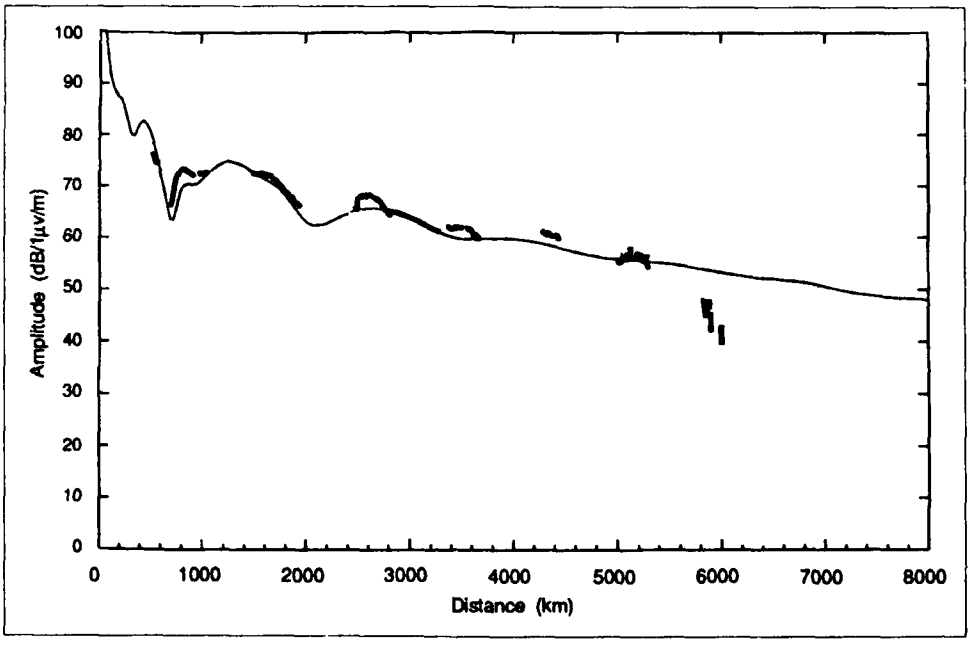

Figure 9: A single trip of the Callaghan; daytime data only.

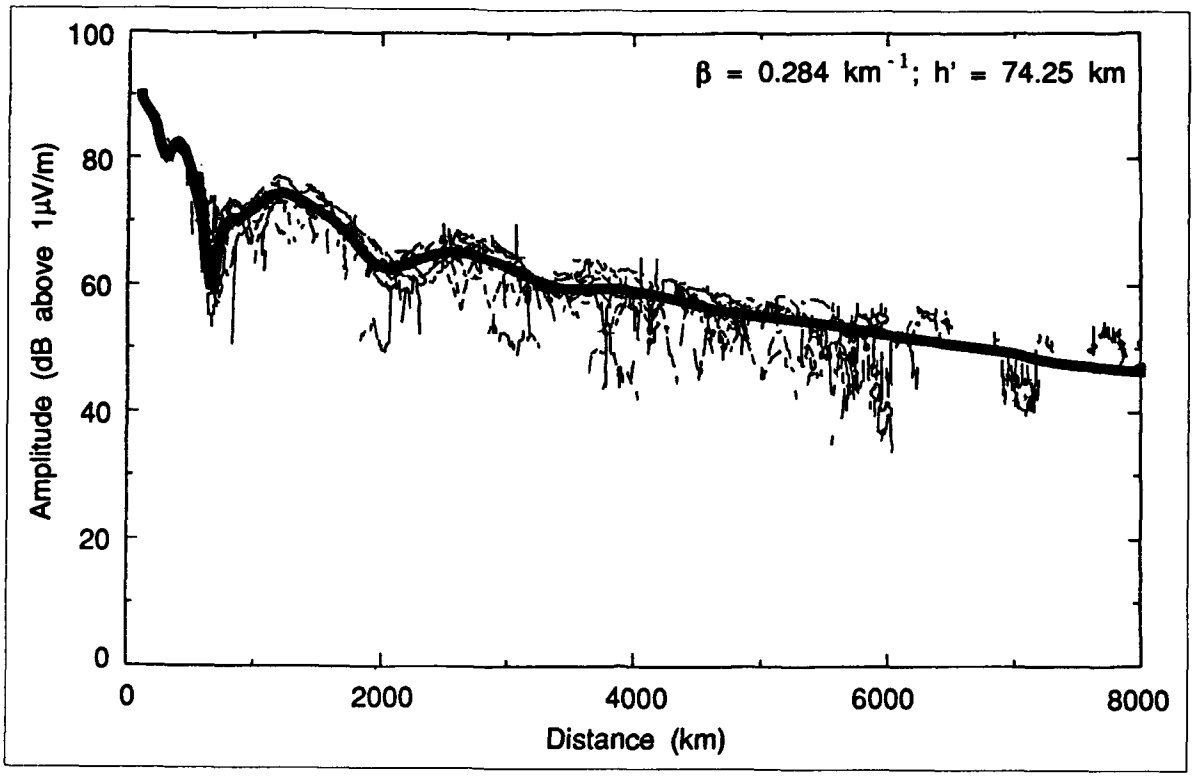

Figure 11: All day data with best fit profile.

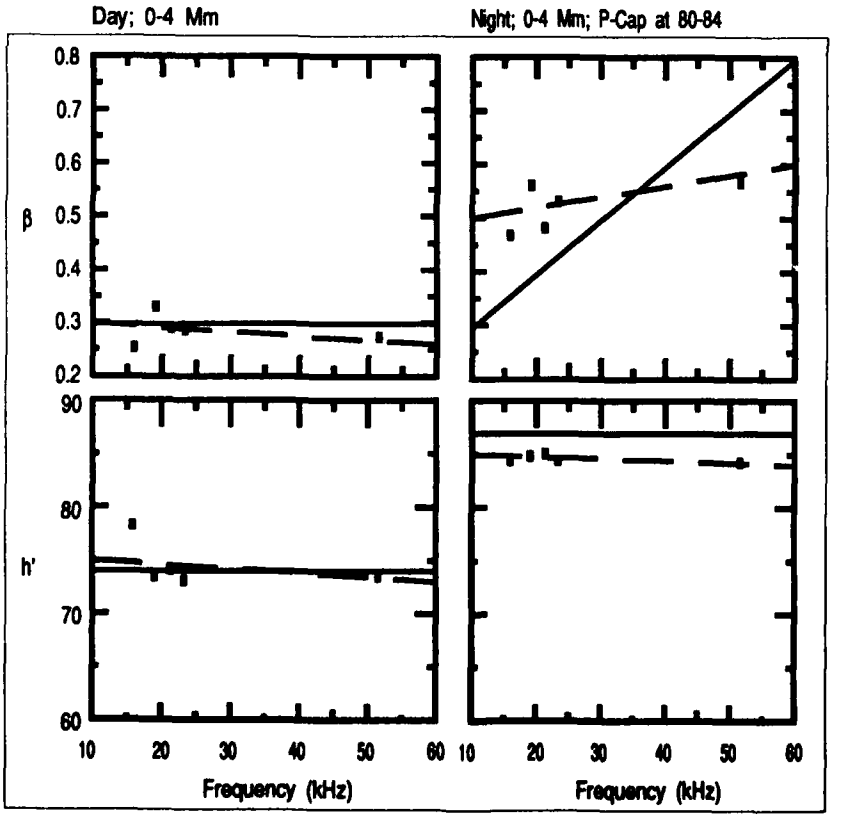

Figure 12: β and h' vs. frequency from contour analysis.

Discussion

U.S. INAN (US)

Your exponential profiles have very low electron densities at low altitudes, say below about 40-50 km. Have you done any modeling with profiles that are described by three parameters, maybe having two different slopes (b) above and below 40-50 km? Are your results sensitive to ionization (or lack of it) at these altitudes?

AUTHOR'S REPLY

We have not made detailed analyses of such perturbations to the exponential model. My intuition tells me that such a modification would provide a means for adjusting the attenuation rate without modifying the excitation factor. However, such an analysis would presume strict homogeneity along the measurement path.

ELF PROPAGATION HIGHLIGHTS

PETER R. BANNISTER
U.S. NAVAL UNDERSEA WARFARE CENTER
NEW LONDON, CT 06320 USA

INTRODUCTION

Elf electromagnetic waves (30-300 Hz) have a remarkable ability to propagate with very little attenuation in the earth-ionosphere waveguide. The resulting fields are also able to propagate to moderately great depths in the ocean in spite of the higher conductivity of the sea water. After considering the costs and benefits of various systems for communications with its submarines, the US Navy made the positive decision to build an operational long range ELF communication system using a single dual sight ground based transmitter. The ELF system became operational in late 1989.

One of the reasons that the US Navy chose this submarine communication system over the alternatives is that, for the most part, the overall variation of the ELF system sizing parameters (propagation, earth conductivity, antenna steering, receiver performance, and atmospheric noise at sea) is small and predictable. Furthermore, the ELF system is relatively inexpensive, and it can provide continuous year round operation.

The general nature of ELF propagation in the earth-ionosphere waveguide has been the subject of theoretical and experimental study for many years and is, apparently, well understood. The texts by Wait (1970), Galejs (1972), and Burrows (1978) describe the theory in the form accepted today and provide a bibliography of earlier work. Reference may also be made to Special Issues of the IEEE transactions edited by Wait (1974) and Burrows (1984), review papers by Bernstein et al. (1974) and Wait (1977), and a collection of papers by Bannister (1987) and Bannister, et al. (1980, 1987). Since nearly ten years have elapsed since the last special issue devoted to ELF communications, this paper will summarize recent events. Particular attention will be paid to ELF propagation highlights.

FIELD STRENGTH CALCULATIONS

At ELF, the effective waveguide height h is of the order of 45 to 90 km. Because h is much less than a free-space wavelength λ, the waveguide is below cutoff for all but the lowest order mode (i.e., the TEM mode). The electric and magnetic fields are wholly transverse to the direction of propagation, with the electric field vertical and uniform and the magnetic field horizontal and uniform. In practice, inhomogeneities and nonuniform surface conditions perturb the ideal TEM field configuration and the result is the quasi-TEM mode.

Attenuation in the earth-ionosphere waveguide at ELF for the quasi-TEM mode is low, on the order of 1 to 5 dB/Mm. The effective conductivity of the ionosphere (10^{-5} - 10^{-7} S/m) is usually much lower than that of the ground 10^{-4} -5 S/m), and so the surface impedance of the ground (n_g) is typically much smaller than the surface impedance of the ionosphere. Thus the attenuation in the guide is attributable mainly to power absorption by the ionosphere. The expressions most often employed for calculating the fields in the earth-ionosphere waveguide are based upon a simple theoretical model that assumes the earth and ionosphere to be sharply bounded and homogeneous. But the ionosphere is neither homogeneous nor sharply bounded. Therefore, a question arises concerning the usefulness of a simple model.

It is necessary to know whether there are simple curves showing the variation with frequency of parameters equivalent to those of the h, S, and n_g parameters of the simple theory, that can be used to calculate the fields with sufficient accuracy for communication system design. (The real part of S is c/v, the ratio of the speed of light in free space to the wave speed in the guide. The imaginary part is proportional to the attenuation rate in the guide.) The real ionosphere may be essentially different in its properties from a well behaved, sharply bounded model. In fact, theoretical calculations using certain layered ionospheric structures have produced propagation data exhibiting resonant absorption and strong dispersion (Galejs, 1972, pp. 254ff; Barr, 1974; Pappert and Moler, 1978; Pappert, 1980; Pappert and Shockey, 1978). On the other hand, experimental measurements of the properties of the guide have consistently shown them to be, on the average, relatively stable and predictable and, in particular, to be accurately represented by the simple formulas (Burrows, 1978).

The experimental corroboration of the simple formulas does not, of course, mean that the ionosphere is actually sharply bounded and homogeneous; direct measurements of its conductivity profile show that it is not. Rather, the corroboration supports the view that, over the frequency range of interest, simple curves

exist of parameters equivalent to h, n_g, and S that can be used in the formulas to obtain accurate field estimates.

The next question to be asked about the simple theory is whether the parameters (e.g., the effective ionospheric height and propagation constant it requires as input) can be readily obtained. It seems likely, based on the theoretical work of Jones (1967, 1970); Greifinger and Greifinger (1978, 1979); Bannister (1979, 1985); Booker (1980); Behroozi-Toosi and Booker (1980), and the experimental propagation measurements of Ginsberg, (1974) ; Bannister, (1974, 1975, 1987); Bannister et al. (1980, 1987); White and Willim (1974) that they could be calculated accurately if enough ionospheric data were available. However, the calculation would not be wholly convincing without periodic experimental verification. The experimental verification in itself is a measurement of the parameters, and so establishes their magnitudes and behavior in time and space directly. Then the interpretation in terms of ionospheric physics is superfluous, apart from the reassurance that it can give that the measurements are consistent with other data (Burrows, 1978).

The substantial body of propagation data now available from measurements of sferics (the propagating electromagnetic pulse originating from a lighting stroke), from Schumann resonances and measurements of signals radiated from man-made sources presents a coherent quantitative description of propagation parameters. Thus, estimates of numerical values to be used for the parameters can be obtained from existing data.

Instead of the parameters h, n_g, and S appearing in the theoretical propagation model, it is convenient to measure a composite of the three called the excitation factor, E, defined by

$$E = \left| \frac{\eta_g}{h\sqrt{\omega\mu_0 S}} \right| \qquad (1)$$

and also the modified form of S, which is the attenuation factor as defined by

$$\alpha = 0.0290\ \omega\ |\ Im\ \{S\}\ | \qquad (2)$$

giving the attenuation in dB/Mm. (It should be noted that the E defined here is not the same as the excitation factor Λ_n used by Wait (1970) and Galejs (1972) for a different purpose.) The utility of these two factors is demonstrated by substituting them in asymptotic form for the horizontal electric current source. Thus,

$$|(H_\phi)_d| \sim I\,dl\,E \left[\frac{k_o}{2\eta_0}\left(\frac{\omega\mu_0}{2\pi}\right)^{1/2}\right]\left(\frac{\rho/a}{\sin\theta}\right)^{1/2} \cdot \frac{10^{-\alpha\rho/2 \times 10^3}}{(k_0\rho)^{1/2}} \cos\phi \qquad (3)$$

There are essentially six distinct factors in this propagation formula. The first is the source strength I dl. The second is E. The third is a collection of free-space parameters, all of which are determined exactly once the frequency is specified. The fourth is the spherical focusing factor. The fifth is the radial propagation loss factor, including both the exponential decay due to absorption and the $\rho^{-1/2}$ decay due to spreading. The sixth defines the directional dependence of the radiated field. Once the current moment I dl, frequency ω, and coordinates ρ, ϕ of the field point are specified, only two parameters are left undetermined, *i.e.*, E and α. Thus, when these two are evaluated, the field calculation can proceed (Burrows, 1978).

IONOSPHERIC CONDUCTIVITY PROFILE PARAMETERS

Greifinger (1978, 1979), Booker (1980) and Behroozi-Toosi and Booker (1980) have derived simple-form approximate expressions for the TEM eigenvalues (propagation constants) for ELF propagation in the earth-ionosphere waveguide. They demonstrated that eigenvalues obtained by their methods were in excellent agreement with full-wave numerically calculated eigenvalues. The Greifinger's showed that the propagation constant depends on four parameters, two altitudes and a scale height associated with each. The lower altitude is the height at which the conduction current parallel to the magnetic field becomes equal to the displacement current. The associated scale height is the local scale height of the parallel conductivity. Under daytime ionospheric conditions, the upper altitude is the height at which the local wave number becomes equal to the reciprocal of the local scale height of the refractive index. Under the simplest nighttime conditions, the second set of parameters is replaced by the altitude of the E-region bottom

and the local wave number just inside the E-region. The relative phase velocity depends, in first approximation, only on the ratio of the two altitudes. The attenuation rate depends on the other two parameters, as well. The two principal attenuation mechanisms are Joule-heating by longitudinal currents in the vicinity of the lower altitude and energy leakage of the whistler component of the ELF wave at the upper altitude.

In a lesser known publication, the Greifingers (1979b) have extended the results presented in their earlier two papers to a more general class of ionospheric conductivity profiles. Their expressions allow the rapid computation of ELF phase speeds, attenuation rates, and excitation factors for a wide range of ionospheric conditions without the necessity of lengthy fullwave computer calculations. The results can be applied to the rapid evaluation of the effects of a variety of ionospheric disturbances, both natural and artificial, on ELF communication systems.

Booker (1980) has combined the reflection theory of Booker and Lefeuvre (1977) with the Greifingers treatment (1978, 1979) of the effect of ionization below the level of reflection. The theory allows for the influence of the earth's magnetic field, reflection from the gradient on the under side of the D region (or, at night, or a ledge below the E region), reflection from the gradient on the underside of the E region, and reflection from the gradient on the topside of the E region.

For daytime propagation, the Greifingers' expressions for α and c / v are

$$c / v \sim (h_1 / h_0)^{1/2} \qquad (4)$$

and

$$\alpha \sim 0.143\, f \frac{c}{v}\left(\frac{\zeta_0}{h_0} + \frac{\zeta_1}{h_1}\right) \sim 0.143\, f \frac{\zeta_0}{h_0}\left[\frac{(c/v)^2 + 1}{c/v}\right] dB / Mm \qquad (5)$$

where h_0 is the altitude where $\sigma = \omega\varepsilon_0$; h_1 is the altitude where $4\omega\mu_0\sigma\zeta_1^2 = 1$; and ζ_0 and ζ_1 are the conductivity scale heights at altitudes h_0 and h_1, respectively.

From (4) and (5) we can see that the phase constant depends primarily on the two reflecting heights and is essentially independent on the conductivity scale heights. On the other hand, for a single scale-height conductivity profile (*i.e*, $\zeta_1 = \zeta_0$), the attenuation rate is directly proportional to scale height.

The single scale-height profile employed by Wait (1970) for determining VLF propagation parameters is

$$\omega_r(z) = \sigma(z) / \varepsilon_0 = 2.5 \times 10^5\, e^{[(z-H)/\zeta_0]} \qquad (6)$$

where H is the (arbitrary) reference height. The altitudes h_0 and h_1 may be determined from

$$h_0 = H - \zeta_0 \ln\left(\frac{2.5 \times 10^5}{2\pi f}\right) \qquad (7)$$

and

$$h_1 = h_0 + 2\zeta_0 \ln\left(\frac{2.39 \times 10^4}{f\zeta_0}\right) \qquad (8)$$

Note that in (6), (7) and (8) all heights and scale heights are in kilometers.

The Greifingers (1979b) have also shown that the effective waveguide height of reflection is roughly h_0 , rather than the higher reflecting height h_1. This is in excellent agreement with the effective reflection heights inferred from the Sanguine/Seafarer propagation measurements. The fact that it is the lower height is not really that surprising since the horizontal rate of energy flow is essentially constant up to an altitude h_0, above which it falls off very rapidly with altitude.

The most common values of H and ζ_0 employed in interpreting VLF daytime propagation measurements are H = 70 km and ζ_0 = 1/0.3 = 3.33 km. By using these values in (4), (5), (7), and (8) we can readily determine h_0, h_1, c/v, and α at ELF. For example, at 75 Hz, h_0 ~ 49.1 km, h_1 ~ 79.5 km, c/v ~ 1.26, and α ~ 1.5 dB/Mm. Furthermore, at 1000 Hz, h_0 ~ 57.7 km, h_1 ~ 70.8 km, c/v ~ 1.10, and α ~ 16.6 dB/Mm.

The theoretically determined values of the ELF daytime attenuation rate are plotted in figure 1 for frequencies of 5 to 2000 Hz. Also plotted, are various experimentally determined values of α. These are all determined from controlled source measurements, except for the 7.8, 14, and 20 Hz attenuation rates, which were inferred from Schumann resonance measurements (Chapman et al., 1966). The 45 and

75 Hz data points are average values determined from the 1970-72 Project Sanguine/Seafarer propagation measurements (Bannister, 1975), the 156 Hz value is from Ginsberg (1974), and the 400 Hz value is from Kuhnle and Smith (1964). The 630-1950 Hz data points were obtained by employing the Navy VLF antenna at Jim Creek, WA, as the source (Ginsberg, 1974). From figure 1 it can be seen that there is excellent agreement throughout the ELF range between the theoretical (employing the Wait exponential ionospheric - conductivity profile) and experimentally determined values of ELF daytime attenuation rates.

The theoretically determined values of the ELF daytime phase velocity are plotted in figure 2 for frequencies of 5 to 1000 Hz. Also plotted are various experimentally determined values of c/v. These values were all determined from measurements of atmospherics. The 7.8, 14, and 20 Hz values were inferred from Schumann resonance measurements (Chapman *et al.*, 1966), the 50-225 Hz values are from Hughes and Gallenberger 1974, and the 300-900 Hz measurements are the two station results of Chapman et al. (1966). From figure 2 we see that there is excellent agreement between the theoretical and experimentally determined values of c/v for frequencies greater than 50 Hz and fair agreement for frequencies less than 50 Hz.

Under nighttime propagation conditions, a sharp E region bottom is usually encountered before the altitude h_1 is established. The electron density undergoes a very sharp increase in passing through the bottom, above which it can be quite variable. The Greifingers' (1979) have considered the simple model where the density above this bottom varies slowly on the scale of the local wavelength. The result is

$$c / v \sim (h_E / h_0)^{1/2} \qquad (9)$$

and

$$\alpha \sim 0.143 f \frac{c}{v} \left(\frac{\zeta_0}{h_0} + \frac{1}{\pi k_0 \eta_E h_E} \right) \qquad (10)$$

where h_E is the altitude of the E region bottom and $k_0 n_E$ is the E region local wave number. Comparison with the daytime results (4) and (5) shows that the altitude of the E region bottom has replaced the frequency-dependent altitude h_1 as a parameter and the local wavelength just inside the E region, has replaced ζ_1.

We have also employed Waits' nighttime ionospheric conductivity model (with a reference height of 90 km and scale height of 1/0.4 = 2.5 km) in conjunction with the Greifingers' nighttime theory. We also assumed the height of the E region bottom was 90 km and its conductivity was approximately 8×10^{-6} S/m. The theoretically determined values of the ELF nighttime attenuation rate are plotted in figure 3 for frequencies of 40-1000 Hz. Also plotted are various experimentally determined values of α. These were all determined from the previously mentioned controlled source measurements. From figure 3 we see that, for frequencies from 45 to 800 Hz, there is excellent agreement between the theoretical and experimentally determined values of the ELF nighttime attenuation rates. Also, the 45-, 75-, and 156-Hz effective waveguide reflection heights (approximately 75 km) are in excellent agreement with those inferred from the Sanguine-Seafarer measurements.

We have also considered the inverse problem (Bannister, 1985). We used experimentally determined values of the ELF effective attenuation rate and excitation factor, along with a modified theory of Greifinger and Greifinger, to establish representative ionospheric conductivity parameters for each propagation path over which ELF measurements were made from 1966 to 1982. Both daytime and nighttime (ambient and disturbed) propagation conditions were considered. The representative ionospheric parameters include the reflection height h_0, scale height ζ_0, and reference height H.

For ambient daytime propagation conditions, the individual path variations in the reflection height h_0, the inverse scale height β (which is equal to $1/\zeta_0$), and the reference height H of the equivalent exponential ionospheric conductivity profile were 43-57 km, 0.24-0.32 km^{-1}, and 67-82 km, respectively.

For ambient nighttime propagation conditions, the individual path variations in h_0, β, and H were 56-91 km, 0.21-0.49 km^{-1}, and 74-107 km, respectively.

We have also established representative ionospheric conductivity parameters for the disturbed propagation period of November/December 1982 (Katan and Bannister, 1987). The largest value of inferred attenuation rate during SPE (solar proton events) disturbed propagation conditions were for the WTF/Gulf of Alaska path (2.51 dB/Mm at night and 2.6 dB/Mm during the day). In fact during the November 23, 1982, minimum nighttime field strength period of 0630-0830 GMT, the apparent attenuation rate for this path exceeded 3 dB/Mm. These attenuation rates are substantially higher than those measured during

ambient propagation conditions on WTF/east-and-northeast paths (~1.0 dB/Mm at night and ~1.25 dB/Mm during the day).

The probable reason for the higher effective attenuation rates observed on the WTF/Gulf of Alaska path is that this path is nearly tangent to the exterior boundary of the disturbed polar cap. That geometry causes lateral refraction of the TEM mode and thus shadow zones (Field and Joiner, 1982; Field *et al.*, 1986).

For ambient nighttime-propagation conditions, the average interpreted values of the reflection height, h_o, the scale height, ζ_0, E layer reflection height, h_E, and the reference height, H, of the equivalent exponential ionospheric-conductivity profile are 77.5, 2.47, 93.0 and 92.8 km, respectively (Bannister, 1985). During SPE disturbed nighttime-propagation conditions, the average inferred attenuation rate and excitation factor were 1.88 dB/Mm and -1.4 dB(0.85). The average interpreted values of h_o, ζ_0, H, and h_E were 59.6, 5.18, 92.0, and 91.0 km, respectively, i.e., the average reflection height was decreased by about 20 km and the scale height was doubled.

For 76 Hz daytime propagation, the representative ionospheric conductivity parameters can be calculated from the inferred values of α and E by employing the following seven-step procedure (Bannister, 1985):

1. Estimate ζ_0 from

$$\zeta_0 \approx 2.25(\alpha / E) \qquad (11)$$

2. Determine χ from

$$\chi \sim \ln(314.5/\zeta_0) \qquad (12)$$

3. Determine c/v from

$$c/v \sim (1 + 0.09\,\alpha\chi)^{1/2} \qquad (13)$$

4. Determine h_o from

$$h_0 \sim \frac{55.90}{E(c/v)^{1/2}} \qquad (14)$$

5. Determine h_1 from

$$h_1 \sim h_0(c/v)^{1/2} \qquad (15)$$

6. Determine ζ_0 from

$$\zeta_0 \sim \frac{9.201 \times 10^{-2}\,\alpha h_0\, c/v}{(c/v)^2 + 1} \qquad (16)$$

7. Determine H from

$$H \sim h_0 + 6.26\,\zeta_0 \qquad (17)$$

The first check on the accuracy of this procedure uses the determined values of ζ_0, h_o, and c/v in

$$\alpha \sim 10.868\,\frac{\zeta_0}{h_0}\left[\frac{(c/v)^2 + 1}{c/v}\right] dB/Mm \qquad (18)$$

This result should yield the starting value of α within 0.01 dB/Mm.

The second check uses the determined values of ζ_0, h_o, and χ in

$$h_1 \sim h_0 + 2\zeta_0\chi \qquad (19)$$

The resulting value for h_1, from (19), should be within 2% of the value obtained from (15).

As an example of the above procedure, consider the March to April 1971 results for the WTF Utah-Hawaii path. For this path, the inferred daytime attenuation rate was 1.50 dB/Mm and the excitation factor was +0.3 dB (1.035) (Bannister, 1975). From (11) -(17), $\zeta_0 \approx 3.25$ km, $\chi \sim 4.57$, c/v ~ 1.27, h_o ~ 47.9 km, h_1 ~ 77.4 km, ζ_0 ~ 3.21 km, $\beta \sim 0.31$ km^{-1}, and H ~ 68.0 km. Using (18) and (19) as checks results in $\alpha \sim 1.50$ dB/Mm and h_1 ~ 77.3 km, which are well within 1% of the determined results. Also note that the initial estimate of ζ_0 is within 1% of the determined value.

RECENT MEASUREMENTS

Many of the earlier controlled source ELF field strength measurements were solely amplitude only measurements (i.e., the relative phase ($\Delta\phi$) between the daytime and nighttime periods was not measured). This oversight has been corrected in recent measurements.

At the present time, the U.S. Navy has land based ELF receiving sites located in New London, CT; Norfolk, VA; Kings Bay, GA; and Pearl City, HI. Their distances from the dual ELF transmitter site (WTF/MTF) are 1.50, 1.54, 1.85, and 6.67 Mm,

respectively. Typical daily plots of signal (both amplitude and relative phase) and atmospheric noise field strengths are presented in figures 4 and 5. If the excitation factor is assumed to be identical at the Hawaii site and one (or all) of the closer in sites, the effective attenuation rate is just equal to the difference of the normalized field strengths divided by their difference in distance from the transmitter. (The normalized field strength is equal to the measured field strength with the spreading loss added and WTF/MTF pattern factors subtracted.) That is,

$$\alpha \sim \frac{\tilde{H}_{\phi 1} - \tilde{H}_{\phi 2}}{\rho_2 - \rho_1} \; dB/Mm \qquad (20)$$

where

$$\tilde{H}_{\phi 1} = 20 \log H_{\phi 1} + 10 \log \left[a \sin \left(\frac{\rho_1}{a} \right) \right] - 20 \log \left[\frac{F(\phi)}{B} \right]_1 \qquad (21)$$

is the normalized field strength at the closer site (located at a distance ρ_1)
and

$$\tilde{H}_{\phi 2} = 20 \log H_{\phi 2} + 10 \log \left[a \sin \left(\frac{\rho_2}{a} \right) \right] - 20 \log \left[\frac{F(\phi)}{B} \right]_2 \qquad (22)$$

is the normalized field strength at the farther site (located at a distance ρ_2). For dual site omnidirectional operation, the pattern factors vary from 7.2 to 7.6 dB for the above mentioned four sites.

When the effective attenuation rate has been determined, the effective excitation factor can be determined by adding a constant (139.1 dB at 76 Hz) and the product of the effective attenuation rate times the measurement distance to the normalized field strength at either site. That is

$$20 \log E = \tilde{H}_{\phi 1} + 139.1 + \alpha \rho_1 \; dB = \tilde{H}_{\phi 2} + 139.1 + \alpha \rho_2 \; dB \qquad (23)$$

For a day, D, to night, N, path change, the corresponding relative-phase change at each received site would be

$$\Delta \phi = \left(\frac{2 \pi \rho}{\lambda} \right) \Delta \left(\frac{c}{v} \right) \qquad (24)$$

where $\Delta(c/v) = (c/v)_D - (c/v)_N$, and λ is the free-space wavelength.

Therefore, from the Hawaii and one (or all) of the closer in sites measured field strengths (both amplitude and relative phase), we can determine the effective daytime and nighttime attenuation rates and excitation factors, as well as the average relative phase velocity difference between daytime and nighttime propagation conditions [$\Delta(c/v)$]. In these interpretations, particular emphasis should be given to the Hawaii relative phase measurements, since a 0.03 change in $\Delta(c/v)$ corresponds to a 18° change in $\Delta\phi$, while the corresponding $\Delta\phi$ change for the closer in sites is only 4° to 5°.

Many years ago (Bannister, 1975), we plotted inferred values of α versus inferred values of E. These 75 Hz values, which are presented in figure 6, were obtained from controlled source propagation measurements taken during 1970 - 72. This procedure, which does not depend upon the selection of a particular ionospheric model, yielded $\alpha \approx 1.4E$ dB/Mm at 75 Hz for both daytime and nighttime 1970 - 72 propagation periods. The fact that α is proportional to E is not really so surprising since, for both isotropic and exponential ionospheric conductivity models, both α and E are inversely proportional to the effective ionospheric reflecting height h_o.

From (1) and (5) for a single scale height exponential ionospheric conductivity profile (for a frequency of 76 Hz):

$$\frac{\alpha}{E} \sim 0.1944 \, \zeta_0 \left(\frac{c}{v} \right)^{1/2} \left[\frac{(c/v)^2 + 1}{c/v} \right] \qquad (25)$$

The average phase velocity ratio inferred from the daytime propagation measurements made during 1970 and 1972 was $c/v \sim 1.25$ (Bannister, 1975). This ratio results in the quantity

$$\left[\frac{(c/v)^2 + 1}{c/v} \right] \approx 2.05 \qquad (26)$$

Note that this estimate is good within 2% when $1.15 \leq c/v \leq 1.35$. For ambient nighttime propagation ($1.05 \leq c/v \leq 1.15$), this quantity ≈ 2.01. With a little bit of hindsight , if we let the relative daytime and

nighttime phase velocity ratios be 1.25 and 1.12, respectively, then

$$\frac{\alpha}{E} \approx 0.445\ \zeta_0 \qquad (27)$$

for daytime propagation conditions and $\approx 0.414\ \zeta_0$ for nighttime propagation conditions. That is, the ratio of α to E is directly proportional to the scale height of the ionospheric conductivity profile. Thus, we can obtain a very good initial estimate of the scale height ζ_0 from the inferred values of α and E. That is,

$$\zeta_0 \approx 2.25(\alpha/E) \qquad (11)$$

for ambient daytime propagation conditions and

$$\zeta_0 \approx 2.41\,(\alpha/E) \qquad (28)$$

for ambient nighttime propagation conditions. Employing (11) and (28) with the average inferred values of α and E obtained from the 1970 - 72 propagation tests results yields $\zeta_0 \approx 3.3$ km ($\beta \approx 0.3$ km^{-1}) for both daytime and nighttime 1970 - 72 propagation periods. Also, $\alpha/E \approx 1.42$ which is almost identical to the experimentally determined results plotted in figure 6.

Presented in tables 1 and 2 are recent 75 Hz band interpretations for ambient daytime and nighttime propagation conditions. The representative daytime ionospheric parameters were obtained from the inferred values of α and E and (11) through (17). The nighttime relative phase velocity ratio $(c/v)_N$ was obtained by subtracting the measured value of $\Delta(c/v)$ from the calculated value (13) of the daytime relative phase velocity ratio $(c/v)_D$. The representative nighttime values of the reflection height, scale height, and reference height were then calculated from (14), (16), and (17), respectively.

Tabulated in the last column in tables 1 and 2 are the scale heights calculated from the approximations (11) and (28). Note that these approximate values of scale height are almost identical to those calculated from the more rigorous formula (16).

Both the daytime and nighttime inferred values of excitation factors and daytime attenuation rates listed in tables 1 and 2 are in good agreement with previous 75 Hz band measurements taken over various propagation paths (see tables 1 and 3 of Bannister (1985)). However, the summertime nighttime attenuation rates are substantially lower (~ 0.6 dB/Mm compared to ~ 1.0 dB/Mm). Also, the summertime daytime attenuation rates (~ 1.25 dB/Mm) are lower than measured during other times of the year (~ 1.50 dB/Mm). This apparent seasonal effect will be investigated further.

DISCUSSION

A convenient quantity to describe the characteristics of the lower ionosphere is the "conductivity parameter" ω_r, which is defined by

$$\omega_r = \omega_0^2/\nu \qquad (29)$$

where ω_0 is the (angular) plasma frequency of the electrons and ν is the effective collision frequency (Wait, 1970). The plasma frequency at a particular height is determined directly by the electron density profile. Experience has shown that simple exponential models of the electron density and collision frequency in the lower ionosphere are adequate to describe ELF/VLF/LF radiowave propagation in most cases. The exponential height profile of the conductivity parameter ω_r successfully employed by Wait and Spies (1964) is

$$\omega_r(z) = 2.5 \times 10^5\ e^{[-\beta(H-z)]} \qquad (30)$$

where β is equal to $1/\zeta_0$ and H is the (arbitrary) reference height.

From tables 1 and 2 we see that, on the average, $\beta \sim 0.30$ km^{-1} and H ~ 75 km for ambient daytime propagation conditions. For ambient nighttime propagation conditions, $\beta \sim 0.36$ km^{-1} and H ~ 95 km.

Figure 7 shows four typical height profiles of the conductivity parameter ω_r. These profiles are representative of (1) ambient daytime (β = 0.30 km^{-1}, H = 75 km), (2) disturbed daytime (β = 0.18 km^{-1}, H = 74 km), (3) ambient nighttime (β = 0.36 km^{-1}, H = 95 km), and (4) disturbed nighttime (β = 0.19 km, H = 92 km) propagation conditions.

Typically, the electron density profile will change from day to day, even during magnetically quiet periods. As a consequence, the profile of the conductivity parameter ω_r will be somewhat variable. Nevertheless, it is not unreasonable to suggest that a suitable analytical model for the lower ionosphere is described by an effective conductivity that varies exponentially with height.

It should also be mentioned that heavy ions will contribute to the effective value of ω_r. In fact, if the frequency of interest is much less than the ion collision frequency, the lower ionosphere may still be represented by an effective conductivity that is numerically equal to $\varepsilon_0\omega_r$ (see chapter VIII of Wait (1970)).

CONCLUSION

In this paper, we have presented a tutorial overview on ELF propagation. We have also compared the Greifingers simple form approximate expressions (which relate ELF propagation constants to realistic ionospheric conductivity profiles) with experimentally derived results for both daytime and nighttime ambient propagation conditions.

The inverse problem has also been considered. We have used the experimentally determined values of effective attenuation rate and excitation factor, along with the modified Greifinger equations, to establish representative ionospheric parameters for each propagation path considered. These parameters include the reflection height h_o, the inverse scale height β (which is equal to $1/\zeta_o$), and the reference height H of the equivalent exponential ionospheric conductivity profile.

We have recently analyzed some of the field strength data taken at the U.S. Navy's four land based ELF monitoring sites (New London, CT; Norfolk, VA; Kings Bay, GA; and Pearl City HI). Both the daytime and nighttime inferred values of excitation factors and daytime attenuation rates are in good agreement with previous 75 Hz band measurements taken over various propagation paths. However, the summertime nighttime attenuation rates are substantially lower (~ 0.6 dB/Mm compared to ~ 1.0 dB/Mm). Also, the summertime daytime attenuation rates (~ 1.25 dB/Mm) are lower than measured during other times of the year (~ 1.50 dB/Mm).

REFERENCES

Bannister, P. R. (1974), "Far-field Extremely Low Frequency (ELF) Propagation Measurements." 1970-72, IEEE Trans. Commun., COM-22(4), 468-474.

Bannister, P. R. (1975), "Variations in Extremely Low Frequency Propagation Parameters, J. Atmos. Terr. Phys.," 37(9), 1203-1210.

Bannister, P. R. (1979), "Some Notes On ELF Earth-ionosphere Waveguide Daytime Propagation Parameters", IEEE Trans. Antennas Propagat., AP-27(5), 696-698.

Bannister, P. R. (1985), "The Determination of Representative Ionospheric Conductivity Parameters for ELF Propagation in the Earth-Ionosphere Waveguide", Radio Sci., 20(4), 977-984.

Bannister, P. R. (1987), "ELF Propagation Measurements and Interpretations," Vol III, NUSC Scientific and Engineering Studies, Naval Underwater Systems Center, New London, CT 06320.

Bannister, P. R., et al (1980, "Extremely Low Frequency (ELF) Propagation," NUSC Scientific and Engineering Studies, Naval Underwater Systems Center, New London, CT 06320.

Bannister, P. R., et al (1987), "ELF System Parameter, Variations," Vol II, NUSC Scientific and Engineering Studies, Naval Underwater Systems Center, New London, CT 06320.

Barr, R. (1974), "The Effect of Sporadic-E on the Nocturnal Propagation of ELF Radio Waves", J. Atmos. Terr. Phys., 39(11/12), 1379-1387.

Behroozi-Toosi, A. B. and H. B. Booker (1980), "Application of a Simplified Theory of ELF Propagation to a Simplified Worldwide Model of the Ionosphere", J. Atmos. Terr. Phys., 42(11/12), 943-974.

Bernstein, S. L., M. L. Burrows, J. E. Evans, A. S. Griffiths, D. A. McNeill, C. W. Neissen, I. Richer, D. P. White and D. K William (1974), "Long Range Communication at Extremely Low Frequencies," Proc. IEEE, 62(3), 292-312.

Booker, H. G. (1980), "A Simplified Theory of ELF Propagation in the Earth-ionosphere Transmission Line, J. Atmos. Terr. Phys.," 42(11/12), 929-941.

Booker, H. G. and F. Lefeuvre (1977), "The Relation Between Ionospheric Profiles and ELF Propagation in the Earth-ionosphere Transmission Line", J. Atmos. Terr. Phys., 39(11/12), 1277-1292.

Burrows, M. L., *ELF Communications Antennas* (1978), Peter Peregrinus Ltd., Stevenage, England, 245 pp.

Chapman, F. W., D. Llanwyn Jones, J. D. W. Todd and R. A. Challinor (1966), "Observations on the Propagation Constant of the Earth-ionosphere Waveguide in the Frequency Band 8 c/s to 16 kc/s", Radio Sci., 1(11), 1273-1282.

Field, E. C. Jr., and R. G. Joiner (1982), "Effects of Lateral Ionospheric Gradients on ELF Propagation", Radio Sci., 17(3), 693-700.

Field, E. C. Jr., C. R. Warber, and R. G. Joiner (1986), "Focusing and Shadowing of ELF Signals", Radio Sci., 21(3), 511-517.

Galejs, J. (1972), *Terrestrial Propagation of Long Electromagnetic Waves*, Pergamon Oxford, 362 pp.

Ginsberg, L. H. (1974), "Extremely Low Frequency (ELF) Propagation Measurements Along a 4900 km Path", IEEE Trans. Commun., COM-22(4), 452-457.

Greifinger, C. and P. Greifinger (1978), "Approximate Method for Determining ELF Eigenvalues in the Earth-ionosphere Waveguide", Radio Sci., 13(5), 831-837.

Greifinger, C. and P. Greifinger (1979a), "On the Ionospheric Parameters Which Govern High-latitude ELF Propagation in the Earth-Ionosphere Waveguide," Radio Sci., 14(5) 889-895.

Greifinger, C. and P. Greifinger (1979b), "Extended *Theory for Approximate* ELF Propagation Constants in the Earth-Ionosphere Waveguide", DNA Report No. 5561T, R&D Associates, Marina del Rey, CA 90291, 1 September.

Hughes, H. G. and R. J. Gallenberger (1974), "Propagation of Extremely Low Frequency (ELF) Atmospherics Over a Mixed Day-Night Path, J. Atmos. Terr. *Phys.", 36(10), 1643-1661.*

Jones, D. L. (1967), "Schumann Resonances and ELF Propagation for Inhomogeneous Isotropic Profiles", J. Atmos. Terr. Phys., 29, 1037-1044.

Jones, D. L. (1970), "Numerical Computations of Terrestrial ELF Electromagnetic Wave Fields in the *Frequency Domain", Radio Sci., 5(5), 803-809.*

Katan, J. R. and P. R. Bannister (1987), "Summary of ELF Propagation Variations at Mid and High Latitudes During the November/December 1982 and February 1984 Solar Proton Events", Radio Sci., 22(1), 111-124.

Kuhnle, P. I. and R. D. Smith (1964), "Experimental Research Investigation of Extremely Low Frequency Propagation", Rome Air Development Center, Rome NY, Rep. RADC-TDR-64-360 (AD609719), December.

Pappert, R. A. (1980), "Effects of a Large Patch of Sporadic-E on Nighttime Propagation at Lower ELF", J. Atmos. Terr. Phys., 42(5), 417-425.

Pappert, R. A. And W. F. Moler (1978), "A Theoretical Study of ELF Normal Mode Reflection and Absorption Produced by Nighttime Ionospheres, J. Atmos. Terr. Phys.", 40(9), 1031-1045.

Pappert, R. A. and L. R. Shockey (1978), "Effects of Strong Local Sporadic-E on ELF Propagation", NOSC TR 282, 15 August.

Wait, J. R. (1970), *Electromagnetic Waves in Stratified Media*, Pergamon, NY, 608 pp.

Wait, J. R. editor (1974), "Special Issue on Extremely Low Frequency (ELF) Communications", IEEE Trans. Commun., COM-22(4).

Wait, J. R. and K. P. Spies, "Characteristics of the Earth-Ionosphere Waveguide for VLF Radio Waves", NBS Tech. Note 300, 1964.

White, D. P. and D. K. Willim (1974), "Propagation Measurements in the Extremely Low Frequency (ELF) Band", IEEE Trans. Commun., COM-22(4), 457-467.

TABLE 1. 75Hz BAND INTERPRETATIONS FOR AMBIENT DAYTIME PROPAGATION CONDITIONS

PATH	DATE	α_D (dB/Mm)	E_D (dB)	α/E	c/v	h_o (km)	ζ_o (km)	β $(km)^{-1}$	H (km)	Approx $\zeta_o=2.25\ (\alpha/E)$ (km)
Alaska-Saipan	5/72	1.60	-0.7	1.73	1.28	53.8	3.84	0.26	77.8	3.89
WTF-E & NE	1977-78	1.25	-1.0	1.40	1.23	56.5	3.18	0.31	76.4	3.15
WTF-N & NW	1977-78	1.50	+0.3	1.45	1.27	47.9	3.21	0.31	68.0	3.26
Conn-Hawaii	6/90	1.31	-1.0	1.47	1.24	56.3	3.32	0.30	77.1	3.31
Conn-Hawaii	7/90	1.31	-0.8	1.44	1.24	55.0	3.24	0.31	75.3	3.24
Kings Bay-Hawaii	7/91	1.25	-0.8	1.37	1.23	55.3	3.11	0.32	74.8	3.08
Conn-K.B.-Hawaii	8/91	1.13	-1.4	1.33	1.215	59.6	3.04	0.33	78.6	2.99
Conn-Hawaii	11/91	1.48	-0.2	1.51	1.265	50.9	3.37	0.30	72.0	3.40
Norfolk-Hawaii	3/92-4/92	1.45	-0.6	1.55	1.26	53.4	3.47	0.29	75.1	3.49
AVERAGE		1.36	-0.7	1.47	1.25	54.3	3.31	0.30	75.0	3.31

TABLE 2. 75Hz BAND INTERPRETATIONS FOR AMBIENT NIGHTTIME PROPAGATION CONDITIONS

PATH	DATE	α_N (dB/Mm)	E_N (dB)	α/E	Meas $\Delta(c/v)$	c/v	h_o (km)	ζ_o (km)	β $(km)^{-1}$	H (km)	Approx. $\zeta_o=2.41(\alpha/E)$ (km)
Alaska-Saipan	5/72	0.8	-4.5	1.34	0.16	1.12	88.6	3.24	0.31	108.9	3.23
WTF-E & NE	1977-78	0.9	-3.8	1.39	O.15	1.08	83.3	3.44	0.29	104.8	3.36
WTF-N & NW	1977-78	0.9	-2.1	1.15	0.13	1.14	66.7	2.74	0.36	83.9	2.76
Conn-Hawaii	6/90	0.54	-4.0	0.86	0.11	1.13	83.3	2.05	0.49	96.1	2.07
Conn-Hawaii	7/90	0.62	-3.6	0.94	0.12	1.12	79.9	2.26	0.44	94.0	2.26
Kings Bay-Hawaii	7/91	0.73	-3.1	1.04	0.09	1.14	74.8	2.49	0.40	90.4	2.51
Conn-K.B.-Hawaii	8/91	0.65	-3.5	0.97	0.115	1.10	79.8	2.37	0.42	94.6	2.35
Conn-Hawaii	11/91	0.89	-2.5	1.19	0.145	1.12	70.4	2.86	0.35	88.3	2.86
Nortolk-Hawaii	3/92-4/92	1.06	-2.5	1.41	0.13	1.13	70.1	3.39	0.29	91.3	3.41
AVERAGE		0.79	-3.2	1.14	0.13	1.12	77.4	2.76	0.36	94.7	2.76

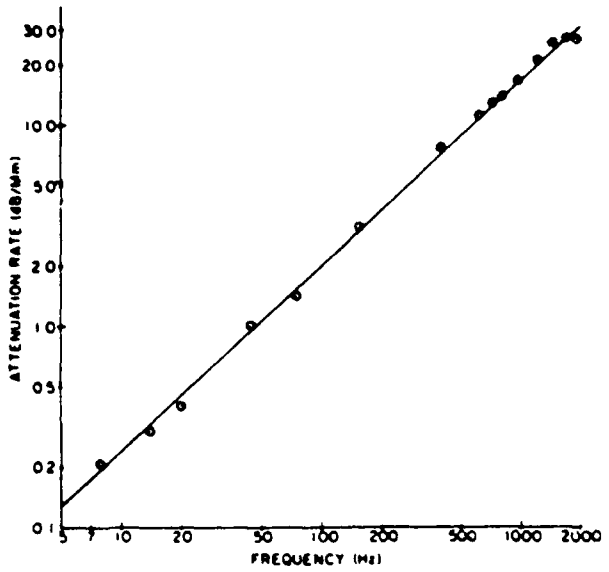

Fig. 1. Comparison of theoretical and experimentally determined ELF daytime attenuation rates. ⊙ Measurements.

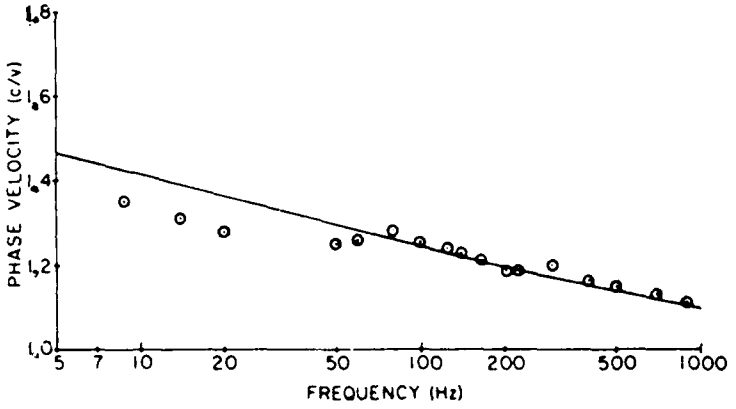

Fig. 2. Comparison of theoretical and experimentally determined ELF daytime phase velocities. ⊙ Measurements.

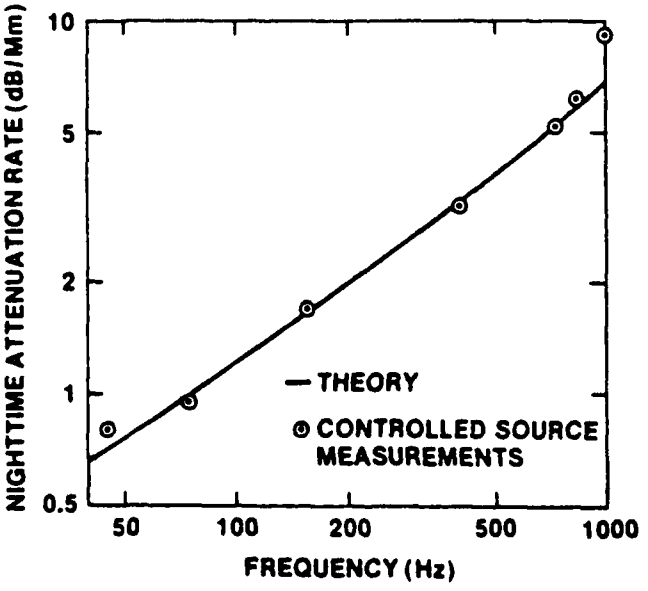

Fig. 3. Comparison of theoretical and experimentally determined ELF nighttime attenuation rates.

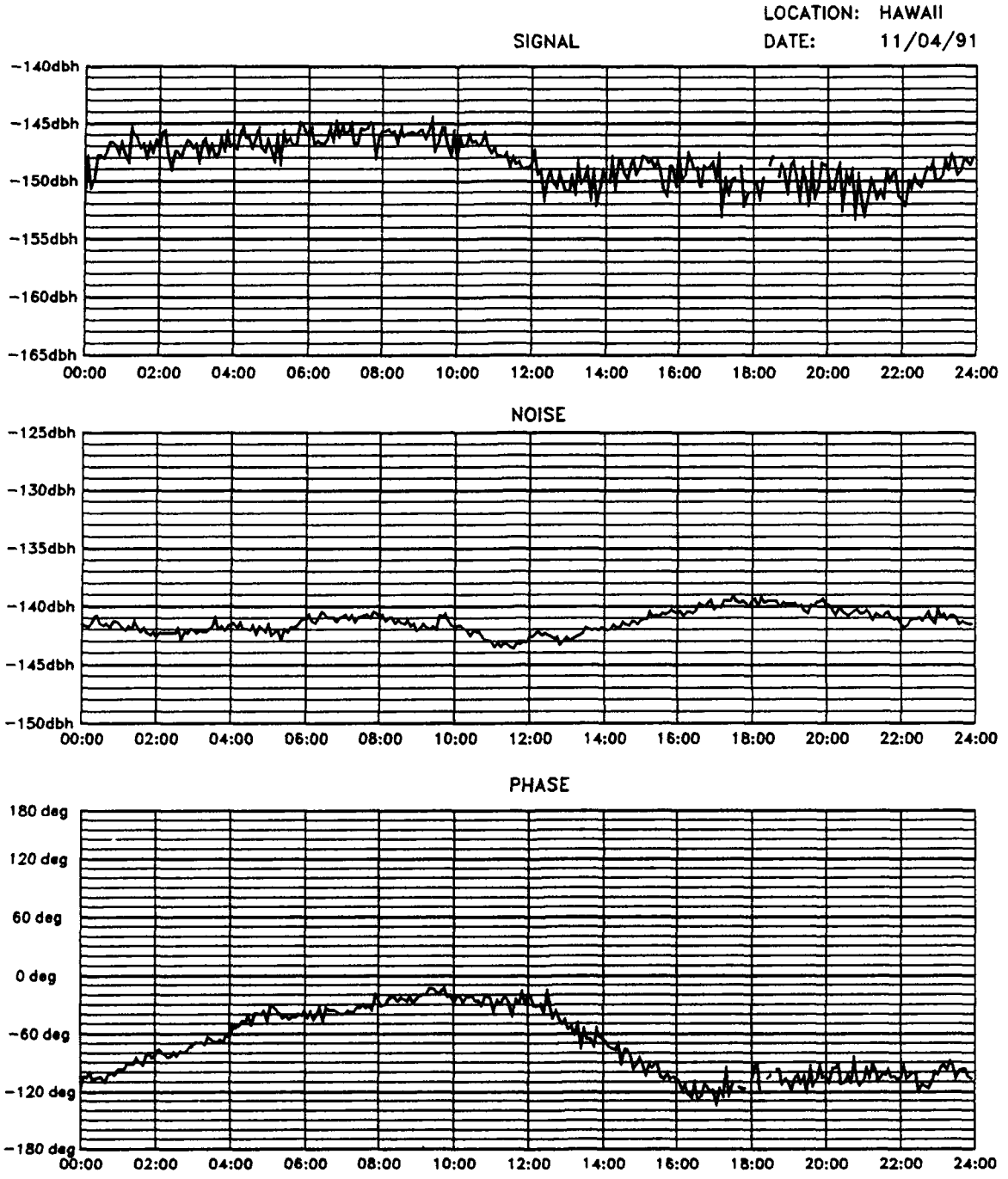

Fig. 4. Typical Hawaii signal and noise data

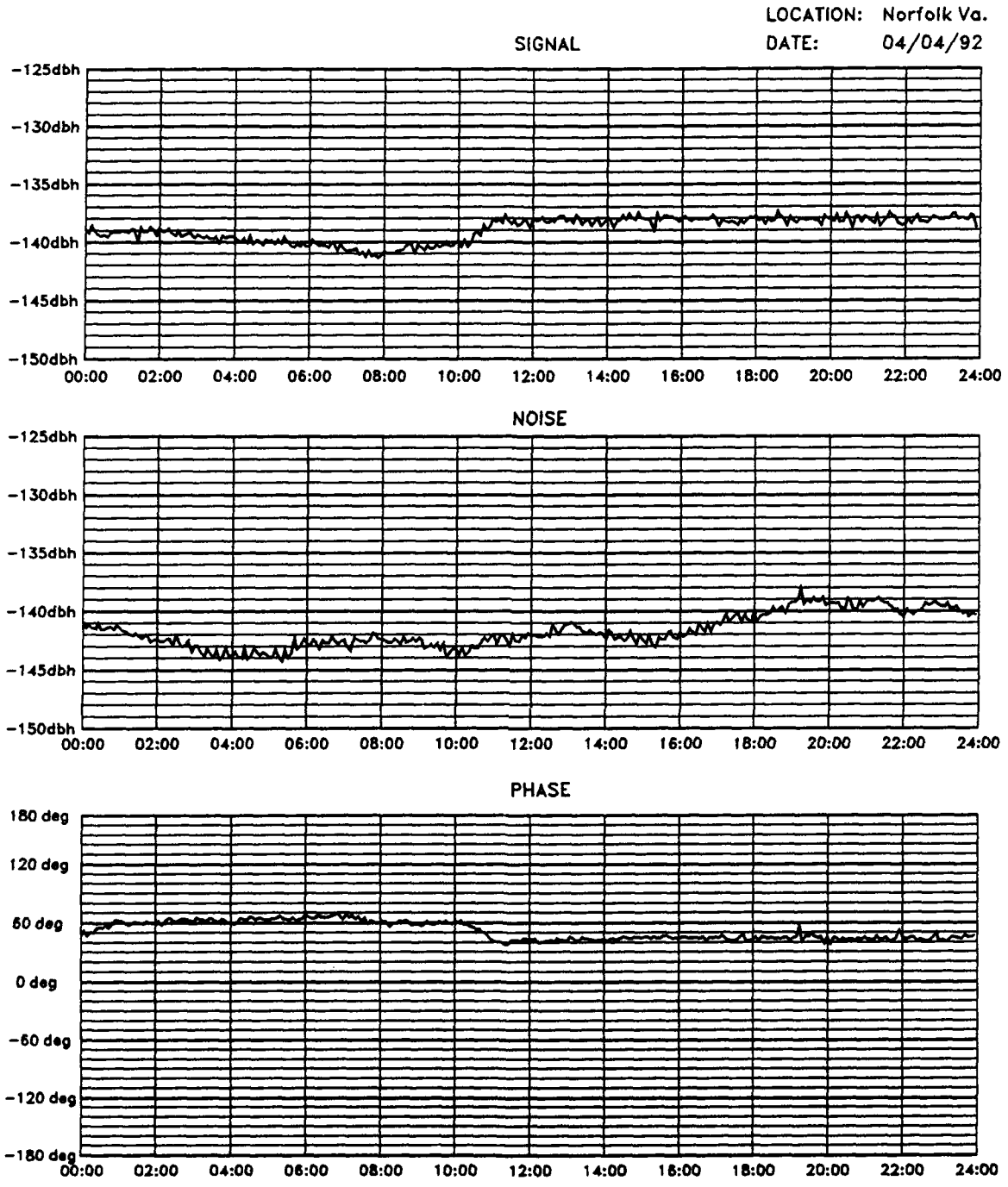

Fig. 5. Typical Norfolk signal and noise data

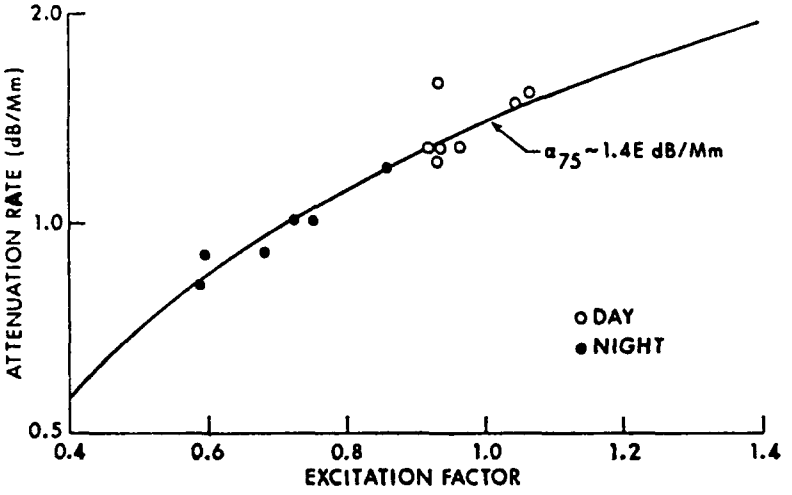

Fig. 6. 75-Hz attenuation rate vs. excitation factor.

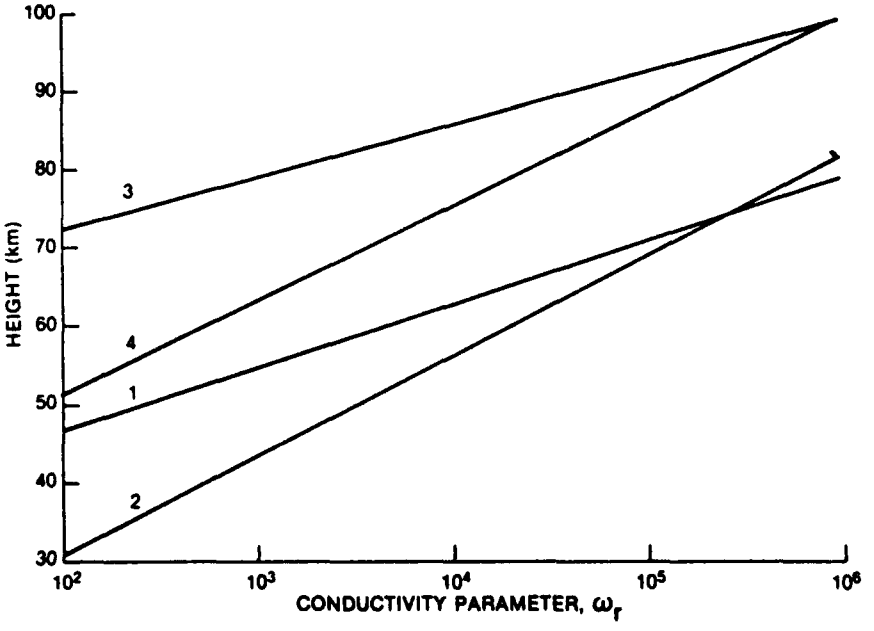

Fig. 7. Conductivity parameter ω_r as a function of height for (1) ambient daytime, (2) disturbed daytime, (3) ambient nighttime, and (4) disturbed nighttime propagation conditions.

Discussion

V. LAMMERS (US)

In view of the high man made interference levels at or near your frequency and the limited ability to discriminate directionally, what bandwidths do you have to employ to communicate successfully?

AUTHOR'S REPLY

The transmitting antenna system bandwidths are of the order of 16 Hz, while the receiving system bandwidths are the order of 1 Hz or less.

P. KOSSEY (US)

In deriving the exponential electron density models from the ELF data, do you include the effects of ions, as well as electrons?

AUTHORS' REPLY

Heavy ions will contribute to the effective value of ω_r. As Jim Wait has pointed out, the lower ionosphere may still be represented by an effective conductivity that is numerically equal to $\varepsilon_o\omega_r$

The Greifingers' have shown that the reflection height at ELF is equal to the height where $\sigma = \omega\varepsilon_o$. Therefore, ELF waves will be reflected from heights where the value of ω_r (ho) is much less than it is at VLF (10^5 to 10^6 radians). In particular the 76 Hz value of ω_r (ho) is approximately equal to 500 radians.

U.S. INAN (US)

I am very pleased to see the good agreement between data and modeling and the fact that ELF modeling is quite insensitive to magnetic field and directional effects, this might mean that ground conductivity models may be improved as a result of such measurements. Would you like to comment on the use of ELF measurements for geophysical prospecting?

AUTHOR'S REPLY

At the present time, the dual site ELF system is operated in an encoded MSK mode; the signals can only be received by the operational ELF receiver. If, at some future time, the system was operated in the CW mode, the signals could be received by a simple ELF receiver (such as modified wave analyzer). In the CW mode, the dual site ELF transmitter could be used as a controlled source for ELF surface impedance measurements - which would make it a very useful geophysical tool.

THE CONE STRUCTURE AND FOCUSING OF THE ELECTRIC FIELD OF VLF AND LF WAVES AT HIGH ALTITUDES OF THE IONOSPHERE

Ya.L. Alpert
Harvard Smithsonian Center for Astrophysics
60 Garden Street
Cambridge, MA 02138, USA

J.L. Green
Goddard Space Flight Center
NASA
Greenbelt, Maryland 20771, USA

SUMMARY

This paper presents a short review of the frequency and angle dependencies of the electric field radiated by an electric dipole $\mathbf{E} = \mathbf{E_0} \cos \omega t$ in a magnetoplasma and detailed results of numerical calculations of $|\mathbf{E}|$ in the **VLF** and **LF** frequency bands $0.02\mathbf{f_b} \leq \mathbf{F} \leq 0.5\mathbf{f_b}$ in the ionosphere and magnetosphere in the altitude region $\mathbf{Z} = (800 - 6000)\ km$ ($\mathbf{F} \sim (4 - 500)\ kHz$ and $\mathbf{f_b} \simeq (1.1$ to $0.2)\ MHz$ is the electron gyro-frequency).

The amplitudes of the electric field have large maxima in four regions: close to the direction of the Earth magnetic field line $\mathbf{B_0}$ (it is the so called Axis field $\mathbf{E_0}$), in the Storey $\mathbf{E_{St}}$, Reversed Storey $\mathbf{E_{RevSt}}$, and Resonance $\mathbf{E_{Res}}$ Cones. The maximal values of $\mathbf{E_0}$, $\mathbf{E_{Res}}$, and $\mathbf{E_{Rev.St}}$ are the most pronounced close to the low hybrid frequency, $\mathbf{F} \sim \mathbf{F_L}$. The flux of the electric field is concentrated in very narrow regions, with the apexes angles of the cones $\Delta\beta \simeq (0.1 - 1)\ degree$. The enhancement and focusing of the electric field increases with altitude starting at $\mathbf{Z} > 800\ km$. At $\mathbf{Z} \geq 1000$ up to $6000\ km$, the relative value of $\mathbf{E}$, in comparison with its value at $\mathbf{Z} = 800\ km$ is about (10^2 to 10^4) times larger. Thus, the flux of **VLF** and **LF** electromagnetic waves in the Earth magnetoplasma produces and is guided by very narrow *pencil beams*, similar, let us say, to laser beams.

1. INTRODUCTION

The linear theory of radiation of an electric dipole in a homogeneous magnetoplasma, used in this study, was developed by Alpert, Alpert & Moiseyev, and by Alpert, Budden et al. (see [1], [2], [3], [4]). The general theoretical results obtained in these papers, the formulae, the computer analysis and the general physical understanding of this problem, are used in this study.

The main features of the electric field studied in [1] to [4] are the following:

a. In the vicinity of the direction of the magnetic field $\mathbf{B_0}$, when the angle between the direction of the group velocity of ELF-LF electromagnetic waves $\beta \to 0$, the amplitude of the electric field $|\mathbf{E}|$ strongly increases. This important characteristic of the field was omitted in the earlier studies of this problem (see [5]).

b. The electric field also increases strongly in the, so called, Storey and Reversed Storey Cones, namely around the angles β_{max} and β_{min} of the maximum and minimum of the $\beta(\Theta)$ dependence (see below Fig.1), where Θ is the angle between the wave vector k and $\mathbf{B_0}$. The enhancement of the field is especially large in the Reversed Storey Cone. This characteristic of the field was also omitted because in the earlier studies, the influence of the ions was not taken into account. Due to the ions, the minimum of $\beta(\Theta)$ and the Reversed Storey Cone are produced.

c. The fourth field growth region is near the resonance frequencies, in the so called Resonance Cones.

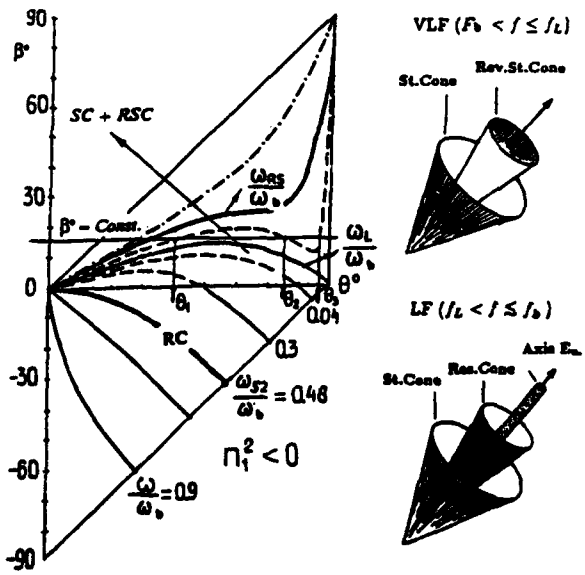

Fig 1. The dependence of the angle β between the group velocity U and the magnetic field $\mathbf{B_0}$ on the angle Θ between the wave number vector k and $\mathbf{B_0}$.

The enhancement of the field is especially large by approaching the low hybrid frequency. In the following parts of the paper, all these characteristics are described in more detail by analyzing results of calculations of the electric field $\mathbf{E}$ at high altitudes of the ionosphere.

2. STATEMENT OF PROBLEM, FORMULAE.

A homogeneous cold magnetoplasma, which is characterized by a superimposed magnetic field $\mathbf{B_0}$, by an electric permitivity tensor ε_0 and a refractive index n is considered. The magnetic field $\mathbf{B_0}$ is parallel to the z axis in the cartesian (x, y, z) and in the cylindrical (ρ, φ, z) coordinate systems. The refractive index is thought as a vector n with components

$$\begin{aligned} n_x &= n\sin\Theta\cos\varphi, \quad n_y = n\sin\Theta\cdot\sin\varphi, \\ n_z &= n\cos\Theta, \quad n_\varphi^2 = (n_x^2 + n_y^2) = n^2\sin^2\Theta, \end{aligned} \tag{1}$$

where Θ is the angle between the wave normal vector $\mathbf{k}$ and the z axis, $\mathbf{z} \parallel \mathbf{B_0}$. The electromagnetic waves $\mathbf{E}, \mathbf{H} \sim e^{i\omega t}$, generated in the magnetoplasma, are produced by an electric dipole of moment $\mathbf{I}e^{i\omega t}$, $\omega = 2\pi F$ or $\omega = 2\pi f$ is the angular frequency of the waves. The electric dipole is parallel to the z axis, i.e. $\mathbf{I} \parallel \mathbf{B_0}$. The source dipole is placed at $x = y = z = 0$. The receiving point is at a distance $r = \sqrt{x^2 + z^2}$ from the source in a direction β to the magnetic field $\mathbf{B_0}$ and

$$x = r\sin\beta, \quad y = 0, \quad z = r\cos\beta \tag{2}$$

since the plasma has rotational symmetry around the z axis.

The general solution of the system of the Maxwell equations of this problem is described by a sum of complicated integrals (see [2], [3]). The integrands of these integrals are rapidly oscillating functions. They are described by the Bessel functions $J_0\left(n_\perp, \frac{\omega}{c}\rho\right)$ and $J_1\left(n_\perp, \frac{\omega}{c}\rho\right)$, and the derivatives $\frac{dn_\parallel}{dn_\perp}$ where

$$n_\perp = n\sin\Theta, \quad n_\parallel = n\cos\Theta, \quad n^2 = n_\perp^2 + n_\parallel^2.$$

These integrals can only be studied by numerical methods. The *method of the steepest descents*, i.e. *the stationary* phase method, was used for this purpose. Certainly, the accuracy of this asymptotic method is sufficiently high only in the far zone from the source, namely, when

$$\frac{\omega}{c}\sqrt{\rho^2 + z^2} = \frac{\omega}{c}r \gg 1. \tag{3}$$

The *main contribution* to the field is made by saddle points. Two cases are considered by analyzing the integrals. Namely these cases characterize the basic physical properties of the field.

The first case is when the observation point is at very small horizontal distances from the source, namely, when $x \sim 0$ (i.e. the angle β of the ray direction is very small). In this region the field is growing larger and *becomes very strong* close to the direction of the magnetic field. This is called the *Axis field* $\mathbf{E_0}$. The saddle points are estimated in this case by the equation

$$\frac{dn_\parallel}{dn_\perp} = 0 \tag{4}$$

The Axis field *enhancement* appears at frequencies $\omega \geq \omega_L$ ($\omega_L = 2\pi F_L$ is the low hybrid frequency). For many decades, it was believed that the field disappears close to the direction of the magnetic field $\mathbf{B_0}$ (see, for example, Arbel and Felson [5]).

The second important case is when $n_\perp\rho \gg 1$ and the observation point is sufficiently far from the axis, from the direction of the magnetic field $\mathbf{B_0}$, and the asymptotic of the Bessel function

$$J_0, J_1 \sim (2\pi n_\perp\rho)^{1/2} exp\left[-i\left(n_\perp\rho - \frac{\pi}{4}\right)\right] \tag{5}$$

may be used. The saddle points are estimated in this region by the equation

$$\cos\beta\frac{dn_\parallel}{dn_\perp} + \sin\beta = 0 \tag{6}$$

The field is enhanced in that region again because of the contributing of two saddle points of the integrands when they are close together - they coalesce. In this case the field is enhanced at different angle intervals β. These field enhancements are the $\mathbf{E_{St}}$ and $\mathbf{E_{Rev.St}}$ and form Storey and Reversed Storey cones. They respectively exist in the frequency bands $F_{RS} \leq F \leq F_{S2}$ and $F_{RS} \leq F \leq F_L$ (see below Fig.1). The field $E_{Rev.St}$ becomes especially strong at frequencies $\omega \leq \omega_L$.

One more region of the enhancement of the field E_{Res} is the *resonance cone*. It occurs when the coefficient of refraction $n \to 0$. At the resonance

$$\Theta - \beta = \pm\frac{\pi}{2}, \quad \tan^2\beta = -\frac{\varepsilon_{xx}}{\varepsilon_{zz}}, \tag{7}$$

where ε_{xx} and ε_{zz} are the elements of the tensor ε_0. In our case, in the cartesian coordinate system

$$\varepsilon_0 = \begin{bmatrix} \varepsilon_{xx} & \varepsilon_{xy} & 0 \\ \varepsilon_{yx} & \varepsilon_{yy} & 0 \\ 0 & 0 & \varepsilon_{zz} \end{bmatrix}, \quad \varepsilon_{xx} = \varepsilon_{yy} \tag{8}$$

The computer analysis and formulae used in the paper cited above by Alpert, Budden, etc. [4] for numerical calculations of the moduli $|\mathbf{E}|$ was developed by K. Budden. The first order descents evaluation of the integrals used by these calculations give the contribution of the saddle points of the Axis and of the both Storey and Reversed Storey cone fields.

The field $\mathbf{E_0}$ is expressed by an algebraic combination of the both Bessel functions $J_0(n_\perp, \rho)$ and $J_1(n_\perp, \rho)$ (see (5)), and also by a combination of the components of the refraction index n and of the elements of the tensor ε_0 of the plasma. The fields $|\mathbf{E_{St}}|$ and $|\mathbf{E_{RevSt}}|$ are expressed by a combination of the Airy integral function $A_i(p)$ and its derivative $A_i'(p)$, and also by n and ε_0. The field in the resonance cone $|\mathbf{E_{Res}}|$ is much simpler and is expressed by an algebraic combination of the elements of the tensor, and of the refraction index n. Certainly, all these formulae depend on the angular frequencies ω and the angle of the ray direction β.

The general formulae of $|\mathbf{E}|$ and the formulae used in the computer analysis are complicated. For orientation, only schematic formulae were given here. They show the distance and angle dependence of the moduli of the field used in this study

$$|\mathbf{E}| = \left(|E_x|^2 + |E_y|^2 + |E_z|^2\right)^{1/2}. \tag{9}$$

These asymptotic formulae are of the following shape:

The Axis field

$$|\mathbf{E_0}| \simeq \left(I\frac{\omega^3}{c^3}\right) n_\rho^2 \left(\frac{2\pi n_z}{\frac{\omega}{c}z}\right)^{1/2} \cdot exp\left[-i\left(\frac{\omega}{c}zn_z \pm \frac{\pi}{4}\right)\right] \times \times F_{Ax}[J_0,\ J_1,\ \mathbf{n},\ \varepsilon_0], \quad (10)$$

where all the values of $F_{Ax}[\ldots]$ depend on ω, β and on the characteristics frequencies of the magnetoplasma.

The field in the two Storey cones

$$|\mathbf{E_{St}}| \simeq \left(I\frac{\omega^3}{c^3}\right) \cdot \frac{\sqrt{\pi} \cdot exp(-i\{\ldots\})}{\left(\frac{\omega}{c}r\right)^{5/6} \cdot (\cos\beta)^{1/3} \cdot (\sin\beta)^{1/2}} \times \times F_{St}\left[A_i(p),\ A_i'(p),\ \mathbf{n},\ \varepsilon_0\right], \quad (11)$$

where all the values of $F_{St}[\ldots]$ depend on ω, β, etc., $A_i(p)$ and $A_i'(p)$ are the Airy function and its derivative,

$$p = \left(\frac{dn_\parallel}{dn_\perp} + \frac{\rho}{z}\right) \cdot \left(\frac{2}{n_\parallel}\right)^{1/2} \cdot \left(\frac{\omega}{c}z\right)^{2/3}, \quad (12)$$

and $F_{St}\{\ldots\}$ is determined by some parameters of the magnetoplasma, by ω and β.

The field in the Resonance cone

$$|\mathbf{E_{Res}}| \simeq \left(I\frac{\omega^3}{c^3}\right) \cdot \frac{n_\rho n_z exp\left[-i\frac{\omega}{c}r(n_\rho \sin\beta + n_z\cos\beta)\right]}{\left(\frac{\omega}{c}r\right)} \times \times F_{Res}[\mathbf{n}(\omega,\beta),\ \varepsilon_0(\omega,\beta),\ \beta]. \quad (13)$$

3. FREQUENCY, ANGLE DEPENDENCIES OF |E|.

The structure of the electromagnetic field in a full ionized and homogeneous magnetoplasma discussed here was initially studied by detailed investigations of the behavior of the direction of the group velocity vector $\mathbf{U} = d\omega/d\mathbf{k}$ in a magnetoplasma. The dependence of the angle β between the vectors $\mathbf{U}$ and $\mathbf{B_0}$, and the angle Θ between the wave vector $\mathbf{k}$ and $\mathbf{B_0}$ reveals the basic features of the field (see [1]).

The vector $\mathbf{U}$ and the Pointing vector $\mathbf{S}$ are collinear in an non-absorbing plasma (see [6]). This theorem is applicable because the collision frequency ν of the ionospheric plasma used in this study is very small (see below). Let us illustrate here the behavior of $\beta(\Theta)$ by the following two figures.

In Fig.1 the dependence of β on Θ is shown. It is determined by

$$\beta = \Theta - \arctan\left(\frac{1}{n}\cdot\frac{\partial n}{\partial\Theta}\right), \quad (14)$$

where $n = n(\Theta,\varepsilon,\omega)$ is the coefficient of refraction of the magnetoplasma. By calculation of $\beta(\Theta)$ given of Fig.1 and of different dependencies of the electric field given in this section, we used the following model of a magnetoplasma, consisting only of one kind of ions (namely protons H^+):

$$f_0 = 3.39\cdot10^6\ Hz,\ f_b = 1.194\cdot10^6\ Hz \quad (15)$$
$$F_L = 2.49\cdot10^4\ Hz,\ \nu_{ei} = 10^2\ sec^{-1}, \frac{m}{M_{H_1}} = 5.44\cdot10^{-4},$$

where f_0 and f_b are the electron Langmuir and gyro- frequencies respectfully ν_{ei} is the electron-ion collision frequency, m and M_{H_1} are the electron and proton masses. This model is close to the parameters of the plasma in the vicinity of the maximum of the ionosphere. This figure and Fig.2, where a schematic frequency dependence of the coefficient of refraction $\mathbf{n}$ is given, demonstrate the distribution of the angles and the characteristic frequencies of the cones formed in a magnetoplasma in the **VLF** and **LF** frequency bands.

The generatrix of the Storey cones, shown in Fig.1 contains the maxima angles β_M of the angle dependencies $\beta(\Theta)$. The maximal value of $\beta_{M,max} = \beta_{St,M}$ corresponds to the upper frequency limit ω_{RS}/ω_b, ($\omega_{RS} = 2\pi F_{RS}$), where the Storey cones and Reversed Storey cones disappear and is determined by the point of inflection of $\beta(\Theta)$. The generatrix of the Reversed Storey cones contains the angles β_m of the minima of $\beta(\Theta)$. The upper frequency limit of $\beta_{m,max} = \beta_{M,max}$ also corresponds to ω_{RS}/ω_b, where both the maxima and minima of $\beta(\Theta)$ approach each other and disappear. The low frequency limits of the Storey and Reversed Storey cones correspond to ω_{S2}/ω_b and ω_L/ω_b ($\omega_{S2} = 2\pi F_{S2}$), where again the maxima and minima of $\beta(\Theta)$ disappear (see Figs. 1 to 3). Thus, the frequency bands of the Storey and Reversed Storey cones respectively are: (ω_{RS} to ω_{S2}) and (ω_{RS} to ω_L), the frequency $\omega_{RS} \ll \omega_L$. In the model of the magnetoplasma used in this section (see (15)) these characteristic frequencies F and the characteristic angles β of both of the Storey cones are equal to:

$$F_{St,Max} = \frac{\omega_{RS}}{2\pi} = 2.6\cdot10^{-3}\ Hz\ ,\ \beta_{St,Max} = 21°;$$
$$F_{St,0} = \frac{\omega_{S2}}{2\pi} = 0.48 f_b\ Hz\ ,\ \beta_{St,0} = 0°; \quad (16)$$
$$F_{Rev.St,0} = \frac{\omega_L}{2\pi} = 2.087\cdot10^{-2}\ Hz\ ,\ \beta_{Res.St,0} = 0°$$

The resonance cones are formed in the frequency band (F_L to f_b) and in the angle region (0 to 90)°.

Angular dependencies of the electric field in different cones and of the Axis field at different frequencies ratios F/f_b are shown on Fig.3. It is natural that the Axis field and the fields inside both Storey cones are oscillating because they are formed by superposition of two modes (mathematically by contribution of the saddle points, see previous section II). The maximal values $Max|\mathbf{E}|_{max}$ of $|\mathbf{E}|_{max}$ of these oscillations of the Axis field and Reversed Storey cones are closer to the direction of $\mathbf{B_0}$. They are determined below by the notation β_{max}. The resonance field has only one maximum. It is formed only by one saddle point and it is also denoted by β_{max}.

Let us note here that the notations $Max|\mathbf{E}|_{max}$ both of $|\mathbf{E_0}|_{max}$, $|\mathbf{E_{Rev.St}}|_{max}$, $|\mathbf{E_{St}}|_{max}$ and of $|\mathbf{E_{res}}|_{max}$ are used below in this and in the following sections. The values of β shown in the figures and in the tables below are also the values β_{max} of these fields.

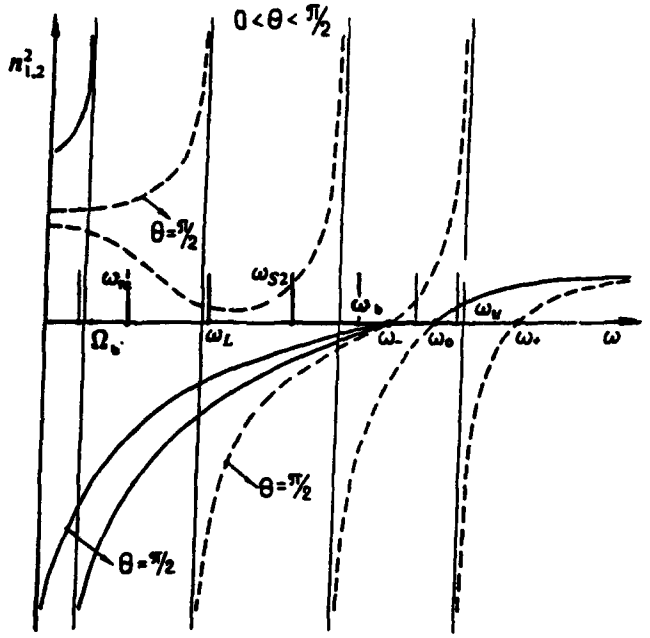

Fig 2. The coefficient refraction n depending on the angular frequency $\omega = 2\pi f$.

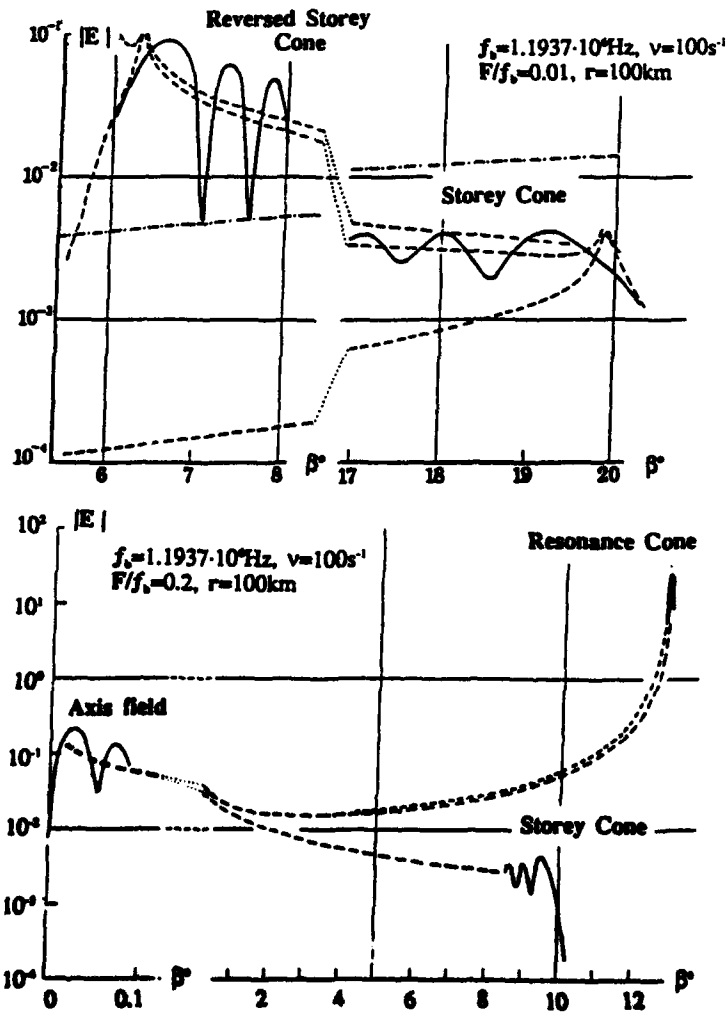

Fig 3. Angular dependencies of E.

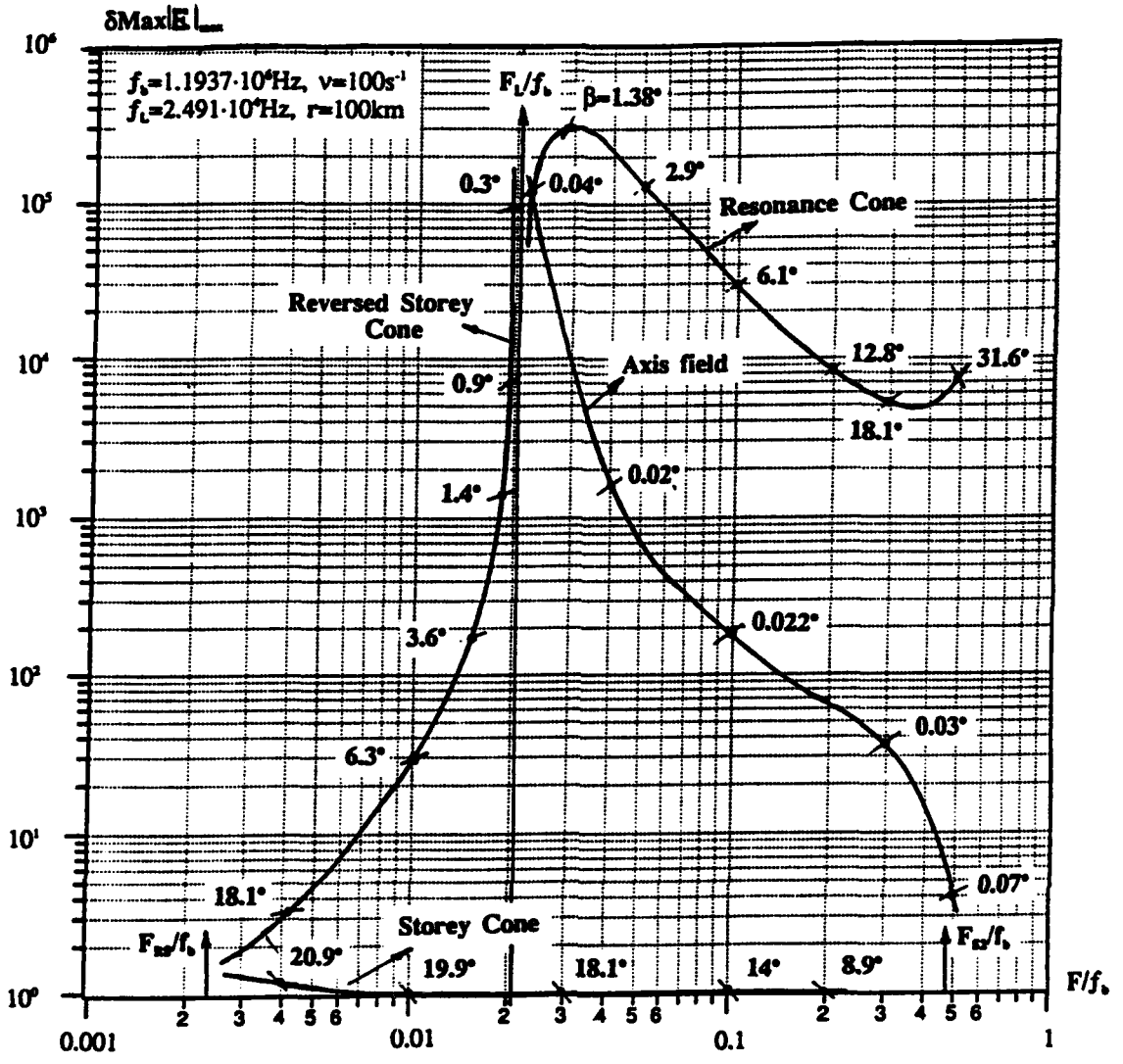

Fig 4. Normalized frequency dependencies of the moduli of the electric field. The numbers near curves are the values of β_{max}.

Frequency dependencies $\delta_{Max}|\mathbf{E_0}|_{max} = \frac{Max|\mathbf{E}|_{max}}{Max|\mathbf{E_{St}}|_{max}}$ namely of the normalized maximum values of the Axis fields $|\mathbf{E_0}|_{max}$, $|\mathbf{E_{St}}|_{max}$, $|\mathbf{E_{Rev.St}}|_{max}$ and $|\mathbf{E_{Res}}|_{max}$ are given in Fig.4 and in the Table I. The values of $|\mathbf{E}|$ were normalized to the field of the Storey cone $|\mathbf{E_{St}}|_{max}$ in the frequency band $\mathbf{F/f_b}$ = (0.01 to 0.2) because in this frequency band $|\mathbf{E_{St}}|_{max}$ is almost a constant magnetude.

The values of β of the Storey cones are changing in the frequency band $\mathbf{F/f_b} \sim 0.1$ to 0.28 from $\beta_{max} = 21°$ up to 8.9°, and $\beta_{max} \to 0°$, when $\mathbf{F/f_b} = 0.48$. The amplitudes of the electric field $|\mathbf{E_{St}}|_{max}$ are about (10 to 10^2) times larger than the predicted electric field in free space, however, much smaller than the Axis field and the field in the Reversed Storey and Resonance cones.

The enhancement of the field by approaching the low hybrid frequency is absent in the Storey cone because it is formed by the oscillations of the electrons and depends very little on the oscillations of ions which produce the low hybrid resonance and the Reversed Storey cone. In the earlier studies, the influence of the ions was not taken into account by discussing the guiding of LF waves, i.e. of the electron whistlers, along $\mathbf{B_0}$, and the formation of the Reversed Storey cone, was omitted.

Table I. Normalized values $\delta_{Max}|\mathbf{E}|_{max}$

$\mathbf{F/f_b}$	St.C.	Rev.St.C.	Axis field	Res.C.
0.003	1.2	1.9	-	-
0.005	~ 1	4.8	-	-
0.008	~ 1	19	-	-
0.01	~ 1	24	-	-
$\mathbf{1.88 \cdot 10^{-2}}$	~ 1	1502	-	-
$\sim$ 0.02	~ 1	-	$2.4 \cdot 10^5$	$1.4 \cdot 10^5$
0.03	~ 1	-	$1.9 \cdot 10^4$	$3.1 \cdot 10^5$
0.05	~ 1	-	670	$1.1 \cdot 10^5$
0.1	~ 1	-	215	$3 \cdot 10^4$
0.3	0.47	-	36	$5.1 \cdot 10^3$
0.5	0.024	-	4	$8 \cdot 10^3$

From Fig.5 it follows that both the Axis field and the fields in the Reversed Storey and Resonance cones are very large and increase very quickly, especially by approaching the low hybrid frequency F_L. The maximum values of $|\mathbf{E}|$ become in this region about 10^5 times larger than in the Storey cone and the directions (angles β_{max}) of the maximum values of $|\mathbf{E}|$ become closer to the direction of the magnetic field $\mathbf{B_0}$. The apexes of the cones, where most of the flux of the field is concentrated, become very narrow. This effect is shown in the next section in more detail, by presenting the results of calculation of $|\mathbf{E}|$ at high altitudes of the ionosphere and in the lower magnetosphere.

4. THE ELECTRIC FIELD $|\mathbf{E}|$, $Z = (800 - 6000)km$.

The altitude behavior of the electric field in the ionosphere and magnetosphere is presented in this section by detailed calculations of the Axis field $|\mathbf{E_0}|$ and resonance field $|\mathbf{E_{res}}|$. By calculation of $|\mathbf{E}|$, both in this and in the previous sections, the factor $\left(\mathbf{I}\frac{\omega^2}{c^2}\right)$ is omitted (see formulae (10) to (13)). This factor is only used on the dependencies shown on Fig.4 and 9 by normalization of $|\mathbf{E}|$ and by comparison of $|\mathbf{E_0}|$ and $|\mathbf{E_{res}}|$.

Preliminary calculations have shown that the amplitude of $|\mathbf{E}|$ is growing up very quickly in the altitude region $Z = (400$ to $800)km$. For example, at $Z = (400,\ 500,\ 800,\ 1000)km$ the maximum values of $|\mathbf{E_0}|$ of the Axis field are equal to $Max|\mathbf{E_0}|_{max} \simeq 6.6 \cdot 10^{-2}$, 2.9, $9.5 \cdot 10^2$, $1.4 \cdot 10^5$; and at $Z = (800,\ 1000)km$, the values $Max|\mathbf{E}_{res}|_{max} \simeq 28$ and 1887. Thus, the enhancement of the flux of **VLF** and **LF** electromagnetic waves in the Earth magnetoplasma, caused by the *caustic focusing*, is especially pronounced at high altitudes greater than or equal to 800 km.

By these calculations we used the model of the ionosphere and magnetosphere given in Table II. This model is representative of day-time middle latitude conditions. The notations used in the table are: Z is the altitude above the Earth's surface, $N_{n,e,i}$ are the densities of the neutral particles, electrons and ions, $T°$ and B are the temperature

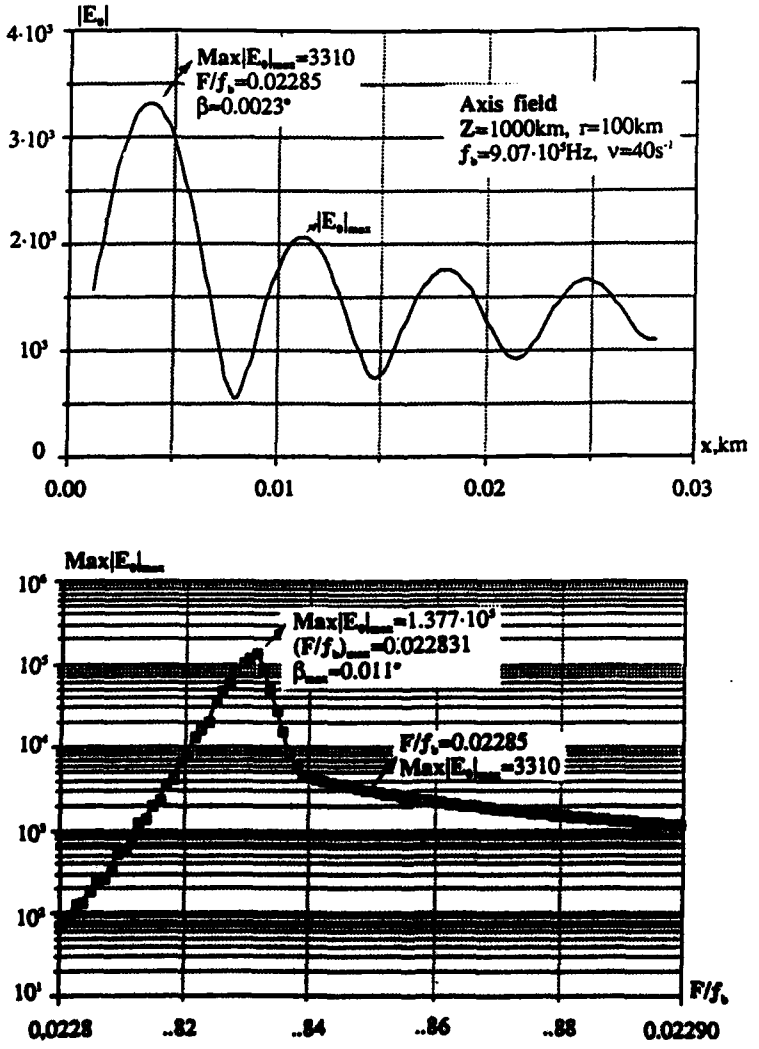

Fig 5. The Axis field $|\mathbf{E_0}|$

in Kelvin degrees and the magnetic field in gammas along the Earth's magnetic field line, ν_{en} and ν_{ei} are the collision frequencies between the electrons and the neutral particles and the ions, f_0 and F_0 are the Langmuir plasma frequencies of the electrons and ions, f_b, F_b, F_L are the electron's and ion's gyro-frequencies and the low hybrid frequency of the ions where:

$$F_L = \left(\frac{f_b F_b}{1 + \frac{f_b^2}{f_0^2}} \right)^{1/2} . \qquad (17)$$

Up to the altitude about $(800 - 1000)$ km the ionosphere consists of a noticeable number of oxygen and helium ions (O_1^+ and He^+) including protons $\left(H_1^+\right)$. Therefore, in the lower part of the ionosphere, we use by calculations of the electron and ion gyro- frequencies f_b and F_b, the effective mass of the neutral particles

$$M_{eff} = M_{H_1} \left(\sum_{s=1,2,3} \frac{N_{is}}{N_{ei}} \cdot \frac{M_{H_1}}{M_{is}} \right)^{-1} , \quad s = 1,2,3. \qquad (18)$$

In (18), N_{is} and M_{is} are, respectively, the ion densities and masses of H_1^+, He^+ and O_1^+. For fixed altitudes Z, the results of the calculation of $|E_0|$ and of $|E_{res}|$ are shown for illustration on Figs. 5 to 8. The main characteristics of these fields are given in the Tables III and IV.

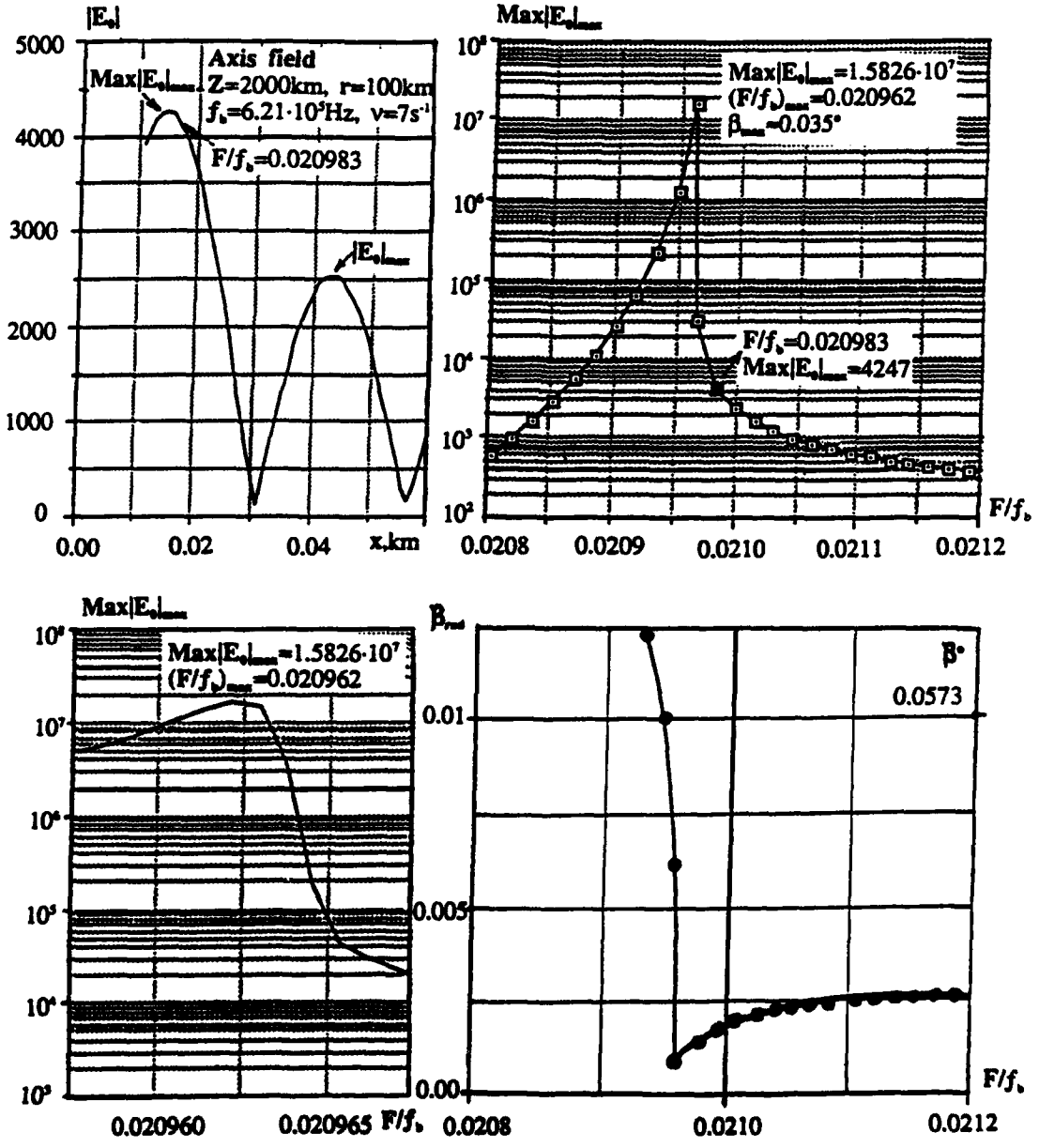

Fig 6. The field $|E_0|$ and the frequency dependence of β of the Axis field.

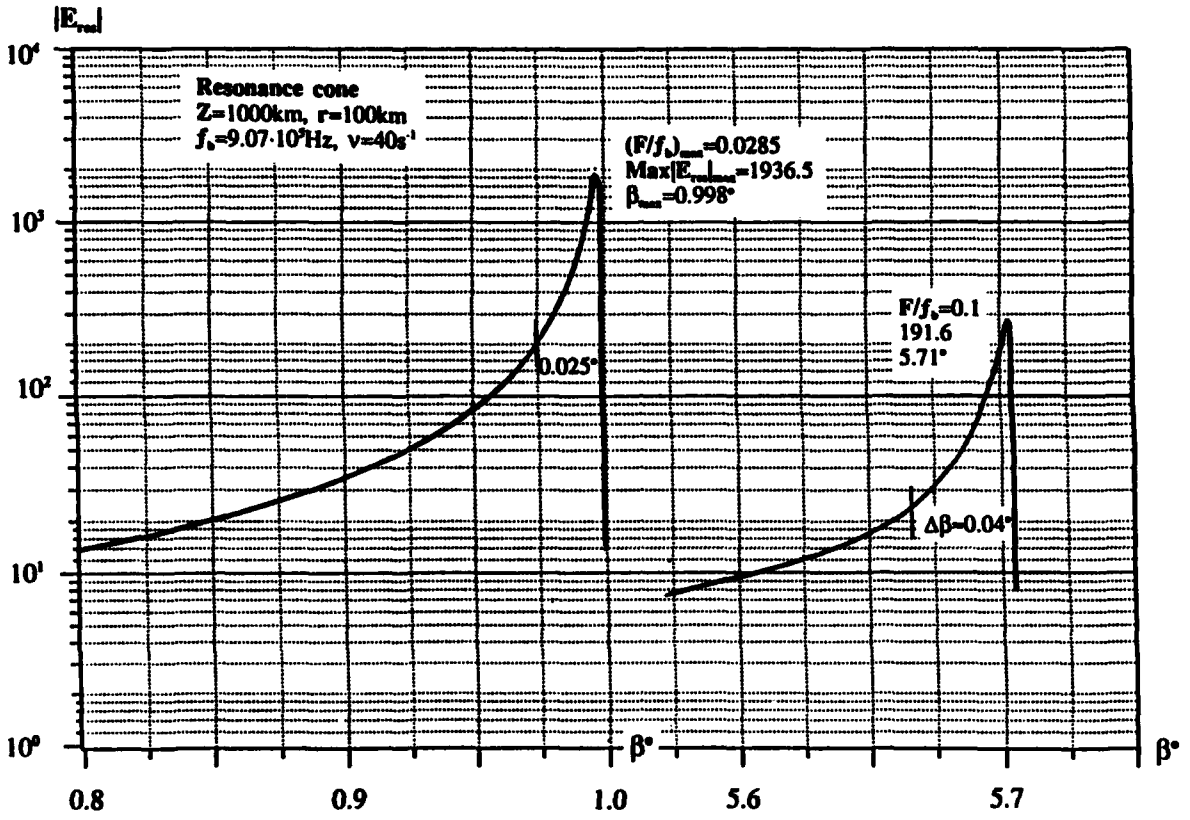

Fig 7. Angle dependencies of $|E_{res}|$.

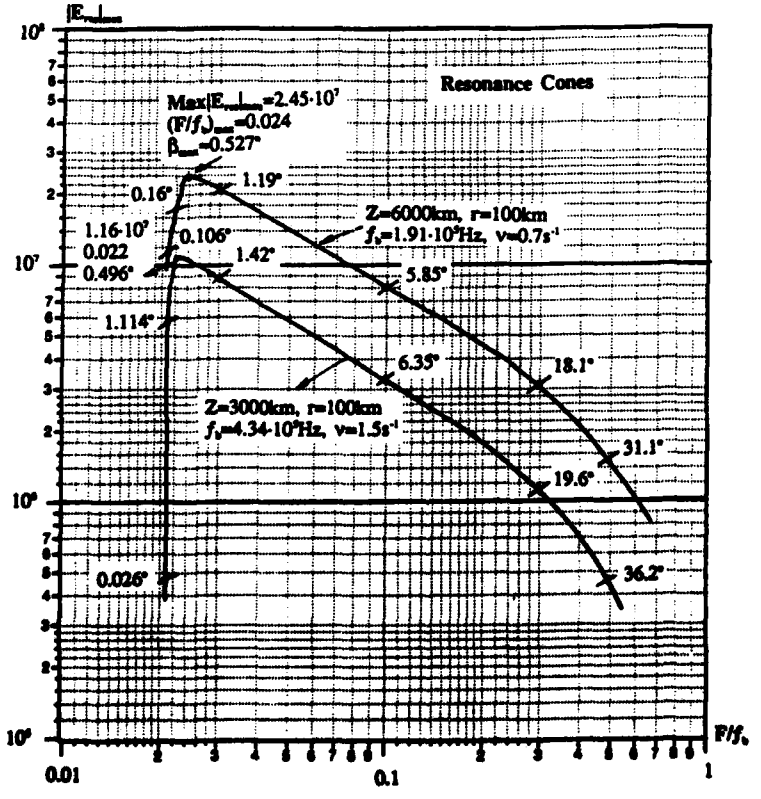

Fig 8. Frequency dependencies of $|E_{res}|$.

Table III. Data of the Axis field $|\mathbf{E_0}|$.

Z , km	F_L/F_b	F_{max}/F_b	F_{max} , kHz	$Max\|\mathbf{E_0}\|_{max}$
800	0.02088	0.02297	22.60	951
1000	0.02281	0.022831	20.71	$1.38 \cdot 10^5$
1500	0.02226	0.02227	16.59	$2.17 \cdot 10^6$
2000	0.02101	~ 0.021	13.02	$1.58 \cdot 10^7$
2500	0.02029	0.02030	10.33	$8.285 \cdot 10^7$
3000	0.02048	0.02062	8.951	$1.116 \cdot 10^8$
4000	0.02115	0.02126	6.825	$1.557 \cdot 10^8$
6000	0.02236	0.022345	4.264	$2.109 \cdot 10^8$

Table IV. Data of the resonance field $|\mathbf{E_{res}}|$.

Z , km	F/F_{max}	F_{max} , kHz	$Max\|\mathbf{E_0}\|_{max}$	β_{max} , deg
800	0.03	29.6	27.7	~ 1.12
1000	0.0285	25.85	1937	0.0998
3000	0.0220	9.548	$1.157 \cdot 10^7$	0.496
6000	0.0240	4.584	$2.449 \cdot 10^7$	0,527

5. DISCUSSION OF THE PROPERTIES OF $|\mathbf{E}|$.

The dependencies of $|\mathbf{E_0}|$ on x and of $Max|\mathbf{E_0}|_{max}$ on F/f_b shown in Figs.(5 and 6) demonstrate their oscillating character by moving away from the magnetic field line $\mathbf{B_0}$ ($\beta = 0$) and the very pronounced $Max|\mathbf{E_0}|_{max}$ of the electric field $|\mathbf{E_0}|$ depending on F/f_b. Besides, the closest maximum of $\mathbf{E_0}$ to $\mathbf{B_0}$ is $Max|\mathbf{E_0}|_{max}$; it is characterized by the angle $\beta_{max} = \arctan x/r$. These angles are very small, and increase with altitude as the following:

$$\begin{aligned} Z, km &= 800,\ 1000,\ 1500,\ 2000,\ 2500 \\ \beta, deg &= 0.014,\ 0.02,\ 0.04,\ 0.06,\ 0.07 \end{aligned} \qquad (19)$$

The frequency dependence $\beta(F)$ has a minimum which is a little shifted from the frequency F_{max} and $\beta(F)$ increases when approaching the low hybrid frequency F_L (see Fig.6). The dependence of $Max|\mathbf{E_0}|_{max}$ on frequency in the neighborhood of $F = F_{max}$ is also given on this figure. A very important characteristic of the frequency dependence of the Axis field is its *narrow-band character* of the value F_{max} in the vicinity of $Max|\mathbf{E_0}|_{max}$. Namely, about 99% of the flux of these electromagnetic waves are concentrated in the frequency bands

$$\Delta F_{max} \sim (2 \cdot 10^{-3}\ to\ 9 \cdot 10^{-4}) F_{max} \qquad (20)$$

at the altitudes Z = (800 to 6000)km.

The behavior of both the electric fields $|\mathbf{E_{res}}|$, shown on Figs. (7 and 8) and of $|\mathbf{E_{St}}|$ and $|\mathbf{E_{Rev.St.}}|$, (see Figs. 3 and 4), differs, in many respects, from the behavior of the Axis field $\mathbf{E_0}$. The maxima $Max|\mathbf{E_0}|_{max}$ of these fields are also pronounced close to the low hybrid frequency at $\mathbf{F_L}$. However, the value of β_{max} changes considerable with frequency. For example, at $F/f_b = (F/f_b)_{max}$, 0.03, 0.1, 0.3, 0.5, the values $|\mathbf{E_{res}}|_{max}$ are conformed to the following values of β_{max} at Z = (1000, 3000 and 6000) km:

$$\begin{aligned} \beta_{max} &= (0.496,\ 1.42,\ 6.35,\ 19.6,\ 36.26),\ deg, \\ \beta_{max} &= (0.53,\ 1.19,\ 5.84,\ 18.1,\ 31.10),\ deg. \end{aligned}$$

The *narrow-angle character* in the vicinity of $F = F_{max}$ (see Fig.7) is also an important characteristic of $|\mathbf{E}|_{res}$. At these frequencies about 99% of the flux of the electromagnetic waves is concentrated in very narrow angles namely $\Delta\beta \leq (10^{-1} - 10^{-2})\ deg$.

To compare the data discussed above of the altitude dependence of $|\mathbf{E_0}|$ and $|\mathbf{E_{res}}|$, the values of $Max|\mathbf{E_0}|_{max}$ and of $Max|\mathbf{E_{res}}|_{max}$ were normalized to $Z = 800\ km$, namely the dependencies

$$\delta|\mathbf{E}|_{max} = \frac{(Max|\mathbf{E}|_{max} \cdot F^3_{max})_Z}{(Max|\mathbf{E}|_{max} \cdot F^3_{max})_{Z=800\,km}} \qquad (22)$$

were calculated. The results of these calculations are shown in Fig.9 and in Table V, where the altitude dependence of these fields and the values of $F = F_{max}$ at different altitudes of the Axis field and Resonance field are also given. It is seen that the behavior of the relative values of the maximum of the Axis and Resonance fields are in general similar. The values of $|\mathbf{E}|$ increase very quickly by a factor $\sim 10^4$ in the altitude region Z = 800 to 2400 km, and diminish slow at higher altitudes. The frequencies F_{max} are also comparable, but $F_{0,max}$ is a little smaller than $F_{res,max}$. The direction of the maximum values of $|\mathbf{E}|$, namely the angles β_{max}, given above in the Tables III and IV, are also commensurable.

Table V. Normalized data of $|\mathbf{E_0}|$ and $|\mathbf{E_{res}}|$.

Z , km	$\delta\|\mathbf{E_0}\|_{max}$	$\|F_0\|_{max}$, kHz	$\delta\|\mathbf{E}_{res}\|_{max}$	$\|F_{res}\|_{max}$, kHz	$\frac{Max\|E_0\|_{max}}{Max\|E_{res}\|_{max}}$
800	1	20.60	1	29.6	32
1000	111.34	20.71	43	25.85	71
1500	902.32	16.59	-	-	-
2000	$3.18 \cdot 10^3$	13.02	-	-	-
2500	$8.32 \cdot 10^3$	10.33	-	-	-
3000	$7.29 \cdot 10^3$	8.95	$1.3 \cdot 10^4$	9.55	9.6
4000	$4.51 \cdot 10^3$	6.82	-	-	-
6000	$1.49 \cdot 10^3$	4.26	$3.03 \cdot 10^3$	4.58	81

The dependence of the $|\mathbf{E_0}|$ on the collision frequency ν_{ei} at z = 1000 km is shown for illustration in Fig.10, where $\frac{\nu}{F_{max}} \simeq 1.93 \cdot 10^{-3}$ when $\nu_{ei} = 40\ s^{-1}$. The maximum of $|\mathbf{E_0}|$ diminish with ν_{ei} about 10 times when $\frac{\nu_{ei}}{F_{max}} \simeq 4.8 \cdot 10^{-3}$, namely when $\nu_{ei} \sim 100\ s^{-1}$. Thus, the enhancement of the amplitude of the field is very sensitive to the ion-electron collision frequency which dominates in the altitude region of interest here.

BRIEF CONCLUSIONS.

It is important to note that the most interesting and important feature of the electric field $\mathbf{E}$ intensity of a radiating dipole in the ionosphere at $Z = 800 - 6000\ km$ is the concentration and focusing of the field in the VLF and LF frequency band by a factor of 10^2 to 10^5 and more in cones by approaching the low hybrid frequency. Due to the caustic focusing, the flux of the electromagnetic waves produces in the magnetoplasma very *narrow pencil beams*. The apexes of these cones are about (0.1 to 1) degrees and under certain condition even less.

It is very important and interesting to investigate in detail these predicted theoretical results in situ by experiments on satellites. Such experimental data will help both, to better understand the physics of different processes in the magnetosphere and also to improve the existing theories of these phenomena. Further theoretical investigation should be done for the study of the guiding of these waves along the magnetic field lines $\vec{B}_0$ with apogees up to (5 -

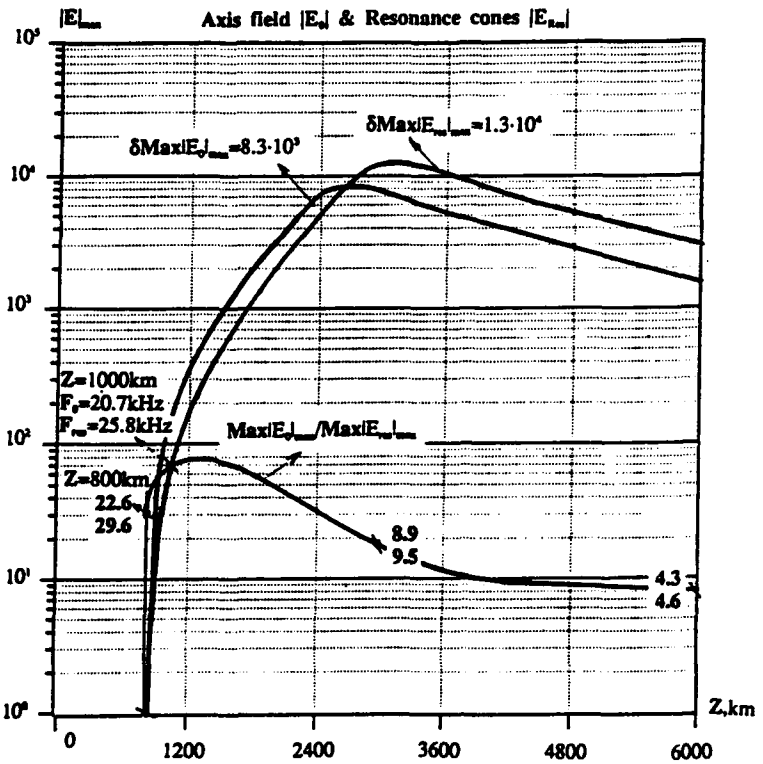

Fig 9. Altitude dependencies of the normalized values of $|E_0|$ and $|E_{res}|$.

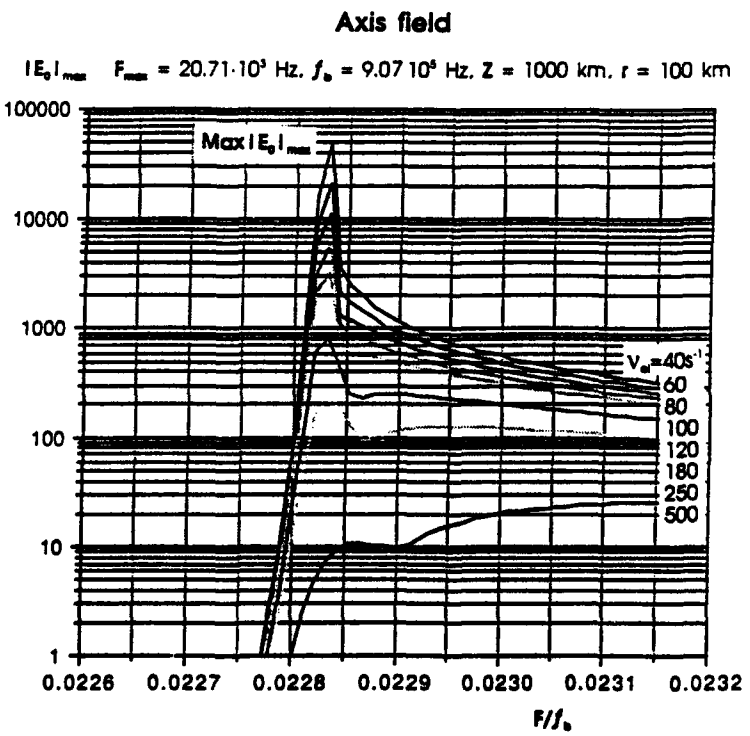

Fig 10. Frequency dependencies of $|E_0|$ for different collision frequencies ν_{ei}.

6) Earth radii. This theory should be also developed for an inhomogeneous magnetoplasma.

Acknowledgements. We thank Lara Aist-Sagara for her help in performing many of the computer calculations.

REFERENCES.

1. Alpert Ya.L., "The direction of the group velocity of e.m. waves in a multicomponent magnetoactive plasma", Journ. Atm. Terr. Phys. **42**, 1980, pp. 205-216.

2. Alpert Ya.L. & Moiseyev B.S., "On the distribution of the field of electromagnetic waves emitted by a dipole in a homogeneous magnetoactive plasma", Journ. Atm. Terr. Phys. **42**, 1980, pp. 521-528.

3. Alpert Ya.L., Budden K.G., Moiseyev B.S. & Stott C.F., "Electromagnetic radiation from a dipole source in a homogeneous magnetoplasma", Phil. Trans. Roy. Soc., London **A 309**, 1983, pp. 503-557.

4. Alpert Ya.L., "On the field of the electric Hertzian dipole in a cold magnetoplasma", Ann. of NY Acad. Sci. **401**, 1983, pp. 1-22.

5. Arbel E. & Felsen F.B., "Electromagnetic Theory and Antennas", Oxford, Pergamon Press, edited by B.C. Jordon, Part I, 1963, 421 pages.

6. Alpert Ya.L., "Trajectories of e.m. rays in the ionosphere", Izv. Akad. Nauk, Ser. Fis., **12**, *N°*3, 1948, pp. 241-266, (in Russian). See also Doklady Akad. Nauk **53**, *N°*8, 1946, pp. 703-706.

Discussion

HILDEBRAND
COMMENT. As an experimentalist I am impressed with the strong confinement of the EM propagation to a narrow path/cone. Do you have a feel/estimate for the effects caused by an inhomogeneous ionosphere along the propagation path?

AUTHOR'S REPLY
It seems to me that the inhomogeneity of the magnetoplasma (ionosphere), due to ionized clouds, will produce more than one narrow beam in any characteristic direction of the cones. Thus, multilobe structure of the electric field, will be produced by the ionized clouds.

TACCONI
COMMENT. The interesting phenomenon of superdirectivity which you have presented appears to be fairly unstable. Can you say something on possible applications in case the instabilities will be overcome?

AUTHOR'S REPLY
I have not a good answer to this question. It is a new problem. An important problem indeed.

VLF/LF PROPAGATION MEASUREMENTS

John E. Bickel
Ocean and Atmospheric Sciences Division
Naval Command, Control and Ocean Surveillance Center
Research, Development, Test and Evaluation Division
San Diego, CA 92152-5000, USA

1. SUMMARY

The Research, Development, Test, and Evaluation (RDT&E) division of the Naval Command, Control and Ocean Surveillance Center (NCCOSC), (NRaD, which is the abbreviated logo for "NCCOSC Research and Development"), and its predecessors, Navy Electronics Laboratory (NEL), Naval Electronics Laboratory Center (NELC), and Naval Ocean Systems Center (NOSC), have had a continuing program to develop a reliable VLF/LF communications coverage prediction capability for the U.S. Navy (ref.1). This involves the measurement of field intensity of many communication stations, the development of propagation models to fit the data measured, and the validation of these models to verify predictions for all seasons world-wide, including possible solar cycle effects.

During the current campaigns, data have been recorded using various platforms, including numerous aircraft, six ships, three submarines, and up to 28 fixed sites since 1981. Currently, data are being recorded aboard two ships and at seven fixed sites. An attempt is made to maintain an overall root-mean-square (rms) accuracy of 0.5 dB, with system calibration and stability measured to the order of 0.1 dB rms. The goal for the model under development is to fit these data and extrapolate predictions to other propagation conditions to within 1 dB. This has been a challenging task where local environmental effects can cause significantly larger perturbations.

A review of the literature is presented summarizing and comparing methods and techniques used by other researchers in the field. This is followed by discussion of the commercial equipment used, the calibration and recording procedures followed, a comparison of results obtained simultaneously using various platforms and sites, and an estimate of the overall accuracy/reliability of the data obtained.

2. EARLY MEASUREMENTS

The first measurements made of radio waves were by Heinrich Hertz in about 1885. His apparatus included a "vibrator", an induction coil with a Leyden jar or a pair of plates for a capacitor, to form a resonant circuit (ref. 2). When this circuit was set into oscillation, the presence of RF fields was detected by the "resonator", a piece of copper wire bent into a circle, or square, with conducting balls spaced closely together at the ends of the wire. The spacing was precisely adjusted by an insulating screw. In the presence of a properly oriented oscillating magnetic field, Hertz observed sparks between the balls, and the brightness of the sparks was an indication of the field strength. This "resonator" was used to map the position and direction of the magnetic field produced by the vibrator.

Marconi received the first trans-Atlantic radio signal on 12 December 1901 at St. Johns, Newfoundland, from England (ref. 3). The first permanent commercial public service radio station in the United States was constructed at Avalon, Santa Catalina Island, in 1902. By 1907 there were over 300 stations in the United States equipped with transmitters of U.S. manufacture and by 1915 the number was over 1100 (ref. 4).

In 1905, Duddell and Taylor made the first accurate measurement of wireless signal strength (ref. 5). Louis W. Austin published a series of reports of VLF/LF field intensity measurements made between 1922 and 1925 and a summary of these measurements showing the 5-year annual variation of several stations is published in ref. 6. These data illustrate the diurnal, monthly, and annual variations, and show a correlation with magnetic storms, but not with sun-spot number or "the weather at the receiving site in Washington, D.C." In 1928, A. Bailey et al. (ref. 7) concluded lower frequencies near 60 kHz were best for trans-Atlantic radio-telephone transmissions and that a wave-antenna in Maine provided a 20,000 times improvement over a loop antenna in New York in reception of English transmitting stations. Lloyd Espenschied, C.N. Anderson, and Austin Bailey (ref. 8) reported two years of trans-Atlantic field intensity data recorded between 1923 and 1924 of frequencies from 15 kHz to 60 kHz. From these data they noticed the "remarkable correlation between the signal level and the intensity of the earth's magnetic field." They developed the famous empirical formula, which bears their name, that provided a best fit to daytime propagation data recorded on the New York-London path.

Round et al. (ref. 5) report measurements made in 1922 and 1923 aboard ships during cruises from England to Australia via the Panama Canal, and from Australia to England via the Suez Canal. It was Hollingworth (ref. 9) that first reported, in 1926, the oscillatory variation of signal level with distance that is due to interference between the ground wave and the ionospherically reflected sky wave. His measurements were made of 5 stations, at 4 fixed locations, and with a portable system, simultaneously. From these measurements he deduced an effective height of ionospheric reflection to be 75 km in the day and 90 km at night. He attempted to avoid making measurements near hills, long distance telegraph wires, and heavily wooded areas.

During these earliest years of radio, a common method of making quantitative measurements of the strength of radio waves consisted of injecting an RF signal into the front end of the receiving equipment, adjusting its amplitude until it sounded to the ear to be the same level as the radio signal received by the antenna, then determining the level of the injected signal with a galvanometer and attenuator. This is particularly true of distant transmitters producing signal levels which were frequently exceeded by spherics. The spherics would drive a galvanometer erratically, making accurate quantitative measurements impossible. In 1921, Vallauri published the first results on the use of the comparison method (ref. 5). He used two loops at right angles, one to receive the signal to be measured and the other, which nulled the radio signal, received atmospherics and the injected C.W. signal. The injected signal was adjusted until it sounded like the same signal to noise ratio as the keyed radio signal, and then measured. Tremellen later improved on this, using a "chip-in" technique, where the calibration signal is injected into the receive antenna only at the end of a message (of Morse Code) or during a pause (ref. 5). Austin (ref. 6) refined the procedure with the use of a dummy antenna. After properly adjusting the level of the calibration signal, he replaced the antenna with the dummy antenna to measure the level of the injected signal without the interference of spherics.

In 1925, three long-wave field intensity measuring systems were compared with each other at the Bureau of Standards in Washington, D.C. (ref. 6). They differed primarily in the way the local reference signal was injected. The Bell Laboratories system (ref. 10) injected an RF signal across a 1 ohm resistor into the antenna coil. The Radio Corporation of America system (ref. 11) introduced the RF calibration signal using "a calibrated mutual inductance". The Bureau of Standards system (ref. 12) used a "telephone comparator" in which an audio frequency signal of measured amplitude is matched against the signal heard in the "telephones" (ear phones) of the receiving set. The agreement between the three systems, when disturbances were not too heavy, was generally less than 20 per cent (about 1.7 dB). The accuracy of manually recorded field intensity data was about $\pm$ 25% in 1922, $\pm$ 20% in 1923, $\pm$ 15% in 1924 and 1925, and $\pm$ 10% in 1926 to 1930 (ref. 13).

During the late 1920s, continuously recording field intensity meters were being developed which had gain stabilities of $\pm$ 15% and over-all precision of measurement estimated at $\pm$ 20% (ref. 14). The Bureau of Standards began recording long wave stations in 1915 and by 1930 was recording 14 stations (ref. 15). This data was being used to develop propagation prediction formulas. Empirical formulas representing mean daytime propagation conditions were developed by Austin and Cohen (ref. 16) and Espenschied, Anderson, and Bailey (ref. 8). Austin Bailey et al. (ref. 17) analyzed the diurnal sunset dip and solar eclipse effects on long path signals in an attempt to develop a method to predict their behavior.

During the 1930s and 1940s, more and more VLF/LF work was devoted to making measurements of the sky wave at short ranges to determine the reflecting properties of the ionosphere (ref. 18,19,20). However, Brown (ref. 21) measured the strength the Annapolis (MD) 15.5 kHz signal which had traveled completely around the world. The delay time measured on two occasions was 0.1365 and 0.1373 seconds. Reviews of early long range VLF/LF propagation measurements prior to World War II can be found in references 2, 5, 22, and 23.

3. LONG DISTANCE PROPAGATION MEASUREMENTS AFTER WORLD WAR II

3.1 Surface Measurements

As radio developed during the 1930s, it was learned that high frequencies would propagate reliably to great distances, with less power required, and at less cost for equipment. As a result, less and less emphasis was put on the study of VLF/LF propagation. However, the U.S. Navy had an interest in maintaining its transmitting stations for shipboard and submarine communications and after World War II supported an increased effort in VLF/LF propagation studies. The Bureau of Ships, of the U.S. Navy Department, had the Stoddard Aircraft Radio Company build the Radio test set AN/URM-6 (also known as the NM-10A) which, for a while beginning in 1949, became the standard equipment for making VLF/LF propagation measurements. Baldwin, a principal author of the Baldwin-McDowell empirical propagation formula (see ref. 22), was instrumental in having the field strength meter built.

Using this equipment, Pierce (ref. 24), under contract to the Office of Naval Research, obtained measurements of field intensity on 5 frequencies, between 30 and 104 kHz, recorded at 8 locations in the continental United States and the Pacific Ocean during the summer of 1951. From these and other data previously published, he developed the empirical formula which bears his name. It predicts daytime field strength as a function of time, frequency, latitude and distance. Dinger et al. (ref. 25) used the equipment to measure, at 5 locations in Alaska, transmissions from an experimental balloon-lifted transmitting antenna on the USS Burton Island ice breaker in the Bering Sea, and from other VLF/LF stations.

Several methods are used to calibrate the URM-6. The equipment is provided with a built-in standard noise source which is used to inject a reference signal into the front end to check and re-set the overall gain of the receiver, if needed. More accurate calibrations are made by using an external signal generator and the Stoddard "loop calibration network" to apply a known voltage across a 0.1 ohm resistor which is in series with the loop antenna. Dinger et al. (ref. 26) developed the shield injection method that involved applying an RF voltage across the gap in the metal shield of the loop. A resistor in series with the loop shield was selected so that the field strength indication in microvolts per meter

is equal to the signal generator output in microvolts.

Beginning in 1958, Pickard and Burns, Inc., under the sponsorships of the Bureau of Ships and using the URM-6 equipment, recorded up to 6 VLF stations at up to 9 recording sites in the North Pacific Ocean and two in the Arctic. They also recorded data aboard two ships making several cruises across the Pacific Ocean, and across the Atlantic Ocean and into the Mediterranean (ref. 27). The measurement program provided a complete year of field intensity data. The data were initially used to develop improvements to empirical VLF propagation prediction models.

Maxwell (ref. 28) reported the measurement of transmissions from Hawaii on 5 VLF frequencies during May to July 1965. The data were recorded at Guam, Japan, and Boulder (CO). Rhoads et al. (ref. 29,30) recorded aircraft measurements during the same tests. This was part of a test to demonstrate the best operating frequency to be assigned to the station Lualualei in Hawaii. A similar test was conducted using station H.E. Holt (North West Cape, Australia) when it was completed and ready for service in 1967. It sequentially operated on 6 VLF frequencies during September, October, and November 1967 while its signal field strength was recorded by the Naval Research Laboratory personnel at Bahrain, Choshi (Japan), and Tanarive (Madagascar) (ref. 31).

In 1963, Parks et al. (ref. 32) made measurements of all 6 field components (the x, y, and z components of both the magnetic and electric fields) of VLF propagating waves. Calibrated field intensity measurements were recorded at Perth (Australia) and at Tracy (CA) of signals from Cutler (ME), Rugby (England), Jim Creek (WA), Lualualei (HI), and Balboa (Panama). Each E field antenna consisted of two plates, 16 feet wide and 30 feet long, spaced 15 inches apart. The magnetic field antennas were one turn loops of aluminum pipe. The Ez/Hy fields ratio (Ry), where Ez is the vertical electric field component, and Hy is the horizontal magnetic field component which is perpendicular to the direction of propagation, was computed and plotted versus time to show a time variation of this impedance quantity, which would be constant at 377 ohms in free space. Figure 1 is an example

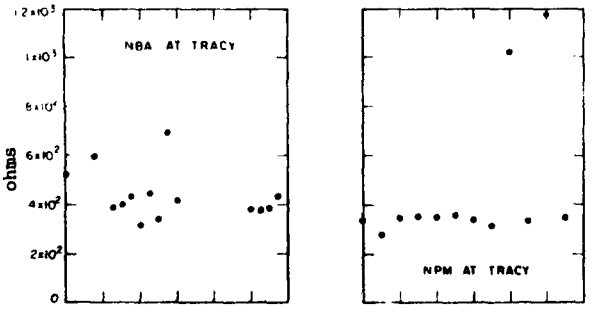

Fig. 1. Magnitude of Major-Axis-E-To-Transverse-H Ratio for 18 Aug. 1963, NBA and NPM signals (from ref. 32).

showing Ry is relatively stable at 377 ohms for NPM (Lualualei, HI) most of the time at Tracy, but it deviates during sunrise and sunset on the propagation path. Three other examples illustrate that field intensity measurements using the E field antenna and the H field antenna differed by as much as 6 dB much of the time.

Chilton et al. (ref. 33) reported measurements of the phase and amplitude of the Balboa 18.0 kHz signal at Boulder (CO) and Tucamon (Argentina) that indicated a difference in the diurnal phase height change, and in the signal level which is significantly lower at Tucamon than at Boulder. They suggested the difference results from a latitude variation in ionization due to cosmic rays. Ishii (ref. 34) compared four years of Jim Creek 18.6 kHz signal field intensity with sunspot data but found no significant correlation.

3.2 Airborne Measurements

It was in 1953 that Budden (ref. 35) reported measurements made aboard an aircraft of the GBR 16.0 kHz signal level as a function of distance. The data were recorded by K. Weeks on daytime flights between England and Cairo in June-July 1950 and show for the first time the modal interference pattern out to a distance of 4000 km. From these data, Budden deduced the height of ionospheric reflection was 69.1 km, and the electron density there was between 135 and 400/cc.

A review of Budden's report prompted the Navy Electronics Laboratory (NEL, a predecessor to NRaD) to record aircraft data of U.S. Navy VLF stations. Bickel et al. (ref. 36) reported data recorded on both day and night flights across the Pacific ocean made in September 1954, December 1954, and August 1955. This included flights from San Diego to San Francisco, Hawaii, Wake Island, Tokyo, Adak, Kodiak, Seattle, and back to San Diego. To convert the relative signal voltage recorded aboard the airplane to absolute field strength, the system was calibrated in flight using two methods: (1) The aircraft was flown at a low altitude over a ground monitor with known calibration; and (2) was flown for some distance in the field of a transmitter of known radiated power where the field intensity was varying inversely with distance. However, when the data are normalized to one kilowatt of radiated power, it is not necessary to use either the calibration factor for the aircraft receiving/recording system or the actual radiated power of the transmitter. All the data values are adjusted so that the data which varies inversely with distance are equal to 69.3 dB above 1 μV/m when adjusted for a distance of 100 km.

Aircraft measurements made during an extensive set of flights in the north western hemisphere and Arctic were reported by Bickel (ref. 37). The flights were at night during November and December 1957 and at day during June and July 1958. In figure 2 are shown the flights made in 1958, the earlier flights over the Pacific Ocean area (ref. 36), and the cruise of the USS Catamount from Seattle to Alaska aboard which some VLF data were recorded. The effect of the variable low ground

conductivity on the propagation path from Jim Creek at Seattle, and across Canada and Greenland to Norway, is illustrated by the high attenuation rate shown in figure 3. Also shown is an averaged equivalent single mode signal level decreasing with distance that approximates a dominant wave guide mode. Data values read from the equivalent single mode, for all the flights shown in figure 2, are used in figure 4 to construct the estimated contours of equal field intensity illustrated. The very high attenuation of signals propagating over Greenland, and other regions of low conductivity, is one of the more dominant features illustrated by the contours.

Watt et al. (ref. 38), determined from 98.5 kHz and 82.05 kHz aircraft data, recorded on flights between Goose Bay, Labrador and Thule, Greenland, that regions of ice cap or permafrost cause very great propagation attenuation and sky wave antenna cutback. Belrose et al. (ref. 39) determined D region electron density profiles, down to 59 km and 30 electrons per cc, using 80 kHz aircraft data recorded to 1,300 km on an Ottawa to Churchill flight and partial reflection measurements at these locations. Rogerson (ref. 40,41) and Bickel (ref. 42) reported aircraft measurements, and Snyder et al. (ref. 43) reported ground-based measurements, made in Africa at the antipode of VLF transmitters located in Hawaii. The predicted large increase in signal level at the antipode was observed. The data were used to deduce average daytime seawater attenuation rates of the dominant waveguide mode, and indicated a diurnal variation in the location of the signal maxima and significant time-varying multi-path interference.

In January 1969, Bickel et al. (ref.44) made airborne measurements of the NPM signals while flying radials at night through Ontario (CA), Samoa, and Wake Island. The modal interference pattern recorded varied significantly with direction of propagation relative to the earth's magnetic field and showed remarkable agreement with theoretical calculations made using NELC's waveguide mode propagation prediction program. During the same flights, data were recorded on the aircraft by Naval Weapons Center (NWC) China Lake personnel using a sounder transmitter operating on ten frequencies simultaneously from 9 to 56 kHz. Analysis of this data was first reported by Morfitt (ref. 45). Morfitt also reported on the analysis of as much other data as he could find in order to determine ionospheric profiles that provided the best fit between the propagation predictions and all the data (ref. 45,46). From 1965, NWC personnel conducted additional studies of long path VLF/LF propagation on the Hawaii to Southern California propagation path using the multiple-frequency and pulse sounding techniques described in ref. 47. The broad band transmitting antenna needed, designed by Seeley (ref. 48), was a stagger tuned horizontal dipole laid out on the lava beds in the saddle between Mauna Loa and Mauna Kea on the island of Hawaii. A description of the sounder transmitting and receiving equipment is given by Wulfing et al. (ref. 49).

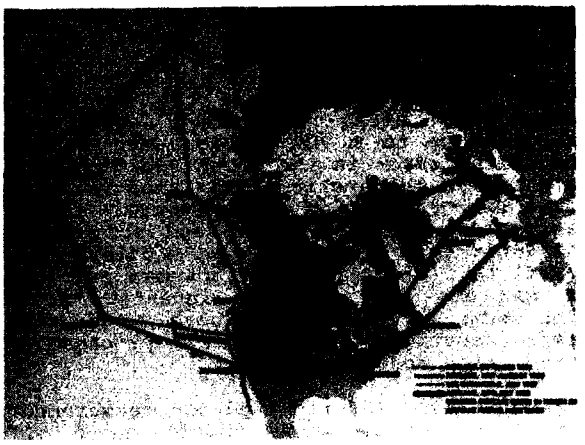

Fig. 2. An azimuthal-equidistant projection map centered on Washington, D.C., showing approximate flight paths flown, and the cruise of the USS Catamount.

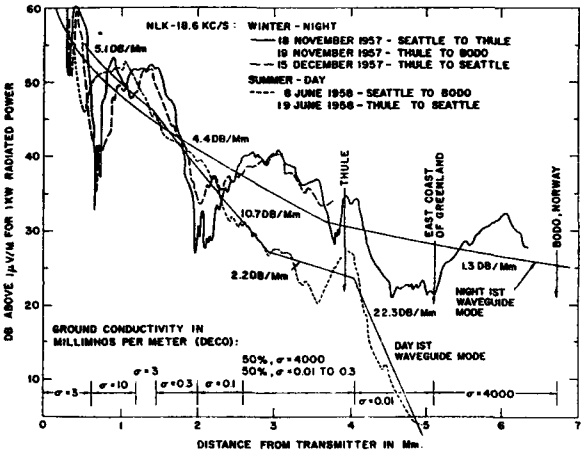

Fig. 3. Airborne data recorded of NLK/NPG on 18.6 kHz during flights across Canada and the Greenland ice cap to Norway.

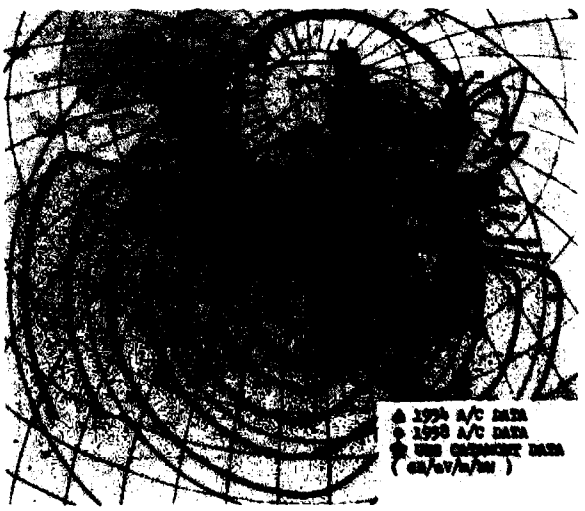

Fig. 4. Daytime contours of equal field intensity of the Jim Creek 18.6 kHz signal.

In 1972, Bickel (ref. 50) reported on measurements made aboard a Piper Aztec airplane of TE and TM signals produced by a TACAMO aircraft during daytime and nighttime propagation conditions. Gallenberger et al. (ref. 51) describes an attempt to measure TE noise at 20,000 ft. altitude but it was below the aircraft generated noise level.

Another extensive set of aircraft data was collected by Naval Electronics Laboratory Center (NELC) personnel during October 1973 and January 1974 using an Air Force KC-135 aircraft outfitted with both TE and TM loop receiving antennas and a long wire E field antenna. A map showing the routes flown is shown in figure 5. In- flight data were recorded of signals from shore-based communications transmitters, airborne TACAMO and ABNCP transmitters, and 10 frequency sounder transmitters located at Hawaii and the NELC field site at Sentinel (AZ). The Sentinel antenna was a north-south oriented grounded dipole 8.5 km long and which was end-fed using a transmitter as its center and a reflection transformer at one end. A ten-frequency sounder receiver was located at Glasgow, Canada. Using data from these flights, and all other data available to him, Ferguson (ref. 52) developed a revision to the recommended ionospheric profiles to use for making communication system coverage predictions. Both TE and TM field strength measurements generally agree with computed fields as predicted using the waveguide theory developed by Pappert (ref. 53).

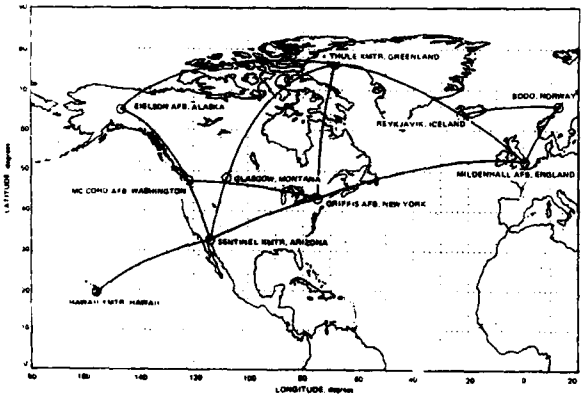

Fig. 5. Routes flown by the KC-135 aircraft in October 1973, and January 1974.

The TE measurements made aboard the Piper Aztec aircraft (ref. 50,51) were made at 10,000 and 20,000 feet altitude and aboard the KC-135 aircraft at 30,000 feet. Kossey et. al. (ref. 54) report measurements made aboard a U2 aircraft at 60,000 feet of TE and TM fields produced by an airborne transmitter. Bickel (ref. 55) developed an antenna system which is placed against the inside surface of aircraft windows to receive TE and TM fields. This was tested on numerous commercial passenger flights between 1972 and 1974, but the aircraft noise level was high and the range of reception was limited to about 2000 km. The relative TM calibration of the antenna system was obtained by recording data while flying level within the inverse distance field of a station of known radiated power, and the TE calibration was obtained while the aircraft is in a bank, at a low altitude, in a known TM field. Kelly et al. (ref. 56) reports measurements of LF transmitters during 1976 and 1977 flights from Washington, D.C. to Europe, through the Mediterranean, and return. Also, Kelly, et al. (ref. 57) report VLF measurements in the Arctic at Spitsbergen, Norway and aboard an aircraft.

The Naval Ocean Systems Center (NOSC) made measurements of Omega Navigation system signals aboard inflight aircraft as part of the Omega Navigation System validation program. This program was designed to evaluate the coverage and accuracy of the Omega navigation system in most regions of the world. Airborne data were recorded in the Western Pacific Ocean in 1977, North Atlantic Ocean in 1978, North Pacific Ocean in 1979, South Atlantic Ocean in 1980, Indian Ocean in 1983, South Pacific Ocean in 1985, and again the Western Pacific Ocean in 1986 (because the Australian Omega Station had not been installed in 1977), and in the Mediterranean Sea in 1987. The measured data analyzed included the amplitude and phase of various Omega signals ranging from 10.2 to 13.6 kHz. Similar data were recorded also at more than a couple dozen fixed monitoring sites located worldwide. The primary information developed was the area of the world covered by signals from each of the Omega stations and the measured navigation error in the various regions. Maps of contours delineating the boundary between regions of coverage and no coverage were prepared. Some of the aircraft amplitude data were compared with waveguide propagation predictions to evaluate the accuracy of the predictions. This program was sponsored by the Omega Navigation System Center (ONSCEN) in Washington, D.C. Omega validation reports were prepared for each of the seven regions validated (ref. 58, 59, 60, 61, 62 ,63 , and 64).

Height-gain measurements of VLF/LF signals have been made by balloons and rockets to 500 kilometers altitude. Measurements were reported by Orsak et al. (ref. 65) of several stations, up to 200 to 400 kilometer altitude. Harvey et al. (ref. 66) presented day and night data recorded at Elgin AFB, Florida in 1965, and day data recorded at Natal, Brazil in 1969, and at Fort Churchill in 1971. At each site, data were recorded on 3 to 6 stations to heights of 70 to 500 kilometers. The stations were at ranges from 1300 to 15,500 kilometers. Harrison et al. (ref. 67) reported daytime measurements of TE and TM fields from an airborne transmitter, with a "nearly-horizontal antenna", at 31,000 feet and a range of 1,300 km. Planck (ref. 68) recorded with rockets TE and TM fields to 250,0000 feet altitude from TACAMO aircraft at 725 n. mi. range. Two daytime rocket launches 30 minutes apart illustrated a change in the recorded height gain profile during this interval. The TE and TM height gain profiles recorded at Thule, Greenland of nine U.S. and European stations, and a

TACAMO aircraft, were published by Turtle (ref. 69). Okada et al. (ref. 70) recorded the altitude dependence of the signals from Yosami (17.44 kHz) and three of the Omega Navigation System signals from the Japan Omega station.

All of the height gain data available from the references cited should provide a valuable source of information for validating the height gain predictions possible from the NRaD propagation prediction code.

4. NRaD MEASUREMENT PROGRAM FROM 1984

Beginning in June 1984, NOSC, now NRaD, began its current effort to develop a reliable VLF/LF system coverage prediction computer program. The procedure is to first record appropriate VLF/LF propagation data in regions of operational interest where there is an uncertainty regarding signal level prediction accuracy. The ionospheric profiles used in the long-wave prediction code are then modified in appropriate ways to fit, on a global scale, all reliable data available. During the past eight years, data have been recorded aboard numerous inflight aircraft, six ships, three submarines, and up to 28 shore locations, with varying degrees of success and accuracy. The receiver used at all locations has been the Hewlett-Packard 3586C selective level meter. It is automatically tuned throughout the VLF/LF band with a bandwidth of 20 or 400 Hz.

Figure 6 is an example of a 24-hour plot of data recorded aboard the ship GTS Callaghan and is typical of the data recorded at fixed locations as well. Under computer control, the HP 3586C receiver samples the amplitude of 20 signals, or noise channels, once every six minutes using the 400 Hz bandwidth setting. This requires about 1 to 1 1/2 minutes to complete. The upper curve of figure 6 is a plot of these six-minute readings of the 24 kHz Cutler signal. During the 4 1/2 to 5 minutes available between these readings, the computer stepped the receiver from 23.0 kHz to 25.0 kHz in 25 Hz steps, to record a 2 kHz spectra. A 20 Hz bandwidth is used for the spectra. It is recorded four times per day, centered on each of the 20 frequencies recorded using the 400 Hz bandwidth. The time of day the spectra are recorded is indicated by the position of the vertical dotted line on the X axis. This spectra allows an evaluation of S/N ratio, or possible interference, from stations nearby in frequency. Aboard aircraft, the 20 frequencies were recorded continuously, using the 400 Hz bandwidth, except when the spectra were recorded occasionally at times selected manually by the operator.

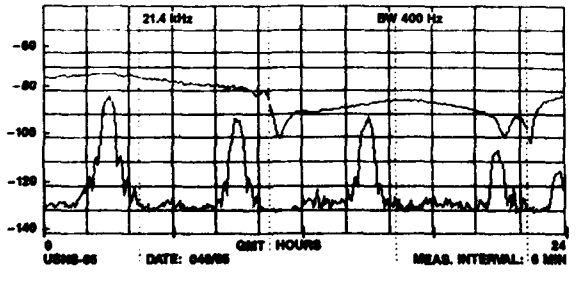

Fig. 6. Annapolis 21.4 kHz data recorded aboard the GTS Callaghan on 17 Feb. 1985.

Several campaigns, described below, have been conducted to resolve propagation prediction uncertainties and allow improvement in the propagation prediction code.

4.1 North Atlantic Campaign

The first campaign, beginning in 1984, was in the North Atlantic operational area. Hepner (ref. 71) describes the recording of VLF/LF amplitude data aboard aircraft and a ship. The aircraft data were recorded on C-141 transport aircraft during 55 regularly scheduled U.S. Military Airlift Command (MAC) freight and passenger service flights in June 1984, February 1985, and September 1985. A map showing the flight paths (as well as the ship GTS Callaghan tracks) is shown in figure 7. The equipment used on the aircraft consisted of an HP model 3586C selective level meter and an HP85 desktop computer. The E field aircraft antenna was a blade bolted to the outside of an escape-hatch cover and its battery-operated pre-amp was attached to its inner surface. Upon boarding the aircraft, the equipment was strapped down, the existing aircraft escape hatch was replaced with the one which had the blade antenna bolted to it, and the antenna coaxial cable and power cable were put in place. The installation took about 15 minutes and was completed before passengers were boarded.

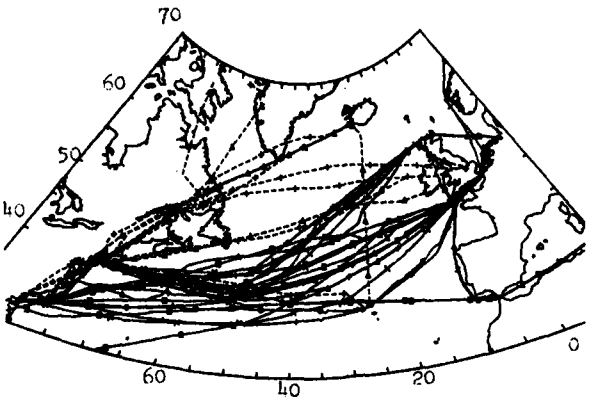

Fig. 7 C-141 aircraft (dashed lines) and GTS Callaghan (solid lines) tracks in 1984 and 1985.

The shipboard data was recorded on the GTS Callaghan during 15 round trip crossings of the Atlantic Ocean from March 1985 to April 1986, sailing primarily between New York and Bremerhaven, Germany. It is described in ref. 71 as well. Figure 8 is a block diagram of the equipment used on the ship and at fixed recording sites.

4.2 Trans-CONUS Campaign

Between September and December 1986, the VLF/LF receiving/recording equipment was installed at 10 locations on the great circle path between Annapolis (21.4 kHz) and the Jim Creek (24.8 kHz) (ref. 72). Data were also recorded aboard an NRL P-3

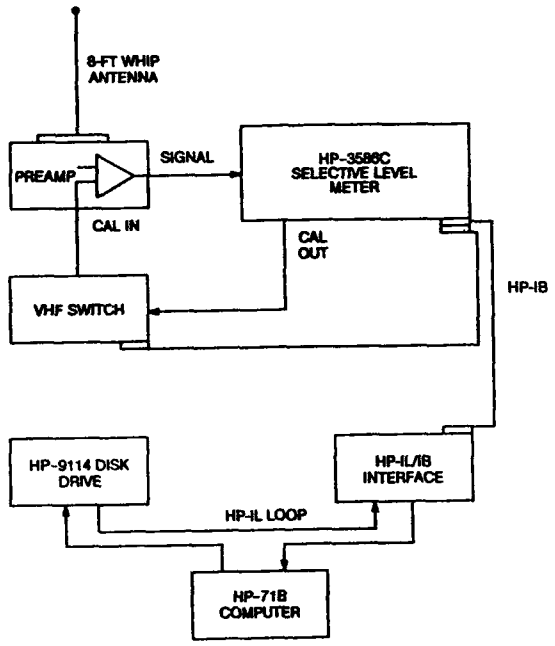

Fig. 8 Block diagram of the receiving and recording system used on ships and at fixed sites.

aircraft during three overflights of the recording sites. This data recording campaign was carried out partly to evaluate the time variability of aircraft data, primarily of concern during nighttime propagation conditions, and to determine the extent to which this variability influences the best fit ionospheric profile determined from aircraft data. The mean of 7 consecutive days of noon data values, plotted with the predicted field intensity, is shown in figure 9. At distances between 3 and 4 megameters, the averaged data are about 2 dB below the predictions.

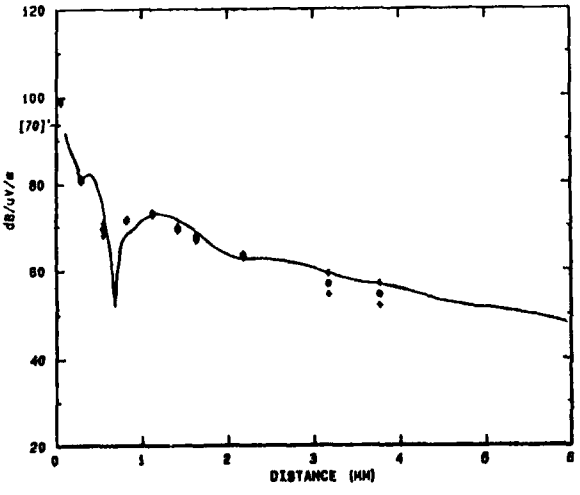

Fig. 9. Trans-CONUS daytime weekly average data and prediction of Annapolis 21.4 kHz signal.

4.3 The Arctic Campaign

The Arctic Campaign, described in ref. 73, included data recorded at Fairbanks (AK) and Thule, Greenland during 1987 to 1989, and aboard two ice breakers which sailed into the Arctic Ocean during this period. In April 1988, a receiving/recording system was installed on the USCGC Northwind at its home port of Wilmington (NC). Data were recorded aboard her during cruises across the North Atlantic Ocean to Iceland, Greenland, and Norway. At Tromso, Norway on 2 September 1988, a VLF/LF system was installed on the Norwegian ship MVS Polarbjorn. The Northwind then escorted the Polarbjorn into the central icepack north of Svalbard (Spitsbergen), where the she was left to become frozen into the ice pack and drift free to the south of Svalbard the following spring. The Northwind then returned to Wilmington via England. This campaign was designed to record diurnal and seasonal changes of US Navy operational communication stations in the Arctic region. Figure 10 shows the Northwind's track from Wilmington to Tromso and return. The Polarbjorn ended its Arctic expedition at Tromso on 22 May 1989.

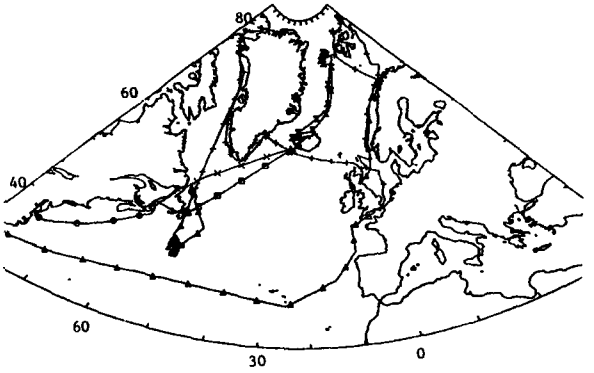

Fig. 10. USCGC Northwind navigation tracks in 1988.

4.4 Auroral Zone Campaign

The purpose of the auroral zone campaign was to detect and document the anticipated variation of VLF/LF long path propagation into and through this geophysical feature. The 6 fixed recording sites, shown in figure 11, were selected based upon the positions of the propagation paths from the VLF stations at Cutler and Annapolis relative to the auroral zone. These paths include one perpendicular to the auroral oval (to Thule), one tangent to the ring of maximum visual auroral activity, (to Fort Smith and Fairbanks), and to Meanook, Bangor, and San Diego with propagation paths which are at increasingly greater distances relative to the auroral ring. It was anticipated that the more intense a "magnetic storm" became, the effect on the D region, and therefore VLF propagation, would extend to increasingly lower geomagnetic latitudes.

4.5 Solar Effects Campaign

Previous researchers have looked for a correlation between VLF/LF propagation and the solar sunspot number. The effect of solar flares on VLF/LF propagation is immediate and well-known, but there's an

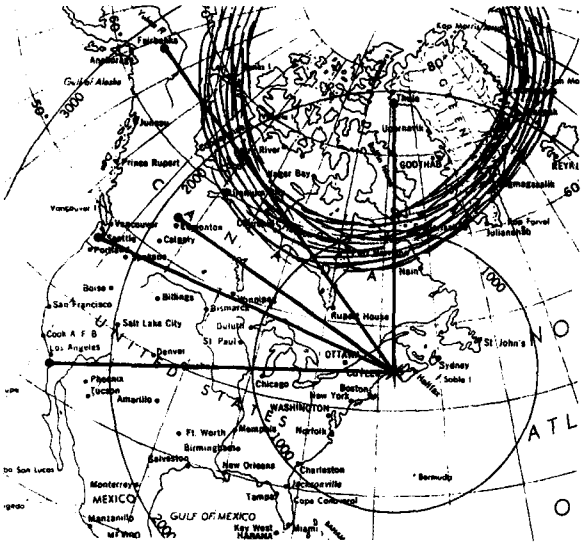

Fig. 11. Propagation paths from Cutler 24.0 kHz to Thule, Fairbanks, Meanook, Bangor, and San Diego, and the auroral zone.

uncertainty regarding an averaged long-term, perhaps subtle, change in the background ionospheric D layer with sunspot number. The GTS Callaghan data (ref. 1, 71) was recorded during the previous sunspot minimum. Between June 1991 and February 1992, solar maximum data has been recorded aboard the Sea-Land container ship Ile de France during its regularly scheduled round trips between New York and Bremerhaven, Germany, every four weeks. Figure 12 shows a composite of its tracks to date, which covers the same general area as the routes sailed by the GTS Callaghan in 1985 and 1986 (shown in figure 7). The plan is to conduct the same analysis of the Ile de France data as had been used to determine ionospheric profiles from the GTS Callaghan data. Any difference in the D region between sunspot minimum and maximum should become apparent.

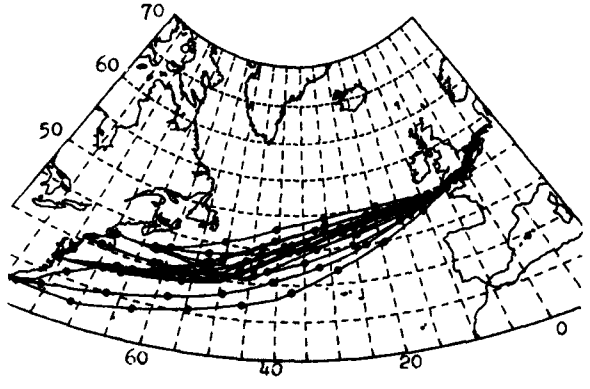

Fig. 12. Tracks of the Ile de France between June 1991 and May 1992.

4.6 Pacific Ocean Campaign

In June 1991, a VLF/LF receiving/recording system was installed on the Sea-Land container ship Spirit, which has been making its regularly scheduled runs from Long Beach to Hawaii, Yokahama, Oakland (CA), and returning to Long Beach, every 4 weeks. Analysis of the data is planned, also in a manner similar to that performed for the GTS Callaghan, to support US Navy VLF/LF systems coverage predictions in the Pacific Ocean.

5. THE RECEIVING/RECORDING SYSTEM, CALIBRATION, AND EXPERIMENTAL ERROR

Much valuable information can be obtained about a physical phenomenon by observing changes in signal level rather than making calibrated observations. For example, in VLF/LF propagation, one can learn about the propagation medium by recording the change in signal level from known locations within the inverse distance field, where no significant ionospherically reflected sky wave is present, to the field at greater distances using an aircraft or other vehicle. However, for observations at distant recording sites only, it is necessary to know the absolute field strength and the radiated power at the transmitting station in order to infer properties of the propagation medium. In this section, the receiving/recording system, the procedures used to calibrate it at its recording site, and the error due to uncertainty in the transmitting antenna radiated power, are discussed.

5.1 The VLF/LF Receiving/Recording System

A block diagram of the generic receiving/recording system is shown in figure 8. The Hewlett Packard 3586C Selective Level Meter shown is a self-calibrating RF voltmeter with a specified accuracy of 0.2 dB in the VLF/LF band. The pre-amplifier is of NOSC design and fabrication and has a nominal 50 ohm output impedance and a gain selectable at 20 dB or 40 dB. The whip antenna is a fiberglass covered wire completely insulated from the environment. Eight ground radials of #16 copper wire are normally extended to about 10-12 feet from the antenna for an antenna system ground plane. Out the back of the HP 3586C is available a 0 ± 0.1 dBm (at 50 ohm) reference signal which is injected into the preamp at the base of the whip through a computer-controlled VHF switch and a 10 pF capacitor. At fixed sites and aboard ships, the switch injects a calibration signal into the pre-amp twice a day and the resulting signal out of the pre-amp is recorded by the 3586C. This recorded calibration signal is plotted and examined to detect any gain drift of 0.1 dB or more or other malfunction of the antenna or pre-amp. The HP 9114 disk drive records propagation and calibration data on a 3 1/2 data disk, and the HPIL/IB interface allows the serial IL data stream from the HP-71 (hand-held) computer to control the IB, or parallel, devices of the system. The system records the RF voltage out of the pre-amplifier in dB relative to 1 volt. The primary requirement for the installation location is that it be an electrically quiet site that provides a good S/N ratio for the stations monitored.

5.2 Calibration

The recording system is calibrated by measuring absolute field intensity (in dB/μV/m) with a second system which is mobile, normally in a car. The difference between dB/μV recorded at the fixed site,

and dB/μV/m measured with the mobile calibrating system, yields dB/m, the calibration factor for the recording system and its E field antenna in its environment. The mobile equipment includes another HP 3586C selective level meter to measure RF voltage from a calibrated loop antenna. Normally, field intensity measurements are made at 4 to 6 selected locations within about 1/2 VLF wavelength of the recording site. An effort is made to choose sites that are at locations where there are no objects or terrain that may distort the loop measurements, such as nearby metal fences or other objects, overhead power lines, buried conductors, railroad tracks, buildings, hills and valleys, etc. If hills and valleys cannot be avoided, then an effort is made to include both so that their effect can be averaged. For example, Korchagin et al. (ref. 74), report a 10 to 16 dB increase in the VLF/LF field intensity on a 60 meter high hill and 8 dB at the peak of a 30 meter hill. Measurements made aboard a helicopter flying from 700 to 7000 feet altitude are reported by Harrison et al. (ref. 75), and indicate a decrease in the field perturbation with altitude above small hills. Bickel (ref. 37) observed the effect while flying over the foothills and high peaks of the Rocky Mountains in northwestern CONUS. Watt et al. (ref. 76) discuss the perturbations in field intensity measurements produced by the objects mentioned above and techniques for mitigating their effect.

The loop antenna used with the mobile calibration equipment is itself calibrated by placing it in an accurately known RF magnetic field and recording its output voltage. Garner et al. (ref. 77) discuss calibration of a loop by the generation of a standard field in a shielded enclosure excited by a wire transmission line that is stretched across the enclosure. Greene (ref. 78), and Jean et al. (ref. 79), analyze the coupling between two loops placed coaxially a distance apart and give equations that describe the coupling between them. This method was used at NELC when the current series of campaigns began in 1984. Today, a two-meter diameter Helmholtz coil, designed by A.D. Watt, is used to periodically calibrate the loop antenna used in the field. This latter method is preferred, since the placement of the loop relative to the source generating the field is not as critical (Smythe ref. 80).

Calibration data are recorded exactly simultaneously (through program control) at the fixed recording site and at the mobile sites. Ten frequencies are used normally, selected to include the strongest VLF/LF stations on the air the day the measurements are made. The system is described by McGrath (ref. 81). These data will yield 4 to 6 values (one for each mobile site) of whip antenna effective height "m", in meters, or dB/m, for each of the signals that are received with a good S/N ratio. Figure 13 is an example of the C-141 aircraft calibration results. These measurements were made with the calibrated loop about 50 ft. in front of the airplane at the various airports where it was parked. Figure 14 is an example of calibration data obtained for the GTS Callaghan on 24 October

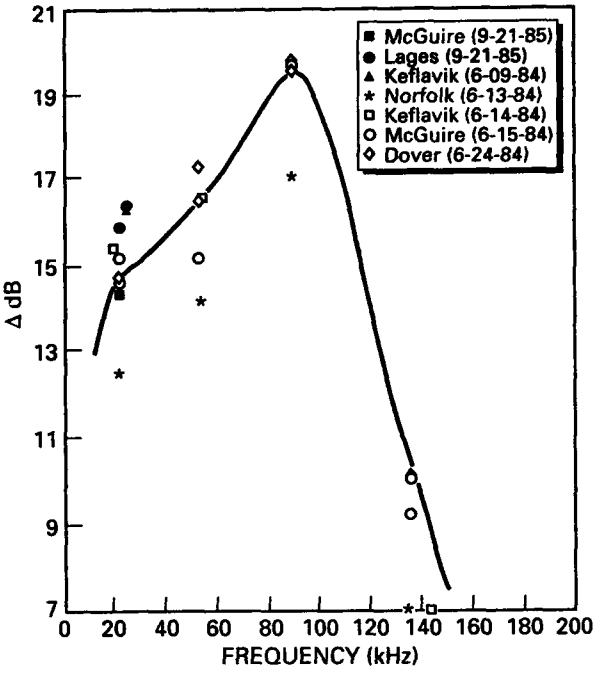

Fig. 13 Calibration factor curve for C-141 flights where the hatch blade antenna and preamp. serial #3 were used.

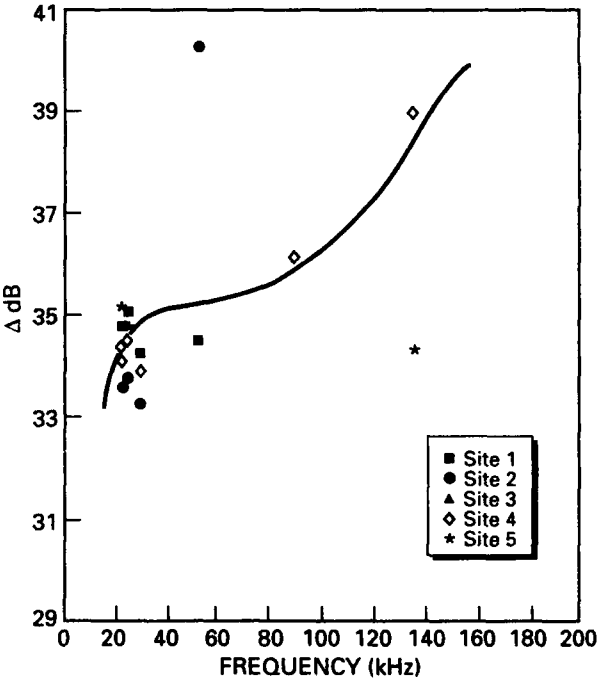

Fig. 14. Calibration curve for preamp. #8 and its 8-foot whip on the GTS Callaghan.

1985 while it was docked in New York harbor. The mobile measurements were made in various parks in the area. The frequency response curves of the pre-amplifiers, shown in both figures, are measured by injecting a constant signal into the antenna input of the preamp through a 20 pF capacitor used as

a dummy antenna. Calibration factors used to reduce recorded data are then taken from the response curve which has been adjusted to be the estimated best fit to the measured data points. Most of the data points in figures 13 and 14 are within ± 1 dB of the respective response curves.

A change in effective height of the shipboard VLF/LF receiving system, when the ship leaves a pier, has been observed. When the calibrated USCGC Northwind departed pier 5 at Norfolk (VA), there was a 1 dB increase in the measured signal level of 4 VLF/LF signals (ref. 73). There was nothing obvious about the environment around the pier that may have been responsible for this increase. Seven hours later, when the ship arrived at a different pier, and between two other large ships, there was a 2 to 3dB decrease, depending upon the frequency. These perturbations need to be allowed for when processing data recorded in open waters. The "pier effect" has not been observed with other ships, even though an effort has been made to look for it.

An indication of the accuracy of data recorded by the C-141 aircraft and the GTS Callaghan is obtained by comparing data recorded by them. During the September 1985 aircraft flights, the aircraft flew closely to the GTS Callaghan on two occasions while the ship was in the English Channel. They were 146 km apart at 1415 GMT on the 17th and 292 km from each other at 1145 on the 18th. Field intensity values of four stations, all beyond 1.5 Mm, were recorded on both platforms. When these data values are adjusted for the relatively small difference in position of the two platforms, the ship data averages 0.9 dB greater than the aircraft measurements, the range of the difference being from -0.4 dB to 2.9 dB. A possible difference due to height gain, where the aircraft altitude is at about 30,000 feet, has not been investigated.

Another comparison can be made using data recorded as the platforms approached, or left the area of, the three Annapolis (MD) transmitters on 21.4, 51.6, and 88.0 kHz, and the Driver (VA) transmitter on 77.15 kHz, where the inverse distance field was recorded. From these data, the radiated power of these transmitters was determined. The ship and aircraft data provided radiated powers that differed from -0.73 dB to 0.55 dB, with an average of - 0.1 dB. In this case, the aircraft was at a lower altitude as it approached or departed an airport.

These comparisons provide an indication of the repeatability, and suggest the accuracy obtained, using the adjusted frequency response curves plotted in figures 13 and 14. Much of the scatter shown is due to field perturbations from the immediate surroundings of the various calibration sites. The averaging of 10 to 20 calibration points leads to a determination of the signal field intensity averaged over the area in which recording site calibration measurements were made with the mobile system.

On a couple of occasions, the calibration measurements were being made near the end of the day when the propagation path involved was in day/night transition. The resulting calibration factor would vary with time. This phenomenon is illustrated in figure 15. Shown is a plot of the relative dB/V of Jim Creek (24.8 kHz) signal recorded at San Diego using the whip antenna, and the dB difference between it and a recording of the relative dB/V Jim Creek signal made using a loop antenna. The dB difference is relatively stable during the all daytime propagation conditions, but varies with time at night. This same phenomenon is being recorded at San Diego of Stockton (CA) on 55.5 kHz, and at Fairbanks of Adak (AK) on 57.9 kHz, and H.E. Holt (Australia) on 22.8 kHz. Parks (ref. 32), reported similar data recorded at Tracy (CA), and at Perth, Australia, (see figure 1). These observations illustrate that measurements made using a loop to calibrate a whip should be made during all-day conditions on the propagation path when modal interference is least likely to be present.

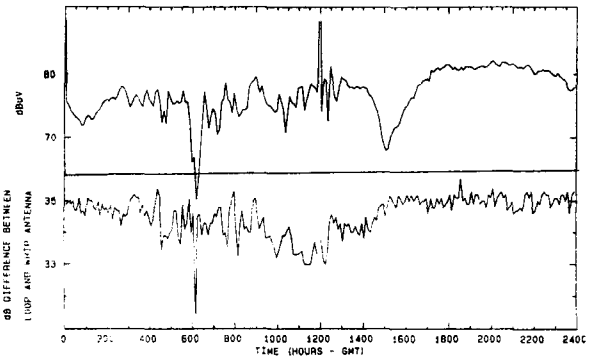

Fig. 15. Upper curve is relative dB/μV of Jim Creek 24.8 kHz recorded at San Diego using a whip antenna. Lower curve is dB difference between the simultaneous whip and loop antenna recordings.

An unexpected phenomenon observed at the HIPAS site near Fairbanks (AK), where the NRaD VLF/LF monitoring equipment is installed, is illustrated in figure 16. Shown is the apparent sinusoidal variation in the recording site calibration factor with direction of arrival of VLF/LF signals. This could possibly result from the very low conductivity permafrost in the area. Because of this, there may be no good ground plane and a buried metal conduit, carrying power lines within the site, can possibly be considered as one side of an asymmetrical dipole receiving antenna, the whip antenna being the other side. This dipole, having a vertical component and perhaps a very large horizontal component, since the effective electrical length of the pipe may be up to a mile long, couples to both a vertical E field and a horizontal E field. The horizontal E field can be present because of the very low conductivity permafrost in the area.

The standard deviation estimated for various sources of error in the NRaD VLF/LF propagation measurements, under ideal conditions, include:

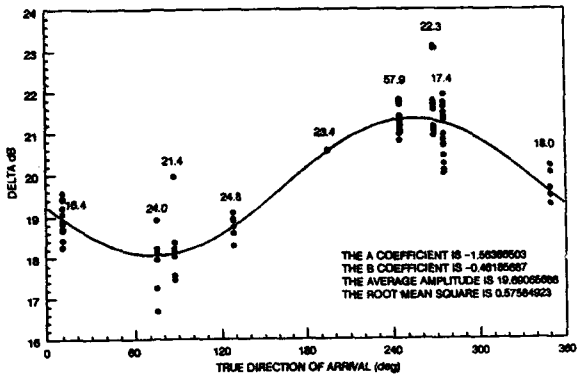

Fig. 16. Fairbanks calibration data vs bearing for preamp. #6, measured on 1 September 1990. The best-fit sine curve clearly illustrates the directional effect.

1. Fixed site HP 3686C recordings, 0.1 dB
2. Mobile site HP 3586C readings, 0.1 dB
3. Absolute cal. of loop antenna, 0.2 dB
4. Environmental variability of site, 0.4 dB
5. Instability of the pre-amp, 0.2 dB.

If each error is normally distributed, and varies independently of the others, the standard deviation of the overall measurement error is the square root of the sum of these uncertainties squared, or 0.5 dB. Therefore, 31% of the data have error greater than 0.5 dB and 5% of the data have error greater than 1.0 dB.

5.3 Transmitter Radiated Power

A knowledge of a station's radiated power may be necessary in order that the data are useful in verifying or improving the propagation prediction model. But, radiated power is derived from field intensity measurements which are made within the radiation field of the transmitting antenna and close enough so that the ionospherically reflected skywave is not significant. Therefore, the measurement is subject to the same error as measurements made in the distant field, or approximately 0.5 dB rms. Since the antenna current is usually measured to an accuracy of 1 % when the radiated power is determined, the 0.5 dB error represents an uncertainty of the radiation resistance of the transmitting antenna.

However, during routine operation of the stations, the antenna current does vary. Tietsworth (ref. 82) has developed and installed at four U.S. Navy LF stations an automatic transmitting antenna monitor that records the antenna RF voltage and current, and computes the radiated power for both the mark and the space frequencies, once per minute. These data show a variability in radiated power with a standard deviation of 0.2 dB. As before, the over all uncertainity of the radiated power of the LF stations is the square root of 0.2 squared plus 0.5 squared, or 0.5 dB rms. The antenna current variability at U.S. Navy VLF stations is generally less than at the LF stations (ref. 83).

6. CONCLUSION

Many environmental factors affect the measurement of VLF/LF field intensity. For the data to be most useful for developing and validating propagation prediction models, the local and environmental perturbations need to be understood and allowed for.

With a 0.5 dB standard deviation in the uncertainty of radiated power, and a 0.5 dB standard deviation in the uncertainty of measured field strength at a distant location, the overall experimental error is 0.7 dB rms. The error will be greater than 0.7 dB 31% of the time, and greater than 1.4 dB 5% of the time.

The above conclusion about experimental error involve the assumption of ideal experimental conditions. Much of the time, ideal conditions do not prevail.

* * * * *

7. REFERENCES

1. Ferguson, J.A., "Numerical Modeling of the Propagation Medium at VLF/LF", in "ELF/-VLF/LF Radio Propagation and System Aspects", AGARD Conf. Proc., Brussels, Belgium, 28 Sept.-2 Oct. 1992, Paper 1.

2. Thomson, J.J., "Notes on Recent Researches in Electricity and Magnetism", Oxford, UK, Clarendon Press, 1893, pp 388-406.

3. Marconi, S.G., "Radio Telegraphy", Proc. IRE, 10, 4 ,1922, p 215.

4. Marriott, R.H., "United States Radio Development", Proc. IRE, 5, 3, 1917, p 179.

5. Round, H.J., T.L. Eckersley, K. Tremellen and F.C. Lunnon, "Report on Measurements Made on Signal Strength at Great Distance During 1922 and 1923 by an Expedition Sent to Australia", IEE Journal, 63, 346, 1925, pp 933-1011.

6. Austin, L.W., "Long Distance Radio Receiving Measurements and Atmospheric Disturbances at the Bureau of Standards in 1925", Proc. IRE, 14, 5, 1926, p 663.

7. Bailey,A., S.W.Dean and W.T.Wintringham, "The Receiving System for Long-Wave Trans-Atlantic Radio Telephony", Proc. IRE, 16, 12, 1928, p 1645.

8. Espenschied, L., C.N. Anderson and A. Bailey, "Trans-Atlantic Radio Telephone Transmission", Proc. IRE, 14, 1926, p 7.

9. Hollingworth, J., "The Propagation of Radio Waves", IEE Journal, 64, 1926, pp 579-589.

10. Brown, R., "Radio Transmission Measurements", Proc. IRE, 11, 2, 1923, p 115.

11. Beverage, H.H. and H.O. Peterson, "Radio Transmission Measurements on Long Wave Lengths", Proc. IRE, 11, 6, 1923, p 661.

12. Austin, L.W. and E.B. Judson, "A Method of Measuring Radio Field Intensities and Atmospheric Disturbances", Proc. IRE, 12, 5, 1924, p 521.

13. Austin, L. W., "Tables of North Atlantic Radio Transmission Conditions for Long-Wave Daylight Signals for the Years 1922-1930", Proc. IRE, 20, 4, 1932, p 689.

14. de Mars, P.A., G.W. Kendrick and G.W. Pickard, "Use of Automatic Recording Equipment in Radio Transmission Research", Proc. IRE, 19, 9, Sept. 1931, p 1618.

15. Austin, L. W., "A Method of Representing Radio Wave Propagation Conditions", Proc. IRE, 19, 9, 1931, p 1615.

16. Austin, L.W. ,"Preliminary Note on Proposed Changes in the Constants of the Austin-Cohen Transmission Formula", Proc. IRE, 14, 1926, p. 377.

17. Bailey, A. and A.E. Harper, "Long-Wave Radio Transmission Phenomena Associated with a Cessation of the Sun's Rays", Bell System Technical Journal, 15, 1, 1936 pp 1-19.

18. Best, J.E., J.A. Ratcliffe and M.V. Wilkes, "Experimental Investigations of Very Long Waves Reflected from the Ionosphere", Royal Society of London Proc., 156A, 1936, pp 614-633.

19. Budden, K.G., J.A. Ratcliffe and M.V. Wilkes, "Further investigations of very long waves reflected from the ionosphere", Royal Society of London Proc., 171A, 1939, pp 188-214.

20. Stanley, J.P., "The absorption of long and very-long waves in the ionosphere", J. of Atmospheric and Terrestrial Physics, 4, 1950, pp 65-72.

21. Brown, J.N., "Round-the-World Signals at Very Low Frequency", J. Geophysical Research, 54, 4, 1949, pp 367-372.

22. Kitchen, F.A., B.G. Pressey and K.W. Tremellen, " A Review of Present Knowledge of the Ionospheric Propagation of Very-Low-, Low-, and Medium-Frequency Waves", IEE Proc., 100, 3, 1953, pp 100-108.

23. Norton, K.A., "Radio-Wave Propagation During World War II", Proc. IRE, 50, 1962, pp 698-704.

24. Pierce, J.A., "Sky-Wave Field Intensity I. Low and Very Low Radio Frequencies", Cruft Laboratory, Harvard University, Cambridge, MA, Technical Report No. 158, 1 Sept. 1952.

25. Dinger, H.E., W.E. Garner and G.E. Leavitt, " Measurements of some Low- and Very Low-Frequency Signal Intensities in the Alaskan Area", Naval Research Laboratory, Washington, D.C., report 3921, 18 Jan. 1952.

26. Dinger, H.E. and W.E. Garner, "A New Method of Calibrating Field Strength Measuring Equipment", Naval Research Laboratory, Memo report no. 83, 14 Nov. 1952.

27. Pickard and Burns, Inc., "VLF-LF Radio Noise and Propagation Measurement and Study Program", P&B Pub. no. 700-1, (prepared for Bureau of Ships) 9 volumes, 31 March 1961.

28. Maxwell, E.L., "VLF Propagation and Noise Measurements in the Pacific", DECO Electronics Inc., report no. 30-F-12, March 1966.

29. Rhoads, F.J. and W.E. Garner, "An Investigation of the Modal Interference of VLF Radio Waves", Radio Science, 2 (New Series), 6, June 1967, p 539.

30. Rhoads, F.J. and W.E. Garner, "An Investigation of the Modal Interference of Very-Low-Frequency Radio Waves", Naval Research Laboratory, report 6359, 27 October 1965.

31. Brookes, C.B. and J.E. Raudenbush, "Field Strength Measurements for NWC, North West Cape, Australia, from September to December 1967", Naval Research Laboratory, report 7148, 23 Sep. 1970.

32. Parks Jr.,G.S., G.H. Price, A.L. Whitson and H.W. Parker, "Measurements of VLF Wave-Front Components Over Long Paths", Stanford Research Institute, contract NObsr 85271 (FBM) with Dept. of Navy, Bureau of Ships, March 1964.

33. Chilton, C.J. and A.H. Diede, "Transequatorial Reception of Very-Low Frequency Transmission", J. of Geophysical Research, 69, 7, 1 April 1964, pp 1319-1328.

34. Ishii, T. and A. Sakurazawa, "Long-Term Amplitude Variation of the NPG-18.6 kc/s Signal on the TransPacific Transmission", J. of Radio Research Laboratories, 10, 54, March 1964, pp 63-74.

35. Budden, K.G., "The Propagation of Very Low Frequency Radio Waves to Great Distances", Phil. Mag. 44, 352, May 1953, pp 504-513.

36. Bickel, J.E., J.L. Heritage and S. Weisbrod, "An Experimental Measurement of VLF Field Strength as a Function of Distance, Using an Aircraft", Navy Electronics Laboratory, report 767, 28 Jan. 1957.

37. Bickel, J.E., "Aircraft Measurements of VLF Field Intensities in the Northern Hemisphere", Navy Electronics Laboratory, report 981, 5 August 1960.

38. Watt,A.D., E.L. Maxwell and E.H. Whelan, "Low-Frequency Propagation Paths in Arctic Areas", J. of Research of NSB, 63D, 1, July-August 1959, p 99.

39. Belrose, J.S. and B. Seagel, "On the Interpretation of CW Propagation Data for Long Radio Waves", COSPAR Conference "Methods of Measurements and Results of Lower Ionosphere Structure", Constance, F.R.G., May 1973, Akademie-Verlag, Berlin, 1974, pp 77-109.

40. Rogerson, J.E., "Airborne Field Strength Measurements in the Region of the NPM Antipode", Radio Science, 2 (New Series), 6, June 1967, p 581.

41. Rogerson, J.E., "Results of Airborne Field Measurements in the Antipodal Region of Radio Station NPM, Hawaii", Naval Research Laboratory, report 6373, 26 April 1966.

42. Bickel, J.E., "VLF Attenuation Rates Deduced From Aircraft Observations Near the

Antipode of NPM", Radio Science, 2 (New Series), 6, June 1967, p 575.

43. Snyder, F.P., J.E. Bickel and M.R. Paulson, "Antipodal-Field Measurements of VLF Transmitter NPM at Stationary Sites", Navy Electronics Laboratory, report 1294, 27 May 1965.

44. Bickel, J.E., J.A. Ferguson and G.V. Stanley, "Experimental observation of magnetic field effects on VLF propagation at night", Radio Science, 5, 1, January 1970, pp 19-25.

45. Morfitt, D.G., "Determination of Effective Ionospheric Electron Density Profiles for VLF/LF Propagation", Defense Communications Agency, report C650-TP-76-4, 1 Jan. 1976.

46. Morfitt, D.G., "Comparison of Predicted VLF/LF Signal Levels with Propagation Data", Defense Communications Agency, 960-TP-74-5, 21 January 1974.

47. Hildebrand, V.E. and D. J. Adrian, "VLF-Propagation Measurement Technique Using Repetitive-Pulse Spectral Lines", Naval Weapons Center, China Lake, CA., report NWC TP 5038, Feb. 1971.

48. Seeley, E.W. and D.A. Wulfing, "Broad-Band VLF Transmitting Stagger-Tuned Dipole", Naval Ordnance Laboratory Corona, Corona, CA, Report 653, 18 May 1966.

49. Wulfing, D.A. and V.E. Hildebrand, "Multiple-Frequency Oblique-Incidence VLF Ionospheric Sounder", Naval Ordnance Laboratory Corona, Corona, CA, report 722, 5 May 1967.

50. Bickel, J.E., "Measurements of Vertical and Horizontal VLF Fields Excited by an Elevated, Arbitrarily Oriented Antenna", Naval Electronics Laboratory Center, TR 1833, 21 July 1972.

51. Gallenberger, R.J. and J.E. Bickel, "Horizontal and Vertical Atmospheric Noise Measurements at VLF up to 20,000-feet Altitude", Naval Electronics Laboratory Center, TR 1793, 7 October 1971.

52. Ferguson, J.A., "Ionospheric Profiles for Predicting Nighttime VLF/LF Propagation", NOSC, TR 530, 25 Feb. 1980, NTIS ADA 085339.

53. Pappert, R.A., "A Numerical Study of VLF Mode Structure and Polarization Below an Anisotropic Ionosphere," Radio Science, 3 (new series), 3, 1968, pp.219-233.

54. Kossey, P.A., E.A.Lewis and E.C. Field, "Relative Characteristics of TE/TM Waves Excited by Airborne VLF/LF Transmitters", AGARD-CP-305, Brussels, Sep. 1981, paper 19.

55. Bickel, J.E., "Aircraft VLF/LF/MF Window Antenna Receiving System," U.S. patent no. 3,977,004, issued 24 Aug. 1976.

56. Kelly,F.J., F.J. Rhoads and J.A. Murray, "Low Frequency Radio Wave Propagation in the Atlantic and Mediterranean Areas", AGARD-CP-305, Brussels, Sep. 1981, paper 24.

57. Kelly, F.J. et al, "Developments in Arctic long-wave propagation theory and experiments", Radio Science, 23, 3, 1988, pp 240-246.

58. Dick, M.J., "Analysis of In-Flight Omega Data", Naval Electronics Laboratory Center, TR 1984, 8 April 1976.

59. Karkalik, F.G., G.F. Sage and W.R. Vincent, "Western Pacific Omega Validation", Systems Control, Inc., report no. ONSOD 01-78, April 1978.

60. Kugel,C.P., J.A. Ferguson, W.R. Bradford and J.E. Bickel, "Airborne and Ground-based Measurements in the Support of the Western Pacific Omega Validation", U.S. Coast Guard Omega Navigation System Operational Detail, report CG-ONSOD-02-78, 31, March 1978.

61. Campbell, L.W., T.M. Servaes and E.R. Grassler, "North Atlantic Omega Navigation System Validation", Analytical Systems Engineering Corp., report no. CG-ONSOD-01-80, 21 July 1980.

62. Levine, P.H., "North Pacific Omega Navigation System Validation", Megatek Corp., report no. CG-ONSOD-01-81, 31 Dec. 1981.

63. Hildebrand, V.E., "South Pacific Omega Validation Analysis", SRS Technologies, report no. CG-ONSCEN 02-89, August 1989.

64. Hildebrand, V.E., "Western Pacific Omega Validation Analysis", Visicom Laboratories, Inc., report no. CG-ONSCEN 03-90, August 1990.

65. Orsak,L.E., L.H. Rorden, G. B. Carpenter and B. P. Ficklin, "VLF Propagation and Noise in the Ionosphere Observed by Sounding Rockets", Stanford Research Institute, Final report on contract NASr-49(01), SRI project 3749, January 1965.

66. Harvey, R.B., R.P. Harrison, V.C. Fields, G.C. Hirst, P.A. Kossey and E.A. Lewis, "Rocket Investigations of the VLF Ionospheric Transmission Window", Air Force Cambridge Research Laboratories, report AFCRL-TR-73-0293, 7 May 1973.

67. Harrison, R.P., G.C. Hirst and E.A. Lewis, "Balloon Measurements of TE- and TM-Polarization in LF Waves From an Airborne Transmitter", Air Force Cambridge Research Laboratories, report AFCRL-TR-75-0613, 1 Dec. 1975.

68. Planck, P.V., R.C. Kahler and J.B. Donohoe, "VLF/LF Long Wave Propagation Study", Megapulse Inc., report RADC-TR-81-313, November 1981.

69. Turtle, J.P., J.L. Heckscher and P.A. Kossey, "TE/TM Height Profile Measurements of Transpolar VLF Signals", Rome Air Development Center, report RADC-TR-87-207, Oct. 1987.

70. Okada, T. and I. Nagano, "Rocket Experiment of VLF and MF Radio Wave Measurement by Using a Single Loop Antenna", Trans. of IEICE, E73, 2, 1990.

71. Hepner, T.A., "GTS Callaghan/C-141 VLF/LF Data 1984-1986" Computer Science Corp., NOSC, TD 1549, July 1989.

72. Hepner, T.A.,"Trans-CONUS 86 VLF/LF Data Acquisition Project", Computer Sciences Corp., NOSC TD 1362, Sept. 1988.

73. Hepner, T.A. and J.E. Bickel, "Arctic VLF/LF Data Acquisition", NOSC TD 2052, February 1991.

74. Korchagin, Yu. A. and I.P. Rozmanov, "VLF Surface Antennas on Surface Protuberances", Telecommunications and Radio Engineering, 40/41, 4, 1986, pp 72-76.

75. Harrison, R.P., J.L. Heckscher and E.A. Lewis, "Helicopter observations of very low frequency radio waves over certain mountains and shorelines", J. Atmos. and Terrestrial Physics, 33, 1971, pp 101-110.

76. Watt, A.D., E.L. Maxwell and R.W. Plush, "DECO VLF Field Strength Measuring Manual", Development Engineering Co (DECO), NRL contract Nonr-3399 (00), 25 January 1961.

77. Garner, W.E. and H.E. Dinger, "The Shielded Transmission Line Method of Generating Standard Fields", Naval Research Laboratory, NRL report 4451, 2 December 1954.

78. Greene, F.M., "NBS Field-Strength Standards and Measurements (30 Hz to 1000 MHz)", Proc IEEE, 55, 6, 1967, pp 970-981.

79. Jean, A.G., H.E. Taggart and J.R. Wait, "Calibration of Loop Antennas at VLF", J. of Res. of NBS, 65C, 3, July-Sept. 1961, pp 189-193.

80. Smythe, W.R., "Static and Dynamic Electricity", Mc Graw-Hill Book Company, New York, NY, 1968, pp 290-291.

81. McGrath, C.P., "PCVLF User's Guide", NOSC TD 2087, March 1991.

82. Tietsworth, S.C., "A New System for Measurement of Low Frequency Radio Transmitting Antenna Parameters in Near Real Time", IEEE Instrumentation and Measurement Society, Tech. Conf. record IMTC/91, Atlanta GA, 14-16 May, 1991.

83. Tietsworth, S.C., private communication.

VLF PROPAGATION MEASUREMENTS IN THE CANADIAN ARCTIC

by

Wilfred R. Lauber & Jean M. Bertrand
Communications Research Centre
3701 Carling Avenue
Ottawa Ontario CANADA
K2H 8S2

ABSTRACT

For the past three years, during a period of high sun spot numbers, propagation measurements have been made on the reception of VLF signals in the Canadian Arctic. Between August and December 1989 the received signal strengths were measured on the Canadian Coast Guard icebreaker, John A. MacDonald in the Eastern Canadian Arctic. Between July 1991 and June 1992 the received signal strengths were measured at Nanisivik, Baffin Island. The purposes of this work were to check the accuracy and estimate variances of the Naval Ocean Systems Center's (NOSC) Long Wave Propagation Capability (LWPC) predictions in the Canadian Arctic and to gather ionospheric storm data. In addition the NOSC data taken at Fort Smith and our data at Nanisivik were used to test the newly developed Longwave Noise Prediction (LNP) program and the CCIR noise predictions, at 21.4 and 24.0 kHz. The results of the work presented and discussed in this paper show that in general the LWPC predicts accurate values of received signal strength in the Canadian Arctic with standard deviations of 1 to 2 dB over several months. Ionospheric storms can cause the received signal strengths to decrease some 10 dB for a period of several hours or days. However, the effects of these storms are highly dependent on the propagation path. Finally the new LNP atmospheric noise model predicts lower values of noise in the Arctic than the CCIR model and our limited measurements tend to support these lower values.

INTRODUCTION

The purpose of this paper is to describe work done to test the validity of several propagation and noise models in the Canadian Arctic. The work began as technical support for the Canadian Submarine Program, to test the accuracy of the Naval Ocean Systems Center's (NOSC) Long Wave Propagation Capability (LWPC) to predict field strengths in the Canadian Arctic. Subsequently we became involved in the ONR/DNA (Office of Naval Research/ Defence Nuclear Agency) noise workshops from which Pacific Sierra produced a new Longwave Noise Prediction (LNP) program. The measurements discussed in this paper relate to both of the above mentioned models.

In 1989 an automatic monitoring system that was installed on a Canadian Coast Guard Icebreaker was used to measure received signal strengths in the Eastern Arctic. In June 1991 a similar system was installed at Nanisivik, on the Northern part of Baffin Island to record received signal strengths for a one year period. Since this measurement period coincided with the peak of the sun spot cycle, it has been possible to observe the effects of several ionospheric storms on received signal strengths. Finally the NOSC data collected at Fort Smith have been used to test the LNP noise model for four seasons. The Nanisivik data can also be used in a similar manner.

1989 MEASUREMENTS

In order to measure the received signal strengths across a wide area of the Arctic it was decided to use a mobile platform. Each year the Canadian Coast Guard has several icebreakers in the high Arctic for the purposes of supplying remote settlements and giving aid to Arctic shipping. In 1989 the ship that was scheduled to go to the highest latitudes and stay the longest above the Arctic Circle was the Canadian Coast Guard Ship (CCGS) John A. Macdonald. This ship was chosen as our monitoring platform. The northern limit of the trip was Tanquary Fiord, 81:30N and the western limit was 100:00W.

The LWPC [Ferguson,1989] was developed from data at mid-latitudes. This series of programs computes the received signal strength as a function of distance for a 1 kW transmitter from inputs of: transmitter location and frequency, date and time, bearing angle from the transmitter to receiver and maximum distance. The signal strengths are computed by obtaining modal solutions to a specific earth-ionospheric waveguide. The propagation path is treated as a series of horizontally homogeneous segments whose parameters are determined by the ground conductivity, height of the ionosphere and slope of the ionospheric profile.

EQUIPMENT

To reliably measure the received signal strengths from a number of existing fleet broadcast transmitters in the hostile electromagnetic environment of a ship and with the minimum of operator intervention, an automatic monitoring system was assembled, consisting of: an active antenna, a programmable field strength meter operating in the RMS mode with a 200 Hz bandwidth and a controlling and data logging personal computer (see Fig.1). With exception of the antenna, the equipment was shockmounted in a rack, which was installed in the ship's radio room.

The system was controlled by a program written in the ASYST control and data logging language. The program: tuned the receiver, calibrated the receiver and measured the actual frequency and

signal level (automatically selecting the input attenuation to ensure an onscale reading). Each of the nine frequencies, as listed in Table 1, was sampled every ten minutes. At the end of the program, which ran for 11.5 hours, the data were written on disk along with the start time, date and the ship's location at the start of the program. A limitation of the software package would not allow the program to run over 2359 to 0001 UT. This was the primary reason for running 11.5 hour programs. It also gave the operator more flexibility, *ie*, a longer time interval in which to restart the program in case he was busy.

Table 1 1989 Monitored transmissions

FREQUENCY	NAME	LOCATION
16.0 kHz	RUGBY U K.	52:22N, 1:11W
19.0 kHz	ANTHORN U.K	54:55N, 3:16W
21.4 kHz	ANNAPOLIS MARYLAND	38:59N, 76:28W
23.4 kHz	RHAUDERFEHN GERMANY	53:06N, 7:35E
24.0 kHz	CUTLER MAINE	44:36N, 67:17W
48.5 kHz	SILVER CREEK NEBRASKA	41:15N, 97:55W
51.6 kHz	ANNAPOLIS MARYLAND	39:00N, 76:30W
73.6 kHz	NEWPORT CORNER N.S.	44:57N, 63:58W
88.0 kHz	ANNAPOLIS MARYLAND	39:00N, 76:28W

The propagation paths for receiving locations in the Canadian Arctic from these transmitters are either South to North over northern Canada or East to West over the Greenland Icecap.

The DUK active vertical antenna was a one-metre whip which had an upper frequency cutoff of 250 kHz. It was mounted on the port crane stanchion post (about 18.3 metres above the water) next to the main HF receiving whip. It was connected to the receiving system with 30 metres of RG-214 coaxial cable. The antenna could not be characterized as a short vertical whip over a perfect ground but was in reality a short vertical whip over a 91.4 metre icebreaker over a perfect ground. Thus, it was necessary to empirically calibrate the antenna in its measurement configuration. Measurements to determine values for the Antenna Factor of the system antenna were made with a calibrated loop antenna while the ship was sailing from St. John's Nfld. to Dartmouth N.S. on August 10th and 11th. One value was also obtained during a sea trial, 8 km outside St. John's harbour on August 9th. Since two of the main calibration signals, *ie*, ANNAPOLIS at 21.4 kHz (except just before reaching Dartmouth) and NEWPORT CORNERS at 73.6 kHz were off the air during this period, measurements were taken on three other strong signals, *ie*, ANNAPOLIS at 18.1 kHz, ANTHORN at 19.0 kHz and NORFOLK VIRGINIA at 77.1 kHz. The loop measurements were made with the loop located on the front deck of the ship (measurements taken at various locations on the ship during the refit in St. John's showed very little variation and the front deck was the least obstructed part of the ship) and simultaneous measurements were made on the system antenna. The values of the Antenna Factor (AF in dB/m) (see Table 2 below) were calculated from the following equation:

AF = FI - SYSTEM

where FI is the received field strength in dB above 1μv/m as measured with a calibrated loop antenna and SYSTEM is the measured antenna reading in dB above 1μV.

Table 2 Antenna Factors of the system antenna

DATE/TIME	FREQUENCY (kHz)					
	18.1	19.0	21.4	24.0	51.6	77.1
Aug 09/15:30ADT					-16	
Aug 10/09:30ADT				-16		
Aug 10/13:00ADT	-16			-15	-16	
Aug 10/18:40ADT				-16		
Aug 11/09:50ADT	-17	-16		-17		
Aug 11/13:30ADT		-17		-16	-14	-17
Aug 11/17:30ADT			-17			

These values were consistant over the frequency range and thus a value of -16 dB/m was used in the subsequent calculations.

DATA COLLECTION

The original plan was for the ship to sail to the Arctic on July 25th. However, delays in a refit put off the departure until August 17th. Spikes on the ship's power supply blew a varistor on the automatic monitoring system's power conditioner before the start of the trip. This subsequently put a ground fault on the ship's power supply. The fault was not discovered until the ship was underway to the Arctic and resulted in the monitoring system being powered down for several days. When the receiver was powered up after being off for several days its frequency calibration had shifted (tests in Ottawa before installation had predicted this type of behaviour since the receiver is tuned by means of a linear VCO but the Ottawa tests did not predict the extent of the shift). After several weeks of operation the frequency calibration stabilized, however, at frequencies 300 to 400 Hz above the correct tuning frequencies. This problem was not corrected until October during a visit to the ship at Nanisivik at which time the system was retuned. After this was done the tuning remained correct for the remainder of the trip. This problem rendered the September data useless for signal strength measurements.

At the end of the trip, in Halifax, the signal levels of each transmitter in a frequency range from -400 Hz to +400 Hz in 50 Hz steps around the nominal frequency were measured (Note: the receiver bandwidth was 200 Hz). This provided correction factors and limitations for recovering some of the off-frequency data.

The data, which consist of sets of amplitude and frequency measurements of the nine monitored transmissions taken ten minutes apart for a period of 11.5 hours (some data cover three or eight hour periods), have been analyzed for the following days: August 22nd to 29th, October 13th to October 31st, November 1st until November 29th (during a fierce storm in Gulf of St Lawrence at the end of the trip).

The August data consist of measurements: along the Labrador coast, in Davis Strait, Baffin

Bay, Jones Sound and up the West coast of Ellesmere Island to Eureka.

The October data consist of measurements: at Nanisivik, across Lancaster Sound, Navy Board Inlet, Eclipse Sound to Pond Inlet, back across Lancaster Sound to Little Cornwallis Island and back to Clyde River.

The November data consist of measurements: from Clyde River to Pangnirtung (in Cumberland Sound), up Baffin Bay to the eastern edge of Lancaster Sound, north of Bylot Island and back down Baffin Bay, Davis Strait, along the coast of Labrador and into the Gulf of St. Lawrence west of Newfoundland.

ANALYSIS

Since the ship could be viewed as a slow moving platform, it was felt that recording its position at the start of each data run would be adequate. In fact, for a significant portion of the trip, the ship was in a specific location for several days.

The diurnal pattern of VLF/LF received signal strength consists of two long periods of stable levels (day and night with the nighttime level being some 10 dB above the daytime level) with two transition periods at sunrise and sunset (sunrise and sunset being defined as the time when the terminator passes between the transmitter and the receiver). Therefore, it was decided to analyze the data at local noon and local midnight for the receiver (1700 UT and 0500 UT), although all the other data do exist. The data for the RHAUDERFEHN transmitter were analyzed at 1600 UT and 0400 UT because 1700 UT and 0500 UT were found to be in the midst of the day-night transition periods.

To test the accuracy of the NOSC propagation model, the following comparison equation was used:

DELTA = CALCULATED FI - MEASURED FI

where MEASURED FI is the received amplitude in dB above 1μV plus the system Antenna Factor (-16 dB/m) and CALCULATED FI is the level for a 1 kW transmitter in dB above 1μV/m plus a POWER term in dB which accounts for the actual radiated power of the transmitter. The following POWER terms were used in this analysis:

16 dB (40 kW)	for RUGBY	at 16.0 kHz
17 dB (45 kW)	for ANTHORN	at 19.0 kHz
23 dB (213 kW)	for ANNAPOLIS	at 21.4 kHz
29 dB (750 kW)	for CUTLER	at 24.0 kHz
18 dB (60 kW)	for SILVER CREEK	at 48.5 kHz
6 dB (4 kW)	for ANNAPOLIS	at 51.6 kHz
22 dB (160 kW)	for NEWPORT CORNER	at 73.6 kHz
7 dB (5 kW)	for ANNAPOLIS	at 88.1 kHz

These values came from various sources. Values for RUGBY, ANTHORN and SILVER CREEK came from Canadian frequency allocation tables. Values for ANNAPOLIS and CUTLER came from NOSC measurement reports [Hepner,1988] and [Hepner,1989]. Finally, the value for NEWPORT CORNER came from private comunications with Canadian Department of National Defence personal.

The LWPC computes the received signal strength as a function of distance for a specific 1 kW transmitter at a specified date and time along a specified bearing. Each profile takes 30 minutes of computer time on the CRC VAX-750 (a newer VAX 3800 has reduced this time to about 5 minutes). To reduce the computer time, profiles were calculated for 5 degree bearing increments and for one date per month. Preliminary runs for the first, middle and end of the month showed no significant differences in the computed profiles, likewise for intermediate bearings. Thus, for the August data, August 25th was the comparison date, for the October data, October 15th was the camparison date and for the November data, November 15th was the comparison date.

The results of this analysis for each transmitter were grouped together to produce a cumulative distribution of DELTA's for each frequency. Because of the relatively low powers, 4 and 5 kW respectively, the received signal levels were too low for the data from ANNAPOLIS at 51.6 and 88.0 kHz to be used in this analysis. The received signal levels from the RHAUDERFEHN transmiter were more variable than the other transmitters. For most of the measurement program it was observed that the transmitter power was cycled between 'high' and 'low' every hour, thus producing a pulsed waveform as a function of time, see Fig.2. The 'high' levels were used in this analysis. The cumulative distributions for all the transmitters are presented in Figs.3 to 6. From the cumulative distributions, as shown in Table 3 below, it appears that the LWPC seems adequate for predicting received field strengths in the Canadian Arctic under normal conditions. Because the ship was a moving platform these results give a variation that consists of both time and location variability.

Table 3 Summary of DELTA

TRANSMITTER	# POINTS	MEDIAN	MEAN	STD DEV
RUGBY	81	+00 dB	1.4dB	5.8dB
ANTHORN	88	+01 dB	2.6dB	7.5dB
ANNAPOLIS	92	-01 dB	-0.5dB	4.6dB
RHAUDERFEHN	65	-26 dB	-24.6dB	7.0dB
CUTLER	89	+02 dB	2.8 dB	6.2dB
SILVER CREEK	46	-07 dB	-6.4dB	8.1dB
NEWPORT CRNR	58	+03 dB	1.2 dB	9.8dB

There was great uncertainty in estimating the radiated power of the SILVER CREEK transmitter. From Table 3, assuming the predictions are accurate, it seems that its true radiated power is about 200 kW. Also, the RHAUDERFEHN transmitter seems to be radiating about 650 kW. The high values of standard deviation are in part caused by including data taken during a major ionospheric storm in October 1989 (the effects of this storm are discussed below).

1991/92 MEASUREMENTS

In order to eliminate the location variability and to collect data over a longer time period it was decided to install a modified version of the monitoring system at Nanisivik, NWT,(74:03N, 84:33W) at the northern tip of Baffin Island, near Lancaster Sound. The choice of this location was based on several

factors, in addition to it being located well above the Arctic Circle and near one of the major sea-lanes in the Arctic. One of these was that this town is very radio quiet, *ie*, no above-ground power lines. The cutoff frequency of the antenna at 250 kHz protects against local broadcast transmitters affecting the results. The operating program was extended to 20 hours, with a four-hour leeway for the operator. The data disks were mailed to CRC on a weekly basis. This allowed for corrective action to be taken if the system started to drift off frequency.

The list of the nine monitored frequencies, as shown below, in Table 4, was modified to include JIM CREEK, a West to East path and AGUADA, a long South to North path. The path lengths vary from 3.2 to 4.5Mm except for AGUADA which is 6.2Mm.

Table 4 1991 Monitored transmissions

FREQUENCY	NAME	LOCATION
16.0 kHz	RUGBY U K.	52:22N, 1:11W
19.0 kHz	ANTHORN U.K	54:55N, 3:16W
21.4 kHz	ANNAPOLIS MARYLAND	38:59N, 76:28W
23.4 kHz	RHAUDERFEHN GERMANY	53:06N, 7:35E
24.0 kHz	CUTLER MAINE	44:36N, 67:17W
24.8 kHz	JIM CREEK WASHINGTON	48:12N, 121.55W
28.5 kHz	AGUADA PUERTO RICO	18:24N, 67:11W
48.5 kHz	SILVER CREEK NEBRASKA	41:15N, 97:55W
73.6 kHz	NEWPORT CORNER N.S.	44:57N, 63:58W

The antenna, which was the same antenna as was used in the 1989 measurements, was mounted on a steel mast, 9.75m above the ground at Nanisivik. As in 1989 the antenna was calibrated *in situ* to determine values for the Antenna Factor. Measurements were made on two nights in June 1991 and repeated in 1992 with the results shown below in Table 5.

Table 5 Antenna Factors of the system antenna at Nanisivik

DATE	FREQUENCY (kHz)				
	21.4	23.4	24.0	24.8	48.5
Jun 22/91	-24		-25	-20	-26
Jun 24/91	-26	-20	-26	-20	-25
Jun 11/92	-24	-19	-27	-20	-24
Jun 12/92	-24	-20	-25	-20	-23

These values were consistant over the frequency range and thus a value of -25 dB/m was used in all the subsequent calculations.

DATA COLLECTION AND ANALYSIS

Measurement data were collected continuously from June 1991 until June 1992 with very few missed days. Since these were the first data collected by us over the winter period, this paper presents the results of the analysis of the measurement data from December 1991 until May 1992 inclusive for: RUGBY, ANTHORN, ANNAPOLIS, RHAUDERFEHN, CUTLER and JIM CREEK.

To test the accuracy of the NOSC propagation model, the comparison equation defining DELTA, as used in the 1989 analysis, was used here:

DELTA = CALCULATED FI - MEASURED FI

where MEASURED FI is the received amplitude in dB above 1μV plus the system Antenna Factor (-25 dB/m) and CALCULATED FI is the level for a 1 kW transmitter in dB above 1μV/m plus a POWER term in dB which accounts for the actual radiated power of the transmitter. The following POWER terms were used in this analysis:

16 dB (40 kW)	for RUGBY	at 16.0 kHz
17 dB (45 kW)	for ANTHORN	at 19.0 kHz
23 dB (213 kW)	for ANNAPOLIS	at 21.4 kHz
28 dB (650 kW)	for RHAUDERFEHN	at 23.4 kHz
29 dB (750 kW)	for CUTLER	at 24.0 kHz
24 dB (250 kW)	for JIM CREEK	at 24.8 kHz

These values came from various sources. Values for RUGBYand ANTHORN came from Canadian frequency allocation tables. Values for ANNAPOLIS, JIM CREEK and CUTLER came from NOSC measurement reports [Hepner,1988] and [Hepner,1989]. Finally, the value for RHAUDERFEHN came from the 1989 results as shown in Table 3 above.

The model and the measurements were compared at 1700 and 0500 UT. The data were divided into two seasons; Winter (December, January and February) and Spring (March, April and May). Cumulative distributions of the DELTA's for each frequency and season were produced (see Figs. 7 to 10) and summarized in Table 6

Table 6 Summary of DELTA

TRANSMITTER	# POINTS	MEDIAN	MEAN	STD DEV
	WINTER			
RUGBY	180	+06 dB	6.8dB	7.4dB
ANTHORN	181	+04 dB	6.4dB	6.2dB
ANNAPOLIS	169	-02 dB	-1.2dB	1.4dB
RHAUDERFEHN	182	+02 dB	2.3dB	3.5dB
CUTLER	170	+06 dB	7.1 dB	3.0dB
JIM CREEK	162	+00 dB	0.7 dB	2.6dB
	SPRING			
TRANSMITTER	# POINTS	MEDIAN	MEAN	STD DEV
RUGBY	162	+10 dB	7.7dB	6.3dB
ANTHORN	174	+11 dB	10.3dB	5.3dB
ANNAPOLIS	167	-02 dB	-1.4dB	1.6dB
RHAUDERFEHN	180	+06 dB	7.4dB	6.4dB
CUTLER	169	+05 dB	5.3 dB	2.2dB
JIM CREEK	176	+01 dB	1.6 dB	1.6dB

To explain these results one must consider a number of factors: transmitter power, path, and monitoring system calibration. For ANNAPOLIS the transmitter power is known and, as seen from the measured data, it does not seem to vary. The signal path passes over very little poorly conducting soil, *ie*, it traverses Hudson Bay and then small land areas of the Arctic. Therefore, the one to two dB difference is very easily explained by measurement system uncertainties. The standard deviation of 1 - 2 dB shows very consistent results. Similar comments apply to JIM CREEK except that it's signal path traverses a large portion of Arctic tundra. The low values of

DELTA and standard deviation show that the model is accurate for this area. However, for the Cutler path there seems to be a problem. The signal path traverses a large portion of the Canadian Shield. The 1991/92 results seem different from those in 1989 (see Table 3. One explanation is that the transmitter was only radiating about 400 kW in 1991/92.

The signal paths for the other three transmitters cross the Greenland icecap. The RHAUDERFEHN winter data show good agreement with the model predictions. However, the spring data seem to be affected by a lower transmitter power for part of April and May. Both RUGBY and ANTHORN seem to be operating at regular power and at one quarter power (*ie* 40 to 45kW and then 10 to 11kW) for most of the measurement time . This showed up as a double peak on the density distribution of the DELTA data and then as a step in the curve of the cumulative distribution as shown in Figs.8 and 10. Separating out these data would show a much clearer picture.

STORM DATA

The causes of ionospheric storms and their effects on VLF signal strengths have been discussed in the past [Field,1970]. However, very little data show the occurrence rate, *ie*, how many per year or month. Also, as far as the NOSC LWPC is concerned, Polar Cap Absorption events (PCAs) are an anomaly and are not dealt with in the model statistics.

There was a major ionospheric disturbance in October 1989 (see Proton Flux in Fig.11a [US Department of Commerce,1989]) that affected the received signal levels from the different transmitters to varying degrees from the 19th until the 26th. From time plots of the DELTAs (Calculated FI - Measured FI) from four transmissions, two North/South and two East/West over the Greenland icecap into the Lancaster Sound area during the storm one can make some interesting observations (see Fig.11b,c,d,e). Note that a positive DELTA means an attenuated signal. Also the - - - mean no data were available. The reception of the ANNAPOLIS, 21.4 kHz, transmission which was on a path over a small part of the Canadian Shield and then over Hudson's Bay was attenuated only for periods of a few hours on the 20th and the 23rd. The CUTLER, 24.0 kHz, transmission which was on a path over a major portion of the Canadian Shield was attenuated in two stages for several days at a time. The first was from the 19th to the 21st and the second more serious attenuation from the 22nd to the 27th. Both the RUGBY, 16.0 kHz, and ANTHORN, 19.0 kHz, transmissions which were on paths over the Greenland icecap were attenuated during the early part of the storm from the 19th to the 24th, with the RUGBY transmission recovering more quickly than ANTHORN.

One can use the NOSC model to explain what was happening to the earth-ionospheric waveguide during the storm. The ionospheric profile model is defined by an exponential in conductivity with height specified by a slope, β, in km^{-1} and a reference height, h, in km. For the daytime period the standard model values for these parameters are $\beta = 0.3$ km^{-1} and $h = 74$ km During a storm the reference height is lowered, thus, increasing the signal attenuation. For the ANTHORN data, signal level predictions were computed for various values of h and compared with the measured results. Values of 45, 30 and 24 dB above 1 μV/m were calculated for reference heights of 74, 60 and 56 km respectively at 1700 UT. On October 19th and 21st the measured field intensity from ANTHORN at 1700 UT was 24 dB above 1 μV/m. Also on October 22nd the measured field intensity was 29 dB above 1 μV/m. These results show that the storm lowered the reference height to about 56 km for the period from the 19th to the 21st and then the reference height recovered to about 60 km by the 22nd. Over the same period of time the measured field intensity of 29 dB above 1μV/m at 0500 UT was compared with calculated values of 49, 51, 44, 34 and 29 dB above 1 μV/m for reference heights of 80, 70, 60, and 56 km respectively. Again these show the reference height was depressed to about 56 km during the peak of the storm.

During the measurements at Nanisivik three ionospheric storms occurred; one in August 1991, and one in February 1992 and one in May 1992. The August storm occurred between August 26th and about the 30th peaking on the 28th (see Proton Flux in Fig.12a [US Department of Commerce,1991]). The ANTHORN transmitter was off during this storm. Also the monitoring system was experiencing tuning problems on the RUGBY and JIM CREEK frequencies. The effects of this storm do show up on the ANNAPOLIS data (for one day) and the CUTLER data as shown in Fig.12b,c. The February storm occurred between February 7th and 9th (see Proton Flux in Fig.13a [US Department of Commerce, 1992]). It had a negligible effect on the ANNAPOLIS and JIM CREEK paths as shown in Fig.13b and c and a small effect on the CUTLER path, Fig13d. The RUGBY path, Fig 13e, showed the largest effect.This storm also had very little effect on the RHAUDERFEHN transmission (see Fig 13f). The May storm occurred late on May 9th and continued for several days (see Proton Flux in Fig 14a [US Department of Commerce, 1992]). Unfortunately the system was off on May 9th. The effects of the storm were only seen on the RHAUDERFEHN path, Fig 14b. the North American paths from ANNAPOLIS, CUTLER and JIM CREEK were unaffected as shown in Figs 14c,d,e.

NOISE MEASUREMENTS

Over the years there has been some doubt concerning accuracy of CCIR atmospheric noise predictions in the Canadian Arctic. With the release of the new LNP model it was decided to test the CCIR model [CCIR,1988] and the new Longwave Noise Prediction (LNP) model [Warber & Field,1991, Warber,1991] with some NOSC data being collected in the Canadian Arctic. The operational characteristics of these channels were used to our advantage, *ie*, when a transmitter is off then no one else is on the frequency. It has been observed that the CUTLER transmitter at 24.0 KHz is regularly shut down on Mondays during the daytime and the ANNAPOLIS transmitter at 21.4 KHz is regularly shut down on Tuesdays during the daytime.The NOSC data were collected at Fort Smith (60:00N, 112:00W) between December 1989 and November 1990 using an RMS measuring circuit with

a bandwidth of 400 Hz and a short vertical monopole antenna. The measured data were in terms of received Field Strength, the LNP model gives the noise in terms of received Field Strength and the CCIR model gives the noise predictions in terms of Field Strength (EN) with the following equation:

$$EN = Fa + 20 \log F - 95.5 + 10 \log b$$

where Fa is the CCIR noise parameter, F is the frequency in MHz and b is the bandwidth in Hz.

The data were compared with the CCIR predictions for the 0800 to 1200 local time period and for 1600UT (0830 local time) for the LNP model. The median and standard deviation for the CCIR model, the LNP model and the measurements are shown in the Table 7. N is the number of measurement points. Figs.15 to 18 show the median values for the two models and the measurements.

Table 7 Noise field strength at Fort Smith

SEASON	CCIR		LNP		MEASURED		
FREQ	MEDIAN	STD	MEDIAN	STD	MEDIAN	STD	N
SPRING							
21.4	31.2	3.9	27.7	4.0	24	6.8	13
24.0	29.0	4.1	26.1	3.9	22	2.1	15
SUMMER							
21.4	36.2	3.5	32.8	4.6	32	0.9	7
24.0	34.2	3.7	30.9	4.6	29	3.5	13
AUTUMN							
21.4	34.5	5.0	33.4	4.6	23	2.5	11
24.0	32.7	5.2	32.0	4.6	22	3.4	10
WINTER							
21.4	32.4	5.6	23.0	4.1	20	3.3	11
24.0	30.3	5.8	21.9	4.2	24	2.8	9

The data tend to favour the new theoretical LNP model over the empirical CCIR model. However, as shown in Fig.18, there is a problem with the frequency variation predicted by the LNP model for the winter season. The general shape of the noise level versus frequency graph was expected to be monotonically decreasing with frequency as was seen in the figures for the other three seasons. At this site the two models predict quite different values except for the autumn season. Also the LNP model always predicts the lower value of the two models.

CONCLUSIONS

1) The LWPC seems to be able to predict accurate values of the received signal strength in the Eastern Canadian Arctic. When the radiated power is known the standard deviation may be as low as 1 to 2 dB over several months. However, during periods of ionospheric storms (possibly three times a year near sunspot maximum) the received signal strengths will decrease some 10 dB for a period of several hours or days. The effects of such storms are highly dependent on the propagation path, with paths crossing the Greenland icecap being most affected.

2) The new theoretical LNP atmospheric noise model predict lower values of noise in the Arctic than the CCIR empirical model and measurements tend to support these lower values.

ACKNOWLEDGEMENTS

We would like to thank Captain D.H. Johns of the Canadian Coast Guard for permission to use the CCGS John A. Macdonald in this work. We would also like to thank Captain G. Barry and the crew of the CCGS John A Macdonald, especially the radio operators, W.E. Fontaine and J.W. Walker for their cooperation.

We would like to thank W. McNeil, manager of Nanisivik Mines Limited for permission to locate our equipment at Nanisivik. We especially thank R.K. Light for his cooperation and E.T. Rowan our operator at Nanisivik for his cooperation.

REFERENCES

CCIR, "Characteristics and Applications of Atmospheric Radio Noise Data", Report 322-3, International Telecommunications Union, Geneva Switzerland, 1988.

E.C. Field, "The Effects of Ions on Very-Low-Frequency Propagation During Polar-Cap Absorption Events", Radio Science, Vol 5 Number 3, Pages 591-600, March 1970.

J.A. Ferguson, F.P. Snyder, "Long-Wave Propagation Capability Program Description and User's Guide", Naval Ocean Systems Center Technical Document 1449, San Diego, California, January 1989.

T.A. Hepner, "TRANS-CONUS 86 VLF/LF Data Acquisition Project", Naval Oceans Systems Center Technical Document 1362, San Diego, California, September 1988.

T.A. Hepner, "GTS Callaghan/C-141 VLF/LF Data 1984 - 1986", Naval Ocean Systems Center Technical Document 1549, San Diego, California, July 1989.

Preliminary Report and Forecast of Solar Geophysical Data, US Department of Commerce, Space Environment Services Center, weekly bulletin, Boulder Colorado, weekly 1989, 1991, 1992.

C.R. Warber & E.C. Field, "Long Wave Noise Prediction; Vol. 1 Physical Basis of the Model, Pacific Sierra Research Corporation Report 2137, Los Angeles California, April 1991.

C.R. Warber, "Long Wave Noise Prediction; Vol. 2 User's Guide to the Computer Code LNP Version 1.1, Pacific Sierra Research Corporation Report 2137, Los Angeles California, September 1991.

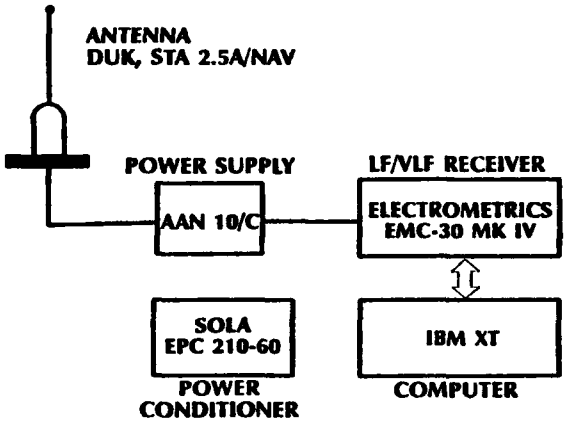

Fig.1 Block diagram of automatic monitoring system on the CCGS John A. MacDonald

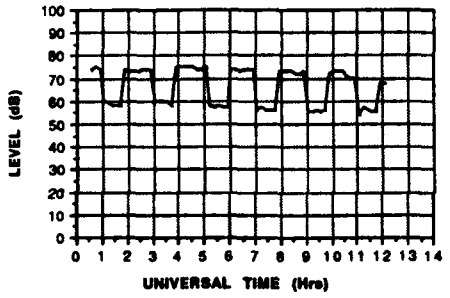

Fig.2 Time waveform of the RHAUDERFEHN signal, Nov 20, 1989

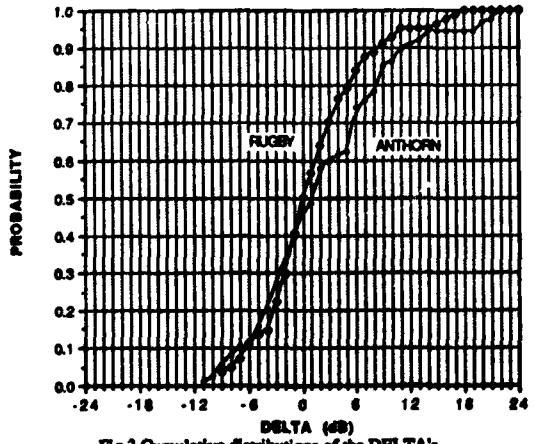

Fig.3 Cumulative distributions of the DELTA's from the CCGS John A. MacDonald

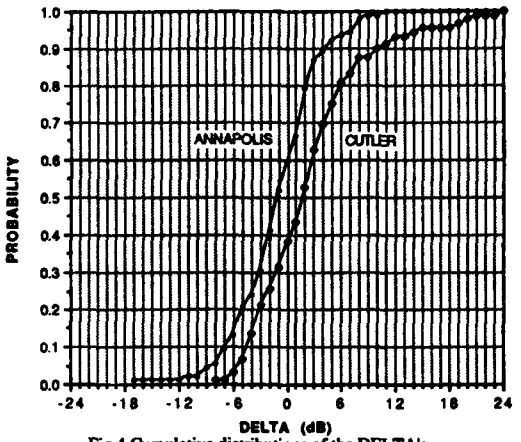

Fig.4 Cumulative distributions of the DELTA's from the CCGS John A. MacDonald

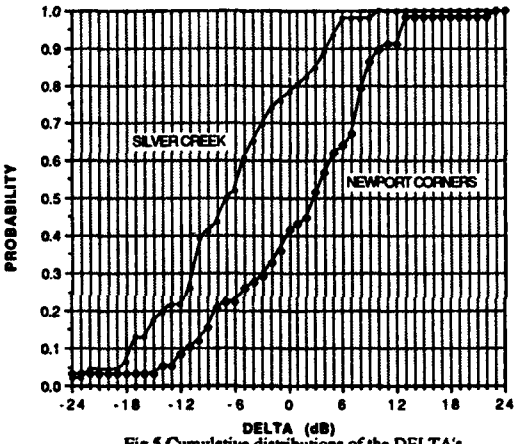

Fig.5 Cumulative distributions of the DELTA's from the CCGS John A. MacDonald

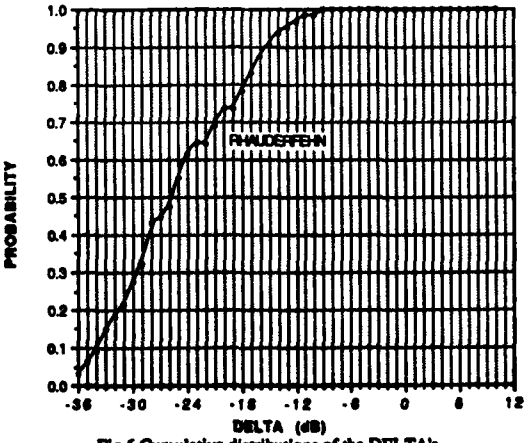

Fig.6 Cumulative distributions of the DELTA's from the CCGS John A. MacDonald

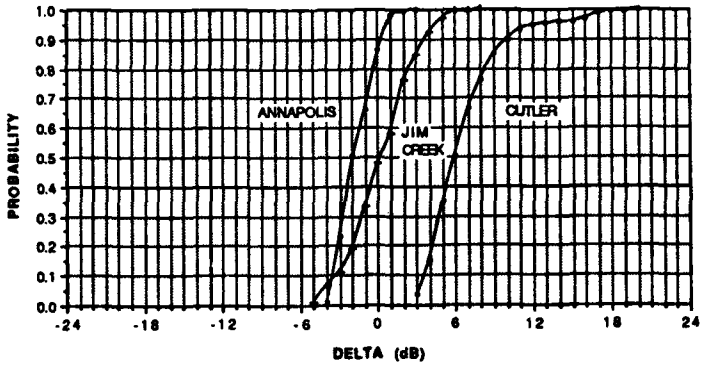

Fig.7 Cumulative distributions of the DELTA's as measured at Nanisivik in Winter

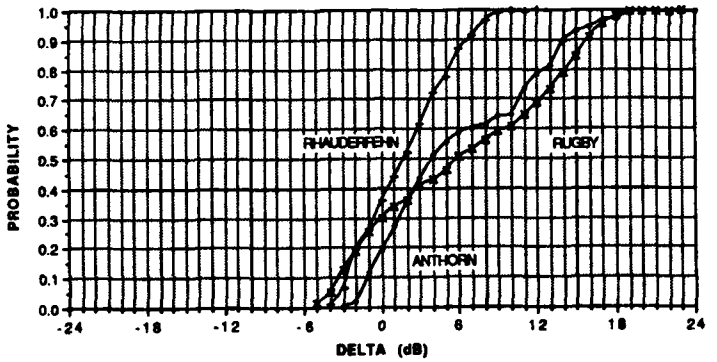

Fig.8 Cumulative distributions of the DELTA's as measured at Nanisivik in Winter

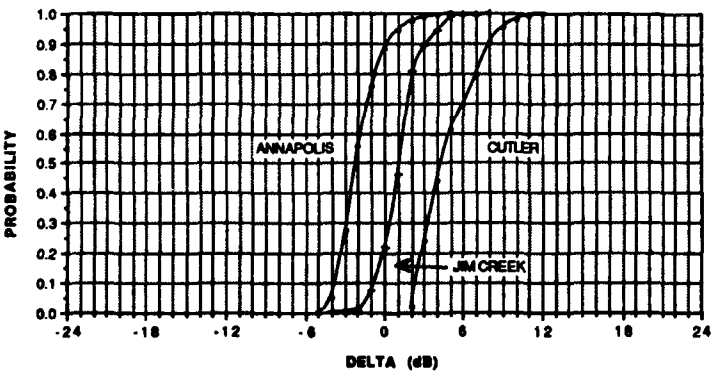

Fig.9 Cumulative distributions of the DELTA's as measured at Nanisivik in Spring

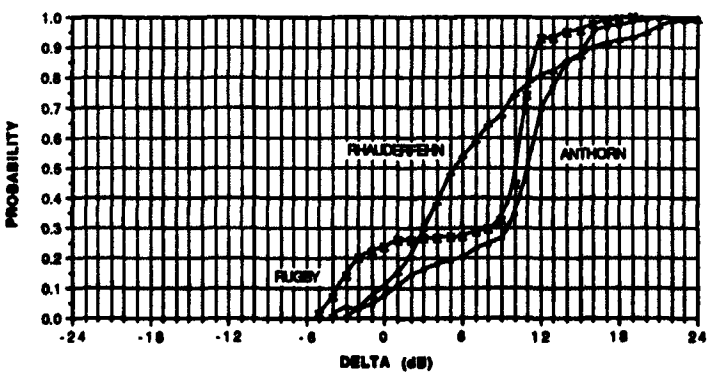

Fig.10 Cumulative distributions of the DELTA's as measured at Nanisivik in Spring

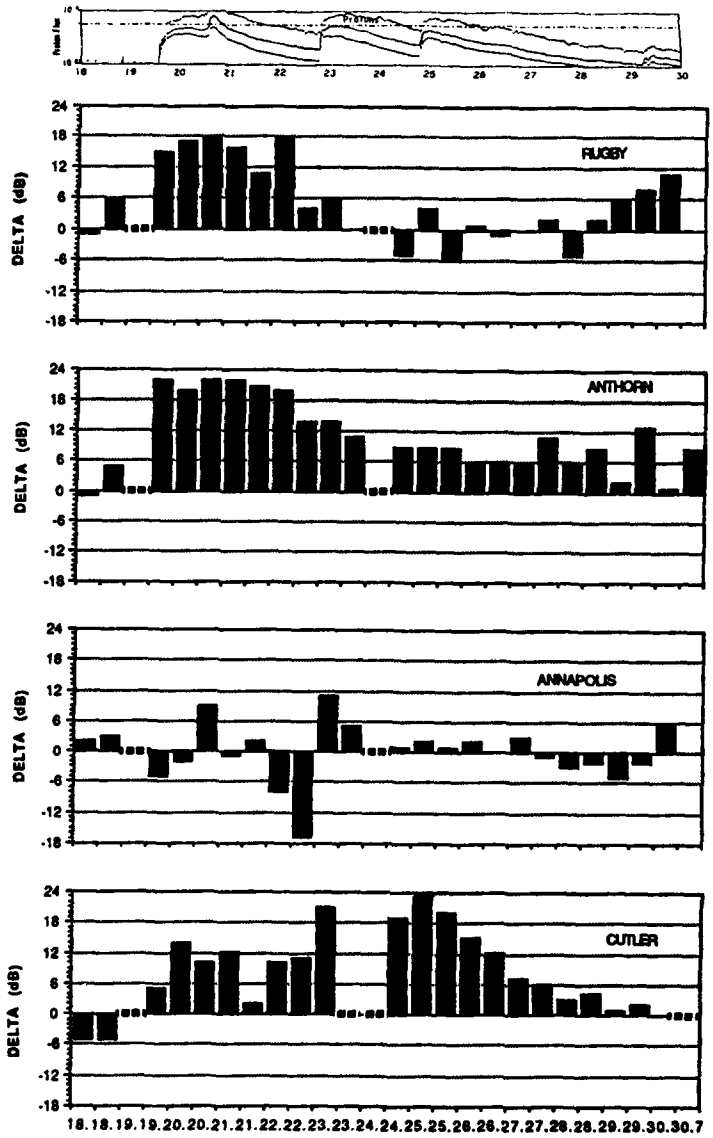

Fig 11a Proton flux for October 18th to 30th 1989

Fig.11b,c,d,e Effects of the October 1989 storm on signals as measured on the CCGS John A. MacDonald

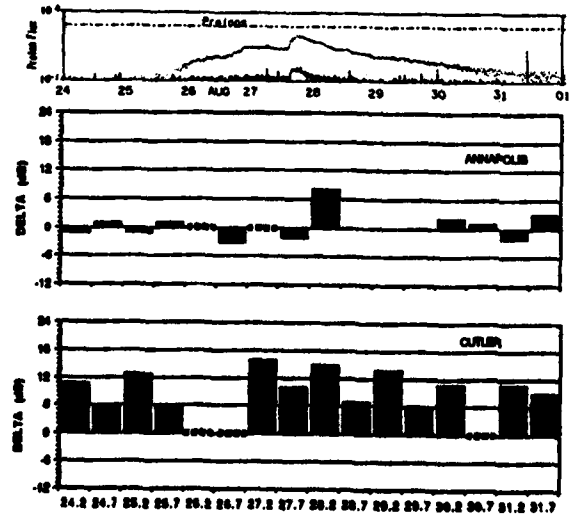

Fig.12a Proton flux for August 24th to September 1st 1991

Fig.12b,c, Effects of the August 1991 storm on signals as measured at Nanisivik

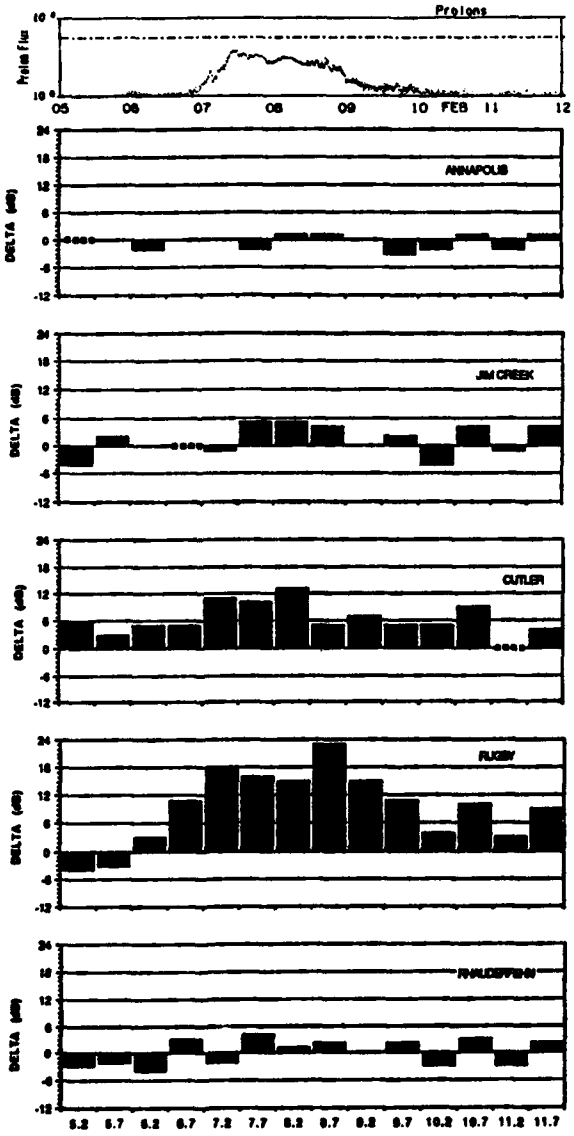

Fig.13a Proton flux for February 5th to 12th 1992
Fig.13b,c,d,e,f Effects of the February 1992 storm on signals as measured at Nanisivik

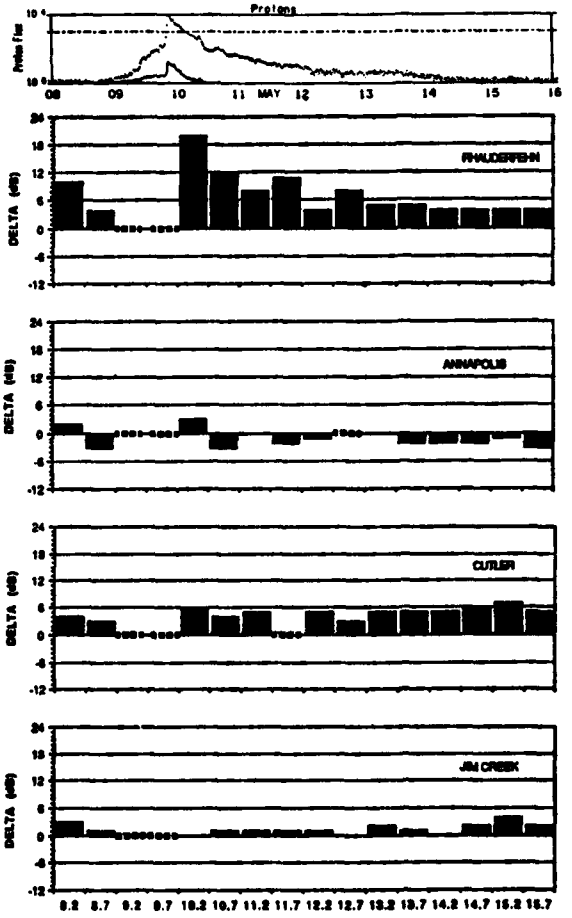

Fig.14a Proton flux for May 8th to 16th 1992
Fig.14b,c,d.e Effects of the May 1992 storm on signals as measured at Nanisivik

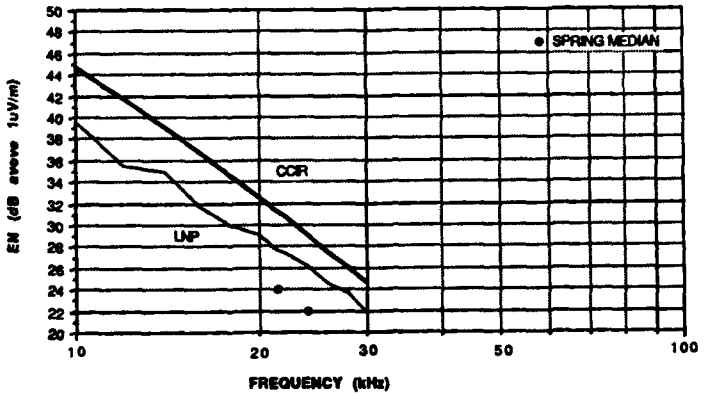

Fig.15 Atmospheric noise measurements at Fort Smith, Spring 1990, 0800 to 1200 LST

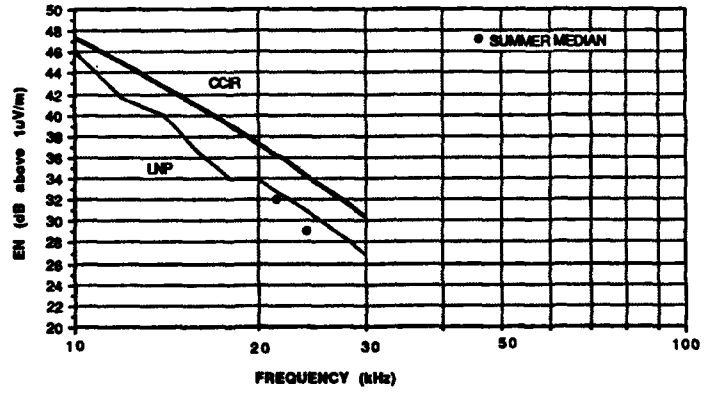

Fig.16 Atmospheric noise measurements at Fort Smith, Summer 1990, 0800 to 1200 LST

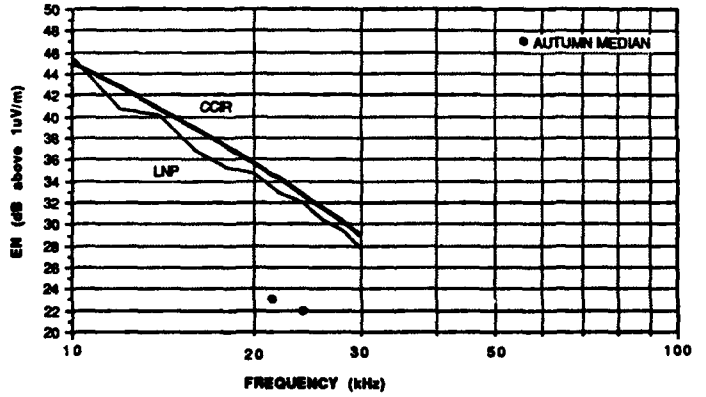

Fig.17 Atmospheric noise measurements at Fort Smith, Autumn 1990, 0800 to 1200 LST

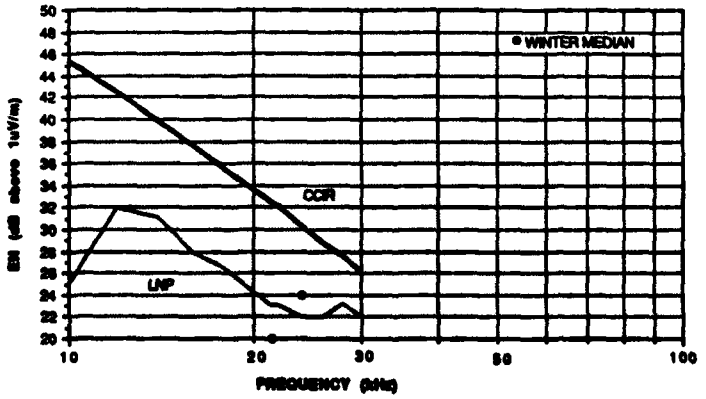

Fig.18 Atmospheric noise measurements at Fort Smith, Winter 1990, 0800 to 1200 LST

Discussion

U.S. INAN (US)

You showed an example of a geomagnetic storm during which the RHAUDERFEHN path (over Greenland) was not affected but the Cutler path (at lower latitudes) was perturbed. Was this storm a particularly intense one? I am thinking that in a relatively intense storm, the auroral electrojet may extend to lower latitudes, and that VLF paths lying to the north of the electrojet may not be as affected.

AUTHORS' REPLY

No, the May storm (where RHAUDERFEHN was affected) was more intense than the February storm (where RHAUDERFEHN was not affected). It should be noted that, at the time of the February storm, the receiving site was mostly in darkness with a brief period of sunlight near noon, i.e., the terminator may have a greater affect on this path at this time.

THEORETICAL AND EXPERIMENTAL COVERAGE ANALYSIS OF A VLF TRANSMITTER

Detlev Borgmann
TELEFUNKEN SYSTEMTECHNIK
Radio Communications Subdivision
P.O.Box 1730, D-7900 Ulm, Germany

SUMMARY

The coverage area of a VLF transmitting station, located in the northern part of Germany, should be analysed. In order to predict the availability of receiving skin depth for the complete operation area of the VLF station some investigations have been made in theoretical propagation models. Then a computer program based on the wave guide mode theory was implemented. To verify the validation of the theoretical model, measurements of field strength in some specific areas were carried out.

The first part of the paper is concerned with a description of the theoretical approach of the coverage analysis. The second part describes some properties of the operation area and gives in detail results from measurements. And finally a comparison of theoretical and measured data then shows the quality of agreement between theory and praxis.

1. INTRODUCTION

A VLF transmitting station for radio communication to submerged submarines was installed in the northern part of Germany. In order to predict the system availability the receiving skin depth for the complete operation area of the VLF station must be calculated. This analysis should be based on a theoretical simulation of the field strength supported by an empirical evaluation of physical parameters of the transmission path. These parameters e.g. ionosphere reflection profile must be estimated by specific measurements.

The problem now consisted of finding a suitable calculation method which, by simple variation, would allow the ionosphere's influence factors to be examined. In a comparison of calculated field strengths with measured values, the aim was to find a set of ionospheric parameters. With this ionospheric data, obtained by targeted measurements, the field strength analysis should then be extended over the entire area of propagation.

With the knowledge of the field strength above the sea surface at any point of the coverage area and the physical constants of the sea water an estimation of the receiving skin depth is possible.

2. COVERAGE AREA

The coverage area of this radio system shown in Figure 1 is the Baltic Sea and parts of the North Sea. For the field strength calculation the area was covered with a net of radials. Different land/sea transition phases characterize this area and complicate the calculation.

3. THEORETICAL PROPAGATION ANALYSIS

To calculate the field strengths over water, a simulation model was sought which on the one hand would take into account all possible variants and influence factors of the ionosphere and, on the other hand, would enable verification of the selected ionosphere parameters by specific measurements. Fundamentally only the WAVEGUIDE MODE method was suitable for the theoretical analysis [1]. Various methods of calculation are described in the literature [2-4] which are exclusively based on the WAVEGUIDE MODE theory.

In the examination of the VLF field strength, the method for determining waveguide constants "MODESRCH" [2] and the mode conversion procedure "GRNDMC" [4] were employed. With the MODESRCH procedure, the mode constants can calculated depending on the homogeneous characteristics of the earth and ionosphere. MODESRCH has the advantage that the characteristics of the ionosphere (conductivity profile) are describable by two parameters. Compared to three-parameters ionospheric models, the two parameter description simplifies the verification by measurements. A detailed analysis of two-parameter ionospheric models is described in [5]. It serves as a basis for the coverage analysis.

VLF mode conversions coefficients and mode sum for an earth-ionosphere waveguide which is inhomogeneous along the direction of propagation can be determined with the procedure GRNDMC.

Using the methods described in [2] and [4], a calculation concept was developed (Figure 2) which consists of a total of six steps and establishes as a result the course of the field strength on the ground. The coverage area was overlaid with a network of radials (Figure 1) on which the field strengths were calculated.

At the beginning of a field strength simulation the parameters of the VLF channel to be calculated have to be fixed in an initial step. This means that all the waveguides parameters which influence wave propagation were assigned according to the geographical and physical circumstances. Figures 3 and 4 show examples of the modelling of a propagation channel. The marked land/sea transitions describe the lower boundary of the waveguide. The ionosphere in Figure 3 is assumed with constant daytime propagation, whereas dawn/dusk propagation was approximated in Figure 4 with a stepped model of the ionosphere.

To calculate the mode constants with the aid of the mode search procedure [2], the waveguide has first of all to be divided into sections with homogeneous values. The mode constants are then calculated for each further homogeneous waveguide section. The determination of the mode conversions coefficients of each section follows in the next step. The subsequent mode summing procedure is followed by the calculation of field strength along the direction of propagation. A field strength plot completes the calculation.

The current local ionospheric parameters are determined in principle via a comparison of measured field strengths with theoretically determined field strengths. By varying certain simulation parameters (ionospheric conductivity coefficient), the calculated field strength curves are so altered until congruence with the measured values is achieved.

The ionospheric conductivity coefficients can be derived via an exponential electron density profile. According to [1], two parameters are sufficient to describe the profile. The parameter Beta (km^{-1}) defines the vertical gradients of the electron density whilst the term H' (km) represents a reference height. By varying both factors, all conceivable ionospheric states can, in principle, be simulated.

The reports [5] and [6] describe detailed examples for effective electron density distributions serves as a basis for simulation of the ionosphere's parameters. A variation of the reference height H' = 70 km to H' = 76 km at a constant electron density gradient of Beta = 0.3 km^{-1} appeared to be the most sensible way to simulate daytime propagation for this specific coverage area. Figure 5 shows the field strength for variations of the ionosphere's height. Mainly the position of the distinct maximum of interference (minimum of field strength) is influenced by the variation of the reference height. As the position of the interference can be precisely determined by measuring the field, the ionosphere's parameters can thus be verified relatively accurately.

In chapter 4, some examples of day and night simulations are compared in detail with measurements.

An investigation of the influence of day-to-night transitions for possible field strength changes took on particular significance. Observations of field strength carried out earlier had, in certain areas, resulted in particularly severe field strength reduction during the dawn/dusk period. The theoretical investigation was intended to provide information about the fundamental behaviour of the field strength during dawn/dusk. To this end, an ionospheric night-to-day transition model was designed (Figure 7) which, verified by measurements, enabled the field strength curve at dawn/dusk to be calculated. Figure 8 shows, as an example, a calculation of the field strength curve for the night-to-day transition on a west-east land path. The transition curves from night to day is vividly discernible. Distinctly conspicuous is a drop in field strength at a certain distance and at a certain time of the transitional phase. This field strength minimum was confirmed by measurements.

Continued investigations of dawn/dusk occurrences [7] confirmed that the simulation method is also fundamentally suitable for calculating dawn/dusk influences theoretically and enabling them to be analysed.

4. MEASUREMENT RESULTS

During extensive measuring activities in 1983/84, field strength measurements were taken by a ship and an aircraft. The measurements took place on several singular radials in winter as well as in summer to take into account area and seasonal influences. The flight measurements proved to be best suited for field strength analysis and ultimately the determination of the mode parameters. Additional positional measurements with a ship supplemented the analysis.

The objective of the measuring was to determine field strength curves for daytime, night-time and dawn/dusk propagation in summer and winter in order to verify current ionosphere parameters. Figure 10 shows the field strength curve resulting from daytime flight measurements in summer over a distance of approximately 2000 km. In principle, two curves can be perceived which represent the outward and return flights respectively. The slight shift of the curves can be explained by the deviation in time of the two sets of measurements. This meant that the ionospheres characteristics had already changed somewhat between the outward and return flights.

A comparison of the in-flight data readings with theoretically determined curves (Figure 9) shows that for the outward and return flights (Figure 11 and 12) there is very good concurrence with the parameters H' = 74 km resp. H'= 75 km and Beta = 0.3 km^{-1}. Particularly pronounced was a drop in field strength at around 600 km. Further comparisons with other in-flight data readings led to similar findings.

The ionosphere data for night-time propagation were considerably more difficult to determine. Figure 14 shows, as a typical example, the data readings for a night flight. The field strength curve shows a plot with several drops in signal strength which is typical for night-time propagation. Also noticeable is a shift in data readings from the outward and return flights. But a comparison with calculated data (Figure 13) does not lead to such clear concurrence as in the case of daytime readings. Figures 15 and 16 show a comparison for the outward and return flights respectively. The theoretically determined curve is based on the ionospheric parameters H' = 83 km (outward flight) resp. H' = 81 (return flight), Beta = 0.5 km^{-1}.

Further night-time measurements taken in summer as well as in winter, also produced similar results. Unlike the daytime propagation, a pronounced null in the field strength curve could not be observed. The in-flight measurements were supplemented by shipboard measurements at certain locations (in the area where field strength minima were to be expected).

5. CONCLUSION

As the result of the VLF propagation analysis the following ionospheric coefficients for the specific coverage area can be determined:

Day	Summer	H' = 75 km	Beta = 0.3 km^{-1}
Day	Winter	H' = 77 km	Beta = 0.3 km^{-1}
Night	Summer	H' = 80 km	Beta = 0.4 km^{-1}
Night	Winter	H' = 85 km	Beta = 0.6 km^{-1}

With the aid of the ionospheric parameters determined by the measuring, field strength calculations were carried out for the entire area of operation. Based on these calculations, the attainable depths were calculated for reception when submerged. It then emerged that there was an area, approximately 600 km distant, in which underwater reception was no longer possible due to an extreme drop in field strength during daytime.

As these reception limitations, especially in this area, were unacceptable for operational reasons, it was examined in the further analysis to what extent the null could be shifted or reduced by selecting a new frequency. Figure 6 shows the simulated field strength curves for various frequencies under daytime condition. The investigation demonstrated that the reception limitations in this particular area could be avoided by shifting the frequency.

6. REFERENCES

[1] Budden, K.G., "The waveguide-mode theory of wave propagation", Prentice Hall

[2] Morfitt D.G., Shellmann C.H.," MODESRCH , An Improved Computer Program for Obtaining ELF/VLF/LF Mode Constants in an Earth-Ionosphere Waveguide", Interim Report 77T, Naval Electr. Lab. Center, San Diego, 1976

[3] Pappert RA, Shockey LR, "Simplified VLF/LF Mode Conversation Program with allowance for elevated, arbitrary oriented electric Dipole Antennas", Interim Report 771, Naval Electr. Lab. Center, San Diego, 1976

[4] Morfitt D.G., "Simplified VLF/LF Mode Conversion Computer Programs;GRNDMC and ARBNMC", Technical Report 514, Naval Ocean System Center, San Diego, 1980

[5] Morfitt DG, "Effective Electron Density Distribution VLF/LF Propagation Data", Technical Report 141, Naval Ocean System Center, San Diego, 1977

[6] Ferguson, J.A., "Ionospheric profile for predicting nighttime VLF/LF propagation", Technical Report 530, Naval Ocean System Center, San Diego, 1980

[7] Borgmann D., "Methode zur Berechnung des Feldstärkeverlaufs bei VLF-Ausbreitung", Technical Report Nr. 12.051/83, AEG-Telefunken

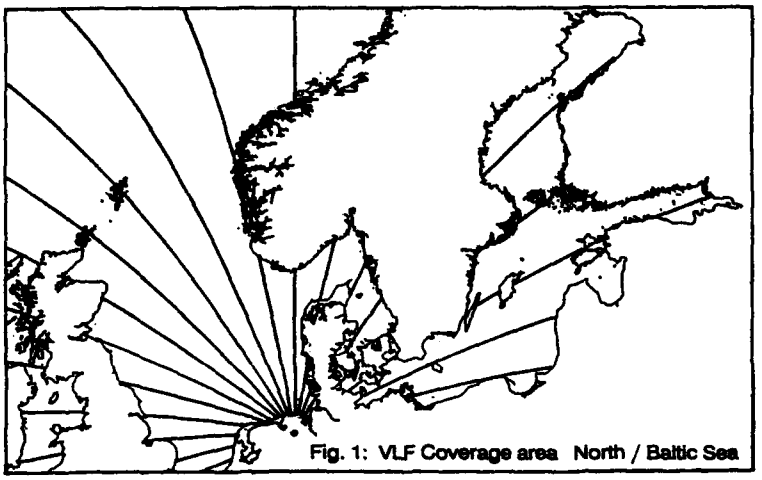

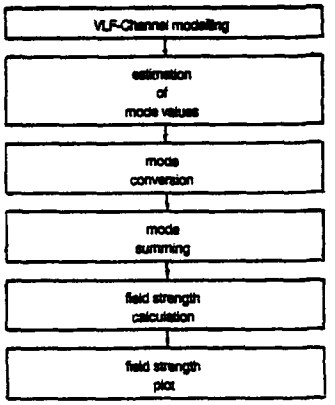

Fig. 2: Wave guide mode field strength prediction procedure

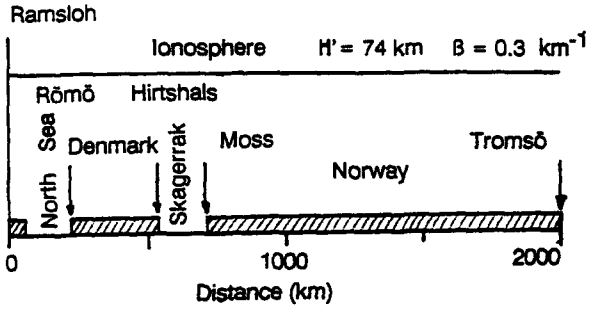

Fig. 3: Example for non homogeneous wave guide; Day

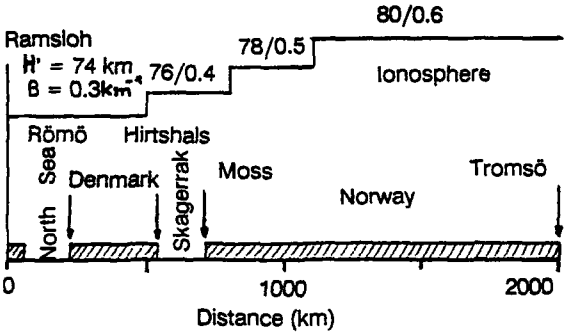

Fig. 4: Example for non homogeneous wave guide; Dawn/Dusk

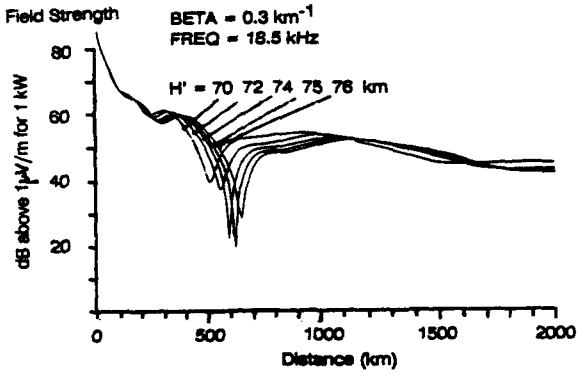

Fig. 5: Field strength curves for various reflection heights

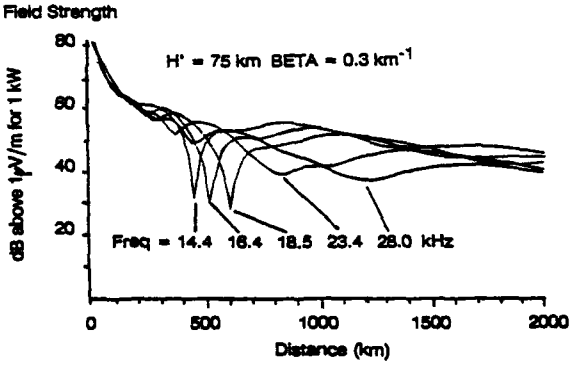

Fig. 6: Field strength curves for various frequencies

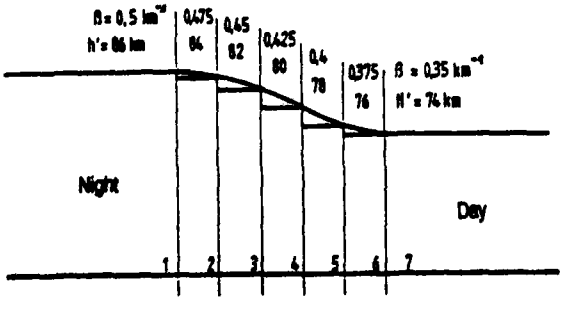

Fig. 7: Ionospheric night to day transition

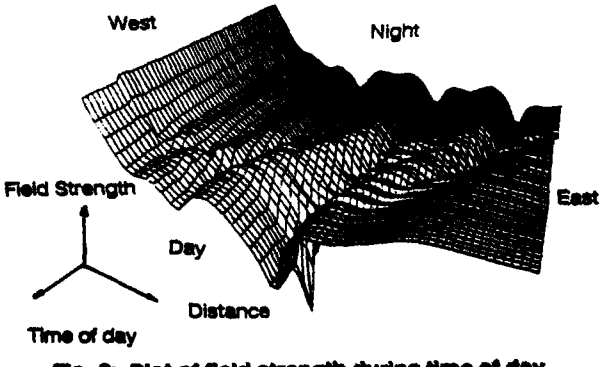

Fig. 8: Plot of field strength during time of day

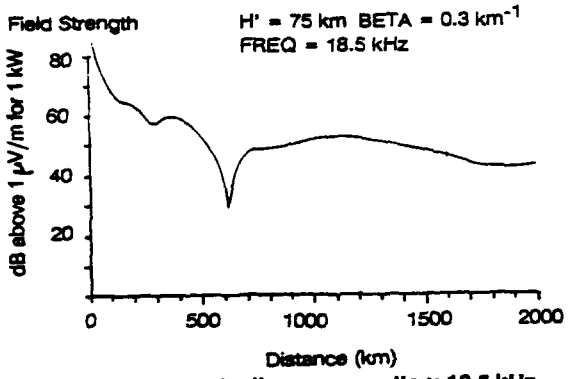

Fig. 9: Typ. daytime propagation; 18.5 kHz

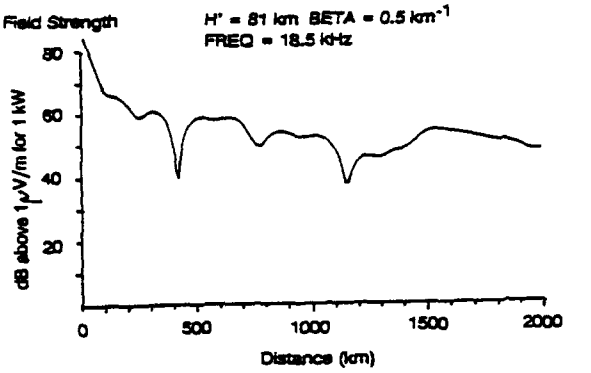

Fig. 13: Typ. night-time propagation; 18.5 kHz

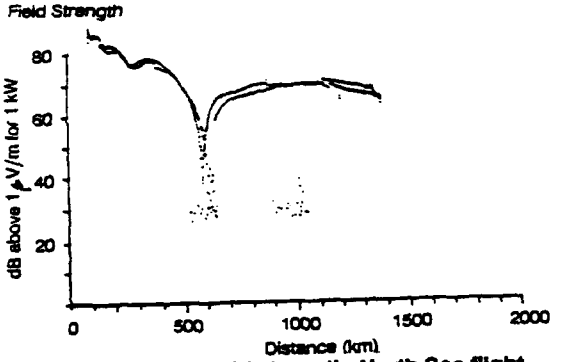

Fig. 10: Measured field strength; North Sea flight, daytime, 18.5 kHz

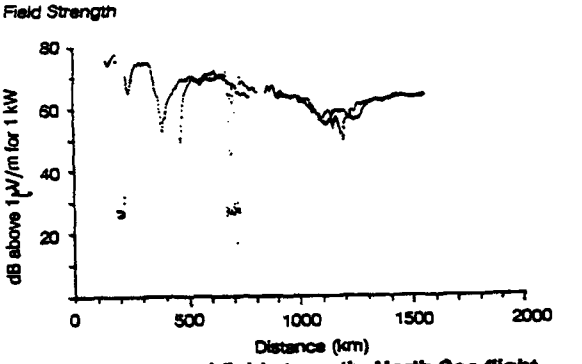

Fig. 14: Measured field strength; North Sea flight, night-time, 18.5 kHz

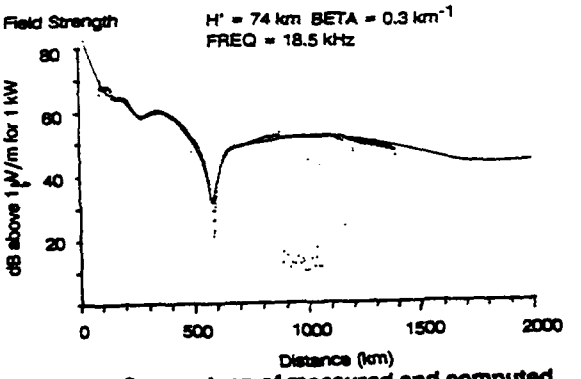

Fig. 11: Comparison of measured and computed daytime field strength; Outward flight

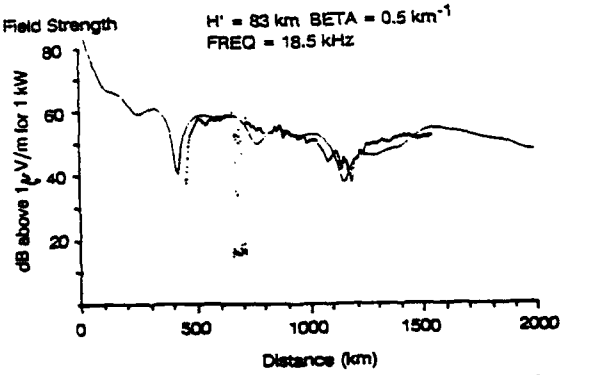

Fig. 15: Comparison of measured and computed night-time field strength; Outward flight

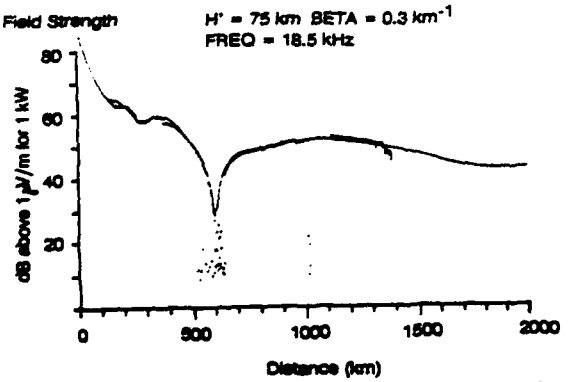

Fig. 12: Comparison of measured and computed daytime field strength; Return flight

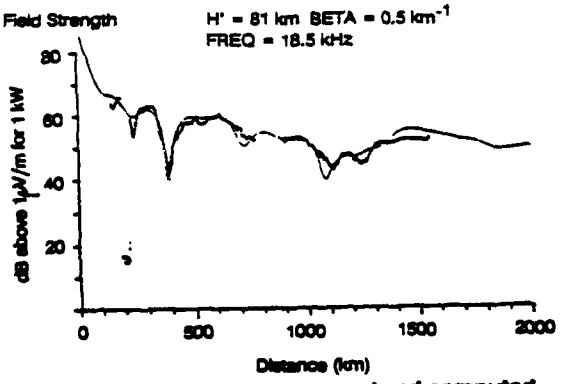

Fig. 16: Comparison of measured and computed night-time field strength; Return flight

INVESTIGATIONS OF EQUATORIAL IONOSPHERE NIGHTTIME MODE CONVERSION AT VLF*

Verne Hildebrand
IWG Corporation, 1940 Fifth Avenue, Suite 200, San Diego, CA 92101, United States

Summary: Research to define equatorial zone nighttime modal interference for VLF signals is described. Modal effects are examined in relation to plausible ranges of ionosphere parameters, propagation path orientation and VLF frequency. Results of various comparisons are described where VLF signal amplitude and phase calculations for low latitude and transequatorial paths are matched to measurements. D-region ionosphere models, used as input to a fullwave VLF propagation computer program, are iteratively adjusted to improve the agreement between calculations and measurements. Findings are interpreted with respect to (1) the feasibility of exploring equatorial zone ionosphere dynamics, and (2) the value of using Omega signals to build propagation models for predicting VLF communications coverage.

Introduction: VLF Radiowave propagation provides one of the few viable tools for exploring the properties of the lower D-region ionosphere. Conversely, VLF communications coverage analysis and prediction is directly dependent on the quality of models for the D-region ionosphere. The VLF Omega navigation signals are an excellent and under-utilized resource for conducting D-region research in direct support of VLF communications. Stations are well placed for investigating polar, mid latitude and equatorial phenomena. Much can be learned by fully utilizing the very stable signals radiated at five frequencies, available from each of the eight transmitters, and taking full advantage of modal structure. While the Omega signals, 10.2 to 13.6 kHz, are well below the VLF communications band, we contend that much of the knowledge gained on D-region characteristics can be directly applied at the higher frequencies. The opportunity offered by Omega needs to be exploited now! With the Global Positioning System (GPS) coming on board as the prime means for global navigation, pressure is mounting to phase out Omega. In this paper we describe how we are using Omega along with computer codes of fullwave VLF propagation, provided to us by the U. S. Naval Ocean Systems Center (NOSC), for ionosphere research and by example illustrate the potential for other investigations.

Background: Under a grant from the U. S. Office of Naval Research, we are studying the dynamics of the equatorial zone nighttime D-region ionosphere, using mode conversion effects on VLF signals as sensors of ionosphere variation. Our research interests are to determine if large dynamical processes are occurring in the equatorial nighttime ionosphere and, if so, to attempt to relate them to geophysical processes.

During previous analysis of VLF propagation in the Western Pacific, we observed some unusually large phase changes at nighttime on several signals undergoing transequatorial propagation. As illustrated in Figure 1, for a path from Omega Japan to Brisbane, the deviation from a normal nighttime phase can be an appreciable part of the normal diurnal change. The phase scale is in CentiCycles (CECs), a commonly used measure for Omega navigation. For the two dates shown, the diurnal phase plots for all three frequencies undergo a near normal sunset transition between 0400 and 1200 GMT. Later in the night, for both dates, the measured phases undergo an additional shift, indicating a further increase in ionosphere reflection height. These later phase shifts are anomalous perturbations that, while occurring infrequently, can approach 50 percent of the day/night phase shift. We suspect that such large phase perturbations may be unique to equatorial propagation as we have not found similar perturbations on other paths. The propagation path for Figure 1 is outside the equatorial modal conversion zone. We noted these phase changes on paths that both did and did not incur modal conversion. An example of a large phase deviation where modal effects are strong, is shown in Figure 2. Here, the Omega Australia signals measured in Japan, show strong modal effects occurring quite consistently during the middle of the night, for six consecutive days. In this case the 13.6 kHz phase follows a fairly normal diurnal pattern. Part of the large phase changes can be attributed to receiver performance. The modal effects seem to suggest that the ionosphere changes primarily occur in the equatorial zone. The times of occurrence often are near or after midpath midnight, as further illustrated in Figure 3, for Omega Japan measured at Cubi Point in the Philippines. Arrows point to the disturbance onset for each night. In these three figures we show quite different phase effects, with each example likely to have different information content regarding derivation of ionosphere parameters associated with the perturbations.

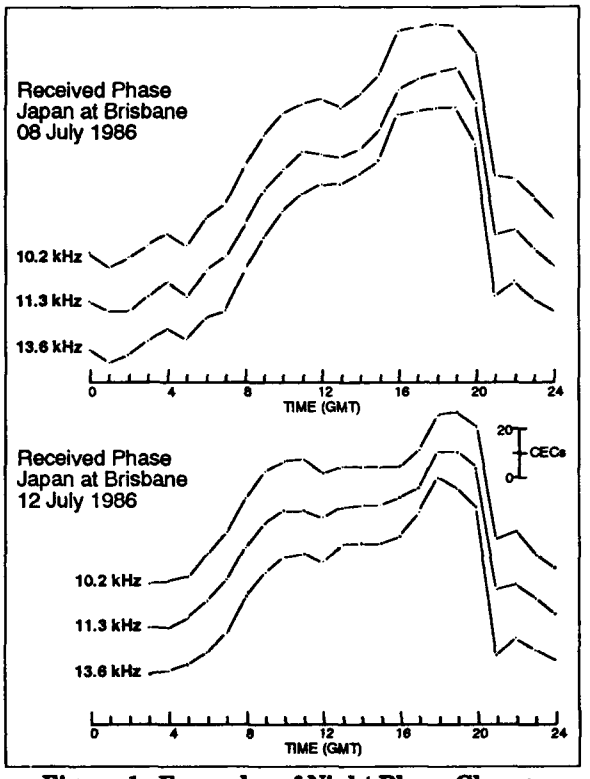

Figure 1. Examples of Night Phase Change

* Analysis sponsored by the U. S. Navy, Office of Naval Research

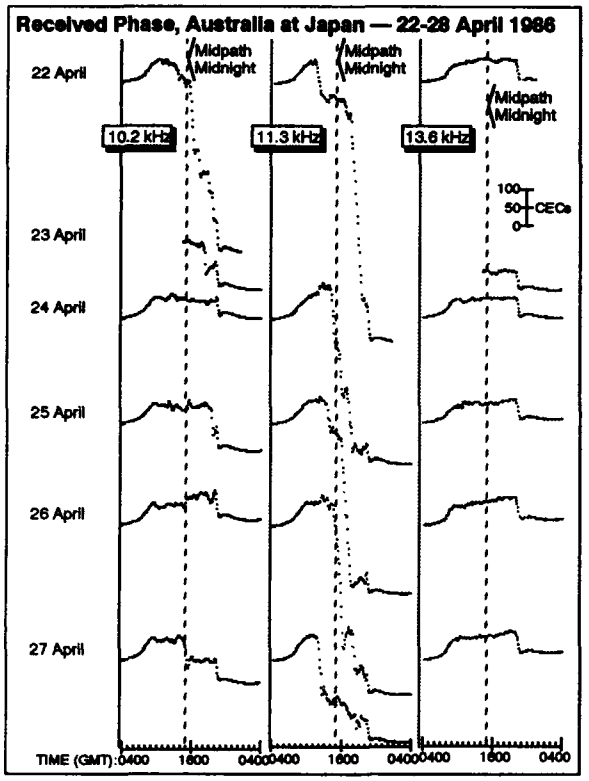

Figure 2. Ionosphere Dynamics

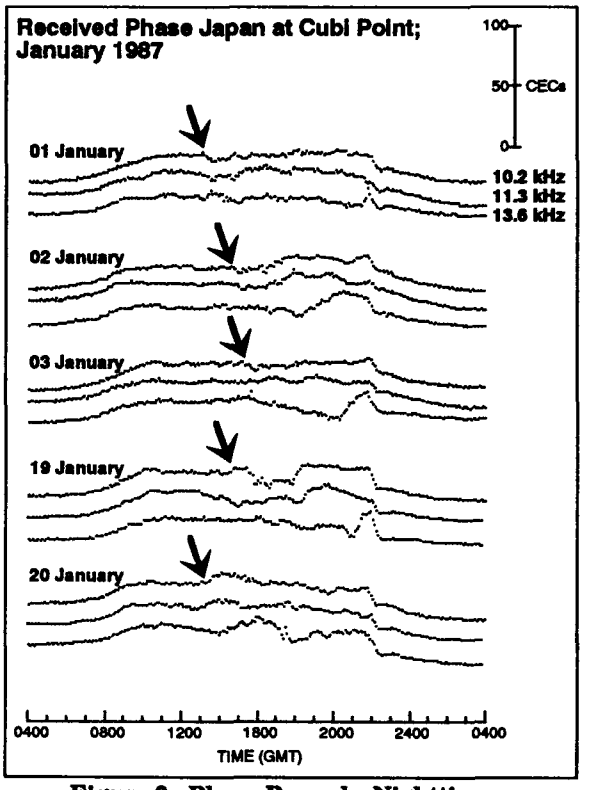

Figure 3. Phase Records, Nighttime Ionosphere Dynamics

Based upon these observations, we have addressed two questions: (1) does the geophysics literature indicate that large D-region perturbations occur, particularly at equatorial latitudes, and (2) can more definitive measurements be made? In regards to question one, we have not found any information specific to the altitude interval important to VLF propagation. However the literature, in general, clearly shows that the equatorial ionosphere dynamics at higher altitudes are much different than at mid or high latitudes and that major perturbations do occur. We will briefly address question one and then turn to question two as the main topic for our paper.

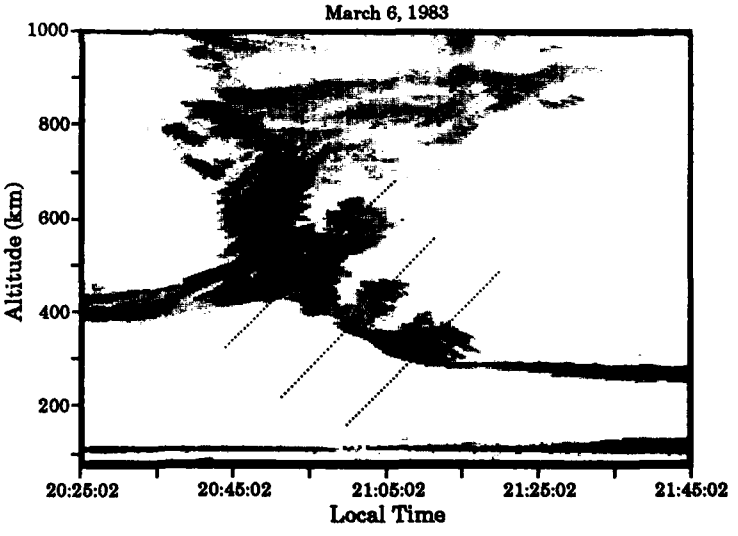

Figure 4. Electron Depletion Plume; Jicamarca Radar

At higher altitudes, the Equatorial Spread-F (ESF) is characteristic of the large scale dynamics that could be of interest to us. Spread-F is a disturbed nighttime condition that is characterized by large scale plasma "bite-outs." Bite-outs are complicated ionosphere plumes or "holes" that can extend 100 km in diameter and have ionization depletions up to three orders-of-magnitude. An example of the Jicamarca (Peru) radar detection of such a plume is shown in Figure 4 (KELLY et al 1986). It is noted that the plume height can extend over an altitude range of 400 km. A time slice example of theoretical plume modeling (shown in Figure 5), taken from an analysis of plume development, indicates the geometric extent (ZALESAK et al 1980). Each contour line represents a factor-of-two change in electron density. The contours inside the plume show decreases in electron density relative to the plume boundary. We note that the observed plumes have a very complex shape in both space and time. Several plumes may be generated in time sequence from a given region of instability and also within a general geographic area. While the measurement tools are insensitive to the D- and E-regions, we see evidence in the data of disturbances associated with the plume development occurring at or below 100 km. The equatorial spread-F is a nighttime phenomena, occurring at approximately 2300 local time ±3 hours, centered about the geomagnetic equator, ±20° latitude. Our interest in spread-F is enhanced because, much evidence exists to indicate that the triggering source for the initial instability originates below the F-region, possibly within

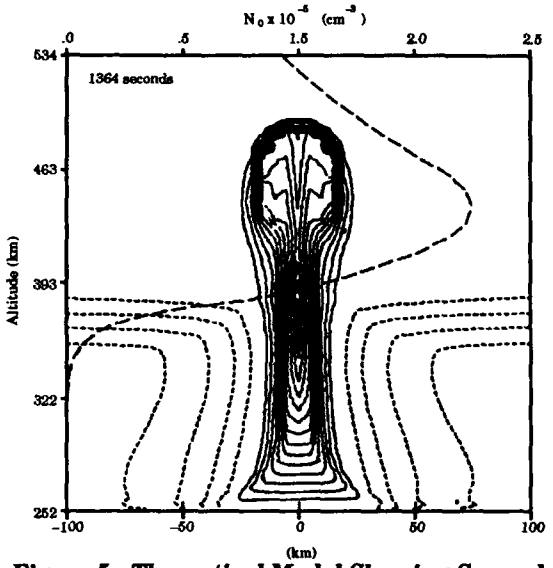

Figure 5. Theoretical Model Showing Several Orders of Magnitude Depletion

the lower atmosphere. Argo (ARGO et al 1986), in analysis of digital ionosound measurements at Huancayo in Peru, suggests seeding of F-region disturbances by gravity waves of local origin, possibly from thunderstorms in the rain forests to the east or from the Andes mountains. If this is so, the D-region must also undergo disturbances. We emphasize that the above evidence only suggests a rationale for study of the D-region.

With respect to question two above, our conjecture is that the equatorial mode conversion phenomena gives an opportunity to obtain more definitive data. Equatorial mode conversion occurs as a result of the earth's magnetic field influence on VLF reflection. The efficiency of conversion is dependent on the orientation of the path to the magnetic field and on ionosphere and collision frequency profiles. For each transmitter, equatorial zone modal conversion occurs over a confined geographic region. Most of our research to date has been to establish boundaries of modal conversion zones and to explore amplitude and phase effects in relation to path orientations and profile parameters. With the knowledge and insights gained, we believe that we truly can make and interpret more definitive measurements. Being able to interpret modal effects is as big an adventure as being able to make good measurements.

Our analysis makes extensive use of the Long-Wave Propagation Capability (LWPC), software package developed at NOSC (FERGUSON et al 1989) and adapted by us to the Macintosh personal computer. We find that this software works very well. Our investigations are to evaluate and devise geophysical models to be used with LWPC in assessing VLF communications and navigation coverage and performance. This study is viable because of the interactive tools we have developed for the Macintosh, which allow us to make extensive graphical comparisons between various hypotheses and to obtain calculation results while the questions are still fresh in our minds.

Presently, our calculations are limited to using electron density profiles where the density increases exponentially with increasing height. Representative profiles are shown in Figure 6. The values ß and h' designate the slope and reference height after the notation established by Wait (WAIT 1964). While we use nominal or average profiles for guidance, our interests are to derive specific profiles for specific measurement events. Though, these profile models frequently give surprisingly good fits to data, we find many cases where we believe a more complex shape is needed. Also, we need a capability to vary the profile along a propagation path. We hope to have the needed computer code modifications completed soon.

To date, our research has focused on (1) assessing the geographic extent and propagation characteristics of the equatorial mode conversion phenomena, (2) gaining experience in using the NOSC VLF propagation model to interpret modal conversion measurements, and (3) designing experiments than can best utilize the mode conversion process.

We have described our research on the equatorial zone modal conversion phenomena and criteria for establishing a zone's geographic boundaries in several papers (HILDEBRAND 1991, 1990). The conversion zones shown in Figure 7, for three Omega transmitters, Hawaii, Australia and Japan, are of particular interest to us because of unique possibilities and availability of some data from the Omega Validation Program. In this paper, we focus on propagation from Hawaii, examining radials in and near the eastern edge of the Hawaii Omega signal mode conversion zone. The radials we examine are shown in Figure 8. The analysis we describe is in preparation for the more complex task of attempting to interpret modal conversion measurements. Along the way we make several comparisons between analysis at Omega frequencies and at 23.40 kHz, from NPM in Hawaii.

Computer Exploration of Mode Conversion: Our first goal is to understand the equatorial zone mode conversion process in relation to geography, ionosphere parameters, and propagation frequency. We are concentrating on exploring potential information content of various sight selection and measurement choices. In the process we are building a database of calculations to help us design a measurement program. As we will show, there are many factors and trade-offs to consider.

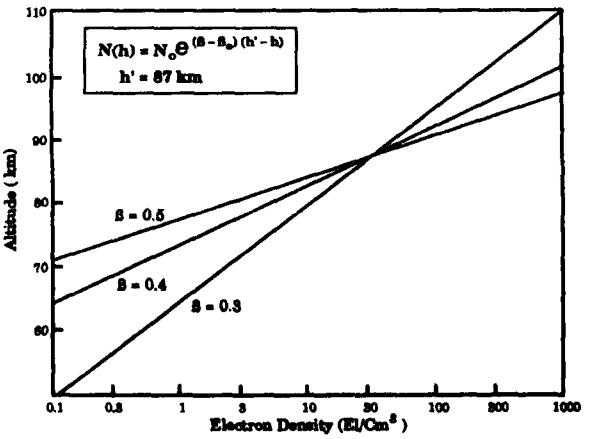

Figure 6. Electron Density Profiles

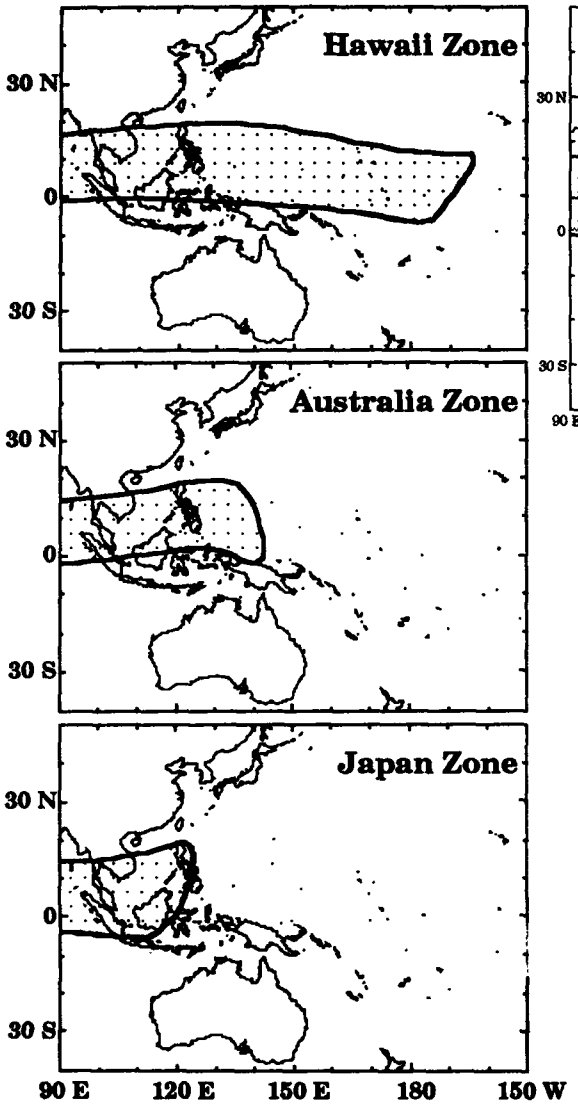

Figure 7. Omega Modal Conversion Zones

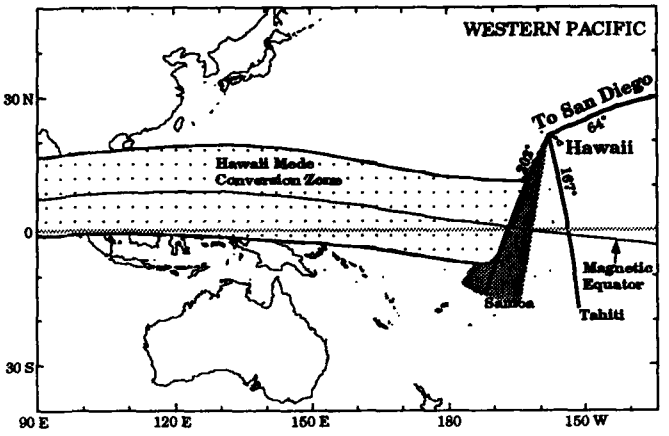

Figure 8. Propagation Paths Used for Diurnal Analysis

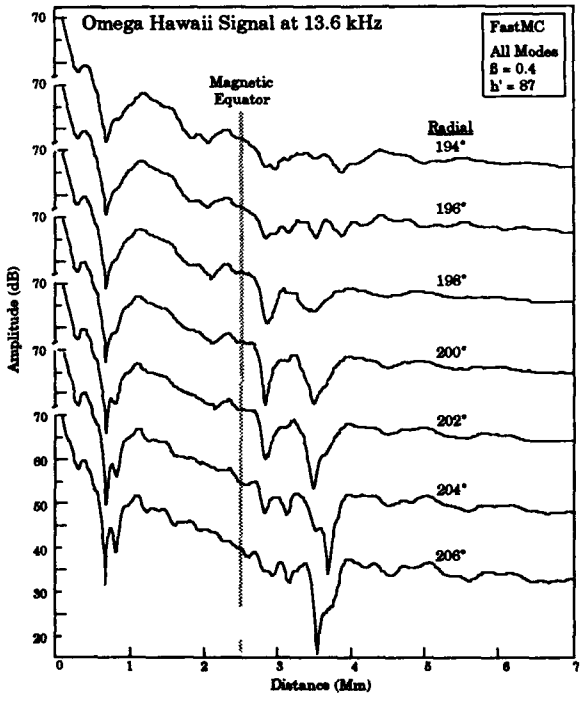

Figure 9. Modal Effects Versus Propagation Path Radials; ß 0.4 Ionosphere

Our original concept in proposing to use modal conversion was to select a geometry where only the last portion of a propagation path incurred modal conversion; the idea being, that with proper experiment design, we could localize the profile derivation to a small area in the equatorial zone. The ideal experiment would locate several receivers along a radial, one before modal conversion occurs and several within the region of modal conversion. These within would be spaced to record maximum differences in modal structure in both distance and frequency space. Simultaneous measurement along several radials would be a significant bonus. The zone boundaries, shown in Figure 7, were derived from a rather simple and static model. This model needed to be refined for our purposes. As we will show, the model is quite complex; with path bearing, profile height, profile gradient and signal frequency all contributing to the observable modal effects. Presenting a complete picture would require publishing a Compact Disk (CD), so a few examples will have to suffice.

In Figure 9, we show computed modal effects on signal amplitude versus distance and path bearing from Hawaii (194° to 206°), for the Omega Hawaii 13.6 kHz signal. From this figure we note, for this ionosphere model (ß 0.4, h' 87 km), that (1) modal effects are most obvious over a distance interval between 2.5 and 4 Mm, (2) their onset is beyond the magnetic equator, (3) their magnitude increases with increasing bearing, and (4) beyond 4.5 Mm negligible amplitude change occurs with increasing bearing that can be attributed to modal conversion. The modal effect would be hard to measure on the 194° radial, but would be quite pronounced beyond 200°. In Figures 10, 11a and 11b, we show similar calculations for respectively, Omega Hawaii and NPM at 23.4 kHz for an ionosphere model of (ß .5, h' 87 km). We note that the modal effects on the Omega signal are stronger than in Figure 9, yet the curves are very similar from 0 Mm to 2.5 Mm, the magnetic equator. Modal effects could easily be measured on the 196° radial. For the NPM signal (Figure 11a and 11b), the modal effects first become clearly evident on the 198° curve. By the 204° radial, the modal

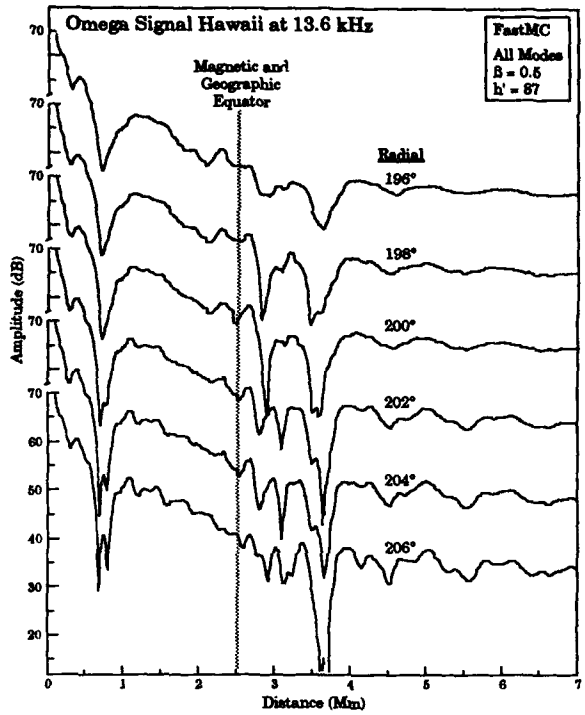

Figure 10. Modal Effects Versus Propagation Path Radials; ß 0.5 Ionosphere

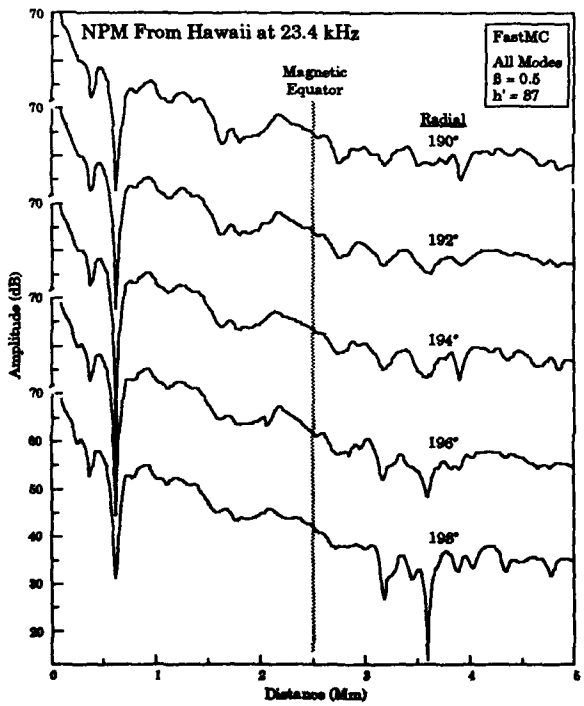

Figure 11a. Modal Effects Versus Propagation Effects; NPM Signal

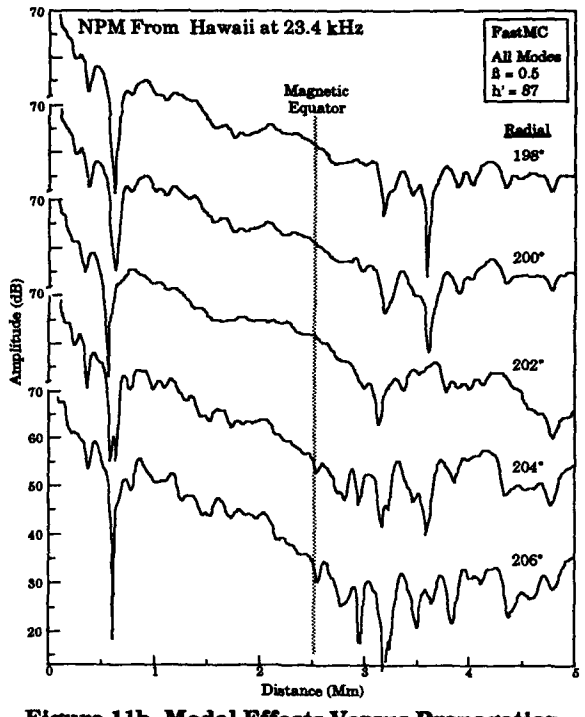

Figure 11b. Modal Effects Versus Propagation Effects, Continued; NPM Signal

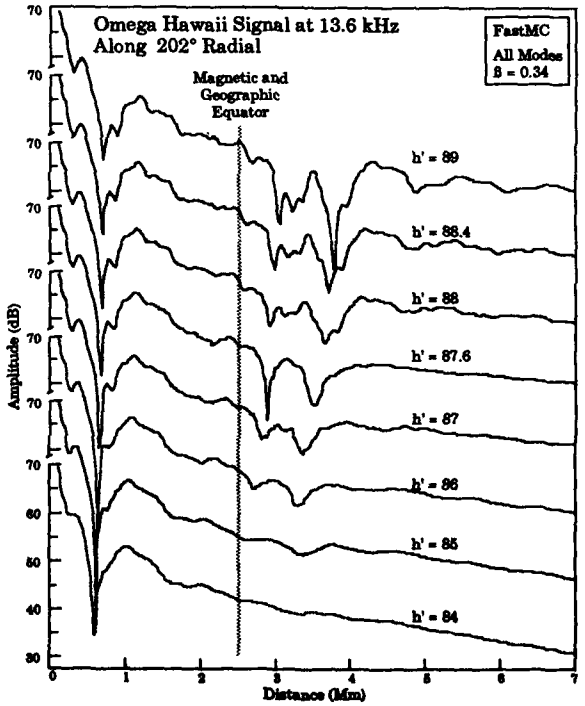

Figure 12. Modal Effects Versus Ionosphere Height; Omega Signal at 13.6 kHz

pattern becomes very complex and changes significantly over a 2° interval.

Varying the reflection height (h'), also causes significant variation in modal conversion as shown in Figure 12 for a ß .34 ionosphere on a 202° radial. The modal structure gradually increases with increasing height, starting near 85 km. Note that the height is varied in 0.4 km intervals from 87.6 to 88.4 km. In Figures 13a and 13b, we show a similar calculation for NPM, but for a ß .5 ionosphere and on a radial of 206°. With the steeper gradient (larger ß), greater bearing, and higher frequency, the onset of recognizable modal pattern begins about 82 km. Above 84 km, the structure becomes very complex, changing in a very complex way with changing height. Modes originating at the transmitter begin to extend to and beyond the magnetic equator, thus adding to the signal complexity. Features of these close in modes are readily traceable

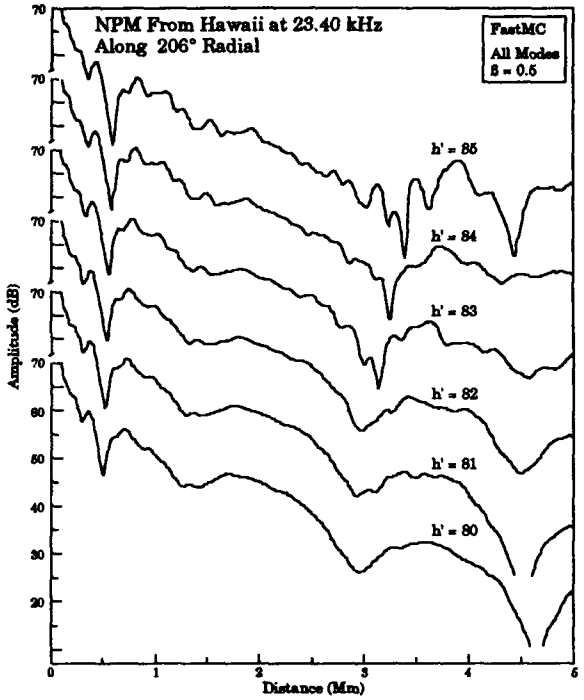

Figure 13a. Modal Effects Versus Ionosphere Height; NPM 23.4 kHz

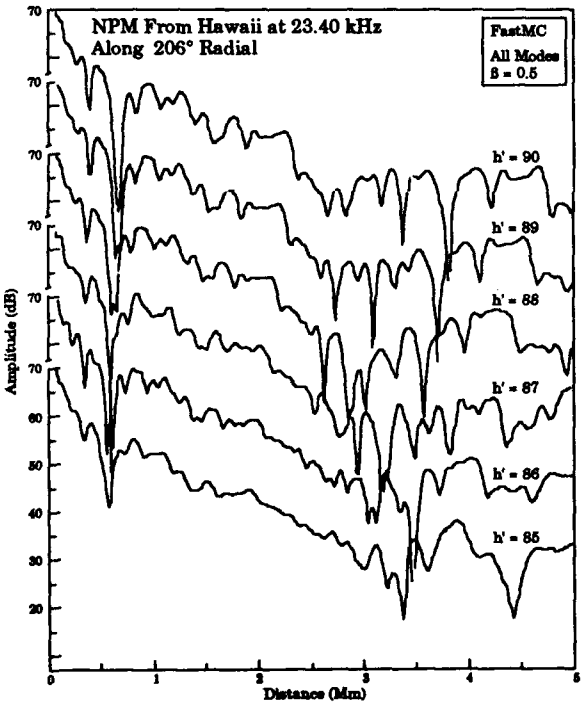

Figure 13b. Modal Effects Versus Ionosphere Height, Continued; NPM 23.4 kHz

from curve to curve, with a feature moving to a greater distance with increasing reflection height. Features beyond the magnetic equator are also traceable, but with somewhat more difficulty. Beyond the equator, the features that move outward with increasing height move at a faster rate with increasing distance along the path. For example, the small peak occurring at 1.5 Mm on the 85 km curve moves outward by 0.31 km as h' increases to 90 km, whereas the peak occurring at 3.9 Mm moves outward by 0.76 km over this height interval. We believe that reflection heights may vary over this range from 85 to 90 km.

Varying ß and frequency have similar effects. In Figures 14 and 15, we show modal structure on the Omega Hawaii signal propagated along a 204° radial as a function of ß with h' = 87 km for respectively, 10.2 and 13.6 kHz. For both frequencies, the mode structure increases with increasing ß. Modal interference is stronger and more

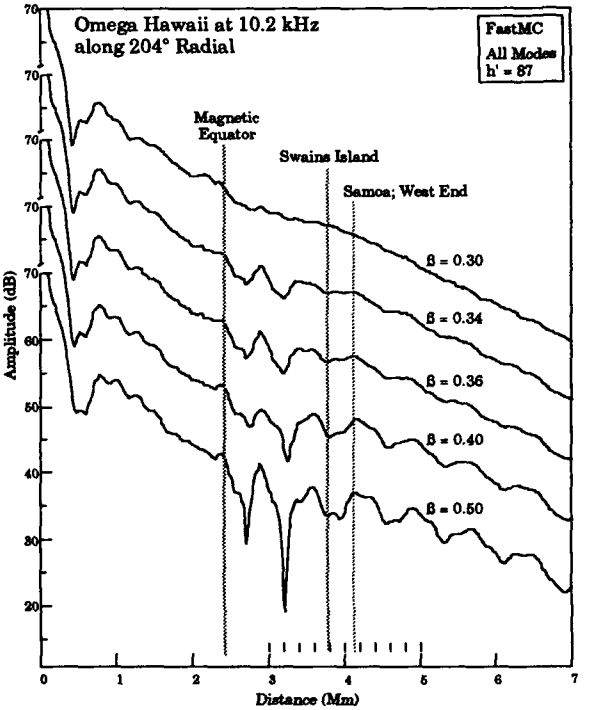

Figure 14. Hawaii Signal Amplitude at 10.2 kHz

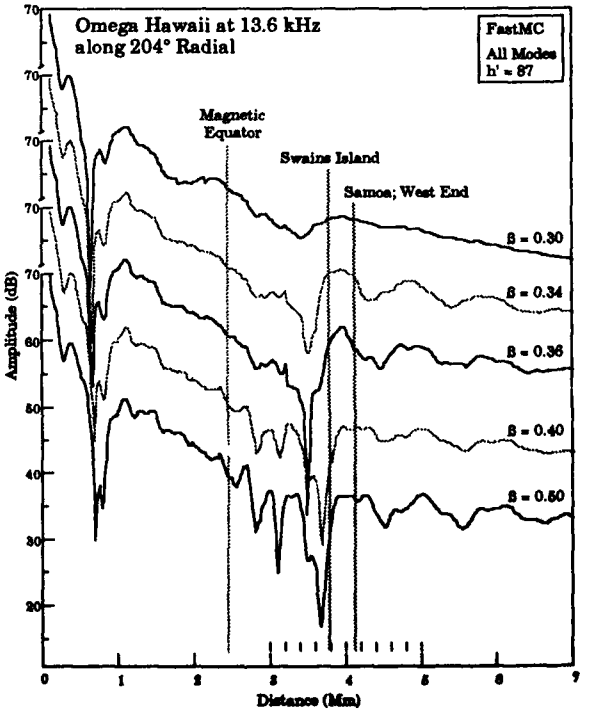

Figure 15. Hawaii Signal Amplitude at 13.6 kHz

complex at 13.6 kHz for any ß. We also show the locations of two possible measurement sites in close proximity to this radial. The space between the magnetic equator and Swains Island is all open ocean.

From an experiment design viewpoint, several things are evident from our calculations. First, for a profile (ß .3, h' 87 km) which is commonly used to model nighttime propagation at Omega frequencies, we should not observe modal effects in the vicinity of Samoa. Either ß or h' has to be larger. The best place to make measurements is within a megameter of the magnetic equator. For frequencies above the Omega band, the modal structure rapidly becomes very complex, which we interpret to mean much more difficult to analyze. For each transmitter, there is an optimum sector of radials for making measurements. As we showed in Figure 9, the modal effects are too small until a certain radial is reached. Further rotation to a more westward equator crossing improves the measurement potential, but a radial is eventually reached where modes originating at the transmitter extend into the equatorial zone and mask the equatorial effects. For Omega Hawaii this occurs around 210/212° depending upon the ionosphere model. From a very large set of calculations, we have derived the three most optimum measurement regions which are shown in Figure 16. While these are the best choices for using Omega, none are particularly good for site placement or logistics. Finally, a lot of variables are involved which leads to a lot of uncertainty. Any bounds that can be placed on parameters is very helpful in experiment design. We are now comparing calculations with propagation measurements to attempt to establish better bounds.

Ionosphere Profile Derivation: We hope to gain considerable insights into the nature of equatorial mode conversion phenomena by studying transequatorial propagation on radials from Omega Hawaii. We are comparing paths that lie both outside and inside of the conversion zone. Our first step is to model the nighttime path from Hawaii to Tahiti using data collected from the Omega validation program (HILDEBRAND 1989). In Figure 17, we show measured diurnal phase for four successive days on three Omega frequencies. We selected this data for two reasons, it is representative of this path and we have flight measurements for the night of 13 February.

In Figure 18, we compare Omega hourly PPC calculations for 10.2 kHz with measurements for these four days. The

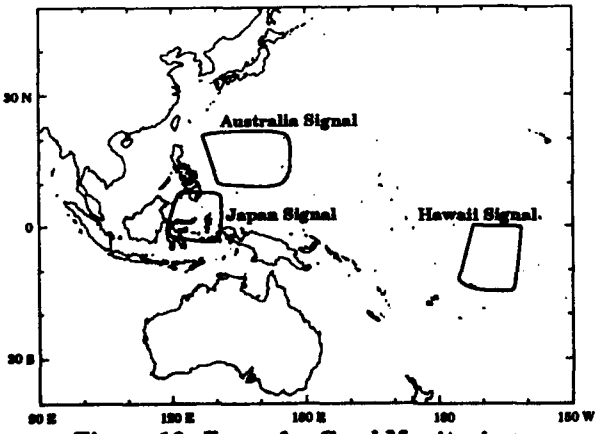

Figure 16. Zones for Good Monitoring

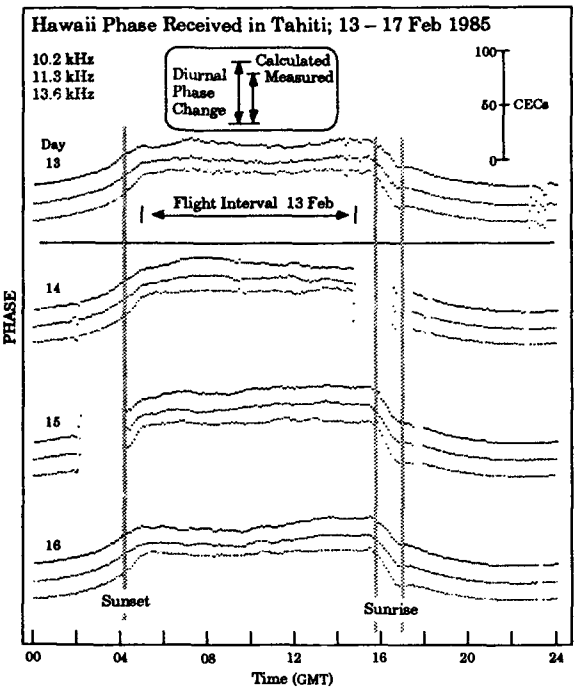

Figure 17. Measured Omega Phase

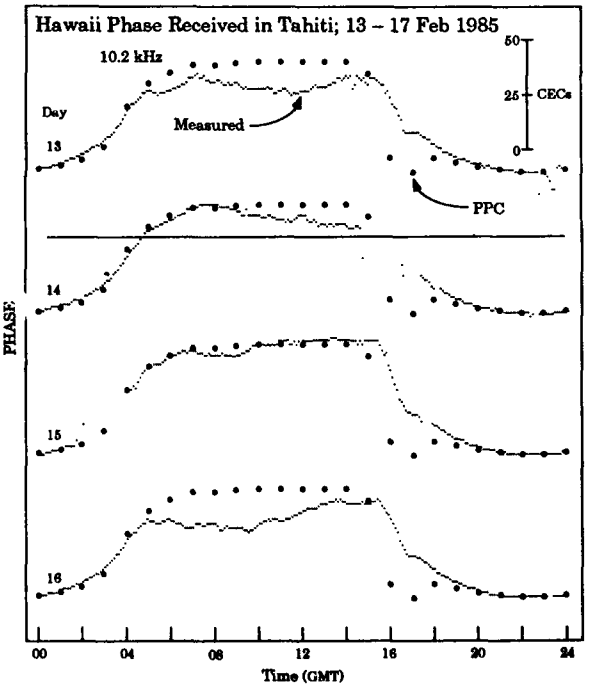

Figure 18. Measured Phase Compared to Propagation Phase Correct Ions (PPC)

measured phase values are set to the PPC values at 0000 GMT because we have not referenced the measured phase to the transmitted phase. The PPC model gives no information on ionosphere profiles but it does model changes over time. We note that the predictions fit very well for the daylight interval between 1900 and 0500 GMT. During nighttime, the measured values vary quite a bit, both with time and between dates. Particularly for 13 and 16 February, the phase is less than predicted. The PPC values aid us by providing a good reference for comparing propagation from night-to-night and for assigning a phase

velocity. For our comparison, we used LWPC to calculate the day/night values of phase, respectively selecting the commonly used values of (ß .3, h' 70 km) and (ß .5, h' 87 km). As noted in Figure 17, the calculated phase values versus time differ markedly from those measured. Again, we have normalized the 0000 GMT measured and computed daytime phases. The reference height interval chosen, 70 to 87 km, gives too large a diurnal change in phase, by about 20 centicycles. The question is, which profiles should we adjust, day or night, or both?

To address this question we turn to measurements aboard aircraft on radials flown from Hawaii. An example of daytime measurements using three frequencies of a multifrequency sounder on a 64° radial is shown in Figure 19. Using a profile of (ß .32, h' 71 km) resulted in a very good fit. We caution that this is only one sample. Our problem is that we have very few samples. In Figure 20 we show a nighttime sample measured on the same radial which we compare with calculations using a (ß .4, h' 85 km) profile. We note that the overall fit is reasonably good in terms of matching the distance interval of signal minima and the magnitude of the modal structure. This fit is definitely better than from any of the h' = 87 km profiles we examined. We also have Omega flight data recorded on 13 February 1985 on the radial to Tahiti that we show in Figure 21. We get a our best match to these measured nulls when a (ß .3, h' 85 km) profile is used. However, this model produces signal levels that are too high for distances beyond the 1.6 Mm maxima at 10.2 kHz and correspondingly at progressively greater distances for the higher frequencies. In Figure 22 we compare a calculation that gives a better fit to the data beyond 2 Mm but which lacks the structure to match the data within 2 Mm. None of our attempts have produced an acceptable fit to the modal structure in the distance interval from 0 to 2 Mm. We are convinced that the electron density profile was changing during the course of this flight. A good indication of this change is the amplitude decrease

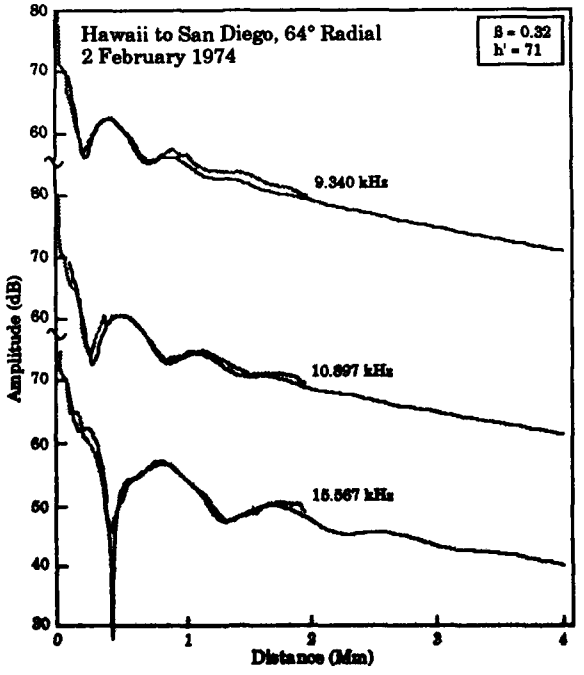

Figure 19. Multi-Frequency Sounder Data

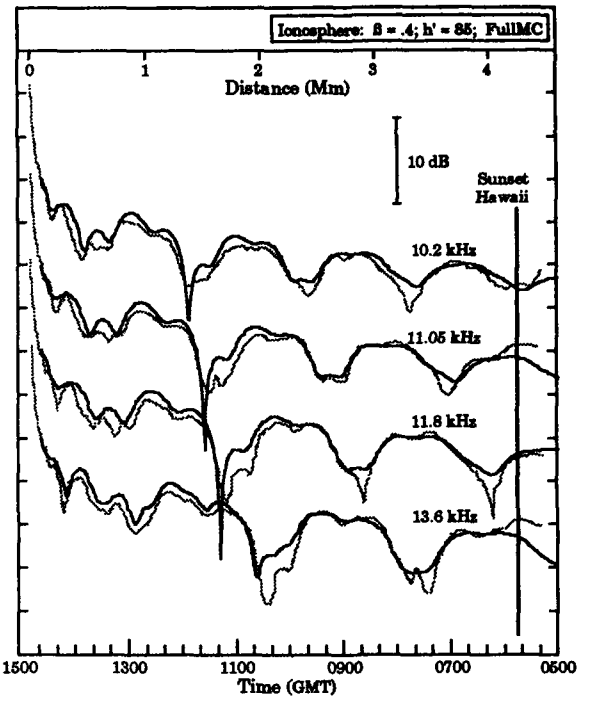

Figure 20. Hawaii to San Diego; 17 August 1983

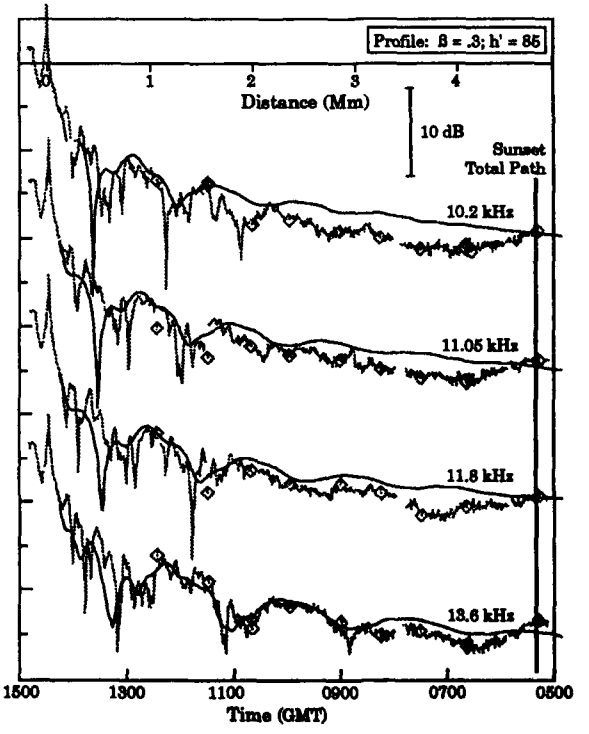

Figure 21. Hawaii to Tahiti, 187° Radial; 13 February 1985

in all signals between 0500 and 0630 GMT as the aircraft flew toward Hawaii. To explain this data we are going to have to undertake a much more complex analysis. We believe that this data does support using a reflection height around 84/85 km. Our other analysis, while not extensive, also indicates that a reference height below 87 km is needed.

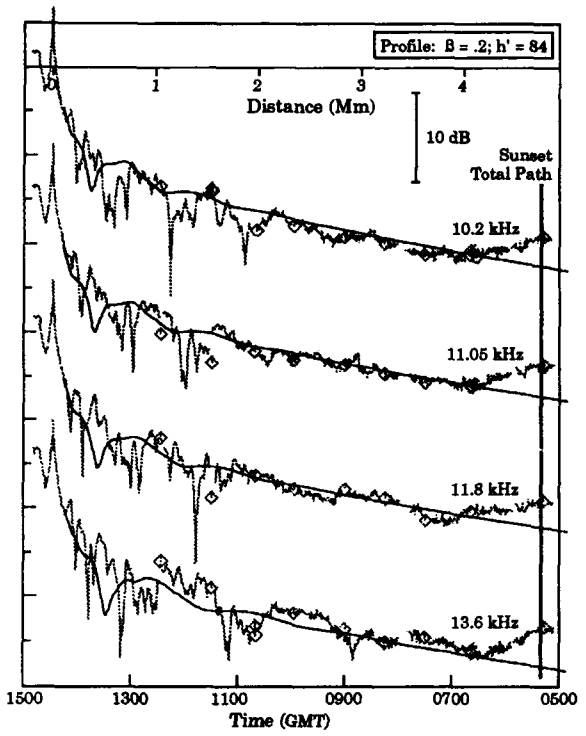

Figure 22. Hawaii to Tahiti, 167° Radial; 13 February 1985

In honor of this meeting, John Bickel of NOSC provided us with measurements of NPM Hawaii at 23.4 kHz obtained on a flight from Hawaii to Samoa and return. We show this data in Figures 23 and 24 along with our best match of calculations. Both sets of data show strong and quite different equatorial zone modal structure as well as other differences. Clearly different profiles are needed to match each measurement. Our fits are less than ideal, but we believe the agreement is sufficient to demonstrate that for both nights the ionosphere height increased with time. For 29 January (Figure 23), the signal null at 0.8 Mm is best fit using an h' of 84 km. The h' then gradually increases to a height above 86.4 km by the 4 Mm distance. For 31 January (Figure 24), the flight started at 4 Mm where the h' was about 90 km. We estimate that h' was about 92 km at 1.5 Mm. Both flights spanned most of the night.

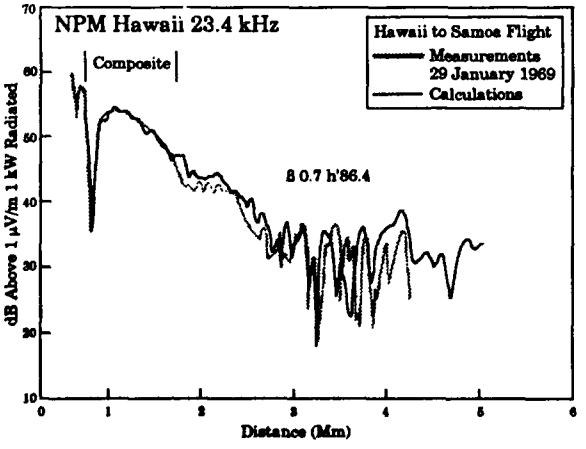

Figure 23. Comparing Measured and Computed Signal Level for 29 January 1969

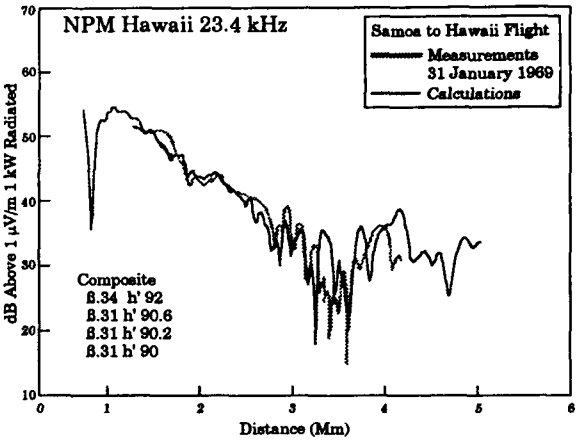

Figure 24. Comparing Measured and Computed Signal Level for 31 January 1969

Analysis Interpretation: We believe that assessment of equatorial zone modal effects requires the use of a fullwave VLF propagation computer code along with representative geophysical parameters. We find that the LWPC developed by NOSC is an excellent program. However, our matches to data often leave much to be desired; we believe because the ionosphere model in not good enough. The ionosphere parameters we have previously used to model transequatorial propagation are largely derived from mid latitude measurements. Our analysis to date suggests that for the paths studied, the ionosphere gradients (β), need to be increased for both day and night and the reference height (h'), probably needs to be slightly raised for daytime and lowered for night. We expect that with lower nighttime reference heights the ionosphere gradients will have to increase significantly to explain measured modal effects. We know from experience in matching flight data, that to get a close fit the profile must be adjusted throughout the flight. This implies that we really need to adjust the profile along the path. Also, we expect that a much more complex ionosphere profile shape than the simple exponential will be required to model the equatorial zone modal structure.

Finally, we are dealing with large amounts of data, both from measurements and calculations. Interactive computer displays are essential for efficient comparison of data. The emerging display capabilities and analysis tools are as important to our progress as the computer propagation models. Apple computer has recently published Macintosh system software called "QuickTime" that allows us to paste a sequence of computer images into movie frames and then play the movie either as a movie or frame by frame. Forward and backward sequences can be played. In Figure 25 a,b,c,d we show frames of a movie clip depicting computer amplitude and phase for a sunset interval. The movie is built by adding a calculation for the next successive time to the previous calculations. Parts a and c show the last frame of the sequence where the transition has been made from full-day to full-night. Very interesting patterns are produced over time that can be studied in detail. Parts b and d are stepped backwards to reveal the most pronounced modal interference. What is most important for analysis, is that this clip can be played over and over, stopped at any point, sequenced frame-by-frame or about any combination

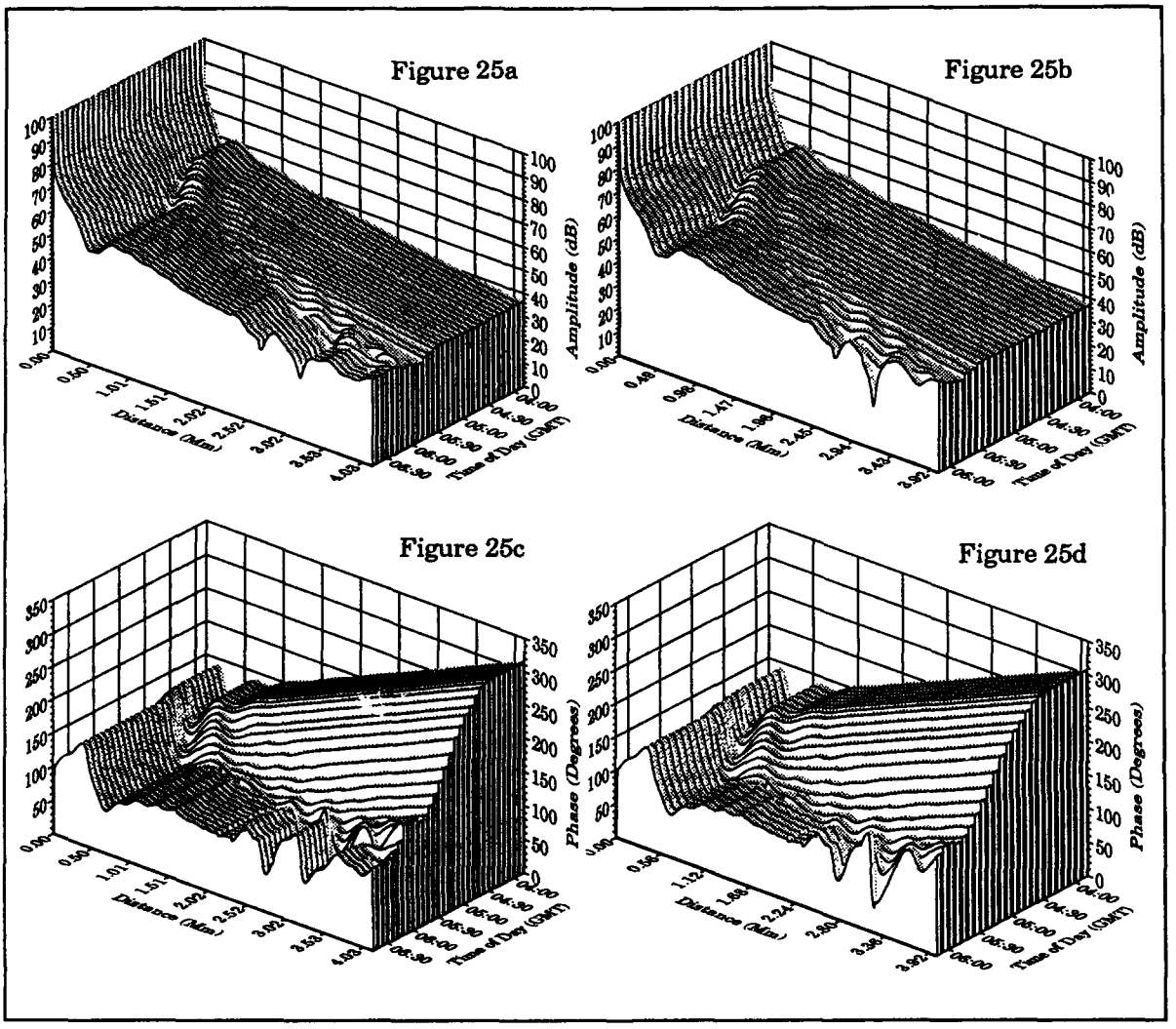

Figure 25. Sunset Transition Along 202° Radial; Hawaii to Samoa at 10.2 kHz

that is useful. This is a personal computer! We are excited about what we can do.

We clearly have a lot of learning ahead of us to be able to interpret equatorial ionosphere dynamics using VLF measurements. With respect to communications modeling, we expect that it will be much easier to initially explore ionosphere parameters using Omega frequencies rather than higher ones.

References:

Kelly, M.C., J. LaBelle, E. Kudeki, B.G. Fejer, Sa. Basu, Su. Basu, K.D. Baker, C. Hanuise, P. Argo, R.F. Woodman, W.E. Swartz, D.T. Farley, and J.W. Meriwether, Jr., "The Condor Equatorial Spread F Campaign: Overview and Results of the Large-Scale Measurements," *J. of Geophys. Res.*, 91, 5487, 1986.

Zalesak, S.T., and S.L. Ossakow, "Nonlinear Equatorial Spread F: Spatially Large Bubbles Resulting From Large Horizontal Scale Initial Perturbations," *J. of Geophys. Res.*, 85, 1231, 1980.

Argo, P.E., and M.C. Kelly, "Digital Ionosonde Observations During Equatorial Spread F," *J. of Geophys. Res.*, 91, 5539, 1986.

Ferguson, J.A., F.P. Snyder, D.G. Morfitt, and C.H. Shellman, "Software Program Long-Wave Propagation Capability and Documentation," Naval Ocean Systems Center, Technical Document 1518, March 1989.

Wait, J.R., and K.P. Spies, "Characteristics of the Earth-Ionosphere Waveguide for VLF radiowaves, NBS Tech. Note 300, 1964.

Hildebrand, V.E., "Practical Implications for Omega Navigation Derived From Modeling Analysis of Equatorial Zone Mode Conversion of Omega and VLF Signals," Proc. 16th Annual Meeting of the Int. Omega Assoc., Vancouver, British Columbia, Canada, 5–9 August 1991.

Hildebrand, V.E., "Omega Western Pacific Validation Highlights," Proc. 15th Annual Meeting of the Int. Omega Assoc., Sanur Beach, Bali, 24–28 September 1990.

Hildebrand, V.E., "Omega Validation Highlights," Proc. 14th Annual Meeting of the Int. Omega Assoc., Long Beach, CA, 2–6 October 1989.

Discussion

J.A. FERGUSON (US)

Have you considered the effect of ionospheric structure in the equatorial region?

AUTHOR'S REPLY

We are concerned with two types of structure - profile variation along the path and profile shape with height. We are in the process of adapting our computer program to study each type of structure. Our philosophy is to determine if measurements can be explained with exponential profiles and if not what structure is needed.

J.H. Richter (US)

In your modeling, you use a simple, two parameter electron density profile and assume horizontal homogeneity as well as temporal persistence. Is it appropriate to match individual segments of measured data and relate the profile parameters providing such a match to dynamic ionospheric properties (e.g., reference height).

AUTHOR'S REPLY

My use of a two parameters horizontally homogeneous profile is for only initial studies. I am now adapting the computer program to handle arbitrary profile shapes and variation of profiles along a path. Two points: (1) the simple model gives information about the need for added complexity. Often the simple profile fits quite well. (2) my analysis shows that the profile changes with time, i.e. during the night. However, the changes are sufficiently slow that at any one time the profile likely is about the same along the path. Exceptions do occur. Matching individual segments to describe an aircraft measurement is necessary because the flight takes a long time (6 hours). I contend that, if the profile changes are consistent with a reasonable physical model and, if the model fits "many" measurements, the process is valid.

Transient (≈10 s) VLF amplitude and phase perturbations due to lightning-induced electron precipitation into the ionosphere (the "Trimpi effect")

A.J. Smith
P.D. Cotton[1]
J.S. Robertson
British Antarctic Survey
High Cross, Madingley Road
Cambridge CB3 0ET, UK

SUMMARY

This paper describes certain characteristics and statistics of the Trimpi effect, as observed near to and equatorward of the Antarctic Peninsula region, inferred using data from specially designed narrow-band OPAL (Omega Phase and Amplitude Logger) receivers deployed in 1989 at Faraday and Halley stations, Antarctica. The amplitude and phase of signals from four Omega VLF transmitters were recorded in each Omega segment (8 segments per 10 s). A 12-month-long data set has been scanned for Trimpi events which, however, were observed on only three of the eight paths, namely Hawaii–Faraday, Argentina–Faraday, and Argentina–Halley, due to inadequate signal-noise ratio on the other paths. The great majority of the ~3500 observed events occurred at night. For the all-sea Hawaii–Faraday path at night, with a single mode dominant at the receiver, lightning-induced electron precipitation (LEP) was inferred to be occurring up to ~1.8 Mm from Faraday. A scatter plot of Trimpi amplitude versus phase for this path is interpreted to infer that LEP regions responsible for the events occurred mostly in the L-range 2–3, with the horizontal size of an affected region in the ionosphere being typically 50 km latitudinally and 200 km longitudinally.

1 INTRODUCTION

It is now recognised that interactions between whistlers (originating in lightning) and energetic electrons trapped in the earth's magnetosphere, can cause scattering which leads to the precipitation of electron bursts into the ionosphere, known as LEP (Lightning-induced Electron Precipitation). The incidence of precipitation bursts with energies greater than about 40 keV can be detected over a wide area from ground stations by means of the secondary ionisation enhancements they produce in the lower ionosphere (40–80 km altitude), which in turn cause transient disturbances to the long-distance propagation of VLF radio signals. The ionisation enhancements have been termed lightning-induced ionisation enhancements, or LIEs (Ref [1]), whilst the propagation perturbations, which generally occur in both the amplitude and phase of the received signal, are known as Trimpi events after their discoverer (Ref [2]). Trimpi events are readily recognisable from their asymmetric time variation, having an onset time of order 1 s (determined by the precipitation flux time profile) and a recovery time in the range 10–30 s (determined by ionospheric relaxation time constants). The magnitude of the perturbations is typically a few degrees in phase and a few tenths of a dB in amplitude. Perturbations may be of either sign, though phase advances combined with amplitude decreases are the most common, as predicted by the simplest model of increased phase speed under a temporarily lowered ionosphere (Ref [3]).

In this paper we briefly note relevant previous work on the Trimpi phenomenon and describe recently established VLF 'imaging' networks, in which intersecting paths between widely spaced transmitters and receivers are used to locate and delineate the precipitation regions associated with Trimpi events. Results from one such network, OPALnet, in which Omega transmissions are received in Antarctica, are presented here. We show the statistics of the phenomenon in terms of the occurrence as a function of local time and season, and also the distribution of signed amplitude and phase perturbations which are observed. From these observations, inferences are drawn regarding the size and location of the LIEs giving rise to the Trimpi events. This report is a only a summary; full details will be given in a paper to be submitted for publication elsewhere.

2 OBSERVATIONS OF TRIMPI EFFECTS

The Trimpi effect was first reported nearly 20 years ago ([2]) but has recently been the subject of increasing attention. References to work on the topic prior to 1990 are given in Ref [4].

The importance of the effect is twofold. Firstly it can be used as a technique for studying LEP which is both a loss mechanism for the trapped radiation belts and a source of energy input to the upper atmosphere. Indeed, because the altitude of the LEP is generally too low for satellite observations (although a few experiments have been done—see e.g. Ref [5]), VLF measurements of Trimpi effect seem at present the only feasible technique for the systematic study of LEP characteristics.

Secondly, as far as the user of VLF transmissions is concerned, the effect is an additional source of lightning associated noise. Greater knowledge of its properties could be used as input data when engineering improved VLF communications or radio-navigation systems.

Much early work on the Trimpi effect used observations made at a single receiver site, and most experiments ob-

[1]Now at James Rennell Centre for Ocean Circulation, Southampton SO1 7NS, UK

served just the signal amplitude and not the phase (see e.g. Ref [6]). More recently, multi-point receiver networks have been deployed specifically for Trimpi studies, and phase as well as amplitude measurements have been more commonly made. Such networks are increasing in number and currently exist in North America, Australasia, Europe, South Africa, and Antarctica.

Inan et al. (Ref [7]) have recently described such a network in North America for 'imaging' LIEs. The method assumes that a LIE will result in a Trimpi event on a particular received signal only if the transmitter-receiver great circle path (TRGCP) passes through or very close to it (Ref [8]). With this assumption, a network of intersecting TRGCPs can be used to map the location and shape of LIEs over a wide area, including simultaneous regions in opposite hemisphere (Ref [9]). However Dowden and Adams (Ref [10]), citing theoretical work by Wait (Ref [11]), have argued that this geometrical optics approach is valid only for large LIEs in which the ionisation enhancement at the edge decrease as a Gaussian function. ('Large' in this context means greater in horizontal extent transverse to the TRGCP than $\sim \sqrt{\lambda s}$ where λ is the radio wavelength and s the transmitter–receiver distance; this is typically of order $\sim$ 300 km in problems of practical interest.) Non-Gaussian or small LIEs can scatter radiation incident upon them, to produce observable Trimpi events, even when well off the TRGCP; Adams and Dowden (Ref [12]) have reported such 'echo' Trimpis arising from LEP occurring up to 1000 km from the TRGCP.

Apart from the wide-area networks, Dowden and Adams (Ref [13]) have also shown the importance of closely-spaced (less than a wavelength) receiver arrays, in determining the direction of arrival of the perturbation signal, as additional information for locating the LIE regions.

3 THE OPALNET EXPERIMENT

OPALnet is a network of OPAL (Omega Phase and Amplitude Logger) receivers set up in 1989 as a joint experiment between British Antarctic Survey and the University of Otago, New Zealand. Figure 1 shows a map of the network. Seven of the eight globally spaced Omega transmitters are shown. Receivers were placed at Faraday (65° 15′ S; 64° 15′ W; L = 2.3) and Halley (75° 36′ S; 26° 36′ W; L = 4.3), Antarctica, and at Dunedin, New Zealand. The map shows a selection of possible transmitter– receiver paths. Other OPAL receivers were operated for a time in Norway (Ref [14]) and Macquarie Island. In this paper we will discuss only the data collected at Faraday and Halley.

Each OPAL receiver was capable of receiving signals from four of the Omega transmitters. Those chosen for the Faraday and Halley receivers are indicated in Figure 1,

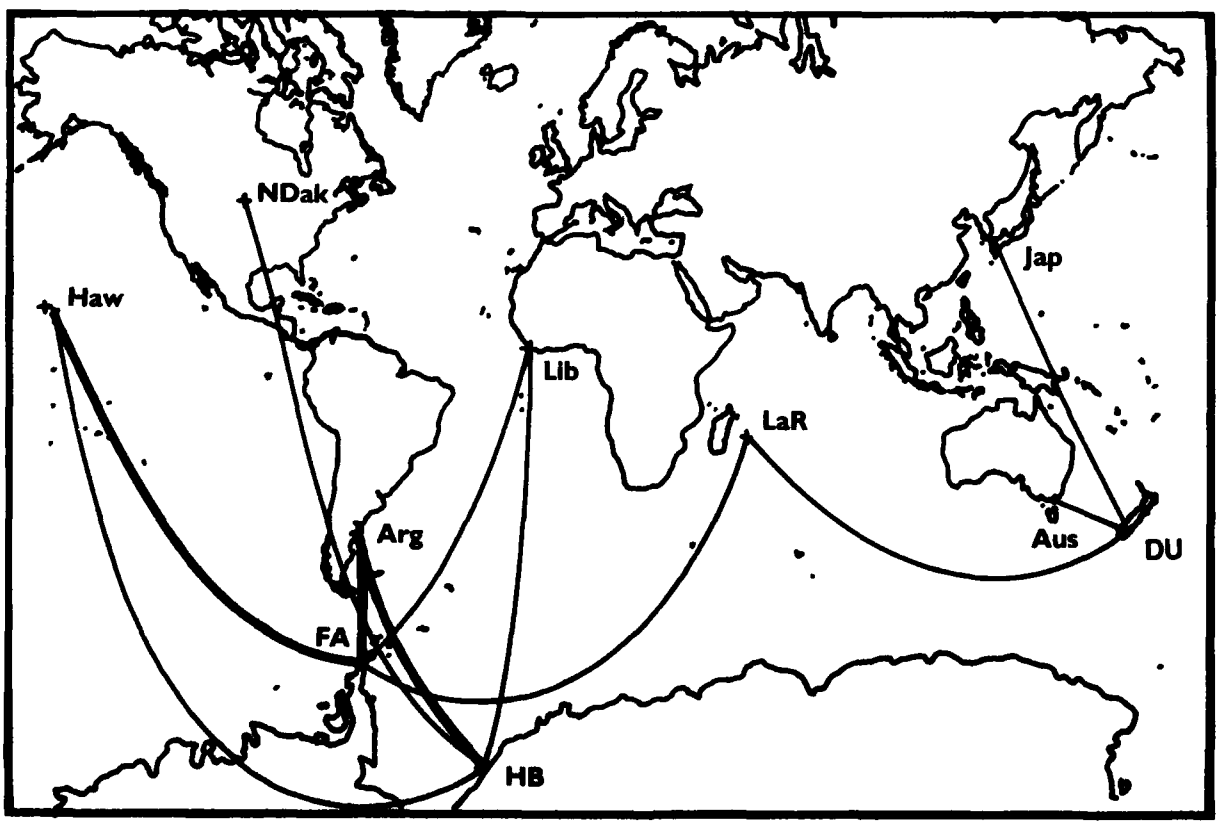

Figure 1. Map of the OPALnet experiment. OPAL receivers were located at Faraday (FA), Halley (HB) and Dunedin (DU). During the 12 months beginning April 1989 the Faraday and Halley OPALs each received signals from four of the Omega transmitters, as shown by the corresponding TRGCPs. Trimpi events were observed only on the three paths shown as thick lines.

and were expected to give the highest signal amplitudes (shorter paths, or paths not crossing the Antarctic ice sheet). In each Omega segment (8 segments per 10 s), the average amplitude and phase (relative to a local reference) were measured and recorded digitally by a host computer on to floppy disc. The receiver firmware was programmed with the Omega transmission format and therefore 'knew' which frequency, either unique or one of the four common frequencies, to expect to receive in each segment. Figure 2 shows two examples of the data including some typical Trimpi events. The events are best seen in the top panel corresponding to the unique frequency (12.9 kHz for the Argentina transmitter in this case), because there are four unique frequency transmissions per 10 s Omega repetition cycle, giving an average time resolution of 2.5 s; in contrast, each common frequency is transmitted in only 1 segment (10 s time resolution).

During the 12 months beginning April 1989, both Halley and Faraday receivers operated essentially continuously. All the data produced during this period have been examined for the occurrence of Trimpi events, using a combination of visual examination of paper charts and an automatic searching routine (see Ref [15]). For each unambiguously identified event (3489 events in all), the onset time was noted, and the maximum amplitude and phase excursions seen in the unique frequency were scaled. Events were seen on only three of the possible eight paths: those for which the typical nighttime received signal amplitude was $\gtrsim 1$ pT rms (300 μV rms), i.e. Argentina–Faraday, Hawaii–Faraday and Argentina–Halley. For the effective receiver bandwidth of about 1 Hz (averaging was done over one Omega segment) and ambient noise levels, the signal/noise ratios for these paths were $\gtrsim$ 30 dB. For the other paths observed, Trimpi events of typical size would not have been detectable above the noise.

4 DIURNAL/ SEASONAL OCCURRENCE

Figure 3 shows the occurrence of Trimpi events observed on the Hawaii to Faraday path over the 12-month period. Time of year is plotted horizontally and UT vertically. For each hour of each day the corresponding pixel

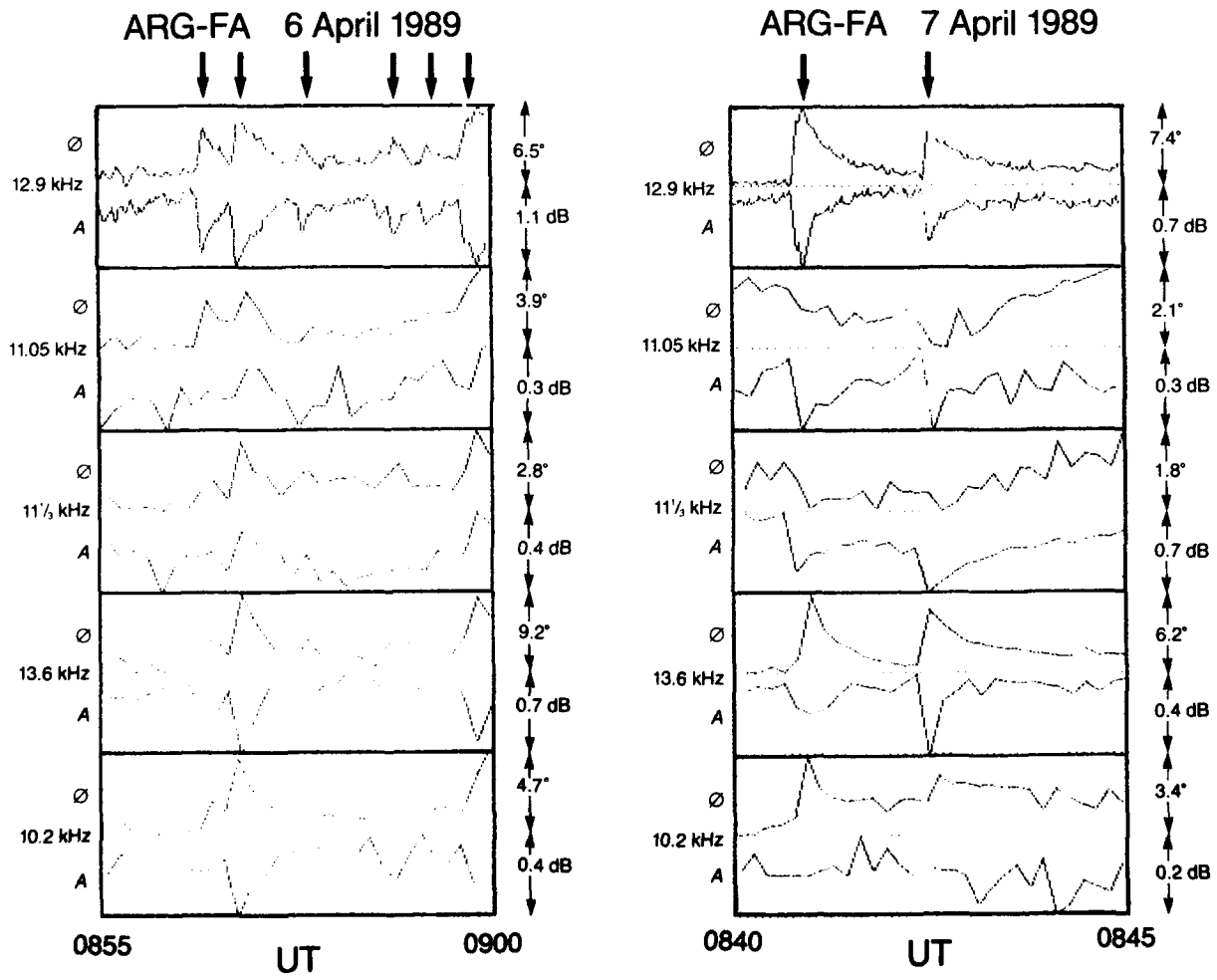

Figure 2. Example of data from one of the OPAL receivers. Two five-minute frames are shown, for each of which is plotted the amplitude and phase variation of the signal from Omega-Hawaii, received at Faraday, for the unique frequency (12.9 kHz) and the four common frequencies. All panels are auto-scaled and so are not directly intercomparable; the full-scale range for each panel is indicated at the right. Examples of Trimpi events are indicated by arrows in the top margin; some additional smaller events may also be discerned.

is grey or black if one or more events were observed, and is otherwise white. Data gaps are indicated by shading. It is well known from earlier studies, e.g. at Palmer (Ref [16]), that events are invariably observed when the ionospheric region affected by the associated LEP is in darkness; energies of the precipitating electrons are generally insufficient to penetrate to the lower effective reflection height of the daytime ionosphere. This explains the lack of events around the December (local summer) solstice when the ionosphere above Faraday is permanently sunlit, and at UTs corresponding to local day-time for the propagation path. If all LIEs corresponding to observed Trimpis occurred at the same geographic point, we would expect the day-night terminator for that point, when plotted on the time-of-year vs. UT plot, to act as a separatrix between occurrence and non- occurrence. In fact for terminator plots corresponding to all points on the Hawaii-Faraday TRGCP, the best fit is that shown in Figure 3 which corresponds to a point 1.8 Mm from Faraday and 80 km altitude (cf. Ref [17]).

We note in the figure that occurrence is greater at equinox than winter solstice, and greater post- than pre- midnight, in agreement with earlier work at Palmer (Ref [16]). This is thought to be a consequence of the greater occurrence of lightning whistlers at these times. Similar results were found for the other two paths (Argentina-Faraday and Argentina-Halley) except that in these cases a small fraction of the events ($\sim$ 6%) occurred at times when the entire TRGCP was in daylight, presumably indicative of unusually energetic LEP.

5 AMPLITUDE AND PHASE OF THE PERTURBATIONS

In the scatter plot of Figure 4a, each point represents for a single Trimpi event the magnitude and sign of the maximum perturbation of the amplitude (ΔA) and phase ($\Delta\phi$) with respect to the unperturbed signal. The 865 events observed on the Hawaii-Faraday path at 11.8 Hz (the unique frequency) during the 12-month period are plotted. The bands devoid of points, near to both axes, represent the limit due to noise. The ratio of the scales on the two axes is such that lines of slope ± 0.14 dB/degree (shown dotted) bisect the four quadrants. In this representation, the perturbation phasor (see Ref [18]), i.e. the perturbed signal phasor minus the unperturbed signal phasor, is represented in amplitude and phase by the magnitude and direction of a vector from the origin (Ref [1]).

The great majority of events ($\sim$ 90%) lie in the top left quadrant, corresponding to phase-advance amplitude-decrease Trimpi events, though a few lie in the other quadrants. The problem here involves a subionospheric signal which effectively consists of a single mode; the 12.3 Mm long all-sea path results in the first mode being at least 40 dB greater than the second mode at Faraday at all the Omega frequencies. This, together with the assumption that mode conversion at the LIE is negligible, allows us to draw some conclusions from the scatter plot regarding the size and shape of the LIEs giving rise to the Trimpi events. Corresponding plots for the other two paths show a similar behaviour.

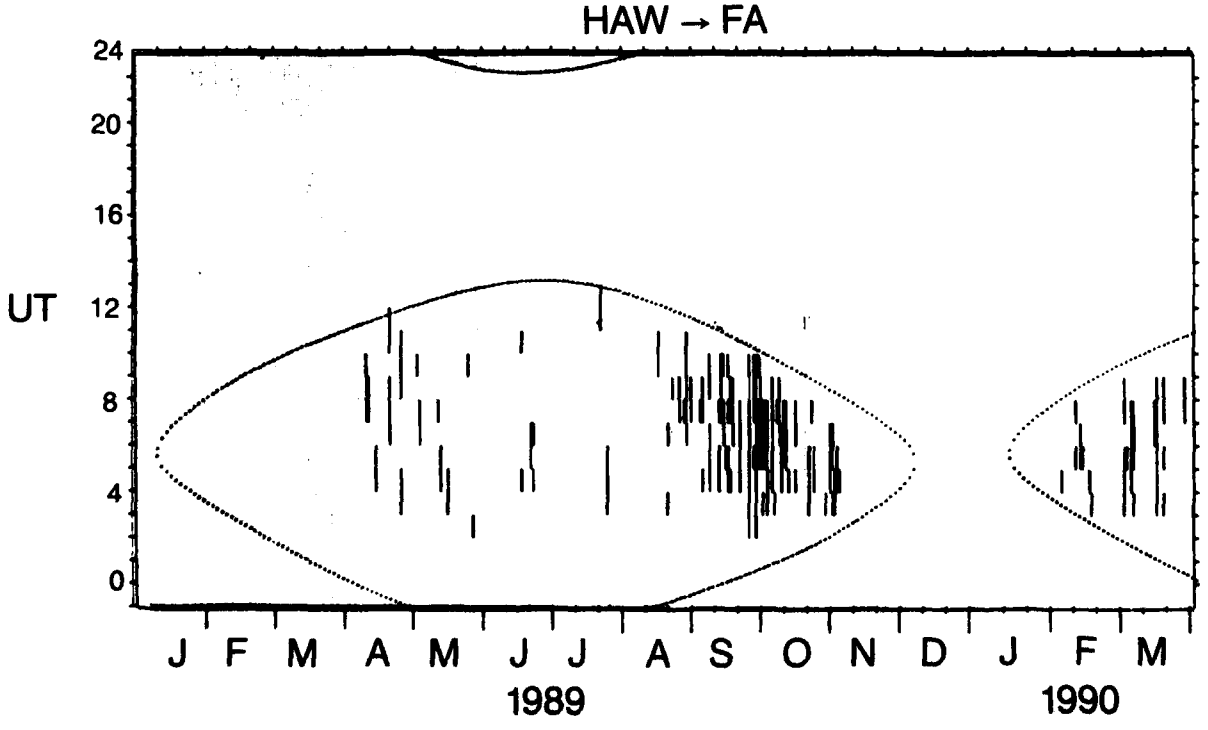

Figure 3. Occurrence of Trimpi events observed at Faraday on the unique frequency from Omega-Hawaii, versus UT and time of year, for the 12 months from April 1989. See text for details.

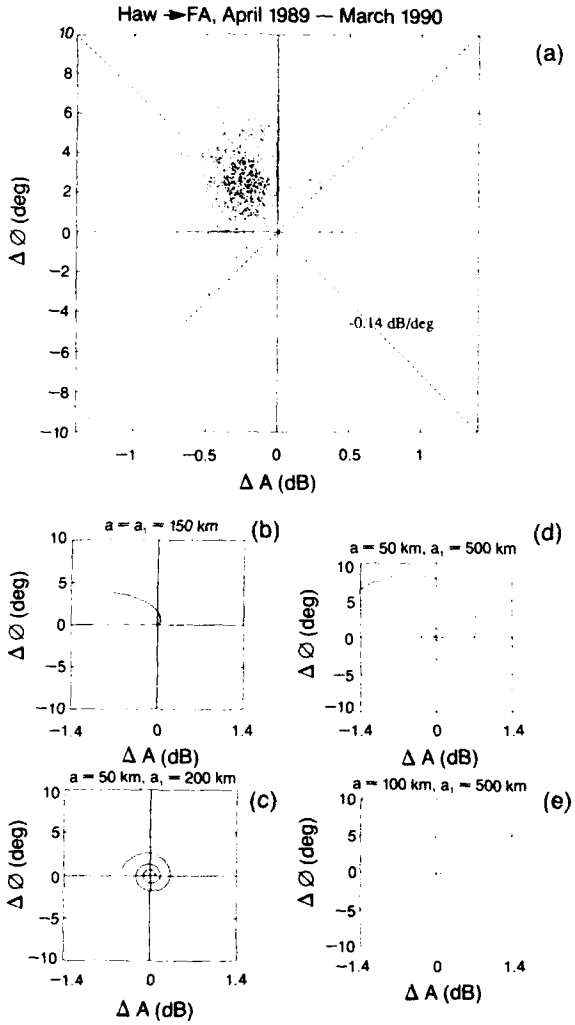

Figure 4. (a) Scatter plot showing Trimpi amplitude (ΔA) and phase ($\Delta\phi$) for all events seen at Faraday on the unique frequency from Omega-Hawaii, for the 12 months from April 1989. (b)–(e) Spiral plots of calculated ΔA vs. $\Delta\phi$ dependence as a LIE of horizontal dimension a (along the TRGCP) and a_1 (transverse to the TRGCP) is displaced away from the TRGCP. Poulsen's scattering algorithm is used (Ref [4]). See text for more details.

6 DISCUSSION

For a simple model in which all LIEs giving rise to Trimpi events straddle the TRGCP and are large in their dimension perpendicular to the TRGCP, and in which the LIE is considered as a region of lowered effective reflection height and thus increased phase velocity, ΔA and $\Delta\phi$ will be negative and positive respectively, and the $\Delta A/\Delta\phi$ ratio will be a constant (−0.48 dB/deg for the NPM–Palmer case considered by Inan and Carpenter, Ref [3]). This is clearly not the case for the present data, so the above assumptions cannot be valid.

On the other hand, the Dowden and Adams model of small scatterers distributed over a range of distances from the TRGCP (Ref [19]) predicts an equal distribution of points in all four quadrants (Ref [1]). This is illustrated by the model plots of Figure 4b–4e, in which the Poulsen et al. (Ref [8]) scattering algorithm is used (see Ref [20]) to estimate the amplitude and phase of a perturbation due to a LIE of width (transverse to the TRGCP) a and length (along the TRGCP) of a_1, distance 1 Mm from Faraday. When the LIE is on the TRGCP, the perturbation phasor is in the top left quadrant. The spiral represents how the phasor changes for a LIE further and further displaced from the TRGCP (see Ref [19]). For the circular 150 km LIE, the spiral winds up rapidly, i.e. it produces Trimpi events only when close to the TRGCP. For smaller a the wind-up is much slower because the LIE can fit within a single Fresnel lane (an elliptical annulus with the transmitter and receiver as foci, within which all scatterers produce perturbations with phase within a 180° range, see Ref [1]) up to considerable distances from the TRGCP, although the size of the perturbation is smaller unless a_1 is increased to compensate. For a statistical sample of Trimpi events from such LIEs, we would expect a spread of distances from the TRGCP to occur, and therefore phasors to be scattered more or less evenly in all four quadrants.

The fact that the distribution of points in Figure 4a is as shown, and points lie neither on a line in the top left quadrant, nor evenly distributed around all quadrants, coupled with the single mode assumption, implies that the typical LIE sizes transverse to the TRGCP are comparable to that of the first Fresnel lane, i.e. in the case of the Hawaii–Faraday path about 50–100 km. Note that for points on the path close to the receiver, where the TRGCP is roughly east-west, this corresponds approximately to the latitudinal dimension. The size of the observed events, interpreted by a simple scattering model as illustrated in Figure 4b–4e, suggests that typical sizes along the TRGCP (i.e. in longitudinal extent near Faraday) are of order 100–500 km. These conclusions are in agreement with the work of Carpenter and LaBelle (Ref [6]).

Similar distributions of events in ΔA vs. $\Delta\phi$ plots were found for the other two paths. Although for those cases the interpretation is more complicated, owing to the possibility that more than one mode needs to be considered, it seems that a similar interpretation is plausible. Figure 5 shows the three paths together with the appropriate first Fresnel lane for the unique frequencies, and summarises our conclusions. LIEs giving rise to observed Trimpi events are inferred, from the results of Section 4, to occur only south of the points on each path marked by a cross. In this sector of the path, the typical LIEs dimensions transverse to the TRGCP are comparable with the size of the Fresnel lane width, i.e. 50–100 km. It is clear that such regions would be unlikely to produce a response on more than one of the paths. This is confirmed by the finding that almost all ($\geq$ 95%) of events were non-coincident (not within 5 s) of an event seen on a different path.

It is interesting to note the differences between the results reported here for the Hawaii–Faraday path and the results for NWC (22.3 kHz) to Dunedin reported by Dowden et al. (Ref [1]), in which they mostly found small scattering regions well off the TRGCP. Although the path lengths (12.3 Mm for the former and 5.7 Mm for the later), and frequencies were somewhat different in the two experiments, in other respects they were rather simi-

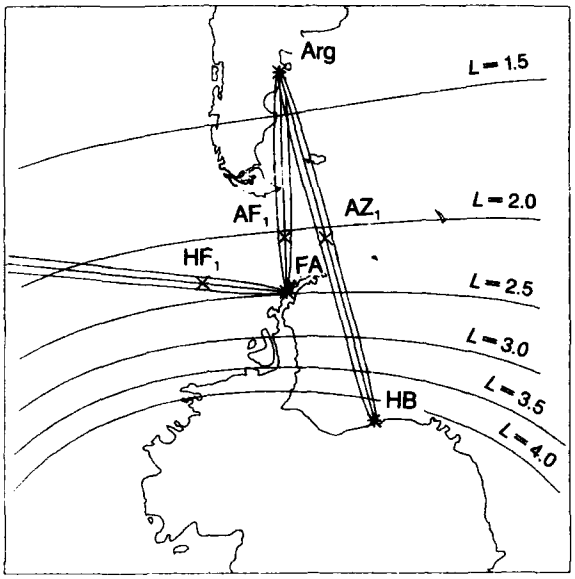

Figure 5. The three paths on which Trimpi events were observed, shown with their corresponding first Fresnel lanes. Corresponding LIEs were inferred from the diurnal/seasonal occurrence to lie mostly between the receiver and the point on the path marked by a cross. The constant L contours show that this corresponds to a region with $L \gtrsim 2$ in agreement with previous work (Ref [6]).

lar, i.e. west-to-east paths all or nearly all over sea, with a receiver at a similar L-shell ($L = 2.3$ for Faraday; $L = 2.7$ for Dunedin). This suggests that the properties of LEP are probably longitude dependent, which may be related to longitudinal variations in whistler activity (Ref [21]) and in loss cone angles of magnetospherically trapped energetic electron populations (Ref [22]).

REFERENCES

1. Dowden, R.L., Adams, C.D.D. and Cotton, P.D., "Use of VLF transmissions in the location and mapping of lightning-induced ionisation enhancements (LIEs)", J. Atmos. Terr. Phys., *54*, 1992, pp 1355–1373.

2. Helliwell, R.A., Katsufrakis, J.P. and Trimpi, M.L., "Whistler induced perturbation in VLF propagation", J. Geophys. Res., *78*, 1973, pp 4679–4688.

3. Inan, U.S. and Carpenter, D.L., "Lightning-induced electron precipitation events observed at $L \sim 2.4$ as phase and amplitude perturbations on subionospheric VLF signals", J. Geophys. Res., *92*, 1987, pp 3292–3303.

4. Smith, A.J. and Cotton, P.D., "The Trimpi effect in Antarctica: Observations and models", J. Atmos. Terr. Phys., *52*, 1990, pp 341–355.

5. Voss, H.D., Imhof, W.L., Walt, M., Mobilia, J., Gaines, E.E., Reagan, J.B., Inan, U.S., Helliwell, R.A., Carpenter, D.L., Katsufrakis, J.P. and Chang, H.C., "Lightning-induced electron precipitation", Nature, *312*, 1984, pp 740–742.

6. Carpenter, D.L. and LaBelle, J.W., "A study of whistlers correlated with bursts of electron precipitation near $L = 2$", J. Geophys. Res., *87*, 1982, pp 4427–4434.

7. Inan, U.S., Knifsend, F.A. and Oh, J., "Subionospheric VLF "imaging" of lightning-induced electron precipitation from the magnetosphere", J. Geophys. Res., *95*, 1990 pp 17217–17231.

8. Poulsen, W.L., Bell, T.F. and Inan, U.S., "Three-dimensional modeling of subionospheric VLF propagation in the presence of localized D region perturbations associated with lightning", J. Geophys. Res., *95*, 1990, pp 2355–2366.

9. Burgess, W.C. and Inan, U.S., "Simultaneous disturbance of conjugate ionospheric regions in association with individual lightning flashes", Geophys. Res. Lett., *17*, 1990, pp 259–262.

10. Dowden, R.L. and Adams, C.D.D., "Lightning- induced perturbations on VLF subionospheric transmissions", J. Atmos. Terr. Phys., *52*, 1990, pp 357–363.

11. Wait, J.R., "Influence of a circular ionospheric depression on VLF propagation", J. Res. NBS, *68D*, 1964, pp 907–914.

12. Adams, C.D.D. and Dowden, R.L., "VLF group delay of lightning-induced electron precipitation echoes from measurement of phase and amplitude perturbations at two frequencies", J. Geophys. Res., *95*, 1990, pp 2457–2462.

13. Dowden, R.L. and Adams, C.D.D., "Location of lightning-induced electron precipitation from measurement of VLF phase and amplitude perturbations on spaced antennas and on two frequencies", J. Geophys. Res., *95*, 1990, pp 4135–4145.

14. Dowden, R.L., Adams, C.D.D., Rietveld, M.T., Stubbe, P. and Kopka, H., "Phase and amplitude perturbations on subionospheric signals produced by a moving patch of artificially heated ionosphere", J. Geophys. Res., *96*, 1991, pp 239–248.

15. Hurren, P.J., Smith, A.J., Carpenter, D.L. and Inan, U.S., "Burst precipitation induced perturbations on multiple VLF propagation paths in Antarctica", Ann. Geophys., *4A*, 1986, pp 311–318.

16. Carpenter, D.L. and Inan, U.S., "Seasonal, latitudinal and diurnal distributions of whistler-induced electron precipitation events", J. Geophys. Res. *92*, 1987, pp 3429–3435.

17. Leyser, T.B., Inan, U.S., Carpenter, D.L. and Trimpi, M.L., "Diurnal variation of burst precipitation effects on subionospheric VLF/LF signal propagation near $L = 2$", J. Geophys. Res., *89*, 1984, pp 9139–9143.

18. Dowden, R.L. and Adams, C.D.D., "Phase and amplitude perturbations on subionospheric signals ex-

plained in terms of echoes from lightning-induced electron precipitation ionization patches", J. Geophys. Res., *93*, 1988, pp 11543–11550.

19. Dowden, R.L. and Adams, C.D.D., "Phase and amplitude perturbations on the NWC signal at Dunedin from lightning-induced electron precipitation", J. Geophys. Res., *94*, 1989, pp 497–503.

20. Cotton, P.D. and Smith, A.J., "The signature of burst particle precipitation on VLF signals propagating in the Antarctic earth-ionosphere waveguide", J. Geophys. Res., *96*, 1991, pp 19375–19387.

phys. Res., *96*, 1991, pp 19375–19387.

21. Smith, A.J., Carpenter, D.L., Corcuff, Y., Rash, J.P.S. and Bering, E.A., "The longitudinal dependence of whistler and chorus characteristics observed on the ground near $L = 4$", J. Geophys. Res., *96*, 1991, pp 275–284.

22. Bering, E.A., Benbrook, J.R., Leverenz, H., Roeder, J.L., Stansbery, E.G. and Sheldon, W.R., "Longitudinal differences in electron precipitation near $L = 4$", J. Geophys. Res., *93*, 1988, pp 11385–11403.

LIGHTNING-INDUCED EFFECTS ON VLF/LF RADIO PROPAGATION

by

U. S. Inan and J. V. Rodriguez
Space, Telecommunications and Radioscience Laboratory, Stanford University
Stanford, California 94305
USA

1. SUMMARY

In recent years, at least two different ways in which energy from lightning discharges couples into the lower ionosphere and the radiation belts have come to fore. In this paper, we briefly review these recent results especially from the point of view of their effects on VLF/LF radio propagation in the earth-ionosphere waveguide. We separately discuss two different mechanisms of coupling, namely (i) lightning-induced electron precipitation, and (ii) lightning-induced heating and ionization of the lower ionosphere. We also discuss a planned active VLF wave-injection experiment designed to investigate ionospheric heating by VLF waves under controlled conditions and to generate ELF waves by modulated VLF heating.

2. LIGHTNING-INDUCED ELECTRON PRECIPITATION

Many aspects of the physics of Lightning-induced Electron Precipitation (LEP) have now been relatively well documented, based on extensive measurements of associated ionospheric disturbances as subionospheric VLF/LF amplitude and phase changes [*Inan et al.*, 1990] as well as satellite measurements [*Voss et al.*, 1984] and theoretical modeling [*Chang and Inan*, 1985]. The LEP phenomenology and the associated ionospheric disturbance is depicted in Figure 1.

The subionospheric VLF method of detection of LEP associated ionospheric disturbances is illustrated in Figure 2. VLF/LF signals propagating in the earth-ionosphere waveguide provide a sensitive means for detection of ionospheric disturbances at altitudes of 60-90 km. At night, the 'reflection height' for VLF/LF waves is ~85 km, so that the subionospheric VLF signal characteristics (e.g., amplitude and/or phase) depend most sensitively to conductivity changes (either due to electron density or temperature changes) near ~85 km. In recent years, perturbations with a characteristic time signature, involving rapid onset (<2 s) followed by slower recovery (10-100 s) (see Figure 4), and referred to as 'Trimpi Events', have been measured in association with lightning discharges and/or whistlers [e.g., *Burgess and Inan*, 1990]. These events have been interpreted as ionospheric signatures of LEP bursts. Both theoretical [*Poulsen et al.*, 1990] and experimental work [*Inan et al.*, 1990] indicates that the disturbed ionospheric regions associated with LEP events are in most cases within <~ 200 km of the perturbed VLF great circle paths.

An unusually high rate of LEP event activity observed on 23 February 1990 is illustrated in Figure 3, showing individual events simultaneously registered on three different collinear VLF paths (NLK-HU, 48.5-HU, 48.5-AR). The path nomenclature (i.e., NLK-HU) refer to the transmitter (as identified either by call sign or frequency as listed in Table 1) and the receiver sites, which in this case are Arecibo (AR), Puerto Rico, and Huntsville (HU), Alabama. The fact that the NAU-HU signal is not perturbed is consistent with the disturbed ionospheric region being located between the 48.5 kHz transmitter and Huntsville (HU), near the perturbed collinear VLF paths.

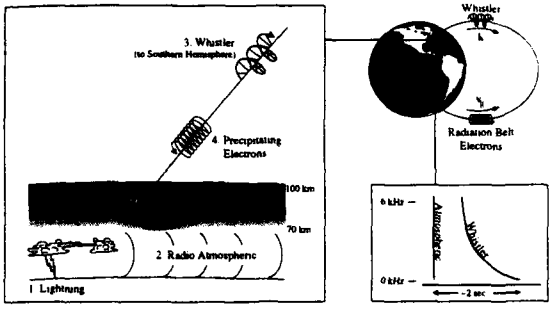

Figure 1: Lightning discharge (1) launches a radio atmospheric, or 'sferic' (2), which propagates in the Earth-ionosphere waveguide and is often strong enough to be detectable all over the planet. Enhancements of the plasma above the ionosphere, aligned with the geomagnetic field and known as 'ducts,' can trap a portion of the sferic energy and cause it to propagate along a field line to the opposite hemisphere as a whistler (3). During its journey the circularly-polarized whistler can interact with gyrating energetic radiation belt electrons, scattering them in pitch angle so that some escape from their geomagnetic trap (4). Upon striking the ionosphere, the precipitating electrons cause significant secondary ionization (5). Meanwhile, the whistler emerges from its duct and can be observed, along with the subionospherically propagating 'causative' sferic, with broadband VLF radio equipment in the opposite hemisphere.

TABLE 1. VLF/LF Transmitters.

Call Sign	Transmitter	Frequency	Latitude	Longitude
NSS	USN Maryland	21.4 kHz	39°N	76°W
NPM	USN Hawaii	23.4 kHz	21°N	158°W
NAU	USN Puerto Rico	28.5 kHz	18°N	67°W
NAA	USN Maine	24.0 kHz	45°N	67°W
NLK	USN Washington	24.8 kHz	48°N	122°W
	USAF Nebraska	48.5 kHz	42°N	98°W

Data from the National Lightning Detection Network (courtesy of Vince Idone of State University of New York (SUNY) in Albany) for 0900-1000 UT on 23 February 1990 shows (Figure 3) an isolated storm center (+'s represent locations of CG lightning) well south-east of the region of overlap of the collinear VLF paths as the only thunderstorm active at this time. Temporal association between some of the lightning discharges from the storm and some of the VLF perturbations is used to establish a causative connection, similar to previous cases studied in detail [*Inan et al.*, 1988b; *Yip et al.*, 1991]. That the storm center is not near the perturbed VLF paths is consistent with the dependence of the ionospheric disturbance location on the availability of magnetospheric propagation paths (i.e., 'ducts') and/or energetic particle distributions [*Yip et al.*, 1991].

Expanded record of one event shown in Figure 4 illustrates typical detailed temporal features consistent with whistler-induced electron precipitation as the causative agent, including; (i) ~ 1 s *delay* between the causative radio atmospheric and the event onset representing the time-of-travel of of both the whistler wave and the electrons respectively to and from the high altitude (equatorial) interaction region, (ii) onset *duration* of ~1-2 s, representing the duration of the whistler-induced electron precipitation burst [*Chang and Inan*, 1985]. The relatively slow (10-100 s) event *recoveries* are consistent with expected relaxation times for secondary ionization produced in the D-region by precipitating energetic electron bursts [*Glukhov et al.*, 1992]. While the LEP event signatures shown in Figure 3 are events with negative amplitude changes, in general both negative and positive changes can occur [*Inan et al.*,1990].

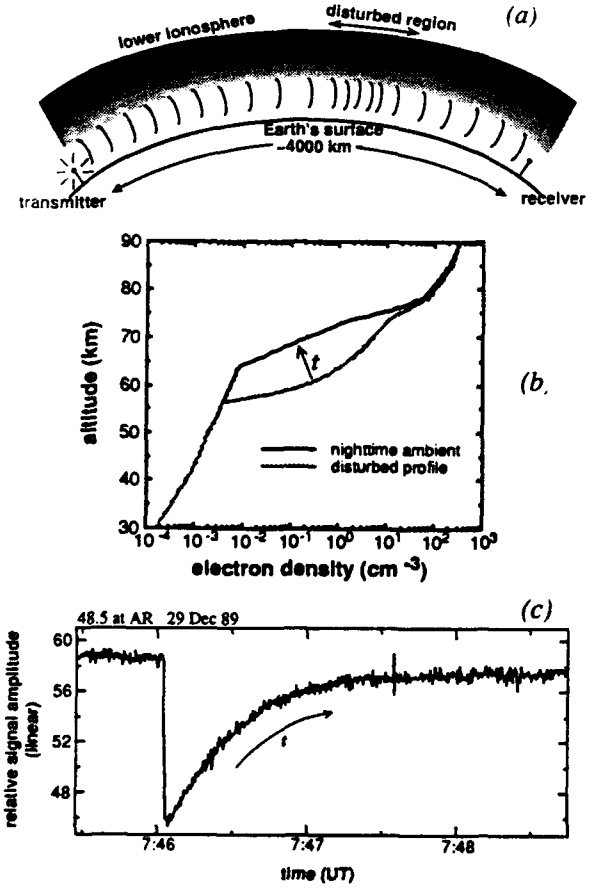

Figure 2: (a) Schematic description of the disturbed ionosphere. (b) Representative electron density profile within the disturbed region. (c) A typical VLF/LF perturbation signature of a lightning-induced electron precipitation burst observed on the 48.5 kHz signal (see Table 1) at Arecibo (AR), Puerto Rico (see Figure 4 for propagation path). The signal amplitude A is plotted using a linear scale, with $A = 0$ representing absence of signal.

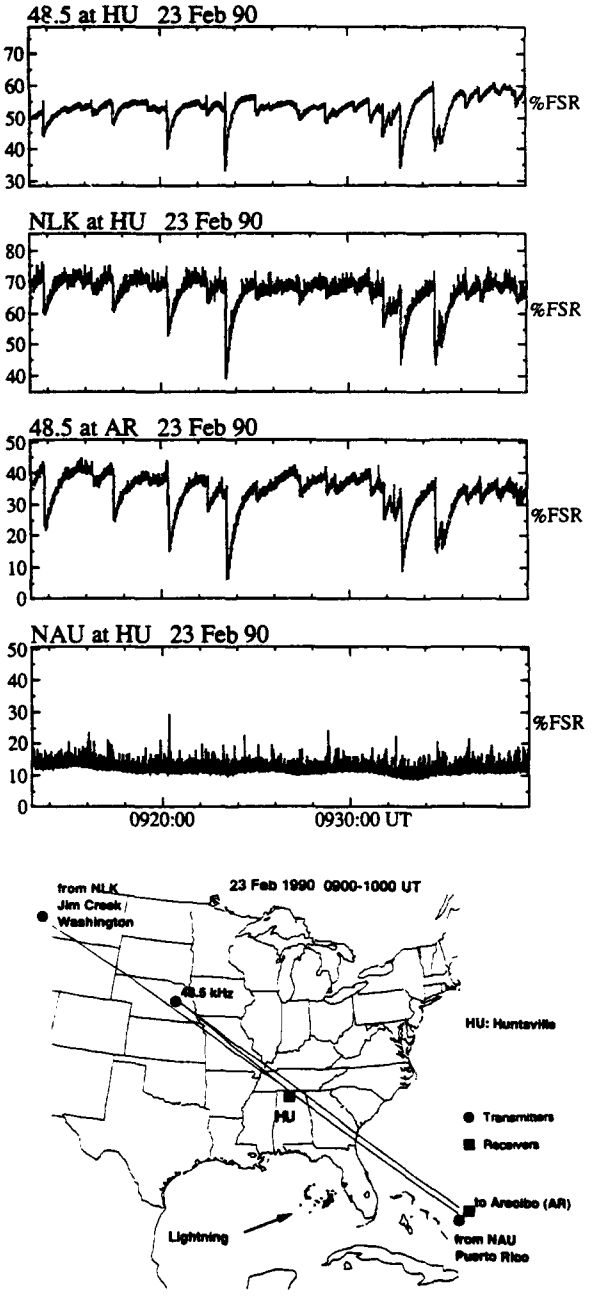

Figure 3: The top three panels show a sequence of events observed on the nearly collinear subionospheric VLF/LF paths illustrated in the lowest panel. A thunderstorm center off the coast of Florida is shown, with the '+"s indicating the location of cloud-to-ground flashes which were recorded during 0900-1000 UT. All signal amplitudes (A) are plotted in linear arbitrary units, with $A = 0$ representing absence of signal. The largest perturbations on the 48.5-HU signal (third panel from top) involve ~ 14 dB reduction in amplitude.

In recent years, Stanford University has developed a network of observation sites across the continental United States and at Palmer Station, Antarctica, which enables the simultaneous monitoring of conjugate ionospheric regions as illustrated in Figure 5. These observations led to the discovery that geomagnetically conjugate ionospheric regions are commonly disturbed simultaneously (within 1 s) in single lightning events [*Burgess and Inan*, 1990]. A 10-minute sequence of events observed on 19 April 1990 are illustrated in Figure 6,

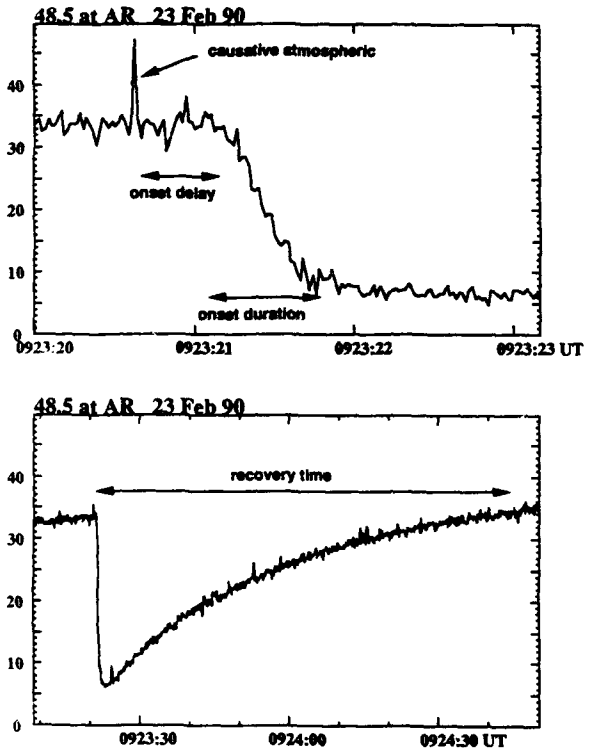

Figure 4: Typical temporal signatures of LEP events illustrated using an expanded record of one of the perturbations from Figure 3.

where many VLF/LF paths lying in the northern and southern hemispheres are simultaneously perturbed. Detailed analysis [*Burgess and Inan*, 1992] indicates that for the case shown, 22 individual events were detectable on the NPM-HU path during the period shown, 21 of which were time-correlated with 21 out of a total of 23 observed whistlers originating in northern hemisphere lightning and propagating along the magnetic field lines to be observed at Palmer Station (see Figure 1). Expanded record of one of the events and the accompanying whistler are shown in Figure 6. All 21 of the correlated whistlers were measured to be arriving from the direction of the NPM-PA signal, indicating that they exited from a duct located on or near this path. The two whistlers which were not accompanied with VLF perturbations were determined to be arriving from directions not overlapping with VLF paths monitored at Palmer Station.

In terms of the effect of such lightning-induced ionospheric disturbances on VLF/LF communications, it is useful to note that event occurrence rates are now known to sometimes reach >40 events per hour [*Inan et al.*, 1990], with amplitude changes ranging from a fractions of a dB to up to ~ 15 dB, as shown in the 48.5-AR panel of Figure 3. Quantitative interpretation of the observed VLF/LF amplitude and phase changes in terms of the altitude profile of enhanced ionization and the transverse structure of the disturbed ionospheric regions must rely on accurate models of VLF/LF propagation in the earth-ionosphere waveguide. For this purpose, a new three dimensional model has been developed at Stanford, which is based on the NOSC LWPC code but which accounts for the presence of localized disturbances located on or off the great circle path [*Poulsen et al.*, 1990;1993]. Application of this model to the NSS-Stanford path for a typical disturbance located near the middle of the path is illustrated in Figure 7. Future interpretation of data such as that shown here will rely heavily on the use of this new three dimensional VLF/LF propagation modeling capability.

3. LIGHTNING-INDUCED HEATING AND IONIZATION OF THE LOWER IONOSPHERE

Subionospheric VLF perturbations which are clearly associated with lightning, radio atmospherics have recently been

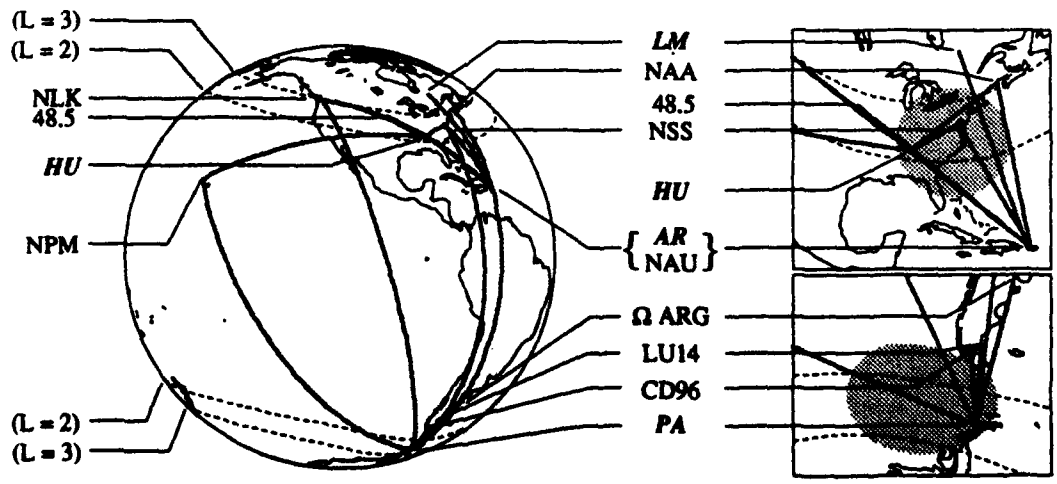

Figure 5: The great-circle paths of some of the signals monitored in Stanford experiments. The transmitters are listed in Table 1; all other locations are receivers. The right-hand panels show closeups of some of the path segments. The shaded areas indicate a 2000 km diameter region in the Northern Hemisphere and its geomagnetic conjugate in the Southern Hemisphere, representing zones which have a relatively high 'conjugate coverage' of monitored signal paths.

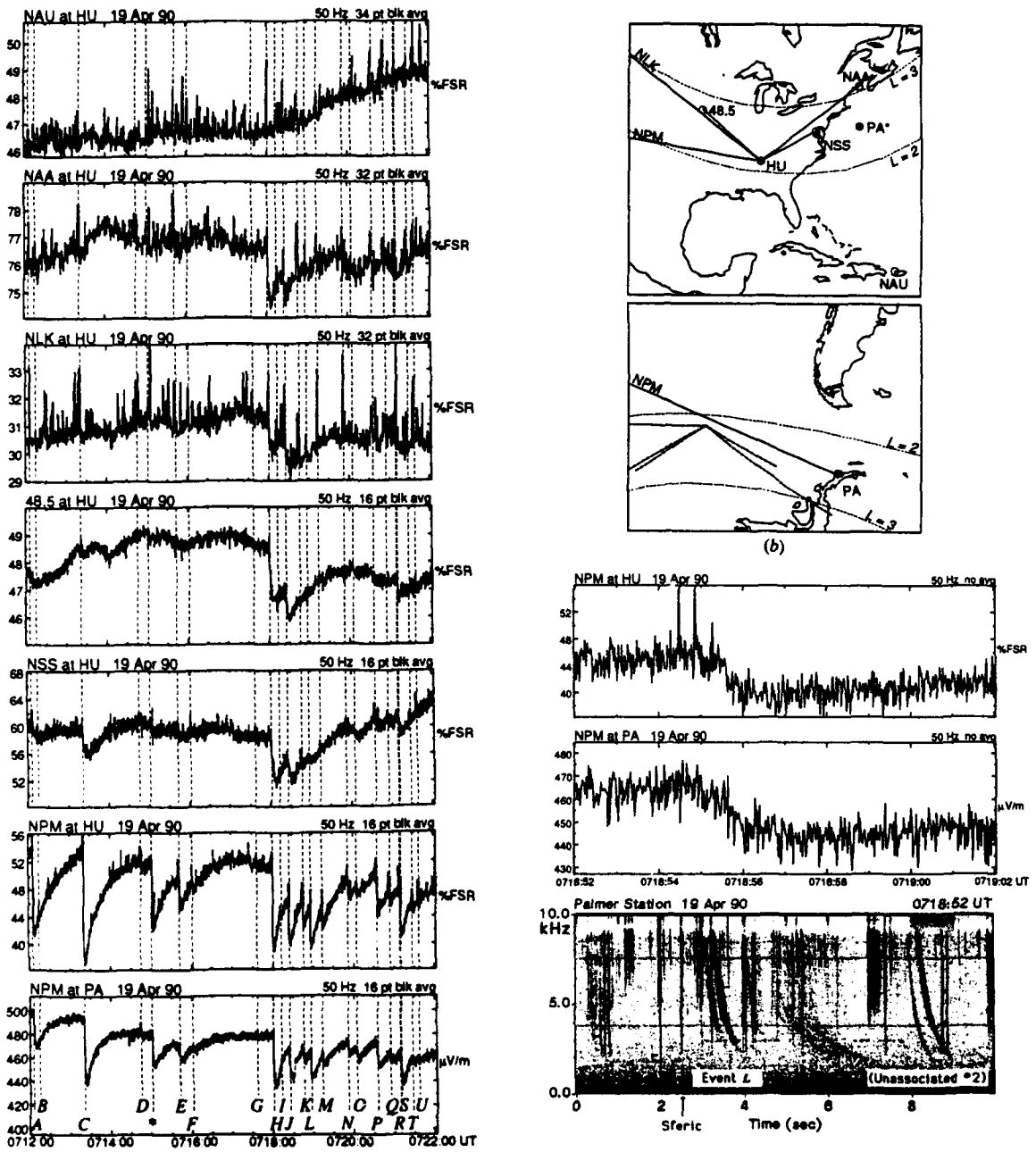

Figure 6: (*a*) A ten-minute period of simultaneous signal perturbations on six signal paths observed on 19 April 1990. NAU–HU was not perturbed but is shown at top for reference. Dashed vertical lines indicate the onset times for 22 perturbations observed on NPM–HU, 15 of which were nearly simultaneous (±1 s) with perturbations of NPM–PA. These events are marked *A* through *U* (no broadband data were available for the event marked with an asterisk). (*b*) The format of the map is identical to that in Figure 5. AR and LM are not shown because no data were available from those sites. The configuration of perturbed signal paths suggests the presence of one or more ionospheric disturbances in the vicinity of HU. On the lower right corner, expanded records are shown of two signal perturbations and the associated whistler and the lack of perturbations associated with a whistler arriving from another direction [Figure taken from ***Burgess and Inan***, 1992].

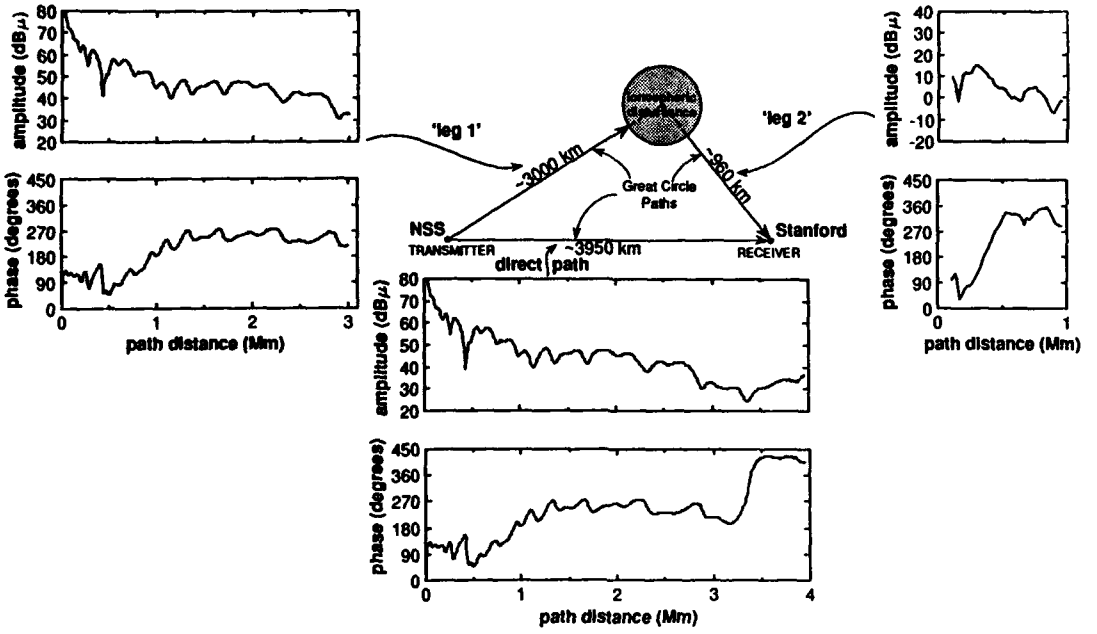

Figure 7: Amplitude and phase plots of a signal propagating along the three great circle paths shown for one particular example of a localized ionospheric disturbance near the NSS to Stanford path. The effective radius of the disturbance in this case was taken to be ~ 100 km, with its center located 3000 km along the path and at a transverse distance of 100 km from the 'direct' path. The lengths of the three paths are given in the center part of the Figure. (Note: not drawn to scale.) [Figure taken from *Poulsen et al.*, 1993].

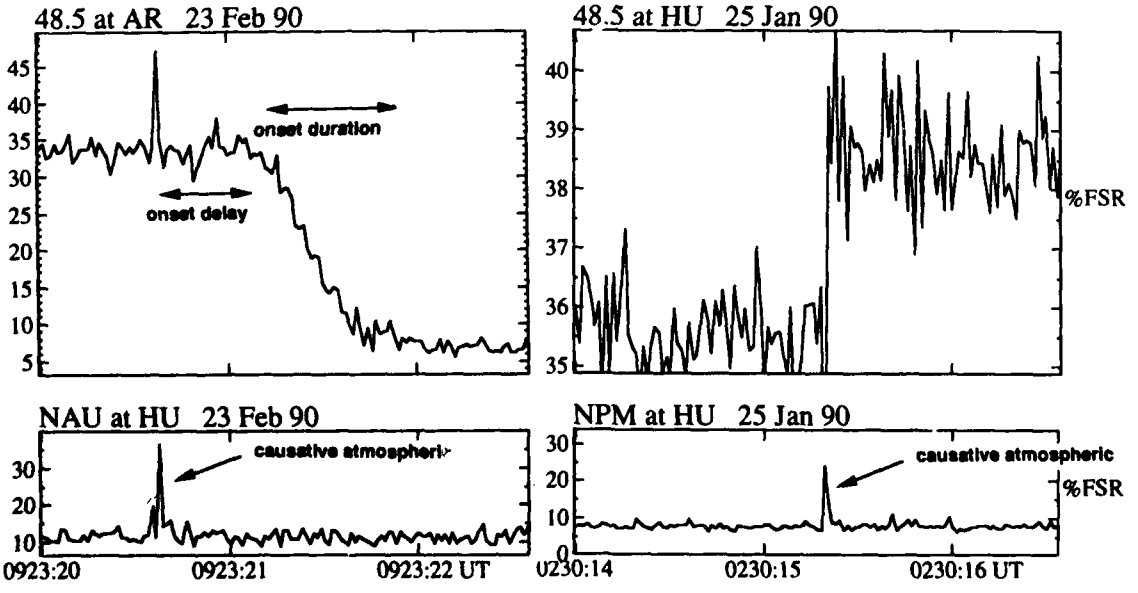

Figure 8: Comparison of the VLF/LF signatures of LEP events and early/fast events. The latter are believed to result from direct heating and ionization of the lower ionosphere by lightning radiation, as depicted in Figure 9.

observed and/or whistlers, but which do not exhibit the onset *delay* and *duration* features shown for the 23 February 1990 case . In such cases, the onset of the VLF perturbation was found to be within <50 ms of the causative atmospheric (i.e., an *early* event) [*Inan et al.*, 1988b]and/or the onset duration has been measured to be <50 ms (i.e., a *fast* event) [*Inan et al.*, 1988a]. In Figure 8, the temporal signatures of *early/fast* events are contrasted with those of LEP events. Illustrating an early/fast event observed on the 48.5-HU path, using an expanded scale comparable to that used in Figure 4. With the 20 ms resolution available in the data shown, no significant onset *delay* or onset *duration* is visible. Recovery signatures of early/fast events usually appear similar to those of LEP events, with somewhat longer recovery times observed in the few cases studied. That these events do exhibit 10-100 s recoveries is strong evidence that *enhanced secondary ionization in the D-region is a resultant feature* of the physical process which leads to these unusual signatures. Both the *early* and *fast* aspects of such events are inconsistent with a high altitude whistler-particle interaction as the causative agent, and suggest direct upward coupling of lightning to the overlying ionosphere (Figure 9).

Heating of *D*-region electrons by the intense radio impulse from lightning leading to the production of secondary ionization [*Inan et al.*, 1991] was proposed as a possible cause of such events. Such heating and ionization of the lower ionosphere by energy from lightning represents a new means of electrodynamic, thermal and aeronomic coupling of energy from lightning to the lower ionosphere and is in retrospect fully consistent with the measured intensities of radio impulses produced by lightning, which range from an 'average' of 5 V/m to > 20 V/m (10% of the time) at 100-km distance [*Krider and Guo*, 1983]. That lightning-induced ionospheric heating would lead to an *early* VLF perturbation is clearly evident. In cases of individual isolated flashes, the onset duration would be < 100μs (i.e., *fast*); however, longer onset durations may occur due to multiplicity of flashes.

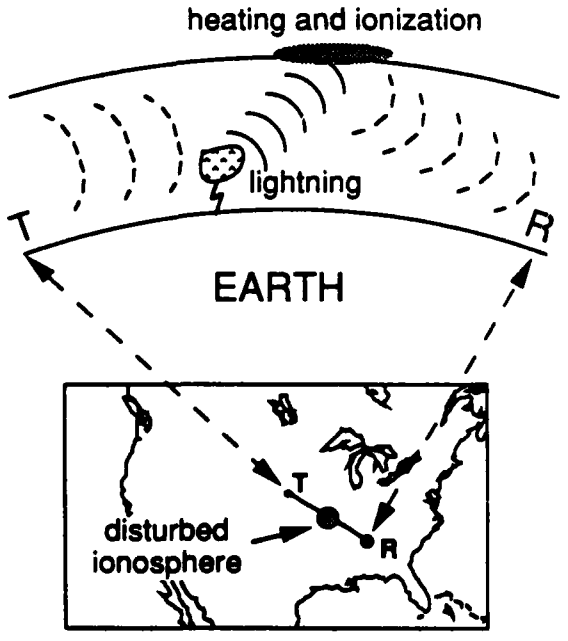

Figure 9: Depiction of a VLF/LF signal being perturbed due to an ionospheric disturbance created by direct interaction of lightning radiation with the lower ionosphere.

The heating process is inherently nonlinear, since absorption of the wave energy increases the electron temperature which in turn leads to enhanced absorption (i.e., self-absorption). The dependence of the amount of secondary ionization generated via the impact excitation of N_2 by the heated electrons is also highly nonlinear [*Inan et al.*, 1991]. While the electron temperature is increased by factors of 100-500 above the ambient during the lightning pulse (i.e., 50-100 μs), cooling occurs within 1-10 μs of pulse termination. Thus, heating of electrons is not by itself sufficient to explain the early/fast subionospheric VLF changes, which do exhibit 10-100 s recoveries as shown. The effects of discharge orientation and radiated electric field on the transverse structure and magnitude of the heating and secondary ionization were described recently using a simple model by *Rodriguez et al.*[1992].

Examples of *early/fast* VLF events observed in association with an isolated thunderstorm on 13 March 1987 off the east-coast were reported previously [*Inan et al.*, 1988b]. One of these events, evidenced as an amplitude change on the 28.5 kHz signal from the NAU transmitter observed at Lake Mistissini (LM), Quebec, is shown in Figure 10. The data from another narrowband channel (in this case the 24.8 kHz NLK channel) shows the impulsive radio atmospheric, which can also be seen on the frequency-time spectrogram below. The event shown, and two others observed during the period 0000-0130 UT, were time-correlated with CG flashes detected by the east-coast lightning detection network [*Inan et al.*, 1988b]. The CG flash which was correlated with the event shown had an electric field intensity as measured (by the network) at 100-km distance of $\sim$ 30 V/m [*Orville*, 1991].

The altitude profile and transverse extent of secondary ionization (ΔN_e) produced as a result of heating of lower ionospheric electrons by a 30 V/m (at 100-km distance) CG flash are shown in Figure 11. The theory used to estimate the structure of the heated region is described by *Rodriguez et al.* [1992].

An unusually high rate of *early/fast* VLF perturbation events observed on 25 January 1990 is illustrated in Figure 12, showing individual events simultaneously registered on three different collinear VLF paths (NLK-AR, 48.5-HU, 48.5-AR), presented in the same format as Figure 3. The fact that the NAU-HU signal is not perturbed is again consistent with the disturbed ionospheric region being located between 48.5 kHz transmitter and Huntsville (HU), near the perturbed collinear VLF paths. Data from the National Lightning Detection Network (courtesy of Vince Idone of State University of New York (SUNY) in Albany) for 0200-0245 UT on 25 January 1990 shows two main thunderstorm centers (+'s represent locations of CG lightning) one very near the perturbed collinear VLF paths in central Missouri and another well southward of the paths in Louisiana. A few other scattered lightning is also recorded between the two centers.

That these VLF events exhibit *early/fast* signatures is illustrated in Figure 13, where one event is shown with high time resolution together with the causative radio atmospheric and associated CG lightning. The signal amplitude in the 23.4±0.25 kHz channel is used as a measure of radio atmospherics. The second within which a CG flash was recorded by the network is indicated with CG.

A total of 33 *early/fast* perturbations were observed during 0200-0245 UT on the 48.5-HU signal, all positive changes in amplitude. The onsets of 7 out of these 33 events occurred within 1 second of a CG flash located within < 50km of the VLF path (i.e., from the storm center ON the collinear paths).

None of the *early/fast* events were correlated with lightning from the Louisiana region. The intensities of the correlated CG flashes as recorded by the network ranged from 6 to 15 V/m normalized to 100-km distance.

In summary, *early/fast* subionospheric VLF amplitude changes provide clear evidence of direct coupling of electromagnetic energy from lightning to the lower ionosphere. The temporal signatures of these events are distinctly different from those produced by lightning-induced electron precipitation (LEP) bursts. In all cases analyzed so far, lightning associated with *early/fast* events is found to be nearby the perturbed VLF paths. In contrast, lightning activity associated with VLF perturbation signatures of LEP events can often be far away from the affected VLF paths.

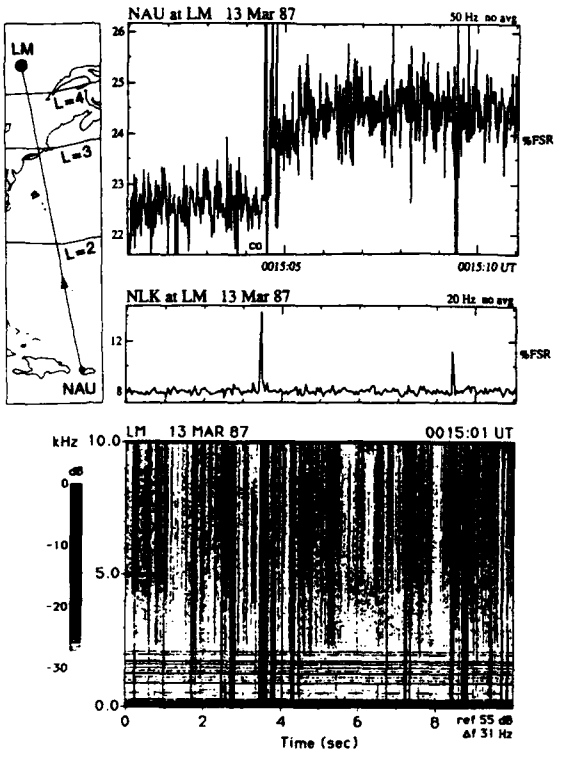

Figure 10: An example of a VLF/LF signature of lightning-induced ionospheric heating and ionization. The observation shown was made during an isolated thunderstorm off the east coast of the United States, as represented by the cloud-to-ground (CG) lightning discharges shown as +'s in the upper left corner. The lightning data was recorded by the SUNY-Albany lightning detection network. The data display on top shows an individual perturbation event on the 28.5 kHz NAU signal received at Lake Mistissini (LM), Quebec. The vertical axes show signal strength (A) in linear arbitrary units, with A=0 representing absence of signal. The lower panel shows the signal intensity in the 24.8 kHz (NLK) channel, which shows the signature of the impulsive radio atmospheric from a cloud-to-ground lightning discharge recorded by the network during the same second [*Inan et al.*, 1988b]. The lower panel shows a 0-10 kHz dynamic spectrogram of the causative spheric originating in the CG flash.

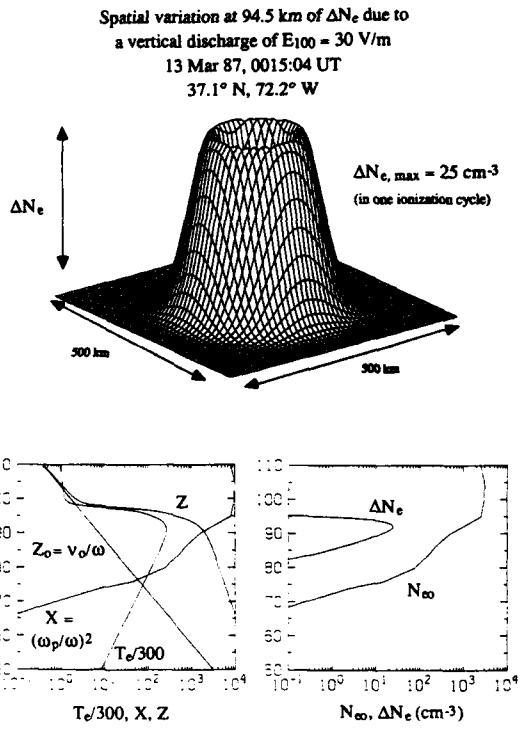

Figure 11: Structure of the ionospheric region disturbed by the CG flash displayed in Figure 10, estimated in the same manner as described by *Rodriguez et al.* [1992]. The lower panels show the altitude profile of temperature T_e and collision frequency ν on the left and electron density N_e on the left. Result shown is for a single ionization cycle; up to 10-15 cycles are expected to occur during a typical 50 μs long lightning radiation pulse [*Inan et al.*, 1991].

If such intense heating of the ionosphere by lightning radiation does indeed occur, as suggested by the data displayed here, a natural consequence would be the excitation of optical emissions from the D-region due to impact of the heated electrons. First quantitative estimates of optical emission intensities indicate that many spectral lines would be excited well above detectable levels, although the duration of the more intense emissions (e.g., first positive of N_2) are short (50-100 μs) [*Taranenko et al.*, 1992b].

4. AN ACTIVE VLF WAVE-INJECTION EXPERIMENT USING THE NAA TRANSMITTER

The first hint that the early/fast VLF/LF events observed in association with lightning may be due to heating of the lower ionosphere was revealed in the context of a controlled experiment in which man-made VLF waves were found to produce detectable ionospheric heating [*Inan*, 1990; *Inan et al.*, 1991]. In an effort to further investigate VLF heating under controlled conditions, and to study the possibility of generation of ELF waves by modulated VLF heating, Stanford University plans to conduct an active wave-injection experiment using the NAA facility at Cutler, Maine, as described in Figure 14a. Stanford equipment has already been deployed at Gander, Newfoundland, and is operating continuously monitoring various VLF transmitter signals, including the 21.4 kHz signal from the NSS transmitter in Annapolis, Maryland.

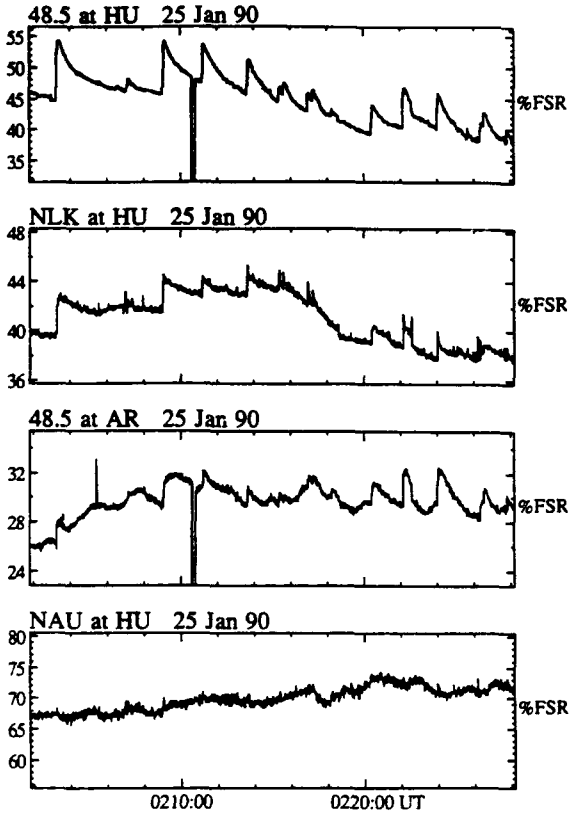

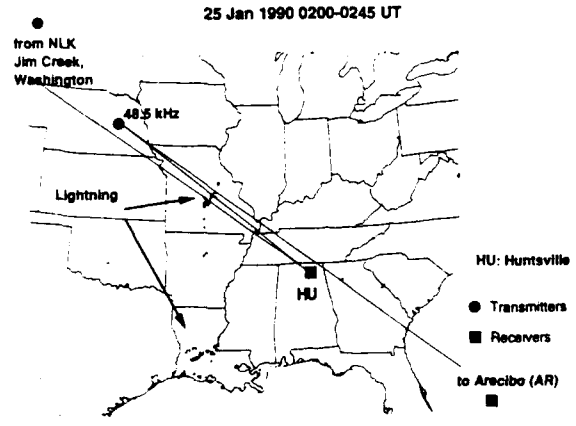

Figure 12: The top three panels show a sequence of early/fast events observed on the nearly collinear subionospheric VLF/LF paths illustrated in the lowest panel. Simultaneous lightning activity is also shown, with the '+"s indicating the location of cloud-to-ground flashes which were recorded during 0200-0245 UT. All signal amplitudes (A) are plotted in linear arbitrary units, with $A = 0$ representing absence of signal.

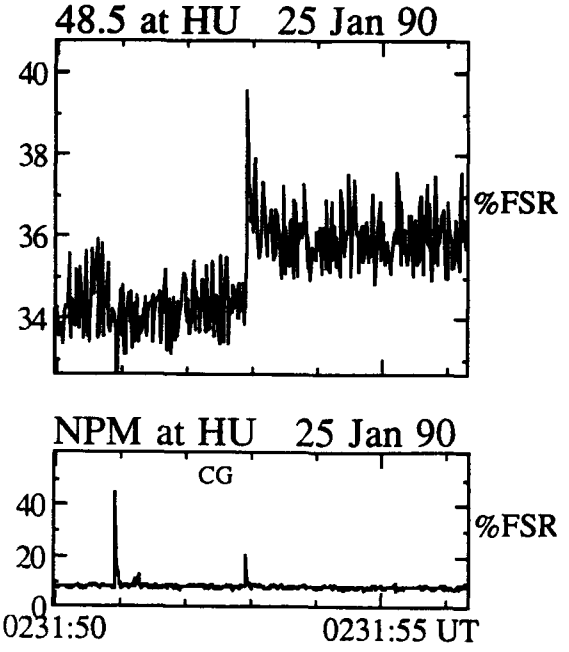

Figure 13: Expanded record of one of the events shown in Figure 12. The lower panel shows the radio atmospheric intensity in the 23.4±0.25 kHz band. The associated radio atmospheric was found to be time correlated with a CG flash occurring during the same second.

Subject to arrangements with the U.S. Navy, plans are to operate the NAA transmitter with specialized formats (typically ON/OFF at ULF (secs) and ELF (10s of milliseconds) rates) for up to 15-30 mins per night. The signatures of heating would be detected as cross-modulation on the NSS signal at Gander. Depending on the size of the heated region, weak effects may also be measured on other signals due to off-great-circle-path scattering. A first estimate of the heated region size, calculated using the model described by *Rodriguez et al.*[1992] is shown in Figure 14b. The asymmetry of the transverse structure of heating is due to the dependence of the heating on the magnetic field [*Inan et al.*, 1992].

Modulation of the VLF heating at ELF rates might lead to the generation ELF waves through auroral current modulation similar to that which commonly occurs in HF heating experiments [*Barr and Stubbe*, 1992]. There is some theoretical evidence that VLF heating might be more effective in generating ELF than HF waves [*Taranenko et al.*, 1992a]. To investigate these possibilities the NAA heating experiments will be closely coordinated with ELF receivers at various sites, such as New Hampshire, Connecticut, Newfoundland, Alaska, and Europe.

Acknowledgement

This research at Stanford University was supported by NSF grants DPP90-20687 and ATM91-13012 and by ONR grants N00014-82-K-0489 and N00014-92-J-1579. J. V. Rodriguez was supported by a NASA GSRP Fellowship. We appreciate Bill Burgess' help with some of the Figures.

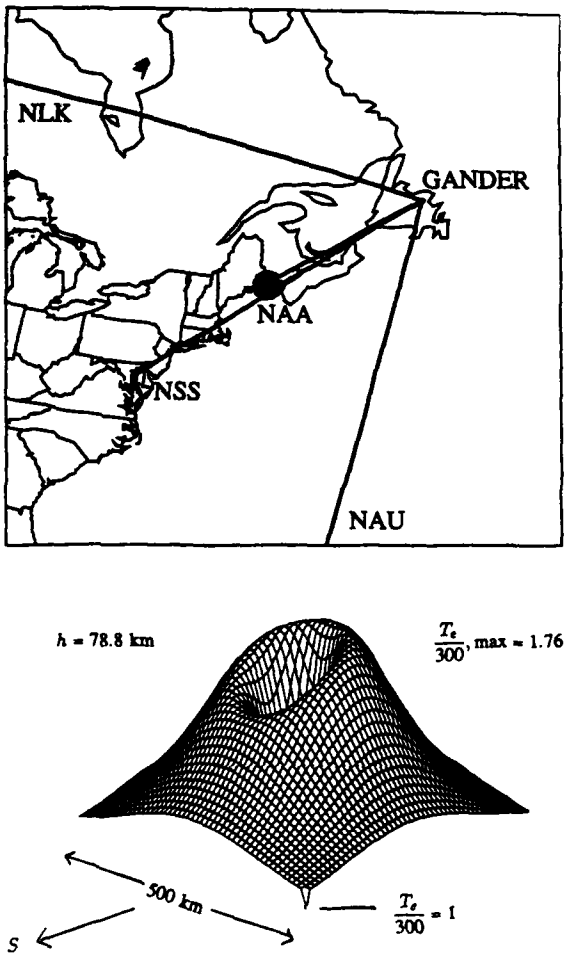

Figure 14: (a) An ionospheric heating experiment with the powerful (1 MW radiated power) NAA transmitter in Cutler, Maine, operating at 24.0 kHz. A VLF receiver in Gander, Newfoundland is used to measure the signal from the NSS transmitter (21.4 kHz), the great circle path from which passes through the heated region. Other signals not going through the modified ionosphere (e.g., NLK kHz and NAU) are used for control. The NAA transmitter would be keyed with special formats (subject to arrangements with the U. S. Navy) for specific periods each night. A similar experiment with the less powerful (0.1 MW radiated power) 28.5 kHz NAU transmitter in Puerto Rico led to the first observation of detectable heating of the nighttime *D*-region by VLF signals from a ground based source [*Inan*, 1990*a*]. (b) The structure of the ionospheric region to be heated by the NAA transmitter, estimated in a manner similar to that described by *Inan et al.* [1992].

References

Barr R. and P. Stubbe, VLF heating of the lower ionosphere: Variation with magnetic latitude and electron density profile, *Geophys. Res. Lett.*, *19*, 1747-1750, 1992.

Burgess, W.C., and U.S. Inan, Simultaneous disturbance of conjugate ionospheric regions in association with individual lightning flashes, *Geophys. Res. Lett.*, *17*, 259, 1990.

Burgess, W. C., and U. S. Inan, The role of ducted whistlers in the precipitation loss and equilibrium flux of radiation belt electrons, submitted to *J. Geophys. Res.* on 25 Nov. 1992.

Chang, H.C., and U.S. Inan, Lightning-induced electron precipitation from the magnetosphere, *J. Geophys. Res.*, *90*, 1531, 1985.

Inan, U.S., T.G. Wolf, and D.L. Carpenter, Geographic distribution of lightning induced electron precipitation observed as VLF/LF perturbation events, *J. Geophys. Res.*, *93*, 9841, 1988a.

Inan, U.S., W.C. Burgess, T.G. Wolf, D.C., Shafer, and R.E. Orville, Lightning-associated precipitation of MeV electrons from the inner radiation belt, *Geophys. Res. Lett. 15*, 172, 1988b.

Inan, U.S., VLF heating of the lower ionosphere, *Geophys. Res. Lett.*, *17*, 729, 1990.

Inan, U.S., F.A. Knifsend, and J.Oh, Subionospheric VLF 'Imaging' of lightning-induced electron precipitation from the magnetosphere, *J. Geophys. Res.*,*19*,2071-2074, 1990.

Inan, U. S., T. F. Bell, and J. V. Rodriguez, Heating and ionization of the lower ionosphere by lightning, *Geophys. Res. Lett.*, *18*, 705, 1991.

Inan, U. S., J. V. Rodriguez, S. Lev-Tov and J. Oh, Ionospheric modification with a VLF transmitter, *Geophys. Res. Lett.*, *19*, 2071-2074, 1992.

Krider, E. P., and C. Guo, The peak electromagnetic power radiated by lightning return strokes, *J. Geophys. Res.*, *88*, 8471, 1983.

Orville, R. E., Calibration of a magnetic direction finding network using measured triggered lightning return stroke peak currents, *J. Geophys. Res.*, *96*, 17,135-17,142, 1991.

Poulsen, W. L., T.F. Bell, and U.S. Inan, Three-dimensional modeling of subionospheric VLF propagation in the presence of localized D region perturbations associated with lightning, *J. Geophys. Res.*, *95*, 2355, 1990.

Poulsen, W. L., U. S. Inan, and T. F. Bell, A multiple-mode three-dimensional model of VLF propagation in the earth-ionosphere waveguide in the presence of localized D region disturbances, *J. Geophys. Res.*, *98*, 1705-1717, 1993.

Rodriguez, J. V., U. S. Inan and T. F. Bell, D region disturbances caused by electromagnetic pulses from lightning, *Geophys. Res. Lett.*, *19*, 2067-2070, 1992.

Taranenko, Y. N., U. S. Inan, and T. F. Bell, VLF-HF heating of the lower ionosphere and ELF wave generation, *Geophys. Res. Lett.*, *19*, 61-64, 1992*a*.

Taranenko, Y. N., U. S. Inan and T. F. Bell, Optical signatures of lightning-

induced heating of the D region, *Geophys. Res. Lett., 19*, 1815-1818, 1992*b*.

Voss, H.D., W.L. Imhof, J. Mobilia, E.E. Gaines, M. Walt, U.S. Inan, R.A. Helliwell, D.L. Carpenter, J.P. Katsufrakis, H.C. Chang, Lightning induced electron precipitation, *Nature, 312*, 740, 1984.

Yip, W-Y, U.S. Inan, and R.E. Orville, On the spatial relationship between lightning discharges and propagation paths of the perturbed subionospheric VLF/LF signals, *J. Geophys. Res., 96*, 249, 1991.

Discussion

SMITH

COMMENT. You have pointed out that for the propagation perturbations associated with lightning induced precipitation the location of the lightning can be well separated for the location of the perturbed region of the ionosphere. For the events with no delay following the radio atmosphere, ascribed to heating, you would expect the disturbed ionospheric region to be approximately co-located with the causative lightning. Have you verified this, in support of your interpretation and if so, what was the result?

AUTHOR'S REPLY

We have very few cases of these direct coupling results that are well studied: for two of these cases, the thunderstorm is indeed directly under the affected VLF paths; for other cases, we have just recently received the lightning data and have not yet checked. I agree that we would expect the lightning induced disturbance in these cases to be within 100-200 km of the VLF paths.

ALPERT

COMMENT. The heading of the ionosphere by the elastic field produced by an atmosphere in the frequency band F $\sim$ 5 - 10 KHz is indeed very large. Thus your idea about the "ionization" of the inosphere (D or E layers) is indeed a good idea. By our you have done these complicated calculations, taking into account the velocities V_l V_i V_h and the diffusion frequencies n_{ln} n_{in} n_{hn} to calculate the temperatures T_l T_i T_h ?

AUTHOR'S REPLY

We have the Budden and Maslin [1974, 75,76] models for heating and used a full magneto-ionic model and a slowly varying (WKB) formulation to calculate the electron temperature T_l. We have also looked at using the Sen and Wyler corrections to n_{ln} but have found that the correction needed is small. For the parameters involved, DT_h , DT_i is very small; we have only calculated DT_l , but using a full model (Appletar Havtree) for the refractive index. The imaginary part of refractive index is ^{c}. We find $iv^c/_c$ to be nearly independent on frequency in the range 100 Hz to 100 KHz.

Studies of the propagation of low frequency (LF) radio waves

E.M. Warrington[1]
T.B. Jones[2]

[1]Department of Engineering
[2]Department of Physics and Astronomy
University of Leicester
University Road
Leicester, LE1 7RH
UK

SUMMARY

Low frequency (30 - 300 kHz) radio waves can propagate to great distances with little attenuation in the cavity formed by the earth and the ionosphere. Because of the relatively high frequency at LF, many active propagation modes can occur between the transmitter and receiver. Changes in the ionospheric conductivity or reflection height can influence the phase and amplitude of these modes and, hence, produce mutual interference. Because of these inference effects, the propagation is less stable than at VLF and the received field strength becomes more difficult to predict. In the present investigation, the WAVEHOP program [1] has been employed in conjunction with a range of ionospheric models to estimate the receiver field strength over a number of experimental paths. The predicted values have been compared with those measured in an attempt to validate the ionospheric models and the method of calculation.

1. INTRODUCTION

As the result of previous work (Jones and Mowforth [2]), several computer programs were available for the calculation of the field strength of VLF and LF signals as a function of distance from the transmitter. Although the theory of the propagation is well defined, considerable uncertainty exists concerning the ionospheric electron density variation with height to which the analysis is applied. It is well known that the lowest region of the ionosphere (the D-region) plays a dominant role in the propagation of VLF and LF radio waves. However, it is extremely difficult to measure the electron density distribution of this layer due to the very low values of the electron density and the relatively high electron collision frequency. The electron density distribution is known to change appreciably with time of day and season and at high latitudes can also be influenced by geomagnetic storm activity.

In order to validate the theoretical modelling work, receiving equipment was deployed at a number of locations world-wide. The amplitudes of several LF transmissions were observed over a period of more than a year at Aberdeen, Scotland and at Tromsø, Norway, and over shorter periods at Clyde River, Baffin Island, Canadian North West Territories and at Gibraltar. The data from these receiving sites provided an indication of the received field strength as a function of time of day and season at a number of frequencies within the band of interest. It must be emphasised, however, that all the measurements are for fixed, though differing, ranges. No attempt was made to measure the field strength variation as a function of distance (i.e. the Hollingworth pattern).

Several features are apparent in the amplitudes of the received signals which are found to be related to the solar zenith angle and to the time of year. WAVEHOP calculations of the signal mode structure for a number of ionospheric models provided an estimate of the expected signal strength and these results are compared with the experimental data in order to assess the validity of the model calculations.

2. SIGNAL STRENGTH CALCULATIONS

2.1 The WAVEHOP program

The WAVEHOP program [1] calculates the amplitude and phase of the vertical electric field on the Earth's surface as a function of distance along the propagation path (assumed to be along the great circle), given a ground-based source of vertically polarised radio waves of known frequency in the VLF or LF bands. The Earth is assumed to be a smooth sphere with known values for the electrical conductivity and dielectric constant and the ionosphere is assumed to be concentric with the Earth and to have known reflection properties. The vertical electric field at the receiver due to a vertically polarised source is the vector sum of several components which travel via different paths to the receiver.

Before the WAVEHOP method can calculate the field strengths, the reflection coefficients of the ionosphere must be determined. These coefficients depend on the height profile of the electron density, the magnetic field parameters (strength, dip angle, azimuth relative to the direction of propagation), the signal frequency, the collision frequency and the angle of incidence. At the frequencies of interest, the ionosphere can change significantly within a path length of one wavelength, therefore a full wave solution is required in order to calculate the reflection characteristics of the ionosphere. The theory has been developed by Wait [3], Berry [4] and Berry, Gonzalez and Lloyd [5], and the propagation characteristics of the wave hops are discussed by Berry [4, 6] and Johler [7]. The WAVEHOP program as

described by Berry and Herman [1] adopts a formula for the reflection height which is correct for high angles of incidence on the ionosphere, but at lower angles of incidence, corresponding to shorter transmission paths, greater accuracy is achieved when the reflection height is calculated from the angle of incidence by the method of stationary phase [8, 9].

The WAVEHOP program has the major limitation that it assumes that the geophysical parameters remain constant over the full length of the path. This is not, in general, the case. For example, the electron density profile is likely to vary over the length of the path due to several causes including, for example, sunrise/sunset effects and changes in latitude. It should be noted that large variations in the electron density will occur in the high latitude auroral regions. Furthermore, the ground conductivity will vary as the signal propagates over different types of terrain (e.g. land, sea, ice, etc.) and local geological discontinuities will also have an affect on the signal strengths. To rectify these limitations would involve comparatively major modifications to the program code, however it is possible to obtain useful information from the program provided these limitations are clearly understood. One of the aims of this investigation was to compare measured signal strength variations with values calculated by the WAVEHOP program in order to quantify the limitations referred to above.

2.2 Interpretation of WAVEHOP results

The WAVEHOP program calculates the amplitude and phase of the vertical electric field at the receiver for each of several propagating modes (ground wave, 1-hop skywave, 2-hop sky wave, etc.) as a function of distance from the transmitter. A typical example of the amplitudes calculated for a test path is presented as the first frame of Figure 1, where the amplitude of the ground wave is represented by a solid line and the amplitudes of the sky waves as dashed lines (1-hop skywave is represented by the least broken dashed line).

These modes are then combined as a vector sum to give the overall amplitude of the signal as a function of the distance from the transmitter. The results of this calculation for the test signal are presented in the second frame of Figure 1. Close agreement between measured and theoretical values at VLF frequencies have been reported by other workers (e.g. Campbell, Jones and Burgess [10]). However, at LF the wavelength is shorter (4 km at 75 kHz) and the predicted phase values are therefore expected to be less accurate than at VLF, resulting in significant errors in the vector sum. The amplitude dependence on the mode phases is illustrated by calculating the mean, the maximum and the minimum signal strengths which can be produced from a summation of the propagating modes (see frame 3 of Figure 1) when their phases are varied. Also shown on this diagram are the maximum and minimum amplitudes which can be produced when a ±6 dB error in the prediction of the sum of the amplitudes of the secondary modes is included.

3. EXPERIMENTAL MEASUREMENTS

3.1 Experimental arrangement

A receiving system was developed which could measure and record in digital form the signal strength at any given frequency in the range 10-200 kHz. The system was based around an HP3561A dynamic signal analyser (an FFT analyser) for signal measurement and an HP85B desktop computer for control of the analyser and for recording the data for subsequent analysis. The antenna was a vertical active whip mounted well clear of local obstacles, either on the roof of a building or on top of a mast. The instrument was calibrated in signal strength by comparison with the output of a Rohde and Swartz ESH 2 signal strength meter monitoring the same "off air" signal. Good linear agreement was achieved between the two systems when both antennas were located on a clear site (see Figure 2).

Measurements were made at four receiving sites during the course of these experiments. The two main sites were at Aberdeen, Scotland and at Tromsø, Norway, with additional sites operational for shorter periods at Gibraltar and Clyde River, Canadian North West Territories (see Table 1 for periods of operation). The principal transmissions monitored covered the frequency range 57.7 kHz to 81 kHz with path lengths well spread between 46 km (Aberdeen - Crimond) and 2654 km (Tromsø - Geneva). The locations of the transmitter and receiver sites are given in Table 2 and the frequencies and path lengths in Table 3.

Table 1. Periods during which the receiving sites were operational.

Aberdeen	4 February 1987 - 22 September 1988 (from 4 February 1988 for signals below 57.7 kHz)
Clyde River	21 July 1988 - 7 August 1988
Gibraltar	22 March 1988 - 26 May 1988, 10 January 1989 - July 1989.
Tromsø	4 - 12 March 1987. 7 June 1987 - 18 June 1988 (from 13 March 1988 for signals below 57.7 kHz)

Table 2. Geographic co-ordinates of the LF sites

	Location	Latitude	Longitude
Receivers	Aberdeen	57.20°N	2.10°W
	Clyde River	70.27°N	68.22°W
	Gibraltar	36.12°N	5.37°W
	Tromsø	69.67°N	19.00°E
Transmitters	Brest	48.42°N	4.23°W
	Criggion	52.72°N	3.07°W
	Crimond	57.60°N	1.92°W
	Denmark	54.37°N	9.47°E
	Geneva	46.40°N	6.25°E
	Inskip	53.43°N	2.78°W
	Rugby	52.37°N	1.18°W
	Trondheim	63.78°N	11.38°E

Table 3. Distances from each LF transmitter to the receiving sites.

Frequency	Location	Aberdeen	Tromsø	Gibraltar	Clyde River
57.700 kHz	Trondheim	1037 km	733 km		3241 km
60.000 kHz	Rugby	541 km	2187 km	1839 km	3871 km
61.835 kHz	Inskip	422 km	2119 km		3715 km
65.800 kHz	Brest	988 km	2765 km	1372 km	4151 km
68.000 kHz	Crimond	46 km	1765 km	2405 km	3355 km
68.900 kHz	Denmark	789 km	1765 km	2330 km	4041 km
73.250 kHz	*Criggion	503 km	2199 km		3773 km
75.000 kHz	Geneva	1391 km	2654 km	1605 km	4776 km
81.000 kHz	Inskip	422 km	2119 km	1938 km	3715 km

* This transmission was from Rugby until 13 March 1987.

The principal aim of this study was to test the effectiveness of the WAVEHOP program in predicting the expected field strength for a range of paths and frequencies and in particular to establish the effectiveness of various ionospheric profiles. In order to minimise the affect of changes in ground conductivity over the length of the path, most measurements were for signals propagating over sea and damp soil (assuming that European ground may be so categorised).

3.2 Observations

As a typical example of the results the amplitude of the 57.7 kHz signal from Trondheim, Norway measured in Aberdeen is reproduced in Figure 3. In this plot the signal amplitude is displayed as a function of (a) time of day along the x-axis and (b) day number from the start of 1987 (1 January 1987 is represented as day 1) along the y-axis. The amplitude level is represented by a grey scale on a logarithmic (decibel) scale relative to the mean signal amplitude observed throughout the entire data set. Periods when data are not available are indicated as white and periods when the signal amplitude is very low (e.g. during transmitter off periods) as black.

As expected, the effects of the changing solar zenith angle and the consequent changes in the electron density profile are clearly evident in the amplitude data. The seasonal change in the day/night transition are particularly evident, as are the differences between day and night time signal amplitudes. The data of Figure 3 have been re-plotted in Figure 4 to illustrate the dependence of the signal amplitude on solar zenith angle. To distinguish between the pre-noon and post-noon periods on the plots, the zenith angles during the morning period are indicated as negative values (i.e. the zenith angle has been multiplied by -1). This is done only to separate pre- and post-noon data and does not imply any physical significance. The largest signal levels occur at night time, during which time there are marked fluctuations in signal strength. In general the night time signal levels exceed those observed during the daytime. The daytime signal level exhibits a solar zenith angle dependence. The signal is weakest during the summer noon period, at which time it is approximately 12 dB less than the night time value. Marked changes in signal level are associated with the dawn/dusk transition periods when strong mode interference effects take place as a result of the rapid change in the electron density height distribution at this time.

Data for some of the other transmissions monitored at Aberdeen are reproduced in a similar format in Figures 5 to 7. The most significant feature of these plots is the rapid change in signal amplitude during the morning at a solar zenith angle of approximately 98°, corresponding to sunrise at an altitude of about 60 km. This is a well known feature of VLF/LF propagation which was first reported in the literature by Bain, Bracewell, Straker and Westcott [11]. The corresponding effect at sunset is not as pronounced since the transition takes place over a longer period. Several other features of the data set also have a pronounced zenith angle dependence, for example the low amplitude observed on the Trondheim - Aberdeen path at zenith angles of less than about 90° during the summer months and the deep fade observed on the Geneva - Aberdeen path at zenith angles of approximately 95°.

Seasonal changes are also evident in the data. For example, the Brest - Aberdeen and Geneva - Aberdeen signals display a marked fade at zenith angles of around 60° and 50° respectively during the first half of the year, whereas this feature is not reproduced during the latter half of the year. This difference is probably related to the change in the geometry of the propagation path relative to the dawn/dusk line. It could also involve the winter anomaly which occurs after the Autumn equinox in the lower D-region electron density distribution. The variation of signal amplitude with the time of day for two of the transmissions (Brest 65.8 and Geneva 75.0 kHz) received at Aberdeen are reproduced in Figures 8 and 9. Deep slow fading is observed on these signals, particularly during the night, which suggests that phase changes between the component modes are producing interference.

The marked modal interference effects at dawn and dusk are a major feature of the diurnal signal strength variation. The number and depth of the signal minima depend on the signal frequency and path length. It is essential that any prediction method correctly reproduces the signal amplitude variations particularly during the transition period. The WAVEHOP program cannot predict short term amplitude changes since only slowly varying models, depending on the solar zenith angle, are considered. Minor changes in the electron density profile will change the relative phases between the component modes, thus it is extremely difficult to model the amplitude fluctuations due to fading. It is, however, possible to estimate the highest (all modes in phase) and lowest (strongest

interference) amplitude limits that might be expected for a particular propagation path from any given ionospheric model. Slowly varying features dependent on the zenith angle, particularly the dawn/dusk transition, should be reproduced by the model calculations.

The data collected at Tromsø are for a much shorter observing period than at Aberdeen but it is clear from the data available that very similar features are present at both sites. There are differences in absolute signal magnitudes and also in some detailed features of the diurnal and seasonal variations. However, the overall propagation patterns are similar at the two sites.

4. INTERPRETATION OF THE OBSERVATIONS

In this section the experimental measurements of signal amplitude over a number of fixed paths are discussed in terms of the predicted values as calculated by the WAVEHOP program. Uncertainties in radiated power, antenna polar diagrams, local conditions around the transmitter and receiver and other factors make it extremely difficult to compare a measured absolute field strength with a calculated value, even for a fixed transmitter and receiver. The theoretical work has, therefore, been confined to attempts to calculate the diurnal and seasonal variations of average field strength and the variability (fading range) of the signals. Field strength calculations from ionospheric models have been made at VLF with considerable success [10] and a similar procedure has been followed here at LF. The analysis presented in this section has been undertaken with the WAVEHOP program and a series of ionospheric models proposed by Bain (unpublished) which include a dependence on the solar zenith angle.

Discussion of the data has been confined to the measurements recorded at Aberdeen since these are the most complete and those from the other receiving sites exhibit similar features.

4.1 Day - night changes

The night-time signal levels are greater than those measured during daytime for all seasons. Moreover, the average night-time value is approximately constant throughout the year, unlike the daytime signal strength which changes markedly with season. The night-time signal does, however, fluctuate over short time scales with fading of up to about 20 dB present on most of the paths (see Figures 8 and 9). The fading period is very variable but the signal is unlikely to remain constant for more than one or two hours. This behaviour results from the low ionisation values present during the night-time and the consequent strength of the lower order modes. Small changes in the electron density profile change the phase relationship between the modes which consequently induce strong mutual interference and hence 'fading' in the total received signal. A comparison of the calculated day and night-time mode amplitudes is given in Figure 10 which confirms the strong propagation of the higher order modes during the night-time at distances greater than about 800 km.

The calculated field strengths of Figure 10 also indicate that the night-time values exceed those obtained from the daytime model (see Figure 1). This is confirmed by the experimental results, although the magnitude of the change depends on frequency and on the path length.

4.2 Diurnal variations

The daytime signal strength depends on the solar zenith angle. For individual days this control is not very strong and the daily changes are dominated by the strong modal interference which occurs at sunrise and sunset (discussed later). However, the seasonal changes are very much in evidence with summer values, some 6 dB smaller than those observed in winter for the Aberdeen - Trondheim (57.7 kHz) path. Similar changes are noted on the other paths monitored, although the weakest signals are not always recorded at summer noon. For example, the Aberdeen - Brest (65.8kHz) path, the weakest signals are recorded in Springtime (see Figure 5) and this is a consequence of the modal structure for this path produced by the ionospheric electron density distribution at this particular time of day and season.

4.3 Dawn - dusk transition

A feature of all the LF signals monitored is the strong modal interference that occurs at sunrise and sunset. This produces major changes (often >30 dB) in signal levels and can therefore greatly influence system performance. The dawn transition takes place over a short time interval (<1 hour) whereas the dusk transition is less abrupt and the change in signal amplitude occurs more slowly (see, for example, the 57.7 kHz Trondheim - Aberdeen signal illustrated in Figure 4). Strong modal interference is present on the Aberdeen - Brest (65.8 kHz) transmission. Again, the dawn transition occurs very quickly and is well defined. The dusk transition is less well defined, particularly in winter. The modal interference produces signal maxima and minima at dawn at the equinox. Two minima and a maximum occur at dusk during summer. A detailed study of these changes has been undertaken for a typical period in summer and winter. The measured changes in signal level are compared with those obtained from the WAVEHOP program for the appropriate frequency, path length and ionospheric model as indicated below.

4.4 Summer conditions

Models of the electron density height profile for summer have been developed by Bain (unpublished). These models can be evaluated for any value of the solar zenith angle (χ). The mode structure to be expected for each of the experimental paths monitored have been evaluated from these summer profiles by means of the WAVEHOP program. The mode structure for the Trondheim - Aberdeen path is reproduced in Figure 11 and the average of measurements on five summer days in Figure 12. The marked difference measured between the night and daytime signal levels are well reproduced in the modelling results. The calculation indicates some modal fading at sunrise and sunset which is not evident in the measured values. A similar comparison is made for the Denmark - Aberdeen path in Figures 13 and 14. Here the day and night signal levels are approximately equal, a feature well reproduced by the model calculations. Some modal interference is present both at sunrise and sunset, the sunrise feature being less in evidence on the observed values (Figure 14). For the Geneva - Aberdeen path, appreciable difference between day and night-time are observed as are strong interference minima at sunrise and sunset (see Figure 16). All these features are well reproduced by the calculated values reproduced in Figure 15. Similar good agreement between the calculated and measured behaviour is obtained for the Brest - Aberdeen path (Figures 17 and 18).

4.5 Winter conditions

The winter electron density profiles [12] are available for a restricted number of zenith cycles only (χ = 75°, 85,° 94,° 95,° 96° and 100°). A comparison of the calculated and measured field strength for winter conditions is presented in Figures 19 and 20. Significant differences are evident between the day and night values. However, there is no strong modal interference for this path. Similar behaviour is observed on the Denmark - Aberdeen path on which the sunrise/set model effects are relatively weak (see Figures 21 and 22). For the Geneva - Aberdeen and Brest - Aberdeen paths (see Figures 23 to 26), modal effects are clearly evident in the experimental data during the morning transition. The time resolution of the theoretical models is not sufficient to reproduce these effects clearly, although there is some evidence of amplitude fluctuations especially in the modelling for the Brest - Aberdeen path. The relatively small change in amplitude from day to night is well reproduced by the model calculation.

5. CONCLUSIONS

The propagation of low frequency waves in the earth-ionosphere waveguide is characterised by modal interference for propagation paths greater than about 500 km. These interference effects are clearly observed at sunrise and sunset when marked minima in signal strengths are evident. These features occur at the same zenith angle throughout the year, which indicates that propagation conditions are sufficiently stable to produce mutual interference between the modes from the appropriate ionospheric model. This is an important conclusion which allows the expected signal levels to be predicted with a high degree of certainty. At night-time the propagation is less stable and small changes in modal structure resulting from changes in the depleted night-time electron density, produce interference leading to fluctuations in signal amplitude with time scales of one hour or less. These 'fading' effects make prediction of the expected signal strength at any given time difficult. It is, however, possible to provide an average night-time value from the model calculations.

During the daytime there is little change in signal level. However, the daytime signal exhibits a marked seasonal dependence with the winter values approximately 6 dB greater than those measured in summer. For some of the paths monitored the minimum signal levels occur during the equinox period and it is suggested that this is a consequence of the modal structure produced by the equinox electron density distribution for those particular paths on which the effect is observed.

The changes between day and night signal levels are well reproduced by the modelling studies and clearly the models can be employed for system design applications. The models can also predict the strong modal effects which occur at both sunrise and sunset for summer conditions. These features are less evident in the winter observations. The winter models are restricted to a limited number of time periods and the time resolution available is insufficient to accurately reproduce the weak modal effects. The models do, however, reproduce the measured day to night changes in signal level.

It is evident that the signal strength prediction based on the WAVEHOP program can reproduce all the main features of the measured data. The calculation of the absolute field strength is probably not possible due to uncertainties regarding transmitter power, antenna polar diagrams etc. The success obtained in predicting the relative change in signal level does, however, have considerable practical benefit in the design and operation of LF communications systems.

ACKNOWLEDGEMENTS

Thanks are due to DRA, Portsdown for their support of this work. We are also grateful to Professor C.T. Spracklen of the University of Aberdeen and to R. Larsen of the Nordlysobservatoriet, Tromsø for their help in running the receiving equipment.

REFERENCES

1 Berry, L.A. and Herman, J.E. A Wave Hop Propagation Program for an Anisotropic Ionosphere. OT/ITS Research Report 11, April 1971.

2 Jones, T.B. and Mowforth, K.E. A review of analytical techniques for determining the phase and amplitude of VLF radio waves propagating in the earth - ionosphere wave guide. AGARD CP 305. Brussels, 1981.

3 Wait, J.R. A diffraction theory of LF sky-wave propagation. J. *Geophys. Res.*, 1961, **66**, number 6.

4 Berry, L.A. Wave hop theory of long distance propagation of low-frequency radio waves. *Radio Science*, 1964, **68D**, number 12.

5 Berry, L.A., Gonzalez, G. and Lloyd, J.L. Wave-hop series for an anisotropic ionosphere. *Radio Science*, 1969, **4**, number 11.

6 Berry, L.A. Wave hop radio propagation theory. *In:* MF, LF and VLF Radio Propagation. IEE conference publication number 36, 1967.

7 Johler, J.R. Spherical wave theory for MF, LF and VLF propagation. *Radio Science*, 1970, **5**, number 12.

8 Bain, W.C. and May, B.R. D-region electron-density distributions from propagation data. *Proc. IEE*, 1967, **114**, pp 1593-1597.

9 Bain, W.C. Wave-hop method of calculating propagation at LF and VLF, and stationary phase. *Proc. IEE*, 1985, **132**, part H, number 2.

10 Campbell, P.H.M., Jones, T.B. and Burgess, B. Experimental studies of daytime LF radio propagation and their implications for D-region electron densities. *J.A.T.P.*, 1988, **50**, pp 725-737.

11 Bain, W.C., Bracewell, R.N., Straker, T.W. and Westcott, C.N. The ionospheric propagation of radio waves of frequency 16 Kc/s over distances of about 540 km. *Proc. IEE*, 1952, **99**, pt. IV, pp 250-257.

12 Jones, T.B. and Spracklen, C.T. Polarisation of v.l.f. radiowaves reflected from the ionosphere. *Proc. IEE*, 1976, **123**, number 2, pp 115-122.

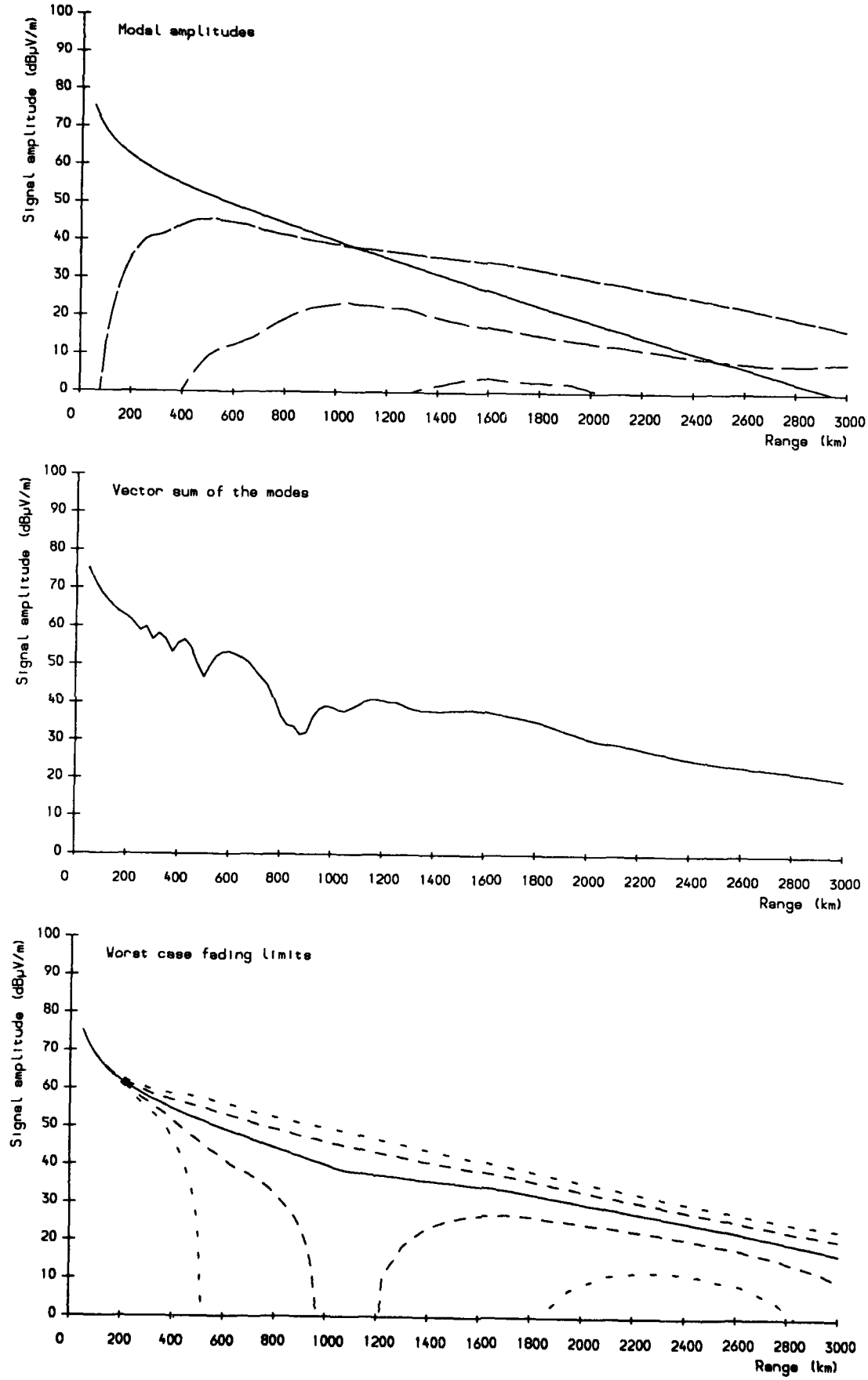

Figure 1. Predicted daytime modal structure for the Trondheim - Aberdeen (57.7 kHz) path.

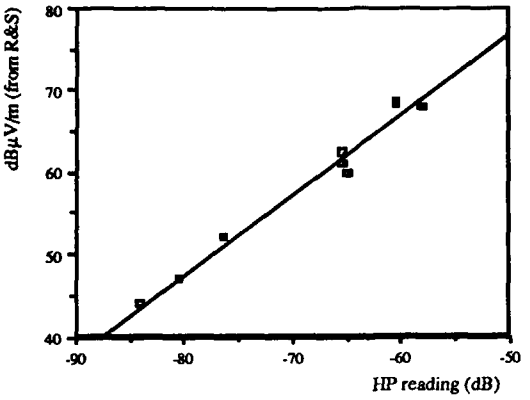

Figure 2. Calibration curve for the receiving equipment.

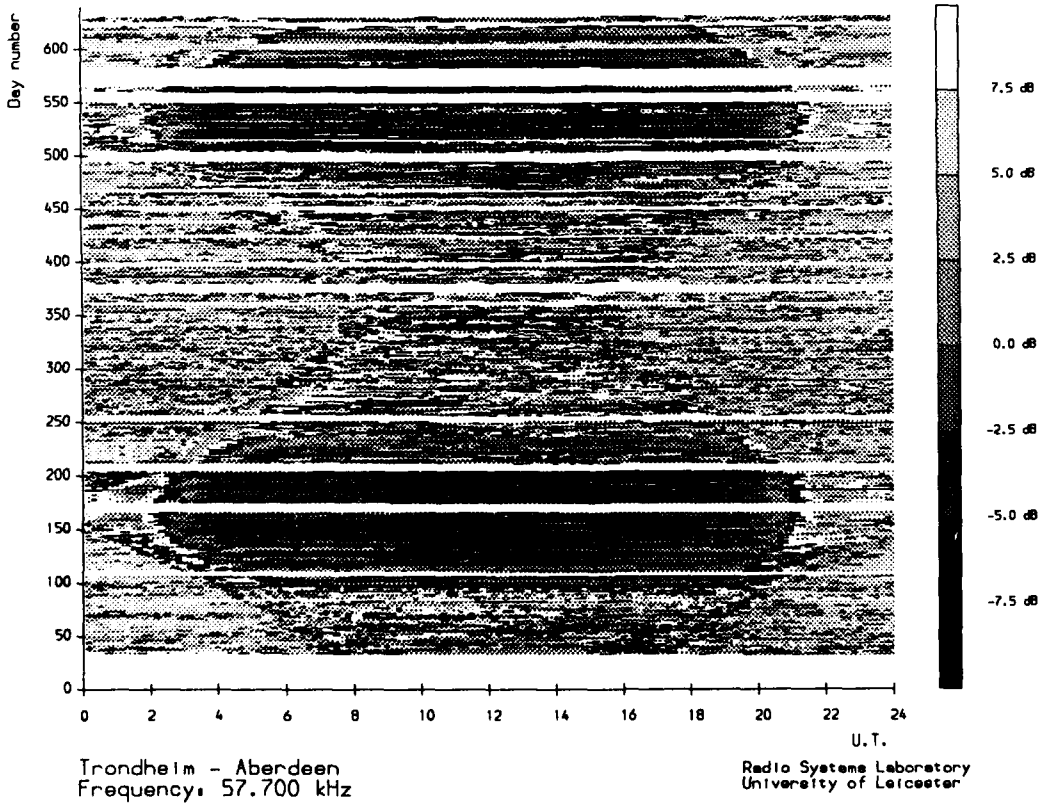

Figure 3. Signal strength variations as a function of time of day and season for the 57.7 kHz Trondheim - Aberdeen signal.

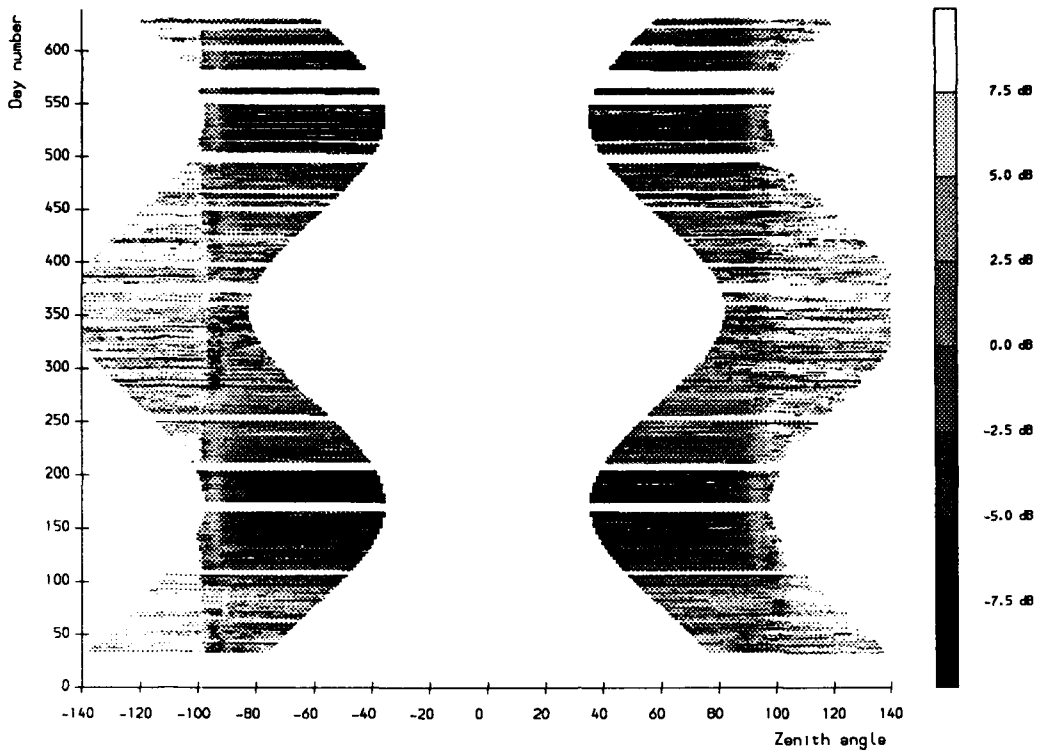

Figure 4. Same data as Figure 3 plotted as a function of solar zenith angle.

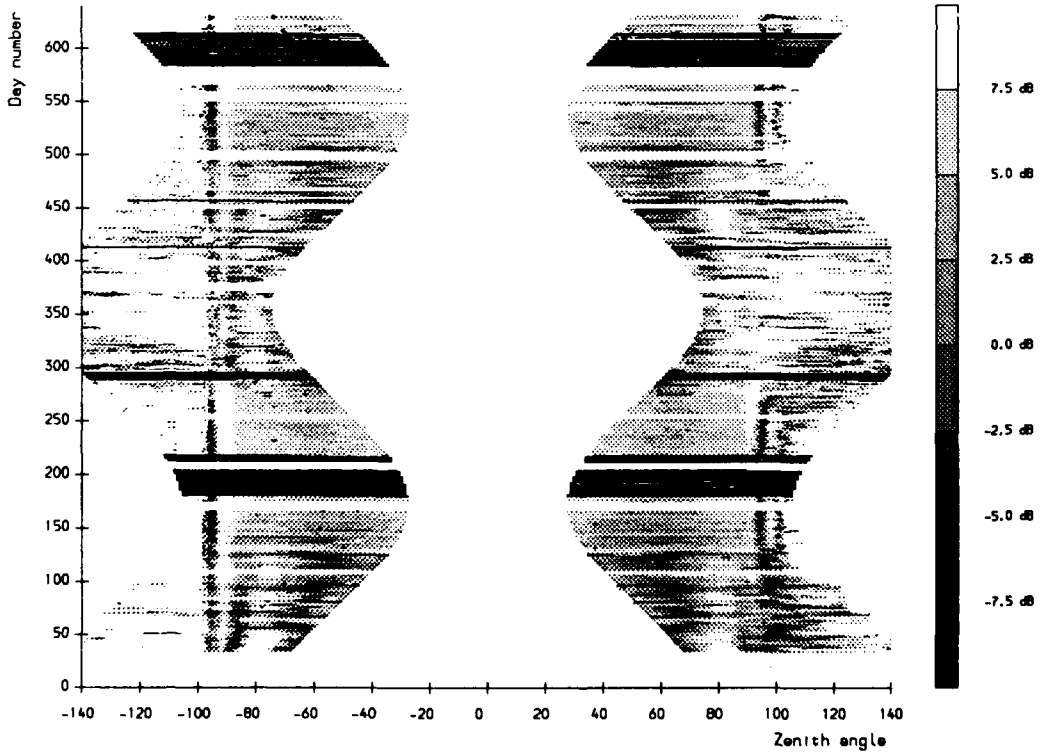

Figure 5. Signal strength variations as a function of solar zenith angle and season for the 65.8 kHz Brest - Aberdeen signal.

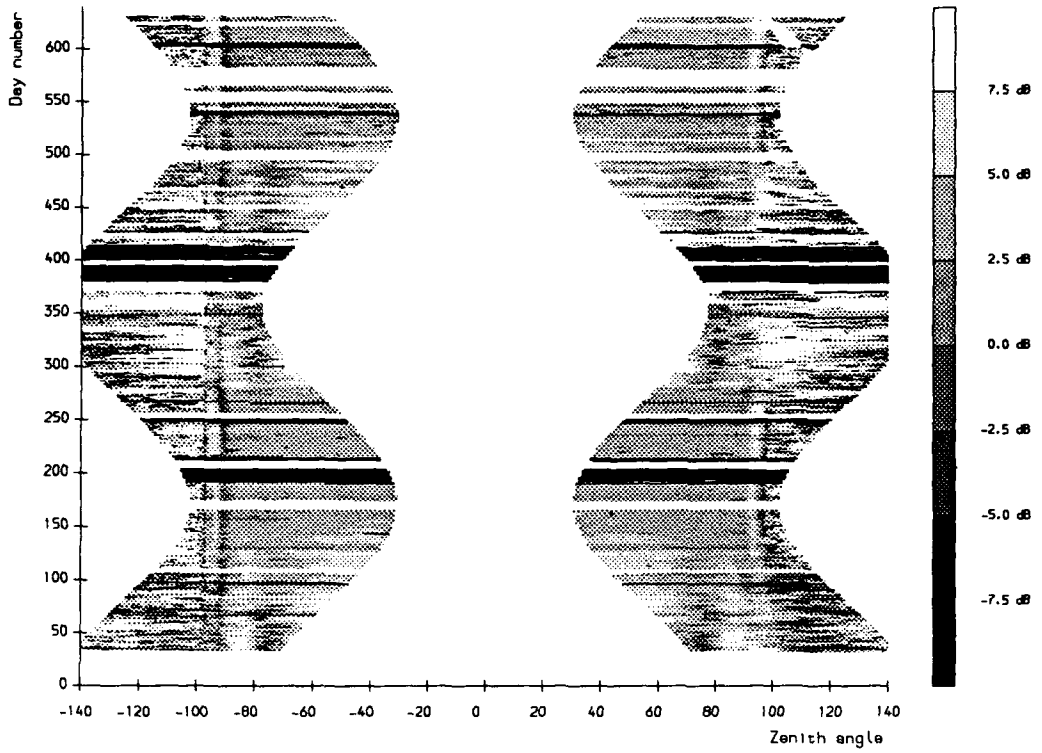

Figure 6. Signal strength variations as a function of solar zenith angle and season for the 68.9 kHz Denmark - Aberdeen signal.

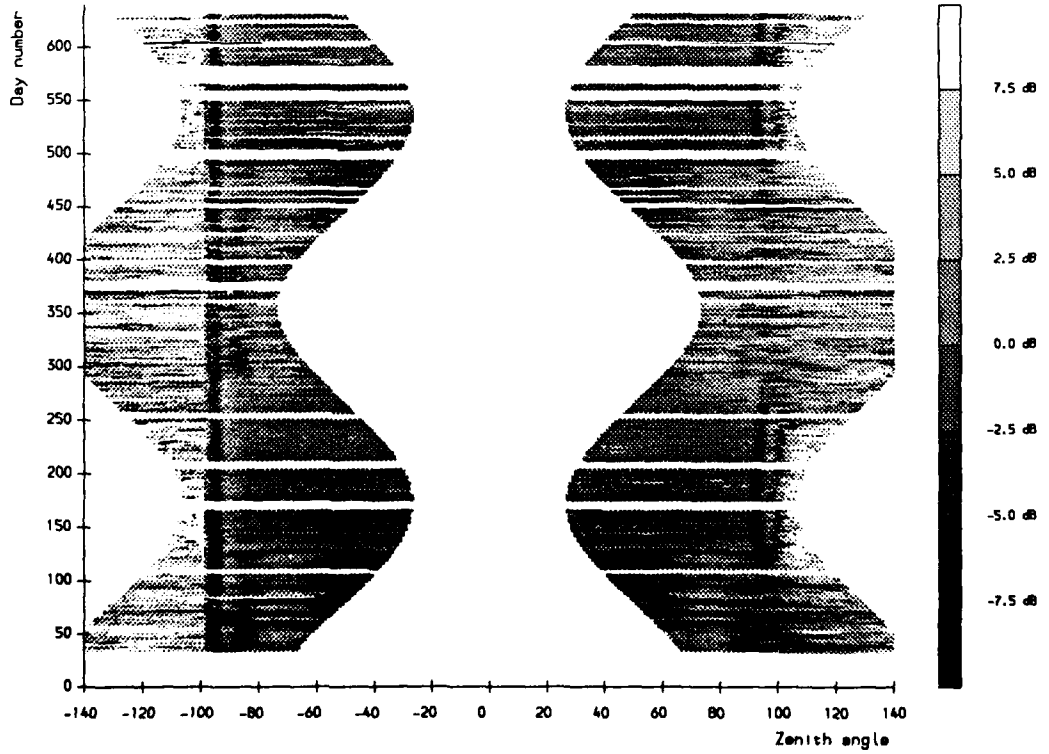

Figure 7. Signal strength variations as a function of solar zenith angle and season for the 75.0 kHz Geneva - Aberdeen signal.

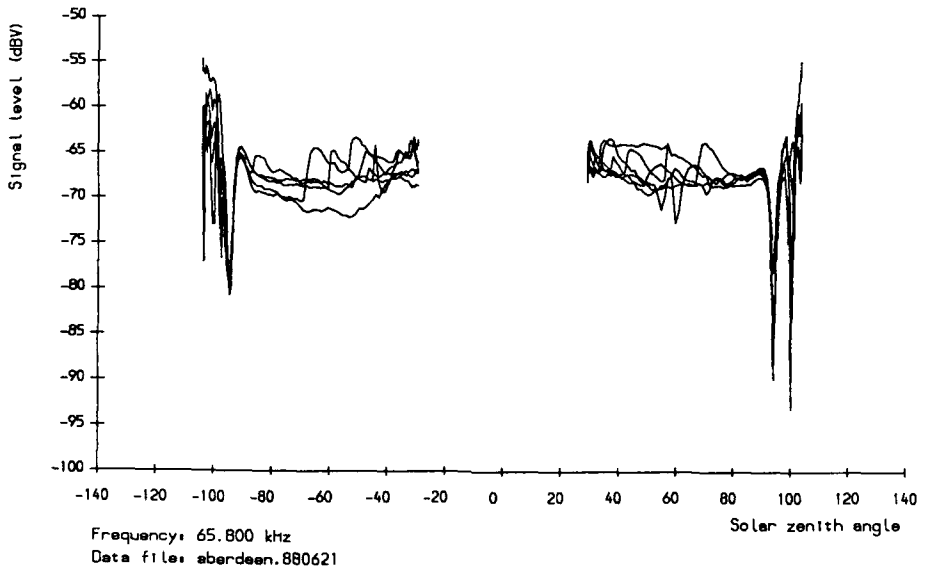

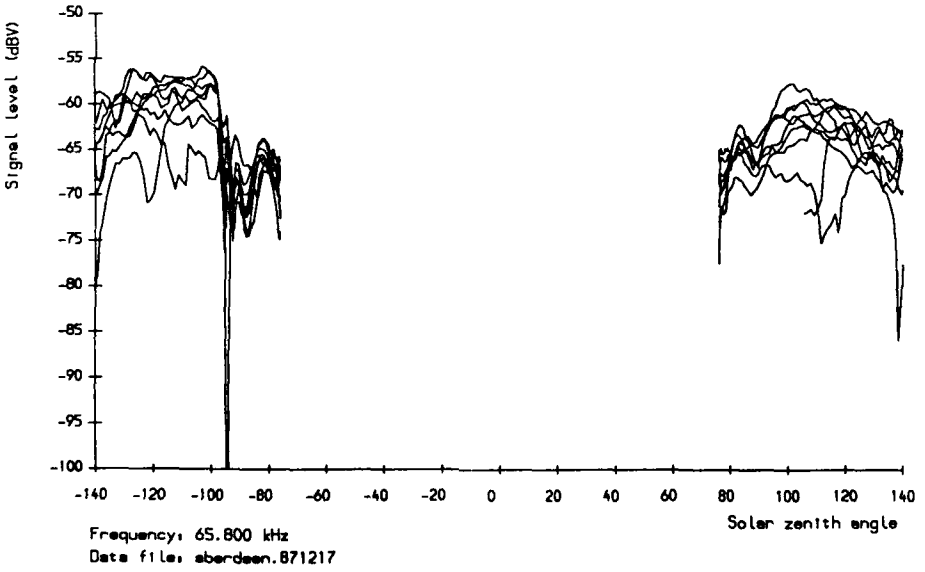

Figure 8. Typical diurnal signal strength variations for the 65.8 kHz Brest - Aberdeen signal. Frame (a) is for summer and frame (b) for winter.

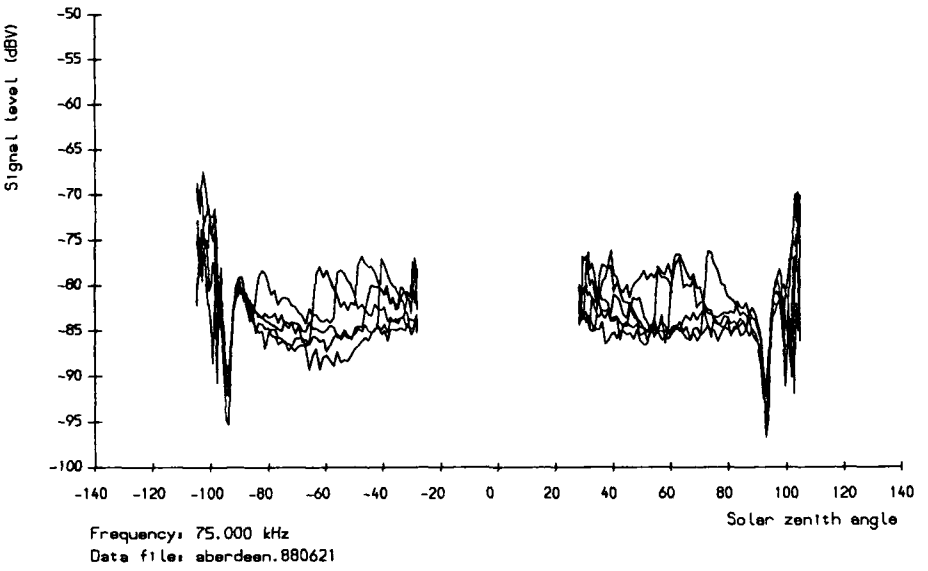

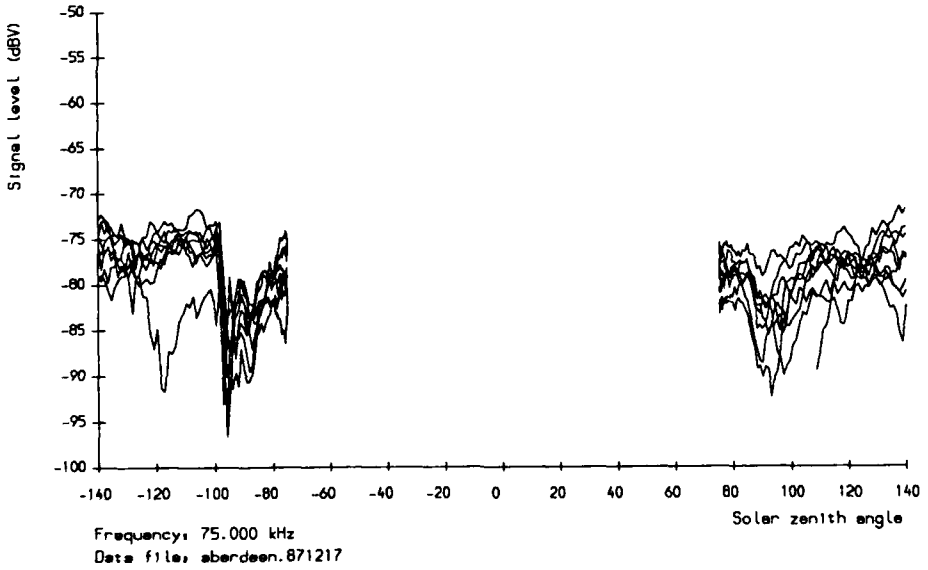

Figure 9. Typical diurnal signal strength variations for the 75.0 kHz Geneva - Aberdeen signal. Frame (a) is for summer and frame (b) for winter.

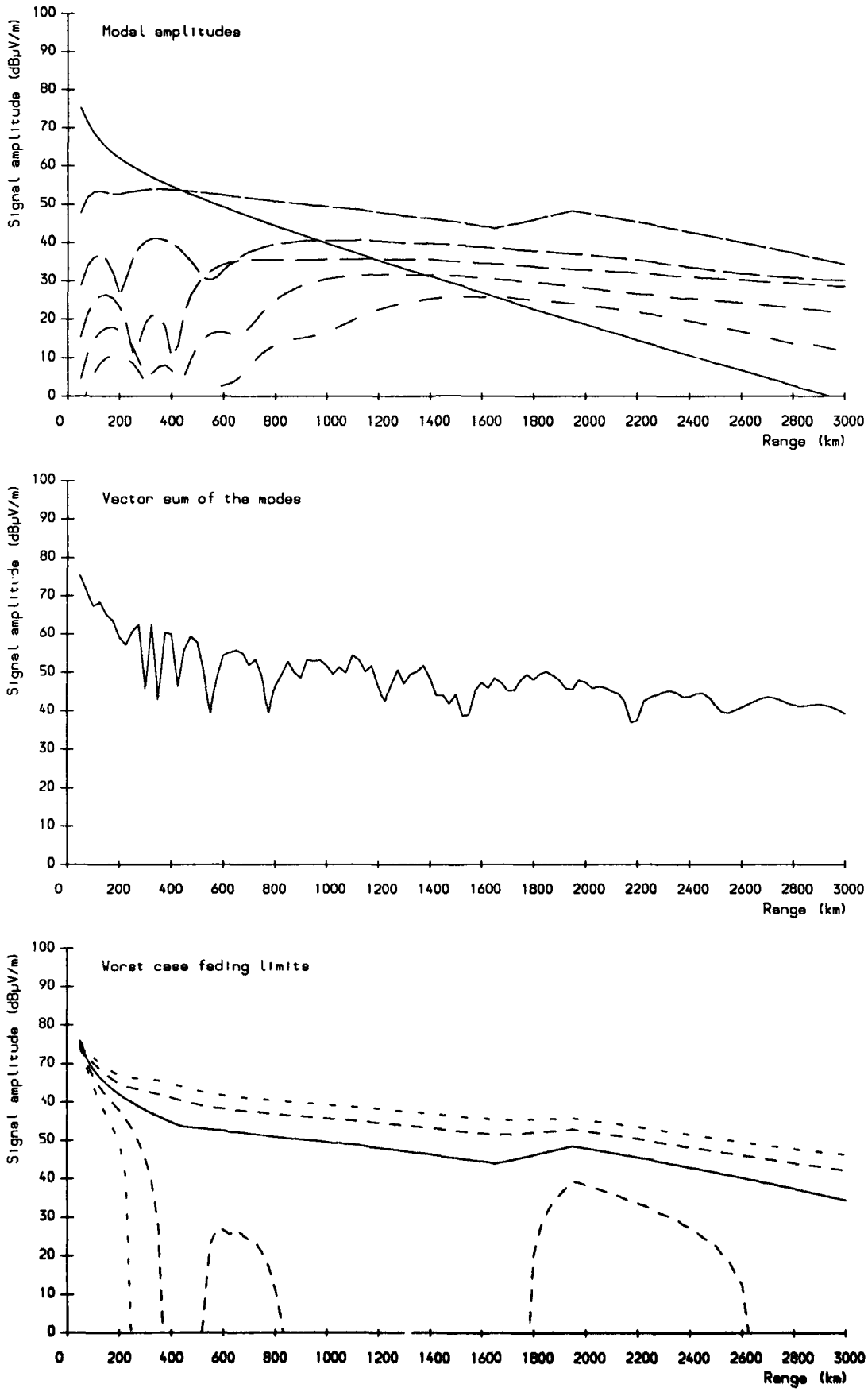

Figure 10. Predicted nighttime modal structure for the Trondheim - Aberdeen (57.7 kHz) path.

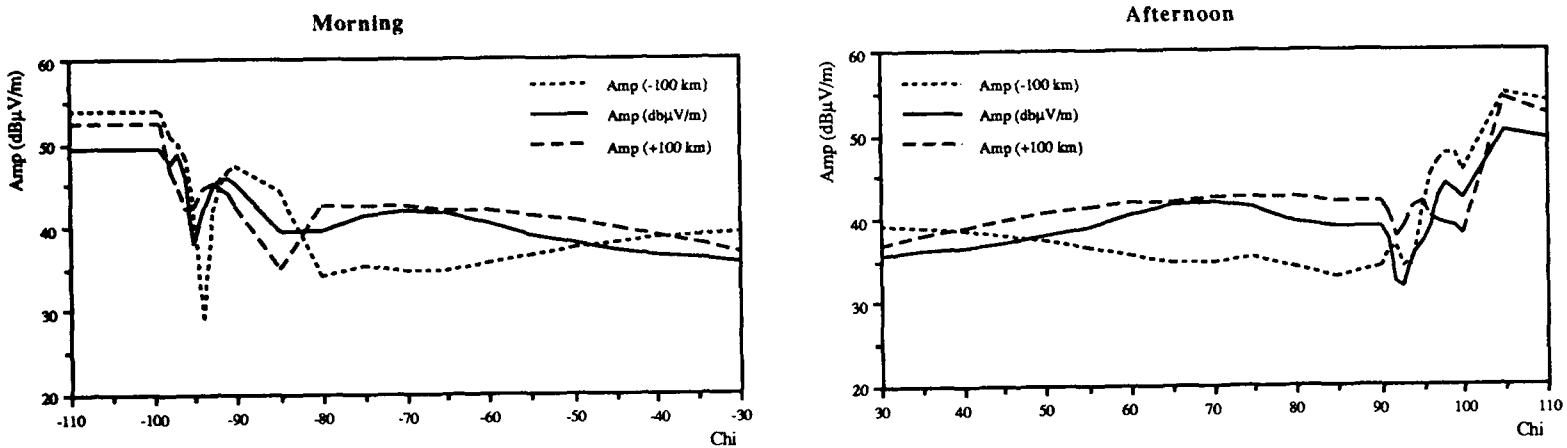

Figure 11. Predictions of the diurnal variation in signal strength for the 57.7 kHz Trondheim - Aberdeen signal for the summer months. To illustrate the likely errors in these predictions, the amplitudes have been calculated at the true range and also at the true range ±100 km.

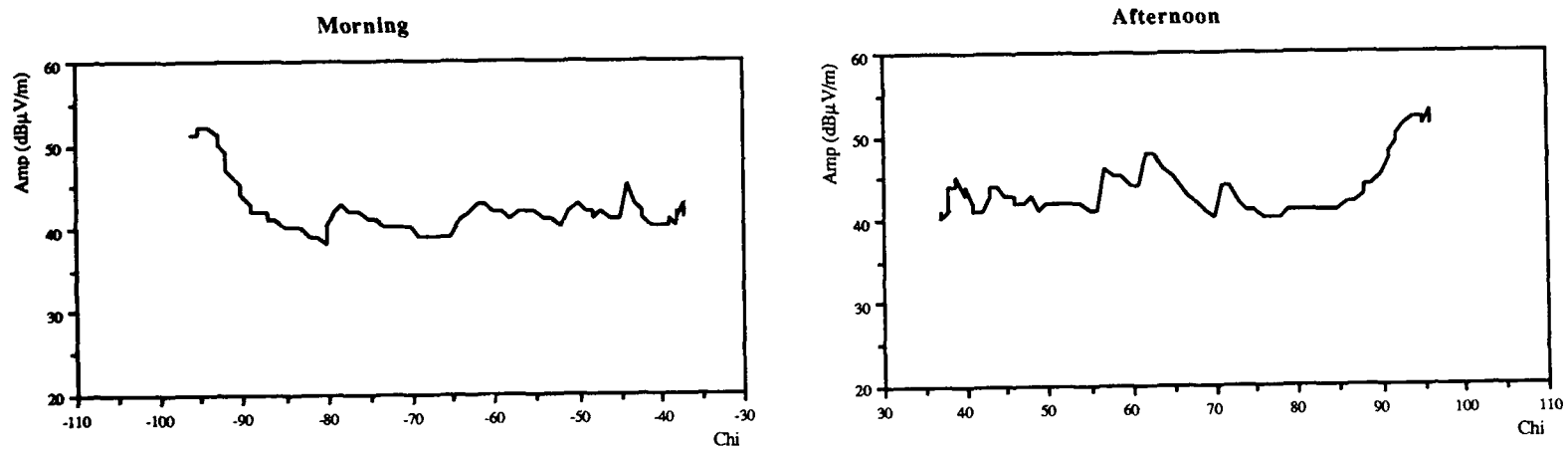

Figure 12. Average measured signal strength over 1 week corresponding to the predictions of Figure 11.

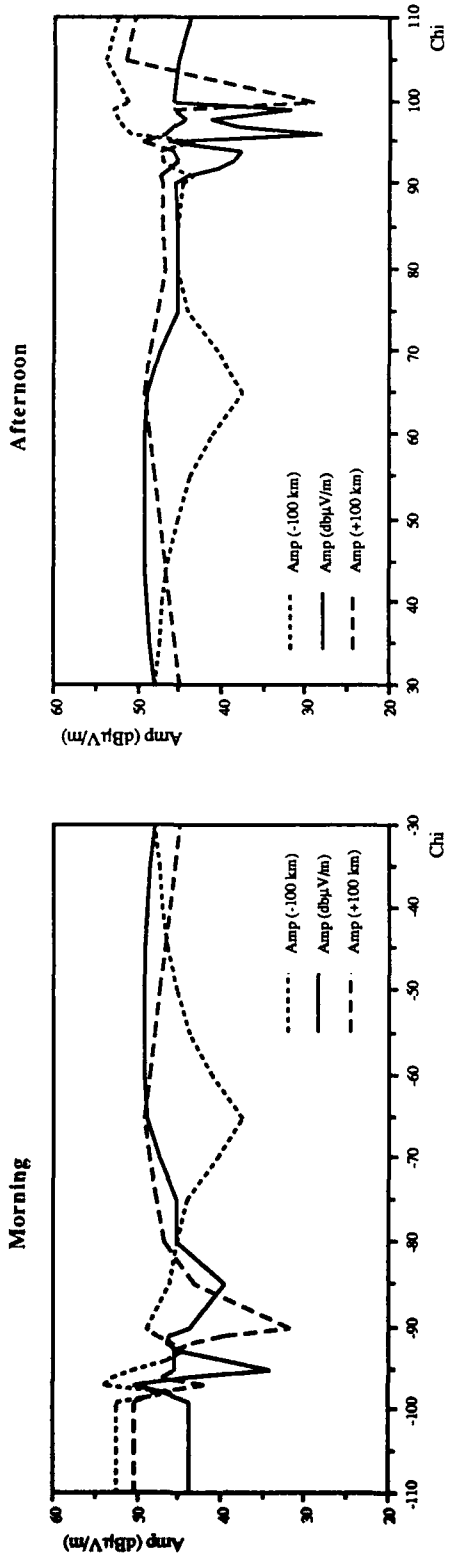

Figure 13. Predictions of the diurnal variation in signal strength for the 68.9 kHz Denmark - Aberdeen signal for the summer months. To illustrate the likely errors in these predictions, the amplitudes have been calculated at the true range and also at the true range ±100 km.

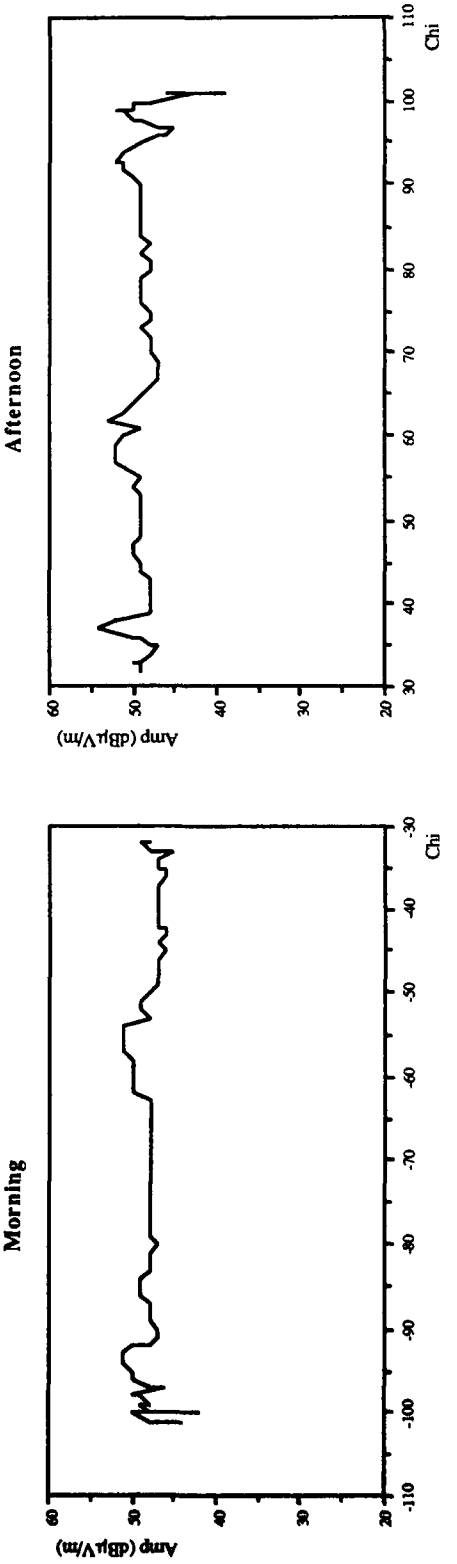

Figure 14. Average measured signal strength over 1 week corresponding to the predictions of Figure 13.

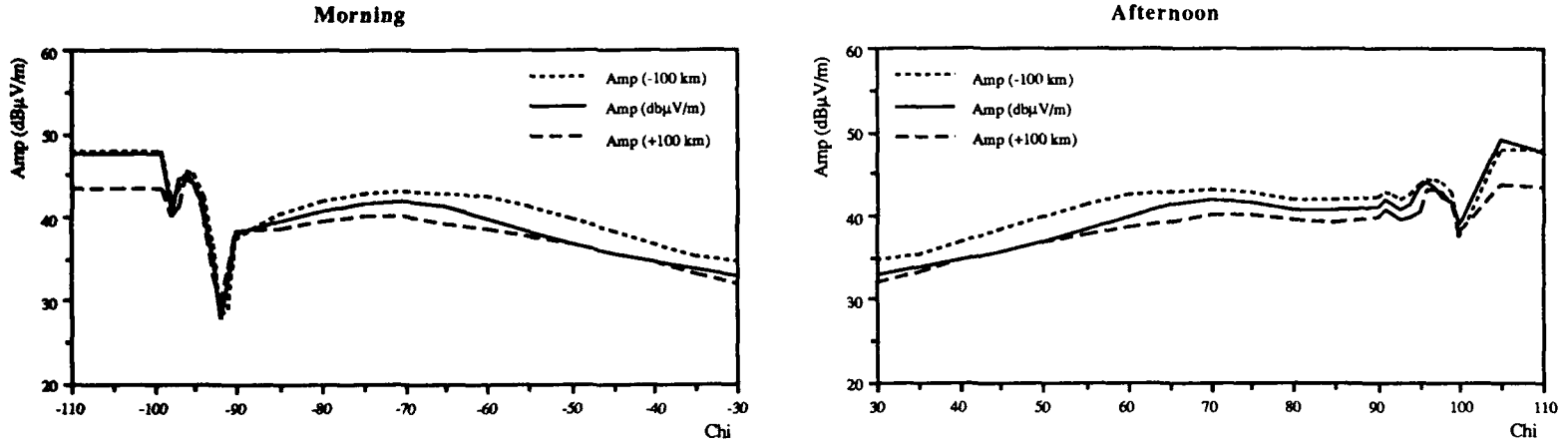

Figure 15. Predictions of the diurnal variation in signal strength for the 75.0 kHz Geneva - Aberdeen signal for the summer months. To illustrate the likely errors in these predictions, the amplitudes have been calculated at the true range and also at the true range ±100 km.

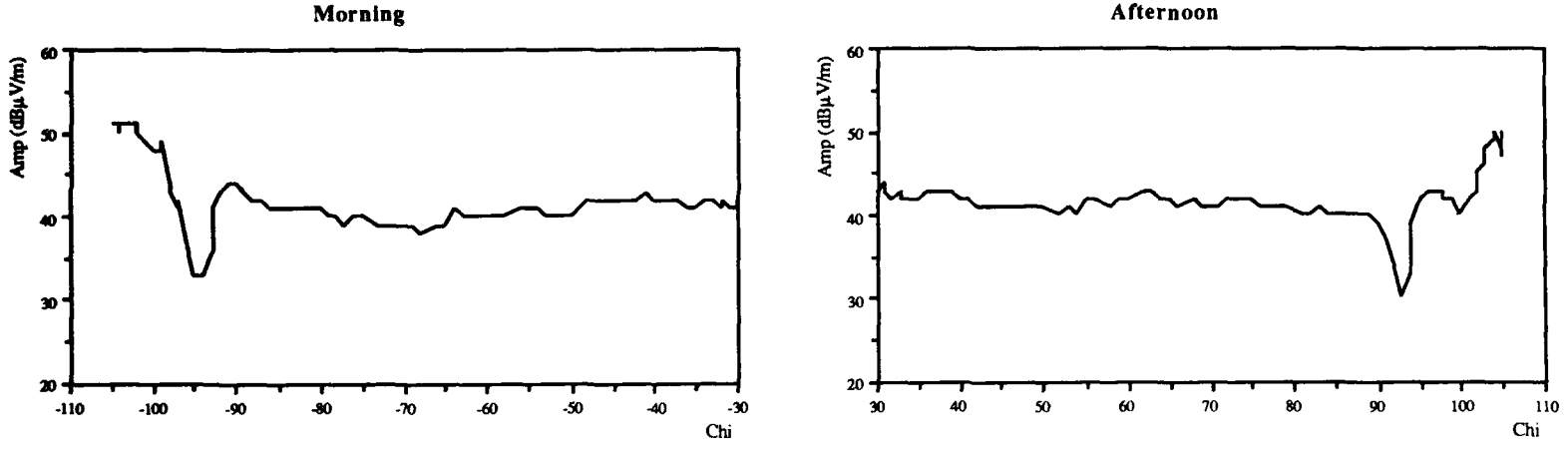

Figure 16. Average measured signal strength over 1 week corresponding to the predictions of Figure 15.

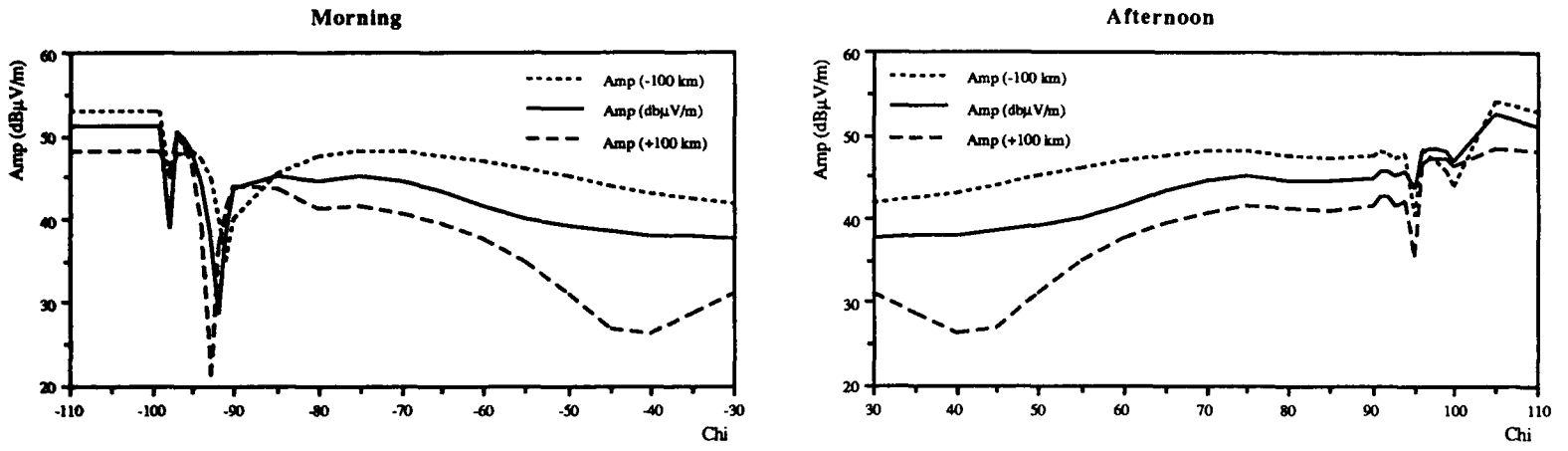

Figure 17. Predictions of the diurnal variation in signal strength for the 65.8 kHz Brest - Aberdeen signal for the summer months. To illustrate the likely errors in these predictions, the amplitudes have been calculated at the true range and also at the true range ±100 km.

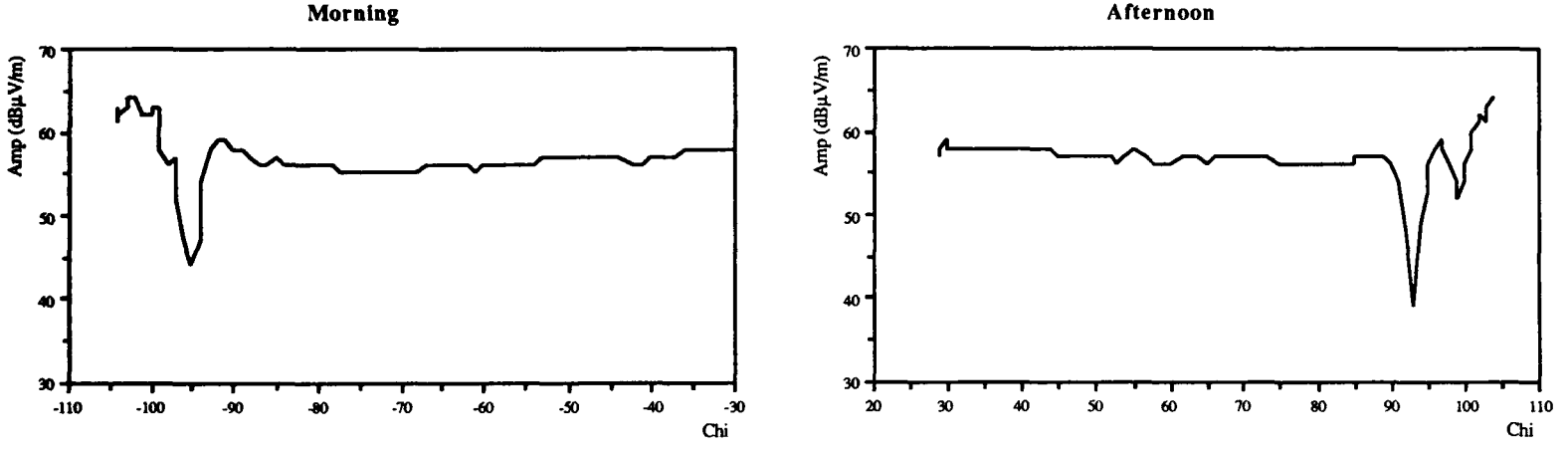

Figure 18. Average measured signal strength over 1 week corresponding to the predictions of Figure 17.

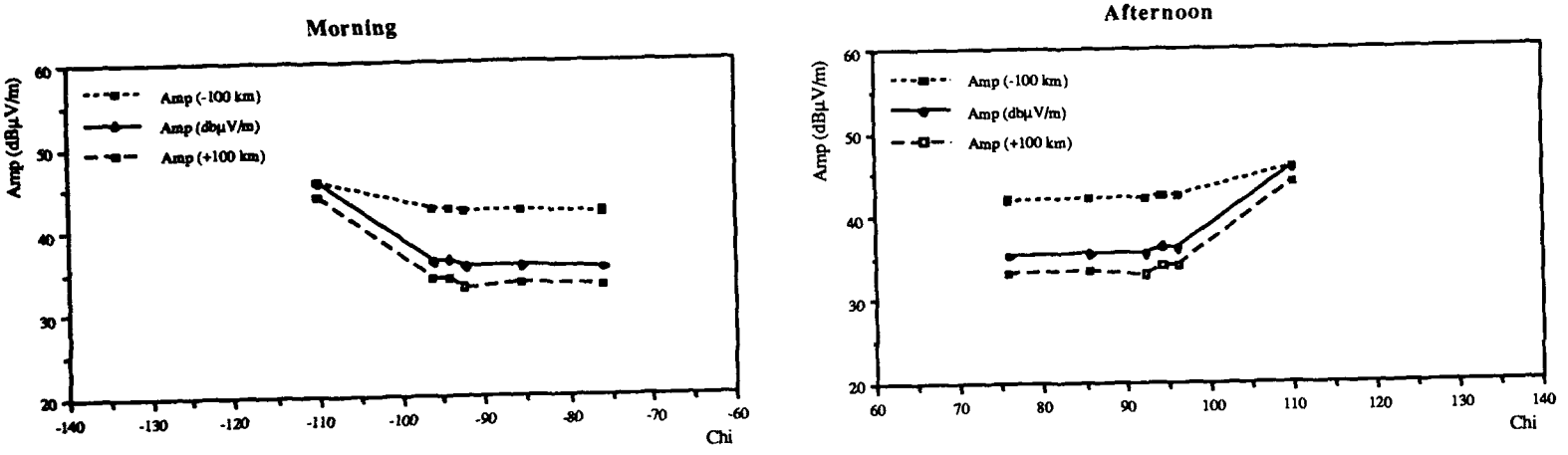

Figure 19. Predictions of the diurnal variation in signal strength for the 57.7 kHz Trondheim - Aberdeen signal for the winter months. To illustrate the likely errors in these predictions, the amplitudes have been calculated at the true range and also at the true range ±100 km.

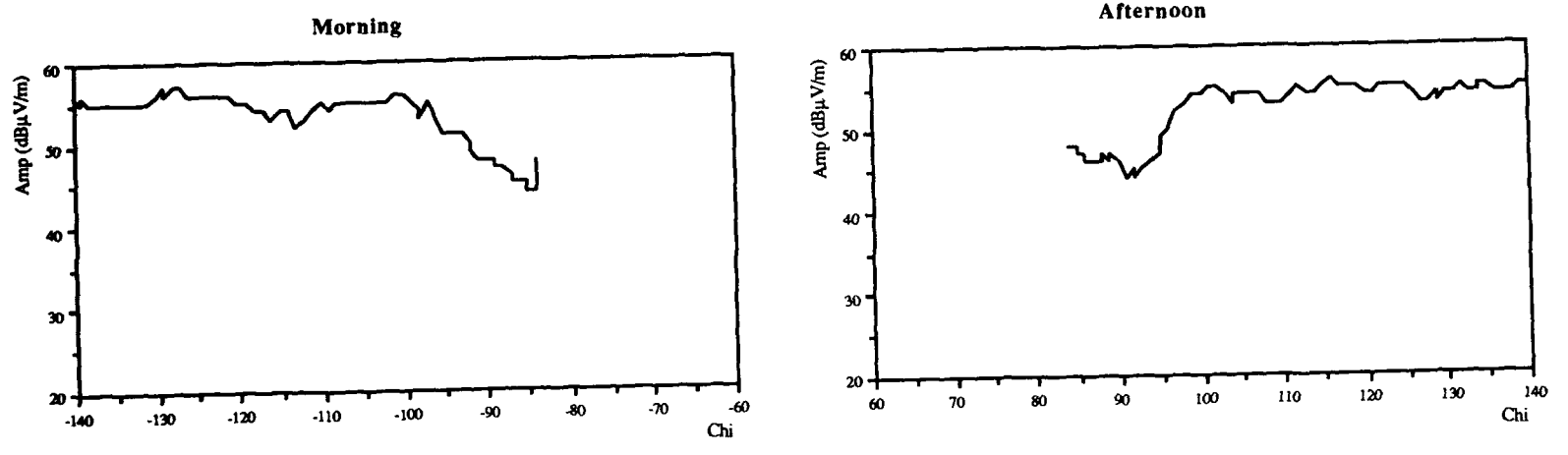

Figure 20. Average measured signal strength over 1 week corresponding to the predictions of Figure 19.

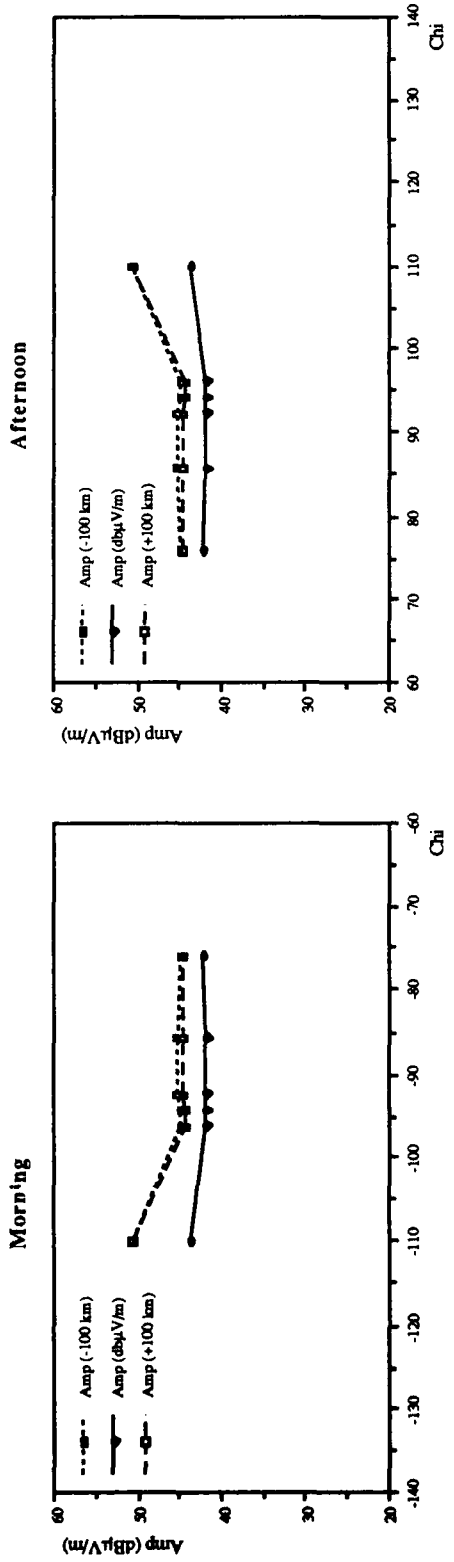

Figure 21. Predictions of the diurnal variation in signal strength for the 68.9 kHz Denmark - Aberdeen signal for the winter months. To illustrate the likely errors in these predictions, the amplitudes have been calculated at the true range and also at the true range ±100 km.

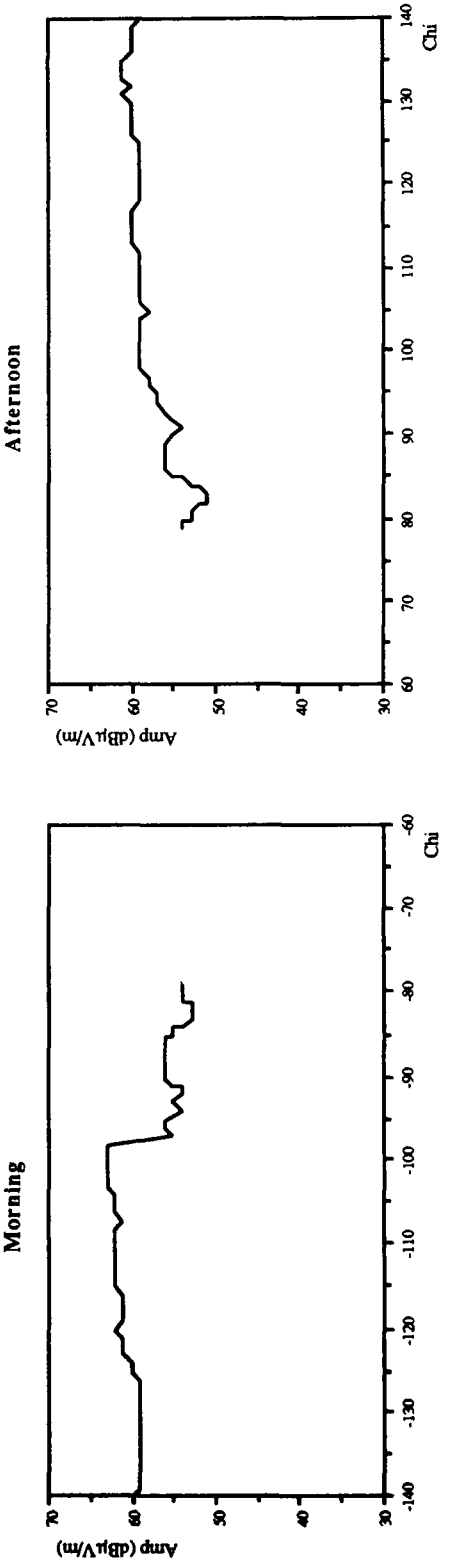

Figure 22. Average measured signal strength over 1 week corresponding to the predictions of Figure 21.

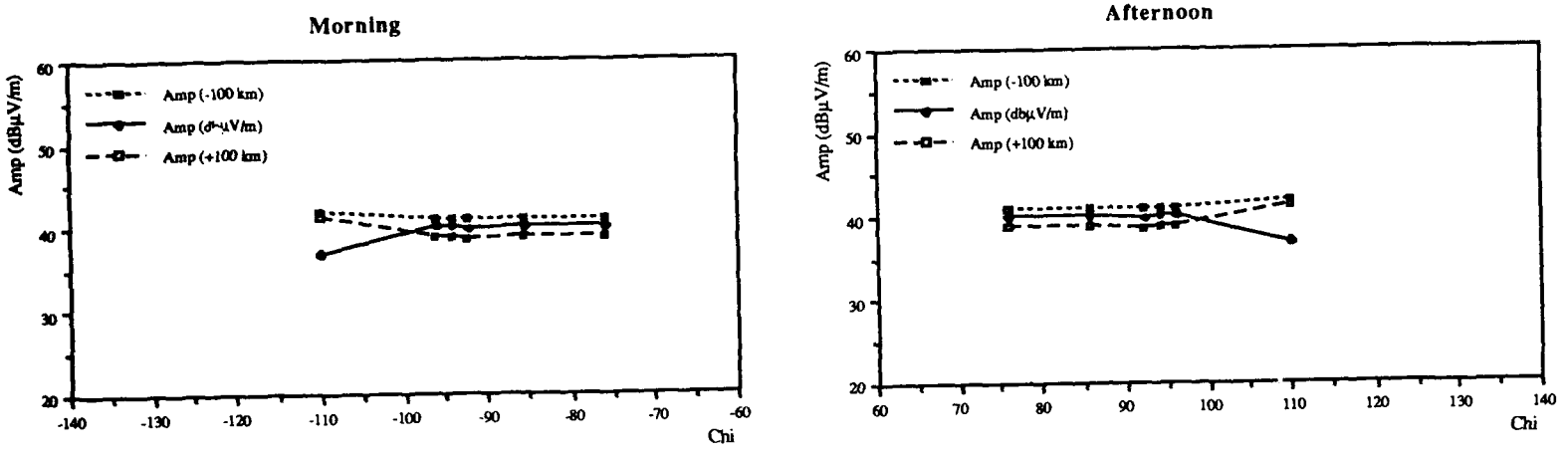

Figure 23. Predictions of the diurnal variation in signal strength for the 75.0 kHz Geneva - Aberdeen signal for the winter months. To illustrate the likely errors in these predictions, the amplitudes have been calculated at the true range and also at the true range ±100 km.

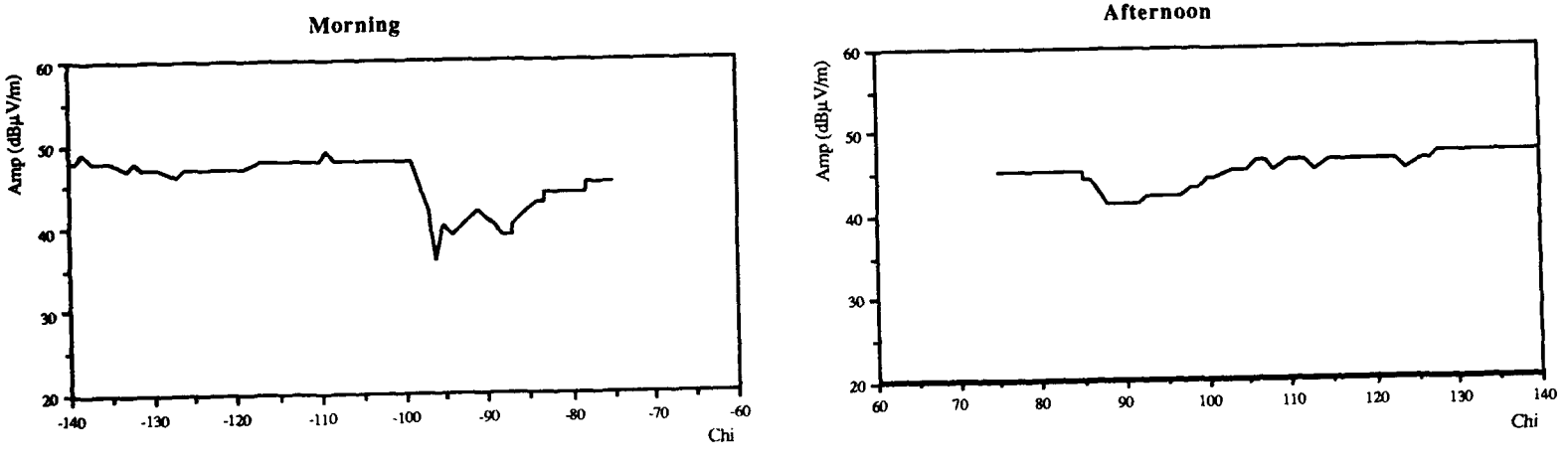

Figure 24. Average measured signal strength over 1 week corresponding to the predictions of Figure 23.

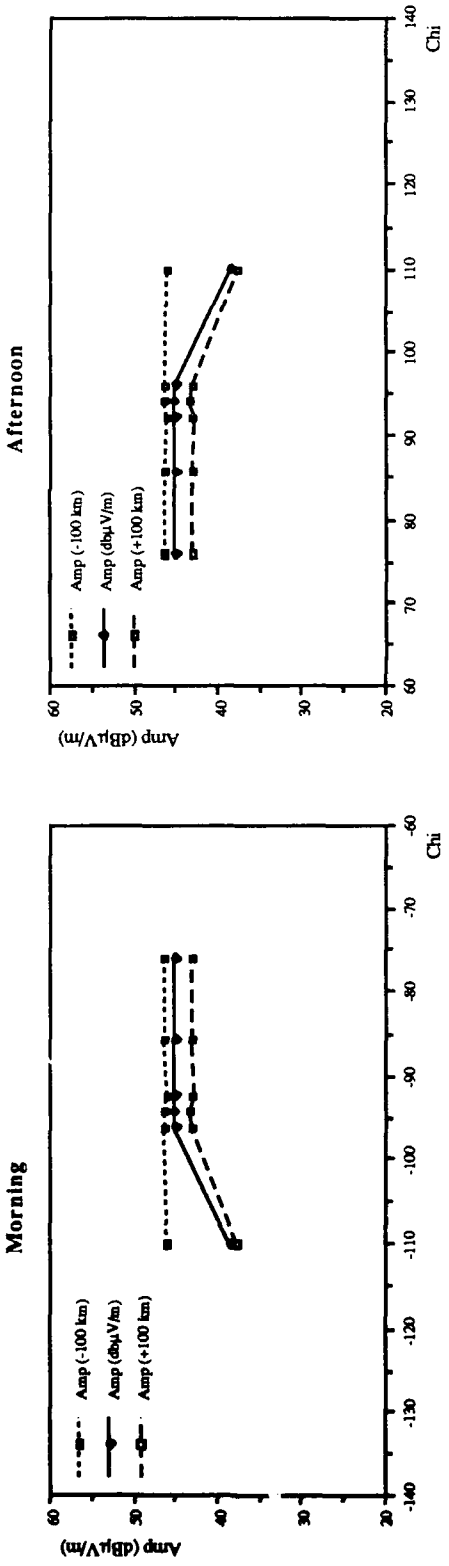

Figure 25. Predictions of the diurnal variation in signal strength for the 65.8 kHz Brest - Aberdeen signal for the winter months. To illustrate the likely errors in these predictions, the amplitudes have been calculated at the true range and also at the true range ±100 km.

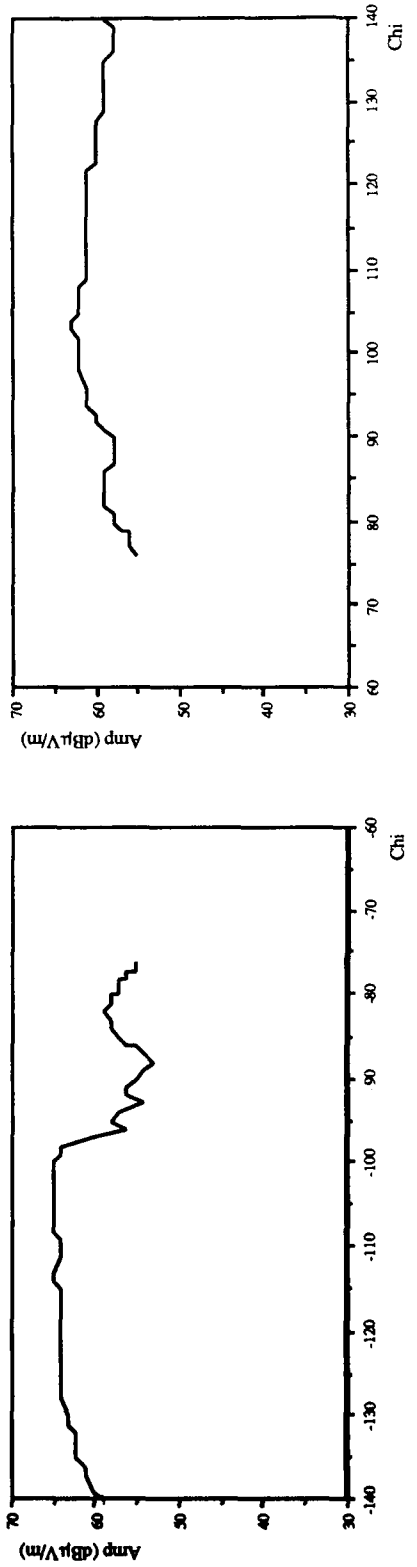

Figure 26. Average measured signal strength over 1 week corresponding to the predictions of Figure 25.

ELF PROPAGATION IN DEEP AND SHALLOW SEA WATER

C.P. Burke
D. Llanwyn Jones
Physics Department, King's College,
London, U.K. WC2R 2LS

ABSTRACT

In this paper electromagnetic wave propagation at Extremely Low Frequencies (ELF) in deep and shallow sea water is considered. The term 'ELF' is used here somewhat loosely to refer to the frequency band 0-3 kHz. The radiation source is considered to be located in the sea water and is taken to be a horizontal electric dipole (HED) or a vertical electric dipole (VED). For the deep water case, a comparison is made between results computed using complex image theory and results calculated using the full Sommerfeld integral formulation. Both these formulations include the lateral waves which propagate along the air-sea interface. Moving on to the case of shallow water, there are two lateral wave modes of propagation - lateral waves which propagate on the sea surface and along the seabed. These modes are included by numerical evaluation of the Sommerfeld integrals which appear in the complete solution. We also compare the relative efficacy of sub-surface horizontal electric dipoles and vertical electric dipoles as radiators. For the case of zero frequency (dc), the Sommerfeld integrals simplify considerably enabling the fields to be evaluated as the sums of infinite series. This dc formulation leads to much reduced computation time. Finally, the effects on propagation of long-wavelength water gravity waves or tides on the surface of the sea are examined by considering these waves as a perturbation to the sea-air interface.

1. INTRODUCTION

Electromagnetic wave propagation in layered or stratified media has been of continued research interest since Sommerfeld's [1] initial pioneering work. Early applications tended to concentrate upon propagation in the Earth-ionosphere waveguide. However, some workers, *e.g.* Wait [2], also examined problems of interest in subsurface geophysical probing. Others, such as Weaver [3] and Seigel and King [4], were concerned with propagation in sea water. Owing to the attenuating nature of sea water, ELF is the most suitable radio band for communication involving subsurface paths. Bannister [5,6], building upon asymptotic expansions due to Wait [7], has developed an approximate theory for calculating the electromagnetic fields in deep sea water, where the effects of the lower (seabed) interface can be neglected.

In this paper we explore the accuracy of Bannister's complex image theory by comparing the fields calculated using Bannister's equations with those computed using the full Sommerfeld integrals for the deep sea water situation. Complex image theory (CIT) has the advantage of allowing the propagation path to be interpreted in simple physical terms but it is not a 'full-wave' formulation.

Moving on to the case of shallow water, we compare the propagated fields for sources situated close to the sea-air interface with those for sources situated close to the sea-seabed interface. We then also compare the fields produced by horizontal electric dipole (HED) sources to those produced by vertical electric dipole (VED) sources. The special case of zero frequency is examined and exact formulas are developed which allow for very rapid computation of the fields due to both HED and VED sources.

Tidal level changes, waves on the surface of the sea and curvature of the sea bed will affect the propagation of radio waves within the sea. Thus we finally examine the effects of slow sea-level changes in the ELF band.

2. DEEP WATER PROPAGATION

We consider an x-directed HED located at $(0, 0, h)$ in infinitely deep sea water as illustrated in Fig.1 and require the fields at a general point (x, y, z).

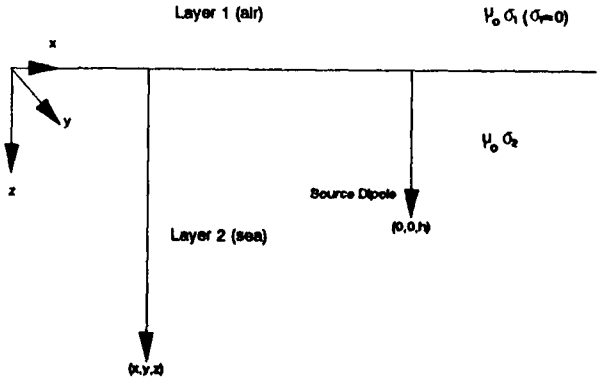

Fig. 1

Deep Water Geometry

The air layer (1) and the sea layer (2) are both are considered to be of infinite extent in the horizontal direction and to have a permeability μ_0 equal to that of free space. An $e^{j\omega t}$ time dependence is assumed. By writing the Hertz vector as

$$\Pi = \Pi^{prim} + \Pi^{sec}, \tag{1}$$

where Π^{prim} is the primary contribution produced by the source in layer 2 and Π^{sec} is a secondary contribution associated with the interface, Sommerfeld showed that the HED fields in layer i (with $i = 1, 2$),can be derived from the two-component Hertz vectors $(\Pi_{xi}, 0, \Pi_{zi})$, the x and z components being given by:

$$\Pi_{x1} = \frac{Idl}{4\pi\sigma_2^*}\int_0^\infty a e^{u_1 z} J_0(\lambda\rho)d\lambda \tag{2}$$

$$\Pi_{x2} = \frac{Idl}{4\pi\sigma_2^*}\int_0^\infty \left(\frac{\lambda}{u_2}e^{-|z-h|u_2 z} + be^{-u_2 z}\right) J_0(\lambda\rho)d\lambda \tag{3}$$

$$\Pi_{z1} = \frac{Idl}{4\pi\sigma_2^*}\frac{\partial}{\partial x}\int_0^\infty c e^{u_1 z} J_0(\lambda\rho)d\lambda \tag{4}$$

$$\Pi_{z2} = \frac{Idl}{4\pi\sigma_2^*}\frac{\partial}{\partial x}\int_0^\infty d e^{-u_2 z} J_0(\lambda\rho)d\lambda \tag{5}$$

in which $\rho = \sqrt{x^2+y^2}$, $u_i = \sqrt{\lambda^2 - k_i^2}$ and $k_i^2 = -j\omega\mu_0\sigma_i^*$ with $\sigma_i^* = \sigma_i + j\omega\epsilon_i$. σ_i^* is the complex conductivity in layer i. In layer (1) σ_1^* is imaginary but for $i > 1$ and layer conductivities and wave frequencies of interest here, σ_i^* is essentially real as the displacement current is negligibly small. The equations above (a) satisfy the relevant Helmholtz equation in each layer, (b) contain the source singularity e^{-jkR}/R where $R = \sqrt{\rho^2 + (z-h)^2}$ as the first term in Π_{x2}, and (c) satisfy the radiation condition at infinity. The fields may then be found from

$$\mathbf{E} = k^2\Pi + \text{grad div } \Pi \tag{6}$$

and

$$\mathbf{H} = \frac{-k^2}{j\omega\mu_0}\text{curl } \Pi \tag{7}$$

where $j = \sqrt{-1}$. Because the permeability is assumed to be the same everywhere, the boundary conditions (continuity of tangential $\mathbf{E}$ and $\mathbf{H}$ at $z = 0$) reduce to the continuity of $k^2\Pi_x$, $k^2\frac{\partial\Pi_x}{\partial z}$, $k^2\Pi_z$ and div Π at $z = 0$. The coefficients a, b, c and d can then be determined. This is the complete, exact or 'full-wave' solution of the two layer problem.

To calculate the fields in the sea (layer 2), only coefficients b and d are required. These are given by

$$b = \frac{\lambda}{u_2}R_{21}e^{-u_2 h}$$

and

$$d = \frac{\lambda}{u_2}(1+R_{21})\left(\frac{k_1^2 - k_2^2}{k_2^2 u_1 + k_1^2 u_2}\right)e^{-u_2 h}$$

where

$$R_{21} = \frac{u_2 - u_1}{u_2 + u_1}$$

The electromagnetic field components can be computed by numerical integration using these expressions. However, much effort has been expended , particularly through the last decade, in attempts to derive analytic or more convergent integral equations. Two complex image theories have been proposed. The first, which has been much developed and promoted by Bannister [5,6] , models the dipole/half-space problem by locating an image dipole at a complex depth and is valid for 'large' source-observer separations and interfaces with a high refractive index. Attention will returned to this approximation shortly. More recently, Lindell and Alanen [8,9,10] have developed an *exact* complex image theory (EIT) for general source-observer distances by taking the Fourier transform of the original Helmholtz equations and then finding the Laplace transform of the reflection coefficient which yields a term interpreted as arising from an extended image of the source. This leads to an integral equation for the Hertz vector which is more convergent than the Sommerfeld integrals (2) to (5) given above.

The advantage of Bannister's formulation is that it leads to simple algebraic equations for the fields produced by different dipoles in two-layered media. Here we concentrate on the fields of the HED in deep sea water. The field equations have three components: 1) a direct wave component, 2) an image component and 3) a lateral wave component. The published expressions [5] are expected to be accurate when (a) $\rho \geq 3(z+h)$ and (b) $|\gamma_2\rho^2/(z+h)| \geq 4c_1$ where $\gamma_2 = jk_2$ and $c_1 = 3, 6, 9, 15$ or 25 depending on the field component.

We now compare some calculated results from Bannister's CIT with data obtained using the full integral approach. For the data presented here we have used equations in Tables II and III of Bannister [5]. As an illustration we consider a HED of unit current moment located at $(0, 0, 100)$ in sea water of conductivity 4 mho/m and calculate the field at $(100, y, 100)$ for frequencies of 10 and 100 Hz. Here, condition (a) is satisfied for $y \geq 592m$. In Fig. 2 the x component of the magnetic field at 10 Hz is plotted using CIT and exact theory. For this field component $c_1 = 6$ so condition (b) is satisfied for $y > 510m$. The dotted line on the graph indicates $y = 592m$. Good agreement can be observed between the two calculations, especially for large source-observer separations. This is reflected in the behavior of the relative errors for the CIT results which are plotted in Fig. 3; these decrease smoothly for large y or ρ. In Fig. 4 the variation of the calculated z component of the electric field at 100 Hz. is shown. For this field component, we have c_1=3, and so condition (b) is satisfied for $y > 181$m. Referring to the graph, we can see that in general there is good agreement between the CIT and exact results. However, if the relative error is plotted as in Fig. 5,

we can see that the error decreases after $y = 592m$ but then *increases* for a while before slowly tailing off. Some care needs to be exercised if precise field values are required from CIT.

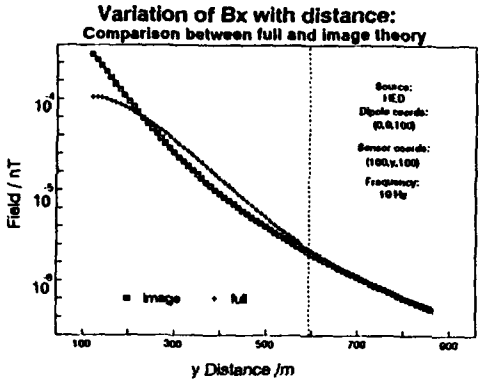

Fig. 2

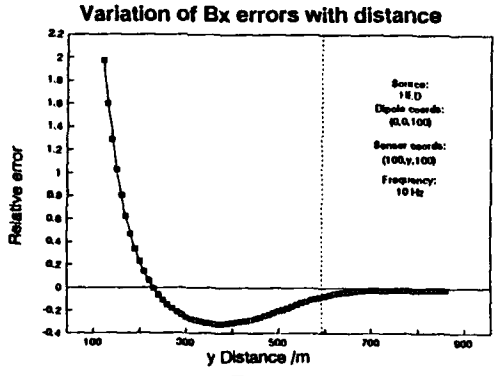

Fig. 3

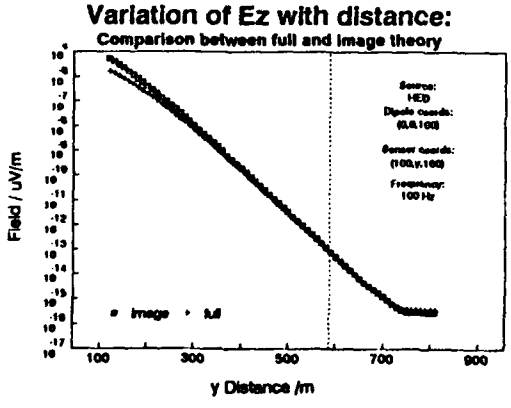

Fig. 4

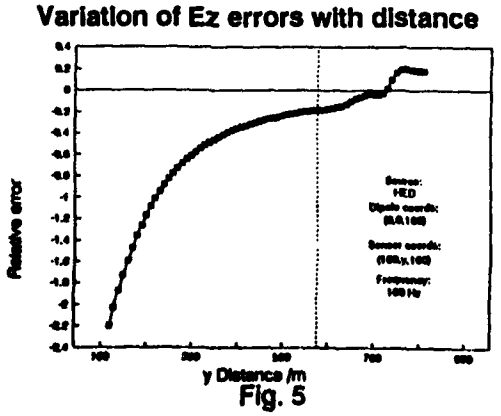

Fig. 5

Thus, in the numerical examples above, CIT gives good agreement when compared to the exact theory, although there are occasions when it can give imprecise answers even when conditions (a) and (b) are satisfied. However, the errors are fairly small. A great advantage of CIT is that it leads to a simple physical interpretation of the modes of propagation in terms of direct, image and lateral wave components. In this case the lateral wave can be thought of as an 'up-over-down' mode, *i.e.* a wave that, in part, propagates just over the sea-air interface during subsurface to subsurface communication. In the case where the sea-air interface can be neglected so that the two important layers are the sea and seabed, the equivalent so called 'down-along-up' mode becomes dominant.

3. SHALLOW WATER PROPAGATION

3.1 The General Case

The shallow water problem is that in which the effects of the sea bed (layer 3) cannot be ignored. To date it appears that CIT has not been developed for the three-layer medium where both an upper and a lower interface are of importance. One condition for the validity of CIT - that the relative refractive index must be large, does not apply to the lower interface in the situation considered here. Wait [11] has shown that the Sommerfeld integrals can be evaluated asymptotically for large source-observer separations using the *saddle-point method*. Here we are concerned with the fields for arbitrary source-observer distances and so evaluate these integrals numerically, enabling us to compare the effectiveness of the 'up-over-down' mode with the 'down-along-up' mode (*i.e.* propagation along the sea-air interface with that along the sea- seabed interface). We then consider the difference in the field amplitudes produced by HED and VED sources.

The geometry for the three layer shallow sea problem is shown in Fig. 6. The sea depth is d, otherwise the notation is as used above. The Hertz vectors for an x-directed HED are:

$$\Pi_{x1} = \frac{Idl}{4\pi\sigma_2^*}\int_0^\infty Ae^{u_1 z}J_0(\lambda\rho)d\lambda \qquad (8)$$

$$\Pi_{x2} = \frac{Idl}{4\pi\sigma_2^*}\int_0^\infty \left(\frac{\lambda}{u_2}e^{-u_2|z-h|} + Be^{-u_2 z} + Ce^{u_2 z}\right) \times J_0(\lambda\rho)d\lambda \qquad (9)$$

$$\Pi_{x3} = \frac{Idl}{4\pi\sigma_2^*}\int_0^\infty De^{-u_3 z}J_0(\lambda\rho)d\lambda \qquad (10)$$

and

$$\Pi_{z1} = \frac{Idl}{4\pi\sigma_2^*}\frac{\partial}{\partial x}\int_0^\infty Re^{u_1 z}J_0(\lambda\rho)d\lambda \qquad (11)$$

$$\Pi_{z2} = \frac{Idl}{4\pi\sigma_2^*}\frac{\partial}{\partial x}\int_0^\infty \left(Te^{-u_2 z} + Se^{u_2 z}\right)J_0(\lambda\rho)d\lambda \qquad (12)$$

$$\Pi_{z3} = \frac{Idl}{4\pi\sigma_2^*}\frac{\partial}{\partial x}\int_0^\infty V e^{-u_3 z} J_0(\lambda\rho)d\lambda \qquad (13)$$

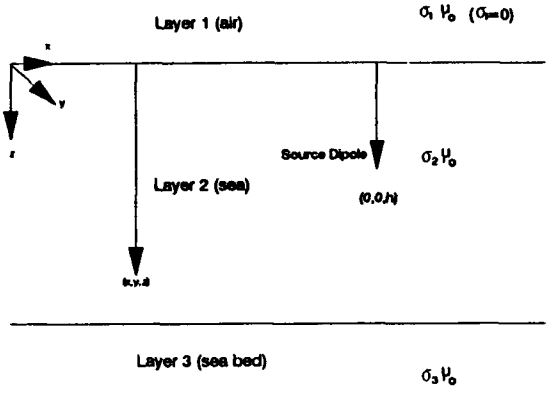

Fig. 6

Shallow Water Geometry

By applying the boundary conditions, we determine the four constants B, C, S and T needed for computing the fields in the sea water. The results are -

$$B = \frac{\lambda}{u_2}e^{-u_2 h}R_{21}\left(\frac{1+R_{23}e^{-2u_2(d-h)}}{1-R_{21}R_{23}e^{-2u_2 d}}\right)$$

$$C = \frac{\lambda}{u_2}e^{-u_2(2d-h)}R_{23}\left(\frac{1+R_{21}e^{-2u_2 h}}{1-R_{21}R_{23}e^{-2u_2 d}}\right)$$

$$T = \frac{H - IR_{21}^{||}e^{-u_2 d}}{1-R_{21}^{||}R_{23}^{||}e^{-2u_2 d}}$$

$$S = \frac{(HR_{23}^{||}e^{-u_2 d} - I)e^{-u_2 d}}{1-R_{21}^{||}R_{23}^{||}e^{-2u_2 d}}$$

$$H = \left(\frac{\lambda}{u_2}e^{-u_2 h} + B + C\right)\left(\frac{k_1^2 - k_2^2}{k_2^2 u_1 + k_1^2 u_2}\right)$$

$$I = \left(\frac{\lambda}{u_2}e^{-u_2(d-h)} + Be^{-u_2 d} + Ce^{u_2 d}\right)\left(\frac{k_3^2 - k_2^2}{k_2^2 u_3 + k_3^2 u_2}\right)$$

in which

$$R_{21} = \frac{u_2 - u_1}{u_2 + u_1}$$

$$R_{23} = \frac{u_2 - u_3}{u_2 + u_3}$$

$$R_{21}^{||} = \frac{k_1^2 u_2 - k_2^2 u_1}{k_1^2 u_2 + k_2^2 u_1}$$

and

$$R_{23}^{||} = \frac{k_3^2 u_2 - k_2^2 u_3}{k_3^2 u_2 + k_2^2 u_1}$$

The R_{ij} and $R_{ij}^{||}$ in the above expressions are reflection coefficients for horizontal and vertical polarisations respectively.

For the VED case, corresponding expressions have been obtained, though only a single-component Hertz vector, Π_z, is then required to satisfy the boundary conditions because there is complete azimuthal symmetry.

Wait's [12] solutions for the three-layer problem (his equations 3.30-3.37) are in agreement with those above, except for missing factors $jk_2/2$ in Wait and differences in the final factors in our formulas for I and H. It is evident that Wait's solutions are valid only if the relative refractive indices of layers 1 and 2 and layers 2 and 3 are large (*i.e.* k_2 is much less than k_1 or k_3). This is the case for the Earth-ionosphere waveguide situation considered by Wait but does not apply for the current problem.

Fraser-Smith *et al* [13] considered propagation in the case where the effect of the upper interface (sea-air) can be neglected. They computed the field when the source was placed near the seabed so that only the 'down-along-up' mode was involved by evaluating the integrals numerically. To compare the relative magnitudes of the 'up-over-down' and 'down-along-up' modes, we consider a sea 10 m deep and two separate cases: (1) the source situated 1 m below the sea surface and compute the fields a distance 1 m below the surface for varying horizontal separations and (2) the analogous situation for the seabed *i.e.* source 1 m above the seabed and point of observation 1 m above the sea bed. The results obtained by numerical evaluation of the Sommerfeld integrals for a HED at a wave frequency of 100 Hz are shown in Figs.7 and 8 for the E_x and B_y field components respectively where the source is loacated at $(0, 0, h)$ and the observations made at $(0, y, h)$. In the case of the E_x component there is relatively little difference in amplitude between the two modes of propagation although as y increases the 'up-over-down' mode appears to propagate with slightly lower loss, as anticipated. This difference is more marked for the B_y component, with the 'down-along-up' mode going through a local minimum near $y = 50m$; thereafter the difference between the two modes is less marked though still considerably greater than for the E_x component.

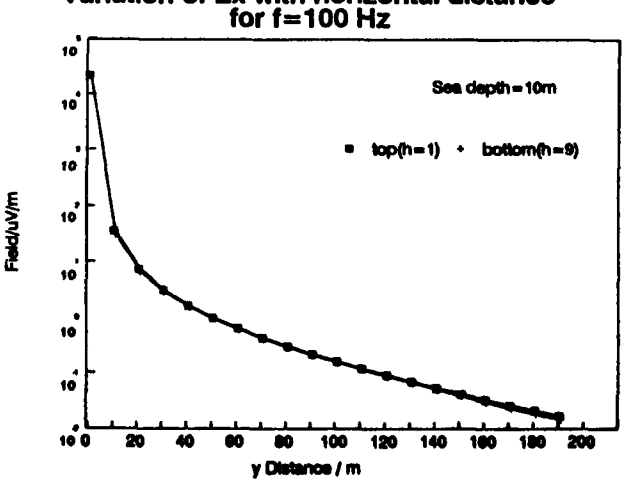

Fig. 7

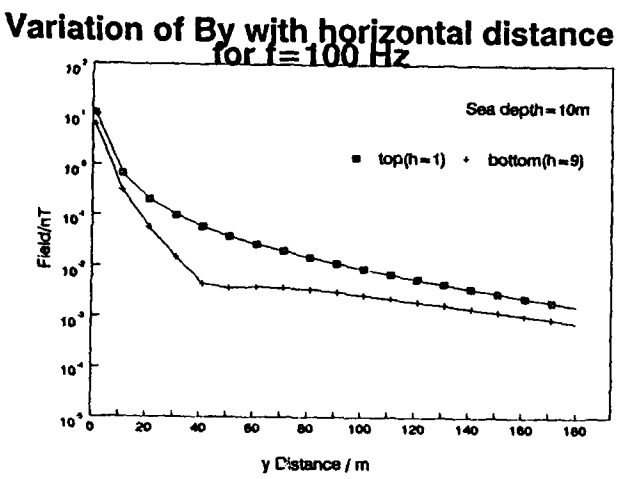

Fig. 8

Figs. 9 and 10 shows a comparison between the fields produced by HED and VED sources located at the same point $(0,0,5)$ in a sea 10 m deep; the diagrams show the field variations along the ray $x = y$. This then means that the x and y field components for the VED are the same. For the major field components the HED is the more efficient radiator. This is the opposite of that which occurs when the dipoles are situated in free space above the Earth or sea. The HED is then a very ineffective radiator at ELF unless it is elevated above the surface by a significant fraction of a wavelength - an HED located *on* a perfectly conducting half-space does not radiate at all!

3.2 The DC Case

At dc ($\omega = 0$) considerable simplification results: as $\omega \to 0$, we have:

$$u_i \to \lambda$$

$$R_{21} \to 0$$

$$R_{23} \to 0$$

and thus both B and $C \to 0$ so that only the first term, which is the primary excitation, contributes to Π_{z2} in (9). Additionally,

$$R^{\parallel}_{21} \to -1$$

and

$$R^{\parallel}_{23} \to R^{\parallel}_{dc} = \frac{\sigma_3 - \sigma_2}{\sigma_3 + \sigma_2}$$

The vertical polarisation reflection coefficients are thus finite but independent of λ. For the z-component of the Hertz vector, the coefficients in the integral (12) then reduce to

$$S = -\frac{1}{D^{\parallel}\lambda}\frac{\sigma_3 - \sigma_2}{\sigma_3 + \sigma_2}\left(e^{-\lambda(2d+h)} + e^{-\lambda(2d-h)}\right) \quad (13)$$

$$T = \frac{1}{D^{\parallel}\lambda}\left(-e^{-\lambda h} + e^{-\lambda(2d-h)}\frac{\sigma_3 - \sigma_2}{\sigma_3 + \sigma_2}\right) \quad (14)$$

where

$$D^{\parallel} = 1 + \frac{\sigma_3 - \sigma_2}{\sigma_3 + \sigma_2}e^{-2\lambda d} \quad (15)$$

The integral equations (8) to (13) can then be evaluated analytically using established formulas for the Laplace transforms of the Bessel functions of order zero and one. The analysis produces an exact infinite series expansion for Π_z which is suitable for computation of the field components. In layer (2), the results obtained for the HED are -

$$\Pi_{x2} = \frac{Idl}{4\pi\sigma_2}\frac{1}{\sqrt{\rho^2 + (z-h)^2}} \quad (16)$$

$$\Pi_{z2} = \frac{Idl}{4\pi\sigma_2}x\left(\frac{1}{R_{10}^2 + R_{10}r_{10}} + s_i\sum_{n=1}^{\infty}\sum_{i=1}^{4}\frac{(-R^{\parallel}_{dc})^n}{R_{in}^2 + R_{in}r_{in}}\right) \quad (17)$$

where the sign $s_i = +1$ for $i = 1$ and 2; $s_i = -1$ for $i = 3$ and 4, and

$$R_{in}^2 = \rho^2 + r_{in}^2$$

$$r_{1n} = 2nd + h + z$$

$$r_{2n} = 2nd - h + z$$

$$r_{3n} = 2nd + h - z$$

and

$$r_{4n} = 2nd - h - z$$

This solution is, in fact, nothing more than the geometrical-optics (or real images) formula which, as is well-known, is valid when the reflection coefficient is independent of the angle of incidence (which in the integral formulation discussed above is contained in the 'dummy' parameter λ). The images associated with a positive sign preceding z in the formulas for r_{in} are in layer (1) and those with a negative sign in layer (3). The series expansion formulas for the individual field components are computed from (6) and (7) with $k^2 = 0$ in (6) and $-k^2/j\omega\mu_0 = \sigma_2$ in (7). These formulas, together with those for the VED, are to be published elsewhere (see [14]). Implementation of this formalism produces a much faster algorithm for computing the field components than any involving numerical integration.

4. EFFECT OF SEA-LEVEL VARIATIONS

Changes in sea-level produced by gravity waves on the surface or tidal variations will affect the field values in the sea. We have calculated the effects of these sea-level variations by writing the Hertz vector as

$$\Pi = \Pi^{prim} + \Pi^{sec} + \Pi^{wave} \quad (18)$$

where Π^{wave} is the perturbation to Π^{prim} and Π^{sec} associated with the change in water level. The results

$$R^s_{12} = \frac{u_1\sigma_2^* - u_2\sigma_1^*}{\sigma_1^* u_2 + \sigma_2^* u_1}$$

$$R^s_{23} = \frac{u_2\sigma_3^* - u_3\sigma_2^*}{\sigma_2^* u_3 + \sigma_3^* u_2}$$

and a_1 is the incident amplitude.

Measurements of Schumann resonances were made over the period September 1988 to August 1989 [15] and the mean electric field in the band 10-45 Hz was measured as 850 $\mu V m^{-1}$. If the energy is distributed evenly over the band this gives a noise field in the air of 144 $\mu V m^{-1} Hz^{-\frac{1}{2}}$ which gives a typical field for the shallow seas considered here of the order of $10^{-2,-3}$ $\mu V m^{-1} Hz^{-\frac{1}{2}}$.

It is interesting to note that the magnetic field (H_y) is continuous across the air-sea interface whilst the electric field is not, so that the electric field in the sea is much smaller than the magnetic field in relation to their amplitudes in air.

6. CONCLUSION

In this paper, ELF electromagnetic wave propagation in deep and shallow water has been discussed. For the deep water case, complex image theory provides a useful and simple approximation for computing the fields providing that the source-observer distance is not too small. However, care must be exercised if precise field values are required.

For shallow water propagation, the amplitudes of the two lateral modes of propagation have been compared. In the numerical examples presented here the 'up-over-down' modes propagated with more effectively than the 'down-along-up' mode. Horizontal electric dipoles have been found to be more efficient radiators than vertical electric dipole sources and this is the opposite of that which obtains when the dipoles are located in free space above the Earth. In the case of zero frequency (dc) the Sommerfeld integrals simplify greatly, enabling the Hertz vectors to be evaluated analytically. This results in series expansion formulas for the fields which produces much faster algorithms than those needed for numerical integration. The effects on subsurface to subsurface propagation of perturbations in sea level such as those produced by long-wavelength gravity waves have also been examined. Finally, an estimate has been made of the natural ELF noise in the sea due to Schumann resonances in the Earth-ionosphere duct.

ACKNLOWLEDGEMENTS

The work described here has been supported by the U.K Defence Research Agency, Maritime Division, Portland, UK.

REFERENCES

[1] Sommerfeld A.N., *Partial Differential Equations in Physics*, Academic Press, New York, 1949

[2] Wait J.R., "The magnetic dipole over a horizontal stratified earth", Can. J. Phys., **29**, 577-592, 1951

See Also Wait J.R. *Geo-Electromagnetism*, Academic Press, New York, 1982

[3] Weaver J.T., "The quasi-static field of an electric dipole embedded in a two-layer conducting half space", Can. J. Phys.,**45**, 1981-2002, 1967

[4] Seigel M. and King R.W.P., "Electromagnetic fields in a dissipative half-space: a numerical approach", J. Appl. Phys., **41**, 2415-2423, 1970

[5] Bannister P.R. "New Simplified Formulas for ELF Subsurface-to-Subsurface Propagation", IEEE J. Oceanic Eng., **OE-9**, 154-163, 1984

[6] Bannister P.R. "Applications of complex image theory", Radio Sci., **21**, 605-616, 1986

[7] Wait J.R. "The electromagnetic fields of a horizontal dipole antenna in the presence of a conducting half-space", Can. J. Phys., **39**, 1017-1028, 1961

[8] Lindell I.V. and Alanen E. "Exact Image Theory for the Sommerfeld Half-Space Problem, Part I: Vertical Magnetic Dipole", IEEE T-AP, **AP 32**, 126-133, 1984

[9] Lindell I.V. and Alanen E. "Exact Image Theory for the Sommerfeld Half-Space Problem, Part II: Vertical Electric Dipole", IEEE T-AP, **AP 32**, 841-847, 1984

[10] Lindell I.V. and Alanen E. "Exact Image Theory for the Sommerfeld Half-Space Problem, Part III: General Formulation", IEEE T-AP, **AP 32**, 1027-1032, 1984

[11] Wait J.R. "Radiation from a vertical dipole over a stratified ground", Trans. I.R.E., **AP-2**, 144-146, 1954

[12] Wait J.R. *Electromagnetic Waves in Stratified Media*, Pergammon Press, London, (1st Ed.) 1962 or (2nd Ed.) 1972

[13] Fraser-Smith A.C., Inan A.S., Villard O.G. Jr, and Joiner R.G., "Seabed propagation of ULF/ELF electromagnetic fields from harmonic dipole sources", Radio Sci., **23**, 931-944, 1988

[14] Llanwyn Jones D. and Burke C.P. " Recipes for computing the DC Field components of the HED and the VED in a three-layer stratified medium", Technical Report RP920617, King's College, London, 1992

[15] Burke C.P. and Llanwyn Jones D. "An experimental investigation of ELF attenuation rates in the Earth-ionosphere duct", J. Atmos. Terr. Phys., **54**, pp243-250, 1992

Discussion

ALPERT
COMMENT. Please give me all the lines of the Schumann resonances, recorded in you experiments.

AUTHOR'S REPLY
We observed resonances up to the seventh or eight Schumann resonance mode. The frequencies of these varied with time of day and season to a small degree. I do not have the values with me but I shall send them to you later.

TACCONI
COMMENT. In the shallow water ELF propagation cone did you consider the sub-bottom contribution?

AUTHOR'S REPLY
In our computational models we have models of two and three layered sea beds. For the sediment layer a conductivity of 4 Sm^{-1} seems appropriate followed by a layer of conductivity of about 10^{-2} or 10^{-3} Sm^{-1} but there are no reliable estimates of the depth of the first sea-bed layer (the sediment).

Comparative study of undersea fields produced by various dipoles

G. ANNAERT, A. BAREL
Free University of Brussels, VUB Dept. ELEC,
Pleinlaan 2
B - 1050 Brussels
Belgium

1. The Abstract.

ELF/VLF/LF- radiation by electric or magnetic dipoles located above or on the surface of the earth or sea is investigated from the exact Sommerfeld potentials. Due to the nonzero conducticvity of the ground or sea water, the waves are strongly attenuated and only a small near field can be effectively used for communication in a low frequency range. The Fresnel coefficient approximation technique, which presumes a planar plane wave propagation, is correct in the far-field but looses great accuracy in a region close to the radiatior. It is the purpose of this paper to review the electromagnetic propagation in layered media based on the rigorous spectral domain method. This theory expresses the Hertz potentials, either of the magnetic type *A* or the electric type *F*, in terms of Sommerfeld integrals. A communication range, as the maximum depth at which satisfactory signal reception is still possible, is derived in function of ground parameters, frequency and dipole orientation.

2. Introduction.

The prediction of the electromagnetic field generated by a dipole near the interface of electrically different regions is important in radio communication. The presence of the boundary makes the field very different from that of the same dipole in free air or above a perfectly conducting half-space. Due to the non-zero conductivity of the earth or sea, only very large wavelengths are usefull since the attenuation factor limits the maximum depth of possible signal reception in the lossy medium. The antennas are electrically small and can be treated as electric dipoles (wire antennas) or magnetic dipoles (loop antennas).

Very often, the waves are treated as planar TE and TM waves. The reflection and transmission waves are calculated using the Fresnel coefficients for optical beams [1]. Although this approach is simple and gives much insight in the distortion due to the interface, it is a wrong representation when the observer is near the interface.

The half-space problem has being solved analytically by Sommerfeld [2]. His work was the fundamental basis for further studies of dipole radiation in stratified media by Wait [3] and Kong [4]. Recently, Mosig [5] reviewed the computation of EM-fields in stratified media using the spectral domain transformation method (SDTM). He intensely applied the method to microstrip antennas [6]. The SDTM method results in Fourier-Bessel integral expressions for the electric and magnetic potentials. These integrals however can't be solved analytically and it is still a challenging task to develop an efficient algorithm for numerical integration. A variety of methods exists for the evaluation of these integrals, but most of them fail when both source and observer are close, in terms of wavelengths, to the interface. The most famous and efficient technique up to now which gives an accurate solution is undoubtedly the steepest descent path (SDP)-method [7], [8]. We have adapted this method so that it can be used even when observer and source are in different media.

In next, the spectral domain technique will be explained and applied to the Maxwell equations to arrive at exact solutions for the electric and magnetic vector potentials. The SDP-method is used to calculate the integrals and a comparison with published far-field patterns derived from the Fresnel approximation is made. Further, our method has been applied to calculate the maximum communication range in the sea in terms of frequency and dipole orientation.

3. The method.

3.1 Spectral Domain Transformation.

Computation of the electric and magnetic field in a layered medium is efficiently achieved via a spectral domain transformation method where the transverse Cartesian coordinates x and y are replaced by their spectral counterparts k_x and k_y according to the double Fourier transform

$$\tilde{f}(k_x,k_y,z) = \frac{1}{2\pi}\int_{-\infty}^{\infty}\int_{-\infty}^{\infty} f(x,y,z)e^{-jk_x x}e^{-jk_y y}dxdy \tag{1}$$

$$f(x,y,z) = \frac{1}{2\pi}\int_{-\infty}^{\infty}\int_{-\infty}^{\infty} \tilde{f}(k_x,k_y,z)e^{jk_x x}e^{jk_y y}dk_x dk_y \tag{2}$$

Useful transform operators from the cartesian to the spectral domain are given by

$$\frac{\partial f}{\partial x} \rightarrow jk_x\tilde{f} \tag{3}$$

$$\frac{\partial}{\partial y}f \rightarrow jk_y\tilde{f} \tag{4}$$

$$\frac{\partial}{\partial z}f \rightarrow \dot{\tilde{f}} \tag{5}$$

The 'del' operator ∇ becomes, in the spectral domain

$$\tilde{\nabla} = j\boldsymbol{k}_\rho + \boldsymbol{e}_z\frac{\partial}{\partial_z} \tag{6}$$

where k_ρ is the radial spectral variable defined as

$$\boldsymbol{k}_\rho = \boldsymbol{e}_x k_x + \boldsymbol{e}_y k_y \tag{7}$$

After introducing the Bessel function of the first kind and zero order J_0, we can express eq. (1) and (2) as

$$\begin{aligned}\tilde{f}(k_\rho,z) &= \int_0^\infty J_0(k_\rho\rho)f(\rho,z)\rho d\rho \\ f(\rho,z) &= \int_0^\infty J_0(k_\rho\rho)\tilde{f}(k_\rho,z)k_\rho dk_\rho\end{aligned} \tag{8}$$

with

$$\begin{aligned}k_\rho &= \sqrt{k_x^2+k_y^2} \\ \rho &= \sqrt{x^2+y^2}\end{aligned} \tag{9}$$

If $\tilde{f}(k_\rho)$ is the transform of $f(\rho)$, then the first order derivative of $f(\rho)$ with respect to $i = x,y$ can be written as

$$\begin{aligned}\frac{\partial f}{\partial i} &= -\left(\frac{\partial}{\partial i}\rho\right)\left(\int_0^\infty J_1(k_\rho\rho)\tilde{f}(k_\rho)k_\rho^2 dk_\rho\right) \\ &= \int_0^\infty J_0(k_\rho\rho)jk_i\tilde{f}(k_\rho)k_\rho dk_\rho\end{aligned} \tag{10}$$

The second order derivative with respect to $i,j = x,y$ is given by

$$\begin{aligned}\frac{\partial^2 f}{\partial i\partial j} &= -\left(\frac{\partial}{\partial i}\rho\right)\left(\frac{\partial}{\partial j}\rho\right)\left(\int_0^\infty \left(-k_\rho J_2(k_\rho\rho)+\frac{1}{\rho}J_1(k_\rho\rho)\right)\tilde{f}(k_\rho)k_\rho^2 dk_\rho\right) \\ &= \int_0^\infty J_0(k_\rho\rho)jk_i jk_j\tilde{f}(k_\rho)k_\rho dk_\rho\end{aligned} \tag{11}$$

Suppose a function ψ satisfies the homogeneous Helmholtz equation

$$(\nabla^2+k^2)\psi(r) = 0 \tag{12}$$

with k the complex propagation constant in the lossy medium, expressed by

$$k = \omega\sqrt{\mu\varepsilon} \tag{13}$$

Then, the spectral transform of ψ is a solution of

$$\left(\frac{d^2}{dz^2}-u^2\right)\tilde{\psi}(k_\rho,z) = 0 \tag{14}$$

where the parameter u stands for

$$u^2 = k_\rho^2 - k^2 \tag{15}$$

The general solution of eq.(14) is given by:

$$\tilde{\psi}(k_\rho,z) = A(k_\rho)\cosh(uz) + B(k_\rho)\sinh(uz) \tag{16}$$

It follows from Maxwell's equations that the components of the electric and magnetic fields, (E_x,E_y,E_z) and (H_x,H_y,H_z), can be associated with the quantity ψ.

For a layered medium, we can only use the normal components E_z and H_z as potentials.

The transverse components are given in the spectral domain by

$$k_\rho^2\tilde{E}_x = jk_x\dot{\tilde{E}}_z + \omega\mu k_y\tilde{H}_z \tag{17}$$

$$k_\rho^2\tilde{H}_x = jk_x\dot{\tilde{H}}_z - \omega\varepsilon k_y\tilde{E}_z \tag{18}$$

$$k_\rho^2\tilde{E}_y = jk_y\dot{\tilde{E}}_z + \omega\mu k_x\tilde{H}_z \tag{19}$$

$$k_\rho^2\tilde{H}_y = jk_y\dot{\tilde{H}}_z - \omega\varepsilon k_x\tilde{E}_z \tag{20}$$

3.2 Boundary conditions.

Next, consider the problem of fig. 1 where we want to express the fields in layers i and $i+1$. Each layer has its own relative permittivity

$\varepsilon_i = \varepsilon'_i - j\frac{\sigma_i}{\omega\varepsilon_0}$ and relative permeability μ_i.

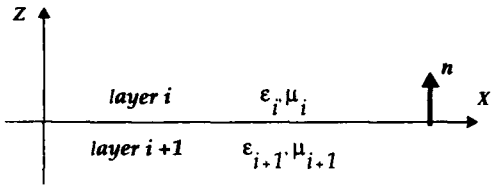

Fig. 1 The half-space problem.

The boundary conditions impose the transverse components to be continuous, when no sources exist on the layers. This implies that at the interface between layer i and i+1 we must have

$$\begin{aligned} \boldsymbol{n}\times\boldsymbol{E}^i &= \boldsymbol{n}\times\boldsymbol{E}^{i+1} \\ \boldsymbol{n}\bullet\varepsilon_i\boldsymbol{E}^i &= \boldsymbol{n}\bullet\varepsilon_{i+1}\boldsymbol{E}^{i+1} \\ \boldsymbol{n}\times\boldsymbol{H}^i &= \boldsymbol{n}\times\boldsymbol{H}^{i+1} \\ \boldsymbol{n}\bullet\mu_i\boldsymbol{H}^i &= \boldsymbol{n}\bullet\mu_{i+1}\boldsymbol{H}^{i+1} \end{aligned} \tag{21}$$

with $\boldsymbol{n}$ the normal vector to the boundary.

In what follows, the tilde (~) denoting a spectral quantity will be dropped. The type of a given quantity is clearly determined by the nature of its mathematical expression and by the context. Working out (21), we derive

$$\begin{aligned} \varepsilon^i E_z^i &= \varepsilon^{i+1}E_z^{i+1} \\ \dot{E}_z^i &= \dot{E}_z^{i+1} \\ \mu^i H_z^i &= \mu^{i+1}H_z^{i+1} \\ \dot{H}_z^i &= \dot{H}_z^{i+1} \end{aligned} \tag{22}$$

Eq. (22) remains valid with the field components expressed in the spectral domain. From (22) we conclude that in the case of planar boundaries E_z and H_z are uncoupled.

3.3 Relations between the magnetic and electric vector potentials *A* and *F* and the z-components of the 2D fields *E* and *H*.

The magnetic (*A*) and electric (*F*) vector potentials are mathematical tools in obtaining solutions for the electric (*E*) and magnetic (*H*) fields. The *A*- and the *F*- potentials present the electric and magnetic current sources respectively.

The relations between $\boldsymbol{E}, \boldsymbol{H}$ and $\boldsymbol{A}, \boldsymbol{F}$ are given by

$$\begin{aligned} \boldsymbol{E} &= -j\omega\boldsymbol{A} + \frac{j}{\omega\mu\varepsilon}\nabla(\nabla\bullet\boldsymbol{A}) - \frac{1}{\varepsilon}\nabla\times\boldsymbol{F} \\ \boldsymbol{H} &= -j\omega\boldsymbol{F} + \frac{j}{\omega\mu\varepsilon}\nabla(\nabla\bullet\boldsymbol{F}) + \frac{1}{\mu}\nabla\times\boldsymbol{A} \end{aligned} \tag{23}$$

3.3.1 The *A*- potential when $F = 0$.

In the two-dimensional case, as depicted in fig. 1, the *A*-potential consists of 2 components A_x and A_z, derived as follows:

$$\mu\boldsymbol{H} = \nabla\times\boldsymbol{A} = \mathbf{1}_x jk_y A_z - \mathbf{1}_y(jk_x A_z - \dot{A}_x) - \mathbf{1}_z jk_y A_x \tag{24}$$

From (24), we obtain

$$A_x = \frac{\mu H_z}{-jk_y} \tag{25}$$

and

$$A_z = \frac{\mu H_x}{jk_y} \tag{26}$$

Using (18) and (26) we attain

$$k_\rho^2 A_z = \frac{\mu k_x}{k_y}\dot{H}_z + j\omega\varepsilon\mu E_z \tag{27}$$

3.3.2 The *F*- potential when $A = 0$.

Two components (F_x, F_z) of the *F*-potential are determined, viz:

$$\varepsilon\boldsymbol{E} = -\mathbf{1}_x(jk_y F_z) + \mathbf{1}_y(jk_x F_z - \dot{F}_x) + \mathbf{1}_z(jk_y F_x). \tag{28}$$

From (28) we obtain:

$$F_x = \frac{\varepsilon E_z}{jk_y} \tag{29}$$

and

$$F_z = \frac{-\varepsilon E_x}{jk_y} \tag{30}$$

Using (17) and (30) we obtain

$$k_\rho^2 F_z = -\varepsilon\frac{k_x}{k_y}\dot{E}_z + j\omega\varepsilon\mu H_z \tag{31}$$

4.0 Fields in layered media.

In this section we present solutions for the functions ψ_E and ψ_H, representing E_z and H_z respectively, where ψ satisfies the Helmholtz equation (14) in each layer. Once E_z and H_z are known, the other components are derived from (17) through (20). Note that in each layer ψ has the form of (16) and on the source-free planar boundary, between layers i and i+1, (22) must be satisfied.

We first introduce dyadics to represent Green's functions relating an arbitrarily oriented dipole to the fields and the vector potential that it creates, viz:

$$dM(r) = \bar{G}_M(r,r')\, I(r')\, dl' \tag{32}$$

with $M = E, H, A$ or F corresponding to the electric and magnetic field and the magnetic and electric vector potentials respectively. The Green dyadic $\bar{G}_M$ in the spatial domain is expressed by

$$\bar{G}_M = \sum_{s=x,y,z} \sum_{t=x,y,z} e_s G_M^{st} e_t \tag{33}$$

where G_M^{st} is the s- component of the quantity M at r due to the t-directed dipole at the source at r'. Note that the Green dyadic can either be expressed in the spectral or spatial domain.

4. 1 Field functions in a half-space layer with source inside.

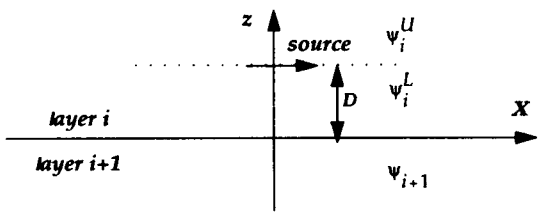

Fig. 2 A half-space layer with source inside, at height D.

In an unbounded medium, the source function, in the spectral domain, is of the form:

$$\psi_i = \begin{cases} U_i e^{-u_i(z-D)}, & z \geq D \\ L_i e^{u_i(z-D)}, & z \leq D \end{cases} \tag{34}$$

with U_i and L_i given in Tables 1 and 2 [9].

Table 1 *Electric dipoles.*

	G_H^{zx}	G_H^{zy}	G_E^{zx}	G_E^{zy}	G_E^{zz}	G_H^{zz}
U_i	$\frac{-jk_y}{4\pi u_i}$	$\frac{jk_x}{4\pi u_i}$	$\frac{-jk_x}{4\pi j\omega\varepsilon_i}$	$\frac{-jk_y}{4\pi j\omega\varepsilon_i}$	$\frac{k_\rho^2}{4\pi j\omega\varepsilon_i u_i}$	0
L_i	U_i	U_i	$-U_i$	$-U_i$	U_i	$-U_i$

Table 2 *Magnetic dipoles.*

	G_E^{zx}	G_E^{zy}	G_H^{zx}	G_H^{zy}	G_H^{zz}	G_E^{zz}
U_i	$\frac{jk_y}{4\pi u_i}$	$\frac{-jk_x}{4\pi u_i}$	$\frac{-jk_x}{4\pi j\omega\mu_i}$	$\frac{-jk_y}{4\pi j\omega\mu_i}$	$\frac{k_\rho^2}{\pi j\omega\mu_i u_i}$	0
L_i	U_i	U_i	$-U_i$	$-U_i$	U_i	U_i

With the planar boundary, we assume a solution of the form

$$\begin{aligned} \psi_i^U &= a^U \cosh u_i z + b^U \sinh u_i z,\ z \geq D \\ \psi_i^L &= a^L \cosh u_i z + b^L \sinh u_i z,\ 0 \leq z \leq D \end{aligned} \tag{35}$$

We then substract the source contributions from (35) to give

$$\begin{aligned} \psi'^U_i &= -U_i e^{-u_i(z-D)} + a^U \cosh u_i z + b^U \sinh u_i z,\ z \geq D \\ \psi'^L_i &= -L_i e^{u_i(z-D)} + a^L \cosh u_i z + b^L \sinh u_i z,\ 0 \leq z \leq D \end{aligned} \tag{36}$$

Now at $z = D$, (36) must satisfy the boundary conditions

$$\begin{aligned} \psi'^U_i &= \psi'^L_i \\ \dot{\psi}'^U_i &= \dot{\psi}'^L_i \end{aligned} \tag{37}$$

So

$$\begin{pmatrix} a^U \\ b^U \end{pmatrix} = \begin{pmatrix} a^L \\ b^L \end{pmatrix} + \begin{pmatrix} -L_i e^{-u_i D} + U_i e^{u_i D} \\ -L_i e^{-u_i D} - U_i e^{u_i D} \end{pmatrix} \tag{38}$$

and $b^U = -a^U$ due to the radiation condition at infinity.

As an example, we derive the function for the z-component of the magnetic field of a HED (Horizontal Electric Dipole) in a half-space bounded by a curve. From Table (1) and eq. (38), we obtain:

$$\begin{bmatrix} a^U \\ -a^U \end{bmatrix} = \begin{bmatrix} a^L \\ b^L \end{bmatrix} + \begin{bmatrix} \frac{-jk_y}{2\pi u_i}\sinh u_i D \\ \frac{jk_y}{2\pi u_i}\cosh u_i D \end{bmatrix} \tag{39}$$

giving

$$b^L = -a^L - \frac{jk_y}{2\pi u_i} e^{-u_i D} \tag{40}$$

and

$$\begin{aligned} \psi_H^{zx} &= a^L e^{-u_1 z} - \frac{jk_y}{2\pi u_i}\sinh u_i z e^{-u_i D}, \quad 0 \le z \le D \\ \psi_H^{zx} &= \left(a^L - \frac{jk_y}{2\pi u_i}\sinh u_i D\right) e^{-u_1 z}, \quad z \ge D \end{aligned} \tag{41}$$

4.2 Field components of a dipole above a planar boundary between two media.

In the following, the different field components of a dipole above a planar interface of two media, as depicted in Fig. 3, are determined. We assume, with no loss of generality, that the relative permeability of both media and the relative permittivity of the upper medium are, each, equal to unity.

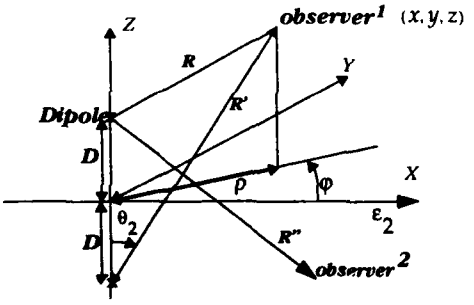

Fig. 3 A dipole source, at height D, in the upper half-space layer separated from the lower half-space layer by a planar interface. The relative permeability of both layers and the relative permittivity of the upper medium are,each, equal to unity.

4.2.1 Arbitrarily oriented electric dipole.

The arbitrarily oriented dipole in the XZ-plane can be decomposed into two components: a vertical component and a horizontal component. Suppose the orientation of the dipole makes an angle ϕ with the X-axis. Then from Table 1 and eq.(38), we have for the electric field

$$\begin{aligned} \psi_E^1 &= a_1^E e^{-u_1 z} + (\cos\phi)\frac{jk_x e^{-u_1 D}}{2\pi j\omega}\sinh u_1 z \\ &\quad + (\sin\phi)\frac{k_\rho^2 e^{-u_1 D}}{2\pi j\omega u_1}\sinh u_1 z \\ \psi_E^2 &= a_2^E e^{u_2 z} \end{aligned} \tag{42}$$

and for the magnetic field

$$\begin{aligned} \psi_H^1 &= a_1^H e^{-u_1 z} + (\cos\phi)\frac{-jk_y e^{-u_1 D}}{2\pi u_1}\sinh u_1 z \\ \psi_H^2 &= a_2^H e^{u_2 z} \end{aligned} \tag{43}$$

Expressing the boundary conditions (22) with the aid of (42) and (43) results in the following equations for the parameters a_1^E, a_2^E, a_1^H and a_2^H

$$\begin{aligned} a_1^E &= \frac{\varepsilon_2 e^{-u_1 D}\left(jk_x u_1\cos\phi + k_\rho^2\sin\phi\right)}{2\pi j\omega(u_1\varepsilon_2 + u_2)} \\ a_2^E &= \frac{e^{-u_1 D}\left(jk_x u_1\cos\phi + k_\rho^2\sin\phi\right)}{2\pi j\omega(u_1\varepsilon_2 + u_2)} \\ a_1^H &= \frac{-jk_y e^{-u_1 D}}{2\pi(u_1 + u_2)}\cos\phi \\ a_2^H &= \frac{-jk_y e^{-u_1 D}}{2\pi(u_1 + u_2)}\cos\phi \end{aligned} \tag{44}$$

which when substituted into (42), and (43) give E_z and H_z in each layer. On the other hand, E_x, E_y, H_x and H_y are found from (17) through (20). Then using the transformation from the spectral to the spatial domain, defined in (8), (10), and (11), results in the spatial components of $\boldsymbol{E}$ and $\boldsymbol{H}$.

A more elegant way to find the spatial components of $\boldsymbol{E}$ and $\boldsymbol{H}$ is by using the magnetic vector potential $\boldsymbol{A}$ since for the electric dipole, $\boldsymbol{F} = 0$.

From (25), (27), (42), (43), and (44) we derive the expressions for the spectral components of the *A*- potential. Using the transformation equations (8) and (10) results in the spatial components given by

$$A_x^1 = \frac{\mu_0\cos\phi}{2\pi}\int_0^\infty J_0 k_\rho\rho \frac{e^{-u_1(D+z)}}{u_1+u_2}k_\rho dk_\rho + \frac{\mu_0\cos\phi}{4\pi}\left(\frac{e^{-jkR}}{R}-\frac{e^{-jkR'}}{R'}\right) \tag{45}$$

$$A_z^1 = -\frac{\mu_0\cos\phi}{2\pi k^2}\left(\frac{\partial\rho}{\partial x}\right)\int_0^\infty J_1(k_\rho\rho)\frac{e^{-u_1(D+z)}}{u_1\varepsilon_2+u_2}(u_1-u_2)k_\rho^2 dk_\rho + \frac{\mu_0\sin\phi}{2\pi}\int_0^\infty J_0(k_\rho\rho)\frac{e^{-u_1(D+z)}}{u_1\varepsilon_2+u_2}\varepsilon_2 k_\rho dk_\rho + \frac{\mu_0\sin\phi}{4\pi}\left(\frac{e^{-jkR}}{R}-\frac{e^{-jkR'}}{R'}\right) \tag{46}$$

$$A_x^2 = \frac{\mu_0\cos\phi}{2\pi\varepsilon_2}\int_0^\infty J_0(k_\rho\rho)\frac{e^{-u_1D+u_2z}}{u_1+u_2}k_\rho dk_\rho \tag{47}$$

$$A_z^2 = -\frac{\mu_0\cos\phi}{2\pi\varepsilon_2 k^2}\left(\frac{\partial\rho}{\partial x}\right)\int_0^\infty J_1(k_\rho\rho)\frac{e^{-u_1D+u_2z}}{u_1\varepsilon_2+u_2}(u_1-u_2)k_\rho^2 dk_\rho + \frac{\mu_0\sin\phi}{2\pi}\int_0^\infty J_0(k_\rho\rho)\frac{e^{-u_1D+u_2z}}{u_1\varepsilon_2+u_2}k_\rho dk_\rho \tag{48}$$

By making use of (23), one gets the spatial components of ***E*** and ***H***.

4.2.2 Magnetic Dipole.

For the arbitrarily oriented magnetic dipole making an angle ϕ with the x-direction, we obtain from Table 2 and eq. (38) for the magnetic field

$$\psi_H^1 = a_1^H e^{-u_1 z} + (\cos\phi)\frac{jk_x e^{-u_1 D}\sinh u_1 z}{2\pi j\omega} + (\sin\phi)\frac{k_\rho^2 e^{-u_1 D}\sinh u_1 z}{2\pi j\omega u_1} \tag{49}$$

$$\psi_H^2 = a_2^H e^{u_2 z}$$

and for the electric field

$$\psi_E^1 = a_1^E e^{-u_1 z} + (\cos\phi)\frac{jk_y e^{-u_1 D}\sinh u_1 z}{2\pi u_1} \tag{50}$$

$$\psi_E^2 = a_2^E e^{u_2 z}$$

Invoking the boundary conditions (22) enables us to define a_1^E, a_2^E, a_1^H, and a_2^H.

$$a_1^E = \frac{\varepsilon_2 e^{-u_1 D}}{2\pi(u_1\varepsilon_2+u_2)}jk_y\cos\phi$$

$$a_2^E = \frac{e^{-u_1 D}}{2\pi(u_1\varepsilon_2+u_2)}jk_y\cos\phi \tag{51}$$

$$a_1^H = \frac{e^{-u_1 D}\left(jk_x u_1\cos\phi + k_\rho^2\sin\phi\right)}{2\pi j\omega(u_1+u_2)}$$

$$a_2^H = \frac{e^{-u_1 D}\left(jk_x u_1\cos\phi + k_\rho^2\sin\phi\right)}{2\pi j\omega(u_1+u_2)}$$

From (29), (31), (49), (50), and (51) we derive the expressions for the spectral components of the *F*- potential. Using the transformation equations (8) and (10) results in the spatial components given by

$$F_x^1 = \frac{\varepsilon_2\cos\phi}{2\pi}\int_0^\infty J_0 k_\rho\rho\frac{e^{-u_1(D+z)}}{u_1\varepsilon_2+u_2}k_\rho dk_\rho + \frac{\cos\phi}{4\pi}\left(\frac{e^{-jkR}}{R}-\frac{e^{-jkR'}}{R'}\right) \tag{52}$$

$$F_z^1 = -\frac{\cos\phi}{2\pi k^2}\left(\frac{\partial\rho}{\partial x}\right)\int_0^\infty J_1(k_\rho\rho)\frac{e^{-u_1(D+z)}}{u_1\varepsilon_2+u_2}(u_1-u_2)k_\rho^2 dk_\rho + \frac{\sin\phi}{2\pi}\int_0^\infty J_0(k_\rho\rho)\frac{e^{-u_1(D+z)}}{u_1+u_2}k_\rho dk_\rho + \frac{\sin\phi}{4\pi}\left(\frac{e^{-jkR}}{R}-\frac{e^{-jkR'}}{R'}\right) \tag{53}$$

$$F_x^2 = \frac{\cos\phi}{2\pi}\int_0^\infty J_0(k_\rho\rho)\frac{e^{-u_1D+u_2z}}{u_1\varepsilon_2+u_2}k_\rho dk_\rho \tag{54}$$

$$F_z^2 = -\frac{\cos\phi}{2\pi k^2}\left(\frac{\partial\rho}{\partial x}\right)\int_0^\infty J_1(k_\rho\rho)\frac{e^{-u_1D+u_2z}}{u_1\varepsilon_2+u_2}(u_1-u_2)k_\rho^2 dk_\rho + \frac{\sin\phi}{2\pi}\int_0^\infty J_0(k_\rho\rho)\frac{e^{-u_1D+u_2z}}{u_1+u_2}k_\rho dk_\rho \tag{55}$$

By making use of (23), one gets the spatial components of ***E*** and ***H***.

4.3. Sommerfeld Integrals.

The integrals appearing in the expressions for the spatial components of the *A*- and *F*- potentials are due to the transformation equations (8), (10), and (11) which are known as Sommerfeld Integrals (SI) . In general, a SI can be written as

$$SI = \int_{-\infty}^{\infty} H_m(k_\rho\rho)h(k_\rho)dk_\rho = 2\int_0^\infty J_m(k_\rho\rho)h(k_\rho)dk_\rho \tag{56}$$

with H_m and J_m the Hankel and Bessel functions of the first kind and order m respectively.

A number of different techniques can be found in the literature to solve a SI . The Steepest Descent Path (SDP)Method first introduced by Parhami et al.[7] and thereafter improved by Michalski [8] is one of the most powerful tech-

niques as long as the source and observer both are away from the interface.

In ref. [8], the SDP method is explained when source and observer are in the upper halfspace. When the observer lies in medium 2, fig. 4, following changes should be made according to the notation of [8].

$$u_2 z - u_1 D = (u_2 - u_1) z - jkr_2 \cos\theta_2 \cos\xi \qquad (57)$$

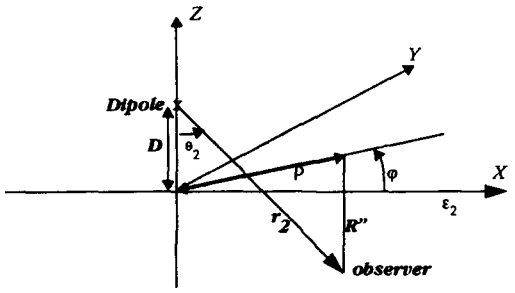

Fig. 4

However, for very small distances of source and observer away from the interface (<1e-4 λ), $h(k_\rho)$ has a very weak exponential decaying and the SDP-method fails. In that case, an improved method based on decomposing part of the integrand in Chebyshev polynomials has been developped [10].

4.4 Fresnel Reflection Coefficient Approximation.

In this part, a "far-field"-approximation for the fields on the boundary is used. It assumes that E and H are perpendicular to each other and $E \times H$ gives us the propagation direction of the plane-wave. A comparison with the rigorous spectral domain theory will be given further in the numerical results.

For the electric dipole the following expressions for the A-potental in terms of the Fresnel plane-wave reflection coefficient [1], [9] are derived.

$$\begin{aligned}
A_x^1 &= \frac{\mu_0 e^{-jkR}}{4\pi R} + \frac{\mu_0}{4\pi}\cos\phi R_{TE}\frac{e^{-jkR'}}{R'} \\
A_z^1 &= \frac{\mu_0 e^{-jkR}}{4\pi R} + \frac{\mu_0}{4\pi}\sin\phi R_{TM}\frac{e^{-jkR'}}{R'} + \frac{\mu_0}{4\pi}\cos\phi R_{TM}\frac{e^{-jkR'}}{R'} \\
A_x^2 &= \frac{\mu_0}{4\pi}\cos\phi T_{TE}\frac{e^{-jkR''}}{R''} \\
A_z^2 &= \frac{\mu_0}{4\pi}\sin\phi T_{TM}\frac{e^{-jkR''}}{R''} + \frac{\mu_0}{4\pi}\cos\phi T_{TM}\frac{e^{-jkR''}}{R''}
\end{aligned} \qquad (58)$$

with

$$\begin{aligned}
R_{TM} &= \frac{\cos\theta_i - Z_g\sqrt{1 - Z_g^2(\sin\theta_i)^2}}{\cos\theta_i + Z_g\sqrt{1 - Z_g^2(\sin\theta_i)^2}} \\
T_{TM} &= \frac{2Z_g\cos\theta_i}{\cos\theta_i + Z_g\sqrt{1 - Z_g^2(\sin\theta_i)^2}} \\
R_{TE} &= \frac{\cos\theta_i - \frac{1}{Z_g}\sqrt{1 - Z_g^2(\sin\theta_i)^2}}{\cos\theta_i + \frac{1}{Z_g}\sqrt{1 - Z_g^2(\sin\theta_i)^2}} \\
T_{TE} &= \frac{2\cos\theta_i}{\cos\theta_i + \frac{1}{Z_g}\sqrt{1 - Z_g^2(\sin\theta_i)^2}} \\
Z_g &= \frac{1}{\sqrt{\varepsilon_2}}
\end{aligned} \qquad (59)$$

and θ_i is the angle of incidence with respect to the surface normal defined by a line from the image point to the observation point.

For a VED, only a TM wave exists while a HED excites both TE and TM waves.

The transmission angle θ_t is related to the incident angle θ_i regarding to Snell's law of refraction

$$k_1 \sin\theta_i = k_2 \sin\theta_t \qquad (60)$$

If k_2 is complex, no radiation in the lossy medium 2 is possible.

If k_2 is real, radiation takes place at an angle

$$\theta_t = arc\sin(Z_g \sin\theta_i) \qquad (61)$$

So the transmitted wave angle is limited to

$$0 \le \theta_t \le \theta_c = arc\sin Z_g \qquad (62)$$

For the magnetic dipole, the F-potental in terms of the Fresnel plane-wave reflection coefficient becomes

$$\begin{aligned}
F_x^1 &= \frac{1}{4\pi}\frac{e^{-jkR}}{R} + \frac{1}{4\pi}R_{TM}\frac{e^{-jkR'}}{R'} \\
F_z^1 &= \frac{1}{4\pi}\frac{e^{-jkR}}{R} + \frac{1}{4\pi}\sin\phi R_{TE}\frac{e^{-jkR'}}{R'} + \frac{1}{4\pi}\cos\phi R_{TE}\frac{e^{-jkR'}}{R'} \\
F_x^2 &= \frac{1}{4\pi}T_{TM}\frac{e^{-jkR''}}{R''} \\
F_z^2 &= \frac{1}{4\pi}\sin\phi T_{TE}\frac{e^{-jkR''}}{R''} + \frac{1}{4\pi}\cos\phi T_{TE}\frac{e^{-jkR''}}{R''}
\end{aligned} \qquad (63)$$

5. Results.

In fig.5, a far-field pattern above the interface is compared using the Spectral Domain technique and the Fresnel Reflection approach. It is seen that the 'geometrical optics' field is a valid representation for the far field.

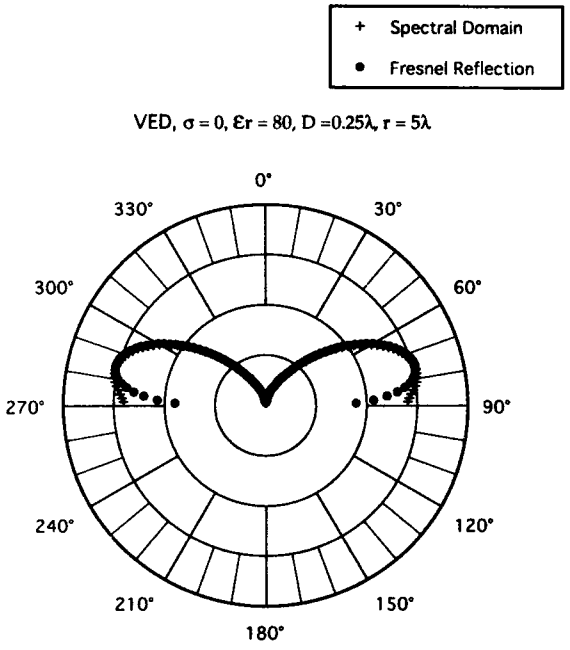

Fig. 6 shows a HED field pattern from the spectral domain technique in a lossless ground for two values of ε_r (ε_r = 80, 10). The improvement of the directivity with increasing ε_r is a general tendency, which is independent of the dipole kind. This is in accordance with (62) where θ_c becomes smaller with increasing ε_r.

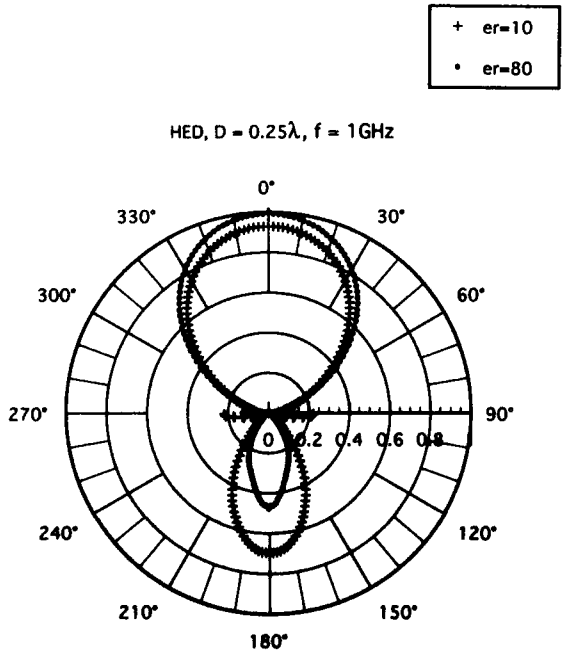

Fig. 7 shows normalised depth sensitivity profiles for the different dipole kinds in sea water (f = 1kHz, f = 10kHz).

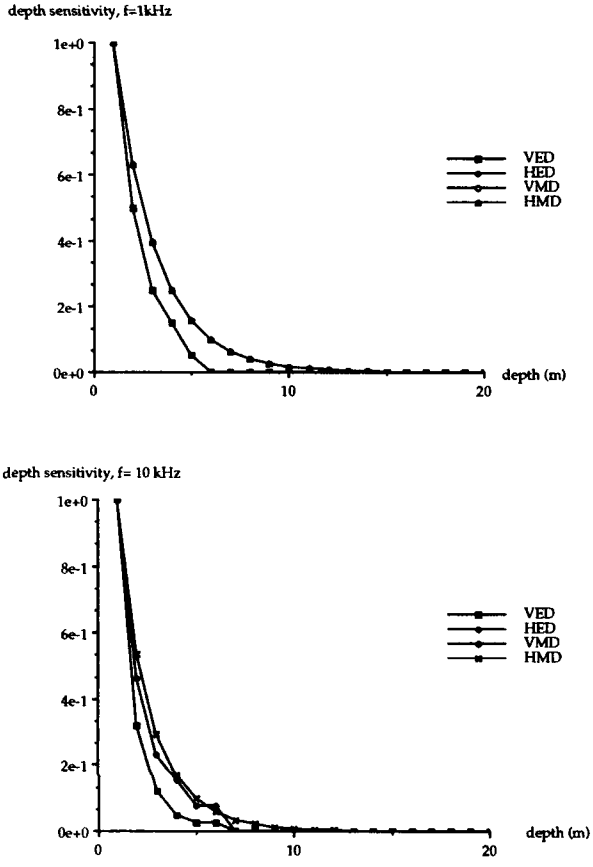

6. Conclusions.

Exact analytical formulations for the electromagnetic fields produced by electric and magnetic dipole sources above a curved interface of 2 media are derived. The method can also handle N layers with arbitrary boundaries.

In the spatial domain, the field components are written in a Sommerfeld integral formulation. Such integrals can efficiently be solved by means of the steepest descent path method which is fully described in the literature [11].

Simulation results of EM radiation in a layered medium with the above method and the extension to three-dimensional layers separated by arbitrary surfaces will be presented later.

References.

[1] G.S. Smith, "Directive Properties of Antennas for Transmission into a Material Half-Space", *IEEE Trans. on Antennas. and Propagat.*, vol AP-32, pp.232-246, 1984.

[2] A. Sommerfeld, Partial Differential Equations in Physics, Academic Press Inc., 1949, pp. 236-289.

[3] J.R. Wait, "Characteristics of antennas over lossy earth", in *Antenna Theory*, part 2, R.E. Collin and F.J. Zucker, Eds. New York Mc Graw Hill, 1969, pp. 386-435.

[4] J. A. Kong, "Electromagnetic fields due to dipole antennas over stratified anisotropic media", *Geophysics*, vol. 376, no. 6, 1972, pp. 985-996.

[5] J.R. Mosig, "Integral Equation Technique", in *Numerical Techniques for Microwave and Millimeter-Wave Passive Structures*, T. Itoh, John Wiley & Sons, 1989, pp. 133-213.

[6] J.R. Mosig, F.E. Gardiol, "Analytical & Numerical techniques in the Green's function treatment of microstrip antennas and scatterers", *IEE proc.*, vol. 130, pt. H, pp. 175-182, 1983.

[7] P. Parhami, Y. Rahmat-Samaii, and R. Mittra, "An efficient approach for evaluating Sommerfeld integrals encountered in the problem of a current element radiating over lossy ground", *IEEE Trans. on Antennas. and Propagat.*, vol. AP-28, 1980, pp. 100-104.

[8] K. A. Michalski, "On the efficient evaluation of integrals arising in the Sommerfeld halfspace problem", Proc IEE, vol. 132, pt. H, 1985, pp. 312-318.

[9] C. A. Balanis, *Advanced Engineering Electromagnetics*, John Wiley & Sons, 1989, Chapter 5, pp. 180-193.

[10] G. Annaert, "Evaluation of Sommerfeld integrals using Chebyshev Decomposition", in press by *IEEE Trans. on Antennas. and Propagat.*

Discussion

ALPERT

COMMENT. The used approximations of Zennech and even of the Sommefield integrals should be checked.

AUTHOR'S REPLY

The Zennech pole in our model is extracted via a pole extraction technique (following Michalski et al. ref. [8] of my paper).

A METHODOLOGY AND TOOL FOR THE PREDICTION OF DEPTH OF RECEPTION IN THE SEA FOR A VLF/LF COMMUNICATIONS SYSTEM

D M Nicholls

DRA, Portsdown,

Portsmouth, PO6 4AA, UK

SUMMARY

This paper describes a method of predicting the depth performance of a VLF/LF (Very Low Frequency/Low Frequency) communications system for submarine reception.

The method uses a Long Wave Propagation Capability program which includes parameters of the system to be considered, such as transmitter power, aerial and receiver sensitivities.

Results from analysis for a particular communications system are presented including an audio visual format to show the expected variations in depth performance with reference to operational frequency, transmitter power, time of day and year and the signal to noise requirements for the system.

The analysis method is flexible and could be adapted for similar communications systems.

LIST OF SYMBOLS

V_i	induced output voltage (V)
E_{sea}	electric field in the sea (V/m)
E_{air}	electric field in air (V/m)
he_{sea}	effective vertical height in the sea (m)
he_{air}	effective vertical height in air (m)
A	effective area (m^2)
λ	wavelength (m)
S/N_{air}	signal to noise ratio in air (dB)
S/N_{req}	signal to noise required (dB)
S_{min}	*minimum signal* (V)
f	frequency (Hz)
α	attenuation rate (dB/m)
ω	angular frequency (rad/s)
σ	conductivity of the sea (mho/m)
μ	permeability

1. INTRODUCTION

Aside from its stable propagation and resilience to exo-atmospheric nuclear disturbances, VLF and to a lesser extent LF, offers useful penetration of the sea due to the low attenuation rates in sea water.

The paper describes a method of analysis to calculate antenna depth and which gives coverage and depth profiles for VLF/LF in the North Atlantic. The predictions utilise the Long Wave Propagation Capability program (LWPC) supplied to DRA by NRAD.

A brief description of the mechanisms involved in propagation and reception at depth in the sea is given followed by a description of the parameters involved and the analysis procedure. Typical results are presented in this paper and in an audio visual format.

2. PROPAGATION THROUGH AIR SEA INTERFACE

As shown in Figure 1, long range VLF and LF transmissions are vertically polarised ie. a vertical electric field and a horizontal magnetic field which propagate via the earth-ionospheric waveguide. Due to the air/sea interface, energy is absorbed from the electric field resulting in it being tilted towards the interface with the absorbed energy giving an electric field along the interface which is approximately horizontal. The magnitude of this field will be reduced compared to that of the vertical electric field as a function of the conductivity of the medium. The magnetic field passes unaffected through the interface since the permeability of the sea is equal to that in air. The resultant propagation of these two horizontal fields is in the downward direction.

If we examine an underwater antenna comprising of a pair of suitably combined orthogonal loops to give omnidirectional reception and consider it as a magnetic antenna then its induced output voltage will be the same just above and just below the surface since the magnetic field is continuous across the interface.

Alternatively, if it is considered as an electric aerial then the induced voltage will be a function of the effective vertical height of the aerial and the electric field. The electric field above and below the surface are at approximately right angles and are different in magnitude but each must produce the same induced output voltage V_i where

$$V_i = E_{sea} \times he_{sea} = E_{air} \times he_{air}$$

and therefore the ratio of the effective heights must be inversely proportional to the ratio of the magnitude of the electric fields.

The propagation wavelength is a function of the conductivity of the medium and will decrease by the same ratio as the electric field decreases since the effective height of the aerial is

$$he = \frac{2\pi AN}{\lambda}$$

then

$$\frac{E_{sea}}{E_{air}} \alpha \frac{he_{air}}{he_{sea}} \alpha \frac{\lambda_{sea}}{\lambda_{air}}$$

To calculate the induced voltage for the aerial either above or immediately below the sea surface we can therefore consider the effective height of the aerial in air and its incident vertical electric field. As the aerial depth is increased the induced voltage will be attenuated at a fixed rate dependent upon the frequency and sea conductivity.

Atmospheric noise, produced by worldwide lightning activity, is the dominant source of noise at VLF and LF and limits the coverage achieved from VLF communication transmitters. Figure 2 shows a diagrammatic view of the relationship between signal to atmospheric noise ratio and depth in the sea. The magnitude of the components of signal and atmospheric noise, shown as S and N at the sea surface, will both be attenuated at the same rate as depth is increased. At point D1, the ratio of S/N will be unchanged but as the depth is increased further the noise of the submarine receive system will become a dominant factor and the ratio of S/N will reduce as shown. At point D2 for example the ratio of S/N is equal to that required to give a specific character error rate for the system, and at this point, the signal S will be the minimum signal required for reception S_{min}. Reception beyond this point will be degraded.

3. DEPTH CALCULATION

To calculate depth we need to determine:

i) S/N_{air} and E_{air}
The signal to noise ratio and the vertical electric field strength in air at the sea surface for any receiver location. These are calculated from the Long Wave Propagation Capability and are dependent upon the operational frequency, radiated power and location of the transmitter, time of day and year and required time availability of the communications link.

ii) S/N_{req}
The ratio of signal to noise required for reception for the system which will achieve a specified character error rate. This will depend upon the modulation scheme implemented. For this paper a range of signal to noise values are considered.

iii) S_{min}
The minimum signal level required by the system to meet the signal to noise requirements and which will be determined by the sensitivity of the system. For the system under consideration in this paper the receiving aerial itself determines the overall sensitivity of the system and is dependent on the operating frequency.

iv) he_{air}
The effective height of the aerial in air which will vary with frequency and is:

$$he_{air} = 0.15 \times f$$

v) α
The attenuation rate, in dB/m, in the sea which is dependent upon frequency and sea conductivity and is calculated from:

$$\alpha = \frac{8.686}{\sqrt{2/\omega\sigma\mu}}$$

For the purpose of the paper it is assumed that the sea conductivity is 4 mho/m

4. LWPC

LWPC is a series of computer programs, designed to run on a VAX system, which can be used to calculate the signal strength (vertical electric field strength), the signal to noise ratio and noise at the sea surface over any given area, given details such as operational frequency, radiated power and transmitter location, time of day and year.

Initially for any selected transmitter and operational frequency the electric field strength is calculated, using a waveguide mode model, at 501 points along a specified bearing from which a data file is created which normally contains results for multiple bearings.

There are two noise models incorporated in LWPC, the UT (Universal Time) numerical mapping coefficients of Zacharisen and Jones OT/ITS Report 2,1970 and the revised CCIR (International Radio Consultative Committee) coefficients of Spaulding and Washburn in NTIA Report 85-173,1985 either of which can be used to evaluate the atmospheric noise at each point along the bearing from which the S/N is calculated. A default condition which uses the CCIR model was implemented. Any required time availabilities for the communication link and the power of the transmitter are taken into account. Jammers and their effect on the Signal to Noise can also be incorporated.

The results of LWPC can be presented as plots of magnitude (programmes PLTSNR and PLTFMC) against range from the transmitter for a single bearing or contour maps (programme PLTOPA).
Further details of LWPC can be found in Reference 1. Discussion of various noise models can be found in Reference 2.

5. ANALYSIS

Depth is determined by amending and incorporating additional calculations and routines into PLTOPA and is renamed PLTDPT. A simplified flow chart for the analysis is shown below.

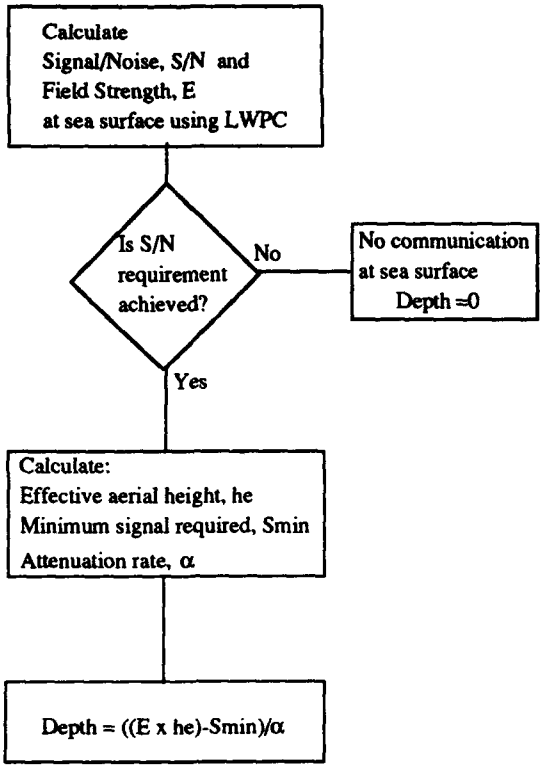

Analysis Flow Chart

Using PLTDPT, at each point along the bearing the Electric Field Strength and Signal/Noise at the sea surface is calculated. If the Signal/Noise does not meet the Signal/Noise required for reception then reception is not possible at this point and the depth of reception at that point is set to zero. However, if the Signal/Noise required for reception is met then the effective aerial height, the attenuation rate and the minimum signal required for reception are calculated. Depth is then calculated as a function of the "excess" signal, which is the difference between the signal at the sea surface and the minimum signal required, divided by the attenuation rate. Depth calculations are placed in a depth data file which has the same format as Signal and Signal/Noise files. The contour plotting functions of PLTOPA which remain in PLTDPT are then used with the depth data file to produce contour maps.

A further adaptation of the program which is called PLTDVAL creates a data file which contains depth values for the defined coverage area. This data file is transferred from the host VAX computer to a Macintosh PC. Using the Macintosh application WINGZ the depth data is read and formatted into a matrix, from which, depth profiles are produced. These profiles have been used to create an Audio Visual presentation of results.

6. RESULTS

A sample of typical results to show the effects of frequency, power, time of day, time of year, S/N requirement and time availability are presented in Figures 3 to 13. Each figure has the default conditions listed below unless specified otherwise.

a) Operational frequency of 16 KHz
b) Radiated power of 40KW
c) 99% Probability of reception
d) S/N requirement of -1.5dB in 1000 Hz BW
e) Reception at 1400 hrs GMT (Day) during July (Summer).

Figures are normally produced in colour but for this report have been reproduced in black and white.

Results are also presented in an audio visual format to show the effect of frequency, power, time of day, time of year, S/N requirement and time availability in much greater detail.

7. DISCUSSION

Figure 3 shows a contour plot produced by PLTDPT. It can be seen that the greatest depth of reception occurs at the location of the transmitter and that depth falls of as a function of range as would be expected. At the edge of reception, indicated as a solid line, depth falls off very sharply which is a typical feature of an atmospherically noise limited system. Three nulls can be seen to the east of the transmitter which are due to interaction between the modes propagating in the earth ionosphere waveguide.

Figure 4 is a depth profile produced using PLTDVAL and corresponds to Figure 3. The sharp fall of in depth of reception at the edge of the coverage area is clearly seen whereas the extent of the nulls are hidden by the perspective view. Depths of reception of greater than 9 metres can be expected over the coverage area.

Figures 5 and 6 show the results for operational frequencies of 51.95 and 81 kHz respectively. The coverage area reduces compared to Figure 4 as does the depth of reception due to higher attenuation rates in the waveguide and the sea. At 51.95 kHz the depth of reception at the edge of the coverage area is 3 metres and at 81 kHz is under 3 metres.

Figures 7 and 8 shows the results for radiated powers of 10 and 160 KW respectively. As would be expected reducing the power reduces the range of reception and for a point by point comparison reduces the depth of reception. Over the reduced coverage area a minimum depth of reception of 9 metres is maintained. Likewise increasing the power increases the range of reception and for a point by point comparison increases the depth of reception. Again a minimum depth of reception of 9 metres is maintained.

Figure 9 shows the result for 0200 hrs GMT (Night). It can be seen that when compared to Figure 4 the depth of reception is similar but there are additional nulls in the coverage. The nulls are due to the ionospheric height increasing at night and causing further interactions between the propagation modes.

Figure 10 shows the results for January (Winter). When compared to Figure 4 (Summer) it can be seen that the coverage area has reduced slightly due to variations in noise levels with the time of year. The noise model used in LWPC varies with season only.

Figures 11 and 12 show the results for S/N requirements of -6 and 6dB respectively. It can be seen that as the S/N requirement is increased to 6dB then the coverage and depth of reception (on a point to point comparison) reduces and the nulls become more pronounced. When the S/N requirement is reduced to -6dB the opposite occurs.

Figure 13 shows the results for a 50% time availability. When compared with Figure 4 it can be seen that the coverage has improved because the noise level has effectively been reduced since noise statistics are those for an exceedence level of 50%. Depth of reception, except that over the extended coverage area, remains unchanged since the signal on the sea surface is unchanged.

Plots have been drawn for a specified system. If aerial/receiver parameters are changed then the programs would have to be modified. The program assumes a sea conductivity of 4 mhos/m which is very generalised. The Arctic waters are likely to have a lower conductivity whilst for the Mediterranean areas it may be greater. The value of conductivity used in the program could be changed but it cannot take account of mixed sea paths.

CONCLUSIONS

Details of a method to predict the depth performance of a VLF system have been given. A representative series of results has been presented for a series of parameters which give a graphic indication of the typical depths of reception and coverage that can be expected.

The depth performance of other VLF/LF communication systems can be predicted.

The calculations are based on the LWPC and it will be the accuracy of that which will determine the overall accuracy of the predictions presented in terms of coverage and depth performance.

REFERENCES

1 NAVOCEANSYSCEN Long Wave Propagation Capability Program

2 DRA/MAR/TM (MCC) 91025, VLF Communication Environment for Future Submarines: Part 1 - Atmospheric Noise, Unclassified, G A Ashdown, September 1991.

ACKNOWLEDGEMENT

This work has been carried out with the support of Procurement Executive Ministry of Defence.

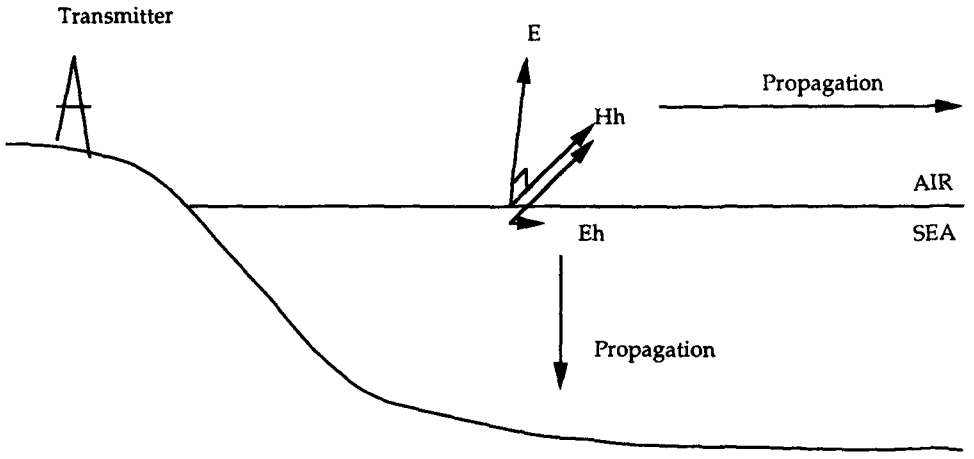

Figure 1 - Electric And Magnetic Fields At The Air Sea Interface

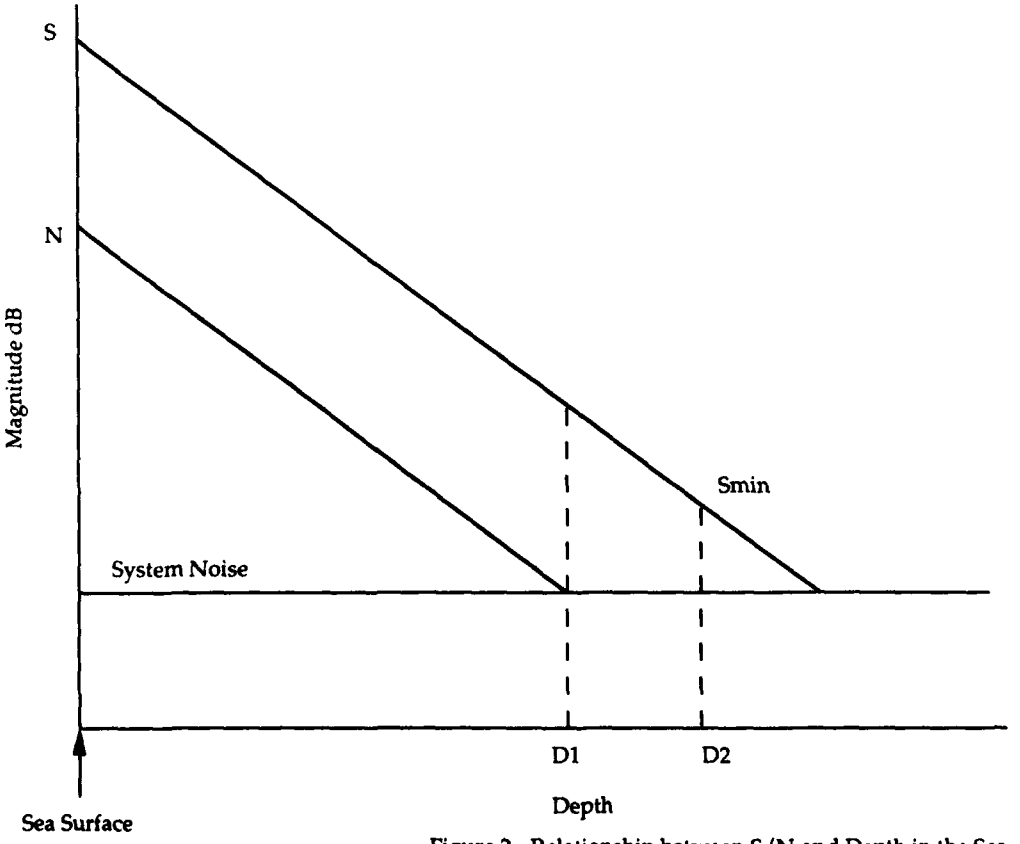

Figure 2 - Relationship between S/N and Depth in the Sea

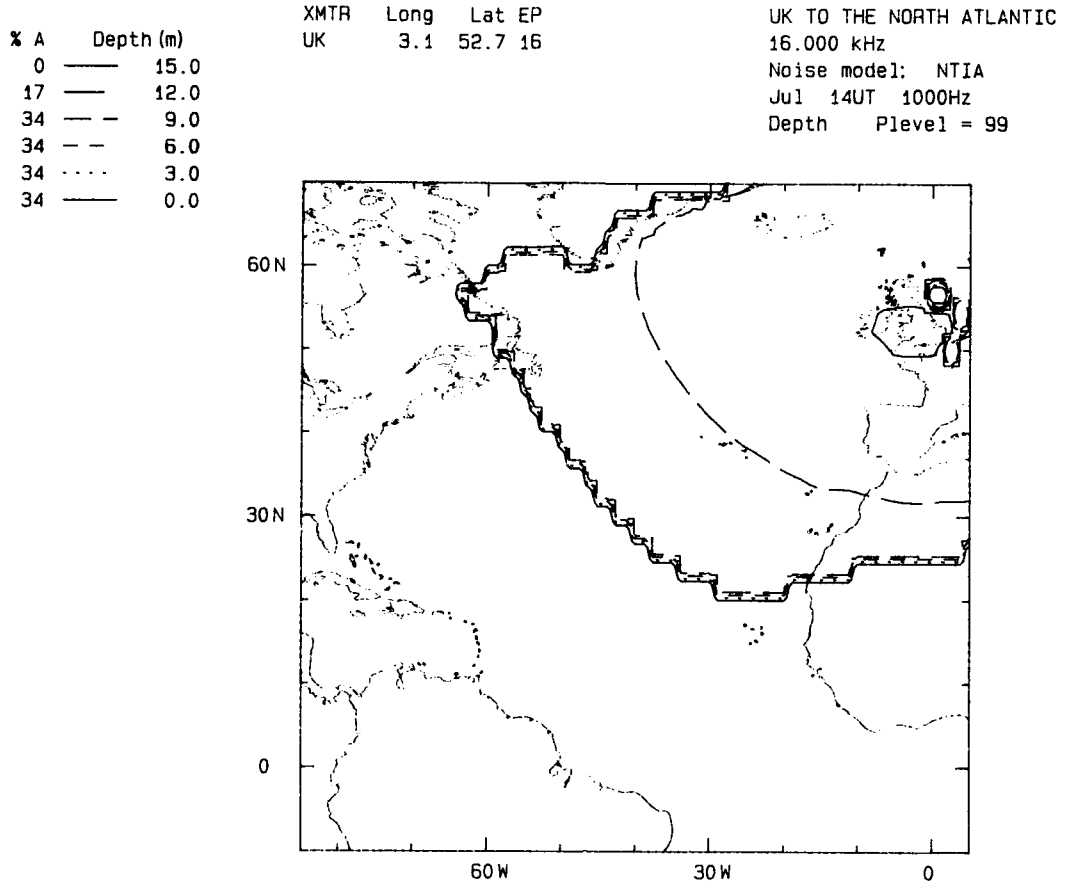

Figure 3 - Contour plot

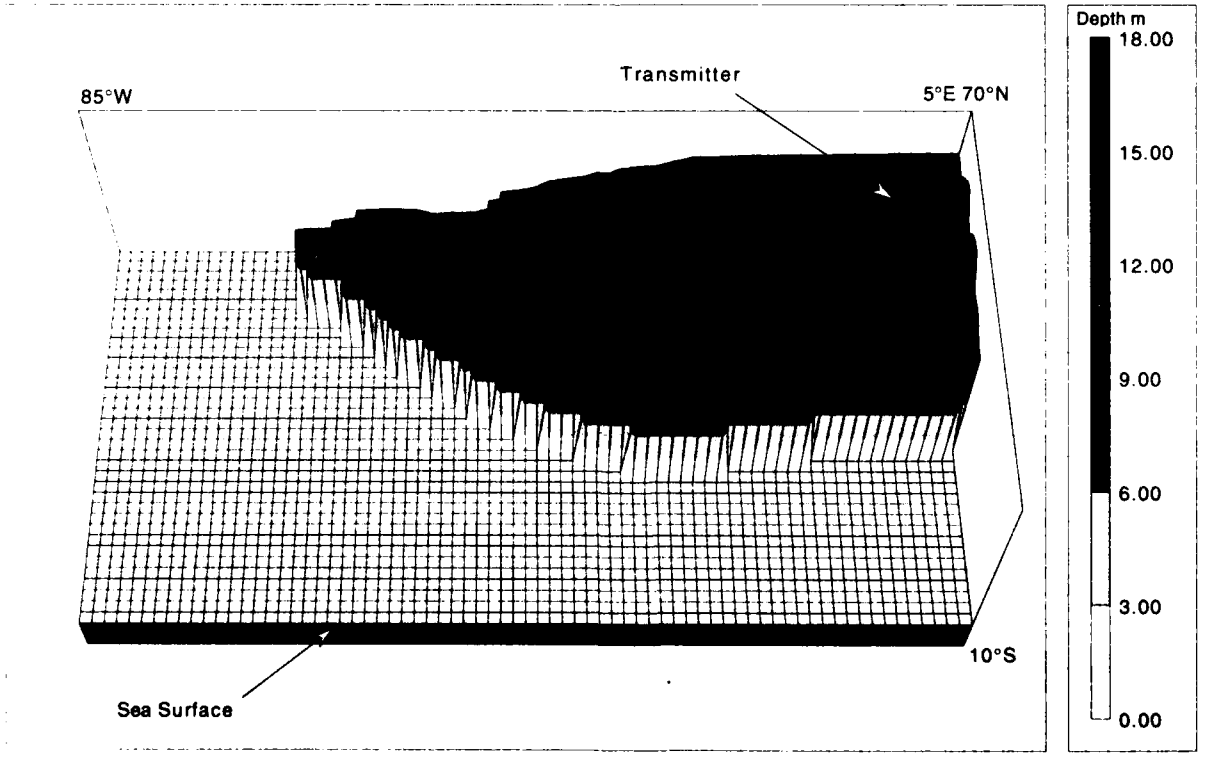

Figure 4 - Depth profile

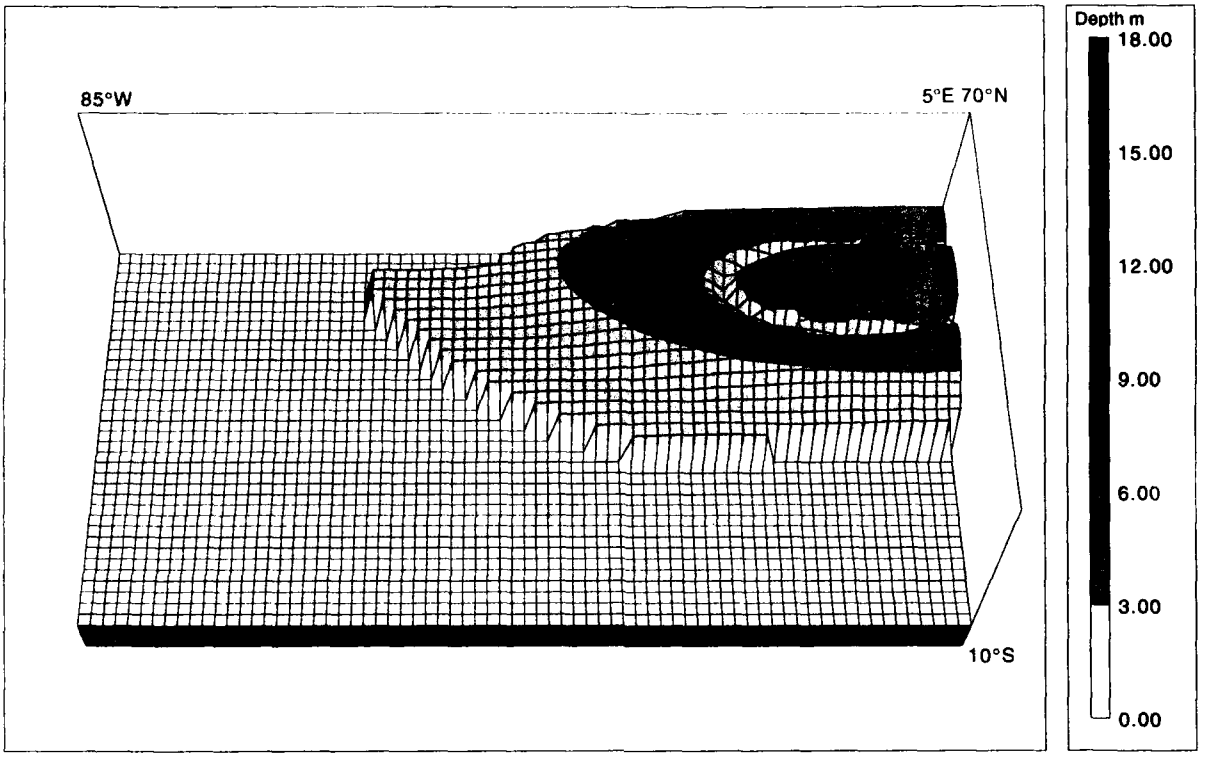

Figure 5 - Frequency, 51.95 KHz

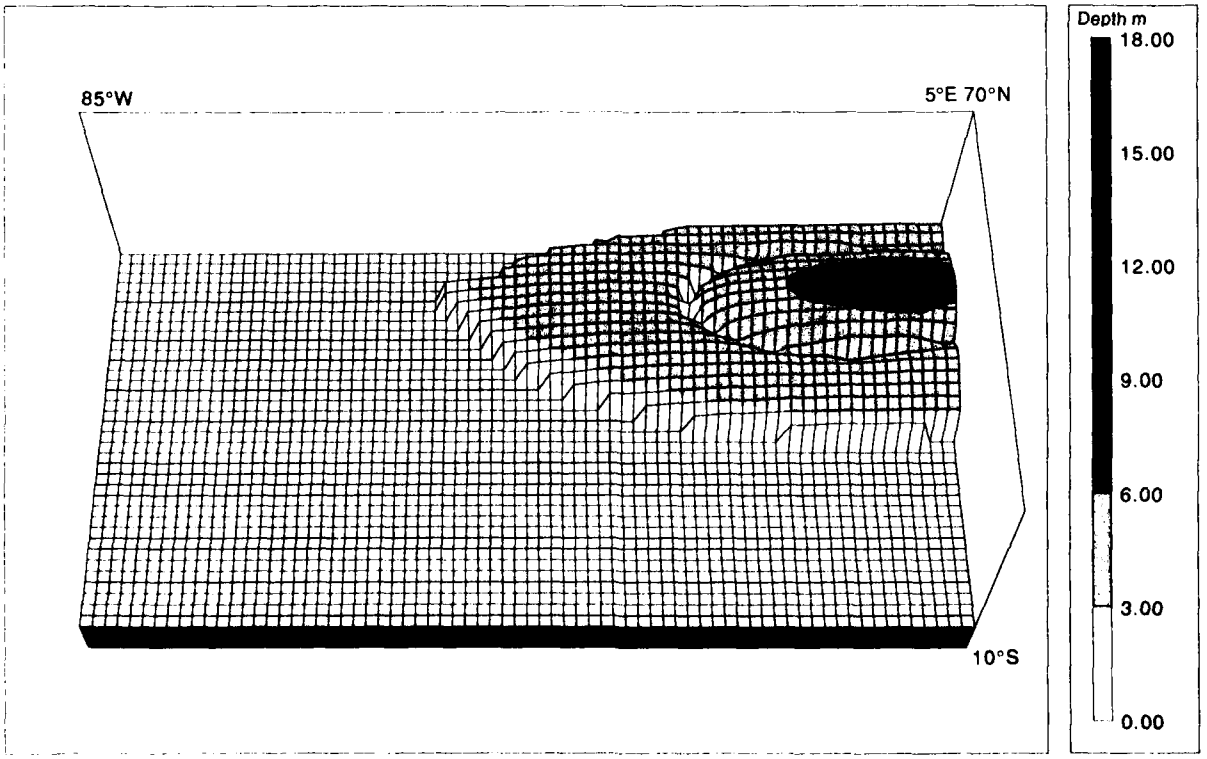

Figure 6 - Frequency, 81 KHz

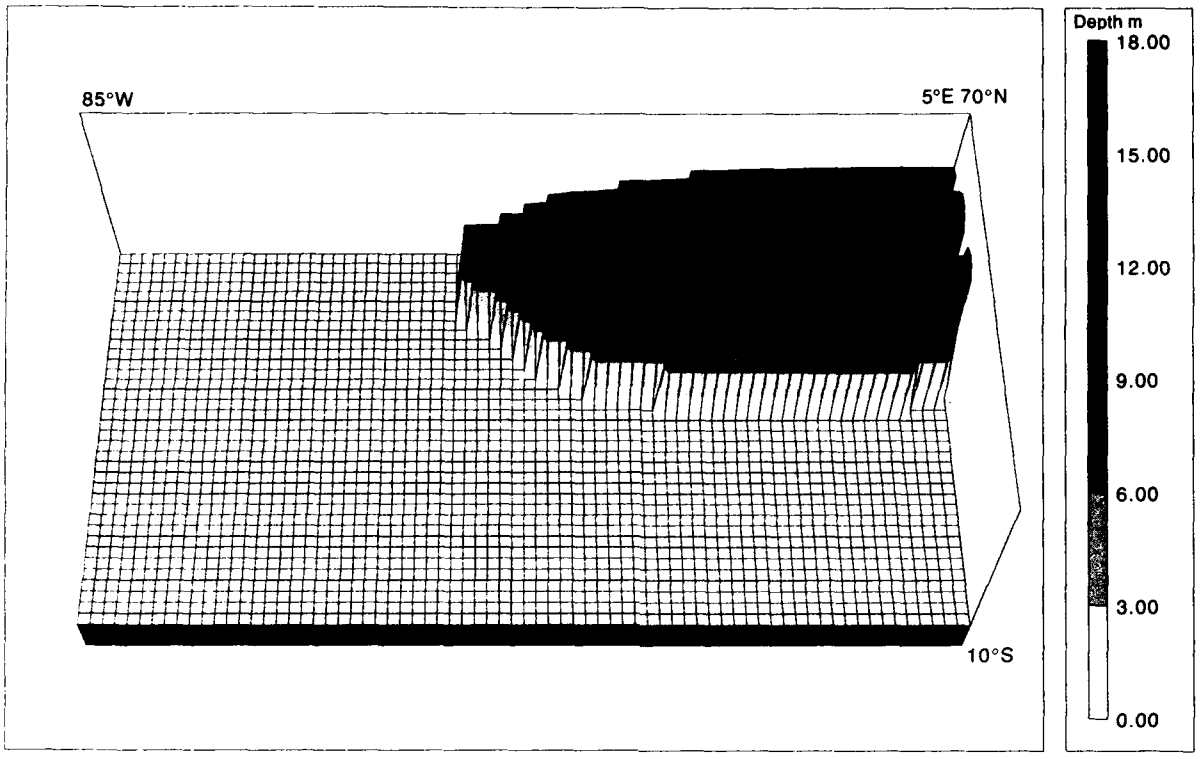

Figure 7 - Radiated Power, 40 KW

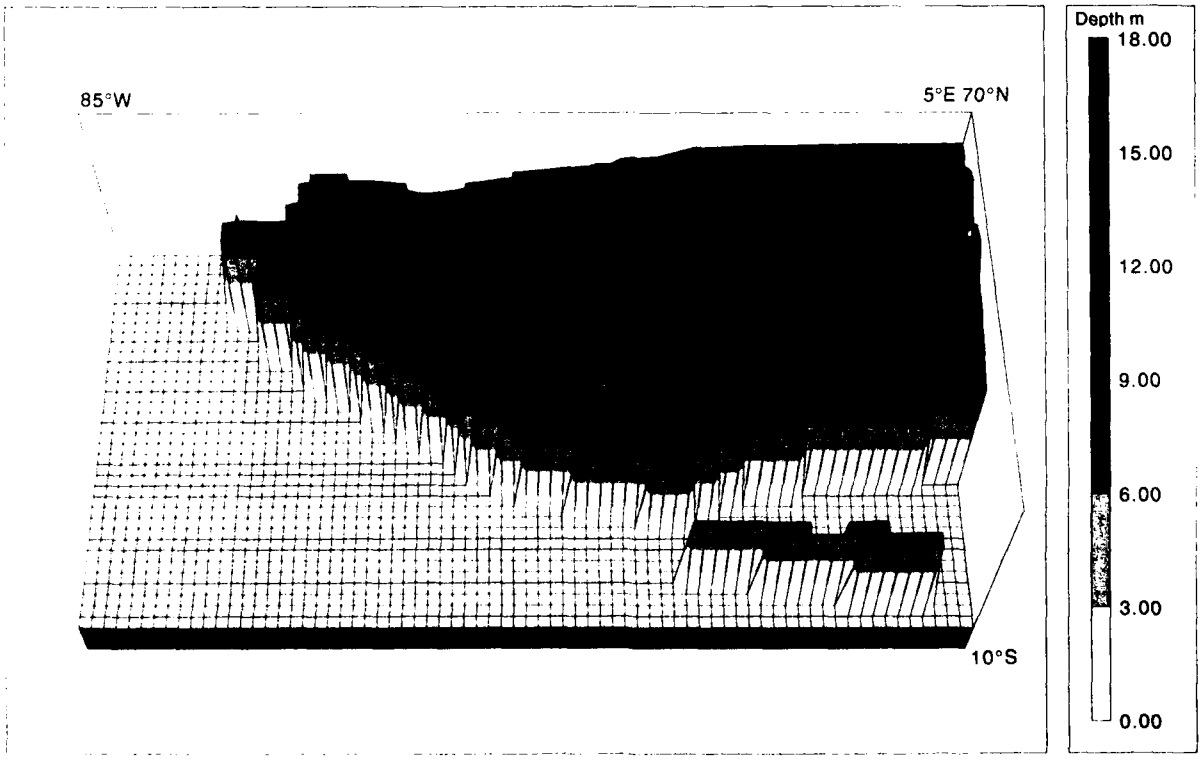

Figure 8 - Radiated Power, 160 KW

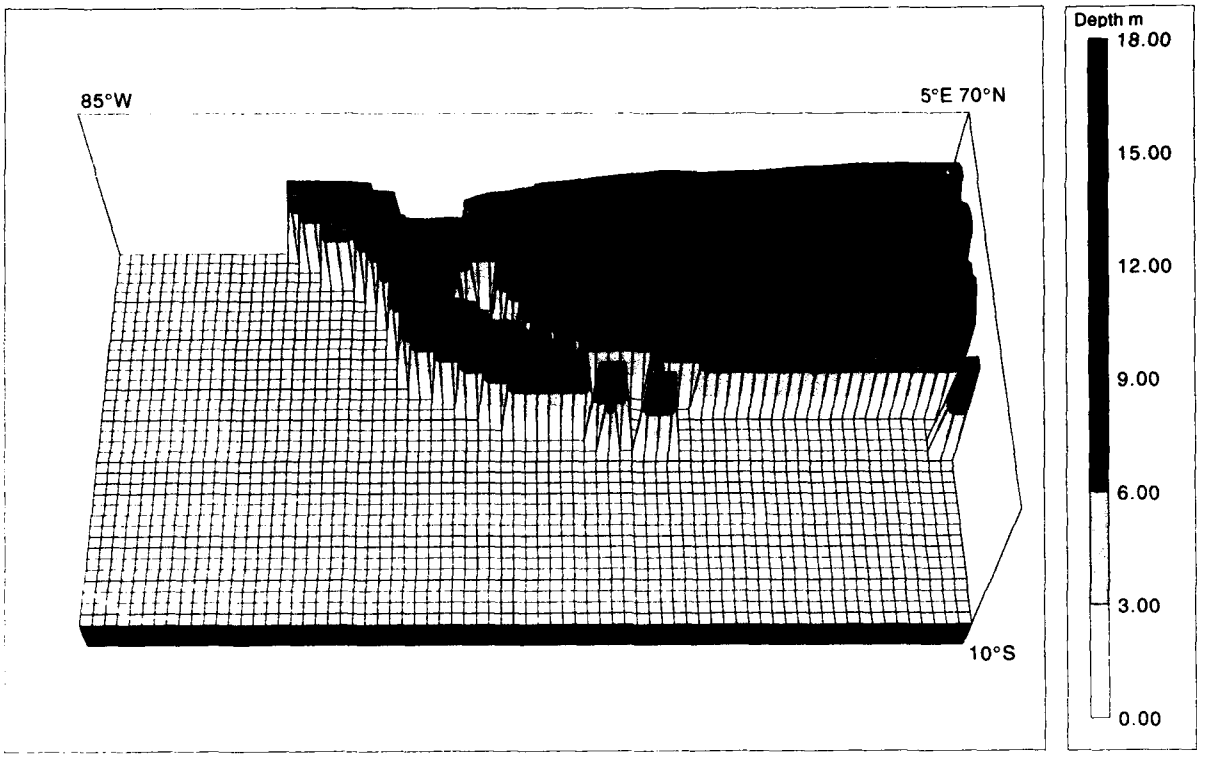

Figure 9 - Time of Day, 0200GMT (Night)

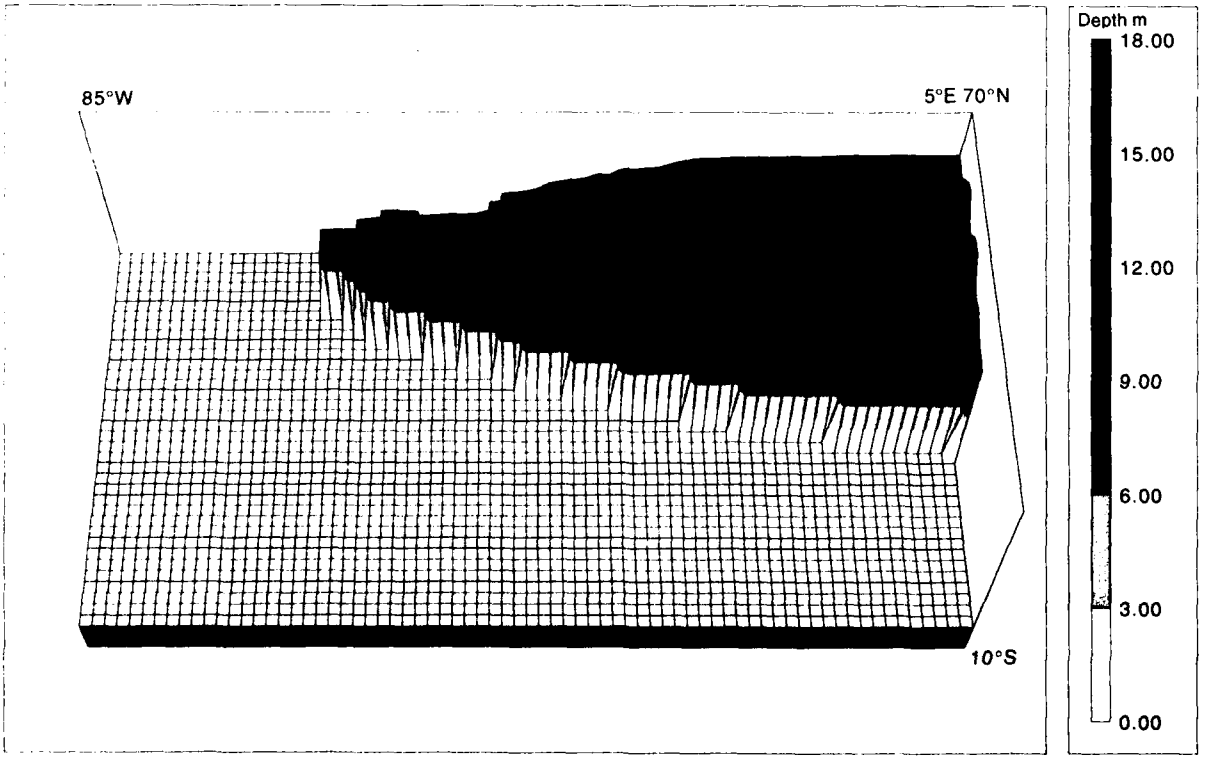

Figure 10 - Time of Year, January (Winter)

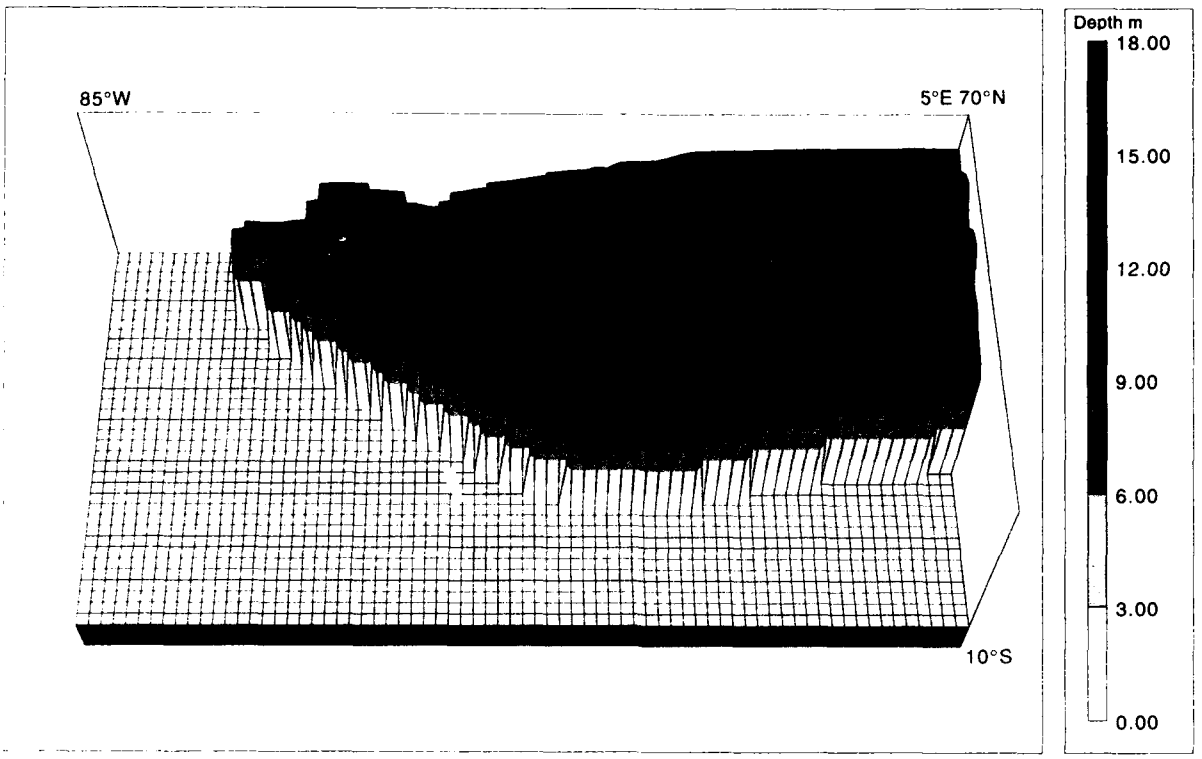

Figure 11 - S/N Requirement, -6dB

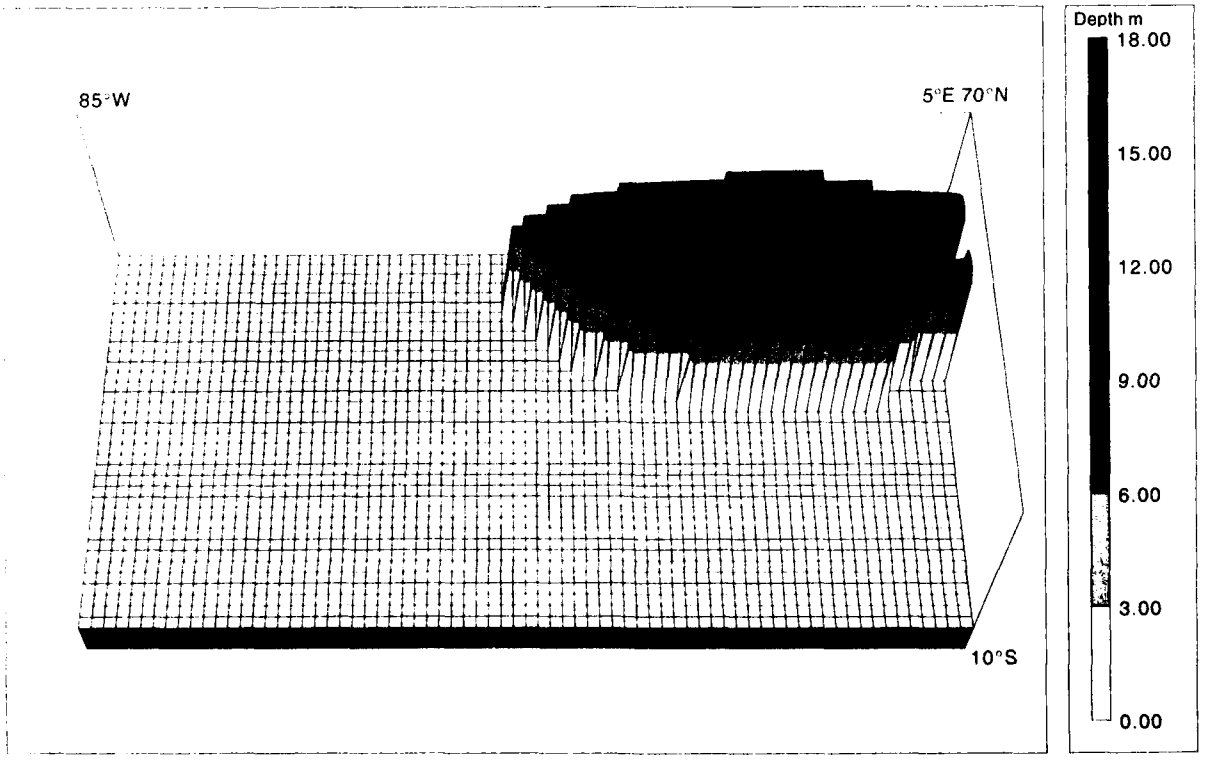

Figure 12 - S/N Requirement, 6dB

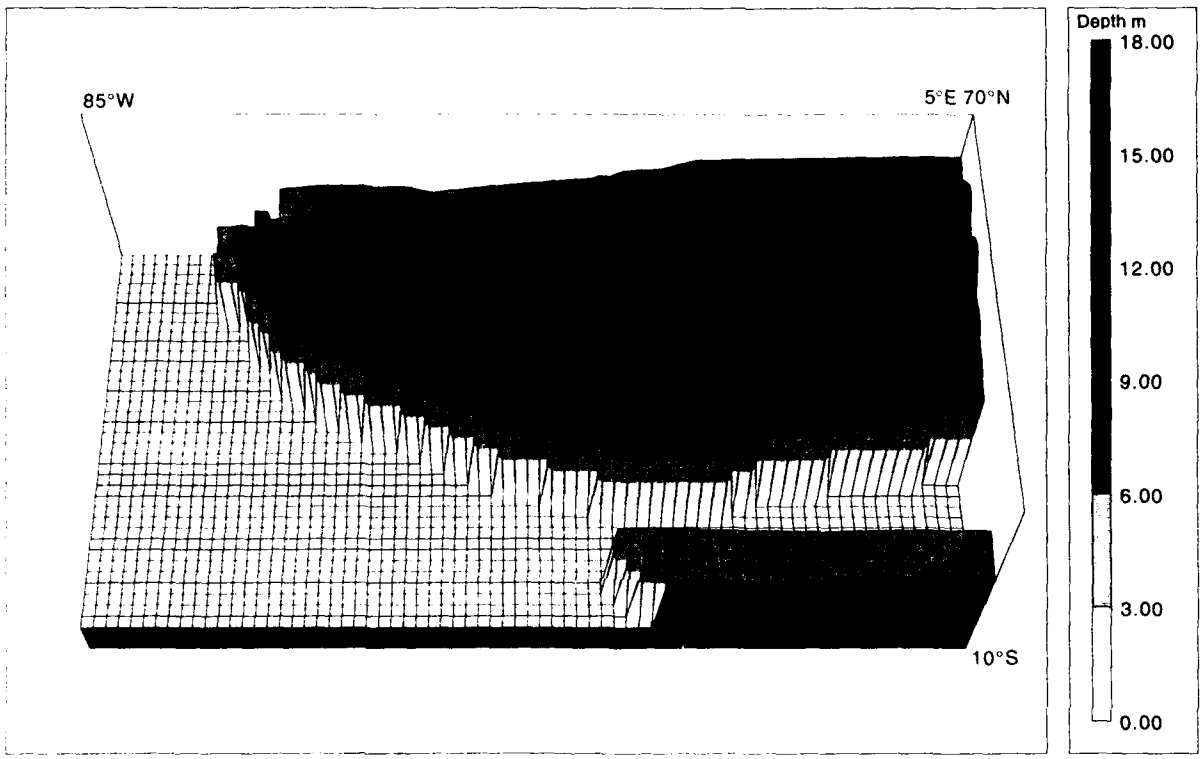

Figure 13 - Time Availability, 50%

Discussion

JONES
COMMENT. Isn't the answer to Dr. Belrose's question that the video we saw does not show simply the radiated field strength but essentially the signal/noise ratio? So it may be it's the noise that is varying and not the propagation.

AUTHOR'S REPLY
The video shows depth performance which is derived from the field strength. The S/N determines if the signal can be received and is purely a yes/no condition.
LNPC predicts noise at 4th time intervals whilst the field strength can be calculated at any time throughout the day. In the case of the video the field strength was predicted for 1/2 intervals. It is therefore both noise and propagation that vary.

INAN
COMMENT. 1) For the calculation of fields inside the seawater do you neglect the displacement current, in other words, do you assume T>>wE. If so, is that valid at 80 KHz? 2) For an atmosphere noise limited sytem, I understand the importance of the S/N requirement. What is the basis of the Smin (signal minimum) requirement? Is this due to the thermal noise in the receiver system?

AUTHOR'S REPLY
1) Yes, we are primarily concerned with VLF frequencies which give the greatest depths of reception and have therefore not considered the validity of the assumption at 80 KHz.
2) Signal minimum is the signal that the receiver system requires to meet the S/N requirement. It will be dependent upon the sensitivity of the system i.e. thermal noise in the receiver system.

A LONG WAVE TE/TM NOISE PREDICTION MODEL

C.R. Warber and E.C. Field, Jr.
Pacific-Sierra Research Corp.
2901 28th Street.
Santa Monica, CA 90405

1. SUMMARY

A computer model that predicts both horizontally and vertically polarized noise in the ELF to LF band (10 Hz – 60 kHz) is described. Since naturally occurring radio noise in this band is produced by lightning, and propagates to the receiver via the earth–ionosphere waveguide, the model starts with average lightning flash density data which it turns into radiated power for horizontal and vertical noise. Adjustments are made to the radiated power to account for seasonal and latitudinal differences in the lightning processes. The noise power is then integrated over fairly large geographic areas into horizontal and vertical equivalent noise transmitters. The power radiated from each of these transmitters is propagated to the receiver location using standard anisotropic long wave propagation algorithms and well-known models of the earth-ionosphere waveguide. From the received power the model predicts RMS noise, standard deviation, voltage deviation V_D, and the amplitude probability distribution of the noise for both polarizations. Since the model is based on theory, it can also predict these parameters under disturbed ionospheric conditions. The model's agreement with data is demonstrated.

2. INTRODUCTION

Long wave communication systems use frequencies between about 45 and 120 Hz in the extremely-low-frequency (ELF) band and frequencies between 10 kHz and 60 kHz in the very-low-frequency (VLF) and low-frequency (LF) bands. In the VLF/LF bands, both vertical and horizontal polarizations are used for links between airborne terminals, whereas only vertical polarization is used for ground-based or submerged terminals. Strategic long wave systems must provide connectivity between mid-latitude transmitters and receivers located at various latitudes, including polar regions. That connectivity must be maintained even when the ionosphere has been disrupted by radiation from nuclear detonations.

When not being jammed, long wave systems are limited by atmospheric noise. Therefore, in order to make performance predictions, it is necessary to specify atmospheric noise for all of the cases just cited. However, no data exists for atmospheric noise in nuclear environments; hardly any data exists for horizontally polarized noise; little data over the ocean regions used by submarines; and –until recently– not enough data existed for ELF noise or noise in polar regions. Empirical models that work well for mid-latitude, vertically polarized VLF/LF noise therefore cannot be applied to a number of important operational conditions, and thus a predictive model is needed.

The best known empirical noise database is that published by International Radio Consultative Committee (CCIR). The latest version of their database, CCIR Report 322-3 published in 1986 [Ref. 1], summarizes data taken on a network of nineteen recording stations over a number of years [Ref. 2]. It consists of contour graphs of the effective antenna noise figure (F_A) at 1 MHz superimposed on world maps. The 24 maps cover four seasons and six diurnal time blocks. In addition to the maps, supporting graphs give additional noise statistics as well as the conversion from 1 MHz to frequencies from 10 kHz to 20 MHz.

Two decades ago, the Westinghouse Georesearch Laboratory (WGL) developed a model to predict ambient VLF noise throughout the world [Ref. 3]. They did this by assuming that lightning flashes are the source of noise. Noise at a particular location was then just the sum of all the noise radiated by storm centers. Although the WGL model was state of the art at the time of its development, it is now limited in several respects. Since data on actual lightning flash occurrence rates were scarce, WGL inferred the rates from records of thunderstorm days (T_D), thus introducing an inaccuracy of unknown magnitude. WGL modeled only radiation and propagation at frequencies between 10 and 30 kHz and neglected the contribution from horizontal lightning entirely. They thus omitted ELF and LF noise and the transverse electric (TE) component of VLF noise, all of which are important to systems deployed during the past two decades. The propagation algorithms used by WGL are crude by present-day standards, particularly in the treatment of non-stratified ground or ionospheres. Finally, the WGL model did not account for ionospheric disturbances, especially those caused by nuclear detonations.

To address these limitations, we undertook a project to produce a modern noise model. The main modernization stems from our use of satellite and ground-based data on the occurrence rate of lightning flashes as a function of longitude, latitude, time of day, and season. Such data circumvent the need to infer lightning occurrence statistics from T_D maps and remove a major uncertainty from the modeling process. We have also benefited from recent data on lightning structure–especially stroke altitude and orientation, which profoundly affects the ratio of TE noise to transverse magnetic (TM) noise.

Computer codes containing the results of this work have been distributed to a number of researchers since 1990. We are continuing to refine the model in accordance with their comments and suggestions. This article presents the results from the current version, called LNP for Long wave Noise Prediction. LNP predicts TE and TM noise in the 50 to 300 Hz and 10 to 60 kHz bands under both ambient and disturbed conditions. The computer code is written in strict FORTRAN 77 for portability. It was designed to be easily extended and upgraded as new data becomes available. We have tested LNP against data from a number of sources including some of the original data used for the CCIR model [Ref. 4] and data from the Stanford University Global Survey of ELF/VLF Radio Noise [Ref. 5].

3. OVERVIEW OF THE NEW PREDICTIVE MODEL

Although man-made or extraterrestrial sources might contribute to long wave noise at certain times or locations, the current version of the model assumes that noise is caused solely by lightning, which radiates strongly in the long wave bands. LNP consists of two submodels: the source submodel, which describes the occurrence rate of lightning flashes throughout the world and the electromagnetic radiation from those flashes; and the propagation submodel, which describes how the energy radiated from numerous worldwide centers of lightning activity propagates in the earth-ionosphere waveguide to the location of a long wave receiver. The total noise at a location is calculated by summing the energy that arrives from all important thunderstorm centers.

LNP uses lightning distribution data taken by a satellite launched from Japan in 1978 called the Ionosphere Sounding Satellite-b (ISS-b). We will discuss this data in more detail below, and compare the flash rates seen by the satellite to data obtained by other means.

The total lightning discharge is called a *flash* and is made up of many components. Among these components are high-current pulses called *strokes*. There are several types of strokes that act as sources of long wave radio noise. If we knew the location of every stroke that occurred over a long period of time and how much power each radiated, we could use standard long wave propagation techniques to determine how much power from each stroke reached a receiving point. Then we could sum the power from all strokes to calculate the total noise as a function of time. In reality, of course, such an approach is impossible. Instead, we assume that each flash can be represented by a collection of a few types of lightning strokes. We then use representations of both the number and power of these strokes

to determine the average noise power radiated by a single flash at a given location and time. The representations we use depend on a number of factors which we will discuss below. Then we combine the radiators from all flashes that occur in a given area, which typically extends over several degrees of longitude and latitude, into a single effective radiatior–an "equivalent noise transmitter" (ENT)–which we assume to be positioned somewhere near the center of the area. The power contributions from all worldwide ENTs are then propagated to the receiver location and summed to get the total average noise.

The propagation is calculated using an almost standard, full-wave, anisotropic waveguide code, with mode coupling calculated at each boundary. We have included some approximations to increase speed. The propagation parameters (attenuation and excitation factors) for a number of different ionosphere models are stored in a database. Both TE and TM modes are handled, and the code is able to determine how many modes to use. The phase of the individual modes is ignored, so the normal summation of complex numbers found in standard waveguide theory is replaced by an RMS sum of real numbers. Since this is a fairly well known procedure, we will not discuss it further. The interested reader is referred to Warber and Field [Ref. 6] for details.

Once the noise from a single noise transmitter is determined, the RMS noise value is added to the RMS sum from the remaining transmitters. The standard deviation is also combined into the total standard deviation. LNP also estimates the amplitude probability distribution and the voltage deviation parameter, V_D.

4. FLASH RATE FROM SATELLITE DATA.

The ISS-b was launched 16 February 1978 from Tanagashima, Japan, into a circular orbit at an altitude of 1100 km, with a 70° inclination [Ref. 7]. This gave the spacecraft a 107 min. orbital period. The orbit was such that the spacecraft was able to observe any region on the earth from 70° North to 70° South at all local times during a 120-day period for high-latitude regions (60 days at low latitudes). The lightning detection experiment was one of four on the spacecraft. The others measured the electron distribution in the upper ionosphere, the positive ion composition, and the temperature and densities of electrons and ions. Each experiment was run repeatedly within a period of 64 s; the lightning detection experiment observed during 20 of those seconds, and took 32 data points per second on each of the four channels. There were about 100 observation periods per orbit. The data in the database was taken from June 1978 to May 1980. The data was divided into four seasons, and within each season, into six 4-h time blocks in universal time, 22-02, 02-06, 06-10, 10-14, 14-18, 18-22 h.

The lightning detection experiment consisted of monitoring a four-channel, narrow-band, HF receiver (frequencies: 2.5, 5, 10, 25 MHz). Noise pulses from lightning should appear on all channels above the critical frequency of the ionosphere beneath the satellite. The location of the pulse can be determined if the location of the satellite is known, since the condition of the ionosphere and the frequency of the receiving channel establish a maximum angle of incidence at which the signal can penetrate the ionosphere to the satellite. Only flashes that occur within the cone defined by this maximum angle will be seen by the satellite. This has been termed the "iris" effect, since it resembles the opening and closing of the iris of a camera. The critical frequency could not be determined in advance, thus four different channels were used. However, since density data was also taken by the satellite, critical frequencies could be determined after the experiment and the field of view estimated. Fields of view with radii as small as 130 km were reported.

After the data was filtered to remove man-made noise, the number of discharges over every observation period normalized by the observation time were summed for each 10°x10° geographic bin. The value thus obtained is defined as the flash rate density (flashes/sec/km^2). Figure 1 is an example of the data for Jun- July -Aug at 2200 to 0200 h. The entire set of 24 maps and tabular data was published [Ref. 8], and has already

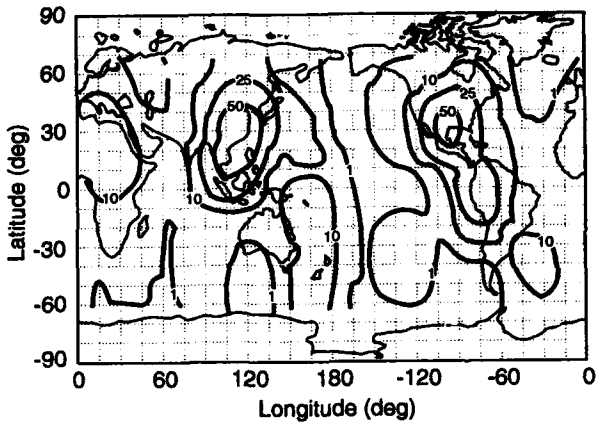

Figure 1. Global distribution of lightning discharges for June-August, 2200-0200 UT. Contour are in units of 10^{-4} flashes/s/km^2

been used to construct models of noise. Kotaki and Katoh [Ref. 9] constructed an HF model for 2.5 to 20 MHz. They claim better agreement with measurements than the predictions of CCIR Report No. 322. Greifinger *et al.* [Ref. 10] report that J. Dea has modified the WGL model to use the satellite data (albeit with a number of shortcuts) and obtained reasonable agreement with 13 kHz data.

Since the flash rate data is central to the operation of the noise model, we have compared the flash rates seen by ISS-b to other flash rate data. Some of these are worldwide flash rates, and others are at specific points. Next we present some of these comparisons. Our effort to validate the lightning database is one of the ongoing areas of research on the model.

The seasonal flash rate can be obtained by multiplying the flash rate density in each geographic bin by the area of the bin, and then summing the contribution from all bins. Results from this calculation are given in Table 1.

Table 1. Seasonal global flash rates obtained from the ISS-b data.

Season	Flash Rate (sec^{-1})
Dec - Jan - Feb	54
Mar - Apr - May	64
Jun - Jul - Aug	55
Sept - Oct - Nov	80

These values agree well with an estimate made by C.E.P. Brooks in 1925 of 100 flashes/s worldwide. This estimate was based on thunder day data. Other estimates of the global flash rates made from satellite observations range from 30 to 120 s^{-1} [Turman and Edgar, Ref. 11, Orville and Spencer, Ref. 12, and Turman, Ref. 13]. These estimates come from studies of optical sensors on board satellites.

Anderson *et al.* [Ref. 14] present flash density data collected over 15 years in Pretoria, South Africa, and over eight years for the entire southern Africa region. Although the annual flash density for Pretoria is fairly constant at about 6.6 km^{-2}, with a maximum value of 10.5 km^{-2} and a minimum of about 4.5 km^{-2}, the monthly flash density values can vary quite a bit. January (summer in South Africa), for example, has a minimum of 0.5 km^{-2} and a maximum of 3.5 km^{-2}. We can estimate the number density over the entire southern Africa region from the data they give to be about 2.8 km^{-2}, which agrees almost exactly with the value of 2.5-3 km^{-2} for the same region in the ISS-b data. The ISS-b data can also be compared to the Pretoria monthly densities if we sum the Pretoria data into seasons and scale the ISS-b data by a factor of 2 to account for the averaging over a wider area. Doing so results in the data shown in Table 2.

Table 2. Comparison of Pretoria and ISS-b flash density data.

Season	Pretoria (km^{-2})	ISS-b (km^{-2})
Dec - Feb	3.5	2.2
Mar - May	1.1	1.6
Jun - Aug	0.0	0.8
Sep - Nov	2.0	2.0

Since the ISS-b data was taken over a relatively short peroid of time, we would like to compare it to data taken over a longer term. Thunder day statistics have been recorded for many years. We removed the dirunal information from the ISS-b data and used a well known approximate relation between thunder day and flash rate to study the dynamic range of the ISS-b data. The World Meteorological Organization (WMO) publishes thunder day data taken over a long period of time. The WMO T_D distributions are published as maps for each month, the four seasons, and the entire year. To convert from flash rate to T_D, we will invert a standard relation between T_D and flash rate. Most investigations of this relation find that the flash rate is proportional to T_D^n, where $n \approx$ 1.1 to 1.5. However a certain amount of caution is needed here, since the data that goes into the fit has a large amount of scatter. It is not unusual for the flash rate to vary by a factor of 10 for a given T_D.

To estimate T_D from the ISS-b data, we sum over the diurnal time blocks and then assume T_D is proportional to the summed flash rate raised to 0.8. Since we are interested in only relative numbers, we set the maximum number to 60 for a season and 200 for a year. We then calculated the T_D number for each 10°x10° bin in the summed data. When we compared the resulting values to values from the WMO maps, taking into account the greater spatial precision of the WMO maps, we found that the sets compare fairly well, except in the Northern Hemisphere during winter, where the ISS-b results can be greater by a factor of on the order of ~10. There are several possible explanations for this, the most obvious one being that a factor of 10 variance is not unusual in lightning parameters; thus the ISS-b data might simply have been taken during an unusually noisy winter. Another possibility is that the relation between T_D and flash rate is not very accurate. For example, the flash rate in Japan varies by an order of magnitude between summer and winter; however, the T_D number is exactly the same~13 T_D/season. The third possibility is that the satellite has problems when the flash rate is too low; note that the discrepancies occur at low flash rates. The satellite might be picking up man-made or extraterrestrial noise and interpreting it as a flash. This would not be a problem when the flash rate is high, since a few extra flashes among several hundred represent only a few percent. Extra flashes among several tens of flashes, however, could represent a major overstatement of the flash rate and cause our noise model to overstate the noise by several decibels. Recently data from the lightning detection network that covers the continential United States has become available to us. The network is a large collection of ground based sensors, and records the time, position and intensitity of cloud to ground flashes. Data is available for the entire U.S. since 1988, and for the east coast area since 1983. We are using this data to help us resolve the difference between thunder days and the ISS-b flash rate, which is confined to mid-latitude, winter noise.

5. POWER RADIATED BY LIGHTNING FLASHES

The lightning rate distribution maps tell us where lightning is occurring. Since the duty cycle of the ISS-b satellite is on the order of a second, we assume that the satellite is recording individual flashes. Thus we have to turn the flash into a series of lightning radiators. This section describes the physics of these lightning radiators and how we model them. We will describe the average power radiated by lightning into the ELF/VLF/LF and how that power is modified by various lightning processes.

The total average noise at the receiver point, P_{R0}, is given by the sum of the instantaneous noise powers arriving from all ENTs at time, T:

$$P_{R0}(T) = \sum_i \wp_{RTi}(T) P_{Ti}(T) \qquad (1)$$

Here we express the latitude and longitude dependence of the functions with the subscripts 0 and i. The power radiated from the ith ENT is P_{Ti}, and $\wp_{RTi}$ represents the propagation of that power from the ENT to the receiver. Note that in the rest of the text, all quantities can be regarded as time or spatial averages unless otherwise noted. Also, they will be functions of both the spatial and time coordinates. We will suppress these coordinates or the average overbar, unless they are needed for clarity or emphasis.

We write the average power radiated by a single ENT as:

$$P_T = N_{TOTAL} \sum_k P_{Sk} N_{Sk} N_{Fk} \qquad (2)$$

where the index, k, denotes the different types of lightning strokes that contribute to the total radiated power; N_{Total} is the total number of flashes of all kinds in the region represented by the ENT; N_{Fk} is the fraction of those flashes that are of type k; N_{Sk} is the number of strokes per flash, and P_{Sk} is the power radiated by a single stroke of type k.

Lightning parameters, such as radiated power or relative occurrence of a given stroke type, depend on a number of factors, which we lump into several multiplicative terms called "modifiers." Thus we write:

$$P_{Sk} = M_{PCk} M_{PSk} M_{PEk} M_{PGk} P_{0k} \qquad (3)$$

$$N_{Sk} = M_{NCk} M_{NSk} M_{NEk} M_{NGk} N_{0k} \qquad (4)$$

where the subscript P or N indicates whether the modifier applies to the power or to the number of strokes per flash that are of type k; M_C is the charge height modifier; M_S is a storm severity modifier; M_E is a terrain effects modifier; and M_G is a land-sea modifier. P_{0k} and N_{0k} denote the average power and stroke-type fraction at the equator, so the modifiers have the effect of normalizing the lightning parameters to their values at the equator. Because most of these parameters have their maximum value at the equator, most of the modifiers are less than unity.

Many of the factors above have either fixed values near one, or are slowly varying. These factors are of minor importance for the results of the model, but are included above for completeness. In the rest of this section we discuss those factors which play a major role in the model and the physical justification for them. Space does not allow a complete discussion of all the terms. A complete discussion can be found in Ref. 6.

5.1. Overview Of The Lightning Discharge.

In order to give some background for what follows, and to define a few terms, we briefly review some facts about lightning. The reader who seeks more detailed information is referred to Uman [Ref. 15], upon which much of what follows is based.

Lightning is a complex, propagating process of gas breakdown that results in a transient, high-current electrical discharge. A discharge typically neutralizes some tens of coulombs of cloud charge over a path length measured in kilometers. Lightning can be classified according to whether or not the discharge channel contacts the earth. A flash that does contact the earth is called a Cloud-to-Ground (CG) flash; one that does not is called an In-Cloud (IC) flash. In addition, we classify individual strokes as vertical or horizontal radiators. Although in the past it was assumed that CG contained basically vertical radiators and IC basically horizontal ones, it is now clear that both CG and IC flashes have horizontally *and* vertically radiating components. Thus we shall use the terms horizontal and vertical, and CG and IC lightning to refer to different aspects of the total discharge.

At VLF there appears to be only two kinds of lightning strokes that contribute significantly. The first is the return stroke, the

most powerful and most widely studied of all lightning components. The second is called a bipolar discharge. Bipolars are small strokes that occur within the cloud and normally precede the return stroke. The power radiated by a single bipolar discharge is usually much smaller than that radiated by a return stroke, but the power spectrums and the relative numbers of these two stroke types are such that the bipolars contribute significant energy near 50 kHz. The return stroke, on the other hand, dominates at 10 kHz. Power spectrums and numbers of strokes per flash are discussed below.

At ELF, only the so-called "continuing current" in the return stroke appears to contribute.

5.1.1. The Cloud-To-Ground Flash.
Figure 2 is a Simplified view of a CG flash. The typical discharge starts in the cloud and eventually neutralizes tens of coulombs of negative cloud charge. The total discharge from start to finish lasts on the order of 0.5 s. In the present model of the thundercloud, positive charge appears at the top of the cloud and negative charge collects in layers at the altitude where the ambient air temperature is near -10° to -20° C. .

The first part of a flash is initiated by a preliminary breakdown within the cloud. Although the exact form and location of this breakdown is uncertain, small volumes of intense space charge in the presence of a strong electric field appear to initiate it. This sets the stage for negative charge to be channeled toward the ground in a series of short, luminous steps called the stepped leader. Typical values for the leader steps are 1 μs in duration and tens of meters in length. The pauses between the steps are on the order of 50 ms. A total of about 5 coulomb of charge is spread out in the lightning channel in tens of milliseconds. The steps have peak currents of around 1 kA, whereas the average leader current is 100 A. The stepped leader channel branches in a downward direction during its development.

As the tip of the leader channel nears the ground, the electric field beneath it becomes very large and causes one or more upward-moving discharges to be initiated at the ground. When one of these upward-moving discharges contacts the downward-moving leader channel, the channel is connected to ground potential. The charge in the leader channel is then discharged by a ground potential wave moving up the channel–the return stroke. Peak currents are on the order of 30 kA, and the total transit time on the order of 100 ms. This much energy in such a small time period heats the air in the channel to near 30,000 K, generating a high-pressure channel that expands and creates the shock wave, which eventually becomes thunder.

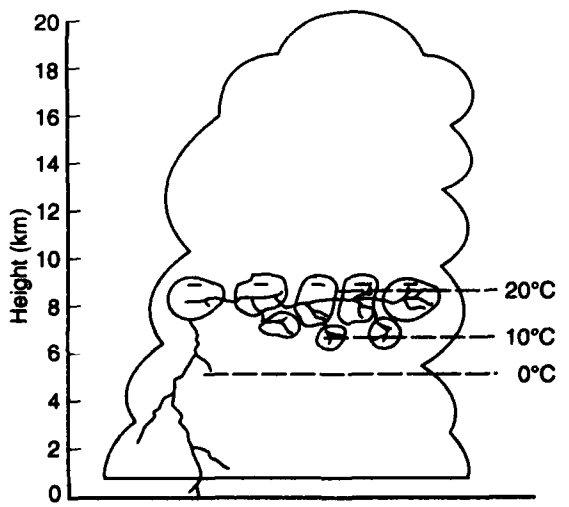

Figure 2. Charge distribution and flash channel for a typical cloud-to-ground flash.

The flash could end at this point. However, more charge is normally made available at the top of the channel by discharges within the cloud, known as J and K processes. This causes a leader to propagate down the channel, lowering about a coulomb of charge with currents on the order of 500 A. This leader (called a dart leader) then initiates a return stroke. This process can occur several times. Typically, a CG flash will be made up of a first return stroke and three subsequent return strokes, although up to 40 strokes in a single flash have been reported. These subsequent strokes have less power than the first return stroke. The time between successive return strokes in a flash is usually 40 to 80 ms. Figure 3 shows a typical return stroke wave form.

The terms J-changes and K-changes refer to mechanisms that distribute charge within the cloud. They are identified by their characteristic signatures on electric field change recordings made during the storm. Associated with the K-changes are a series of bipolar pulses that radiate in the VLF range. Figure 4 shows the wave forms for a burst of these bipolar pulses [Ref. 16]; they appear to be the only other kind of pulse that will radiate strongly at VLF [Ref 10]. These pulses will occur in large numbers during a flash, and since there spectrum peaks about 30 kHz, they dominate at the higher VLF/LF frequencies. The leader pulses will also radiate a significant amount of energy, but their spectrum peaks near 200 kHz, so they will not contribute to the noise at VLF.

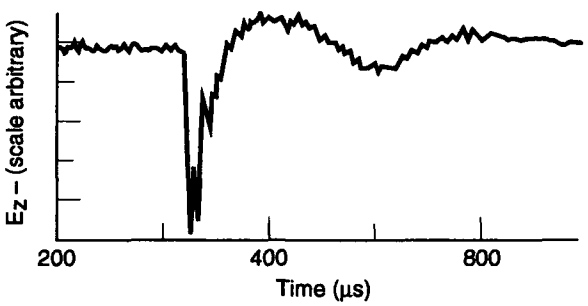

Figure 3. Typical return stroke wave form.

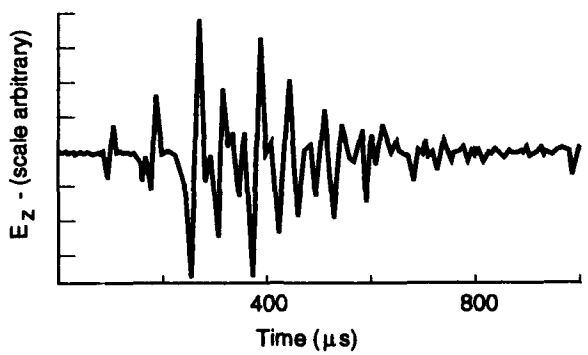

Figure 4. Wave form for a bipolar pulse burst.

The normal return stroke lowers negative charge to the ground and is thus termed negative lightning. It is also possible for a flash to be initiated from the upper positive charge in the thundercloud. This probably occurs when this positive charge becomes horizontally separated from the negative charge beneath it. These discharges lower positive charge to the ground and are thus called positive lightning.

Positive lightning is generally composed of a single return stroke followed by a period of continuing current. The positive return stroke can have a much larger peak current than the more common negative lightning. Positive lightning is relatively common in winter and uncommon in summer. The rate of occurrence of positive lightning appears to depend on the elevation of the cloud above the ground; the rate increases with decreasing altitude. The rate also appears to depend on the wind shear within the thundercloud. Orville *et al.* [Ref. 17] found that, for a severe fall storm, overall only 4 percent of the flashes were positive, but that the rate for positive flashes increased with the age of the storm, reaching 37 percent in the last hour. This behavior has been observed in other storms as well. Using a direction-finding system covering the northeastern United States, Orville et al. [Ref. 18] found that about 80 percent of the return strokes were positive in February 1985, 10 percent were in April, and only a few percent were during the summer. The wave form of the positive return stroke is similar to the negative, except for polarity. The median currents are about the same as the negative return strokes (35 kA for positive, 30 kA for negative), but positive flashes can contain a higher percentage of very large peak currents. The amplitude probability distribution for both kinds of return strokes is given in Fig. 10. LNP does not use a direct positive stroke type in the calculation of average noise power, since the effect of the positive strokes is contained in the modifiers. However, we do use the positive stroke type in the calculation of the amplitude probability distribution of the noise.

5.1.2. The In-Cloud Flash.

Since the IC flash does not reach the ground, it is not as well studied as the return stroke, both because it is of less economic importance and because its discharge channel is remote from measuring instruments. What we term In-Cloud flashes could be further subdivided into those flashes that occur entirely within a cloud (intracloud), those that propagate between clouds (intercloud), and those that propagate from clouds to air. However, the majority of IC flashes are intracloud, and experimental data shows that these three types are very similar. Thus the Noise Model does not distinguish between them.

The IC discharges have a total duration about equal to those of the CG discharges (0.5 s). A typical cloud discharge neutralizes 10 to 30 coulomb of charge. Path lengths of 5 to 10 km are generally accepted, but Richard *et al.* [Ref. 19] suggest that the average path length is greater than this. The discharge is thought to consist of a continuously propagating leader that generates five to six weak return strokes called recoil streamers. These are very similar to the K-changes that occur in CG lightning (except for opposite polarity).

5.2. Average Radiated Power.

In this section we present the models we use for the average radiated power for each of the different kinds of strokes. We discuss the power spectrum of an individual stroke of each type and the average number of strokes per flash we assume for each type. Included in this section is a discussion of the probability distribution of both the power and the number of strokes per flash. We do this first for the return stroke, then for the bipolar stroke, then the ELF component.

Figure 5 shows the power spectrum of the return and bipolar strokes used by the model in the VLF range. We assume that the positive return stroke has the same form as the first negative return stroke, but that it is about 35 percent more powerful to account for its larger average current (35 kA to 30 kA.) Subsequent return strokes also have the same form as the first return stroke, but are about 25 percent weaker. LNP does not include direct positive or subsequent strokes in the calculation of average power, but they are included in the modifiers.

5.3. Numbers Of Strokes.

Figure 6 summarizes the number of return strokes per flash from various studies [Ref. 20]. The average number of strokes per flash is about four, which is also close to the median. This number is in agreement with a later result by Thomson *et al.* [Ref. 21] of 4.0 strokes per flash in Florida and an earlier study of 1800 flashes in South Africa by Schonland [Ref. 22], whose results showed 4.1. LNP uses 4.0 as its base value.

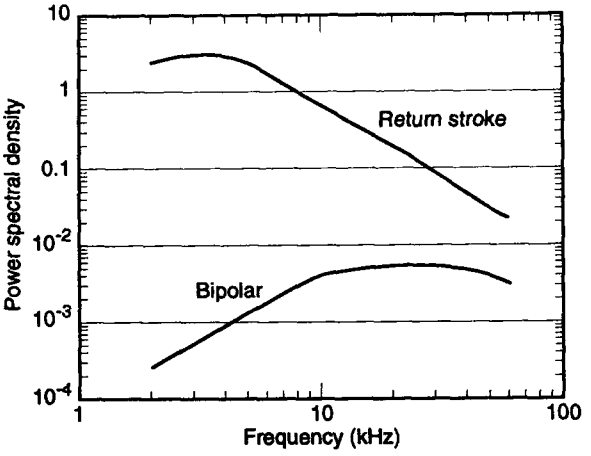

Figure 5. Power spectrum for the two basic types of VLF radiators.

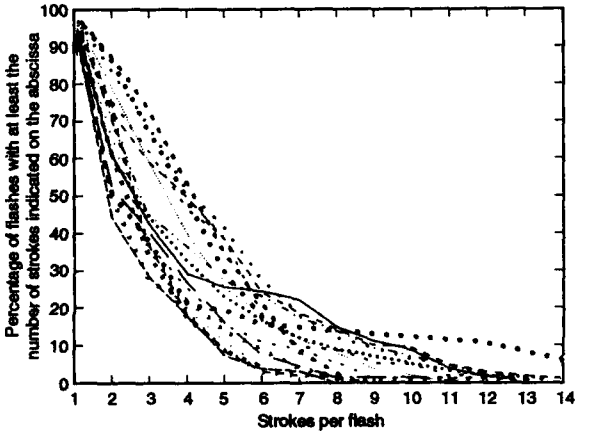

Figure 6. Probablity distribution for number of return strokes per flash form a number of sources.

There seems to be little data on the number of bipolar strokes per flash. Greifinger *et al.* [Ref. 10] recommend using 20 bipolars of the size in Fig. 5 per flash. This recommendation resulted from comparing the spectrum of the bipolars with an approximate spectrum for the entire CG flash and an IC flash. We have made the number of bipolars per return stroke and per IC flash adjustable parameters of the model, and have adjusted them to agree with data at 50 kHz (5 and 20, respectively). We have not found it necessary to make the total number of bipolars different in CG and IC flashes.

For the horizontal radiators, only the bipolars contribute significantly to long wave noise. We have followed the recommendation of Greifinger *et al.* [Ref. 10] and have set the number of bipolars per flash equal to 20. There seems to be no data on this parameter. For the average radiator power, we started with the same average power as the vertical bipolars, and then adjusted to give agreement with data on TE noise from the ALFAN experiment [Turtle *et al.*, Ref. 23].

5.4. Effects Of Charge Height.

The height of the charge center, from which the lightning discharge begins, appears to be a very important parameter in the description of the lightning discharge. A number of other parameters in the model depend on it. Although a number of researchers have looked for latitudinal variations in lightning flash characteristics, Pierce [Ref. 26] appears to have been the

first to suggest the meteorological interpretation for this variation. Since the usual model of the thundercloud has positive charge collecting at the top of the cloud at, say, altitude H, and negative charge collecting in a layer near altitude h, the basic physics of spark breakdown imply that the smaller h is compared to H - h, the greater the chance the discharge will be to the ground.

Krehbiel *et al.* [Ref. 24] found that the charge centers observed in storms tend to collect at altitudes where the ambient temperature is between -10° and -20° C. This result is in agreement with a number of other authors. For LNP, we use the -15° C level as the altitude at which the charge centers collect.

5.4.1. Charge Center Altitude As A Function Of Season.
Oort and Rasmusson [Ref. 25] have published tables of mean temperature as a function of altitude and season. Figure 7 is based on those tables. It shows altitude at the -15° C isotherm as a function of latitude for the four seasons. This figure also contains our analytic fit to that data. Basically, we have:

$$\varsigma = \cos^k(\Theta) \qquad (5)$$

where $\varsigma = h/h_0$, h is the altitude of the charge center, and h_0 is the altitude at the equator (7.5 km). Here k=2 in the winter; 1 in the spring, 0.5 in the summer, and 1.5 in the fall. We call ς the normalized charge center altitude parameter, or the charge height parameter. We will use it to define a number of other parameters that have a latitudinal dependence.

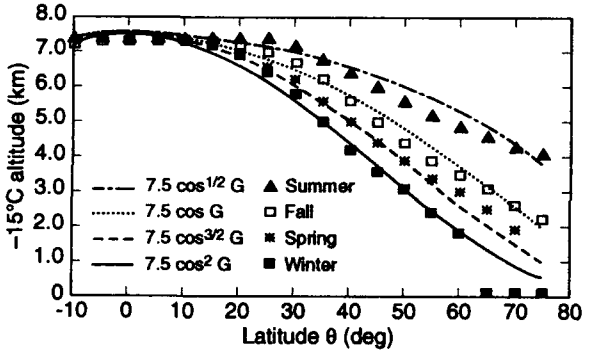

Figure 7. Data analytic fits to the altitude of the -15 C isotherms as a function of latitude and season.

5.4.2. Ratio Of CG To IC Flashes.
Both Pierce [Ref. 26] and Prentice and MacKerras [Ref. 27] have found fits to the CG flashes–IC flashes ratio ($\Xi = N_C/N_G$) as a function of latitude. The Prentice and MacKerras fit is now regarded as the most current:

$$\Xi = 4.16 + 2.16\cos(3\Theta) \qquad (6)$$

We have investigated the relationship between Ξ and the charge height parameter ς of Eq. (5) by plotting the N_G / N_T ratio taken from Eq. (6) as a function of ς in Fig. 8–the fit is almost linear. Thus, the noise model assumes that

$$\Xi = \frac{1}{0.94 - 0.84\varsigma} - 1 \qquad (7)$$

Figure 9 shows the data Prentice and MacKerras used, as well as their fit. In this figure, the points marked Model Summer are the results of Eq. (7) using ς from Eq. (5) for summer. They agree almost exactly up to 60° and, in fact, appear to match the data better at latitudes of 60° and above. The data Prentice and MacKerras used were for summer storms; winter storms have much lower charge centers, so most of the flashes are CG discharges. We have plotted the results for Eq. (7) using winter values of ς in Fig. 9. According to these results, most flashes are CG discharges at high latitudes, which is consistent with experimental data.

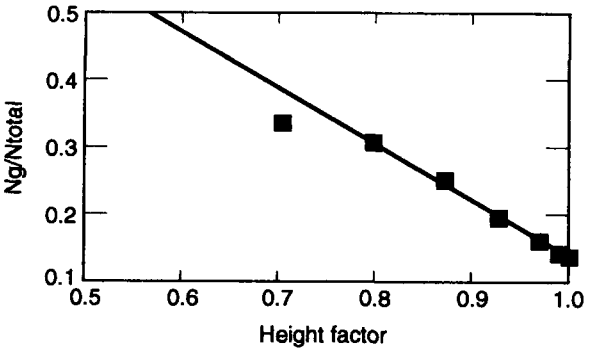

Figure 8. Ratio of CG flashes to total flashes as a function of the height factor.

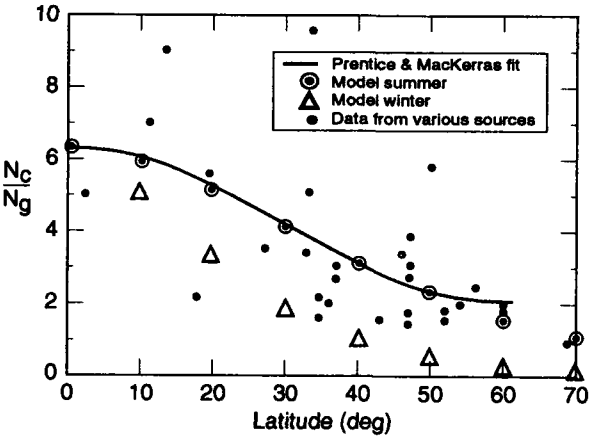

Figure 9. Ratio of CG flashes to total flashes a a function of latitude, showing the Prentice&MacKerras, fit, and the noise model fits.

5.4.3. Positive Lightning.
The recent paper by Biswas and Hobbs [Ref. 28] presented flash rate density data for both negative and positive return strokes along the East Coast of the United States. The ratio of the positive to negative return strokes ranges from 10 to 30 percent. Using data from this and a few other sources (some summarized in Uman [Ref. 15]), we find the following (albeit crude) fit to the percentage of positive lightning in return strokes:

$$\frac{n_P}{n_N} = 1 - \varsigma \qquad (8)$$

5.4.4. Effects On Cloud Size.
Orville [Ref. 29] measured the peak currents in a large number of summer return strokes using the SUNY Lightning Detection Network. This data covers almost the entire United States east of the Mississippi. A clear latitude dependence is seen in the nearly factor of 2 difference in average peak current between Florida and Maine. Orville found that he could account for the difference if there is a dependence of the current on the size of the average cloud. His argument is that the current in the return stroke I depends on the charge Q, which, in turn, should depend on the volume of the thundercloud. Using data from return strokes on Mount San Salvatore near Lugano, Switzerland, Berger [Ref. 30] found that $I \propto Q^{0.7}$. The Noise Model assumes that the cloud dimension d is related to the charge height parameter as $d \propto \varsigma^m$. Here m is a Noise Model parameter, and we are saying that, on average, the closer to the ground the -15° C level is, the smaller the cloud will be. Thus,

$$P \propto \varsigma^{4.2m} \qquad (9)$$

Orville's data suggests $m \approx 1.5$.

At ELF, the published frequency spectrums depend on the model of the return stroke used (see, for example, Galejs [Ref. 31]), a consistent feature being that the spectrum is almost constant over the range of the frequency treated by the model. Rather than select a particular model for the stroke, we have assumed a constant power which has been adjusted to agree with the ELF noise data from the Stanford radiometers. The agreement is very good over the entire 50-300 Hz range.

5.4.5. Bipolar Strokes.
We assume that bipolar strokes occur in all types of flashes. The model assumes that five bipolars occur for every return stroke in a CG flash, and twenty for every IC flash. Thus, in Eq. (4) the average number of bipolar strokes is:

$$N_{0V} = 5N_{0R}n_{CG} + 20(1-n_{CG}) \qquad (10)$$

The bipolar stroke power is taken from Fig. 5. The modifier is:

$$M_{CPR} = \varsigma^{4.2m_C} \qquad (11)$$

We assume that the current in a bipolar is a function of the charge available, as is the current in a return stroke, and so have a modifier for the bipolar power which is the same as Eq. (9).

Lacking data to the contrary, we assume that the modifiers for the horizontally radiating bipolars are the same as for the vertical ones.

5.5. Effects Of Storm Severity.
Large storms produce numerous lightning flashes, and evidence exists that larger storms tend to produce stronger discharges. It is well known, for example, that larger storms tend to have more positive flashes, which can have larger peak currents. We could not, however, find hard data to quantify these effects. Therefore, early versions of the model did not have a storm severity factor. We found that those earlier versions tended to underestimate the noise in the noisiest regions and overestimate it in the quieter ones. Note that all the modifiers we have discussed so far have only the charge height or latitude dependence, so they are the same for regions of low or high flash rate.

The physical justification for a storm severity factor is that large storms tend to have greater updrafts within the clouds. and since updraft speed is related to charge formation, we expect greater power in the flashes. We know that the flash rate, is directly proportional to the updraft velocity [see Vonegut, Ref. 32]; therefore, we base our storm severity factor on this relationship. Thus, we define:

$$M_{SP} = (\dot{N}_T / \overline{\dot{N}}_T)^{m_{SS}} \qquad (12)$$

where $\overline{\dot{N}}_T$ is the average flash rate (≈ 0.1 flashes/s) and m_{SS} = 0.5 if the flash rate is above the average; otherwise, m_{SS} = 2. We take the same factor for all three types of strokes. These parameters have been set to adjust the model predictions to data. The square root is suggested by some results due to Williams [Ref. 33]; WGL also used it. Uman cites reports that indicate that the number of strokes per flash increases as the storm severity increases. However, we could find no hard data on this and so assume that the storm severity modifier on the number of strokes per flash (M_{SN}) is 1 for all types of strokes.

5.6. Terrain Effects.
We have built into LNP a crude terrain map. We speculate that the ratio of CG to IC flashes is greater over mountains, and that the average power radiated per stroke is also greater over mountains. We include the first effect directly by lowering the height of the charge centers based on the average terrain height of the region. However, no data supporting an increase in power per stroke was found, and the effect of ad hoc modifiers was not sufficient to include in the model.

6. LIGHTNING STATISTICS

In this section we discuss how the Noise Model calculates lightning statistics other than the RMS noise value. The model can predict the following statistics: the standard deviation (σ), the voltage deviation [V_D = 20 $\log_{10}$ (RMS / AVG)], and the APD of the noise.

6.1. Lightning As A Random Process.
Lightning is known to be a highly random process, and almost all–if not all–the parameters associated with the model have a probability distribution around their average values. We assume that the density function for most of the quantities we deal with is formulated as:

$$p(x) = \frac{\alpha x^{\alpha-1}}{R^{\alpha}} \exp(-(x/R)^{\alpha}) \qquad (13)$$

This is known as a Weibull distribution. If α = 2, then the distribution corresponds to that of the Rayleigh distribution.
The amplitude-probability distribution is defined to be:

$$\mathrm{APD}(x) = \mathrm{Prob}(X \geq x) = \int_x^{\infty} p(x)dx \qquad (14)$$

Using Eq. (13) in Eq. (14) gives:

$$\mathrm{APD}(x) = \exp(-(x/R)^2) \qquad (15)$$

As an example of this, consider the distribution of peak current in return strokes. In Fig. 10 the curves are fits to data from Berger *et al.* [Ref 34], as shown in Uman [Ref 15]. The axes in Fig. 10 are drawn so that APDs of the form in Eq. (15) are straight lines. The parameters of the fit are given in Table 3.

Table 3. Weibull parameters for peak currents in return strokes.

Type	*a*	R(kA)
First return	1.9	47.5
Second return	1.9	14.9
Positive return	0.85	53.3

The number of subsequent return strokes per flash is drawn in Fig. 11, which is fit to the center of the lines given by Thomson, and plotted in Fig. 6. This gives a fit with α = 1.2 and R = 3.4. We can determine the standard deviation from Figs. 10 and 11, since we know that:

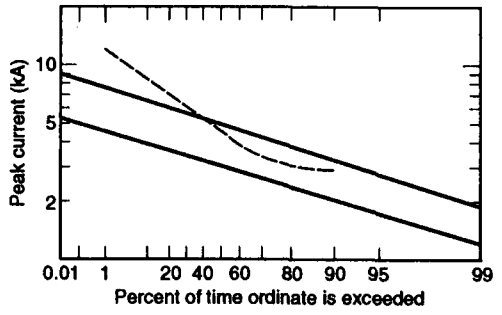

Figure 10. APD of peak currents in return strokes, as a function of type. The solid lines are for negative strokes (upper is first, lower subsequent). Dashed line is for positive strokes.

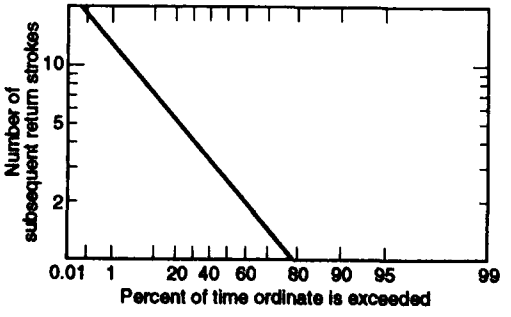

Figure 11. APD of the number of subsequent return strokes per flash.

$$\langle x^n \rangle = \int_0^\infty x^n p(x)dx = R^n \Gamma(1+n/\alpha) \qquad (16)$$

$$\sigma^2 = \langle x^2 \rangle - \langle x \rangle^2 \qquad (17)$$

Thus

$$\sigma^2 = R^2\left[\Gamma(1+2/\alpha) - \Gamma^2(1+1/\alpha)\right] \qquad (18)$$

This leads to Table 4, which expresses the RMS and the standard deviation of return strokes per flash expressed relative to the average.

Table 4. Relative return strokes per flash parameters.

Parameter	RMS / Avg	s / Avg
Negative return	1.14	0.55
Positive return	1.54	1.17
No. of subsequent strokes	1.30	0.83

6.2. Amplitude Probability Distribution (APD) and V_D

Field and Lewinstein [Ref. 35] show that the narrow band APD for long wave noise power can be described by two parameters, which can be determined at the receiver. One parameter, α, characterizes the impulsiveness of the noise from local sources; the other, γ^2, characterizes the ratio of energy in the impulsive-noise component to the energy in the background, non-impulsive component. The parameter α is the same as the parameter in Eq. (13). The method assumes that the local sources have a probability density function given by Eq. (13). The probability density function for the amplitude of the background noise, which is formed by summing the power from many distant lightning storms, will be Rayleigh and can be expressed as:

$$p(y) = \frac{2y}{r}\exp(-(y/r)^2) \qquad (19)$$

Field and Lewinstein show that the APD of the sum of the local and background components can then be written as a function of two parameters: α, and the ratio of the r to R. Since the R's are proportional to the average amplitude of the components, they depend on the average energy in the components; thus, we arrive at the parameter γ^2. Field and Lewinstein found that they could attain agreement with noise data measured at Boulder, Colorado, at 22 kHz in a 5 percent bandwidth, if $\alpha = 0.4$ and $\gamma = 5.50$.

The parameter α depends on the pulse characteristics of the local component and on the bandwidth of the receiver. Typically, α becomes larger as the bandwidth is reduced, reaching 2 for narrow band noise. For $\alpha < 2$, the probability density function Eq. (13) assumes relatively large values for large arguments, indicating the occurrence of intense noise impulses. Thus, the smallest values of α correspond to the most impulsive noise.

As a measure of the impulsiveness of the noise, CCIR 322-3 defines the voltage deviation, V_D, as the ratio in dB of the RMS noise to the average noise. Impulsiveness, when observed at the receiver output, is related to the bandwidth of the receiver. As the bandwidth gets narrower, the noise pulse spreads out in time, so more pulses tend to overlap at the receiver–which decreases the V_D. Pulse spreading (dispersion) becomes more pronounced as the propagation path increases. Thus, the farther away the average lightning is from the receiver, the lower the V_D. Clearly V_D is also related to α and γ.

The noise model estimates V_D and APD by assigning value for the parameters α and γ to each individual ENT. These values are functions of the number and kinds of strokes that make up the ENT. Then LNP adjusts the parameters based on the distance of the ENT from the receiver, and then assigns the noise power from the ENT to either the implusive or Gaussian component of the the total noise based on the value of γ. In this way almost all of the energy from a nearby noise source is put in the implusive component. If the ENT is far enough away, all the energy is taken to be Gaussian. In this way we can determine an effective value for γ. Then LNP uses it and the value of α from the closest ENT to determine the final total values for V_D and APD. The values that LNP calculates are done assuming a five percent bandwidth, and adjusted to other bandwidths using the method described in CCIR 322-3.

LNP adjusts the value of α because of the tendency of noise pulses to spread out in time as they propagate down the earth-ionosphere waveguide. This tendency results from waves with different frequencies propagating with different phase velocities. Thus, the effective α for a particular ENT depends on the distance between the ENT and the receiver.

This method is not an attempt to closely model the physical situation, but can produce resonable agreement with experimental data in most cases. This is an area of continuing research.

7. VALIDATION OF RESULTS

Validation of LNP is an ongoing effort. This work can be roughly divided into three areas. First, we review the physical models we use for the various lightning processes as new data becomes available. Second, as discussed above we are making a major effort to validate the underlying lightning distribution data. Third, we are always comparing the noise predictions of LNP with data. In this section we will present some comparisons of the current model with data. It is not possible here to present all of our validation comparisons due to lack of space, so we have selected some representative results. Because horizontally polarized noise data is so scarce, we will only present comparisons to vertically polarized noise data. In the following, the term *Day* refers to 1500 local time; *Night* means local midnight. When the user requests a prediction at a particular time, LNP determines in which 4 hour time block the time falls and changes the request so that it is at the center time for that time block. The next version of LNP will allow the user to request that LNP do an interpolation between two time blocks.

7.1. July Day, at Several Locations, 13 kHz.

At frequencies near 10 kHz, the power frequency spectrum for bipolar strokes shows that they make almost no contribution to the noise power. Thus noise at this end of the VLF range is entirely due to the return stroke. Since return strokes are so well studied, we expect the internal representations to be fairly accurate. Figure 12 below shows this to be the case. The com-

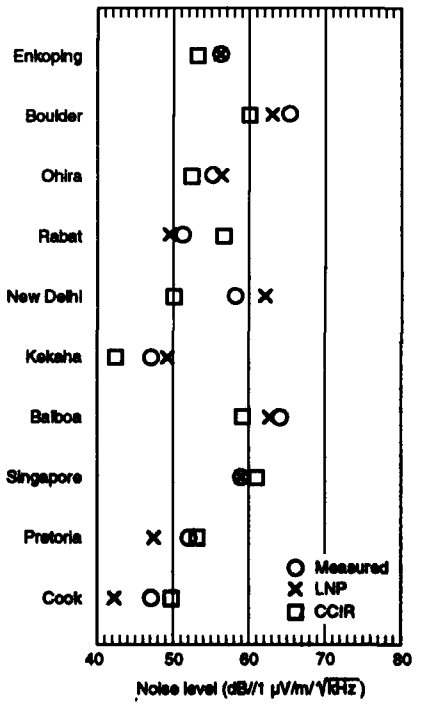

Figure 12. Comparisons at 13 kHz, at Several Locations, for a July Day.

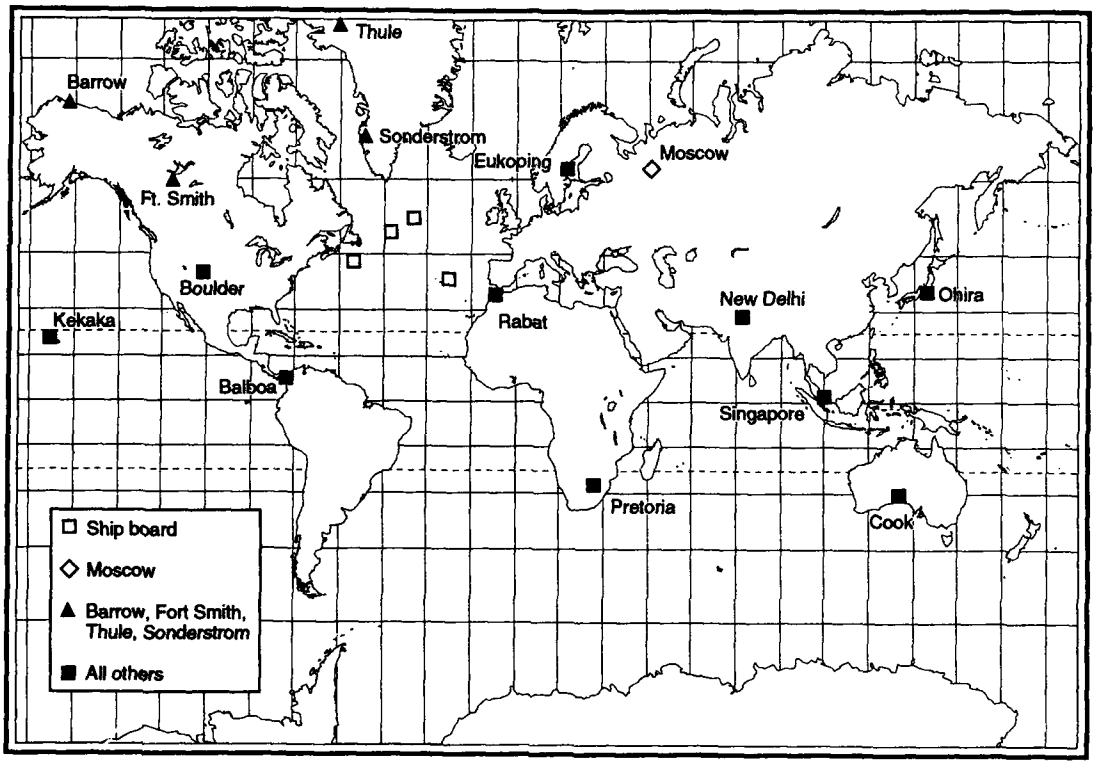

Figure 13 Data Collections Locations used in Comparisons.

parisons in this figure are to data collected for the CCIR database. *Also shown in this figure are predictions from the computerized version of CCIR 322-3 for those locations. We do this in order to give some idea of the degree of variability from the data one might expect from a noise prediction code.*

7.2. January Day, Moscow, 13 to 60 kHz.
Figure 13 presents data at several frequencies at a single location. For the reasons discussed above, it was difficult to produce correct predictions for the winter time block. The figure shows that we have solved the winter day problem.

7.3. July Day, Mid Atlantic Locations, 21 kHz.
Since the CCIR data was taken at land station, an extrapolation scheme was used to produce noise predictions at other locations. Thus we might expect that the predictions from CCIR 322-3 would depart from measured noise the most at locations remote from the data stations, such as in mid ocean. LNP, on the other hand, should have no particular difficulties at these locations. The data in Fig. 14 were taken on board a ship during July. Again the agreement between LNP and the data is very good.

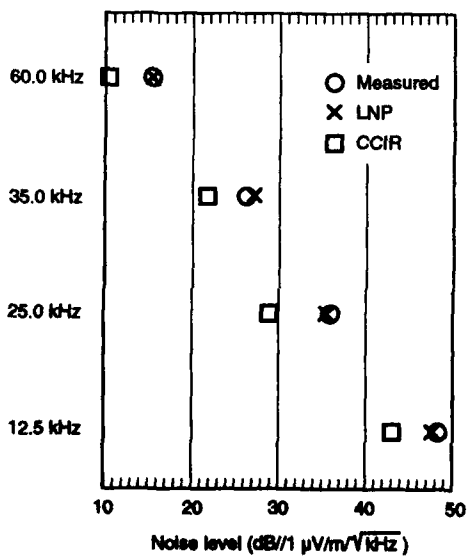

Figure 14 Comparisons for a January Day, at Moscow, Frequencies from 13 to 60 kHz.

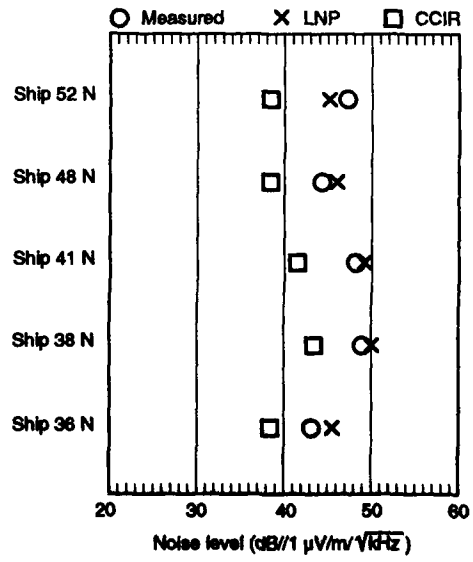

Figure 15. Comparisons at 21 kHz, for Mid Atlantic Locations, July Day.

7.4. July Day and Night at Several Locations, 51 kHz.

At the upper end of LNP's frequency range, the lightning noise power is dominated by the bipolar strokes. Since less is known about the bipolar, we might expect that LNP's predictions would not match the data as closely. From Fig. 15, which shows day time data and predictions, this appears to be the case. Note that LNP gives very good agreement in some cases, specifically Singapore, and Kekaha, but very poor agreement at New Delhi. The agreement is better at night as can be seen from Fig. 16. In general, LNP's night predictions match data better than day predictions. We believe that this is due to the fact that at night the propagation attenuation is less than during the day. This allows noise to propagate over longer distances than during the day. During the day, the noise at a single location tends to be dominated by one or two ENTs because the greater attenuation means that only a small number of ENTs sum to the total noise. At night this tends not to be the case since many more ENTs contribute to the total noise.

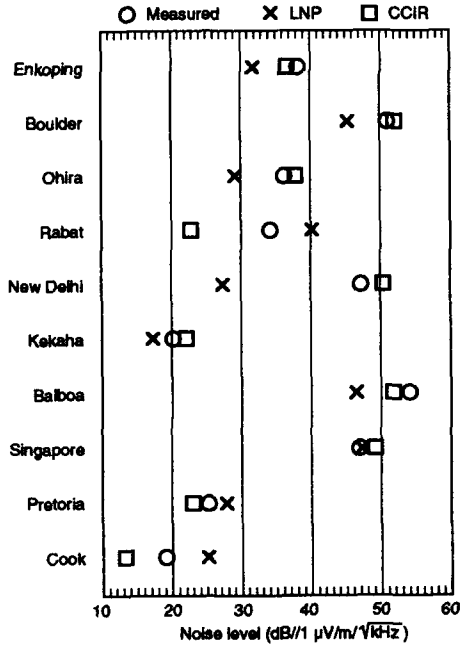

Figure 16. Comparisons at 51 kHz, at Several Locations, for a July Day.

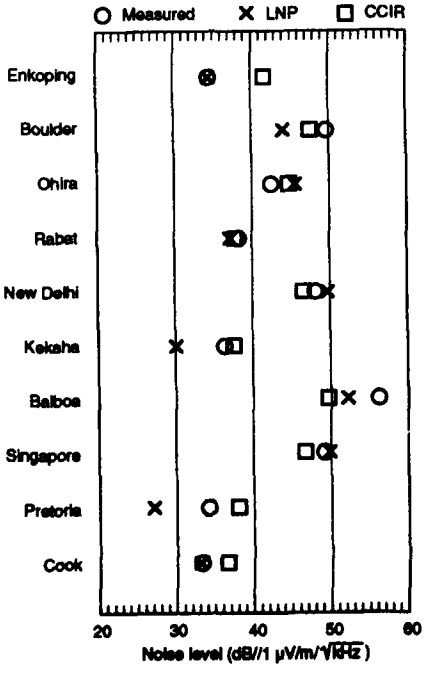

Figure 17. Comparisons at 51 kHz, at Several Locations, for a July Night.

7.5. Noise at High Latitudes.

It is well known that CCIR 322-3 has problems with noise at high latitudes. One of their data stations–Thule Greenland–is believedto be contaminated with man-made noise. In the table below we present data from several high latitude locations compared to predictions from LNP and CCIR 322-3. Two of the locations (Thule and Sondre Stromfjord) are from the Stanford radio noise survey. The data from Fort Smith was taken by Wilfred Lauber [Ref. 36] at frequencies normally used by the Annapolis and Cutler VLF transmitters. This data was taken during periods when the transmitters were off the air for maintenance. It should be noted that there are only a few data points in this data set, not enough for meaningful statistics to be calculated; thus, the data given in the table represents range of noise measurements Lauber found.

Table 5. Comparison of High Latitude Day Data with LNP Predictions.
Data and Predictions in dB//1μV/m.

Location	Frequency (kHz)	Season	Data	LNP	CCIR
Thule	32	Summer	29	31	33
Thule	32	Winter	14	17	30
SondreStrom	32	Winter	12	19	30
Fort Smith	21.4	Summer	32-34	34	38
Fort Smith	24	Summer	28-34	31	35
Fort Smith	21.4	Winter	17-26	23	33
Fort Smith	24	Winter	19-24	22	32

7.6. ELF Results

Figure 18 shows the comparison of a number of high latitude ELF data points with the results of LNP. In general, the agreement of LNP with ELF data in the range from 10 Hz to

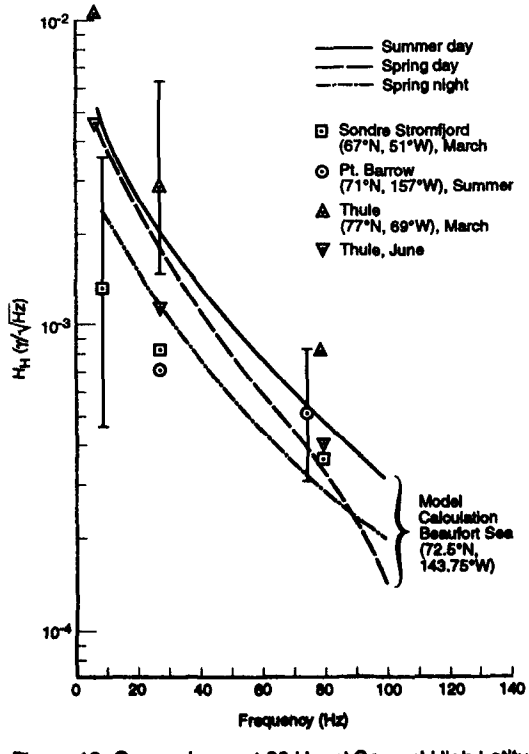

Figure 18. Comparisons at 80 Hz, at Several High Latitude Locations, for a Spring Day.

300 Hz is very good. Table 6 is a selection of ELF data from the Stanford survey compared to the results from LNP.

Table 6. Comparison of Predictions and Data from the Stanford Radio Noise Survey at 80 Hz.

Location	Season	Time	Data	LNP
Stanford CA	Summer	1200	43	44
Stanford CA	Summer	0000	42	47
Dunedin NZ	Summer	1200	37	37
Dunedin NZ	Summer	0000	37	41
Kotchi, Japan.	Winter	1200	40	41
Kotchi, Japan.	Winter	0000	40	46

8. CONCLUSION

LNP was originally conceived as an extension of the WGL model to predict horizontally polarized noise. We found that the original WGL code could not easily be adapted, and so decided to completely abandon it and create a new model. In general, LNP works well. We are continuing to develop the model and validate the code. Since the underlying lightning occurrence database is very important to the results of the model, we are in the process of validating it at the present time. To do this, we are comparing the ISS-b data with ground based lightning occurrence data. In particular we will use data from the lightning detection network that covers the entire continental United States. This should give us a direct comparison to the ISS-b data. In addition, a recent paper by Price and Rind [Ref. 37] gives a method to predict lightning occurrence from cloud height data that is available from weather satellites. This would give us another comparison to worldwide, long term data.

The current version of the model has some problems producing close agreement with experimental data in regions near moutainous terrain. We are adding a terrain map and terrain modifiers to the model to address this problem. Another shortcoming of the model seems to involve receiver locations near, or in, the day-night terminator. We may have to introduce a new propagation model to handle this situation.

Other ongoing research on the model includes an effort to improve the method used to calculate APD and V_D as well as adding short term noise statistics of interest to receiver designers, such as pulse width, spacing, and height predictions. We will also be adding the ability to use specific, as opposed to average, weather patterns as the basis of the predictions.

We are also looking into the general problem of how a noise model can be validated. This involves both developing a master set of reference noise data that the user community believes to be valid and determining what comparisons to that data would be adequate to validate the model predictions. The kinds of comparisons we have shown here only suggest that the model is valid, but they do not really demonstrate it.

9. REFERENCES

1. CCIR (International Radio Consultative Committee), "World Distribution and Characteristics of Atmospheric Radio Noise," International Telecommunications Union, Geneva, Switzerland, Report 322-3, 1986.
2. Spaulding, A. D., and Washburn, J. S., "Atmospheric Radio Noise: Worldwide Levels and Other Characteristics," U.S. Department of Commerce, NTIA Report 85-173, April 1985.
3. Maxwell, E. L., et al., "Development of a VLF Atmospheric Noise Prediction Model," Westinghouse Georesearch Laboratory, Report 70-1H2-VLF No-R1, 30 June 1970.
4. ???
5. Fraser-Smith, A. C., et al., "A New Global Survey of ELF/VLF Radio Noise," Space, Telecommunications and Radioscience Laboratory, Stanford University, presented at the NATO/AGARD Conference on Effects of Electromagnetic Noise and Interference on Performance of Military Radio Communication Systems, Lisbon, Portugal, October 1987.
6. Warber, C. R., and Field, E. C., "Long Wave Atmospheric Noise Model: Phase I--Vol. 2, Mode Parameters," Defense Nuclear Agency, Report DNA-TR-88-239-V2, 14 October 1989.
7. Kotaki, M., et al., "Global Distribution of Thunderstorm Activity Observed with ISS-b," J. Rad. Res. Lab. (Tokyo), *28, 125-126*, March/July 1981, pp 49-71.
8. Radio Research Laboratories, "World Distribution of Thunderstorm Activity Obtained from Ionosphere Sounding Satellite-b Observations," June 1979 to May 1980, Ministry of Posts and Telecommunications, Japan, October 1981, pp 59.
9. Kotaki, M., and Katoh, C., "Global Distribution of Atmospheric Radio Noise Derived from Distribution of Lightning Activity," J. Rad. Res. Lab. (Tokyo), *30, 129*, 1983.
10. Greifinger, C., et al., "Modeling of TM and TM VLF Atmospheric Noise," Research Development Agency, RDA-TR-026128902-001, August 1989.
11. Turman, B. N., and Edgar, B. C., "Global Lightning Distributions at Dawn and Dusk," J. of Geophys. Res, *87, C2*, February 1982, pp 1191-1206.
12. Orville, R. E., and Spenser, D. W., "Global Lightning Flash Frequency," Mon. Weather Rev., *107*, 1979, pp 934-943.
13. Turman, B. N., "Analysis of Lightning Data From the DMSP Satellite," J. Geophys. Res., *83, C10*, October 1978, pp 5019-5024.
14. Anderson, R. B., et al., "Lightning and Thunderstorm Parameters," International Conference on Lightning and Power Systems, London, England, 1984, pp 57-61.
16. Uman, M. A., The Lightning Discharge, Academic Press, Inc., Orlando, Florida, 1987.
17. Rinnert, K., et al., "Characteristics of Magnetic Field Pulses in Earth Lightning Measured by the Galileo Probe Instrument," J. Geophys. Res., *94, D11*, September 30, 1989, pp 13,229-13,253.
18. Orville, R. E., et al., "An East Coast Lightning Detection Network," Bull Am. Meteorol. Soc., *64*, 1983, pp 1029-1037.
19. Orville, R. E., et al., "Cloud-to-Ground Lightning Flash Characteristics From June 1984 through May 1985," J. Geophys. Res., *92, D5*, May 1987, pp 5640-5644.
20. Richard P., et al., "SAFIR: Lightning Monitoring and Warning Systems," presented at 22nd General Assembly of the International Union of Radio Science, Tel Aviv, Israel, 24 August - 2 September 1987, subsequently published by the Office National d'Etudes et de Recherches Aerospatiales, Chantillon-sous Bagneux, France, as TP No. 1988-4.
21. Thomson, E. M. "The Dependence of Lightning Return Stroke Characteristics on Latitude," J. Geophys. Res., *85*, pp 1050-1056.
22. Thomson, et. al. [1984]
23. Schonland, B. F., "The Lightning Discharge," Handb. Phys., *22*, 1956, pp 576-638.
24. Turtle, J. P., et al., "Low-Frequency Transverse Electric Atmospheric Noise: Measurement and Theory," Rad. Sci., *24*, 1989, pp 325-339.
25. Krehbiel, P. R., et al., "Lightning Charge Structure in Thunderstorms," Proc. Atmos. Elect., L. H. Ruhnke and J. Latham (eds.), Deepak Hampton, Virginia, 1983, pp 408-411.
26. Oort, A. H. and Rasmusson, E. M., "Atmospheric Circulation Statistics," NOAA, Department of Commerce, Rockville, MD, 1971.
27. Pierce, E. T., "Latitudinal Variation of Lightning Parameters," J. Applied Meteo., *9*, 1969, pp 194-195.

28. Prentice, S. A. and MacKerras, D., "The Ratio of Cloud to Cloud-Ground Lightning Flashes in Thunderstorms," J. Applied Meteo., *16*, 1977, pp 546-550.

29. Biwas, K. R., and Hobbs, P. V., "Lightning Over the Gulf Stream," Geophys. Res. Let., *7*, June 1990, pp 941-943.

30. Orville, R. E., "Peak-Current Variations of Lightning Return Strokes as a Function of Latitude," Nature, *343*, 1990a, pp 149-150.

31. Berger, K., "The Earth Flash," Lightning, *1*, Chap. 5, R. H. Golde (ed.), Academic Press, New York, 1977, pp 119-190.

32. Galejs, J., "Terrestrial Propagation of Long Electromagnetic Waves," Permagon Press, London, 1972.

33. Vonnegut, B., "Some Facts and Speculations Concerning the Origin and Role of Thunderstorm Electricity," Meteorol. Monogs., *5*, 1963, pp 224-241.

34. Williams, E. R., "Large-Scale Charge Separation in Thunderclouds," J. Geophys. Res., *90, D4*, June 1985, pp 6013-6025.

35. Berger, K., et al., "Parameters of Lightning Flashes," Electra, *80*, 1975, pp 23-37.

36. Field, E. C., and Lewinstein, "Amplitude-Probability Distribution Model for VLF/ELF Atmospheric Noise," IEEE Trans. on Comm., *COM-26*, 1978, pp 83-87.

37. Wilfred Lauber, 1991, private communication

38. Price, C. and D. Rind, "A Simple Lightning Parameterization for Calculating Global Lightning Distributions", JGR, 97,June 1992

Discussion

INAN

COMMENT. 1) Does your model properly calculate the propagation of noise in the wave guide cutoff regions below about 1.8 khz? 2) Can we use the model to estimate atmospheric noise at South Pole?

AUTHOR'S REPLY

1) The current version of the code does not give predictions in the range 500 Hz to 8kHz. This frequency range is out of the "communication band", and there was no interest in this range when we started the project.

2) (See text over).

TACCONI

COMMENT. In your presentation you mention the additional contribution of spiky noise to the previous gaussian distributed noise. Is that addition affecting the gaussianity of the resulting noise?

AUTHOR'S REPLY

The model assumes that the total power that reaches the receiver from a single equivalent noise transmitter can be divided into Gaussian and spiky parts. It keeps track of these components from each equivalent transmitter and uses the totals of these components to estimate the APD and the parameter V_D. There are more details of the procedure in the printed text.

BURKE

COMMENT. Does your model go down to the lower ELF band and if no, can you predict Schumann resonance spectra ?

AUTHOR'S REPLY

Although we allow the user to request predictions down to 10 Hz, the present version of the code is not really designed to predict values less than 50 Hz. Thus we do not predict the Schumann resonance spectra. In principle we could attempt to predict these spectra.

INAN

COMMENT. Concepts such as APD and rms are valid mostly for Gaussian Noise, where as the nature of lightning noise is impulsive. If you had a communication system with 1 Khz bandwidth, say around 20 Khz, then in principle you would have a time resolution of 1 ms. Thus, if you subdivide the time series into intervals of $\sim$1ns, we should see discrete noise and very large variability from one interval to another. Is this the case? I assume this is what you mean by short term statistics?

AUTHOR'S REPLY

I believe that this is correct. Research into our next version of the code, where we will try to predict short term statistics, has not yet begun in earnest.

APPLICATION OF NON-STANDARD SIGNAL PROCESSING TO ELF NOISE CHARACTERIZATION FOR THE TSS1-OESEE PROGRAMME

G. Tacconi (*), A. Tiano (**), S. Pagnan (***)

(*) Department of Biophysical and Electronic Engineering
University of Genova, Via all'Opera Pia 11/A, 16145 Genova, Italy

(**) Department of Information and Systems
University of Pavia, Via Abbiategrasso 21, 27100 Pavia, Italy

(***) Institute of Ship Automation of C.N.R.
Viale Causa 18R, 16145 Genova, Italy

Summary

Within the framework of the TSS1 (Tethered Satellite System)-Project a measurement programme on the electromagnetic background noise has been foreseen. This programme, denominated OESEE (Observation on the Earth Surface of the Electromagnetic Emissions), intends to carry out a number of passive detections of possible emissions by the orbiting tethered system. From theoretical considerations on the cold plasma theory in the ionosphere, the expected frequency band of these emissions should be in the order of about 1 Hz up to 60 hz.

In order to design an optimal receiver of such a signal, the noise statistical characteristics have to be taken into account. From the literature, it has been proved that this noise is characterized, from the statistical viewpoint, by a non gaussian and non stationary behaviour.

This paper outlines some recently proposed applications of non gaussian and non stationary signal processing techniques which can be usefully applied to ELF (Extremely Low Frequency) electromagnetic noise characterization for detection and parameter estimation purposes.

Some simulation examples are presented together with some results obtained from experimental data of natural background noise in the ELF range recorded at Canary Islands as a preliminary test of the TSS1 mission.

The TSS1 (Tethered Satellite System) is a NASA/ASI (Agenzia Spaziale Italiana) research Project.

1. Introduction

The TSS1 is a spatial experiment carried out according to an international cooperation between the NASA (USA) and ASI (Italy). The experiment, described in details in several publications [1,2,3], is essentially based on a space Shuttle vehicle which is towing, by means of a long tether (about 20 Km) a spherical satellite of 1.5 meter diameter. The TSS concept was initially conceived as a pure dynamical system, namely a large, flexible, structure orbiting in the ionosphere and obeying only to mechanical laws. Since, on the other side, the TSS1 contains a long conducting tether, consequently all the orbiting structure will interact also with the environmental earth magnetic field and the ionospheric plasma electrical field, thus implying also electrodynamical effects connected with the experiment.

The TSS1 vehicle orbiting in the ionosphere can be practically regarded as a self powered radiating antenna which transforms kinetic energy into electromagnetic energy. The combined interaction between the orbiting system, the earth magnetic field and the ionospheric plasma produces a complex phenomenon of radiation of electromagnetic perturbations in the ELF bands : the Alfven waves [1] and [2]. The Alfven waves can be interpreted as an example of spontaneous radiations generated by electrodynamic phenomena. The exact wave form, however, is not well known, owing to the complexity of the plasma effects. Another possible artificial electromagnetic radiation source is constituted by the modulation of the current in the tether itself.

The generation of electromagnetic emissions by the tether has been investigated by Grossi and Estes of the Smithsonian Astrophysical Observatory in Cambridge, M.A. (USA) and the main results of such researches are contained in [1].

Accordingly, the following basic assumptions for the estimation of the signal produced by the tether have been formulated :

i) a guided mode of propagation in the earth surface-ionosphere cavity;

ii) a non-guided mode isotropic propagation through the earth atmosphere.

According to such a simplified propagation model, the region of the earth's surface that is "illuminated" by the possible emissions by the tether is a limited area located around the vertical projection of the orbiting TSS. This area can be called "hot spot" and its definition is a consequence of the propagation model (ii) and accordingly the receiving site should be selected as close as possible to the center of this area. On the contrary, in the case of propagation model (i), the reciving site can be everywhere . Pappert [5] and Wait [6] suggest a propagation model according to which the source embedded in the ionosphere can be regarded as an elementary dipole of infinitesimal length, which apparently seems to be an incorrect assumption in the case of 20 or 100 Km tether. A comprehensive essential research programme is therefore needed in order to achieve a better knowledge about the complex underlying physical process. The first step towards this direction is to ascertain theoretically and/or experimentally the structure of the signal radiated by the TSS, while the second is to achieve an appropriate modelling of the real propagation conditions through the real medium from the ionosphere to the earth's surface.

2. The TSS Transmission Channel Model

The general propagation scenario for the TSS1 experiment is represented in Fig.1, and in Fig.2 it is shown a block diagram representing the associated transition channel. As it can be noted, the OESEE programme is mainly concerned within the detection section, but it is worth noting that inputs from the other tasks (transmitter and medium) are essential to the accomplishment of the whole programme.

In spite of the lack of a complete knowledge of the characteristics of the expected signal, some likely hypotheses can be made in order to define a suitable signal processing strategy. For this purpose, it seems to be quite reasonable to make the assumption of being in the presence of a very poor signal to noise ratio.Furthermore, it can also be expected [10], that the ELF noise may exhibit a non gaussian behaviour of the type illustrated in Fig.9.

Consequently, the processing approaches which, in addition to the classical conventional ones, have been considered are :

i) After-the-fact-detection;

ii) Spatial processing;

iii) Non gaussian analysis;

3. After-the-fact-detection

Under the assumption that the emitted signal is due to a known modulation by the TSS in a frequency band for which the far field conditions are accomplished, the physics of the propagation scenario suggests that the expected received signal should consist of an increase of level in the appropriate frequency band, which reaches a maximum value corresponding to the closest point of approach to the receiver and then vanishes on getting away. The received signal is expected to be slightly different from the one which is transmitted owing to the modifications introduced by the interactions with the propagation medium scenario.

The problem, in its general outline, can be therefore formulated as a typical detection of a transiting signal with a poorly known waveform, which is a classic problem in many applications like, for example, seismic processing, sonar and radar surveillance techniques, etc. An extensive research activity has been carried out, during the last decade, in the theoretical and in the practical field concerning detection and estimation. These two techniques have been generally regarded as two separate statistical tasks. The detection in terms of hit probability of detection, which implies the surely presence of the signal, is performed under the simple binary hypothesis which considers the presence or the absence of the signal independently of any signal parametrization. From the statistical theory of decision, it can be shown that the optimum Bayes detector consists of the comparison of a generalized likelihood ratio with a proper threshold fixed by the estimation cost function, [7]. The analysis performed by Esposito [8] shows that the in case of a gaussianity hypothesis concerning signal and noise, the optimum detector is obtained by a Maximum Likelihood principle.

A further interesting result is due to Porat and Friedlander [11], which show that an appreciable improvement in the detector performances can be achieved by including some a-priori information in the detection scheme. This can be done in a quite general fashion, as far as linearity assumptions are valid, by using ARMAX models, which provide a very general tool for modelling, according to a black-box principle,unknown stochastic discrete-time dynamic systems perturbed by gaussian white noises.

A block-diagram of the ARMAX model is illustrated in Fig.3, where the relationship between known modulating input signal x(t), unknown signal s(t), measured signal r(t) and noise n(t) is shown. Such relationship can be expressed by a finite difference stochastic equation of the type :

$$r(t)= \sum_{1}^{p} b_k x(t-k) + \sum_{1}^{p} a_k r(t-k) + e(t) + \sum_{1}^{p} c_k e(t-k) \quad (1)$$

where e(t) is assumed to be a sequence of identically distributed gaussian white noises. According to [11], it is possible to combine detection with parameter estimation by means of a MGLRT (Modified Generalized Likelihood Ratio Test), which estimates the model order p and the unknown parameter vector

$$\theta = [a_1 a_2 .. a_p \; b_1 b_2 .. b_p \; c_1 c_2 .. c_p]^T \quad (2)$$

on the basis of finite time histories of input/output pairs (x(t), r(t)), t=1,..N.

A recently proposed algorithm [12] allows to determine the model order p before any parameter estimation. This approach is based on a SVD (Singular Value Decomposition) algorithm, and attempts to determine the maximum number of eigenvalues different from zero which supplies the best approximation to the sample autocorrelation matrix.

In order to estimate the unknown parameter vector θ, a number of methods can be used, all of which attempt to minimize a preset cost function which takes into account the difference between the observed output signals r(t) and the corresponding model prediction of s(t). A detailed presentations of these methods can be found in [13].

The advantage of the above approach over conventional pure detection methods is shown in Fig.4, where the probabilities of detection of a Energy Detector (E.D.) [14] and the proposed MGLRT are compared on a theoretical basis. In Fig. 6. the same comparison is carried out on the basis of a simulated signal plus noise example modelled by a 2nd order ARMAX, the time history of which is shown in Fig. 5. As it can be appreciated, the probability of false alarm is 0.1, while there is a significant performance improvement for signal-to-noise ratios above -10 dB.

4. Spatial processing

Since the radiating orbiting system will pass close to the vertical of the islands of Mona (Puertorico) and Tenerife (Canaries), these two islands can be used as a dipole which, at least in principle, can process and spatially reduce the background noise in the 15-30 Hz spectral region. In case the radiated signal does not contain a significant energy in such a frequency band, the two-islands system can also be used to detect lower frequency energy by means of different approaches.

The theory and methodology of this spatial processing are reported in details in [9]. The geometry of such a detector is illustrated in Fig.7.

The two islands have a separation of 1/2 wave length at 30 Hz (about 5000 Km) and can be used as the locations for two receivers sets, forming a dipole antenna at this frequency, as shown in Fig.8. It can be shown that such dipole can provide the possibility to perform a spatial processing gain to facilitate detection on the earth surface of radiation from the TSS. A further gain can be achieved by using the after-the-fact detection method of the transiting target in order to esploit the transitory nature of the time domain signal, as discussed in the previous paragraph. In the case of a significative detected energy at an even lower frequency (1-3 Hz), the two-islands approach can be used in an incoherent mode to achieve a gain of about 3-6 dB in addition to the one supplied by the transiting target detector alone.

5. Non gaussian analysis

As it is well recognized, one of the most used tool for signal processing is constituted by Power Spectral Density (PSD) estimation. The different PSD estimation techniques can be divided into different classes, which include :

Fourier methods;

Maximum Likelihood;

Maximum Entropy;

Maximum Energy;

ARMAX;

A very large number of studies have demonstrated that each of the above mentioned methods is characterized by specific advantages and limitations in terms of estimation error, computational complexity ,etc. The suitability of each method generally depend on the intrinsic characteristics of the signal which has to be processed.

It should be noted, however, that most of the above mentioned methods strongly rely on a gaussianity and linearity asssumption concerning the signal and the noise. Therefore, expecially when a poor knowledge is available about the underlying processes, suitable tests are strongly recommended in order to determine if such assumptions are effectively verified in practice.

The most used techniques for testing gaussianity and linearity are based on the analysis of Higher Order Spectra (HOS), and particularly on bispectrum analysis [15]. The main advantages of HOS tecniques can be concisely enumerated :

i) provide information about deviation from a gaussian behaviour;

ii) possibility of a phase estimation for a non gaussian signal;

iii) detection and characterization of non linear properties.

The test based on bispectrum analysis, also called Hinich test [15], applies to every zero-mean stationary time series $\{X(t)\}$, the bispectrum $B(f_1,f_2)$ of which can be defined as a two-dimensional Fourier transform of the bicovariance function :

$$C_{xxx}(n,m)=E[X(t+n)X(t+m)X(t)] \quad (3)$$

given by the generalization of the spectrum relationship:

$$B(f_1,f_2)=\sum_n \sum_m C_{xxx}(n,m)\, e^{-2\pi i(f_1 n+f_2 m)} \quad (4)$$

It can be easily shown that the 3rd order cumulant $C_{xxx}(0,0)$ verifies the following :

$$E[X(t)^3]=C_{xxx}(0,0)=\int_{-1/2}^{1/2}\int_{-1/2}^{1/2} B(f_1,f_2)df_1df_2 \quad (5)$$

The bispectrum can thus be interpreted as a frequency decomposition of the 3rd order moment of a time series. The above relation can be easily extended to higher order moments of the time series.

In order to test gaussianity, however, it is sufficient to limit the analysis to 3rd order moment . In fact, it can be shown [15] that a suitable test is supplied by the relation :

$$\frac{|B(f_1,f_2)|}{S(f_1)\,S(f_2)\,S(f_1+f_2)} = \frac{\mu_3^2}{\sigma^6} \quad (6)$$

where $S(f)$ is the spectrum of $\{X(t)\}$ and the constant μ_3^2/σ^6 is the square of Fisher's skewness measure associated to linear representation of the time series.

From the above relation it follows that ,if one supplies in (6) the corresponding estimates for bispectrum and spectrum, the test allows to conclude that :

i) linearity of $\{X(t)\}$ implies constancy of the ratio for every pair of frequencies f_1 and f_2;

ii) gaussianity implies that the ratio is zero for every pair of frequencies f_1 and f_2.

The test is robust and powerful even on small samples (as low as 256) and is furthermore characterized by nice asymptotic properties.

In Fig.10 an example of bispectrum relative to a non gaussian and non linear process is shown.

Once a given stationary process has been recognized to be non gaussian or non linear, the task of a statistical characterization should be accomplished. We note that the bispectrum itself can supply a qualitative tool by means of the coupling existing between different frequency pairs. The problem of determining a more quantitative characterization is a matter of current research; an interesting approach based on Gabor representation is suggested in [16].

6. Experimental results and conclusions

This presentation has been prepared before the TSS1 mission, which took place from 31th July until 8th August 1992. Consequently its content represents essentially intentional tasks aimed to detect possible radiations from the orbiting TSS1 on the ground track.

The OESEE programme was performed by employing two sets of tri-axial magnetometers (one of the air-coil type and the other one of SQUID type), both located at the Tenerife island in Canaries (Spain). During about 55 hours of continuous recording,while the TSS1 mission took place, about 1.2 Giga bytes of data were collected and are now in the phase of reduction and analysis. Unfortunately, it is not possible to communicate at the moment any relevant result.

A part of real data recorded in December 1989 at Tenerife Islands and at IAN Laboratory in Genoa, have been analyzed by means of conventional signal processing methods as a preliminary integration test of the data acquisition system deployed during the OESEE programme. Some results obtained from the preliminary analysis of such data are concisely presented together with a discussion of the software developed for processing the experimental data.

A block diagram of the computer programs designed and developed for non conventional signal processing is shown in Fig.11.

After a pre-processing phase, which includes conventional statistical analysis (graphical presentations, elementary statistics, spectral analysis, digital filtering,etc.), a transient test is carried out in order to verify if the recorded data can be classified as stationary or not. In the first case, after bispectrum computation, Hinich test is carried out for verifying gaussianity and linearity. In any case, an ARMAX identification is developed for detection purposes, while in case of non gaussianity, suitable qualitative characterizations are performed by an interactive procedure.

In case of a non stationarity assessment, the signal classification is carried out on the basis of Middleton approach [17], [18] and, subsequently, a Gabor detector [16] is applied.

An example of evolutionary Power Spectral Density of vertical ELF background noise recorded over 40 hours by an air-coil sensor in Genoa, is shown in Fig.12. A

highly non stationary behaviour can be noticed.

In Fig. 13 and 14 , PSDs of horizontal and lateral ELF background noise recorded at Tenerife are shown. It is worth noting that from such preliminary anaysis the well known Schumann resonance frequencies are evidentiated with a good approximation.

As a final concluding remark, it is possible to say that the complete analysis of TSS1-OESEE data may be an interesting opportunity for applying challenging non conventional signal processing techniques to an advanced electromagnetic communication problem.

7. References

[1] Grossi M.D. "Spaceborn long vertical wire as a self-powered ULF/ELF radiator", Trans. IEEE JOA, July 1984, Special Issue on ELF Communications, Vol.OE-9,N.3.

[2] Colombo G.,E.M. Gaposchkin,M.D. Grossi and G.C. Weiffenbach "Long-tethered satellite for the Shuttle orbiter", International Conference on Technology of Scientific Space Experiments, Paris, May 1975.

[3] Estes R.D. and M.D. Grossi "Self-powered drag-compenseted tethered satellite system as an orbiting transmitter at ULF/ELF ", NASA/AIAAA/PSN International Conference on Tethers in Space, Washington, 17-19 September 1986.

[4] Estes R.D. "Alfven waves from an electrodynamic tethered satellite system", Journal of Geophysical Research, Vol.), N.A2, pp.945-956, Feb.1988.

[5] Pappert R.A. "Excitation of earth-ionospherewaveguide by point source at satellite heights", Radio Science, Vol.8, N.6, June 1973.

[6] Wait J. and E. Einaudi "Analysis of the excitation of the earth-ionosphere waveguide by a satellite nborn antenna", Canadian Jornal of Physics, 1971.

[7] Middleton D. "Introduction to statistical communications", MacGraw Hill, New York, 1960.

[8] Esposito E. "A class of estimators for optimum adaptive detection", Information and Control, Vol.10, pp.137-148,1967.

[9] Sullivan E.J., P.R. Bannister and G. Tacconi "A possibility of improving the detection of tether electromagnetic radiation by spatial processing", 3rd International Conference on Tethers in Space, S. Francisco, 16 May 1989.

[10] Bernstein S.L., M.L. Burrowos, J.E. Evans, A.S. Griffiths, D.A. McNeil, C.W. Niessen, I.Richter, D.P. White and D.K. Willim "Long-range comminications at extremely low frequencies", Proc. IEEE, Vol 62, N.3, March 1974.

[11] Porat B, R. Friedlander "Adaptive detection of transient signal", IEEE Trans. on ASSP, Vol.6,Dec.86.

[12] Cadzow J.A. , B. Baseghi and T. Hsu "Singular Value Decomposition approach to time series modelling", Proc. IEEE,part F130,1983.

[13] Ljung L. and T. Soderstrom "Theory and Practice of recursive identification", MIT Press, Cambridge (USA), 1983.

[14] Hunt F.V. "Signal rate processing for transit detection", JASA, Vol.51 N.4,1972.

[15] Hinich M. "Testing for gaussianity and linearity of a stationary time series", Journal of Time Series, Vol.3,N.3, 1982.

[16] Friedlander D. and B. Porat "Detection of transient signals by the Gabor representation", IEEE Trans. on ASSP, Vol.37, N.2,1989.

[17] Middleton D. "Procedure for determining the parameters of the first order canonical models of class A and B electromagnetic interference", IEEE Trans. on EMC, Vol.21 N.3,August 1979.

[18] Middleton D. "Canonical non gaussian noise models : their implications for measurement and prediction of receiver performance", IEEE Trans. on EMC, Vol.21 N.3, August 1979.

8. Acknowledgements

The project OESEE-TSS1 has been sponsored by the ASI (Agenzia Spaziale Italiana).
The autors are grateful for the important support, in different ways and forms (logistic, instrumentation, site, facilities, experts etc.), given to the project OESEE by the following organizations:

- ALENIA spa, Torino, IT.
- IAC (Istituto Astrofisico de Canarias) Tenerife, SP.
- IDS (Ingegneria dei Sistemi) Pisa IT.
- 2G Enterprise, Mountain View, CA USA.
- NPGS (Naval Post Graduate School) Monterey, CA, USA.
- NUSC (Naval Underwater System Center) New London CT. USA.
- SACLANTCEN, La Spezia IT.
- PROEL - Firenze IT.
- IESS/CNR - Roma IT.

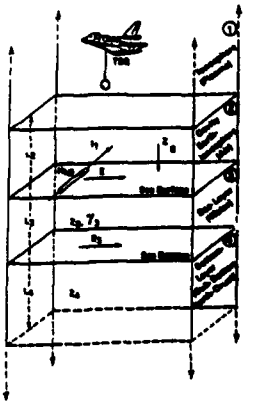

Fig.1 Propagation scenario

THE TSS: TRANSMITTING SYSTEM
Theory of Possible e.m. Emissions:
Tether/Plasma/Earth Magnetic Field Interactions
Smithsonian Astrophisical Observatory
Project EMET, R.Estes omissis

THE PROPAGATION MEDIUM SCENARIO
Transmissions from Ionosphere to Earth surface
Propagation Theoretical Modelling
SAO - MIT,Cambridge Mass.
M.D. Grossi and J.A. Kong omissis

THE GROUND TRACK RECEIVING SYSTEMS

1.EMET-Receiving Test Facilities,R.Estes PI
Mona Island (Portoricc),and Australia
omissis

2.OESEE-Receiving Test Facilities,G.Tacconi PI
Canaries-TFC, Kenya-TFK, Tino-TFT

i. General Planning,Detection,Estimation,
Measurements Theories
DIBE-GE, DMPA-MO,SACLANTCEN;
ii. Coil Detectors:DIBE,IAN-CNR-NUSC-MMI;
iii. SQUID Detectors:DIBE and IDS;
iv. Test Facilities:TFC,IAC-DIBE-IAN.CNR;
TFK,CRA-DIBE-IAN;TFT,MMI-DIBE-IAN.CNR
v. Data Collection and Analysis:DMPA
DIBE, IAN-CNR, SACLANTCEN.

Fig.2- TSS1-ELF Transmission Channel

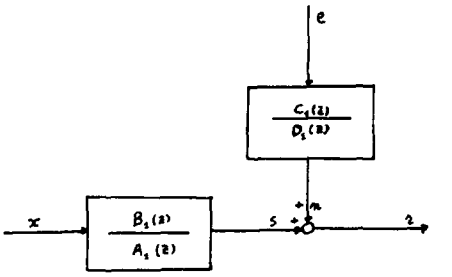

Fig.3- ARMAX modelling of TSS1 signal + noise.

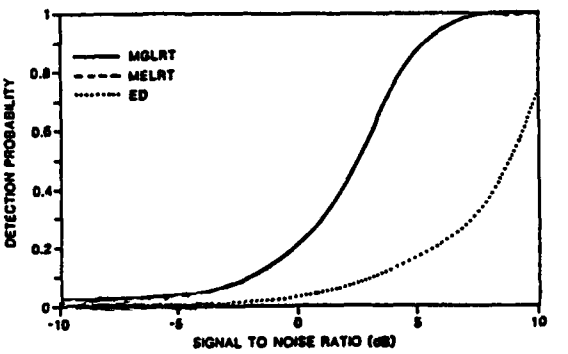

Fig.4- Comparison of detection probability for different detectors.

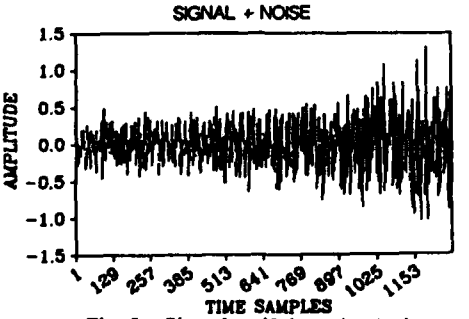

Fig.5- Signal + Noise simulation.

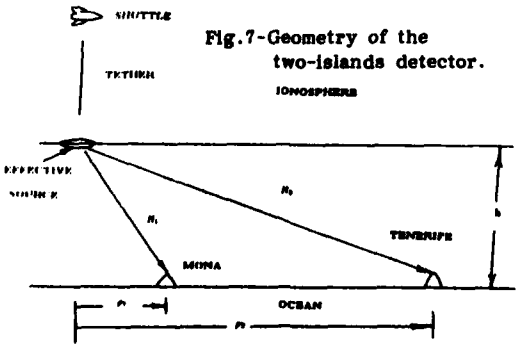

Fig.7-Geometry of the two-islands detector.

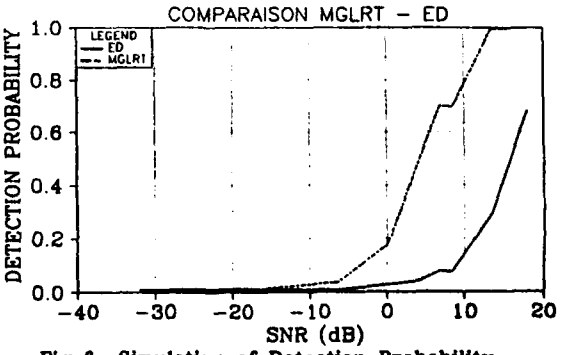

Fig.6- Simulation of Detection Probability.

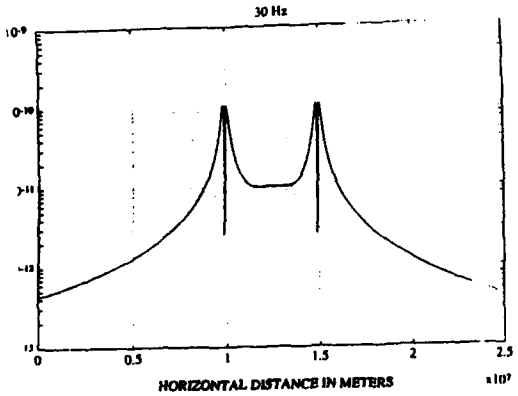

Fig.8-Two-Islands overflight transiting signal (calculated).

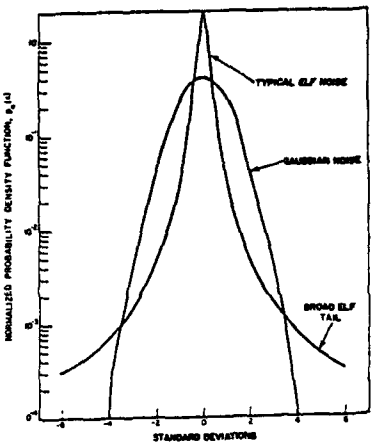

Fig.9- ELF Noise PDF, (Bernstein & Al. Proc.IEEE March 74).

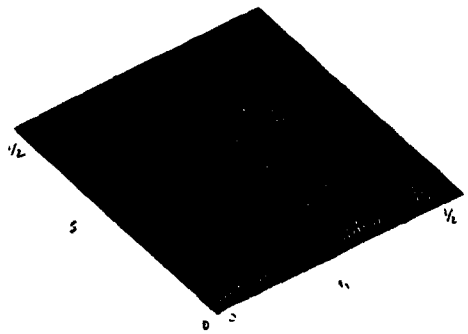

Fig.10 - Bispectrum analysis of a simulated signal.

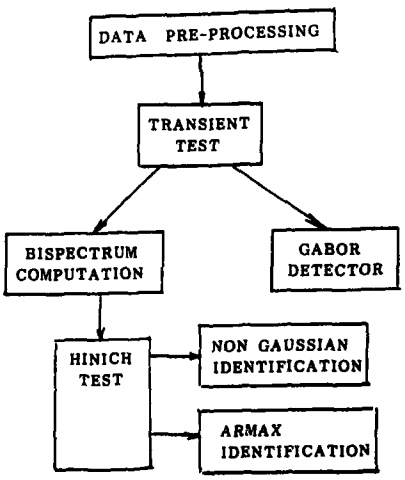

Fig.11- Block diagram of signal processing software.

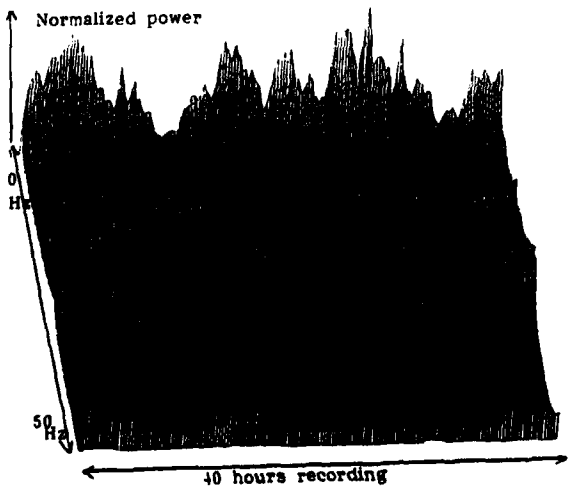

Fig.12- Evolutionary PSD function of vertical ELF noise recorded at IAN/CNR .Genoa IT.

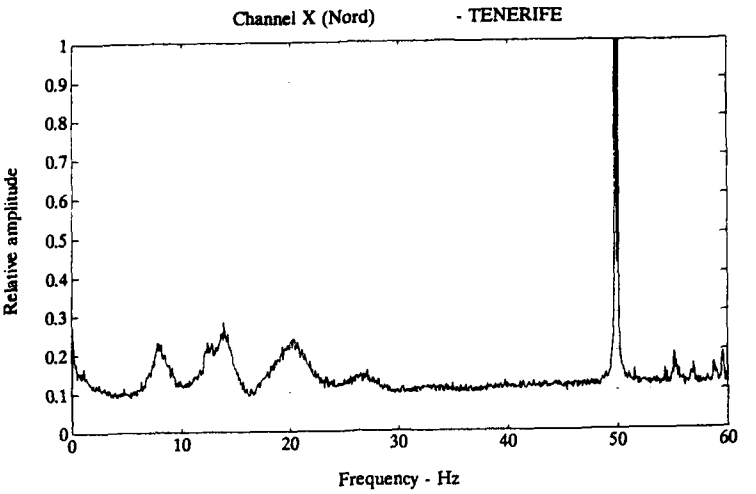

Fig.13 - Power Spectral Density of horizontal ELF signal, recorded at Tenerife,SP.

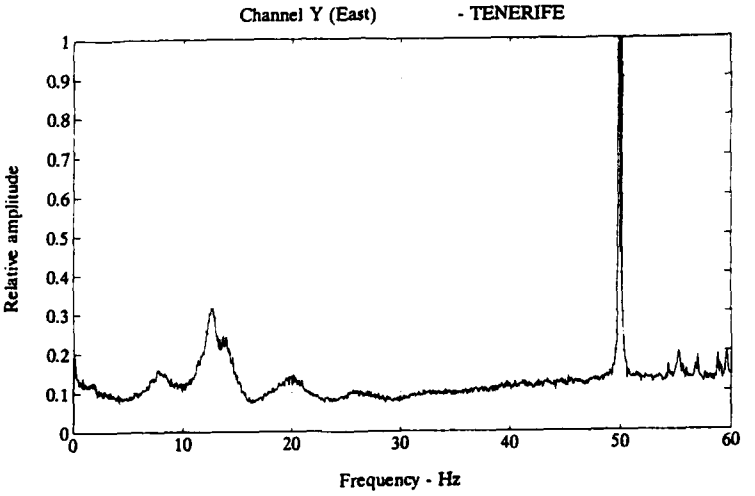

Fig.14 - Power Spectral Density of lateral ELF signal, recorded at Tenerife,SP.

Discussion

BURKE
COMMENT. When do you expect the next deployment of the TSS1?

AUTHOR'S REPLY
Not before 1 year.

ELF/VLF RADIO NOISE MEASUREMENTS AT HIGH LATITUDES DURING SOLAR PARTICLE EVENTS

A. C. FRASER-SMITH
Space, Telecommunicatons and Radioscience Laboratory, Stanford University,
Stanford, California 94305, U.S.A.

J. P. TURTLE
Antenna Technology Branch, Rome Laboratory, Hanscom Air Force Base
Massachusetts 01731, U.S.A.

1. SUMMARY

We report simultaneous measurements of ELF/VLF radio noise (10 Hz – 32 kHz) at three high latitude locations (Thule and Søndrestrømfjord, Greenland; Arrival Heights, Antarctica) during a number of moderately large and large solar particle events (SPE's), including some of the largest that have been observed during the last three decades. Thule is close to the center of the northern polar cap and thus the ELF/VLF noise signals reaching it are particularly exposed to the ionospheric effects of the SPE's, whereas the ELF/VLF noise signals at Søndrestrømfjord and Arrival Heights, which are located closer to their corresponding auroral zones, should be less affected. These general expectations are supported by the results of our measurements, which show major changes occurring in the Thule noise statistics following the start of the polar cap absorption (PCA) caused by the SPEs, and smaller changes at Søndrestrømfjord and Arrival Heights. The changes depend markedly on the frequency of the noise signals. At Thule, for frequencies in the approximate range 250 Hz to 1.5 kHz, the diurnal variation in the rms noise amplitudes is typically suppressed during the 2–3 days following the start of the PCA, and in most of the examples we have examined there tends to be a decrease in the average amplitude. Nevertheless, increases can occur: Following the event of 12 August 1989 the noise amplitudes increased by as much as 10–15 dB. For most other frequencies in the range 10 Hz to 32 kHz there is little change in the noise statistics. However, in the range 3–10 kHz there tends to be a marked decline in the rms noise amplitudes at Thule in the 24 hours following the start of the PCA, after which there is a rapid recovery to the undisturbed levels. At Søndrestrømfjord and to a lesser extent at Arrival Heights the most marked change appears to be the suppression of the diurnal variation noise peaks and thus lower average noise amplitudes in the 2–3 days following the start of the PCA.

2. INTRODUCTION

The STAR Laboratory at Stanford University has been operating three ELF/VLF radio noise measurement systems of advanced design at high latitudes for several years as part of a larger program to improve and expand knowledge of the global distribution of ELF/VLF radio noise [*Fraser-Smith and Helliwell*, 1985; *Fraser-Smith et al.*, 1988, 1991]. These three systems were routinely making measurements during some or all of the latter half of 1989, when an unusually large number of solar particle events (SPE's) occurred in the 4-month period starting July 25 [*Bieber et al.*, 1990]. It is well known that the occurrence frequency and intensity of SPE's and their associated effects on radio wave propagation through the polar regions, including the intense absorption now known as polar cap absorption (PCA), are related to, and vary roughly in phase with, the solar cycle [*Zmuda and Potemra*, 1972; *Duggal*, 1979; *Smart and Shea*, 1989; *Gorney*, 1990]. As a result, it was expected that some SPE's would occur during the 1989–1992 maximum phase of the present solar cycle. Nevertheless, the concentration in such a short interval of seven relativistic SPE's that were detectable with ground-based cosmic ray measuring instruments and which included the largest such event observed since 1956 [*Bieber et al.*, 1990] was a surprise. The occurrence of these SPE's during the operation of three high-latitude ELF/VLF radio noise measuring systems provides a unique opportunity to study the effects of SPE's on naturally-occurring ELF/VLF radio noise in the polar caps.

The three high latitude ELF/VLF measurement systems are located at Thule (TH) and Søndrestrømfjord (SS) in Greenland and at Arrival Heights (AH) on Ross Island in the Antarctic; Figure 1 shows their geographical locations and Table 1 lists their geographic and geomagnetic coordinates. As indicated by these latter data, and shown more fully by *Fraser-Smith* [1987], Thule is particularly close to the north geomagnetic pole, i.e., it is essentially at the center of the northern polar cap. Søndrestrømfjord, on the other hand, is either just outside the polar cap, and thus in the northern auroral zone, or just inside the polar cap, depending on the time of day (on the dayside it is typically located in the auroral zone under the polar cusp; on the nightside it is typically located in the polar cap somewhat to the north

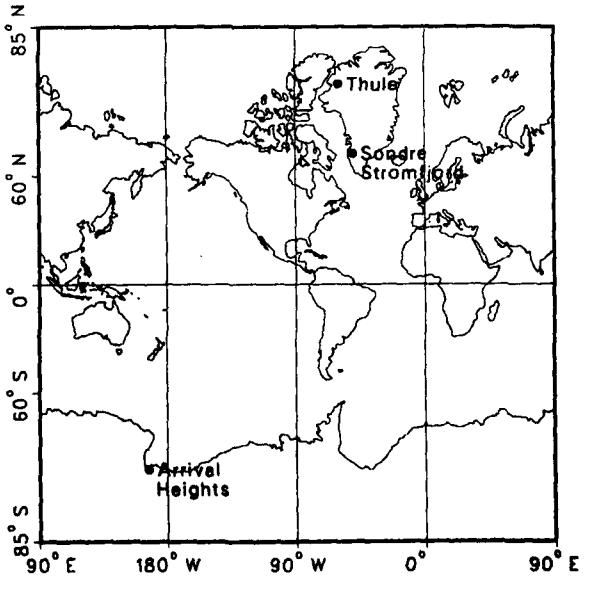

Figure 1. Geographical locations of the Thule, Søndrestrømfjord and Arrival Heights ELF/VLF radiometers.

TABLE 1. Geographical coordinates of the three high-latitude radiometer stations. The geomagnetic coordinates are computed from the 1985 International Geomagnetic Reference Field.

Station	Geographic Coordinates	Geomagnetic Coordinates
Thule, Greenland	76.5°N, 68.8°W	87.5°N, 11.3°E
Søndrestrømfjord, Greenland	67.0°N, 51.0°W	76.8°N, 37.9°E
Arrival Heights, Antarctica	77.8°S, 166.7°E	78.8°S, 66.9°W

of the auroral oval [*Kelly*, 1983; *Wickwar et al.*, 1984]). Arrival Heights is located 2° closer to its geomagnetic pole than Søndrestrømfjord, which means that it is similar geomagnetically to Søndrestrømfjord but that it is also somewhat more frequently located within the (southern) polar cap. However, it must be remembered that there are important differences between the earth's magnetic field configuration in the northern and southern polar regions [e.g., *Dudeney and Piggott*, 1978] that limit the relevance of north-south polar region comparisons based on geomagnetic coordinates alone. Probably the most important of these differences is the much greater distance between the magnetic dip pole in the south from its respective geographic pole [*Dudeney and Piggott*, 1978; *Fraser-Smith*, 1987]. Another important difference between the north and south polar caps that must be taken into account when simultaneous measurements are made is the markedly different aspects presented to the sun by the two polar regions at times other than the equinoxes.

This study addresses the effects produced on ELF/VLF radio noise at high latitudes by eight SPE's. Seven of these SPE's are those referred to above, all of which occurred in 1989 and which started on the following dates: (1) 25 July; (2) 16 August; (3) 29 September; (4) 19 October; (5) 22 October; (6) 24 October; and (7) 15 November. These SPE's are all classified as relativistic events, i.e., the solar particle energies reached levels of 800 Mev or greater. The September SPE and the combination of October SPEs are considered to be among the most severe particle events ever observed [*Gorney*, 1990]. In addition to these seven relativistic SPE's, we will also consider the effects produced by an additional 'softer' event, which started on (8) 12 August 1989 and which is classified as a ground level event (GLE), for which the particle energies must reach a level of 350–400 Mev or greater, but which was not energetic enough to be classified as a relativistic event. As we will show, there clearly are strong SPE effects on ELF/VLF radio noise at high latitudes, but there does not appear to be much distinction between the effects produced by GLE's and relativistic events.

3. PRESENTATON OF DATA

In this section we present representative plots of the ELF and VLF radio noise data recorded at Thule, Søndrestrømfjord, and Arrival Heights during several SPE's. Because of the more complete availability of noise data, and the greater strength of the SPE's, we will concentrate on three SPE intervals for our data presentation, one covering the two August events, another covering the single September event, and the third covering the three October events. In addition, to help characterize the individual SPE's, we will provide reference plots of Thule riometer data. We will start this presentation by considering the interval containing the September event, partly because a study of the changes produced over time by a single relatively isolated event in our high latitude ELF/VLF measurements will provide us with a reference against which we can compare the changes produced by the other groups of SPE's, and partly because it produced the largest enhancements in the measurements made by ground-based particle detectors [*Bieber et al.*, 1990].

3.1. The SPE interval of September 1989

Figure 2 shows a plot of the Thule riometer data for the interval 28 September – 2 October, 1989. It can be seen that the absorption began increasing immediately after 1200 UT on 29 September and rapidly reached a maximum of 8.0 dB at 2100 UT. After a characteristic decline to a low level during the nighttime hours the absorption again increased, reaching a maximum of 7.5 dB at 1800 UT on 30 September (the diurnal variation is characteristic of stations at which the ionospheric D region is alternately sunlit during the day and dark during the night [*Sauer*, 1968]). After a further nighttime decline the absorption again increased to a relatively small third maximum of 2.1 dB on 1 October, after which it declined to zero and the absorption event terminated. As would be expected, plots of the five minute averaged proton flux for proton energies greater than 10, 50, and 100 MeV, as measured by the GOES-7 satellite [*Sauer et al.*, 1990; also see *Gorney*, 1990], show none of the diurnal variation seen in the absorption data. Instead, the particle fluxes begin increasing rapidly shortly before 1200 UT on 29 September, rise to a maximum within the next 12 hours, and then gradually decline to low levels over the next three days.

Figures 3–6 show plots of the one-minute rms average amplitude of the ELF/VLF noise measured at Thule during the interval 26 September – 5 October. The measurements cover 16 frequencies in the overall range 10 Hz – 32 kHz and they are plotted in four groups, each covering four frequencies. Although the measurements are made continuously, they are only shown for two hours of every four hour interval during the 24-hour UT day, starting with 02–04 UT. The data obtained during the alternate two hour intervals are contam-

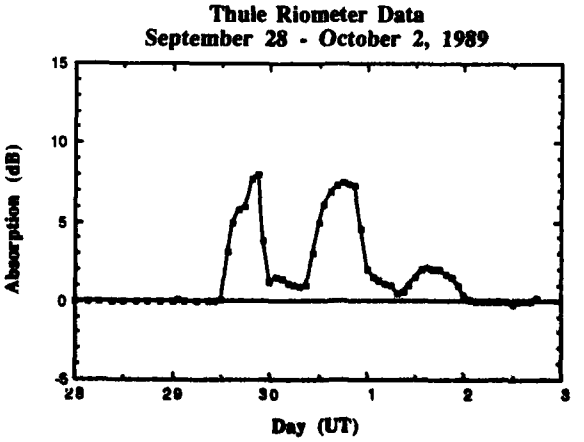

Figure 2. Thule riometer measurements during the interval 28 September – 2 October, 1989.

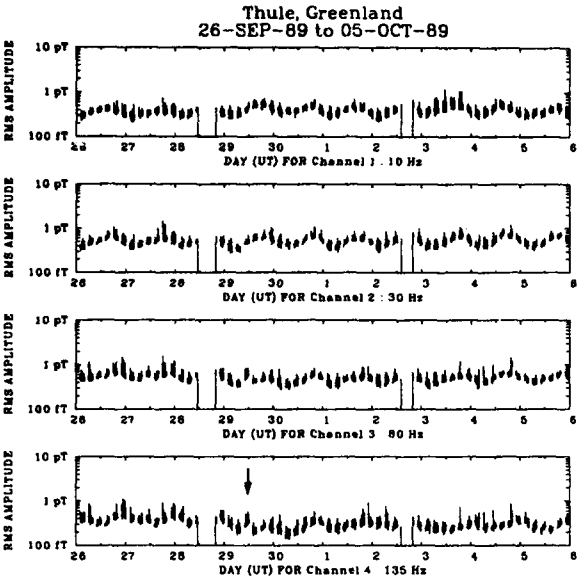

Figure 3. Measurements of the radio noise at Thule during the interval 26 September – 5 October, 1989, for four frequencies in the range 10–135 Hz. The arrow marks the approximate start time of the SPE.

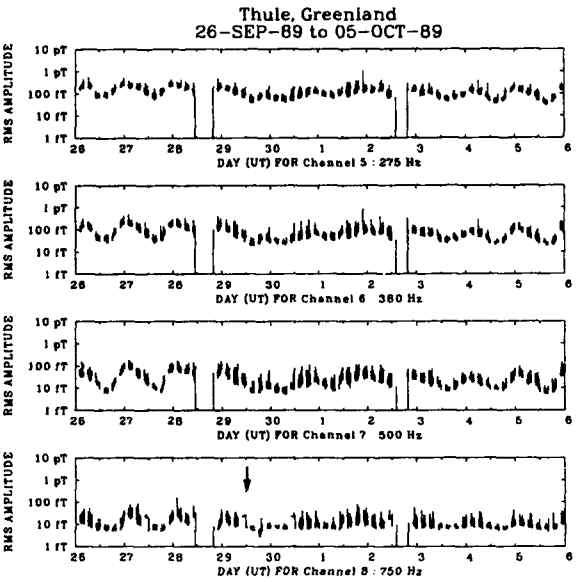

Figure 4. Measurements of the radio noise at Thule during the interval 26 September – 5 October, 1989, for four frequencies in the range 275–750 Hz. The arrow marks the approximate start time of the SPE.

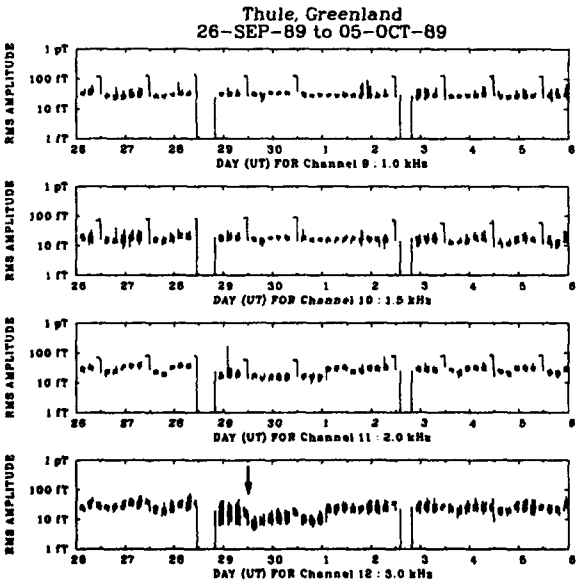

Figure 5. Measurements of the radio noise at Thule during the interval 26 September – 5 October, 1989, for four frequencies in the range 1–3.0 kHz. The arrow marks the approximate start time of the SPE.

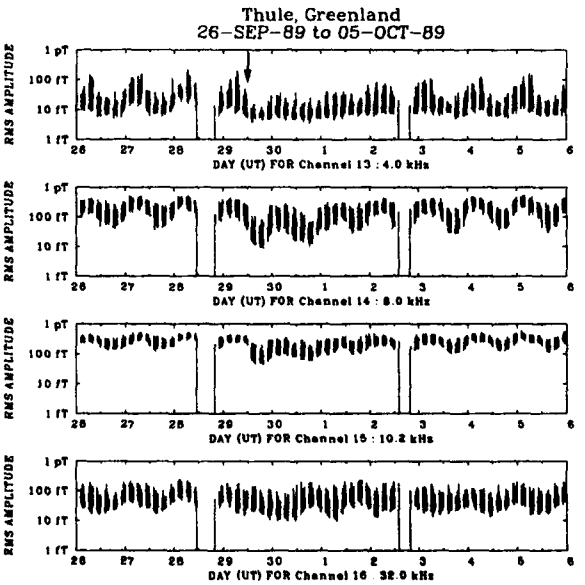

Figure 6. Measurements of the radio noise at Thule during the interval 26 September – 5 October, 1989, for four frequencies in the range 4–32 kHz. The arrow marks the approximate start time of the SPE.

inated by the transmissions from a VLF ionosonde that was operating at Thule during the time interval covered by this communication.

Inspecting the data in Figures 3–6, we see the following general trends during the SPE interval (29 September–2 October): (1) for frequencies in the approximate range 250 Hz – 1.5 kHz, the diurnal variation is suppressed during the 2–3 days following the start of the SPE; (2) for frequencies in the two adjacent ranges 10–250 Hz and 1.5–3 kHz there is little change in the noise statistics, i.e., the SPE appears to have little effect on the noise; and (3) for frequencies in the range 3–32 kHz there is a marked decline in the noise amplitudes in the 24 –48 hours following the start of the SPE, after which there is a rapid recovery to the previous undisturbed levels.

The SPE effects on the ELF/VLF noise at Søndrestrømfjord and Arrival Heights, our two lower latitude stations, are noticably weaker than those we have just described for Thule. At both stations the most marked change appears to be the suppression of the diurnal variation noise peaks and thus lower average noise amplitudes in the 2–3 days following the start of the PCA.

3.2. The SPE interval of August 1989

Figure 7 shows a plot of the Thule riometer data for the interval 11–19 August, 1989. The absorption for this event began increasing immediately after a comparatively sharp dip in absorption at 1500 UT on 12 August and rapidly reached an extended, structured maximum that varied in the range 6.8–9.3 dB from 0400 UT until 2100 UT on 13 August, after which it declined until 0300–0600 UT on 15 October. The absorption then increases slowly up to a maximum of 3.2 dB in the interval 1800–2100 UT, followed by a short decline. The absorption begins to increase again soon after 0300 UT on 16 August, reaching a maximum of 6.0 dB at 1500 UT the same day. Plots of the five minute averaged proton flux for proton energies greater than 10, 50, and 100 MeV, as measured by the GOES-7 satellite [*Sauer et al.*, 1990], show the existence of an SPE, starting a little before 1500 UT on 12 August. There is also a small increase in the energetic particle fluxes starting on 15 August, which accounts for the corresponding small increase in absorption seen in Figure 7 during the latter half of the day. This small increase in energetic particle flux is followed by a larger one starting early on 16 August, which accounts for the increase in absorption on that day. Interestingly, the SPE of 16 August is classified

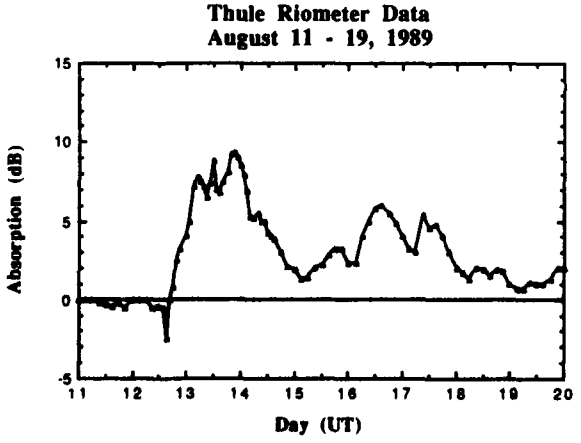

Figure 7. Thule riometer measurements during the interval 11–17 August, 1989.

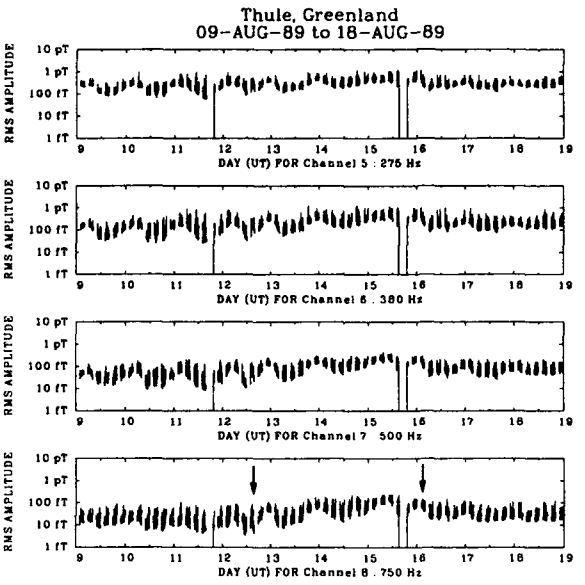

Figure 8. Measurements of the radio noise at Thule during the interval 9–18 August, 1989, for four frequencies in the range 275–750 Hz. The arrows mark the approximate start times of the two SPE's.

as a larger event than that of 12 August, even though, as we have seen, the ionospheric effects of the latter event are greater than those of the first.

Figure 8 shows the changes in the Thule noise measurements for frequencies in the range 275–750 Hz during the interval 9–18 August, and it is clear that the diurnal variation is once again suppressed during the course of the two SPE's. However, unlike the previous event, and unlike the other events for which we have made measurements, there is a small increase in the average noise level during the SPE. Figure 9 shows the corresponding noise amplitudes for frequencies in the range 4–32 kHz, and once again there can be seen to be some marked declines for the frequencies below 32 kHz. At 32 kHz the noise amplitudes do not appear to be significantly changed by the SPE except for an unusual jump in the noise amplitudes in the 6–8 hours immediately following the start of the SPE.

As a final example of the data for the two August events, Figure 10 shows a plot of some of the Søndrestrømfjord VLF noise measurements during the SPE's. For the four frequencies shown, only the amplitudes at 4 kHz show any obvious SPE effect: the diurnal variation, which is not very marked in any event, is eliminated throughout the course of the two SPE's.

3.3. The SPE interval of October 1989

Figure 11 shows a plot of the Thule riometer data for the interval 18–27 October, 1989. It can be seen that the absorption began increasing immediately after 1200 UT on 19 October, after which there is a series of maximums during the latter half (i.e., daylight period) of each UT day until 27 October, when the ionospheric absorption changes return to an approximately normal level. The largest of these repetitive daylight maximums occurs on 20 October, when the absorption reaches a level of 14.0 dB around 1630–1700 UT, which is substantially larger than the maximum absorption

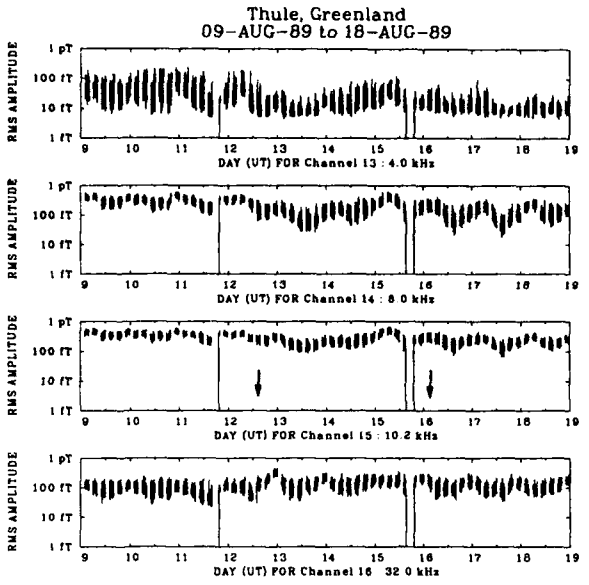

Figure 9. Measurements of the radio noise at Thule during the interval 9–18 August, 1989, for four frequencies in the range 4–32 kHz. The arrows mark the approximate start times of the two SPE's.

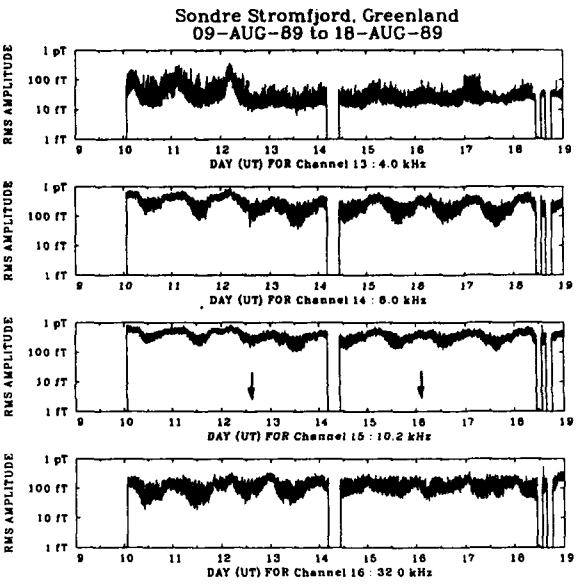

Figure 10. Measurements of the radio noise at Søndrestrømfjord during the interval 9–18 August, 1989, for four frequencies in the range 4–32 kHz. The arrows mark the approximate start times of the two SPE's.

measured during the September event, even though the September event was a stronger event from the point of view of the energetic particle fluxes measured on the ground.

Plots of the five minute averaged proton flux for proton energies greater than 10, 50, and 100 MeV, as measured by the GOES-7 satellite [*Sauer et al.*, 1990; also see *Gorney*, 1990], show that the sequence of absorption maxima in Figure 11 is the result of the occurrence of three SPE's. The first of these SPE's commenced at 1200 UT on 19 October and it was followed by two others starting at about 1800 UT on 22 October and at about 1830 UT on 24 October.

Figure 12 shows the changes in the Thule noise measurements for frequencies in the range 275–750 Hz during the interval 16–25 October, and once again there is a very marked suppression of the noise amplitudes throughout the interval in which the SPE's are occurring. There is still some evidence of a diurnal variation, but it is weak (and was not particularly strong before the SPE's occurred).

Finally, Figure 13 shows the corresponding Arrival Heights noise amplitudes for frequencies in the range 4–32 kHz. The changes closely resemble those observed at Thule, with the exception that the more clearly defined diurnal variation is more evidently suppressed during the course of the SPE's.

4. SUMMARY AND DISCUSSION

We have shown a number of plots of the variations of the ELF/VLF rms noise amplitudes measured at Thule during six large SPE's, and we have supplemented these plots with others showing the variations of the noise amplitudes at Søndrestrømfjord and Arrival Heights. Our analysis of these data, and of other similar data for the other SPE's that occurred during the latter half of 1989, provide us with a general picture of how the noise amplitudes vary at stations in and around the polar caps during SPE's. Although there are changes in detail that vary between SPE events, it is generally true that the SPE effects appear to be concentrated in the two frequency bands 250 Hz – 1.5 Hz and 3–32 kHz. In both bands the diurnal variation is typically suppressed following the start of the SPE and the average amplitude of the noise is decreased. There is, however, a difference in the duration of these effects: they tend to last for 2–3 days in the lower frequency band, whereas in the higher frequency band the changes only last for about 24 –48 hours after which there is a rapid recovery. The decreases in noise amplitudes and suppression of the diurnal variations are not as evident at Søndrestrømfjord and Arrival Heights, which are at lower latitudes and not as exposed to the ionospheric changes produced in the polar caps by the incoming energetic solar particles. Finally, for frequencies in the two ranges 10–250 Hz and 1.5–3 kHz, the SPE's do not appear to produce marked changes in the rms noise amplitudes.

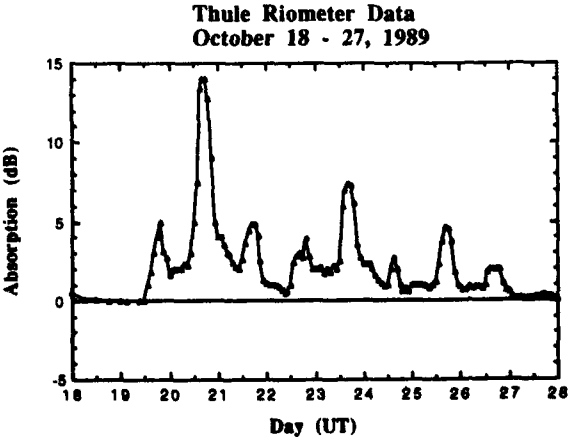

Figure 11. Thule riometer measurements during the interval 18–27 October, 1989.

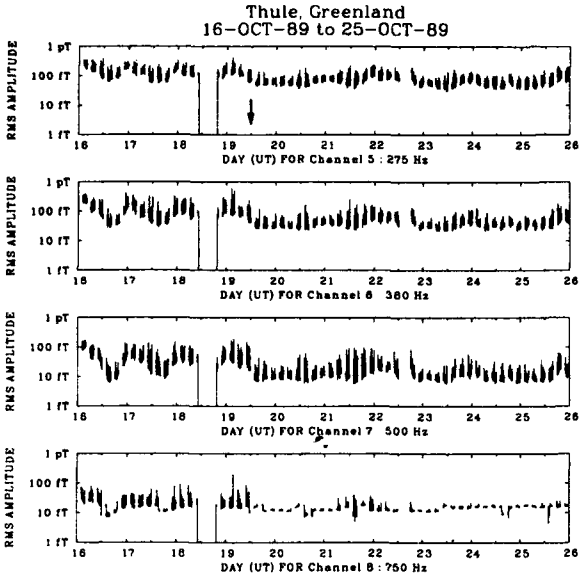

Figure 12. Measurements of the radio noise at Thule during the interval 16–25 October, 1989, for four frequencies in the range 275–750 Hz. The arrow marks the approximate start time of the first of the three SPE's that occurred during the time interval.

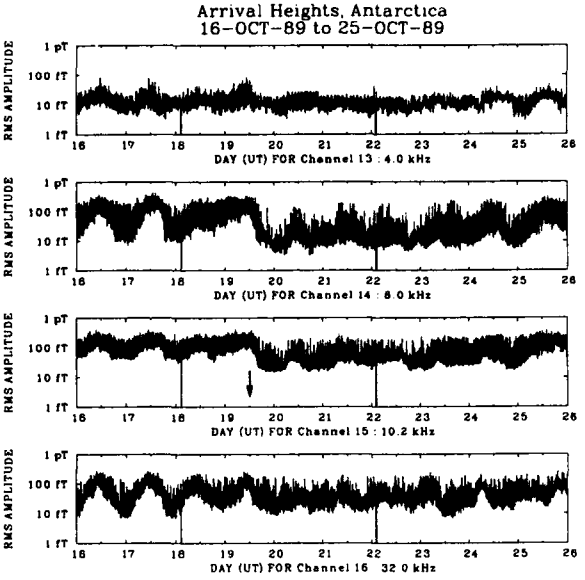

Figure 13. Measurements of the radio noise at Arrival Heights during the interval 16–25 October, 1989, for four frequencies in the range 4–32 kHz. The arrow marks the approximate start time of the first of the three SPE's that occurred during the time interval.

In an earlier study of the effects of an SPE on ELF radio noise at high latitudes, in this case ELF sferics (75 Hz) measured at Byrd Station, Antarctica (which has a geomagnetic latitude of 70.9° S (derived from the 1985 International Geomagnetic Reference Field), and which is therefore not strictly a polar cap station), *Fraser-Smith and Helliwell* [1980] found that there was no polar cap 'blackout' of the sferics, but that there were some significant changes in the median amplitudes and rates of occurrence of the sferics. The first observation, that there was no polar cap 'blackout,' is consistent with our own observation that there are no marked changes in the rms noise amplitudes for ELF radio noise with frequencies in the range 10–250 Hz. However, the second observation appears to be inconsistent. It is possible that there were real differences between the effects produced on ELF radio noise by the 9 June 1968 event analyzed by *Fraser-Smith and Helliwell* [1980] and the SPE's analyzed here. On the other hand, it is also possible that the lower geomagnetic latitude of Byrd Station combined with differences in the amplitude measurements account, at least partially, for the difference. The median amplitudes measured by *Fraser-Smith and Helliwell* [1980] are more sensitive to changes in the amplitudes of the much more frequently occurring smaller sferics than are the rms amplitudes reported here, which are more sensitive to changes in the amplitudes of the largest sferics. Many of the larger sferics reaching Byrd Station must have come from relatively close lightning discharges and they are unlikely to have propagated through the southern polar cap, whereas the smaller sferics, from more distant lightning discharges, are more likely to have propagated through the polar cap and thus to undergone attenuation due to the SPE-induced ionization in the lower part of the ionosphere. In support of this argument, we note that the median amplitudes of the largest sferics measured by *Fraser-Smith and Helliwell* [1980] appear to be affected less by the SPE than the median amplitudes of the smaller sferics.

SPE's are unusual and remarkable events. The results reported here cover only a single aspect of their effects on the earth's upper atmosphere and on radio waves propagating in the earth-ionosphere waveguide in the polar caps. Many other studies, covering a wide range of topics [*Reid*, 1978] are possible, including the influence of SPE's on stratospheric ozone [*Heath et al.*, 1977] as well as additional studies of the effects of SPE's on ELF/VLF radio noise at high latitudes. The occurrence of so many large SPE's in the latter half of 1989 provides us with a unique opportunity to conduct these studies.

ACKNOWLEDGEMENTS

The Stanford University measurements and research at Thule were supported by Rome Laboratory Contract No. F19628-89-K-0015 and by the Office of Naval Research through Contract No. N00014-81-K-0382 and Grants No. N00014-90-J-1080 and N00014-92-J-1576. The measurements at Søndrestrømfjord and Arrival Heights were supported by the Office of Naval Research through Contract No. N00014-81-K-0382 and Grants No. N00014-90-J-1080 and N00014-92-J-1576, and by the National Science Foundation (NSF) through NSF cooperative agreement ATM-88-22560 (Søndrestrømfjord) and NSF Grants DPP-8720167 and DPP-9119552 (Arrival Heights). We are grateful to the Danish Commission for Research in Greenland for its continued approval of our measurements and we thank Drs. J. W. Bieber of the Bartol Research Institute and H. H. Sauer of NOAA's Space Environment Laboratory for much helpful information.

REFERENCES

Bieber, J. W., P. Evenson, and M. A. Pomerantz, "A barrage of relativistic solar particle events," *Eos Trans. AGU, 71*, 1027–1035, August 14, 1990.

Dudeney, J. R., and W. R. Piggott, "Antarctic ionospheric research," pp. 200–235 in *Upper Atmosphere Research in Antarctica* , Eds. L. J. Lanzerotti and C. G. Park, Am. Geophys. Union, Washington, D.C., 1978.

Duggal, S. P., "Relativistic solar cosmic rays," *Revs. Geophys. Space Phys., 17*, 1021–1058, 1979.

Fraser-Smith, A. C., "Centered and eccentric geomagnetic dipoles and their poles, 1600–1985," *Rev. Geophysics, 25*, 1–16, 1987.

Fraser-Smith, A. C., and R. A. Helliwell, "ELF sferic occurrences in the Antarctic during a solar proton event: Case study of occurrences at Byrd Station during the event of 9 June 1978," *J. Geophys. Res., 85*, 2296–2306, 1980.

Fraser-Smith, A. C., and R. A. Helliwell, "The Stanford University ELF/VLF radiometer project: Measurement of the global distribution of ELF/VLF electromagnetic noise," *Proc. 1985 IEEE Internat. Symp. on Electromag. Compatability, IEEE Catalog No. 85CH2116-2*, 305–310, August 1985.

Fraser-Smith, A. C., R. A. Helliwell, B. R. Fortnam, P. R. McGill, and C. C. Teague, "A New Global Survey of ELF /VLF Radio Noise," Conference on Effects of Electromagnetic Noise and Interference on Performance of Military Radio Communication Systems, Lisbon, Portugal, 26–30 October, 1987, published in *AGARD Conference Proceedings No. 420*, pp. 4A-1–4A-7, December 1988.

Fraser-Smith, A. C., P. R. McGill, A. Bernardi, R. A. Helliwell, and M. E. Ladd, "Global measurements of low-frequency radio noise," pp. 191–200 in *Environmental and Space Electromagnetics*, Ed. H. Kikuchi, Springer-Verlag, Tokyo, 1991.

Gorney, D. J., "Solar cycle effects on the near-earth space environment," *Rev. Geophys., 28*, 315–336, 1990.

Heath, D. J., A. J. Krueger, and P. J. Crutzen, "Solar proton event: Influence on stratospehric ozone," *Science, 197*, 886–889, 1977.

Kelly, J. D., "Sondrestrom radar – initial results," *Geophys. Res. Lett., 10*, 1112-1115, 1983.

Reid, G. C., "Polar–cap absorption," pp. 269–302 in *Handbook of Astronomy, Astrophysics and Geophysics, 1*, Ed. C. W. Gordon, V. Canuto, and W. I. Axford, Gordon and Breach, New York, 1978.

Sauer, H. H., "Nonconjugate aspects of recent polar cap absorption events," *J. Geophys. Res., 73*, 3058–3062, 1968.

Sauer, H. H., R. D. Zwickl, and M. J. Ness, "Summary data for the solar energetic particle events of August through December 1989," NOAA Space Environment Lab. Rept., February 21, 1990.

Smart, D. F., and M. A. Shea, "Proton events during the past three solar cycles," *J. Spacecr. Rockets, 26*, 403–415, 1989.

Wickwar, V. B., J. D. Kelly, O. de la Beaujardière, C. A. Leger, F. Steenstrup, and C. H. Dawson, "Sondrestrom overview," *Geophys. Res. Lett., 11*, 883–886, 1984.

Zmuda, A. J., and T. A. Potemra, "Bombardment of the polar-cap ionosphere by solar cosmic rays," *Revs. Geophys. Space Phys., 10*, 981–991, 1972.

Keywords

(1) Longwave radio waves

(2) Solar particle events (SPEs)

(3) Polar caps

(4) ELF/VLF radio

(5) Greenland

(6) Antarctica

(7) Polar cap absorption (PCA)

(8) Sferics

(9) Cosmic rays

(10) stratospheric ozone

Discussion

BENSON
COMMENT. Have you seen evidence of signal enhancements of the radiometer signals just prior to the large absorption events? Such enhancements are commonly observed in the auroral regions, e.g., see Benson et al, La Belle, etc.

AUTHOR'S REPLY
In the radiometer for the SPE event of 12 August 1989 there is a short (1/2 hour) enhancement immediately proceeding the large absorption event! However this is the only such sample of an enhancement that I have observed.

BELROSE
COMMENT. You spoke about the polar cap and the auroral belt or zone with reference to high energy particle events, solar proton and electrons events, but you did not, I feel, provide a clear distinction between polar cap and auroral events. Solar proton events enhance the ionization in the D-region more or less uniformily over the whole of polar cap, down to latitudes dependent on whether a geomagnetic storm is in progress or not. Auroral particle events, and relativistic high energy particle events do occur at auroral latitudes are restricted to the auroral belt.

AUTHOR'S REPLY
Thank you, Dr. Belrose, for the clarification. I must say, though, that I am not convinced at this time that the ionization produced by solar proton events in the D-region is more or less uniform over the whole of the polar caps. Since spherics reach receivers in the polar caps from all directions, they may provide me with a means for determining whether there is more absorption in some directions than others during SPE's which would be indicative of non-uniform ionization over the polar caps.
Since Thule is close to the center of the northern polar cap, it would be an ideal location for this kind of study.

INAN
COMMENT. With respect to the earlier question by Dr. Belrose, I would like to point out that it is well know that PCA or SPE (Solar Protes Events) significantly affect VLF paths. The early works is the 1960's by Potemra at al., and Potemra and Zmuda, and later by Larsen et al. and Reagan et al, precisely were on this topic and they used the effect of SPE's on VLF to derive D-regions profiles.

AUTHOR'S REPLY
Thank you Umran. I think Dr. Belrose was concerned by my use of the term "wiped out" in reference to the effects of an SPE on VLF signals in the polar cap. This would be true for HF signals, but it is less true for VLF signals. The VLF signals reaching stations in a polar cap will be attenuated, perhaps strongly during a strong SPE, but they probably will not be "wiped out".

ELF/VLF SPECTRUM MEASUREMENTS

M. G. Laflin, Member, Technical Staff
U.S. Department of Commerce
National Telecommunications and Information Administration
Institute for Telecommunication Sciences
325 Broadway
Boulder, CO, USA 80303-3328

1. SUMMARY

A 16-bit digital spectrum analysis system was designed and built to provide measurement capabilities not currently available in commercial systems. The system provides the wide dynamic range necessary to observe very weak signals in the presence of strong signals. Large sample size allows for high frequency resolution. System outputs include spectral densities, amplitude probability distributions, diurnal amplitude variations, and time domain plots.

Measurements were made to characterize the ELF/VLF H-field noise environment in a sampling of office buildings. These include two buildings in New York City and two Denver office buildings. Measurements were made for all hours of the day and include business day and weekend coverage.

Results reveal a complicated signal environment. Associated with the power distribution frequencies were strong odd harmonics with higher harmonics evident into the kilo Hertz range; other man-made noise components were also evident.

2. INTRODUCTION

The modern office building presents a very complicated electromagnetic (EM) radiation environment. Strong, localized signals are present, which may be a potential source of electromagnetic interference (EMI). This is especially true in the ELF/VLF frequency range. Office lighting and power distribution systems, fans, and elevator motors generate strong fields at harmonics of 60 Hz. Off powerline frequency man-made noise is also generated by motors and lighting as well as corona discharge, arcing, computers, displays, varying loads, and the like. It is very important to characterize this ELF/VLF noise environment.

Presented in this paper is a brief overview of the measurement system and results from four locations. The first two sites, located in lower Manhattan, represent high density urban environments. Office buildings in Denver represent moderate density urban and low density suburban types of environments. Data were collected during 24-hour periods, covering business and nonbusiness days.

3. MEASUREMENT SYSTEM

The Low Frequency Measurement System (LFMS) was designed to provide a wide dynamic range, run under computer control, and provide a variety of analysis options. Digital time domain data are recorded on digital audio tape for later playback and analysis.

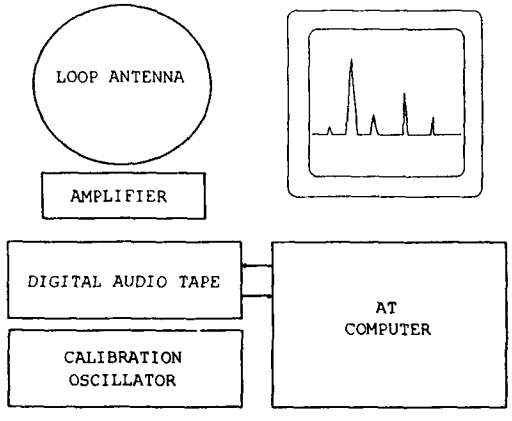

Figure 1. LFMS block diagram.

Figure 1 shows a block diagram of the measurement system. A calibrated loop antenna converts ac magnetic fields to analog electric signals. A digital audio tape (DAT) recorder converts the analog signal to 16-bit PCM data. The digital data are recorded on digital audio tape. A desk top computer is used to control the measurement system, recording data at preprogrammed times, and for analysis. During the analysis phase, data are transferred from

the DAT via an interface, built by ITS, to the system computer for processing.

3.1 Antenna

The system employed a simple loop antenna with an integrated preamp and calibration loop. The antenna has a 3 dB bandwidth extending from 10 Hz to 10 kHz and a response of 50 mV/nT. A 1 dB compression occurs at 112 dBpT (dB relative to one picoTesla) and the second order intercept is at 183 dBpT providing linear response over the expected signal range.

The antenna and amplifier are connected to the DAT with 30 ft of shielded cable.

3.2 DAT

A Panasonic SV-3500 digital audio tape recorder is utilized. It provides a low impedance differential analog input and 16-bit analog-to-digital conversion (ADC). The sample rate is 48 kHz. The dynamic range is greater than 90 dB and has a signal-to-noise ratio (SNR) greater than 93 dB. The DAT is capable of storing 1.3 Gbytes of data.

3.3 DAT-Computer Interface

An interface was designed by ITS to convert digital data available on the DAT's internal serial bus to a format acceptable by an AT&T DSP32C signal processor. The interface board resides inside the DAT housing.

3.4 Computer

The system computer is an AT type personal computer equipped with a math co-processor and a plug-in DSP card. The DSP serial port accepts data from the custom ITS interface and transfers it to the host computer over the computer's ISA bus.

4. DATA ANALYSIS

Four types of output are generated: time plots, spectral density plots, amplitude probability distributions (APD), and diurnal amplitude variation plots.

Once each hour the system records the time wave form for a period of a few minutes. This is done over a 24-hour period and include business and non-business days. This is to provide records for periods of high and low activity.

4.1 Frequency Domain

All frequency domain analysis is based on the Discrete Fourier Transform (DFT). The DFT is implemented on the computer with a base-2 Fast Fourier Transform (FFT) algorithm [1]. To reduce the spectral leakage from the inherent rectangular window, a "minimum four-term Blackman-Harris (BH)" time domain window is used prior to transforming [2]. DFT sample lengths are 32768 and 65536 data points. Noise equivalent bandwidths, based on DFT length and the BH window, are 1.46 and 2.93 Hz.

Spectral density plots are generated in the following manner. The time data for an hourly measurement are uploaded from the DAT and stored in a disk file on the computer. A series of nonoverlapping DFTs are performed on the time record. From these a maximum and rms average flux density is calculated. If any time signal exceeds a limit of 75% of the ADCs maximum input rating, it is discarded. This is to ensure linear operation. These cumulative spectral densities can be combined to generate a maximum and rms average level for an entire 24-hour period. Amplitude is given in decibels relative to a picoTesla (dBpT).

Spectral densities, which represent a single hours measurement, are marked "1 Hr" in the upper right-hand corner of the plot. Plots covering 24-hour periods are marked "24 Hr." Resolution bandwidth and number of "scans" or DFTs are also indicated in the upper right-hand corner.

4.2 Amplitude Probability Distributions

An amplitude probability distribution (APD) is the cumulative probability distribution for the received signal/noise in a given bandwidth. In this case the APD is based on envelope detection. The APDs are generated by comparing the measured power against a set of quantized power levels. A set of bins, each representing a certain power level, is used to keep track of the number of times the corresponding level was exceeded. Each bin corresponds to a 5-dB increment ranging from -30 dBpT to +90 dBpT. This way the distribution is filled in. The sample size must be large enough to intercept low probability events.

APDs for two frequency bands are presented. One covering 10 Hz to 1000 Hz and one covering 3000 Hz to 7000 Hz. These are generated by sequentially comparing the amplitude at each discrete frequency within the band against the quantized bins. This is done for each DFT or "scan" over a 24-hour day. It should be noted that this is not the same as sampling the total power in the band.

4.3 Diurnal Amplitude Variations

Diurnal amplitude variations track the rms average level at a specific frequency for each hourly measurement over a 24-hour day. Powerline harmonics are tracked to give an indication of field strength variation through the day.

5. MEASUREMENT SITES

5.1 Site #1

Site #1 is located in Lower Manhattan, New York City, NY. It was built some time in the 1920s and is of masonry and steel construction with a marble vernier. Site #1 sets among the large cluster of buildings that make up the financial district. During the work day there is a high population density in the area. This site is representative of an older style building in a high density urban environment.

Site #1 has a large amount of electronics and power equipment. A large bank of computers are located on the 22nd floor. The LFMS was placed on the 19th floor in the facilities offices. Within the immediate area of the measurement system there was only a moderate amount of electronics equipment.

5.2 Site #2

Site #2 is also located in Lower Manhattan. Built in the early 1970s, it is of steel and concrete cantilever construction with aluminum skin. It is a modern office complex rising many tens of stories into the air. Power is distributed to the various floors through several parallel power buses. Site #2 is representative of a modern skyscraper in a high-density urban environment.

The LFMS was located on a high floor of building one in a large open plan office area. Work space was separated by soft par itions. Power was distributed throughout the office area via a grid located under the floor. A cluster of desk top workstations were located 20 ft from the antenna. Little other computerized office electronics were present.

5.3 Site #3

Site #3 is located in the downtown Denver, CO, building cluster. Built in the early 1980s, it is about 30 stories tall and is of modern concrete and steel construction. This site is representative of moderate density urban environments.

The LFMS was placed on the 6th floor in a common area for several adjacent offices. At this site there was a large number of word processing terminals attached to a central unit. Supporting the central computer were many printers and data storage devices. These items were between 10 and 20 ft from the antenna.

5.4 Site #4

Site #4 is located in an off-downtown area of Denver, CO. It was built in 1984 and is of concrete and steel construction with an aluminum skin and many windows. Its height is six floors. This site was intended to be representative of urban/suburban low-rise environments.

The measurement system was located on the sixth floor in a large open plan office. Individual office space was separated with soft partitions. A single PC type computer and dot matrix printer were present in the office area and was 14 ft from the antenna.

6. RESULTS FROM FOUR SITES

Results are presented on a site-by-site basis. Discussion of the results and conclusions are given in Section 7 of this paper.

Spectral density plots are presented first. The first two cover 0-600 and 600-1200 Hz, respectively; these ranges are chosen such that powerline harmonics fall on graticular lines. Resolution bandwidth for these spectral plots is 1.46 Hz. The remainder of the spectral densities are given in 3 kHz blocks. Resolution bandwidth for the last three spectral plots is 2.93 Hz. Spectral densities showing the maximum and rms average level for a 24-hour day are given. Reference [3] presents this work in greater detail.

The APDs for both business and nonbusiness days are presented in two frequency bands. Printed on the upper right-hand corner of the APD plots are the rms average noise level in the band.

Diurnal amplitude variations for the first 10 powerline harmonics are shown for both business and nonbusiness days. These are the rms average values for each hourly measurement in a 2.93 Hz bandwidth.

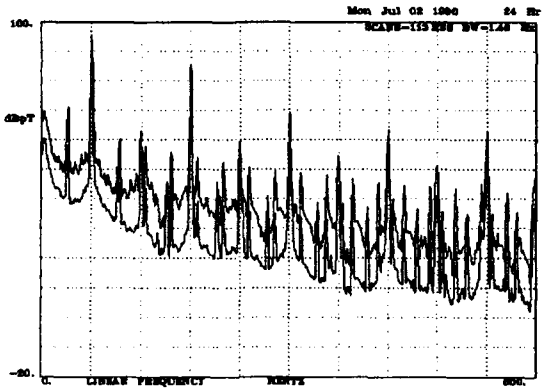

Figure 2. Site #1 spectrum, 0-600 Hz.

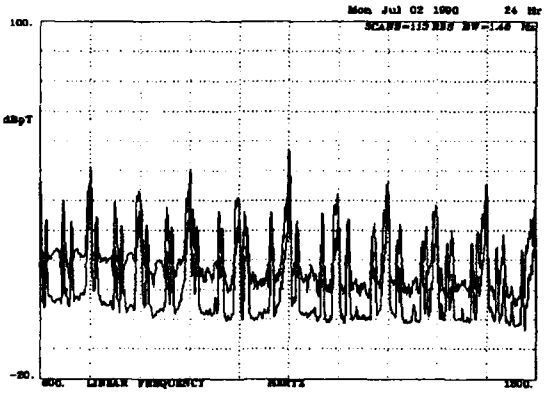

Figure 3. Site #1 spectrum, 600-1200 Hz.

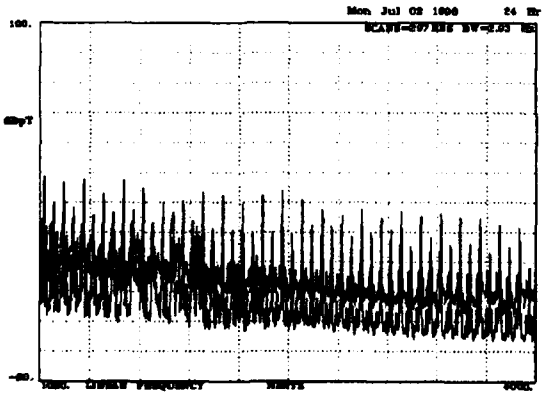

Figure 4. Site #1 spectrum, 1-4 kHz.

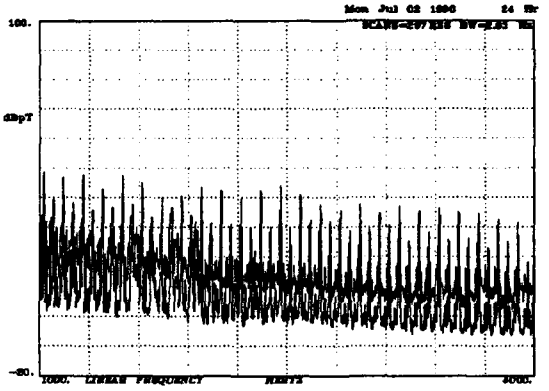

Figure 5. Site #1 spectrum, 4-7 kHz.

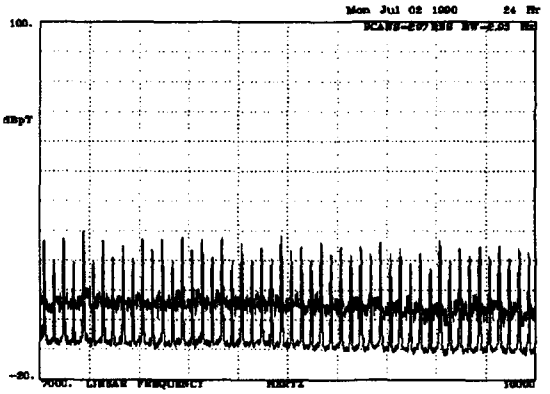

Figure 6. Site #1 spectrum, 7-10 kHz.

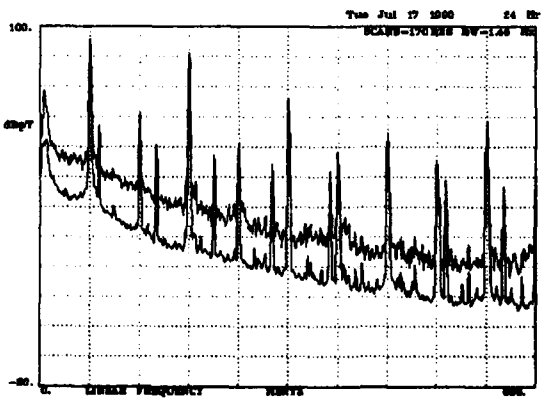

Figure 7. Site #2 spectrum, 0-600 Hz.

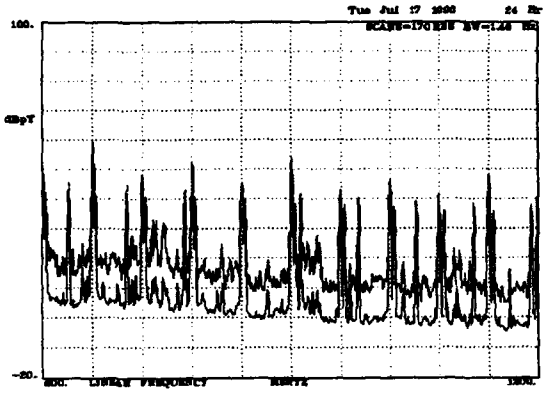

Figure 8. Site #2 spectrum 600-1200 Hz.

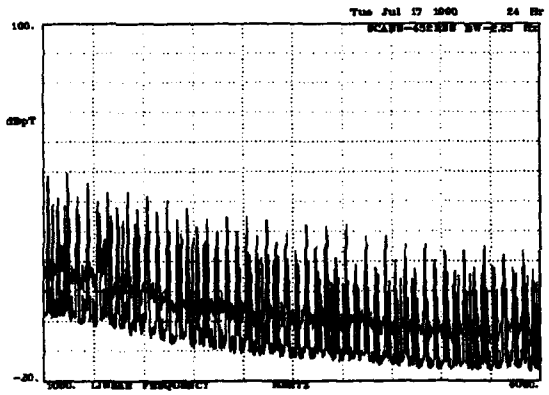

Figure 9. Site #2 spectrum, 1-4 kHz.

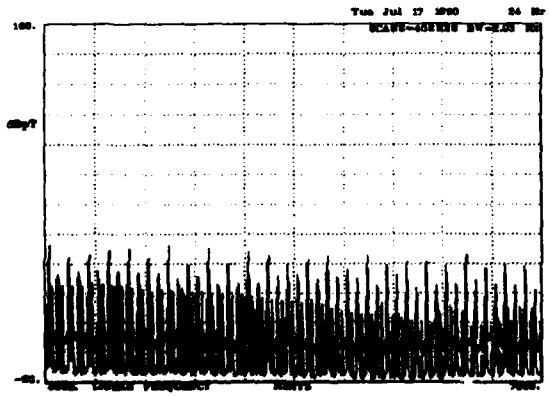

Figure 10. Site #2 spectrum, 4-7 kHz.

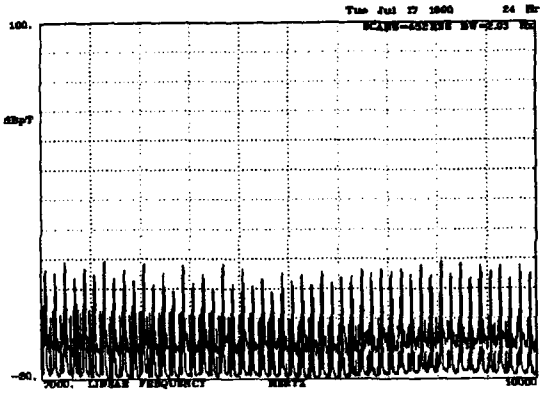

Figure 11. Site #2 spectrum, 7-10 kHz.

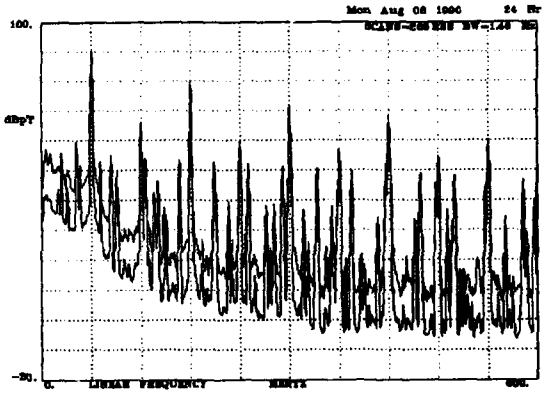

Figure 12. Site #3 spectrum, 0-600 Hz.

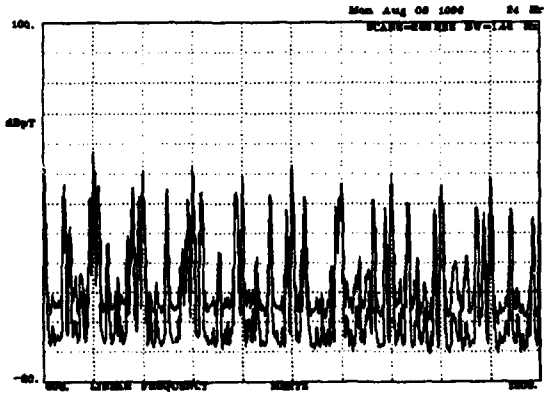

Figure 13. Site #3 spectrum, 600-1200 Hz.

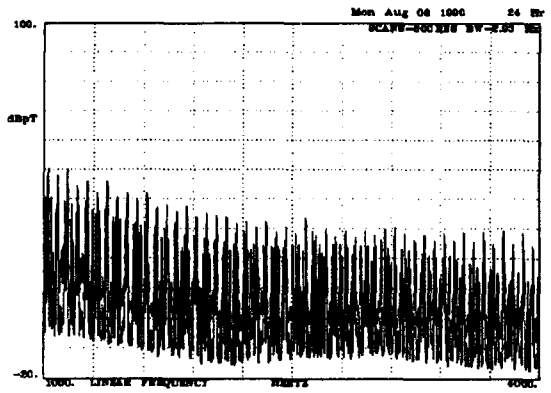

Figure 14. Site #3 spectrum, 1-4 kHz.

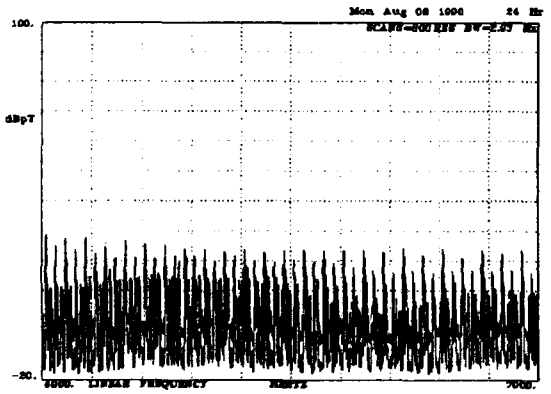

Figure 15. Site #3 spectrum, 4-7 kHz.

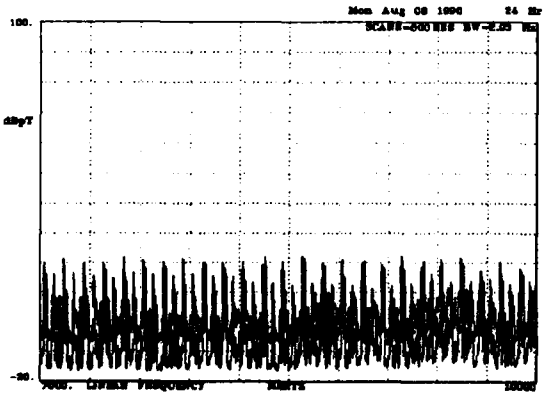

Figure 16. Site #3 spectrum, 7-10 kHz.

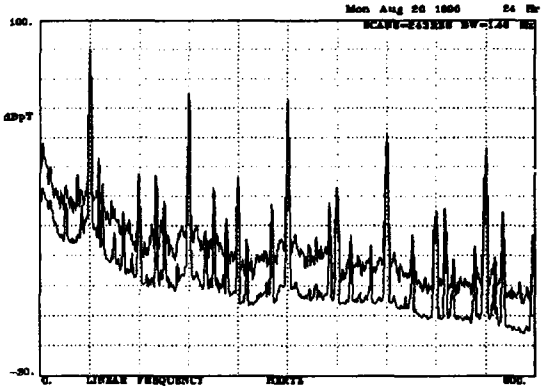

Figure 17. Site #4 spectrum, 0-600 Hz.

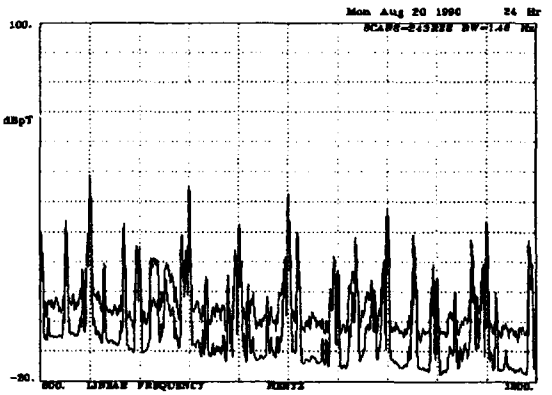

Figure 18. Site #4 spectrum, 600-1200 Hz.

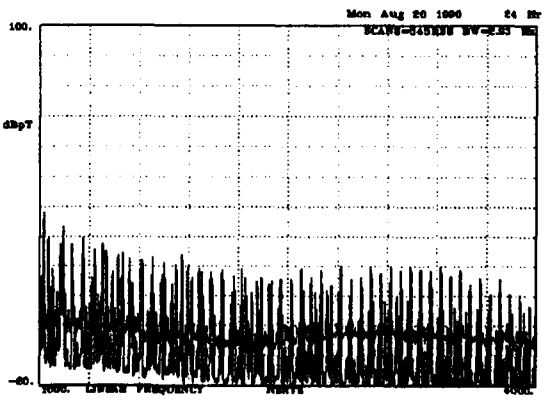

Figure 19. Site #4 spectrum, 1-4 kHz.

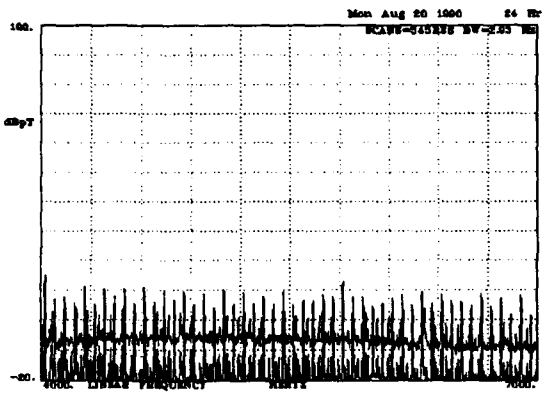

Figure 20. Site #4 spectrum, 4-7 kHz.

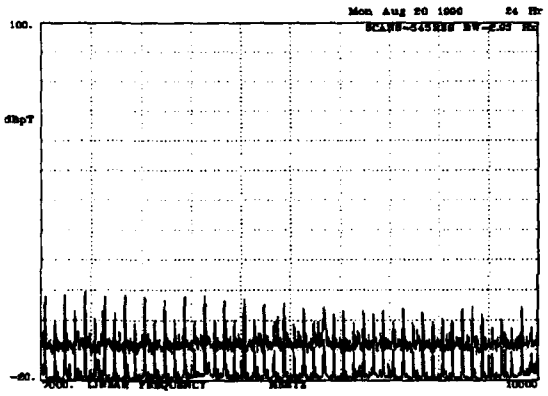

Figure 21. Site #4 spectrum, 7-10 kHz.

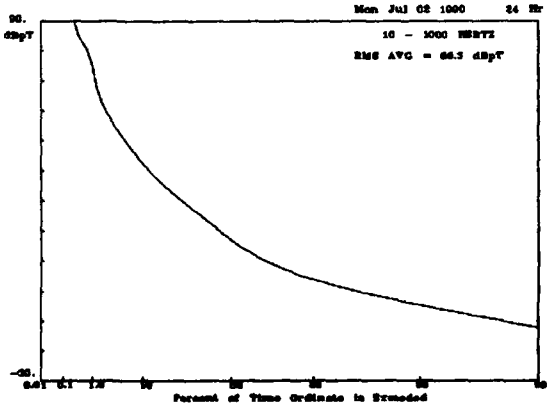

Figure 22. Site #1 APD, business day.

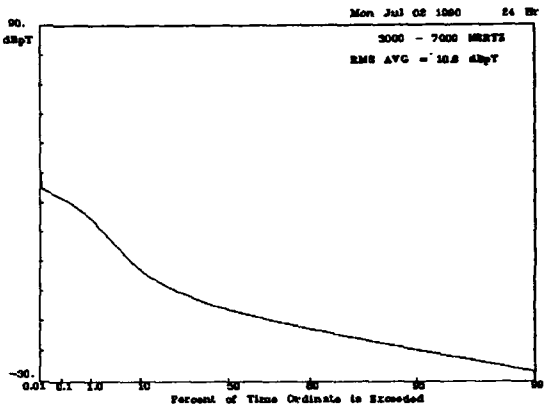

Figure 23. Site #1 APD, business day.

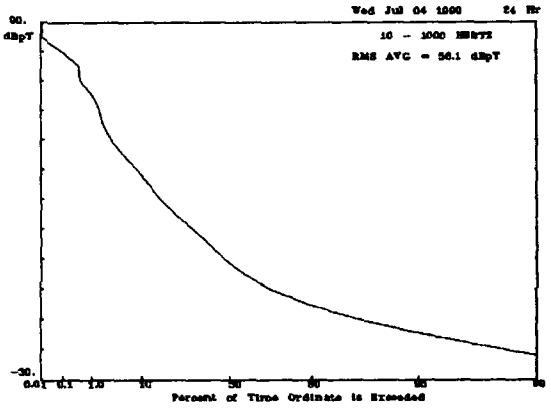

Figure 24. Site #1 APD, nonbusiness day.

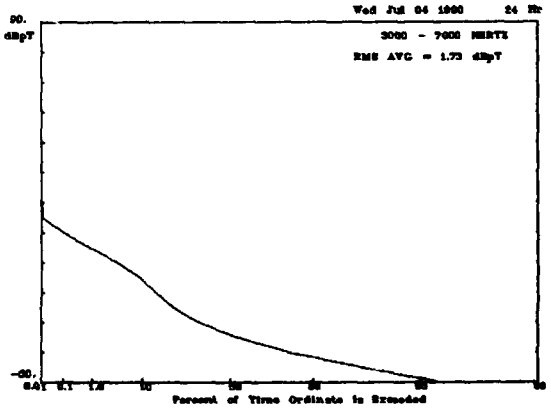

Figure 25. Site #1 APD, nonbusiness day.

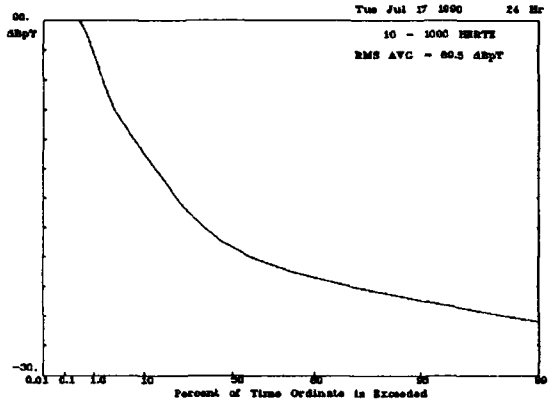

Figure 26. Site #2 APD, business day.

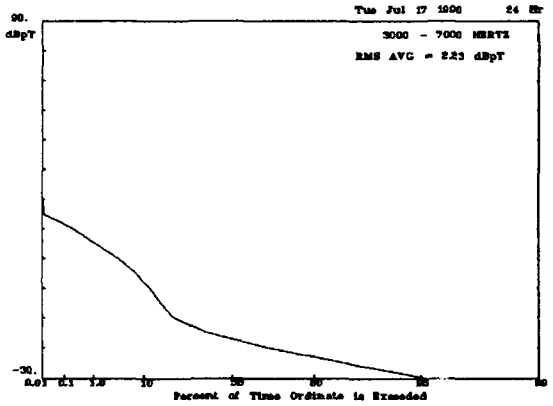

Figure 27. Site #2 APD, business day.

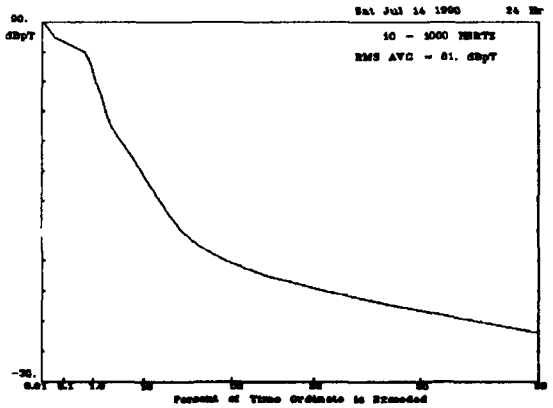

Figure 28. Site #2 APD, nonbusiness day.

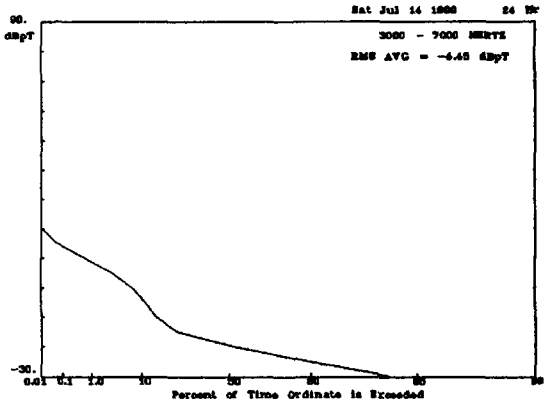

Figure 29. Site #2 APD, nonbusiness day.

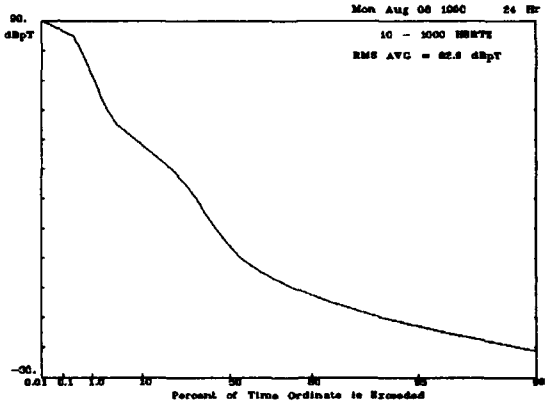

Figure 30. Site #3 APD, business day.

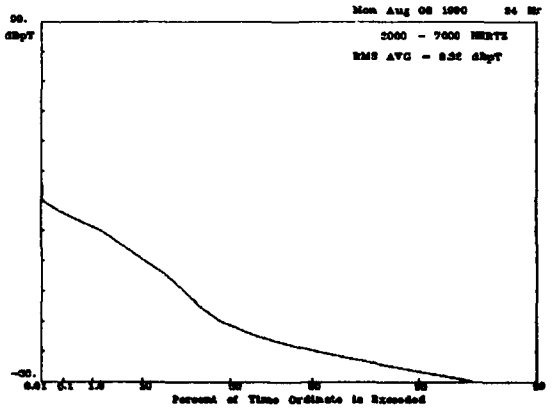

Figure 31. Site #3 APD, business day.

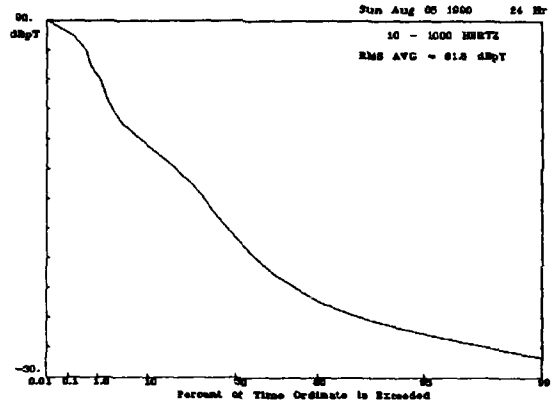

Figure 32. Site #3 APD, nonbusiness day.

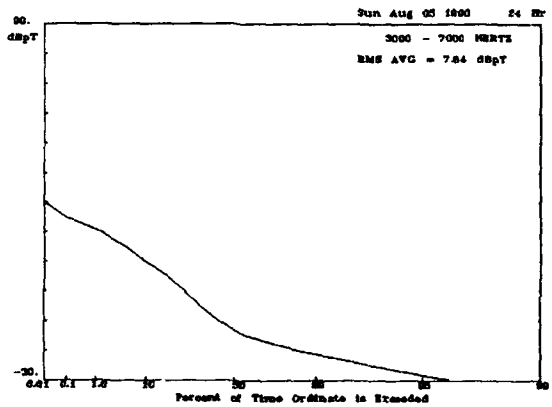

Figure 33. Site #3 APD, nonbusiness day.

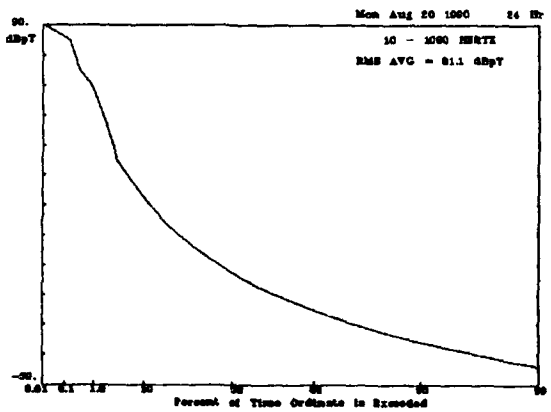

Figure 34. Site #4 APD, business day.

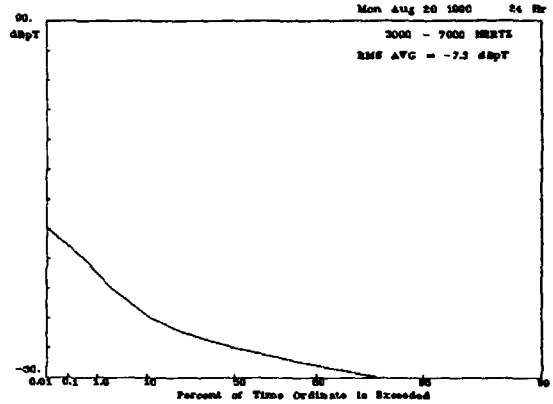

Figure 35. Site #4 APD, business day.

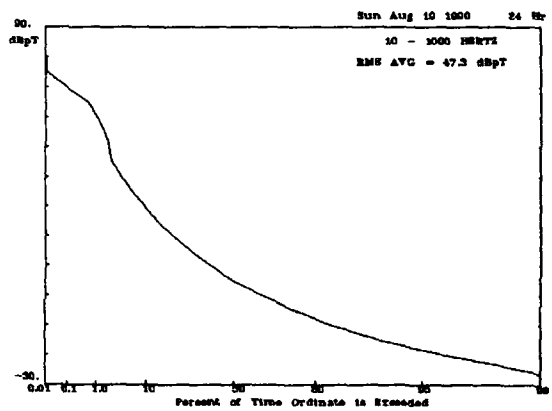

Figure 36. Site #4 APD, nonbusiness day.

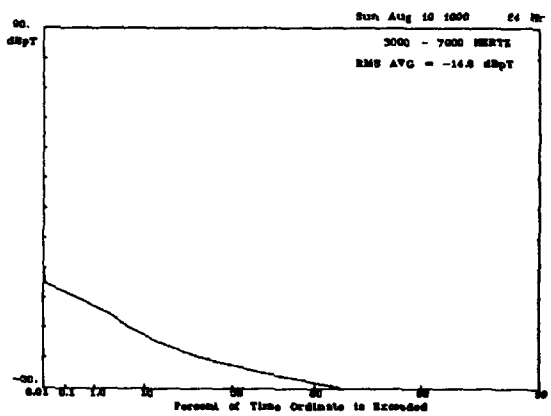

Figure 37. Site #4 APD, nonbusiness day.

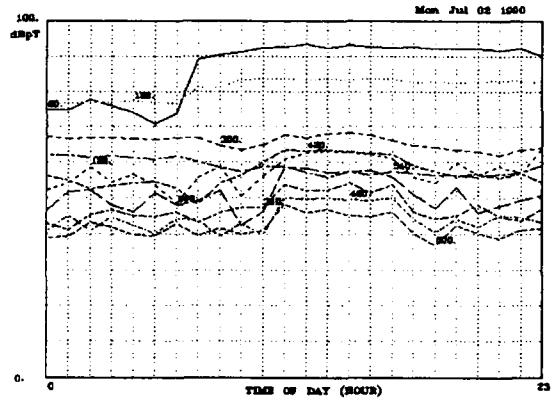

Figure 38. Site #1 diurnal variation, business day.

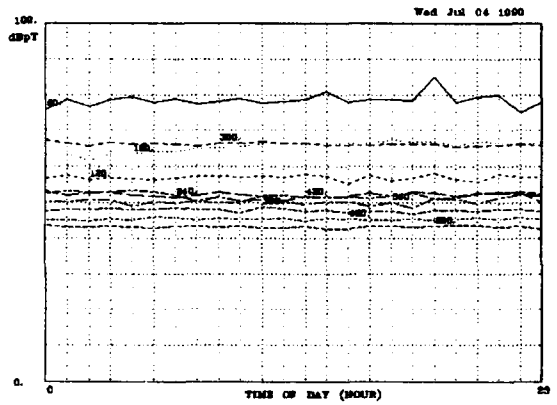

Figure 39. Site #1 diurnal variation, nonbusiness day.

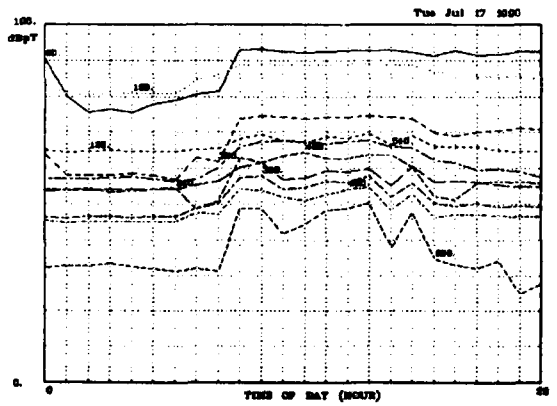

Figure 40. Site #2 diurnal variation, business day.

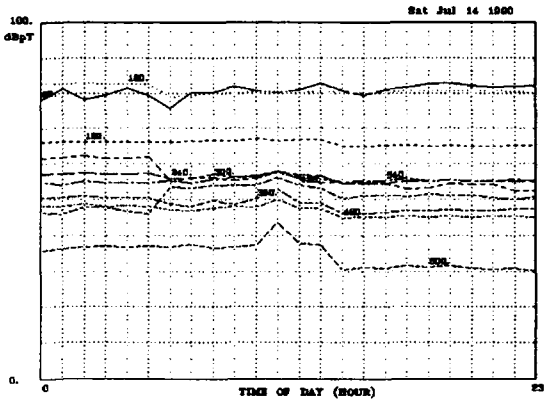

Figure 41. Site #2 diurnal variation, nonbusiness day.

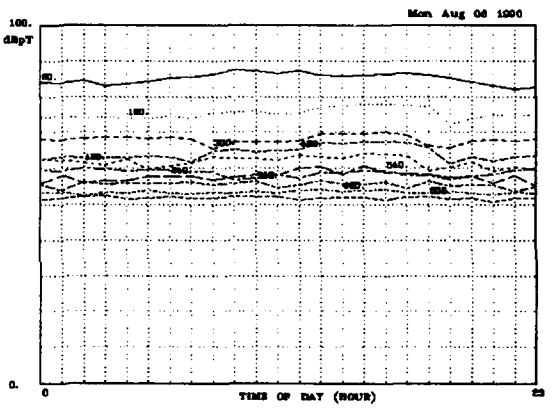

Figure 42. Site #3 diurnal variation, business day.

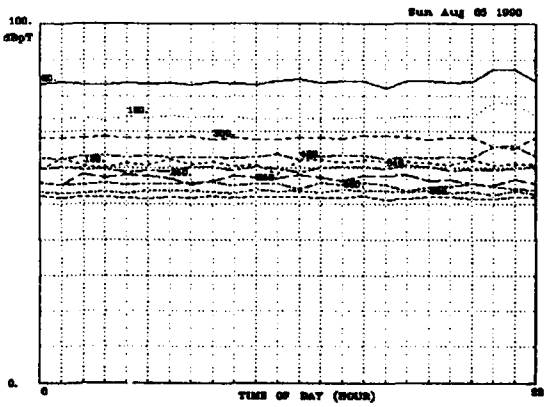

Figure 43. Site #3 diurnal variation, nonbusiness day.

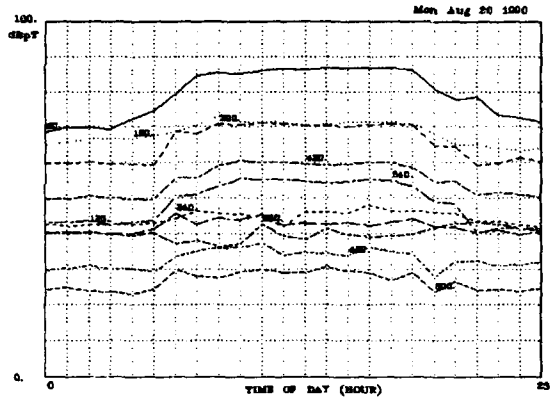

Figure 44. Site #4 diurnal variation, business day.

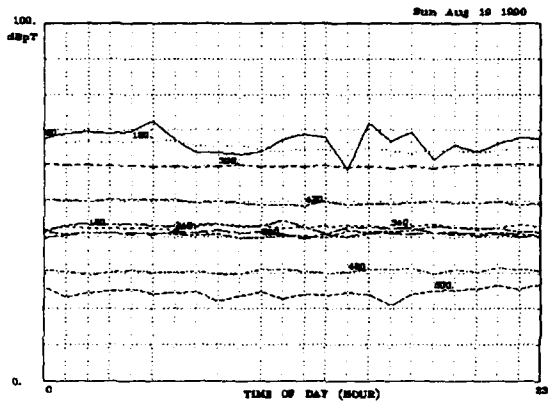

Figure 45. Site #4 diurnal variation, nonbusiness day.

7. DISCUSSION AND CONCLUSIONS

It is the purpose of this section to touch on some of the more obvious results obtained from this series of measurements. No attempt was made to identify the source of the signal/noise although in some cases speculation is made.

7.1 Spectral Densities

This section refers to Figures 2 through 21. Odd powerline harmonics (PLH) are the dominant feature at all sites at frequencies below about 2 kHz. At several of the locations the third PLH is within 10 dB of the fundamental. The mean value of the 60 Hz signal at all sites was 93 dBpT while the third harmonic was 83 dBpT. This implies that a large part of this powerline field is contributed not only by the fundamental frequency, 60 Hz, but by its first several odd harmonics.

Nonpowerline harmonic man-made noise is present at all sites. This is especially true of Site #3 where there was a larger amount of monitors and other computer related equipment. Although the source of the non-PLH frequency spectra was not researched, it is speculated that computer monitors are the primary source. In Figure 2 we see what appear to be PLH subharmonics. Upon closer examination, these are found to occur at 33.3 Hz multiples and are not PLH.

Background noise levels at Site #2 at frequencies below 1 kHz were found to be consistently higher than those at other sites. This is reflected in the higher rms levels indicated in the 10-1000 Hz business day APD (Fig. 26). The cause of this may be the large amount of heavy equipment in use to support operation of such a large structure. It may also have been caused by vibration of the sensor in the earth's dc magnetic field--vibration from building sway and mechanical activity. Above 1 kHz Site #1 exhibited a background level that was on the average 10 dB greater than the other sites.

7.2 Amplitude Probability Distributions

Examination of the amplitude envelope APDs, Figures 22-37, indicate that the distribution is the sum of several statistical processes. A Gaussian or thermal process for low- and mid-amplitude events and an impulsive component (impulsive in time and also in frequency, since the algorithm "sweeps" in frequency over the band) as well as the deterministic PLH noise.

The rms average power over each band is shown for business (Bday) and nonbusiness (nBday) in Table 1. Amplitude values are given in dBpT. A definite difference is seen between business- and nonbusiness-day activity.

Table 1. RMS Power in APD Bandwidth

Sites	Bday 0.01-1	Bday 3-7	nBday 0.01-1	nBday 3-7
#1	68.3	10.6	56.1	1.7
#2	69.5	2.2	61.0	- 4.5
#3	62.9	8.3	61.8	7.6
#4	61.1	-7.3	47.3	-14.9

7.3 Diurnal Amplitude Variations

Figures 38-45 show the H-field variation of the first 10 PLH over 24-hour periods for business and nonbusiness days. Three of the four sites show a definite change during the business day with little activity on the nonbusiness day. Site #3 does not indicate much variation. This is most likely an indication that equipment was left on around the clock.

One note of interest is that the third PLH exceeded the level of the first during low activity hours at all sites except Site #3 (one could say that there is never a period of low activity at this site).

8. SUMMARY

Presented here is an overview of a comprehensive set of measurements designed to characterize the ELF/VLF environment in a modern office building. Odd powerline harmonics are found to be the dominant feature at frequencies up to a few kilo Hertz. Other nonpowerline frequency man-made noise was also evident. APDs indicate a change in noise level between business and nonbusiness day. Definite day-night cycles were observed in powerline H-field levels at three of the four sites.

9. BIBLIOGRAPHY

1. Brigham, E.O., "The Fast Fourier Transform and Its Applications," (Englewood Cliffs, NJ, USA, Prentice-Hall Inc.), 1988, ISBN 0-13-307505-2, pp. 131-166.

2. Harris, F.J., "On the Use of Windows for Harmonic Analysis with the Discrete Fourier Transform," Proc. IEEE, Vol. 66, No.1,January 1978, pp. 51-84.

3. Laflin, M.G., "LF Signal and Noise Measurements in an Office Environment 10 Hz to 10 kHz," NTIA Tech. Report (to be published fall 1992).

RESULTS OF THE JOINT HIPAS/NUWC CAMPAIGNS TO INVESTIGATE ELF GENERATED BY AURORAL ELECTROJET MODULATION

Peter R. Bannister and Raymond F. Ingram
Naval Underwater Warfare Center
New London, CT 06320-5594, USA

and

Michael J. McCarrick and Alfred Y. Wong
UCLA Physics Department, Los Angeles, CA
and
HIPAS Observatory, Fairbanks, AK

SUMMARY

This paper reports the results of the first concerted effort (both experimentally and theoretically) to characterize the various parameters of the ELF HIPAS polar electrojet antenna excited by the HIPAS radiating facility. These parameters include the magnetic dipole moment, excitation height, and range and bearing dependence. The experimentally determined values of these various parameters, using a mobile ELF receiver, as well as a long distance station, are in agreement with predictions.

INTRODUCTION

Two HIPAS/NUWC campaigns were conducted during May-June and September 1990. Each campaign covered 12 consecutive days with six hours of continuous operation per day; this amounts to 144 hours of systematically acquired data. During each experimental run, the HIPAS high-power transmitters were operated at a frequency of 2.85 MHz and a power level of 8 X 100 kW with an effective radiated power (ERP) of 50 MW. The vertically-directed HF power was typically amplitude modulated with a square-wave envelope at 154 Hz. The HIPAS (HIgh Power Auroral Stimulation) ionospheric heater is located in the auroral zone 40 km east of Fairbanks, Alaska. For a detailed description of the HIPAS facility, see Wong, et al, (1990).

Absorption of the extremely-low frequency (ELF) modulated electromagnetic wave in the lower ionosphere results in a periodic modulation of the electron tempeature between approximately 70-90 km altitude. This tempeature modulation causes a modulation of the electron-neutral collision frequency and thereby, a periodic modulation of the conductivity tensor in the region illuminated by the HIPAS beam. In the presence of an auroral electric field, modulated currents will be induced that will radiate at the ELF frequency.

Although the ELF wave is generated in a region of the ionosphere where the dielectric constant is large and negative (*i.e.*, the wave is non-propagating) a fraction of the energy escapes into the region between the earth and the ionosphere and is detectable on the ground. The purpose of the joint HIPAS/NUWC campaigns was to characterize this ELF source by making measurements of the ELF wave both directly below the HIPAS beam and at various distances from the source. These measurements were made under a wide variety of experimental conditions including natural variations of the ionospheric parameters and controlled variations of the HF heater source.

There have been questions in the past regarding the verification of the ionospheric source of ELF produced by modulated HF heating. One of the questions raised is the sensitivity of the ELF receiving system to modulated HF radiation. If the ELF system itself demodulates the HF skywave, for instance, the ELF measurements would be invalidated. In answer to this question, the NUWC group performed laboratory tests to measure the response of their ELF receiver to direct modulated HF radiation as a function of HF power level. During the May 1990 campaign, HF electric field measurements were made in the vicinity of the ELF system. The result was that the observed HF levels were several orders of magnitude below that required to produce detectable demodulation.

Another possible source of artificial ELF signals is the demodulation of the HF signal by nearby conducting structures. A long fence with points of poor contact, for example, could act as an HF receiver/demodulator. In this case, the signal detected by the ELF receiver would be proportional to the amplitude of the HF skywave. To test this possibility, simultaneous measurements were made of the ELF received signal and of the demodulated HF signal using a standard HF receiver. We found absolutely no correlation between the ELF receiver output and the HF modulation amplitude. ELF signals were correlated with auroral currents detected by the magnetometer chain. Thus we believe the ELF signals are of ionospheric origin.

THEORETICAL ESTIMATE

In the usual operating mode, the vertically directed HF power illuminates a circular area of approximately 20 km diameter directly above the HIPAS facility. The equivalent polar electrojet antenna (PEJ) can be thought of as a pair of crossed horizontal electric (HED) or horizontal magnetic (HMD) dipoles - each of magnetic moment m (or m_1 and m_2). For an HMD (see figure 1).

$$m \sim (IL)\Delta z, \; Am^2 \qquad (1)$$

while for an HED

$$m \sim (IL)(\delta/\sqrt{2}), \; Am^2 \qquad (2)$$

where δ is the ionospheric skin depth. For a homogeneous, isotropic ionosphere

$$\delta \sim \left[\frac{\omega^2\mu_0\varepsilon_i}{2}\left(\sqrt{1+\frac{\sigma_i^2}{\omega^2\varepsilon_i^2}}-1\right)\right]^{-1/2} \quad (3)$$

Past measurement [Barr and Stubbe, 1984 a, b; Stubbe *et al*, 1985] have shown that for frequencies of 1 to 200 Hz, the PEJ essentially behaves as an HMD rather than as an HED (i.e., Δz independent of frequency). Typical values quoted are $IL \sim 3$ to 5×10^4 Am and $\Delta z \sim 10$ km, resulting in $m \sim 3$ to $5 \times 10^8 Am^2$.

The HMD (or HED) is located at height h with respect to a cylindrical coordinate system (ρ, ϕ, z) and is assumed to carry a constant current I. The axis of the HED is oriented in the x direction, while the axis of the HMD is oriented in the y direction. The ionosphere is located at the height $z \geq h$ while the earth is located at height $z \leq 0$. The propagation constant in the air is denoted by γ_o ($= ik = i2\pi / \lambda_o$), whereas the effective propagation constants in the earth and ionosphere are denoted by γ_e ($=[i\omega\mu_0(\sigma_e + i\omega\varepsilon_e)]^{1/2}$) and γ_i ($=[i\omega\mu_0(\sigma_i + i\omega\varepsilon_i)]^{1/2}$), respectively. The magnetic permeability of the whole space is assumed to equal μ_o, the permeability of free space. Meter-kilogram-second (MKS) units are employed, and a suppressed time factor of exp ($i\omega t$) is assumed.

When the measurement distance ρ is greater than approximately three ionospheric reflecting heights from the source, each HED and HMD field component expression varies as the Hankel function $H_0^{(2)}(kS_o\rho)$ or $H_1^{(2)}(kS_o\rho)$ (or a combination of the two), where ikS_o is the propagation constant in the earth-ionosphere waveguide. S_o is related to the phase velocity v and attenuation rate α by the formulas $c/v = \mathrm{Re}\, S_0$ and $\alpha = -8.7\, k\, \mathrm{Im}\, S_0$.

At ELF (i.e., 30 to 300 Hz; ITT [1968],

$$H_o^{(2)}(kS_0\rho) \sim H_0^{(2)}(x)e^{-\alpha\rho} \quad (4)$$

and

$$H_1^{(2)}(kS_0\rho) \sim H_1^{(2)}(x)e^{-\alpha\rho} \quad (5)$$

where

$$x = k\rho(c/v) \quad (6)$$

Accounting for ionospheric reflection effects to distances of approximately three reflecting heights (h) is a tedious process involving an infinite sum of images or modes [Wait, 1970; Galejs, 1972; Martin, 1964]. However, by following the procedure outlined by Martin [1964], Bannister and Williams [1974], and Bannister [1986], practical approximate formulas can easily be obtained.

In this article, we will use previously derived [Wait, 1961; Baños, 1966; Kraichman, 1970; Bannister, 1967] quasi-near-field range formulas ($\rho > \lambda_e$, $\rho \ll \lambda_0$, $\rho < h/3$), as well as the Wait [1970] and Galej [1972] formulas ($\rho > 3h$), to find HED and HMD formulas valid at ELF for $R > \lambda_i$ with no restrictions on the ratio of ρ to h ($R = (\rho^2 + h^2)^{1/2}$).

As an example of our derivation procedure, consider the HMD H_ϕ component. When $\rho > 3h$ the higher order evanescent modes can be neglected [Wait, 1970]. Therefore

$$H_\phi \sim \frac{m\cos\phi\, e^{-\alpha\rho}}{2\pi h\rho^2}\left[\frac{\pi}{2}(k\rho)^2\right]\left[H_0^{(2)}(x) - \frac{H_1^{(2)}(x)}{x}\right] \quad (7)$$

For $x \leq 0.25$ and $c/v \sim 1$ (*i.e.*, $\rho \leq 150$ km), (7) reduces to

$$H_\phi \sim \frac{m\cos\phi}{2\pi h\rho^2} \quad (8)$$

For short distances ($\rho < h/3$), the quasi-near range formula is [Bannister, 1967]

$$H_\phi \sim \frac{m\cos\phi}{2\pi h^3} \quad (9)$$

If we let

$$H_\phi \sim \frac{m\cos\phi}{2\pi hR^2} \quad (10)$$

we see that for $\rho > 3h$, (10) reduces to (8), while if $\rho < h/3$, (10) reduces to (9). Therefore, by substituting R for ρ in (7), we obtain the general formula valid for $R > \lambda_i$ (with no restrictions on the ratio of ρ to h). It is

$$H_\phi \sim \frac{m\cos\phi\, e^{-\alpha R}}{2\pi hR^2}\left[\frac{\pi}{2}(kR)^2\right]\left[H_0^{(2)}(x) - \frac{H_1^{(2)}(x)}{x}\right] \quad (11)$$

where x now equals kR (c/v).

FIELD STRENGTH FORMULAS

In this section, we will present approximate formulas for HMD (or HED) ELF radio wave propagation in the earth-ionosphere waveguide. Most of these formulas have been obtained by following the procedure outlined in the previous section. They are valid for the source located at height z = h, the receiver located at the earth's surface (*i.e.*, z = 0), and $R > \lambda_i$ with no restrictions on the ratio of ρ to h.

It should be noted that for 2 Mm $\leq \rho \leq$ 19 Mm, all of the

field strength component formulas presented in this article should be multiplied by the spherical earth spreading factor S, which is equal to

$$S = \left[\frac{\rho/a}{\sin(\rho/a)}\right]^V \tag{12}$$

where V = 1/2 for all E_ρ, E_z, and H_φ components; V = 3/2 for all E_φ and H_ρ components; and a is the radius of the earth (~ 6.37 Mm) [Galejs, 1972]. This factor (12) neglects the antipodal or "round-the-world" signal. Adequate field-strength formulas for this signal are readily available [Burrows, 1978; Wait, 1960, 1970; Galejs, 1972]. For less than approximately 150km:

$$E_z \sim -\frac{i\omega\mu_0 \cos\phi \sin\theta}{2\pi hR} \tag{13}$$

$$H_\phi \sim \frac{m\cos\phi}{2\pi hR^2} \tag{14}$$

$$H_\rho \sim -\frac{m\cos\phi}{2\pi hR^2}\left(1 - \frac{2h^2}{R^2}\right) \tag{15}$$

$$H_z \sim \frac{8m\sin\phi\sin\theta\cos\theta}{2\pi R^3(\gamma_e R)} \tag{16}$$

and

$$\frac{E_\phi}{H_\rho} \sim -\frac{E_\rho}{H_\phi} \sim \eta_e = \sqrt{\frac{i\omega\mu_0}{\sigma_e + i\omega\varepsilon_e}} \tag{17}$$

where $R^2 = \rho^2 + h^2$, $\sin\theta = \rho / R$, and $\cos\theta = h / R$. For the general case (i.e., ρ greater than approximately 150 km)

$$E_z \sim -\frac{i\omega\mu_0 m \cos\phi \sin\theta}{2\pi hR} \times \left[\left(\frac{-i\pi x}{2}\right) H_1^{(2)}(x)\right] e^{-\alpha R} \tag{18}$$

$$H_\phi \sim \frac{m\cos\phi}{2\pi hR^2}\left[\frac{\pi}{2}(kR)^2\right] \times \left[H_0^{(2)}(x) - \frac{H_1^{(2)}(x)}{x}\right] e^{-\alpha R} \tag{19}$$

and

$$H_\rho \sim -\frac{m\sin\phi}{2\pi hR^2}\left[1 - \frac{2h^2}{R^2}\right] \times \left[\left(\frac{-i\pi x}{2}\right) H_1^{(2)}(x)\right] e^{-\alpha R} \tag{20}$$

where x now equals kR (c/v).

Typical values of H_φ are plotted in figure 2. For these plots, m = 3 x 10^8 Am^2, and ϕ = 0°. The 154Hz H_φ plots are for three different values of h - 50, 75, and 100 km. Note that for short distances $H_\varphi \rightarrow h^{-3}$, while for greater distances $H_\varphi \rightarrow h^{-1}$.

We have also derived approximate expressions for a finite length source (L large compared to Δz). For the infinitesimal antenna located along the x axis and $\rho \leq 150$ km:

$$E_z \sim -\frac{i\omega\mu_0 I\Delta z\, x\, dx}{2\pi hR^2} \tag{21}$$

$$H_x \sim -\frac{I\Delta z\, y\, x\, dx}{\pi hR^4} \tag{22}$$

$$H_y \sim +\frac{I\Delta z\, dx}{2\pi hR^2}\left(1 - \frac{2y^2}{R^2}\right) \tag{23}$$

and

$$H_z \sim \frac{4I\Delta z\, y h\, dx}{\pi\gamma_e R^6} \tag{24}$$

The finite length antenna formulas may be determined in a straightforward fashion by integrating (21) through (24) over the length of the antenna (i.e., from $x_1 = x - L/2$ to $x_2 = x + L/2$). The resulting formulas are:

$$E_z \sim -\frac{i\omega\mu_0 I\Delta z}{2\pi h}\ln\frac{R_1}{R_2} \tag{25}$$

$$H_x \sim -\frac{mxy}{\pi h R_1^2 R_2^2} \tag{26}$$

$$H_y \sim +\frac{I\Delta z}{2\pi hr}\left[\left(1-\frac{y^2}{r^2}\right)\times\left(\tan^{-1}\frac{(x+L/2)}{r}-\tan^{-1}\frac{(x-L/2)}{r}\right)-\frac{y^2}{r^2}\left(\frac{(x+L/2)r}{R_1^2}-\frac{(x-L/2)r}{R_2^2}\right)\right] \tag{27}$$

$$H_z \sim \frac{I\Delta z\,yh}{2\pi\gamma_e r^5}\left[3\left(\tan^{-1}\frac{(x+L/2)}{r}-\tan^{-1}\frac{(x-L/2)}{r}\right)+\frac{(x+L/2)r[5r^2+3(x+L/2)^2]}{[(x+L/2)^2+r^2]^2}+\frac{(x-L/2)r[5r^2+3(x-L/2)^2]}{[(x-L/2)^2+r^2]^2}\right] \tag{28}$$

and

$$\frac{E_y}{H_x} \sim -\frac{E_x}{H_y} \sim \eta_e \tag{29}$$

where

$$L = PEJ\ antenna\ length$$

$$r^2 = y^2 + h^2$$

$$R_1^2 = (x+L/2)^2 + r^2$$

and

$$R_2^2 = (x-L/2)^2 - r^2$$

RECEIVING SYSTEMS

The UCLA ELF sensors and data acquisition system [McCarrick, *et al*, 1980] are located at the NOAA tracking station in Gilmore Creek, Alaska. This site is 35 km northwest of the HIPAS Facility. The ELF receiving system consists of a pair of magnetic detectors oriented geographic NS and EW, and a vertical electric field sensor. The magnetic detectors are large, high-permeable coils that are buried for stability. The coils have recently been calibrated in absolute terms. The electric field sensor is more difficult to calibrate and is used as a relative measurement only.

The amplified output of the three ELF channels is digitized and recorded continuously to a large-capacity optical disk. At the same time, the acquisition computer cross-correlates the waveforms with the ELF reference frequency and integrates the result to provide a real-time display of the ELF signal strength and phase. This result is also transmitted to the HIPAS control room via telephone lines so that the signal condition can be monitored while the experiment is in progress.

The NUWC ELF receiver consists of a single air-core loop, preamplifier, and a dedicated digital processor. The receiver is self-contained and portable. During the May 1990 campaign, the NUWC receiver was positioned at a number of receiving sites at distances between 20 km and 300km from the HIPAS transmitting site. During the September 1990 campaign, the NUWC receiver remained at a single location at Talkeetna, Alaska, 330 km southwest of HIPAS.
The NUWC receiver is designed to have maximum sensitivity between 40 Hz and 200 Hz, in contrast to the UCLA receiver, which is most sensitive from approximately 5 Hz to 50 Hz. Most of the experiments were performed at an ELF frequency of 154 Hz. Since the near-field [Gilmore] ELF signal strengths are typically 20 dB higher than signals received at Talkeetna, comparable signal-to-noise ratios were obtained between the two systems despite the reduced sensitivity of the UCLA receiver at this frequency.

A secondary purpose of the May/June campaign was to provide an absolute calibration of the UCLA ELF receiver. Prior to this series of experiments, the response of the UCLA receiver was known approximately within the pass band of 5-50 Hz. However, the response at 154 Hz was not calibrated. In addition, no independent measurement of ELF signals produced by HIPAS modulation had been made. By locating the NUWC receiver side-by-side with the UCLA receiver, we were able to provide this calibration.

Prior to the September campaign, a calibration system was installed for the UCLA magnetic field sensors. This includes a driver coil that was buried at a fixed distance from the sensors, a tunable frequency source, and software to calculate the response based on the calculated coupling between the driver coil and the sensors. The system response is now known absolutely over the full passband. The new calibration agrees extremely well with the previous calibration at NUWC.

CHARACTERIZATION OF POLAR ELECTROJET (PEJ)

The primary goal of the May/June 1990 campaign was to make measurements at multiple distances in order to verify the theoretical H_ϕ versus distance curve and determine the average values of m and h. The secondary goal was to determine the pattern of the equivalent PEJ source. Measurements were made at distances between 20 and 300 km and at various angles with respect to the ionospheric current source.

The EW polar electrojet current flows in the E region at an altitude of approximately 110 km. However, maximum heating takes place in the D region at a typical altitude of 75 km [Tomko, 1981]. This implies that what actually happens is not a direct modulation of the electrojet current but rather a

modulation of the currents in the D region that are mapped down from the electrojet source. Werner and Ferraro [1990] have found that the electrojet mapping through the D region becomes independent of spacial wavelength when the wavelength exceeds 100 km and can be completely characterized in terms of the Pedersen and Hall conductivities. They also found that there will be a NS component of the current density at the altitude of the ELF source, (approximately 75 km), even though there is no NS component at the altitude of the electrojet. This mapping property can be attributed to the anisotropy of the ionosphere.

At HIPAS, the magnetic NS is 28° E of N, while the magnetic EW direction is 118° E of N. If we assume that the equivalent PEJ consists of two equal magnitude, in phase, perpendicular antennas located in the magnetic NS and EW directions, then the resulting source pattern will be equal to cosφ with the φ = 0° direction 45° from either antenna (see figure 3). For this situation, the φ = 0° direction is 17° N of E (or S of W).

The normalized (to φ = 0°) field strength averages measured at each of the eight locations are presented in figure 4. (φ =0° corresponds to 17° E of N (or S of W)). Also plotted in figure 4 is the theoretical field strength versus distance curve (from 19) for the case where m = 1.69 x 10^8 Am^2 and h = 75 km. Note the close agreement between the predicted and measured field strengths. It should also be noted that the September average field strengths were approximately 11 dB greater than the May/June average field strengths (*i.e.*, m = 6 x 10^8 A m^2 and h = 75 km).

The PEJ pattern can also be obtained by measuring two orthogonal horizontal magnetic field components (*e.g.*, H_φ and Hρ) at various distances and angles from the source [Bannister, *et al*, 1974]. A comparison of (19) and (20) results in

$$\frac{H_\phi}{H_\rho} \sim F(f,R)\cot\phi \qquad (30)$$

where F(f, R) is a frequency and range dependent function. For f = 154 Hz and ρ = 300 to 350 km, F(f, R) ~ 1.10.

Presented in figure 5 is plot of the magnitude of H_φ to H_ρ (in dB) versus φ for Talkeetna, AK (ρ = 330 km). The measured value (+ 0.8 dB) is also plotted. A comparison of the predicted and measured values yields φ = 45°, which for the Talkeetna location, also indicates that the PEJ is oriented 17° N or E (or S of W).

FREQUENCY DEPENDENCE OF PEJ DIPOLE MOMENT

Presented in Figure 6 are theoretical plots of magnetic field strength versus distance (from 19) for frequencies of 78, 154, and 198 Hz. For these plots, m = 6 x 10^8 Am^2, h = 75 km, and ϕ = 0° . Note that for constant dipole moment m, the 10 to 150 km field strengths are identical However, at the Talkeetna site (330 km), the 154 and 198 Hz field strengths are 3 to 6 dB greater than the 78 Hz field strength.

Past measurements [Stubbe, *et al.*, 1985] have indicated that the 1 to 200 Hz field strengths (measured at a site 17 km from the Tromso HF heater) were essentially identical, which infers a constant PEJ dipole moment.

During May 28 and 29, the 78 and 154 Hz field strengths were measured at the Gilmore Creek Site and at a 10 km location. The 78 Hz measured field strengths were approximately 3 dB *greater than* the 154 Hz field strengths. On September 24, the 35 km 78 Hz measured field strengths were approximately 2 dB *greater than* the 154 Hz field strengths, while Talkeetna (330 km) 78 Hz field strengths were approximately 1 dB *greater than* the 154 Hz field strengths (rather than the expected 3 dB lower).

These recent measurements suggest that the 78 Hz PEJ dipole moment is approximately 3 dB greater than the 154 Hz dipole moment. That is, the HIPAS PEJ appears to be acting like an HED rather than a HMD. These frequency comparison measurements should be repeated and extended.

DEPENDENCE OF ELF SIGNAL ON IONOSPHERIC PARAMETERS

A number of interesting observations can be made by comparing the ELF signal amplitude and phase with the ionospheric parameters, inferred from the College, AK magnetometer and riometer traces. Figure 7 shows data from 15 September 1990. The most apparent feature of this data is the clear 180 degree phase reversal of the ELF signal as the magnetometer H-trace reverses sign. The H trace shows the horizontal NS component of the magnetic field, with positive defined as northward. An overhead eastward electrojet current will cause a positive H deviation, while a westward electrojet shows up as a negative H deviation. In figure 7 it is clear that as the H component pass through and oscillates about zero, the ELF phase also oscillates about -90 and +90 degrees. When the westward electrojet surges strongly at 1130, the ELF phase finally locks at +90 degrees. It is also apparent that there is not a straightforward correspondence between the amplitude of the ELF signal and the deviation of the magnetometer H component. During the eastward electrojet, there is at least a weak correlation with a peak in the magnetometer around 1000 UT corresponding to a peak in the ELF signal at the same time. On the other hand, the very large currents seen during the westward surge between 1130 and 1300 UT do not produce a larger ELF signal. The large currents are likely due to an increase in conductivity because of increased ionization in the lower ionosphere. This can be seen by inspecting the riometer signal, which shows relative absorption of cosmic 30 MHz noise as it passes through the ionosphere. The abrupt increase in absorption at 1130 UT is coincident with the large negative excursion of the magnetometer H component.

The effect of increased absorption in the lower ionosphere on the ELF signal strength is somewhat indeterminate. Since the modulated current density is proportional to the DC conductivity, one might expect increasing ionization to increase the ELF signal. However, there are two factors which work in the opposite direction. Firstly, under some circumstances the increased conductivity appears to "short out" the auroral electric field. This can be seen in coherent radar data where there is sudden loss of cross-field backscatter coincident with a large absorption event. The mechanism which is responsible for coherent backscatter depends on a threshold value of the electric field. Secondly, under very high absorption conditions, the HF wave may be absorbed very low in the *D* region where the conductivity is extremely low.

LONG DISTANCE PROPAGATION (HIPAS/CONNECTICUT)

Following Bannister [1975], when R>0.2 λ_0 and $\rho > 3h$, the Hankel functions in (19) may be replaced by the first terms of their asymptolic expansions, resulting in (for f = 154 Hz and m = 6 X 10^8 Am^2):

$$H_\phi \sim -123.1 - 20\log h - 10\log c/v - \alpha\rho - 10\log[a\sin\rho/a] + 20\log\cos\phi \quad (31)$$

where h is in km, ρ and a in Mm, and α in dB/Mm. For other frequencies (assuming constant m)

$$H_\phi \rightarrow f^{3/2} \quad (32)$$

Presented in figure 8 are two nighttime plots of H_ϕ versus ρ for measurement distances of 10 km to 10 Mm. For these plots, f = 154 Hz, h = 75 km, α = 1.7dB/Mm, φ = 0°, and m = 1.7 x 10^8 Am^2 (May/June result) or 6 x 10^8 Am^2 (September result).

For the HIPAS/Connecticut path, ρ = 5.2 Mm and φ = 7°. For m = 1.7 X 10^8Am, H_φ ~ - 187 dBA/m, while for m = 6 x 10^8Am^2, H_φ ~ - 176 dBA/m. At the Connecticut site, the typical Winter month's variation of 154 Hz "clipped" atmospheric noise field strength is from -156 to -146 dBA/m/ Hz. Assuming the average value is -151 dBA/m/$\sqrt{Hz}$, then if m = 6 x 10^8, the SNR will be 7.5 dB after 0.5 hr and 10.5 dB after 1 hr integration time - therefore, detectable. However, if m = 1.7 x 10^8Am^2, the HIPAS/Connecticut signals will be undetectable even after an hour's integration time.

154 Hz HIPAS transmissions were successfully received in Connecticut during 5 nights in December 1990/January 1991, and also during 5 nights in September/October 1991. The average field strengths are plotted in figure 9, along with the simultaneous Gilmore Creek AK averages. During these reception periods, the average HIPAS PEJ dipole moments were 4.0 X10^8Am^2 (December 1990/January 1991) and 12 X 10^8Am^2 (September/October 1991). To date, the HIPAS/Connecticut path (5.2 Mm) is the longest path over which ELF PEJ transmissions have been successfully received.

HIPAS PEJ/COMBINED ELF SYSTEM COMPARISONS

Presented in Table 1 are the 154 Hz magnetic dipole moments inferred from the joint HIPAS/NUWC 1990 campaigns. During the May/June campaign, m = 1.69 X 10^8Am^2 (0500 - 1100 UT), 2.12 X 10^8Am^2 (0800 - 1100 UT) and 2.83 X 10^8Am^2 (high value). The high value field strength samples are those whose magnitude exceeded the nightly average value at each measurement location. During the 15 to 25 September period, m = 6.0 X 10^8Am^2 (0800 - 1400 UT), and 9.0 X 10^8Am^2 (high value). However on 26 September, the ELF signal strength was very weak, resulting in m = 2.12 X 10^8Am^2, which was the same as the avg 0800 - 1100 UT May/June inferred value.

For the US Navy's ELF Wisconsin Transmitter Facility (WTF), I = 300A, L = 22.5 km, and σ_e = 3.2 X 10^{-4} S/m. From (2), the WTF 76 Hz magnetic dipole moment is 1.55 X $10^{10}Am^2$. When combined with the Michigan Transmitter Facility (MTF), there is a 6.7 dB gain so that the combined 76 Hz WTF/MTF dipole moment is 3.35 X $10^{10}Am^2$.

Referring to table 1, we see that the 154 Hz magnetic dipole moment was less than the 76 Hz combined WTF/MTF magnetic dipole moment by a factor of 200 (46 dB) during the 0500 - 1100 UT spring period and by a factor of 56 (35 dB) during the 0800 - 1400 UT fall period. In order for the HIPAS PEJ system to be comparable to the WTF/MTF system, it's efficiency (which varies as m^2) must be increased by a factor of 3 X 10^3 to 4 X 10^4. Papadopoulos, et al [1990] have proposed two methods of achieving this increase in efficiency. These, and other methods, will be attempted in future HIPAS PEJ measurements.

CONCLUSION

In this paper, we have presented approximate field strength formulas for both horizontal dipole and finite length polar electrojet (PEJ) sources. These formulas are valid at any range from the source.

We have also shown that the results of the 1990 joint HIPAS/NUWC campaigns to investigate ELF generated by auroral electrojet modulation are consistent with our recently developed theory. The 154 Hz average dipole moments inferred were 1.7 X 10^8Am^2 (spring) and 6.0 X 10^8Am^2 (fall), while the average excitation altitude of the ELF source was shown to be equal to 75 km. The HIPAS PEJ is also characterized by a cos φ dependence, with φ = 0° approximately equal to 17° N of E (or S of W).

Our measurements also indicated that the 78 Hz PEJ dipole moment was approximately 3 dB greater than the 154 Hz dipole moment. That is, the HIPAS PEJ appears to be behaving like an HED rather than an HMD.

We have also shown that in order for the HIPAS PEJ system to be comparable to the ELF combined WTF/MTF system, it's efficiency must be increased by a factor of 3 X 10^3 to 4 X 10^4. Beam painting has been proposed as a way to increase the PEJ efficiency. However, the beam painting experiments to date have been indecisive.

Based upon subsequent measurements, we have shown that he HIPAS/ Connecticut path far field measurements are in agreement with near field measurements. To date, the HIPAS/Connecticut path (5.2 Mm) is the longest path over which ELF PEJ transmissions have been successfully received.

By far, the largest variations in the PEJ produced ELF signal strengths are due to natural variations in ionospheric conditions.

REFERENCES

Bannister, P. R., (1967), The quasi-near fields of dipole antennas, IEEE Trans. Antennas Propagat., AP-15(5), 618-626.

Bannister, P. R., (1975), Variations in extremely low frequency propagation parameters, J. Atmos. Terr. Phys., 37(9), 1203-1210.

Bannister, P. R., (1986), Simplified formulas for ELF propagation at shorter distances, Radio Sci., 21(3), 529-537.

Bannister, P. R., and F. J. Williams, (1974), Results of the August 1972 Wisconsin Test Facility effective earth conductivity measurements,J. Geophys. Res., 79(6), 725-732.

Bannister, P. R., F. J. Williams, A. L. Dahlvig, and W.A. Kraimer, (1974), Wisconsin Test Facility transmitting antenna pattern and steering measurements, IEEE Trans. Commun., com-22(4), 412-418.

Baños, A., Jr., (1966), Dipole Radiation in the Presence of a Conducting Half-Space, Pergamon, New York.

Barr, R., and P. Stubbe, (1984a), The "polar electrojet antenna" as a source of ELF radiation in the Earth-ionosphere waveguide, J. Atmos. Terr. Phys., 46, 315-320.

Barr, R., and P. Stubbe, (1984b), ELF and VLF radiation from the "polarelectrojet antenna," Radio Sci., 19, 1111-1122.

Burrows, M. L., (1978), ELF Communications Antennas, Peter Peregrinus,Stevenage, United Kingdom.

Galejs, J., (1972), Terrestrial Propagation of Long Electromagnetic Waves,Pergamon, New York.

International Telephone and Telegraph (ITT) Reference Data for Radio Engineers, 5th ed., (1968), pp. 1-2, New York, NY.

Kraichman, M. B., (1970), Handbook of Electromagnetic Propagation in Conducting Media, U. S. Government Printing Office, Washington, D.C.

Martin, C. A., (1964), Site evaluation for a Beverage type transmitting antenna, PANGLOSS Task 4 Tech. Note 6, RCA Lab., Princeton, N.J.

McCarrick, J. J., Sentman, D. D., Wong, A. Y., Wuerker, R. F. and Chouindard, "Excitation of ELF waves in the Schumann resonance range by modulated HF heating of the polar electrojet", Radio Sci., 25(6):1291-1298, 1990.

Papadopoulos, D., C. L. Chang, P. Vitello, and A. Drobot (1990), On the efficiency of ionospheric ELF generation, Radio Sci., 25(6), 1311-1320.

Stubbe, P., et al., (1985), Ionospheric modification experiments with the Tromso heating facility, J. Atmos, Terr. Phys., 47, 1151-1163.

Tomko, A. A., (1981), Nonlinear phenomena arising from radio heating ofthe lower ionosphere, Rep. PSU-IRL-SCI-470, Ionos, Res. Lab., Penn.State Univ., University Park.

Wait, J. R., (1960), Mode theory and the propagation of ELF radio waves,Radio Sci., 64D(4), 387-404.

Wait, J. R., (1961), The electromagnetic field of a horizontal electrical dipole in the presence of a conducting half-space, Can. J. Phys., 39(7),1017-1028.

Wait, J. R., (1970), Electromagnetic Waves in Stratified Media, Pergamon,New York.

Werner, D. H. and A. J. Ferraro, (1990), Mapping of the polar electrojet current down to ionospheric D region altitudes, Radio Sci., 25(6),1375-1386.

Wong, A. Y., et al., (1990), High-power radiating facility at the HIPAS Observatory, Radio Sci, 25(6), 1269-1282.

TABLE 1

154HZ HIPAS MAGNETIC DIPOLE MOMENTS

DATES	TYPE OF AVERAGE	$m(Am^2)$	dB relative to $1.69X10^8Am^2$
5/29 - 6/5/90	0500 - 1100UT	$1.69X10^8$	0
5/29 - 6/5/90	0800 - 1100UT	$2.12X10^8$	2.0
5/29 - 6/5/90	HIGH VALUE	$2.83X10^8$	4.5
9/15 - 9/25/90	0800 - 1400UT	$6.0x10^8$	11.0
9/15 - 9/25/90	HIGH VALUE	$9.0X10^8$	14.5
9/26/90	NORMAL MODULATION SAMPLES	$2.12X10^8$	2.0

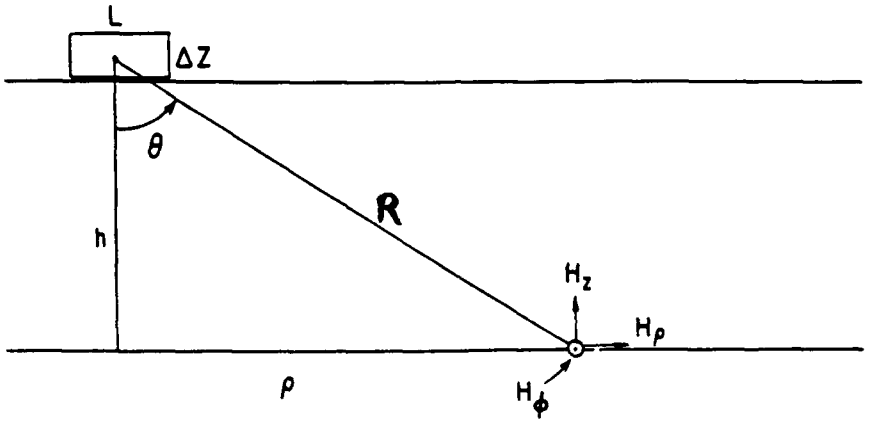

1. Geometry of the theoretical model.

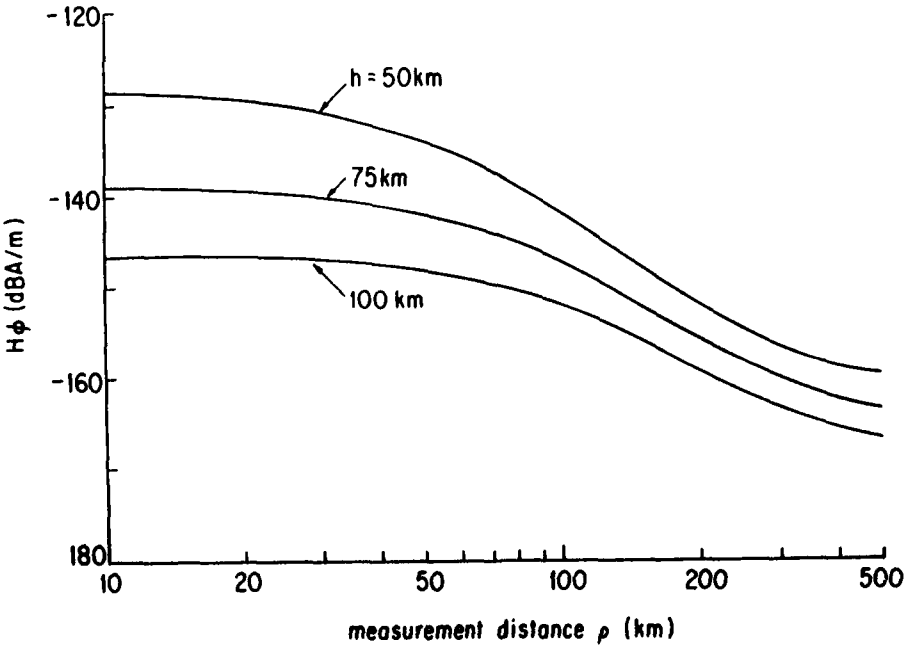

2. H_ϕ versus ρ for f = 154 Hz, m = 3 x 10^8 Am^2, α = 1.7 dB/Mm, ϕ = 0°, and h = 50, 75, 100 km.

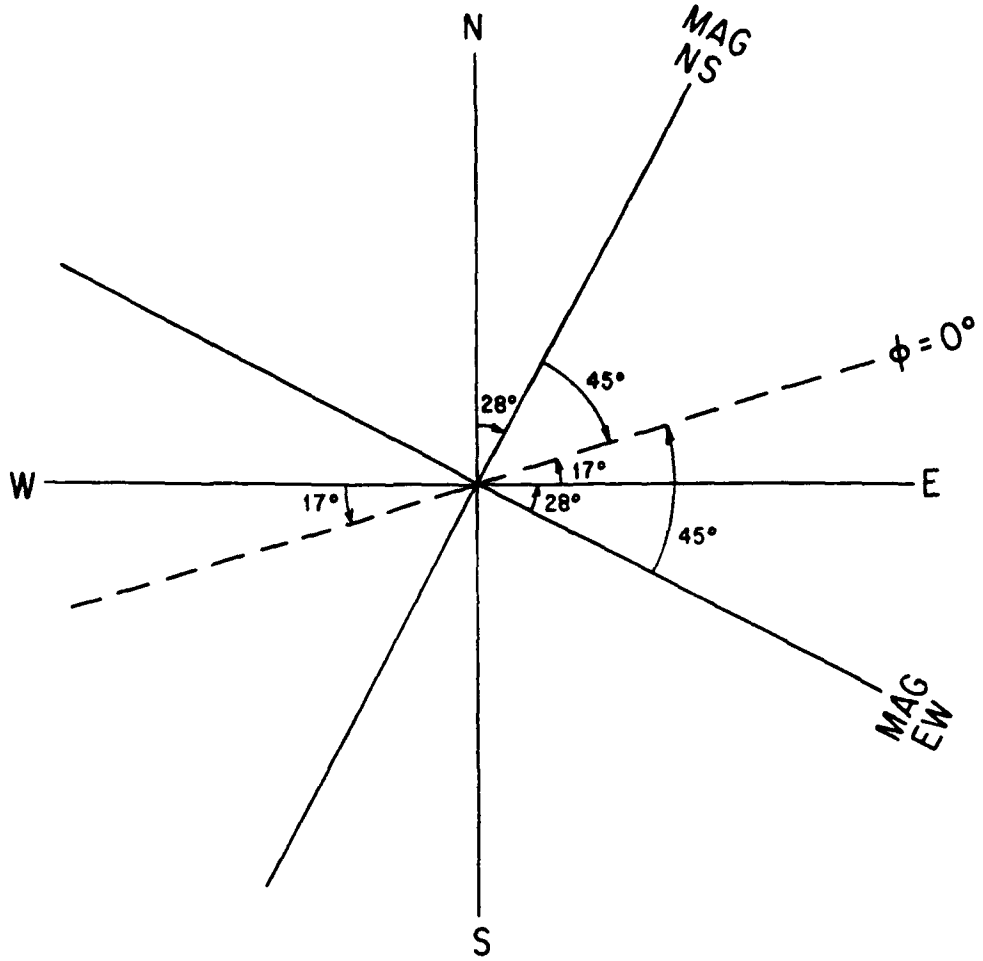

3. HIPAS PEJ crossed dipole system.

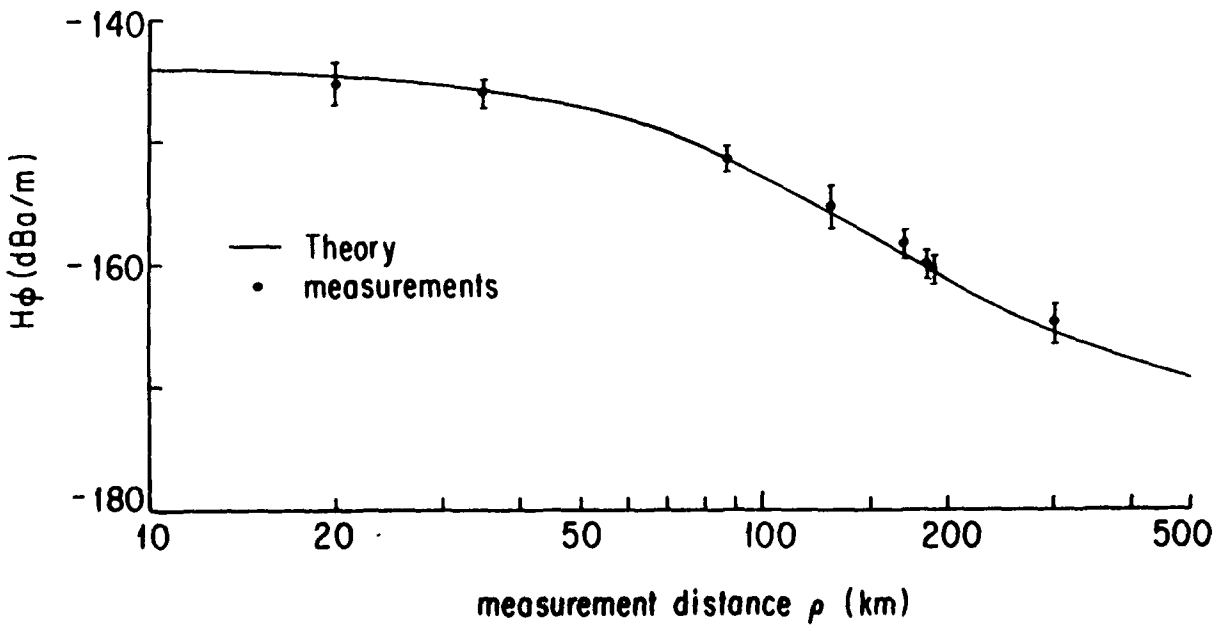

4. May / June 1990 154 Hz 0500 - 1100 UT normalized (to $\phi = 0°$) field strength averages versus distance. (The solid line is a theoretical plot for $m = 1.69 \times 10^8$ Am^2, $h = 75$ km, and $\alpha = 1.7$ dB/Mm.)

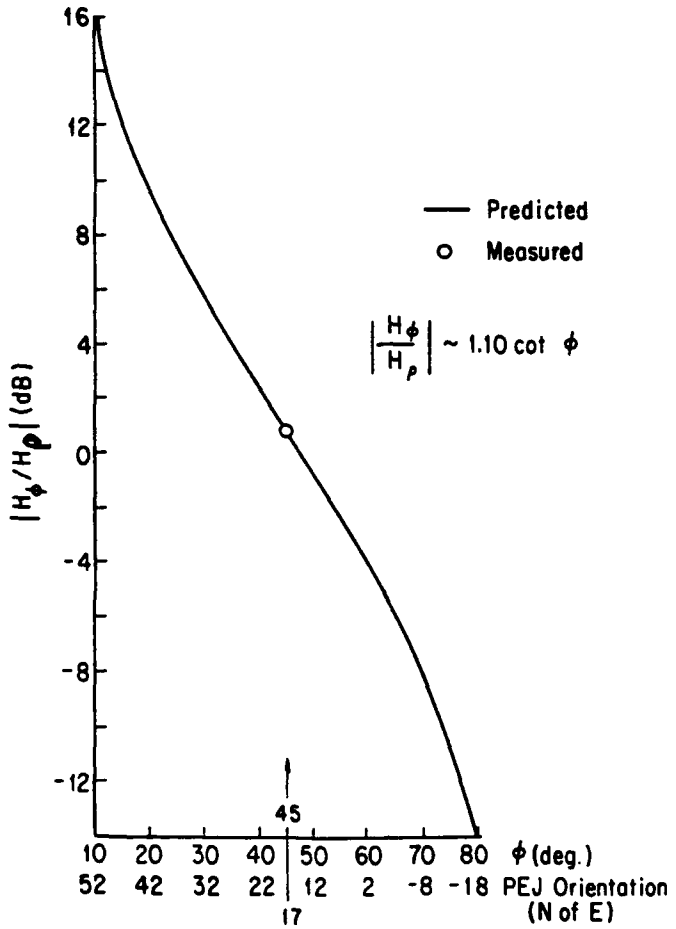

5. $| H_\phi / H_\rho |$ versus PEJ orientation. Talkeetna, Alaska (ρ = 330 km).

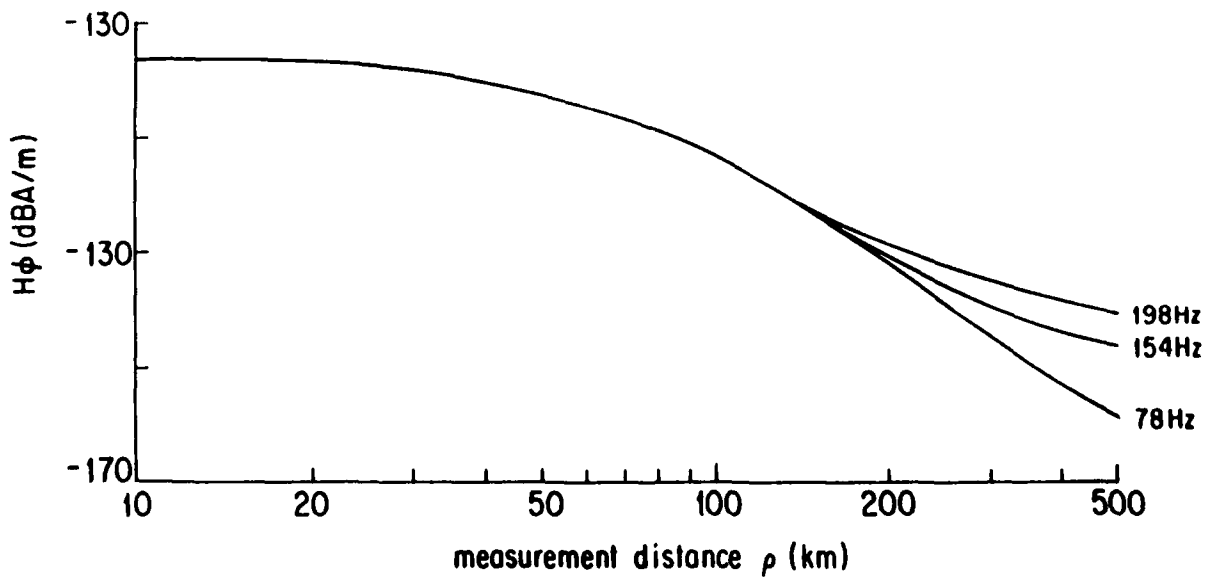

6. Theoretical plots of 78, 154, and 198 Hz magnetic field strength versus distance. $m = 6 \times 10^8$ Am^2, h = 75 km, $\phi = 0°$, and α = 1.7 dB/Mm.

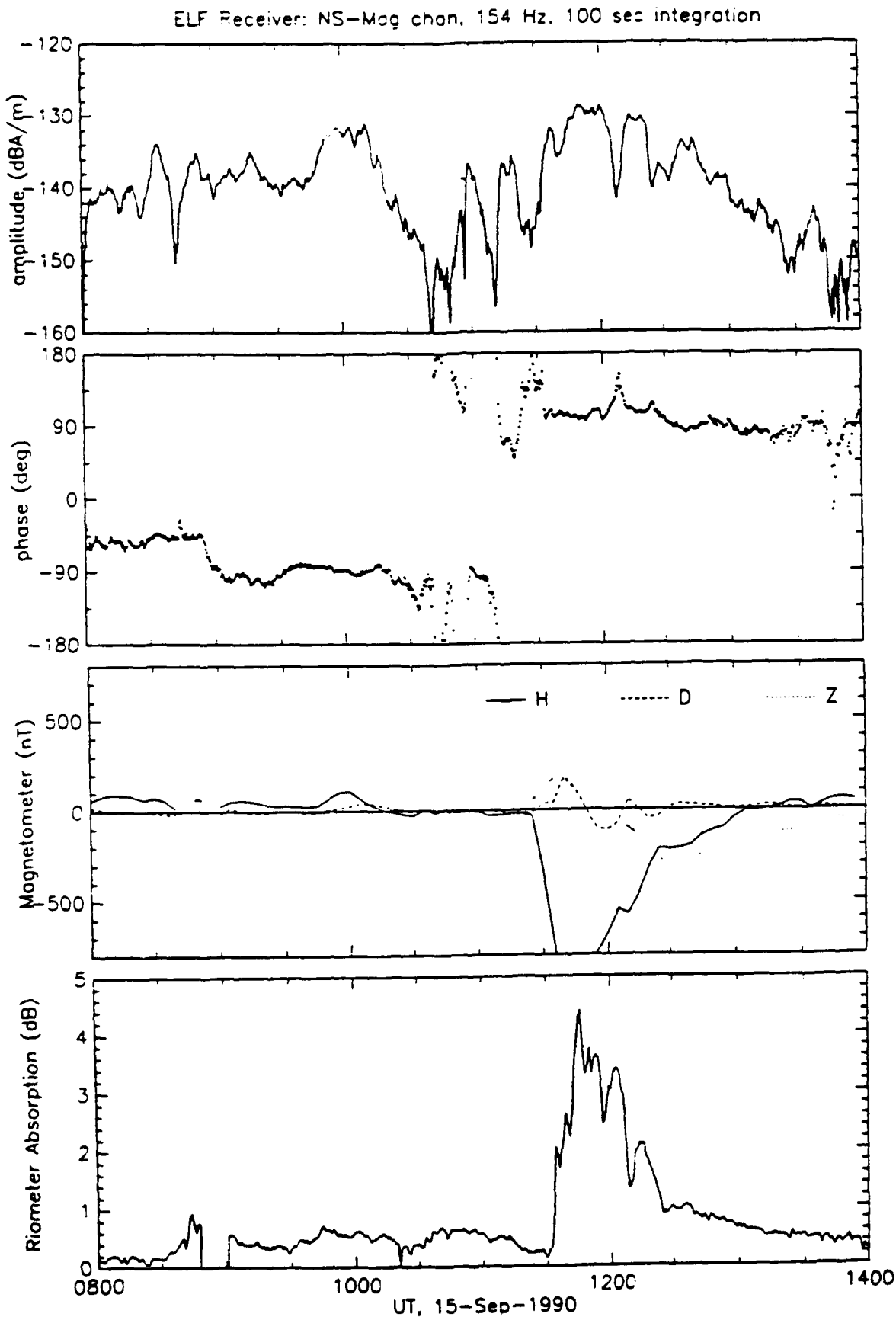

7. Comparison of 15 September Gilmore H_{NS} field strengths with magnetometer and riometer absorption data.

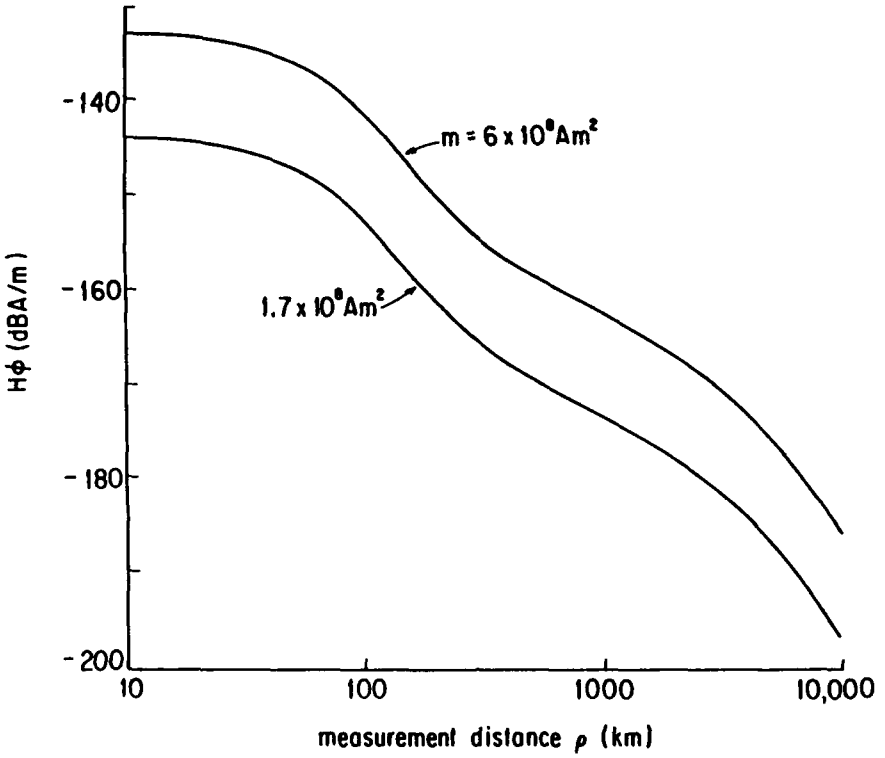

8. 154 Hz nighttime plots of H_ϕ versus ρ for distance of 10 km to 10 Mm. h = 75 km, ϕ = 0°, and α = 1.7 dB/Mm.

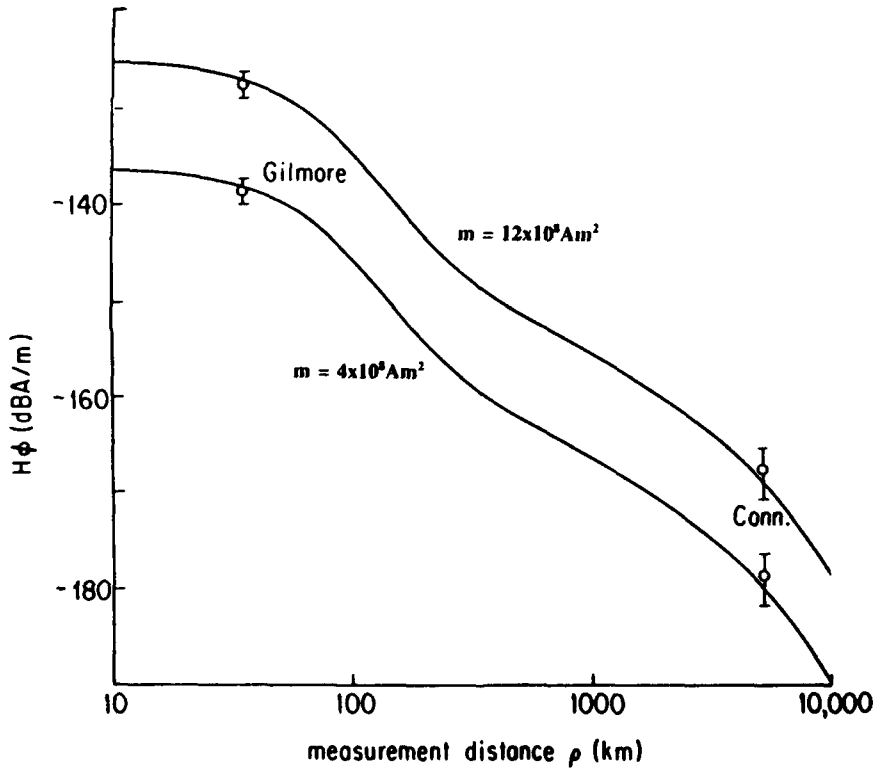

9. December 1990 / January 1991 and September / October 1991 Connecticut and Gilmore Creek, AK, 154 Hz field strength averages. The theoretical plots are for m = 4.0 x 10^8 Am^2 and 12 x 10^8 Am^2, h = 75 km, ϕ = 0°, and α = 1.7 dB/Mm.

VLF/LF Transmitting Antennas

John S. Belrose
Communications Research Centre
P.O. Box 11490 Stn. H
Ottawa ON K2H 8S2
Canada

1. Introduction

VLF transmitting antenna design is a specialized field of engineering that requires the combined skill of radio, civil and mechanical engineers. The antenna systems used for this band (15-30 kHz) are enormous structures; vertical radiators with very extensive top-loading (non-radiating top-hats), necessary because the electrical height of practical towers is small. For tower heights of 300-450 metres (1000-1500 feet) the electrical heights are only fifteen to forty-five one thousands of a wavelength.

Various types or classes of antennas are presently in operational use. Some of the common types are: inverted-L antennas; T-antennas; multi-wire diamond antennas and paralleled combinations of diamonds; down leads from long catenaries with mountain top support (e.g. the USN Jim Creek, WA station); and the fjord mountain antenna, Narvik, Norway are employed. There are about as many configurations as there are antennas [Watt, 1967; Belrose, 1983].

Three very large VLF antennas are more or less scaled versions of each other. These are the USN stations at Cutler, ME and North West Cape, Australia; and the NATO VLF station at Anthorn, England. The top-loading consists of 6-diamond shaped wire panels, see Fig 1, supported by 13-towers of heights 243 - 390 metres high.

While indeed a high radiation efficiency is achieved (> 80% for the USN antennas operating in the 20-30 kHz band), for a new installation, in the authors view, this is not a good antenna design for the following reasons:

1) There are too many tall grounded towers;

2) Even for the largest antenna (the NWC antenna) the effective height of the antenna system is only about one-half the average height of the 13 towers. The decrease is attributed to the sag on the top loading structure, and to the many grounded towers with their extensive guy systems;

3) The top-loading contains many wires, too many wires for places where wind loading is a problem, and too many wires to ice up in a Canadian environment;

4) The star like configuration results in six sharp points, and while this forms a nice snow-flake-like pattern viewed from above, sharp points should be avoided, because of corona problems with the high transmit powers employed. It is clear that precautions were taken to avoid corona, note the large corona rings (Fig. 2);

5) The operational bandwidth, except for the largest, the NWC, Australia antenna, is less than that required for 4-channel MSK (a 200 Hz bandwidth is required). The NWC Australian antenna system is a very large installation. The outer ring of towers for this station are on a diameter of 2.5 kilometers. The problem with bandwidth is particularly a problem for the smallest of the three antenna systems Anthorn. In fact Anthorn employs bandwidth resistors, resulting in a loss in radiated power, in order to realize even a 100 Hz bandwidth.

2. A Need to Overview Antenna Design Concepts

The purpose of a study recently carried out at the Communications Research Centre was to search for new concepts, or revisit old ones; e.g. multiple tuning, an early concept [Alexanderson, 1920], to improve the radiation efficiency and bandwidth of VLF/LF antennas. During the course of the study the author had the opportunity to visit the German Navy VLF Station at Rhauderfehn, near Hanover, Germany. This station employs eight 352.5 m umbrella top-loaded antennas. Each antenna is tuned and separately fed. Since the spacing between the antenna elements is small with respect to a wavelength, the eight elements radiate "in phase", and the far field radiation pattern is omni-directional. In effect this antenna system is a "radiation coupled multiple tuned antenna array". This configuration intrigued the author, and so even prior to his visit to the station he decided to carry out a detailed study

(by numerical and experimental modeling) of a simplified version of such an antenna system, for comparison with a more conventional multiple tuned antenna system.

During the course of the study, five antenna types were considered, some of which were modeled in more detail then others. These were:

1) Conventional antenna systems, like the Anthorn/Cutler/NWC Australia VLF antennas;
2) A single tall umbrella top-loaded radiator;
3) A transmission-line radiator;
4) Radiation coupled multiple tuned antenna arrays (similar in principle to the Rhauderfehn VLF antenna); and
4) Multiple-tuned folded unipole type of antenna arrays (to be described).

Multiple tuned-antenna systems is a principle subject of my paper.

3. Antenna Fundamentals

The input impedance of an electrically short top-loaded vertical radiator $Z_a = R_a - j X_a$. This is the impedance that must be tuned and matched to the characteristic impedance of the transmission feeding the antenna, and to the transmitter output impedance. The antenna resistance R_a (sometimes labeled R_b to indicate that the antenna is base fed) is the sum of the radiation resistance R_r and the ground loss resistance R_g, referenced to the feed point. The resistance R_c of the tuning coil or helix must also be included, and this further increases the antenna system resistance $R_{as} = R_a + R_c$.

The radiation resistance R_r is an important parameter, since the radiated power is

$$P_r = I_a^2 R_r$$

where I_a is the antenna current.

The radiation efficiency η is equal to

$$\eta = \frac{P_r}{P_t}$$

where P_t is the transmitter power.

Since R_r is small for conventional VLF antennas, typically less than 1 ohm, the loss resistances must be small with respect to the radiation resistance for an acceptable radiation efficiency. The loss resistances are the ground loss resistance R_g, and the RF resistance of the tuning coil or helix R_c.

$$\eta = \frac{R_r}{R_r + R_g + R_c} = \frac{R_r}{R_{as}}$$

where R_{as} is the antenna system resistance.

The antenna system bandwidth, for VLF/LF antennas, when the antenna's base reactance $X_a >> R_{as}$ is

$$BW_{as} = \frac{f}{Q_{as}} = \frac{R_{as} f}{X_a}$$

since $$Q_{as} = \frac{X_a}{R_{as}}$$

This formula is an approximation and valid only if the antenna is electrically small and its operating frequency f is low compared to the resonant frequency f_o of the antenna system. The general formula is

$$BW_{as} = \frac{R_{as} f [1 - [\frac{f}{f_o}]^2]}{X_a}$$

This is the bandwidth of the antenna system. When connected to a transmitter the operating bandwidth is increased by a factor of 2. When a signal source (an RF amplifier) is required to deliver power to a load (the antenna system), the power transfer will be a maximum when the load impedance is the complex conjugate of the source impedance. Matching therefore reduces the antenna system Q by a factor of two, and so doubles the bandwidth. However, the the bandwidth calculated above from circuit theory, is the 3dB bandwidth. A more practical operational bandwidth of the antenna system is less than this; more typically the antenna's bandwidth is increased by a factor of 1.5. Hence the operational band width

$$BW_{op} = 1.5 \times BW_{as}$$

An alternative definition of bandwidth useful for numerical modeling is the predicted bandwidth for an arbitrary VSWR, say 1.5:1. This bandwidth is calculated for the numerical model by change of frequency. VSWR is measured with respect to the resonant antenna system impedance. Since the transmitter's RF amplifier is conjugately matched to its load, the antenna system, the operational bandwidth is twice the antenna system bandwidth.

Another important parameter is antenna potential. The base voltage for an electrically short antenna is

$$V_b = I_a X_a$$

The maximum potential existing on the antenna due to potential build-up from its standing-wave potential-distribution pattern is

$$V_{as(max)} = \frac{V_b}{\cos \theta}$$

where θ = electrical height of the antenna system at the operational frequency f

$$\theta = \frac{f}{f_o} 90^o$$

4. Tools For Antenna Modeling

The numerical modeling studies employed the numerical electromagnetic codes NEC-3 and MININEC. Menu driven versions of MININEC, ELNEC and MN are easier to use---we used ELNEC [Belrose, 1992]. The experimental modeling studies were conducted by fabricating a detailed model of the antenna, sometimes including insulated guys, using a scale factor of 1000 for VLF antennas. That is towers 300 meters in height scale to a modeled rods 30 centimeters high, and a full scale frequency of 25 kHz scales to 25 MHz.

4.1 Measuring Antenna System Impedance

The experimental models were placed on a 30 metre diameter elevated ground plane (Fig. 3), so that the instruments to measure impedance and the effective height of an antenna under test could be deployed from beneath the wire grid ground plane (Fig. 4). To measure impedance either a Hewlett-Packard RF Impedance Analyzer Model 8505A or a HP Network Analyzer Model 4194A was employed. The latter instrument was used with a probe (a HP 41194A) so that the impedance could be measured right at the base of the model antenna; or the effect of the measurement coaxial cable could be taken into account using the former instrument.

The modeled antennas were very small with respect to the size of the ground plane, but the radius of the ground plane (15 metres) was not large with respect to the wavelength at the modeling frequency (wavelength 12 metres for a frequency of 25 MHz). Edge effects, because the ground plane was finite affect particularly the measured resistance. The effect on measured reactance is small, since the effective capacity of the ground plane is very large with respect to the capacity of the antenna system. But there is another problem with modeling electrically short antennas. Since the base capacity of the antenna system at the model frequency is small, the base insulator capacity of the model becomes important.

4.2 Measuring Antenna System Radiation Resistance

The radiation resistance is not so easily measured. We have used three methods. Whatever method is employed, measurements have to be made with great precision to achieve accuracy, since the radiation resistances are small (for conventional VLF antennas < 1 ohm).

The three methods that we have used are:

4.2.1 Antenna under test as a Receiver

The effective height of electrically short antennas, but not tuned antennas such as a multiple tuned antenna array, can be determined by measuring the open circuit voltage of the antenna under test (AUT), using the antenna as a receiving antenna. A signal was radiated (using a Hewlett Packard Model 3335 Tracking Synthesizer) from a small loop antenna at the edge of the ground plane. The open circuit voltage was measured using a HP Level Meter Model 3586C with a HP 1124 active probe. The effective height is determined by a comparison with the measured open circuit voltage for an antenna of known effective height. We used a 1-metre whip as the reference antenna.

The input impedance of the probe must be known. In our case the HP active probe had input impedance of 1 MΩ in series with a 10 pf capacity.

The open-circuit voltage of an antenna is

$$V_{oc} = h_e E_i \ \mu V$$

where h_e is the effective height of the antenna (in metres); and E_i is the incident field strength (in $\mu V/metre$).

The reference antenna was a 1 meter whip, whose effective height is known (0.5 m), and so the effective height of the antenna under test can be determined from the difference between the open-circuit voltages of the antenna under test compared with the reference antenna.

The problem with this technique is that the precision of measurement has to be very great, and all parameters have to be accurately measured and taken into account. The reference antenna's capacity was small (our's was 12.4 pf---calculated value); hence the feed through capacity of the base insulator for this reference antenna becomes important (our feed through insulator capacity was 4.6 pf). Any error in the measurement of h_e is squared,

since

$$R_r = 160\,\pi^2\,\frac{h_e^2}{\lambda^2}\ \text{ohms}$$

We have estimated that the accuracy in determining R_r using this method of measurement was something better than a factor of two.

4.2.2 Antenna under test as a Transmitter

A second method is to use the antenna under test as a transmitting antenna. The field strength for a particular power input is measured in the far field, and compared with the field strength for a reference antenna, e.g. a quarter wave whip. This measurement technique is a good one if the model frequency is high. For a scale factor of 1000, and a full scale frequency of 25 kHz, the model frequency is 25 MHz, and a quarter wave whip while larger than at VHF frequencies is still a reasonable size. There are however, errors with this method. Field strength can be measured with an accuracy of ± 1 dB, and so the difference in field strength is measured with a precision of ± 2 dB. Power radiated varies as field strength squared (see below). Since we are trying to measure radiation resistance, antenna current must be measured, and P_r is proportional to I_a^2. Even with great care the uncertainty in determining R_r can be as great as a factor of two.

If the scale factor is 100, the model frequency is 2.5 MHz. The modeled antenna cannot be placed on the elevated ground screen, and a quarter wave whip is unreasonably large. We carried out a series of model measurements using a scale factor of 100.

In this case we measured absolute field strength, and so it was necessary to measure field strength as a function of distance, over say 2 kilometers. From the field strength vs. distance curve, one can deduce the effective ground conductivity of the field site; and, knowing this, one can estimate (using an appropriate theoretical formulation for ground wave propagation) the unattenuated field strength E_u at 1 kilometer. And, since

$$P_r\ (\text{kW}) = 1.111 \times 10^{-5}\ E_u^2\ \text{mV/m}$$

we can determine the radiated power. Again, antenna current must be measured to determine the radiation resistance. This method is quite accurate, since the field strength is determined from a series of measurements, rather than a spot measurement, but it is tedious to do.

Any estimation of the radiation efficiency using this method is low, in fact very low since the ground conductivity should also be scaled. For average ground, conductivity 3 mS/m for the full scale antenna site, the ground conductivity for the modeling site should be 3 S/m. Since the radial ground system cannot be modeled, resonant quarter wavelength elevated radials can be used for the model, since a 3- or 4- elevated radial wire ground system is equivalent to 120 buried radials [Christman, 1989].

5. A Mini-Study of Conventional Antennas

First let us consider several conventional antennas:

1) The Anthorn/Cutler/NWC type;
2) A single umbrella top loaded radiator (Fig. 5); and
3) A transmission line radiator (Fig. 6), which is an antenna system that has been investigated by the author [Belrose, 1983] in previous years. This antenna type was revisited as a part of the present study. The transmission line radiator is an inverted-L type in which the horizontal arm is bent into a multi-side-polygon, or a spiral, of length necessary for resonance.

5.1. A Basic Antenna Element- a Single Inverted-L

The multiple tuned antenna systems which we will be considering here were made up from basic elements, inverted-L type antennas (Fig. 7). This is a commonly used antenna type, which is easy to construct. Therefore the investigation began with a short study of inverted-L antennas.

For our study we supposed that:

1) the vertical radiator was a square or triangular tower 304.8 m high, 4 - 5 m on a side; and
2) the horizontal top loading was a 457.2 m long square cage of four conductors, where the square is 15.24 m on a side. The construction of the horizontal cage and its support by the towers could be similar to that used for EHV (500 KV) power transmission lines.

5.1.1 Idealized Inverted-L

An idealized inverted-L, a base insulated tower with no end support tower is sketched in Fig. 8a. In Fig. 9 we compare the measured antenna resistance R_a and reactance X_a vs. frequency for an inverted-L experimentally modeled, having scaled

dimensions as above, with theoretical values (radiation resistance R_r and reactance X_a) calculated by: 1) a transmission line type of analysis, c.f. Belrose [1983]; and by 2) by ELNEC. Theory and experiment are considered to be in good agreement. The differences are thought to be due to the difficulty with experimental modeling, when such a large scale factor is used; and with the fact that the antenna is mounted on a ground plane of finite size (an elevated ground screen 30 m in diameter). For example, the calculated reactance at 25 MHz corresponds to an antenna capacity for the model of 11 pf, and the difference between this reactance and the measured reactance amounts to a difference of 2.3 pf, which can be attributed to the base insulator capacity for the model. The differences between calculated radiation resistance and measured antenna resistance are attributed to effects associated with the finite size of the ground plane. Although the ground screen looks to be very large with respect to our small model, its radial dimension is only 1.25λ at 25 MHz. It is well known that the resistance of a monopole is modified by currents reflected from the edge of a ground plane of finite size.

5.1.2. Effect of Grounded Towers

The idealized antenna had no end support tower, and no sag on the horizontal arm of the antenna (Fig. 8a). We have investigated the effects of grounded support towers and sag on the horizontal arm by numerical and experimental modeling. Fig. 8b is an inverted-L with an end support tower. The current induced to flow on the grounded support tower, according to ELNEC, is opposite in phase to the current on the radiator. This effect reduces the effective value of the antenna's radiation resistance and reactance. The sag on the horizontal arm further reduces the radiation resistance.

If two towers are employed (Fig. 8c) to support a cage antenna, this further reduces the radiation resistance and reactance.

These effects are summarized in Table 1.

5.1.3. Cage Feed for a Grounded Tower

An arrangement discussed by Belrose [1983] which eliminates the need for an insulated-base tower, a decided advantage if feasible, cf. Fig. 10, is to feed a cage of wires that surround a grounded tower. In fact this method of feed was used for the USN VLF antenna at Northwest Cape Australia. This method of feed (confirmed by experiment and performance at full scale) works well for LF/MF radiators, where the electrical height of the tower is large, large compared with practical antennas at VLF, and the radiation resistance is several ohms, or more. However, according to NEC-3, when the electrical height of the tower is small [Royer, 1991], the 'transmission line' induced current on a grounded tower surrounded by a 9-wire cage (Fig. 8d) reduces the radiation resistance by an intolerable amount (Table 1).

While the antenna's reactance is reduced, which is desirable, the radiation resistance is reduced by a large factor. This means that the ground loss resistance for the same radiation efficiency must be proportionally reduced; and the antenna's bandwidth is less. Thus, unfortunately, this method of feed should not be used at VLF where the highest possible value for the radiation resistance is desired from the point of view of efficiency and bandwidth.

5.2. The Anthorn/Cutler/NWC Type of Antenna

The Cutler and Anthorn antennas are in effect 6-inverted L type antennas fed in parallel, each with a diamond shaped top-loading structure. The antenna system is supported by 13 towers. The NWC antenna uses cage feed with a grounded center tower (a 48-wire cage).

Anthorn is the smallest and the NWC antenna system the largest. The Anthorn antenna is an example of the problem with this type of antenna if its size (in wavelengths) too small. The measured radiation resistance for this antenna at the operating frequency of 19 kHz is only 0.08 ohm (we comment below on factors affecting radiation resistance for this type of antenna); the antenna system resistance including bandwidth resistors is 0.18 ohms; and the antenna reactance -j 85 ohms. The self-resonant frequency 50.1 kHz. The radiation efficiency is 44-percent and the antenna's bandwidth is 100 Hz. Note that the antenna employs bandwidth resistors. Since the antenna is built on land that is partly under water at high tide, the ground loss resistance is very low and the bandwidth is small. Bandwidth resistors are used to achieve a 100 Hz bandwidth [Cook, private communications, 1991].

Why is the radiation resistance so small? For uniform current on a driven tower of height that of the center tower of the Anthorn antenna (228 m), and if there was no sag on the top loading, and if the antenna was supported by insulated towers, the radiation resistance at 19 kHz would have been 0.33 ohms. The difference between this value

and the actual measured value is because: the top loading is insufficient for there to be uniform current on the down-lead; there is a significant sag of the top-loading structure; the grounded towers carry out of phase currents and this effect decreases the antenna system radiation resistance and the antenna's reactance. The effect of the grounded center tower is particularly significant. The center tower supports the driven ends (Fig. 1) of the diamond panels and the 6-downleads that are fed.

In Fig. 11 we show a skeleton model for this type of antenna---skeleton because the diamond panels are made up from perimeter and center wires only, to simplify the numerical model. For this case study the diameter to the open ends of the diamond panels was 1000 meters, and the height of the panels 300 meters. The frequency was 25 kHz. As can be seen by the density of wires at the center of the model, each diamond panel has its own down-lead and all panels are fed in parallel. Table 2 shows the effect of the grounded towers.

The effect of the grounded towers is to reduce the antenna's radiation resistance and the antenna's reactance. The phase of the current on each of the grounded towers is -180^{o} wrt the current on the radiating downleads. The current on the grounded center tower is significant. With a current of 1 ampere flowing on each down-lead (antenna current 6-amperes), the current on the grounded tower is 0.7 amperes. However radiation due to the current distribution on this tower is partially screened by the six down-leads (on a 15m radius about the center tower).

5.3 Umbrella Top Loaded Antenna

Umbrella top loading, see Fig. 5, has been studied by Belrose [1983] and Hansen [private communications, 1988]. The design procedure given by Belrose was a numerical/graphical method, based on experimental modeling studies. Hansen has written a computer programme for use with an IBM compatible PC (ANT 1) based on other model studies

The important parameters for an umbrella top loaded antenna are: the height of the tower h; the number n of active top loading wires (12 is a reasonable number); the tangent of the angle θ between the top loading wire and the tower (1.4 is reasonable but 1.0 has been employed); and the height at which the umbrella wires are broken by an insulator divided by the height of the tower (s/h).

The capacitive reactance is decreased by the use of umbrella wires (or active guys), and as s/h increases the capacitive reactance decreases. As s/h increases the radiation resistance at first increases, and then decreases. The radiation resistance is a maximum when s/h $\approx$ 0.3. This is because current on the umbrella wires has a component opposite in phase wrt current on the tower.

For f = 20 kHz, h = 609.6m, n = 12, tangent θ = 1.4, and s/h = 0.7, the antenna's impedance is

$Z_a = 0.83 - j\ 158$ ohms

For a helix Q-factor = 2000, and a ground loss resistance R_g = 0.25 ohms, the antenna system resistance R_{as} = 1.16 ohms, and the radiation efficiency η = 72 percent. The self resonant frequency f_o of the antenna system is calculated to 39.3 kHz, and so the operational bandwidth of the antenna is 163 Hz. For a transmitter power of 1000 kW, the antenna voltage is high. The end voltage where the umbrella wires are broken by an insulator is 210 kV.

Reducing the height of the tower will reduce the radiation efficiency and bandwidth, and increase the antenna's reactance and antenna voltage (Table 3). A tall tower with an extensive umbrella-hat is required for VLF.

5.4 Transmission Line Radiator

The transmission line antenna, see Fig. 6, has been studied by Belrose [1983]. This antenna was revisited as a part of the present study. A resonant antenna was thought to be a good feature. Since the antenna could be "tuned" by the addition of an end capacitor, it was thought that this could provide a way to dynamically tune the antenna in synchronism with the frequency shift keying for MSK, if its bandwidth was too small. That is the "end" capacity could be switched in synchronism with the frequency shift keying. However, after a detailed experimental/numerical modeling study, it was concluded that this type of antenna was not a useful antenna for high power VLF transmission for the following reasons:

1) A number of towers would be needed, eight or more, to support an extensive top-loading cage;
2) since the antenna system is in effect "quarter wave resonant" the end voltage would be very high for a transmitter power of 1000 kW, and the end tuning capacitor would have to withstand this voltage; and

3) this type of antenna system does not lend itself easily to frequency agility.

6. Multiple Tuned Antenna Systems

As noted above multiple tuning has been used since the beginning of radio, for improving the radiation efficiency of early VLF antennas, where the most adverse conditions of low radiation resistance and high base reactance are encountered, and some extreme measures were necessary to obtain acceptable antenna radiation efficiencies, c.f. Alexanderson [1920]. While the basic principles were understood, little use has been made of multiple tuning since these early antenna systems fell into disuse, until recently, because of the high cost of multiple helix tuning coils, and matching and phasing circuitry, inside physically large copper or aluminum screened tuning huts.

The early history of multiple tuning is summarized in Table 4.

6.1 Radiation Coupled Antenna Systems

The German Navy VLF antenna system at Rhauderfehn, Germany (Figs. 12, 13, 14, 15) is multiple tuned. It comprises eight 352.5 m umbrella top loaded antennas, Figs. 12 and 13. Each antenna is separately fed, and the 8-elements of the antenna array are coupled through radiation.

Our antenna model consisted of four inverted-L antennas, see Fig. 7a, each element tuned with an identical base loading coil. A single inverted-L antenna by itself, with the base loading used, resonated at 25.12 MHz. The impedance (Z, θ) as measured at the base of one of the elements of the coupled antenna system is graphed in Fig. 16. Notice that in the frequency range 23-28 MHz the antenna's reactance was measured to be zero ($\theta = 0$) at five frequencies in this band, 24.15, 24.24, 24.7, 26.3 and 26.815 MHz.

The theoretical impedance curve was calculated by ELNEC, in a like manner with the experiment. That is a base load reactance was chosen such that a single inverted-L antenna was resonant at 25.12 MHz, and this inductance was used as a base load for each of the 4-elements of the multiple tuned antenna system. The resistance associated with these base loads was chosen such that the calculated antenna's impedance at the highest resonant frequency was in agreement with the measured value (at the corresponding resonant frequency). Clearly there is a good qualitative agreement between theory and experiment. The differences are attributed to difficulties with experimental modeling as discussed above, and the simplicity of the numerical modeling.

The multiple resonant frequencies were somewhat unexpected. They are due to the complex interactions between multiple tuned antenna elements that are closely coupled, not because of a misstuning of the elements in the experimental model. It is interesting to note that with 4-towers tuned, there were 5 resonant frequencies; and with 2-towers tuned there were 3 resonant frequencies. It is speculated that with 8-towers tuned, like for example the Rhauderfehn antenna, there would be 9 resonant frequencies. However, according to ELNEC only the two highest resonant frequencies are of practical importance, since for these the antenna's radiation efficiency is high. The radiation efficiency is low for the other 3 resonant frequencies. And, only the highest resonant frequency (26.815 MHz for the model) would be used practically, since VLF antennas are 'current fed.' Therefore in practice such antenna systems should be tuned by incrementally increasing the helix reactances from the high frequency side (minimum inductance) to achieve resonance. It is not known whether this is the tuning procedure used for the German Navy VLF antenna, Rhauderfehn.

However, it should be noted, that for our model studies only one tower was fed. The Rhauderfehn VLF station employs eight towers, and each tower is fed. We have not investigated the frequency response of a radiation coupled antenna system with all towers fed.

6.2 Folded Monopole Type

Two approaches can be taken to achieve a wider bandwidth: increase the effective diameter of the radiator; or multiple tune several vertical towers (or down-leads) sharing a common top-hat. Both approaches are taken in the antenna system to be described.

Let us now consider four inverted-L antennas arranged in the manner just discussed, but with their ends connected, see Fig. 7b. This configuration is more typically like a conventional multiple tuned antenna system where two or more down leads share a common top-load, excepting for the simplicity of the top-loading structure. The antenna to be described is in effect a multiple tuned double folded unipole. The base tuning is an essential part of the antenna system, since this establishes equal and in-phase currents on the vertical elements. The current is zero at the center of the antenna system, as it was at the end of a single inverted-L. It is interesting to note that the antenna can in effect 'be tuned' in

the course of the numerical modeling study by changing the loads to achieve the deepest overhead null in the vertical plane pattern.

For the experimental model, each element of the multiple tuned antenna system was tuned with an identical base loading coil. As for the radiation coupled multiple tuned antenna discussed above, each inverted-L antenna, by itself, with the base loading inductance used, resonated at 25.5 MHz. The measured impedance vs. frequency for this antenna is plotted in Fig. 17. For this multiple tuned antenna, in the frequency range 23-28 MHz, there was only one resonant frequency, 27.2 MHz. Theoretically, according to MININEC, loads of j 652 ohms would be required to tune the antenna to 27.2 MHz, and such a load would tune a single inverted-L to 24.56 MHz.

In accord with early theory the radiation resistance with multiple tuning R^{MT}_r is equal to $n^2 R_r$, where R_r, is the radiation resistance of a single element, n the number of elements, and R^{MT}_r is the radiation resistance with multiple tuning. But this equation does not take account of the mutual inductances between the vertical elements of the multiple tuned antenna, which in effect lower the effective capacity of the antenna system. A larger load inductor must be used to tune to a given frequency, and the increase in the radiation resistance is less. Writing

$$R^{MT}_r = k\, n^2 R_r ,$$

for our experimental model k = 0.87.

The loss resistance associated with each inductor R_C appears at the terminals of the driven element as n R_C, and this same factor n applies for the ground loss resistance R_g attributed to each element of the antenna system. But the effective ground loss with multiple tuning should be less than for single tuning, since with multiple tuning the ground loss is distributed over n times the area. The radiation efficiency can therefore be significantly increased.

The above analysis is for the antenna modeled. That is the antenna is multiple tuned but only one leg is fed. If all four legs are fed the effective radiation resistance attributed to each element is R^{MT}_r divided by four.

7. A Comparison between Performance (Measured and Predicted) for Multiple Tuned Antennas vs. Single Tuned Antennas

In Table 5 we compare the operational performance of two types of multiple tuned antenna systems: 1) the German Navy radiation coupled multiple tuned antenna system (measured performance); and 2) a multiple tuned double folded unipole (predicted performance); with 3) the largest antenna of conventional design in the world, the US Navy antenna system at North West Cape, Australia. The comparison is made at a frequency of 20 kHz.

The predicted radiation efficiency for the double folded unipole multiple tuned antenna system compares favorably with the Northwest Cape antenna, which is the largest VLF antenna in the world, excepting the antenna voltage is high, and the antenna's bandwidth is too narrow for 4-channel MSK. The high value of radiation resistance, 2.3 ohms, which at first sight might seem to be unacceptably high, is due to the fact that all towers excepting for one, the center support tower, radiate in-phase and contribute to the total radiation field. Since the radiation resistance is high, ground loss resistance becomes less important for comparable radiation efficiencies, and in the design of such antenna systems, it would be possible, for example, to use fewer radials in the ground system, to in effect trade radiation efficiency for bandwidth, but still achieve a reasonable radiation efficiency.

When we compare the radiation resistance for multiple tuned antennas with single tuned antennas, we must specify how the multiple tuned antenna was fed. The radiation resistance for the multiple tuned double folded unipole is the source value with four tower fed. This method of feed is operationally convenient, since four transmitters could be used. Hence it would be possible, but with retuning, to remove one or more transmitters for service, with a corresponding decrease in radiated power. The predicted value for the radiation resistance is in more in accord with the 1.9 ohms for the Rhauderfehn antenna, then with other antennas in the world.

If one tower is fed, and the other three towers are grounded through their tuning helixes, the radiation resistance associated with the fed tower would be four times that shown, viz. 9.2 ohms; an unheard of value for VLF!

While the multiple tuned folded unipole antenna has limitations when compared with the largest VLF antenna in the world, the

USN NWC, Australia antenna, let us be clear what we are comparing. The NWC antenna comprises 13 towers, and the diameter of the outer ring of towers is 2.5 kilometers. The double folded unipole multiple antenna comprises 5-towers on a diameter of 914 metres. Clearly, now that we know how to design such an antenna system, we could optimize its characteristics. For example, lengthening the horizontal arms of the antenna will decrease the reactance needed to tune the antenna, and the antenna voltage; and increase the radiation resistance. But additional towers would be needed to support the longer top-loading spans. Finally it should be noted that the comparison was made at 20 kHz. Increasing the operational frequency will result in improved performance.

8. Concluding Remarks

The Folded Unipole type of multiple tuned antenna has a number of attractive features:

1) Its configuration lends itself to a relatively simple mechanical construction;

2) There is a minimum of wire structure in the air, which is subject to environmental stress, such as wind and icing;

3) Since the structure is in effect a system of closed loops sleet melting is made easy;

4) All of the towers contribute to the radiated field (with the exception of the center tower), and since currents on grounded support towers oppose the current on the radiating towers this is a distinct advantage;

5) As is well known with multiple tuning, since current is collected at 2-, 3-, or 4-downleads, depending on design, the radiation resistance is high, and less attention needs be given to reducing the ground loss resistance to a very low value. It is speculated that less wire would be needed in the total ground system;

6) The maximum voltage on the antenna, in contrast with conventional VLF antennas, occurs at the center of the antenna system, at a place where in effect the antenna does not "end". Thus corona problems associated with high powers are minimized; and

7) The theoretical bandwidth far exceeds that for any known VLF antenna system of comparable size and having a similar number of towers.

However, the antenna voltage is high, and several (2, 3 or 4) very large helix inductors are required to tune and phase the antenna. It should be noted that this study is still ongoing. Other configurations for the top-loading structure one under consideration.

This antenna offers an attractive alternative to conventional design for a LF antenna. Here, the length of the top loading elements is more practical, and can be significantly longer in electrical length. Grounded support towers could be used to support a wire cage antenna structure (i.e. down leads could also be cages). A three- or four-element multiple tuned antenna system could be suspended from 4- or 5-grounded towers. While, as noted above, this reduces the antenna's radiation resistance and the antenna's reactance, this configuration lends itself to a practical antenna design.

Acknowledgments

This study was sponsored by the Canadian Department of National Defence. The author benefited from a visit to the German Navy VLF station near Rhauderfehn, and from discussions with Karl Ruf, Telefunken-System Technik, Ulm (Donau), Germany about this unique VLF antenna system. The author thanks Peter Bouliane, who built and meticulously measured the antenna parameters for the experimentally modeled antennas.

References

Alexanderson, E.F., 1920, "Trans-oceanic radio communications". Proc. IRE, 8, 263.

Belrose, J.S., 1983, "VLF, LF and MF Antennas". In The Handbook of Antenna Design Vol. 2 (ed. A.W. Rudge, K. Milne, A.D. Olver and P. Knight), IEE Electromagnetic Wave Series, 553-662.

Belrose, J.S., 1992, "Modeling HF Antennas with MININEC-Guidelines and Tips from a Code User's Notebook". ARRL Antenna Compendium Vol. 3, Newington, CT.

Burke, G.J., 1989, "Recent advances to NEC: Applications and Validations." In AGARD Lecture Series No. 165 Modern Antenna Design using Computers and Measurement: Application to Antenna Problems of Military interest. Avail. NTIS, Springfield, VI (Ref. NASA Acces. No. N90-17932).

Christman, A., "Elevated Vertical Antenna Systems", QST, August 1988, pp. 35-42.

Logan, J.C., and Rockway, J.W., 1986, "The New MININEC (Version 3): A Mini Numerical Electromagnetic Code". Naval Oceans Systems Center TD 938.

Ma, M.T. and R.G. Fitzgerrell, October 1977, "Design of a Van-Top Low-Profile HF Antenna," US Department of Commerce, Office of Telecommunications, OT Report 77-131.

Ray, H.A., March 1982, "Dispensable transmitting antennas VLF/LF investigations," Rome Air Development Center, Griffiss Air Force Base, New York, Final Report RADC-TR-72-28.

Royer, G.M., January 1991, "The Characteristics for an Inverted-L Antenna where the Vertical Driven Element is a Cage of Wires around the Tower," Communications Research Center, Technical Memorandum DRC-91-1.

Watt, A.D., 1967, VLF Radio Engineering, Pergamon Press, 158-164.

Wheeler, H.A., 1975, "Small Antennas". IEEE Trans. AP-23, 462.

Table 1

Effect of support towers, and of physical and feed arrangement on the impedance, according to MININEC, of an inverted-L antenna: height 304.8 mm, diameter 6.35 mm; with 457.2 mm horizontal cage, diameter 10.6 mm; frequency 25 MHz

Configuration	Reference Sketch	Impedance
Base fed, no end support tower	Fig. 2a	0.6 - j 577
Base fed, grounded end support tower*	Fig. 2b	0.52 - j 562
Cage inverted-L radiator suspended between two grounded towers	Fig. 2c	0.35 - j 482
Cage fed grounded tower no end support tower	Fig. 2d	0.125 - j 255

* For a realistic model, with suspended top-loading cage hanging under its own weight, the base impedance Za = 0.4 - j 549

Table 2

Skeleton Cutler/Anthorn/NWC Antenna System

Configuration	Antenna's Impedance	Base Currents on Towers* Outer Ring/Inner Ri (center tower)
No Towers	0.85 - j 200	
12 Towers (No center Tower)	0.55 - j 179	0.085/0.089 $\angle$-180°
13 Towers	0.45 - j 163	0.077/0.0805 $\angle$-180° (0.7 $\angle$-180°

* Antenna current 6.0 $\angle$0° amperes.

Table 3

Predicted performance for an Umbrella-Type Antenna

Reference parameters:
f = 20 kHz
n = 12
tangent θ = 1.4
s/h = 0.7
P_t = 1000 kW
Helix Q-factor = 2000

Tower Height (Metres)	R_r ohms	R_g ohms	-j X_a ohms	BW_{op} Hz	η %	f_o kHz	$V_{as(max)}$ kV
304.8	0.21	0.25	398	46	31	78.7	533
457.2	0.46	0.25	242	88	55	52.5	321
609.8	0.83	0.25	150	163	71	39.3	210

Table 4

Multiple Tuning: Early History

Alexanderson [1920]	Briefly described by Laport [1950]
German VLF Goliath antenna, Kalbe, Germany, mid 40s. Measured data available [Watt, 1967]. Station moved after the war to Gorki, USSR.	Three interconnected hexagonals with 3 insulated 200m central towers, and 15 grounded 170m towers, the three central support towers were tuned, the center down lead was also tuned and fed (in effect this gives 4-down-leads tuned).
Canadian Department of Transport LF transmitter at Beaconsfield, QC (near Montreal)--late 40s - early 50s.	Diamond antenna with four tuned down-leads.
LF Broadcast transmitter Donebach/Odenwald, Germany [CCIR 1966-69 Doc. X 57].	Folded monopole, 3 - 200m towers uniformly spaced about a central tower, tops joined by a 10m flat wire system, all towers tuned (BW 6 kHz achieved at 155 kHz).
USN Stations Annapolis, MD (1941) and Lualualei, Hawaii (1947) [Watt 1967].	12 parallel wires supported by 7-182.9m grounded towers, two down-leads tuned one fed.
Unique antenna system for short (LF/VLF application)/low profile (HF mobile application) [Ray, 1972; Ma and Fitzgerrell, 1977].	Multiple tuned type, but an additional feature was the method of feeding the flat-top; by a wire running up the center of the grounded towers (loading coils said to be effectively in series at the top of the towers but physically placed at ground level).
German Navy VLF Station at Rhauderfehn, nr Hannover, Germany (operationally in use).	8-352.5m umbrella top-loaded antennas, each antenna tuned and separately fed (author visited the station in June 1989).

Table 5

A comparison between performance **of two multiple tuned VLF antennas with the USN NWC VLF antenna, which is the largest antenna in the world.**

Reference parameters:
f = 20 kHz
P_t = 1000 kW
Helix Q-factor = 2000

Antenna	R_r ohms	R_g ohms	j X_a ohms	BW_{op} Hz	η %	$V_{as(max)}$ kV
NW Cape *Australia*	0.25	0.033	38	163	87	123
Rhauderfehn, Germany, Eight umbrella antennas *multiple* tuned, radiation coupled.	1.9	0.15	490	120	85	124
Multiple Tuned Double Folded Unipole	2.3*	0.25	796	106	78	247

* Four inverted-L type antennas, ends electrically connected, four 457.2 m towers tuned and fed, with 457.2 m horizontal arms and grounded center support tower. If only one tower is fed the radiation resistance would be 9.2 ohms, and the associated ground loss resistance 1 ohm.

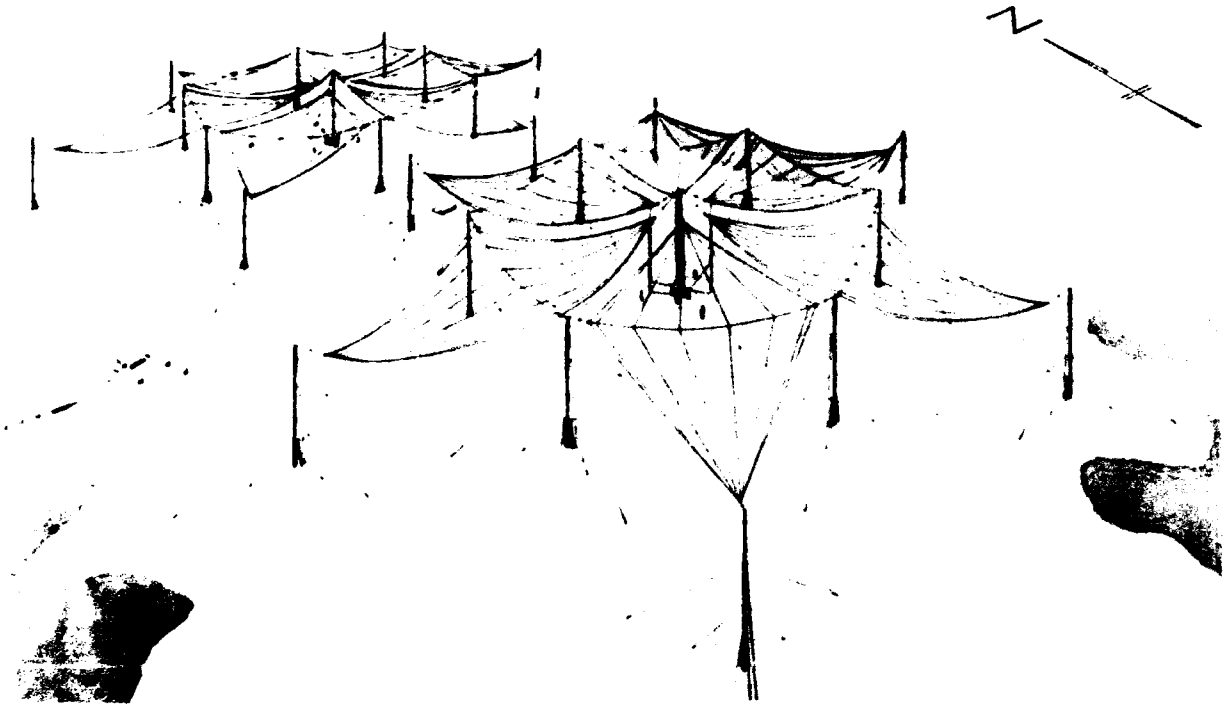

Fig. 1 Pictorial view of the USN Cutler, Maine, VLF antenna [after Watt, 1967].

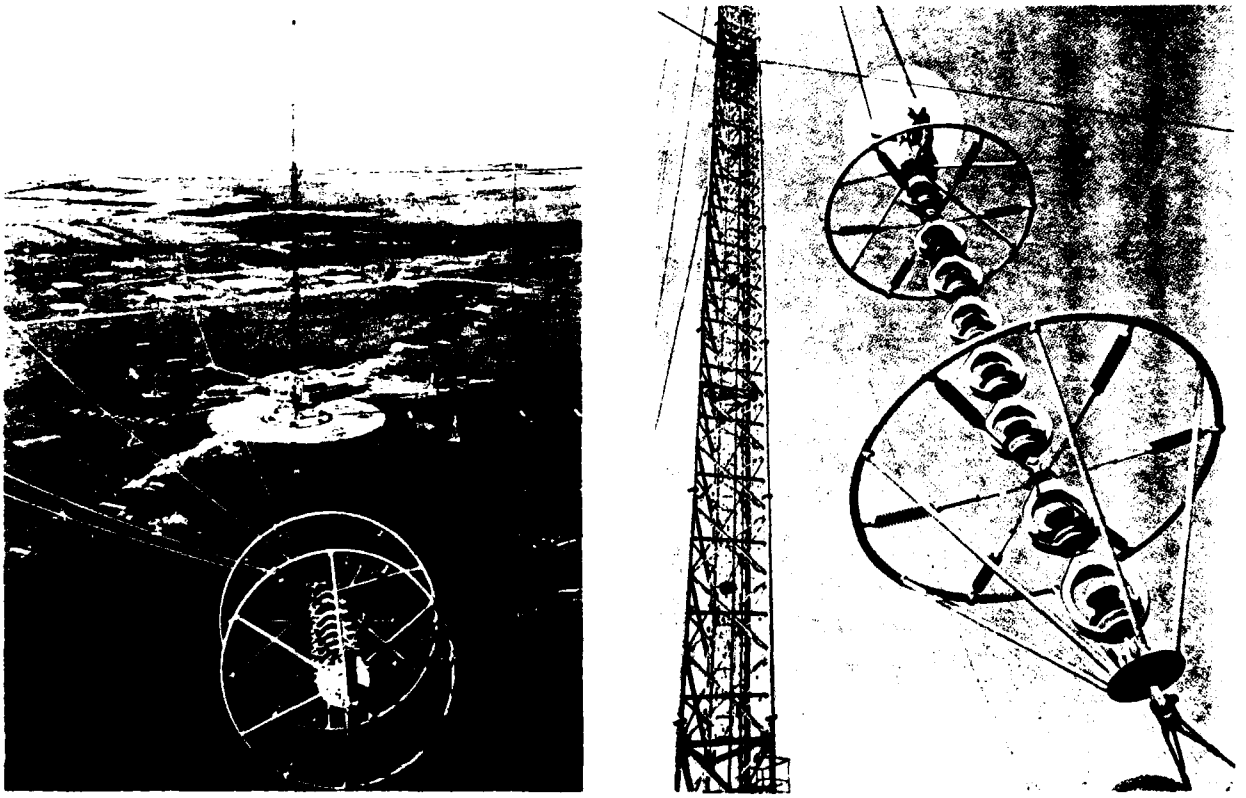

Fig. 2 Bird's eye view from an outer tower of the NATO Anthorn, England, VLF antenna, looking toward the center tower. Antenna insulator strings are 9-metres long and fitted with large coronal rings. Note the engineer at the top for size comparison.

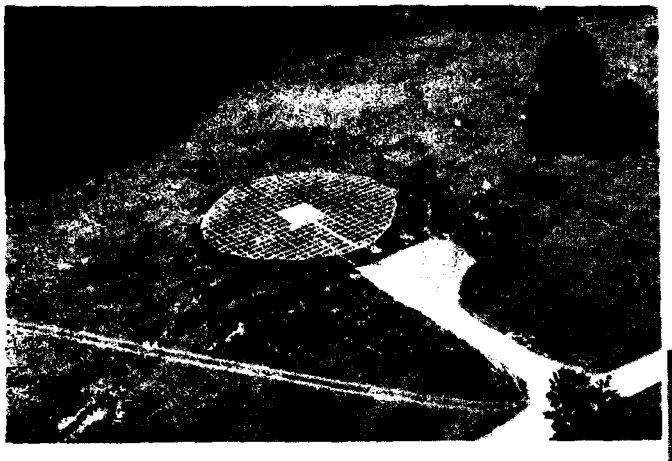

Fig. 3 Left: Aerial view and close up view of the CRC 30-metre elevated ground plane for experimental antenna modelling studies.

Fig. 4 Below: Instruments to measure antenna system characteristics are deployed directly beneath the modelled antenna system, and below the ground plane.

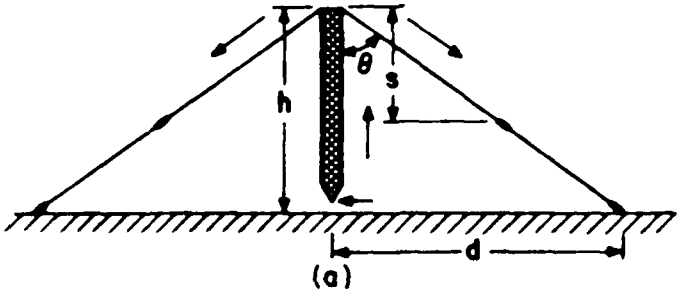

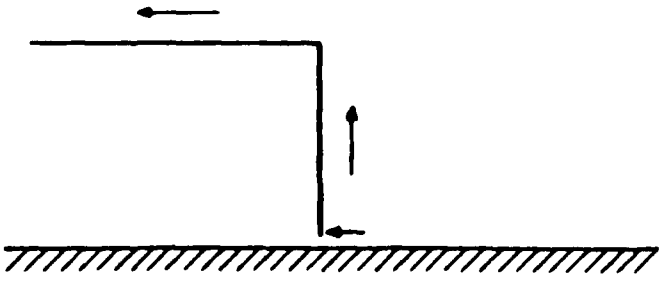

Fig. 5 Sketches illustrating phasing of currents on umbrella and inverted-L type radiators. Note that for the inverted-L currents on the top-load do not interfere with currents on the radiator, but this is not the case for the umbrella antenna.

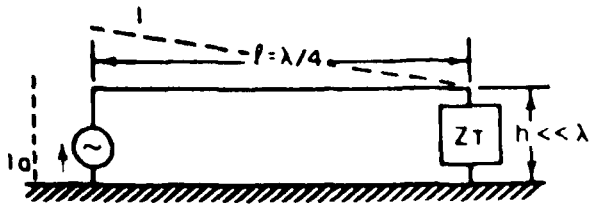

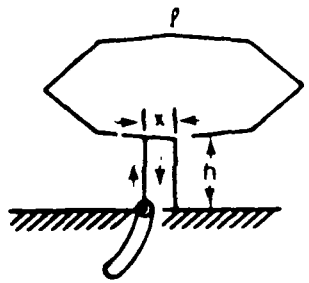

Fig. 6 Sketches for a transmission-line radiator ($h << \lambda/4$). The sketch below shows a practical method of matching and feeding a grounded radiator [after Belrose, 1983].

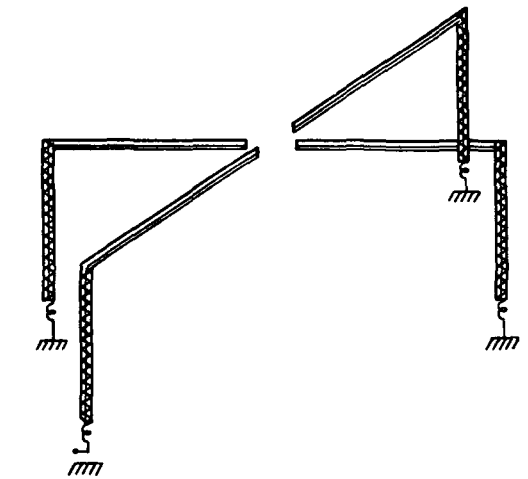

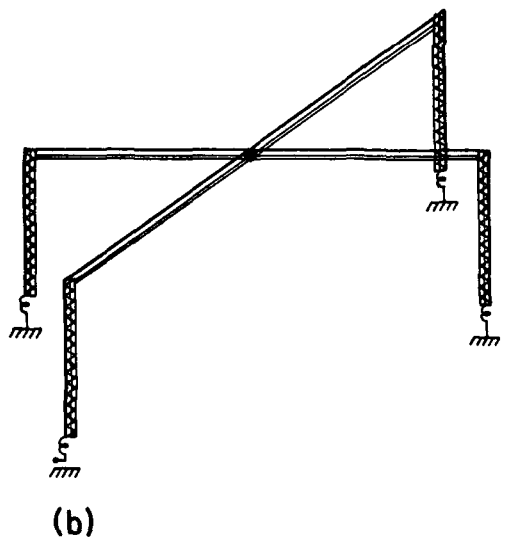

Fig. 7 Sketches of multiple-tuned antenna systems: a) radiation coupled; b) double folded unipole.

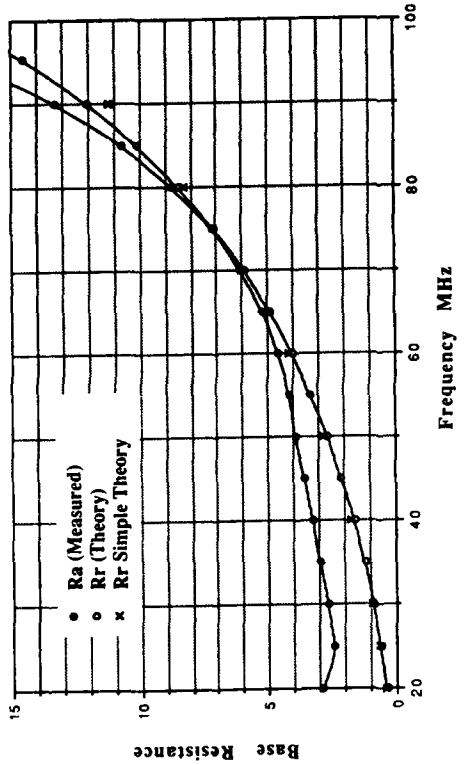

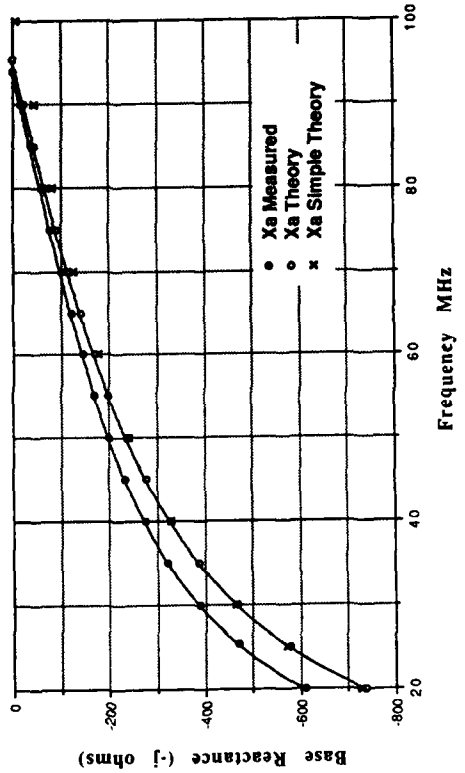

Fig. 9 Measured and predicted impedance *vs* frequency for a modelled inverted-L antenna with no end support tower (Fig. 8(a)'s antenna).

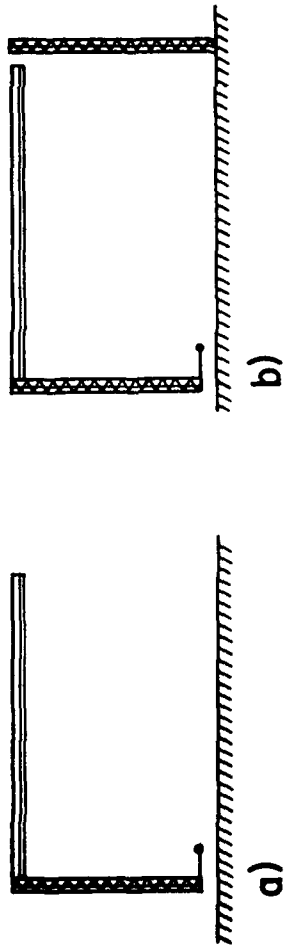

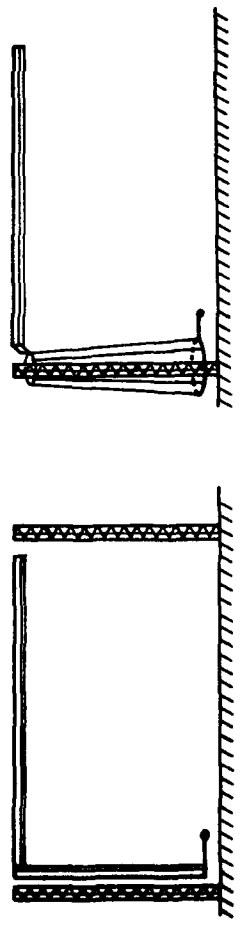

Fig. 8 Sketches for inverted-L type antennas: a) idealized radiator (*no* end support tower); b) with end support tower; c) cage type inverted-L with two support towers; and d) grounded tower with cage feed.

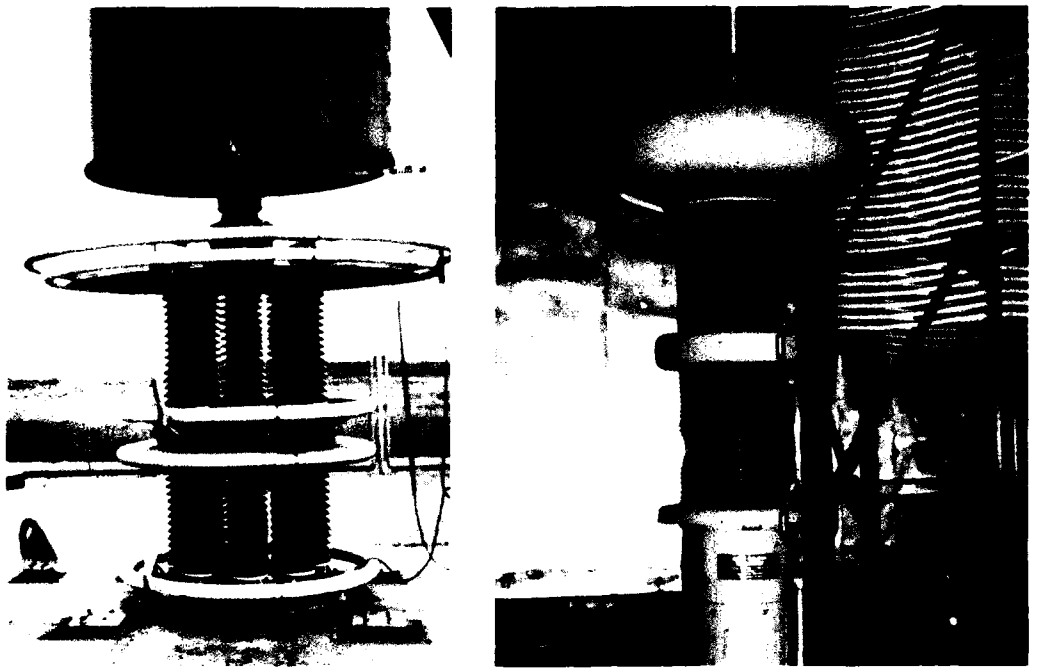

Fig. 10 Photograph of the base insulator for one element of the German Navy Rhauderfehn, FRG, VLF radiation coupled antenna system; and view inside one of the tuning huts. The tower lighting transformer is in the foreground, the main tuning helix in the background. In the case of a grounded tower neither the base insulator or the lighting transformer would be needed.

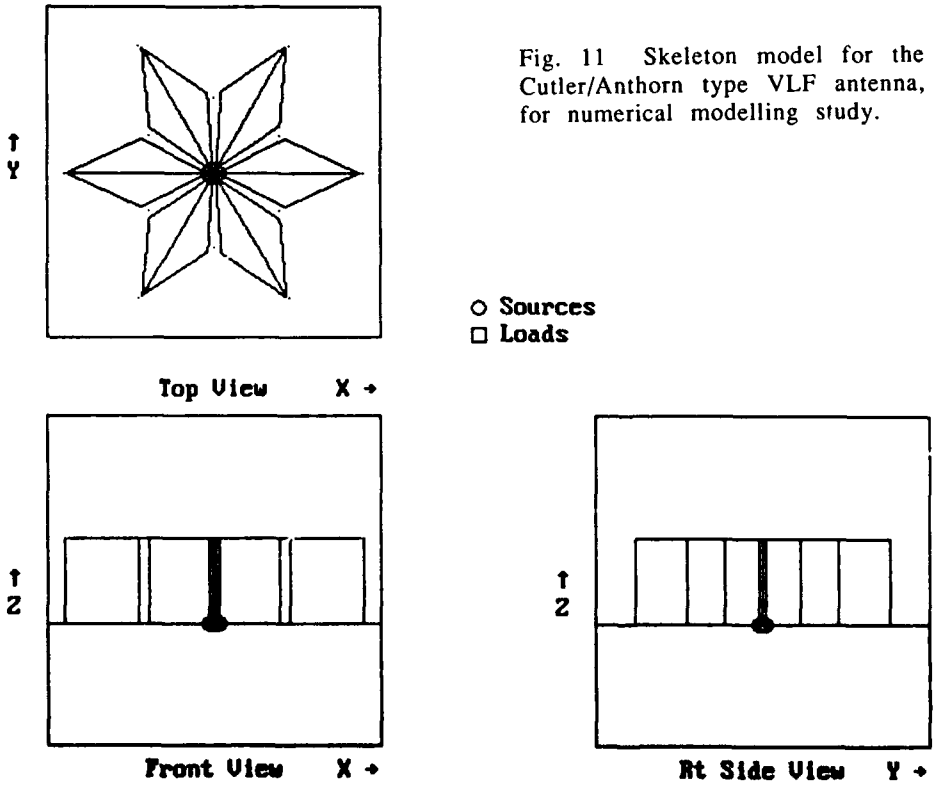

Fig. 11 Skeleton model for the Cutler/Anthorn type VLF antenna, for numerical modelling study.

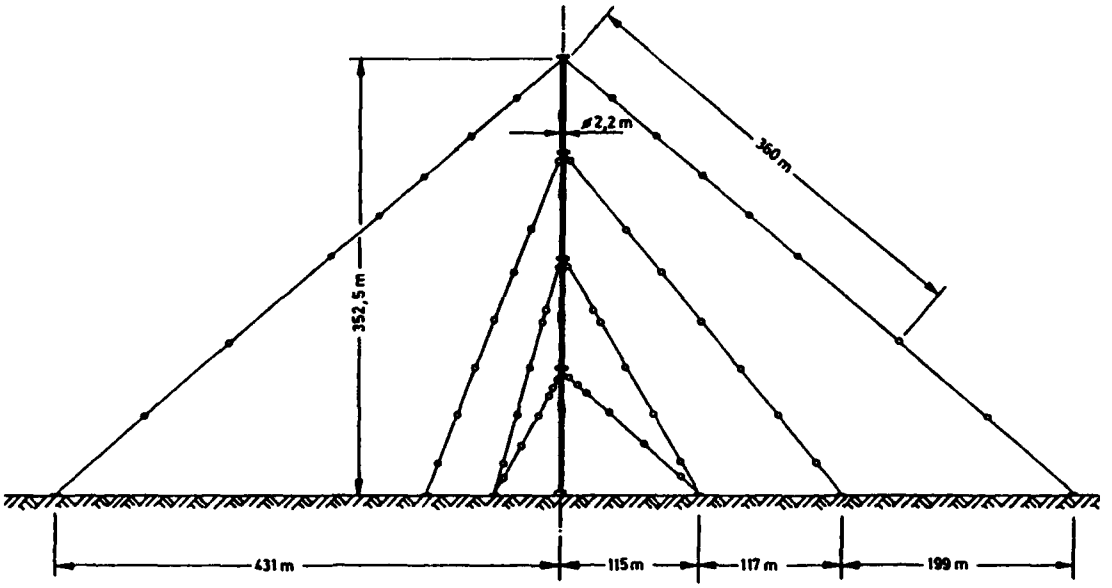

Fig. 12 Sketch of one of the Rhauderfehen umbrella antennas.

- o Insulator
- • Aircraft warning signs
- ▮ Antivibration segments

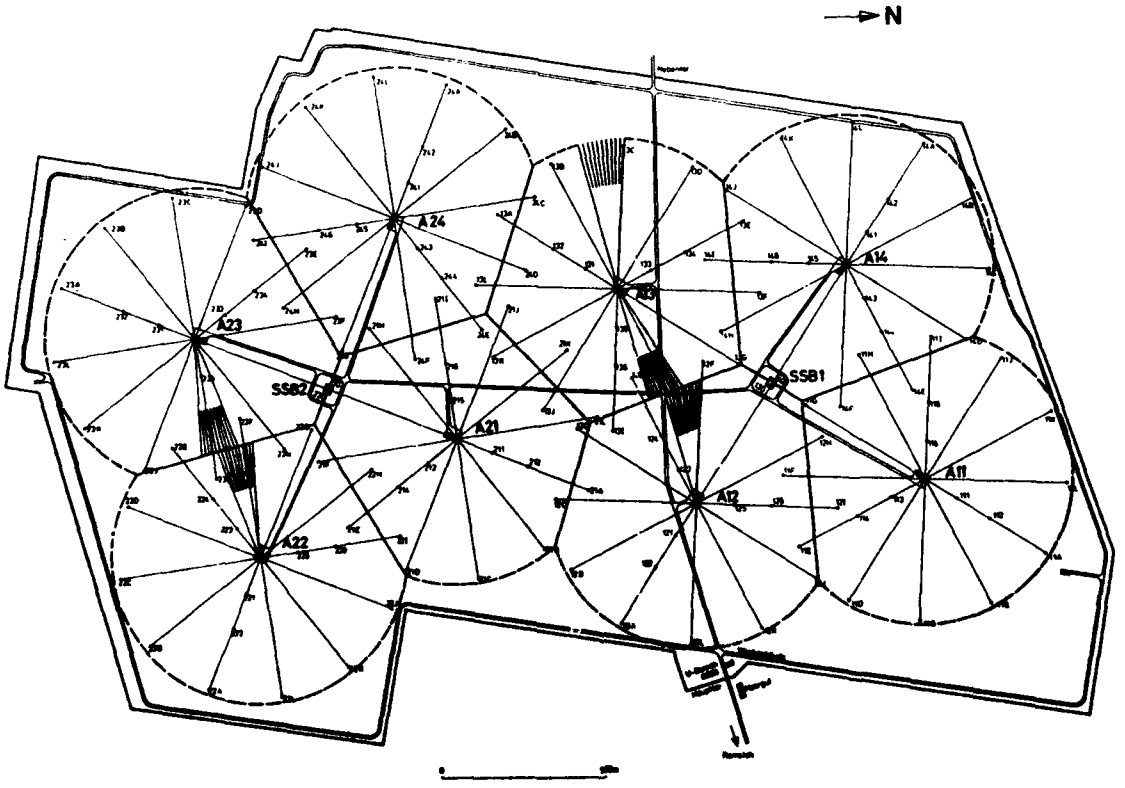

Fig. 13 Site plan for the Rhauderfehn VLF antenna system, showing the position of the towers and arrangement of radial ground system for the eight umbrella antennas.

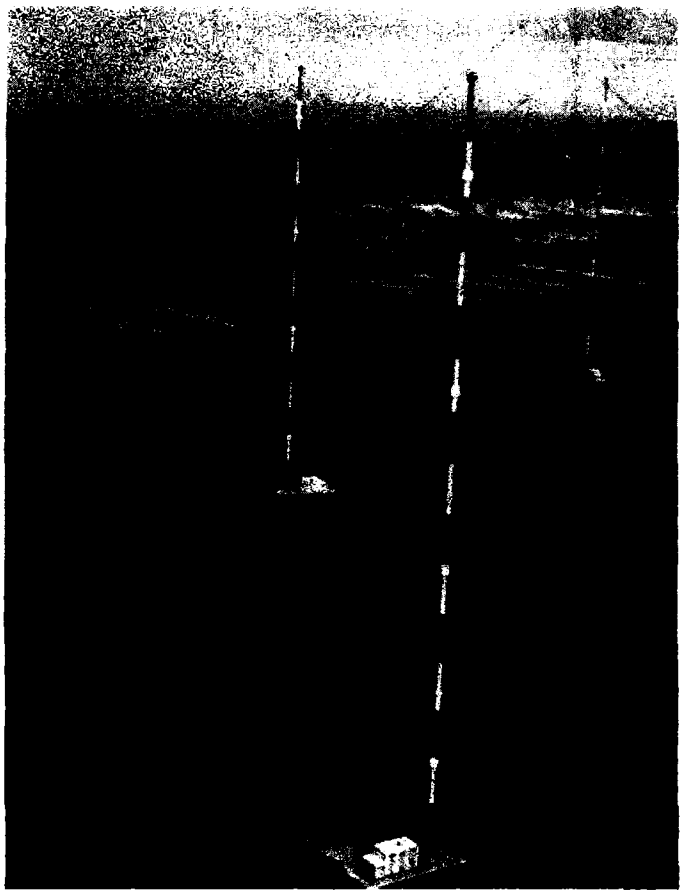

Fig. 14 Photograph of three of the Rhauderfehn towers taken from the top of one of the towers. The tuning huts can be clearly seen, as well as, for the near tower, the antenna lead to a feed through insulator feeding through the roof of the antenna tuning hut.

Fig. 15 View looking up from the base of one of the Rhauderfehn towers. The antivibration segment can be clearly seen, as well as the antenna feed cage (the heavy conductor that appears to be coming in from the top of the photograph).

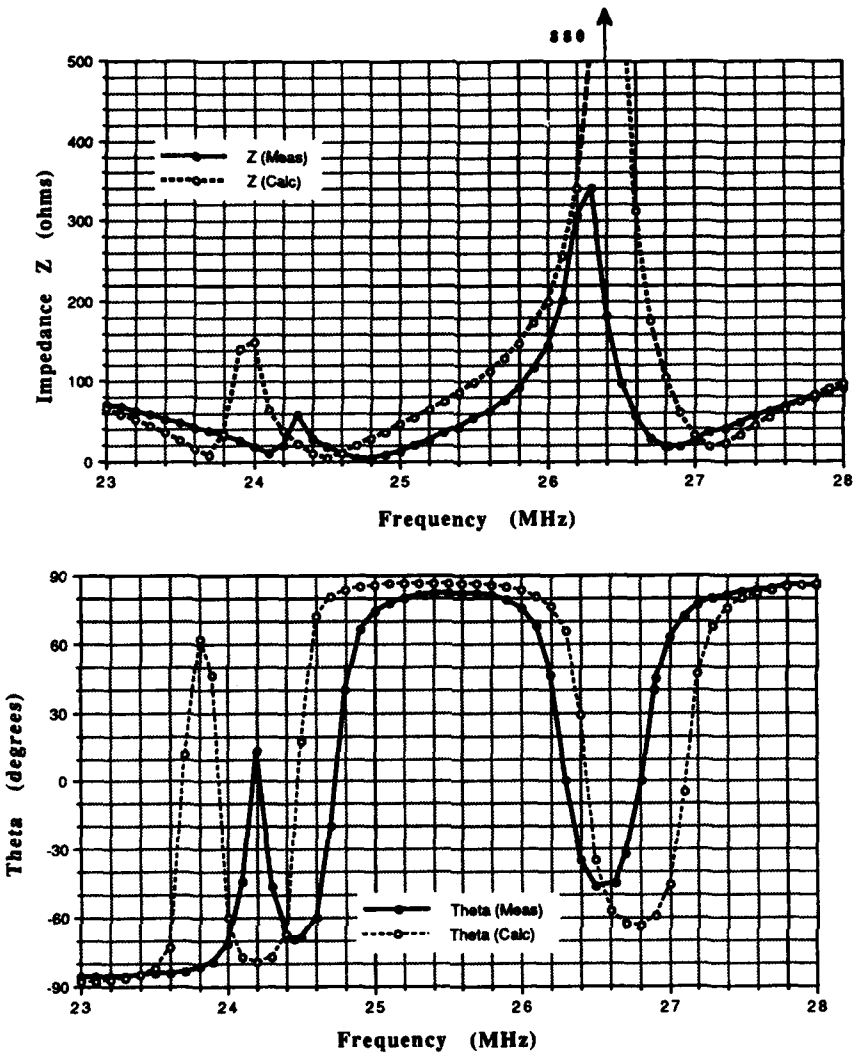

Fig. 16 Measured and calculated impedance (Z, θ) vs frequency for modelled VLF radiation coupled antenna system (Fig. 7a's antenna).

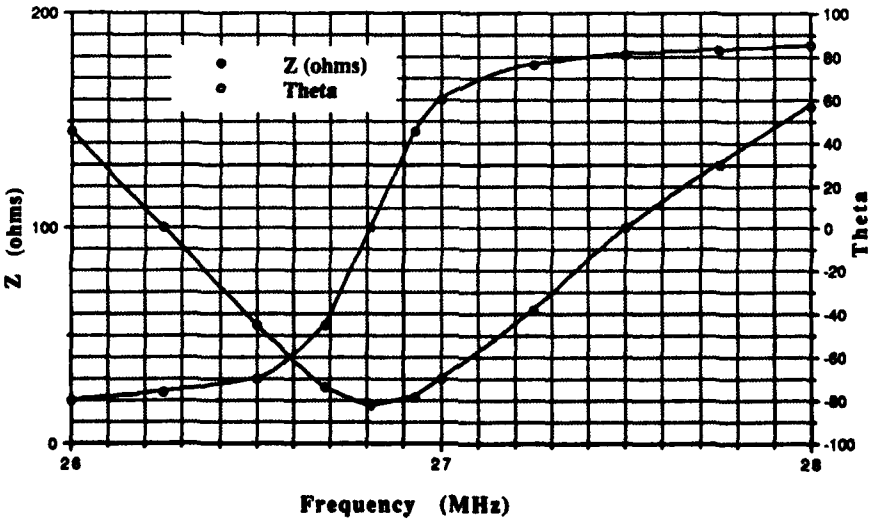

Fig. 17 Measured and calculated impedance (Z, θ) vs frequency for double folded unipole antenna system (Fig. 7b's antenna).

Discussion

V. LAMMERS (US)

In addition to keeping the ratio of radiation resistance to ground loss resistance high for best signal transmission, what can you do by improved grounding to achieve a low take-off angle.

AUTHOR'S REPLY

Improved grounding will not help to achieve a low take-off angle (or efficient coupling into the waveguide mode of propagation). I discussed this briefly in my introductory overview. In the case of MF, where one can certainly describe the propagation via a wave-hop mode, I argued that the ground more than fifty wavelengths in front of the antenna was important in achieving a low take off angle. At 3.75 MHz this distance is 4 km; at 25 kHz (if this concept still has meaning) this distance is 600 km!! Ideally a VLF/LF transmitter should be on an island remote from land, or have the ocean in the preferred direction of propagation. However, as I noted ground of high conductivity can be found in the prairie provinces of Canada.

U.S. INAN (US)

What you just described is also valid for MF Broadcast antennas, which have ground systems underneath essentially vertical monopoles. The purpose of the ground plane is to increase efficiency rather than control the radiation pattern.

AUTHOR'S REPLY

What you have said is only partly correct. The ground system controls and stabilizes the self impedance of the individual antenna elements, and it plays a significant role in stabilizing the antenna's azimuthal pattern, which is important for critical antenna arrays. Some critical broadcast antenna systems have used elevated radials (elevated near the center) or insulated radials, to help stabilize the pattern in the different seasons.

Concerning the desire to achieve a low angle of radiation, we are concerned here with skywave, which is usually considered a nuisance for broadcasters. The MF Broadcast service relies on ground wave, in fact particular attention is sometimes taken to reduce the skywave, and so reduce the interference problem during nighttime hours. The null on the horizon, characteristic of vertical antennas, is a null with respect to the launch of skywave. The total field strength does not have a null in the direction of the horizon -- this is the range of angles in which the ground wave is found.

A Dynamic Bandwidth and Phase Linearity Measurement Technique for 4-Channel MSK VLF Antenna Systems

M.D. HARRINGTON
Defence Research Agency
DRA Portsdown
Portsmouth, Hants PO6 4AA,
UK

SUMMARY

The recent move to multi-channel MSK transmissions on VLF transmitters has lead to a requirement for more stringent performance boundaries on antenna bandwidth and phase linearity parameters. The limitations of traditional 'static' measurement techniques for these parameters are described, and a new 'dynamic' test methodology is discussed. A spectrally matched test waveform is generated in order to fully exercise the antenna system under test. The test waveform also allows real-time quality of tune information to be generated as an operator aid.

LIST OF SYMBOLS

$G_{yx} = (F_y)(F_x^*)$	cross power spectrum
(F_y)	output spectrum
(F_x^*)	complex conjugate of input spectrum
$\gamma^2 = \frac{G_{xy} G_{xy}^*}{G_{xx} G_{yy}}$	coherence
G_{xy}^*	complex conjugate of cross spectrum
G_{xx}	input power spectrum
G_{yy}	output power spectrum

1. INTRODUCTION

This paper presents a method for performing dynamic measurements of antenna bandwidth and phase linearity parameters for VLF transmitter systems. These measurements have been undertaken in support of both National and NATO VLF MSK upgrade programmes, and relate to VLF transmitting antenna characteristics required in order to comply with STANAG 5030 (Ref 1).

The conversion to 200 Baud MSK transmissions (from 50 baud FSK) places strict bandwidth and phase linearity requirements on antenna systems in order to limit phase and amplitude non-linearities which inevitably lead to a degradation in overall system performance. Networks exhibiting phase non-linearity or deviation from a linear phase response produce an output signal which is a distorted and time translated version of the input signal. The result is intersymbol interference and an increase in bit errors. Consequentially, an increase in the bit energy to noise power spectral density ratio will be required in order to maintain a desired bit error probability. This is illustrated at Figure 1 which plots the degradation in bit energy to noise power spectral density as a function of the phase deviation from linearity (only parabolic phase nonlinearities are shown – Ref 2).

STANAG 5030 requires that the phase deviation (from linearity) should be limited to 12 Degrees in order to prevent a degradation of the bit energy to noise power spectral density ratio by more than 0.5 dB. This limit was selected in order to correspond to a probability of bit error which preserves an overall system CER (Character Error Rate) of 1×10^{-3}.

2. MEASUREMENT TECHNIQUES

2.1 Bandwidth Measurement

The general measurement technique used in the past consisted of tuning the system for the desired mode of operation (in this case 200 baud MSK), then removing the modulation and applying a CW tone. This is then altered in discrete steps (typically 10Hz) until the required bandwidth has been determined by amplitude comparison either by monitoring locally or at a remote receiving site.

However, previous work by CCM12 has demonstrated that the above method provides a misleading estimation of the transmitter/antenna system full power instantaneous bandwidth when applied to the non-linear amplifiers typically used at VLF to increase efficiency. By using a static stimulus, the tuned system dynamic response is masked. Furthermore, a stepped CW measurement (usually performed over a period of 15 – 30 minutes) is easily distorted by variability in the site primary power supply and even by local climatic conditions such as cloud cover and wind gust factors. In addition, transmitter down time is increased by the need to continually perform repeat measurements after minor tuning adjustments to correct for asymmetry, an example of which is shown at Fig 2.

The system bandwidth may be more accurately measured (and adjusted) by using an injected real-time dynamic test signal of equivalent power spectral density to the modulation format required.

Since it is impossible in practice to inject Gaussian Noise so as to determine the frequency transfer function, an

alternative is to generate signals which not only allow convenient analysis but are also valid examples of the modulation states used. In this respect, one suitable solution is to use a frequency comb which is envelope matched to the MSK spectral distribution. Such a signal may be conveniently generated using most on-site 4-channel MSK modulators by careful choice of the external traffic data presented to the modulator inputs:

Ch 1	Ch 2	Ch 3	Ch 4
0	1	1	1

The resultant spectrum is shown at Figure 3. By monitoring this signal both locally and at a remote site (using, for example, the test setup shown at Figure 4), a comparison may be made with the original input signal and the bandwidth determined by direct inspection of the experimental data.

Since the received signal contains all the information required for the measurement (i.e. relative tone amplitudes), cross-calibration between site recording equipment is not a significant factor – the limiting requirement is that each signal is captured and re-constructed in a linear manner.

VLF receive antenna and amplifiers of known characteristics were used so as to ensure that the measurements included all signal distortions and frequency response functions that would be referred to a receiver input. All measurements were recorded (and analysed) at 'rf' in order to ensure that no significant error would be introduced by down conversion filtering/front-end effects at the receive site.

It is important that the transmitter system be correctly tuned for 200 baud MSK operation before any measurements are recorded. In particular, over-coupling of the antenna system (manifested as at Figure 5) must be avoided and amplitude symmetry should be established and maintained throughout the measurement. An advantage of using a dynamic test signal is that local monitoring enables detection and correction of these factors in real time.

2.2 Phase Linearity Measurement

A realistic indication of the system phase response can be obtained by performing a cross-spectrum measurement using the same test signal as that described in the bandwidth measurement above.

Cross spectrum - sometimes called "cross power spectrum" - is a measure of the mutual power between two signals at each point in the current frequency span. Such measurements are useful in this instance, since they reveal both phase and magnitude information.

The phase display of the cross spectrum measurement shows the relative phase - at each frequency - between two signals. Because this phase relationship is relative, cross spectrum measurements can be made without the use of a synchronised trigger. All that is required is access to the input and output signals of the network/system under test, as shown at Figure 6.

The measurement is computed by multiplying the complex conjugate of the linear spectrum of the input by the linear spectrum of the output:

$$G_{yx} = (F_y)(F_x^*)$$

where:

(F_x^*) is the input spectrum's complex conjugate

(F_y) is the output spectrum.

The magnitude of the cross spectrum measurement is the product of the magnitudes of the two signals, therefore the measurement can be a sensitive tool for isolating major components common to both input signals – in this case the five test comb frequencies. However, cross spectrum measurements do not necessarily reveal causal relationships, i.e. the analyzer may show signals at the network output not caused by the input. For a much better indicator of causality, the coherence measurement is used.

Coherence is derived from a series of averaged cross spectrum measurements. It shows the portion of the output power spectrum actually caused by the input signal and is an indication of the statistical validity of the cross spectrum measurement. Values are on a scale of 0 to 1, where 1 indicates perfect coherence – poor coherence values are caused by uncorrelated input signals, windowing leakage effects and system non-linearities.

Coherence is calculated by dividing the cross spectrum by both the input and output power spectra:

$$\gamma^2 = \frac{G_{xy} G_{xy}^*}{G_{xx} G_{yy}}$$

where:

G_{xy} is the cross spectrum

G_{xy}^* is the cross spectrum's complex conjugate

G_{xx} is the input power spectrum

G_{yy} is the output power spectrum

The same test setup (Figure 6) is used for this 'confidence check' measurement.

On-site monitoring signal information can usually be obtained using the Transmitter stations own external whip antenna installation. However, the location of this antenna is not usually ideal (leading to inherent proximity effects) and so, where possible, a loop antenna is usually employed as an independent reference.

3. RESULTS

3.1 Bandwidth Measurement

Measurements were made using live test signals injected at the Transmitter site (as described above). The final results were then obtained from an analysis of the off-air signals received both locally and in the UK at DRA Portsdown.

The original input spectrum is shown at Figure 3. The signal received off-air at the UK test site reflects the shaping function of the Tuning and Antenna sub-systems in the relative tone amplitudes. It is important that amplitude symmetry be maintained throughout the measurement – this can be conveniently monitored by comparing matching frequency pairs at the receiving site and relaying asymmetry information back to the Transmitter site for corrective action.

A subtractive analysis is then performed on the two spectra – this can be done directly from the plots, but since all signals are available in digital format at 14 bit resolution from the PCM data recorders, greater accuracy is available by using computer analysis techniques. Figure 7 shows the results of processing the transmitted and 'off-air' spectra as overlays – the parabolic curve fits applied are accurate enough over a 200 Hz bandwidth, however transcendental functions are a better fit for an 'ideal' waveform. Since a parabolic fit is better on the filtered spectrum, it is used as a common reference between the two cases.

3.2 Phase Linearity Measurement

Using the test equipment configuration of Fig 6, the cross-spectrum phase component shown at Figure 8 was obtained. The dwell platforms for each of the five frequencies in the comb are easily discernable from the un-correlated components. The relevant data is re-plotted at Figure 9, along with a linear fit against which phase deviation may be measured.

As a check on the phase data integrity, coherence measurements were performed throughout the tests – an example result is shown at figure 10 – note the maximum value of '1' for all five comb frequencies within the measurement band.

4 CONCLUSIONS

The test method described uses a spectrally matched test waveform which fully energises the antenna system under test and so gives more accurate, operationally useful, measurement results. In addition, the technique greatly reduces the required measurement transmitter down-time by providing feedback quality of tune information to operators in real time. This is particularly useful for those Transmitters which use a bandwidth resistor in the tuning chain, as the effect of varying the bandwidth resistor current on antenna tune-state can be observed by direct inspection.

5 REFERENCES

1. NATO MAS, STANAG No. 5030 (Edition 3 Amendment 2),1989

2. Broome, N.L., "Phase Linearity Requirement for NATO MSK Broadcast", MITRE Corporation Working Paper WP81W00233, 29 April 1981

ACKNOWLEDGEMENT

This work has been carried out with the support of Procurement Executive Ministry of Defence.

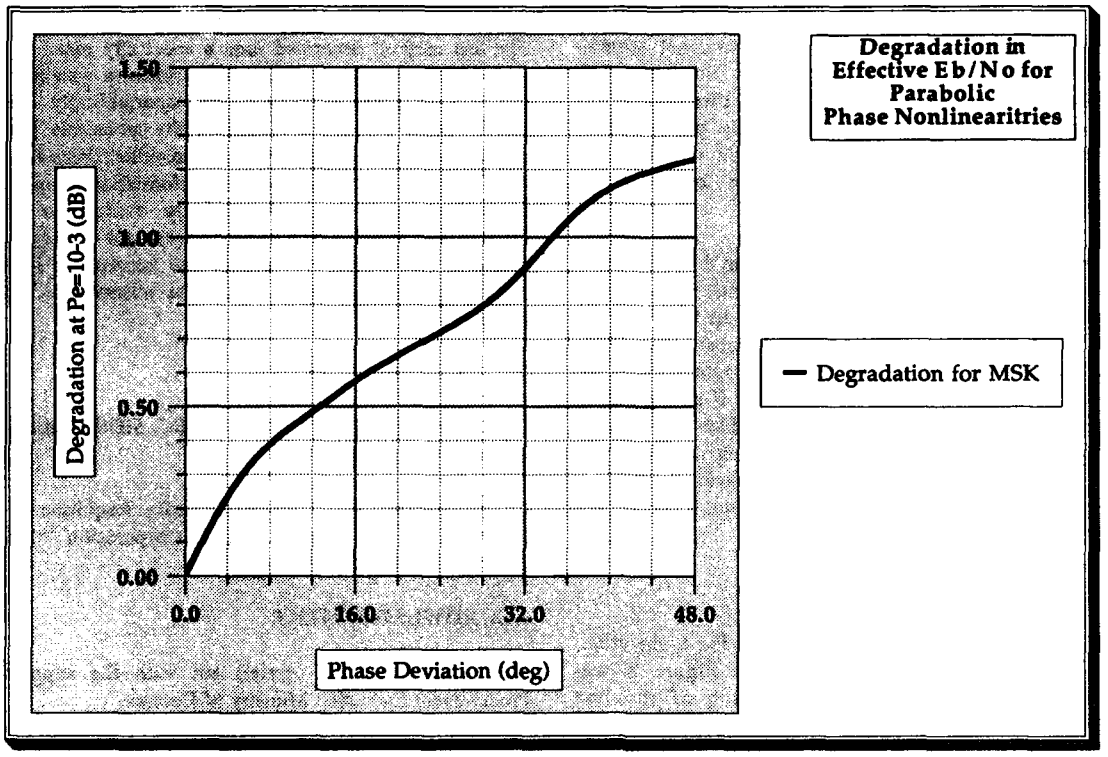

Figure 1. Degradation in Effective Eb/No for Parabolic Phase Non-Linearities (MSK Modulation).

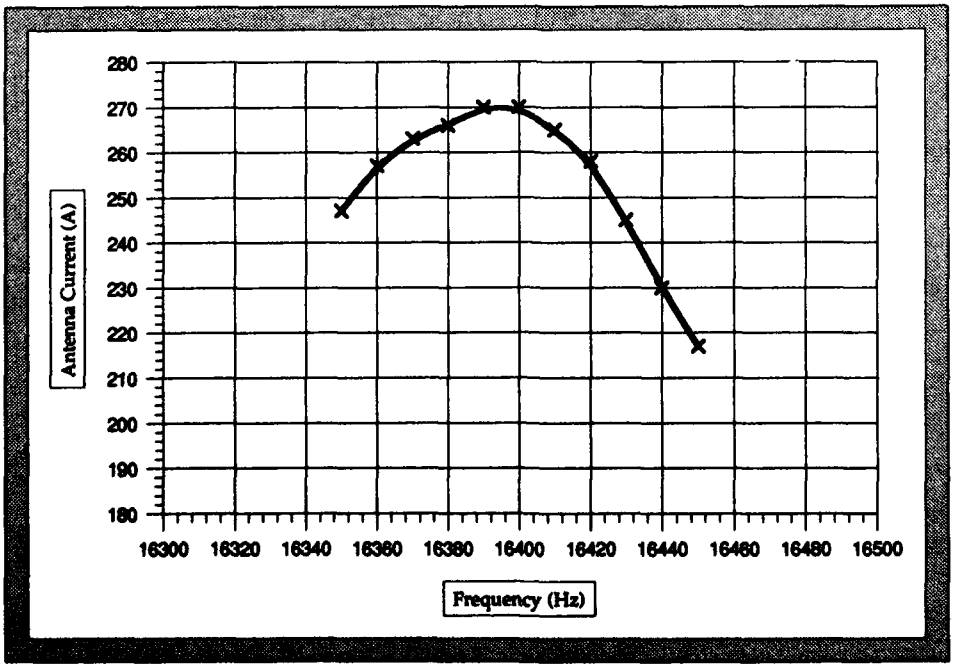

Figure 2. Asymmetric Tune Plotted by Stepped Tone Method.

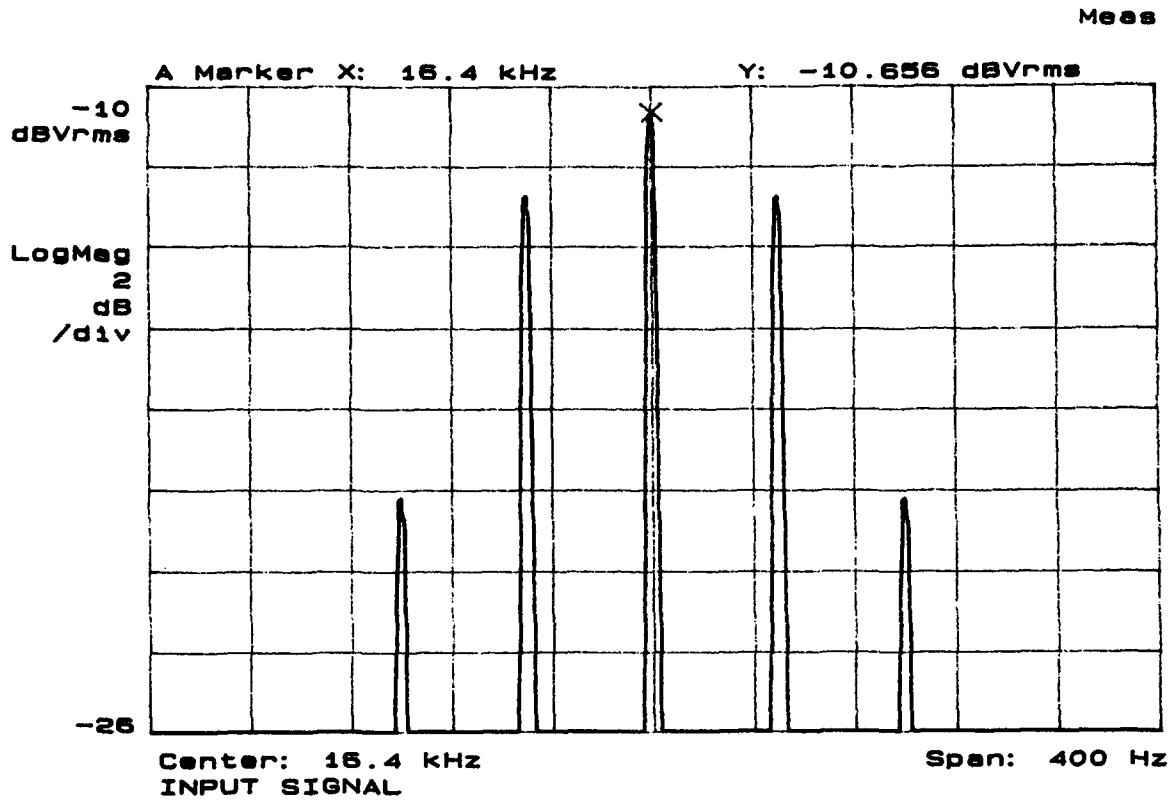

Figure 3. Dynamic Test Waveform Frequency Spectrum.

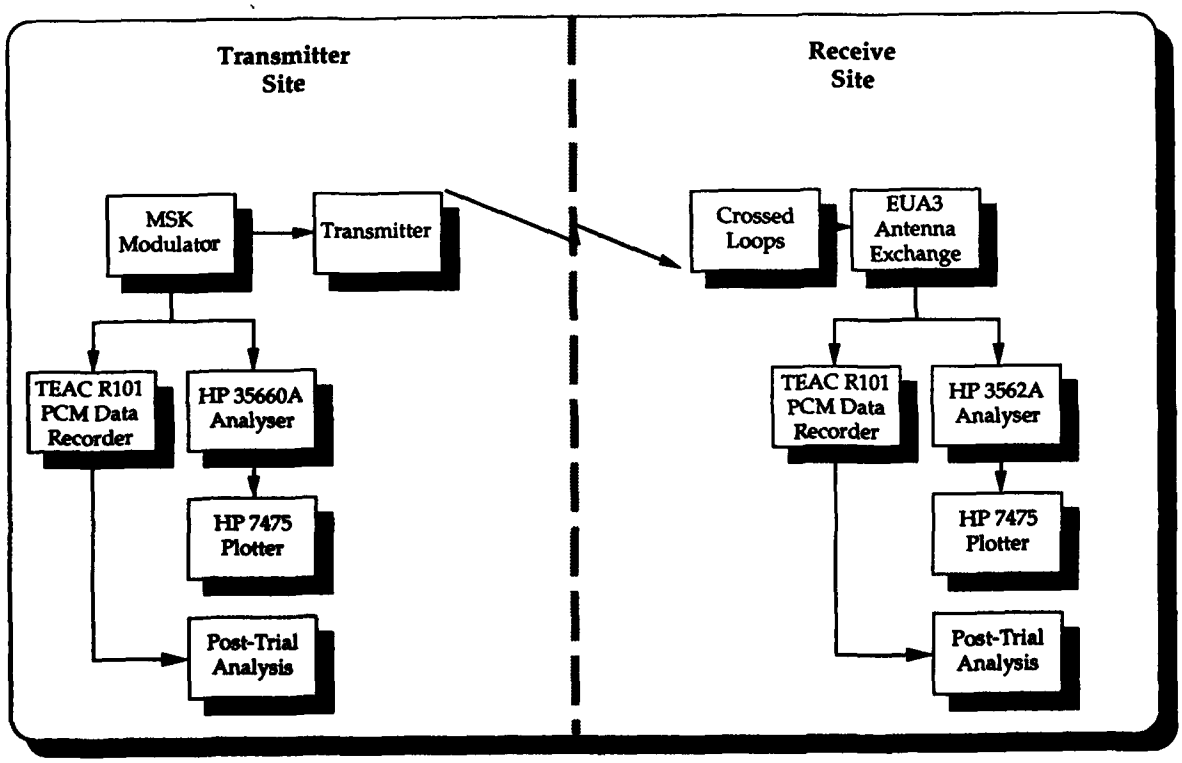

Figure 4. Bandwidth Measurement Test Configuration.

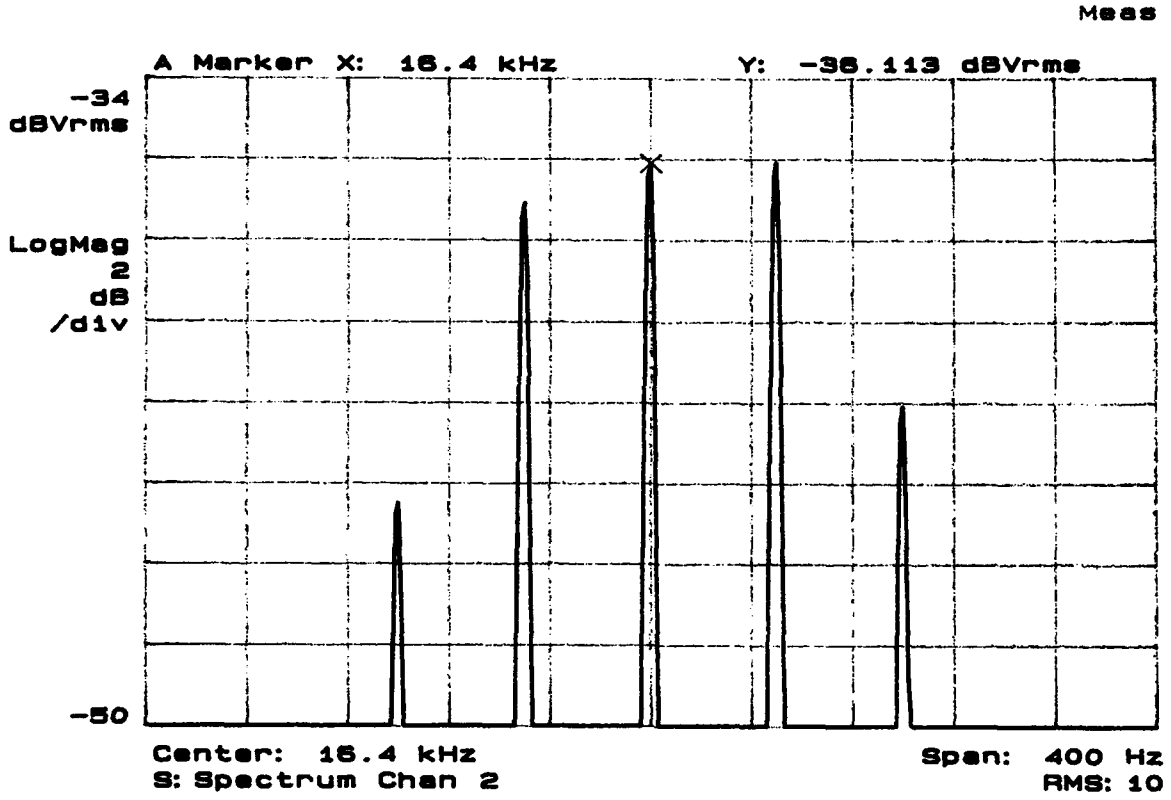

Figure 5. Frequency Response of Over-Coupled Antenna System.

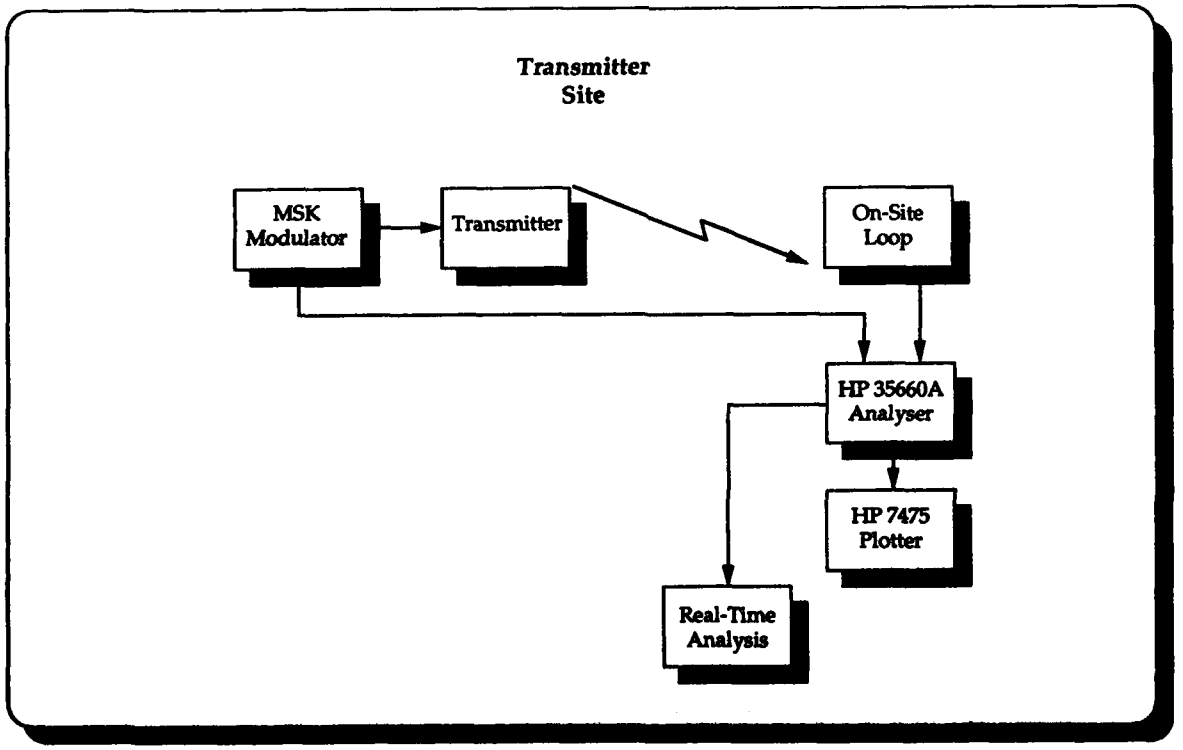

Figure 6. Phase Linearity Measurement Test Configuration.

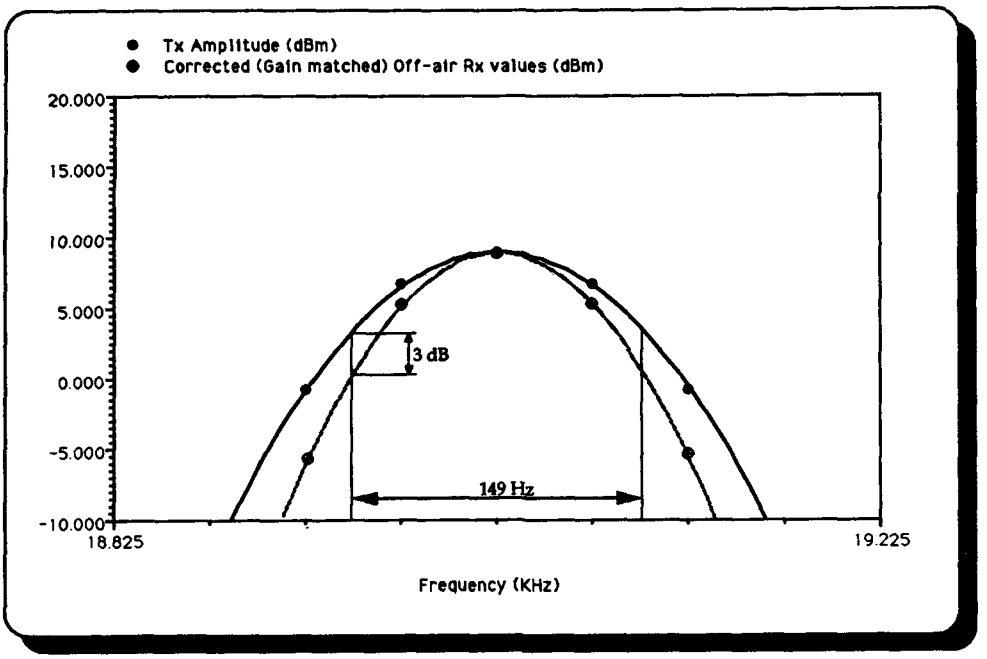

Figure 7. Parabolic Curve Fits on Original/Received Signals.

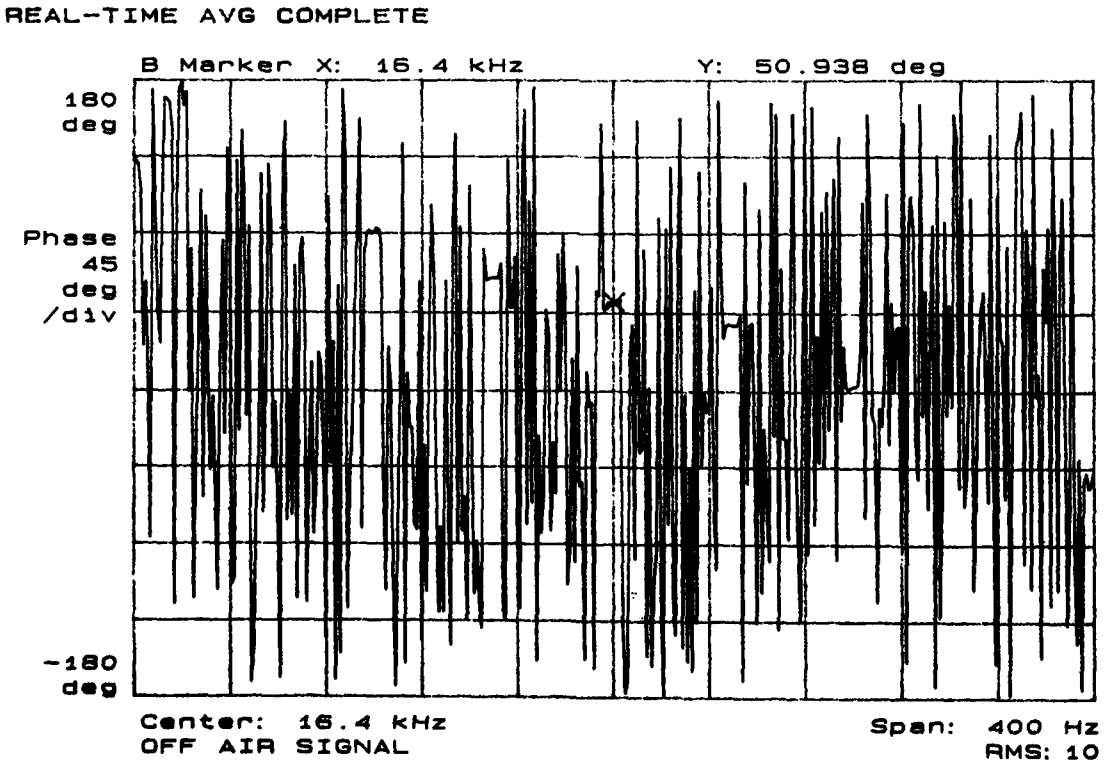

Figure 8. Cross-Spectrum Phase Measurement (Received Signal).

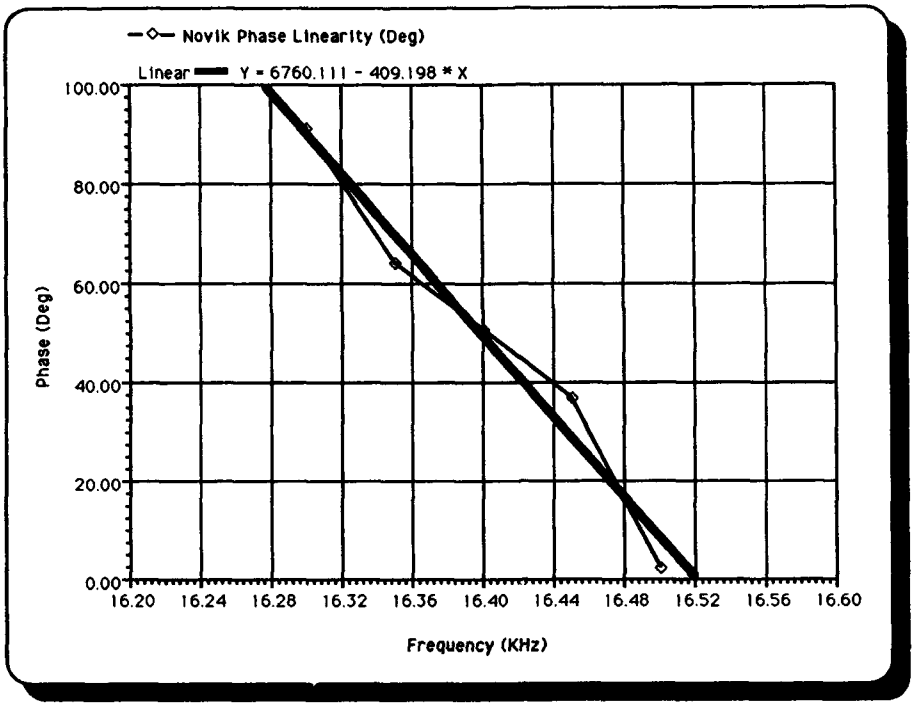

Figure 9. Cross-Spectrum Phase Result.

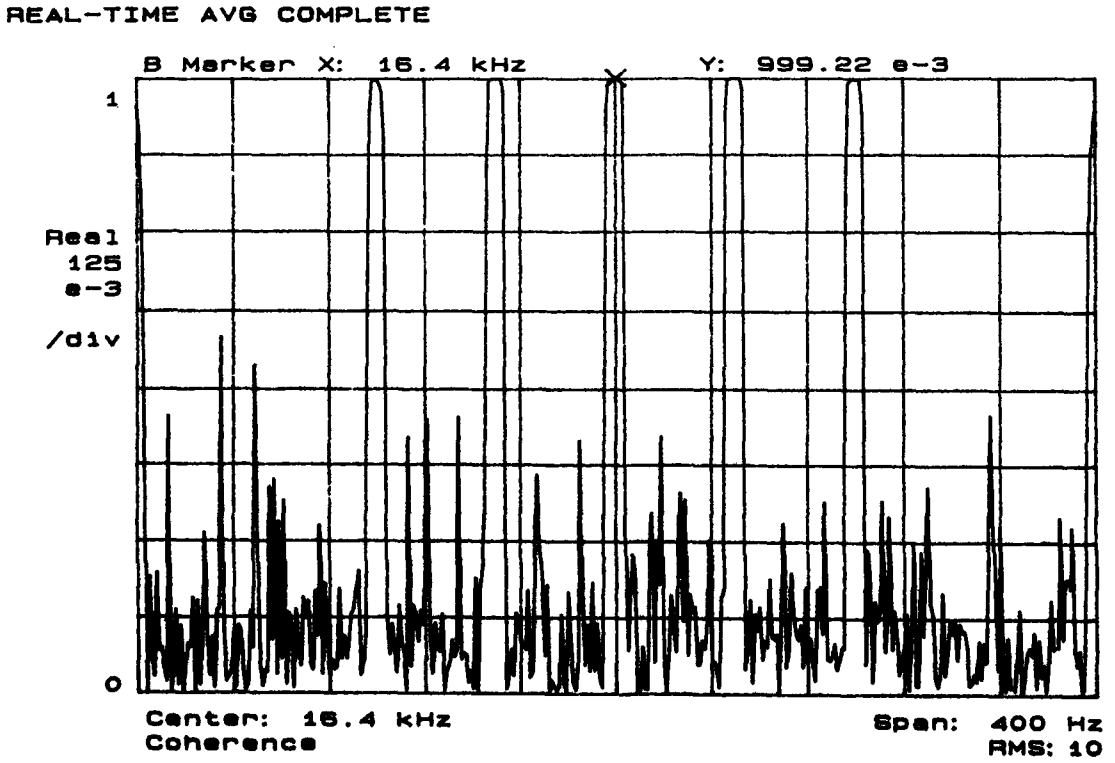

Figure 10. Coherence Measurement.

STUDY OF A VLF DISTRIBUTED ANTENNA ARRAY

G. A. ASHDOWN
Defence Research Agency
DRA Portsdown
Portsmouth, Hants PO6 4AA,
UK

SUMMARY

This study considers the use of an array of VLF antennas distributed throughout the UK, instead of a single, high powered antenna, for submarine command broadcasts. Such an array offers survivability and environmental advantages. The coverage of the array would, however, not be omni-azimuthal, but would have nulls every few degrees as a result of the interference between the signals from the individual antennas.

The study investigates the effect on the array coverage of a number of impairments (operating frequency, phase and frequency errors, and antenna loss), and discusses the advantages and disadvantages of steering the main beam to the receiving platform. Consideration is also given to how the received signal will be distorted depending on the location of the receiving platform. It was concluded that a VLF array would not be suitable for providing wide area continuous and assured communications.

1. INTRODUCTION

The study examined the use of a spatially distributed array of single VLF antennas for submarine command broadcasts, instead of the usual implementation of one or more antennas placed closely together and radiating as one high powered antenna.

The use of a number of widely dispersed, integrated, transmitters offers redundancy advantages with the possibility of lower visual and electromagnetic environmental impact due to reduced element radiating power. This, however, would be offset by the sophisticated arrangements required to ensure that all of the individual antennas acted as in integrated system, despite the distances between them.

2. THE ARRAY

The basic array consists of a number of discrete transmitting elements (antennas). These elements emit the same in-phase signal, and the signals form a spatial interference pattern. The element spacing determines the positions of the (side) lobes and nulls in the interference pattern. (For applications such as radar, half wavelength spacing is generally favoured since it results in a main beam, and low sidelobes. This contrasts with VLF submarine broadcast communications which generally require near omni-azimuthal coverage.)

The way in which the individual signals from the antennas of the array combine at the point of reception (constructively or destructively) depends on the relative phases of the signals, the phase of each signal being a function of the path length, in wavelengths, between antenna and receiver. The radiation pattern of an array can be drawn, which plots gain with respect to a single antenna as a function of the angle from broadside ('broadside' being perpendicular to the array). The calculation involved in producing this plot is analogous to that for classical optics for the far-field.

The shape of a VLF array built in the UK would be dependant on sites available. It is reasonable to expect that the array would not be a straight line, nor would its antennas be equally spaced. At 20 kHz, the UK is approximately 50 wavelengths long. It was assumed for this study that the antenna sites would be randomly positioned (effectively) throughout the length of the UK (thus average antenna spacing would be of the order of seven wavelengths), at varying distances from a nominal North-South line. Broadside to this array, and hence main beam direction, would then be due west. This study used ten antennas, each of power 75 kW, and results were compared to those for a single, omnidirectional, 750 kW transmitter.

The antenna layout used in this study is shown in Figure 1. It was allocated the name "FILEUK". Figure 2 shows the radiation pattern for this array, with the signals transmitted in phase (on this plot, the gain of a single, omnidirectional, 750 kW antenna, is shown by the 10 dB circle). The radiation pattern for a number of layouts were examined, and it was concluded that results obtained for "FILEUK" were typical - it was therefore used throughout this study.

3. IMPAIRMENTS

The effect of the following parameters on the coverage obtained from a VLF array were examined.

- Operating Frequency
- Phase Errors
- Frequency Errors
- Loss of Antennas

These impairments were all applied to the basic system:

- Array Layout "FILEUK"
- Operating Frequency 20 kHz
- No Phase or Frequency Errors

3.1 Operating Frequency

As the transmission frequency varies, the phases of the individual antenna signals at any receiving point will vary (since the distance from the receiver to each antenna, in terms of wavelengths, will alter), and hence the interference pattern will change.

The radiation patterns for a number of frequencies in the VLF band were examined. At 20 kHz, the radiation pattern consists of a mainbeam and numerous sidelobes, with varying gains, up to a maximum of around 17 dB - see Figure 2. The radiation patterns at other frequencies were of the same form, consisting of a comparable number of sidelobes, with a similar distribution of gains, although the exact positions of the sidelobes (and nulls) varied with frequency. It was concluded that, although the exact radiation pattern is very dependent on operating frequency, for a staggered array of the type which would have to be implemented practically, the overall coverage will not be improved (or degraded) by operating at a particular frequency. However, because the positions of the nulls are frequency dependant, once the array layout had been selected its coverage would need to be calculated, and tested practically.

3.2 Phase Errors

For the purposes of this model, random phase errors were generated for each antenna, using a gaussian (normal) distribution with zero mean and a user defined variance.

It would be expected that each transmitting antenna would derive its frequency and time from a high quality frequency standard, which would be synchronised. The accuracy of the transmitters is such that they will drift, relative to each other, by perhaps 1μs per day. This time delay corresponds to a phase offset of 7.2° at 20 kHz, 10.8° at 30 kHz. To model this, 7° was used as the variance in generating random phase errors.

The changes to the radiation patterns, resulting from the introduction of phase errors, were examined for a number of sets of phase errors. Although the effect on the overall pattern did not appear to be very great, especially in the region -90° to +90° which is mainly of interest for North Atlantic coverage, there were slight alterations in the positions of nulls and the gains of the lobes which could be of significance to a platform trying to receive a signal.

In addition to phase errors at the antennas, which could possibly be monitored so that the coverage at any particular moment could be predicted, phase variations could also be introduced by unpredictable aberrations in the ionosphere. However, given the short baseline of the array compared to reception ranges the ionosphere was considered to be similar for each path to the receiving platforms.

3.3 Frequency Errors

If one or more of the antennas transmit the signal at an incorrect frequency, the relative phases of the signals, and hence the total signal at any particular point, will be altered. The frequency accuracy of an individual transmitter is of the order of one part in 10^{12}, which implies an accuracy of the order of $\pm 10^{-8}$ Hz at VLF frequencies - this magnitude of error is not going to affect the array radiation pattern.

There is however a possibility of an error occurring if a transmitter becomes faulty, or an incorrect frequency setting is used. This was investigated for an error at one transmitter of up to 200 Hz - if the 'rogue' antenna was more than 200 Hz out from the operating frequency, its propagation characteristics would be very different, so larger errors were not considered.

A number of different cases were considered, and it was established that the magnitude of the effect on the radiation pattern was dependent on which antenna had the frequency error. For example, a 200 Hz error at antenna 6 appeared to have far less effect than the same error at antenna 2; this is because antenna 2 is further from the phase centre of the array. The changes in the radiation patterns, compared to the 'perfect' case, were small but discernable.

3.4 Loss of Antennas

If one or more of the antennas operate at reduced power, or fail completely, the total power will be reduced. Moreover, since one or more of the individual signals received at any particular point will be changed, the total signal will also be altered, and hence the whole radiated pattern.

An example of the effect of antenna loss is shown in the radiation pattern of Figure 3 - antennas 3 and 7 are off, and antenna 2 is operating at half power. It can be seen that, as expected, the loss of the antennas significantly alters the radiation pattern and, hence the coverage. Consequently, if a transmitter is deactivated, not only would a receiving platform at the limits of the transmitter range no longer be able to receive messages because of the reduction in power, but a platform at a bearing off the main beam may suddenly find itself in the null of the 'new' radiation pattern, even if it is well within the range of the 'old' radiation pattern.

4. IMPLICATIONS OF VLF PROPAGATION

The radiation patterns used so far are quick to produce, and are suitable for a 'first look'. However, the plots assume that at the receiving point, the amplitudes of all the individual signals are equal. At VLF frequencies, the interaction between the modes propagating in the earth ionosphere waveguide mean that signal amplitude is not a simple function of distance, but consists of a number of peaks and nulls due to modal addition. Further, since the height of the ionosphere varies between day and night, VLF propagation also follows a diurnal variation. To take this into account "power plots" were produced.

The power plots show a plan view of the coverage with received power, in dB μV/m indicated by a grey-scale. The plots were produced as follows. At every point on a 100 km xy grid, the distance from the point to each of the antennas was calculated. The relative phases of the signals were found from the differences in path lengths; the amplitude of each signal was found from the propagation curve for the appropriate frequency and time of day, taken from Brookes, McCabe and Rhoades [1]. The signals were

then summed, taking into account both their amplitudes and relative phases.

The day and night power plots for the array "FILEUK", operating at 20 kHz, are shown in Figure 4. The transmitter is at the centre, and received powers have been calculated out to a radius of 7 Mm. No information was available for distances less than 750 km, hence the blank area in the centre. (Note that the main beam points due west, not upwards as in the radiation patterns.)

Power plots were also generated to look at the effect of phase errors. Comparing the resulting plots with those of Figure 4 showed that, although the coverage did not change greatly, nulls were introduced which would mean that, if unpredictable phase errors occurred, the receiving platform could unexpectedly find itself unable to receive communications.

One limitation of the power plots is that they use one propagation curve, a sea path, for all bearings. However, this study is concerned with coverage in the North Atlantic, so a sea path is appropriate for the western half of this plot, and the eastern half is of lesser interest. Obviously, the power plots give a more realistic picture of the coverage achieved by an array than do the radiation patterns, but the power plots are very time consuming to produce, so most of the analysis was done using radiation patterns, or the coverage plots described in section 5.

5. IMPLICATIONS OF ATMOSPHERIC NOISE

At VLF, because of the worldwide propagation of VLF frequencies generated by lightning impulses, atmospheric noise, rather than receiver internal noise, is the limiting factor in long distance signal reception, and this will vary with geographical position. By calculating the SNRs over an area, a coverage plot, showing the geographical limits of reception for a particular transmitter can be constructed. (Because atmospheric noise is a random phenomena, it is described statistically, for example, the noise value (in dB μV/m) which will not be exceeded for 99% of the time (the value used in this study), and hence the SNR and the coverage limits are also given as those correct for a certain percentage of the time.)

The NRaD Long Wave Propagation Capability (LWPC) program [2] calculates the coverage limits (corresponding to a specified SNR) by combining information about signal strength at each location, calculated using standard waveguide mode propagation techniques, and atmospheric noise values taken from a data base. Inputs include frequency, month and time of day, all of which affect both propagation and atmospheric noise parameters. Figure 5 shows the different coverage limits for a 20 kHz transmitter operating at a number of different powers, during the day.

Plots to assess the coverage limits of the array were produced as follows. The gain for the array operating at the required frequency was calculated for every degree between -90° and +90° (these are the values plotted in the radiation patterns). Since broadside is due west, this corresponds to bearings from 180° to 360°. This value for gain is with respect to an individual array antenna; given that each antenna radiates 75 kW, the corresponding power for each bearing could then be calculated.

The assumption was then made that, at a particular bearing, the signal generated by the array is the same as that produced by a single antenna transmitting the power calculated from the gain, and, therefore, the limit of coverage at that bearing will also be the same.

Plots were generated by hand, by overlaying a map showing the coverage limits for a number of powers, for the particular frequency and time of day required (similar to Figure 5), with a plot of the bearing lines (which are not straight because of the projection of this particular map), and then drawing in the the coverage limits along each bearing.

Figures 6 and 7 compare the reception limits for the array and a single 750 kW antenna operating at 20 kHz, for day and night respectively. (Note that at night there are areas within the limit line where no reception is possible; this is shown as a bounded area for the single antenna, and as lines along the bearing curves for the array. For the array, there are also areas beyond the reception limit line where reception is possible - these areas are also shown as lines along the bearing curves.)

Similar plots were generated to show the effect of the various impairments already investigated in section 3. The reception limits for the array with and without phase errors are compared in Figure 8, for 20 kHz day. (The particular phase errors used are given with the figure.) The limits are similar, but it can be clearly seen that some nulls have moved a few degrees. This plot clearly shows how significant the effect of phase errors, even of this magnitude, can be.

6. BEAM STEERING

The obvious method of overcoming the problem of the possibility of the receiving platform being within a null of the radiation pattern, and hence unable to receive any signal, is to steer the main beam to the direction of the platform. This can be achieved by introducing, at each antenna, a phase shift which is a function of the required main beam bearing relative to broadside, the frequency, and the position of the antenna with respect to the array phase centre. Steering the main beam also ensures that the maximum power, and hence the maximum range, is in the direction of interest.

Beam steering has some advantages, but also a number of disadvantages - these are summarised below.

Advantages of Beam Steering

(a) Maximum power, and hence maximum range is in the direction of the receiving platform.

(b) The main beam direction is largely unaffected by phase and frequency errors and loss of antennas, although the rest of the radiation pattern may be changed. (The exception to this is if any phase errors are systematic rather than (apparently) random, in which case the main beam will be pointed in the wrong direction.)

Disadvantages of Beam Steering

(a) The power in the main beam is significantly higher than that in any of the other lobes (by at least 6dB, i.e. 7500 kW as compared to a maximum of around 3500 kW in the sidelobes). It may therefore be relatively easy to establish the bearing at which the maximum power is being transmitted (e.g. using an aircraft with a simple VLF receiver) and hence the bearing of the platform. Since the beamwidth (which is determined by the size of the array) is narrow (3dB beamwidth 1.2°, null-to-null beamwidth 2°), the platform position is defined in azimuth.

(b) The narrow beamwidth implies that the platform position must be accurately known so that the phase shifts needed to steer the beam to the required direction can be calculated. Each antenna would require the facility for introducing the phase shift into the signal. The actual phase shift could either be calculated at a central processor and sent to each transmitter site, or the required steering direction could be passed to each site and the phase shift calculated there. Whichever method were used, the control information (i.e. phase shift or steering direction) would have to be passed to the antenna securely and reliably.

(c) Only one receiving platform can be contacted at a time (unless they are all on the same bearing), so any message requiring transmission to several platforms would have to be repeated for each, reducing message throughput.

(d) A possible way of overcoming problem (a) - i.e. the position of the main beam indicating the bearing of the receiving platform - could be to repeat the message with the beam steered to several different bearings, which may be unrelated to the actual platform bearing. However, this method has the same disadvantage as transmitting to a number of dislocated receivers - dilution of message throughput. Continuous communication to one platform would not be possible.

7. SUMMARY OF ARRAY COVERAGE RESULTS

Because the coverage limits for various transmit powers are so closely spaced for powers in the range 150 - 750 kW (for example, see Figure 5), the coverage limit (as shown by the coverage plots) for the distributed array is fairly close to that of the 750 kW antenna, even though the power in many of the lobes is well below 750 kW. In fact, since the coverage limit for the array tends to hover about the 750 kW limit, it suggests that it is not really necessary to steer the beam unless the receiving platform is near the outer limits of the transmitter range.

The limitation of the distributed array lies, of course, in the existence of the nulls in the coverage. These occur very abruptly, for example, a change in bearing of one degree can result in a drop in apparent radiated power (i.e. value calculated from the radiation pattern gain) from 1280 kW to 14 kW, and hence loss of signal. Similarly, if any impairments occur which alter the coverage, the platform could abruptly lose the signal, even though the platform itself has not moved.

The coverage is totally dependent on the operating frequency used. The coverage could be characterised theoretically, and confirmed by actual measurements, in which case it should be known whether or not a particular platform would be able to receive a message, provided the platform's position were known with sufficient accuracy. However, the high possibility of the introduction of random impairments would mean that these 'perfect' coverage plots would often not reflect reality.

Quite high relative phase errors are possible, both because of drift in equipment, and due to errors in initiating the signal from widely dispersed antennas. These, largely unpredictable, errors can have a significant impact on the positions of the nulls in the coverage limits of the array.

Errors in the frequency at individual antennas are not so likely to occur, but when they do they again affect the coverage pattern. Total or partial loss of any of the antennas also has a significant effect on the coverage, which is dependent on the particular antenna(s) involved. The effect of all possible antenna losses could be modelled, however it would be very time consuming.

These impairments appear to have little effect on the main beam (except for reduction in power due to antenna loss), so many of the problems could be overcome by steering the main beam to the receiving platform. However, there are a number of disadvantages to this method, as listed in section 6.

8. SIGNAL DISTORTION

For adequate communication using signals from a distributed array, the coverage is not the whole story. To consider the problem in the simplest terms, the signals from two transmitters may add constructively at the point of reception, but the difference in the two path lengths may be several wavelengths, and thus the information (for example, one bit) conveyed on the signals may be offset, and hence the resultant will be meaningless. This can be overcome by delaying the start of transmission of the information at one antenna relative to the other, so that the information coincides exactly at the reception point, but the problem will still occur at other locations. The fact that the 'information' will probably alter either the frequency (FSK) or the phase (MSK) of the signal complicates matters even further.

The problem was investigated using two different methods as outlined below. Reception was considered at two locations, Y (30°N 50°W) and Z (60°N 20°W). Additionally, Y was taken to be the centre of a square, side 100 km, whose corners were labelled A, B, C and D (lying due NE, SE, SW and NW of Y respectively).

8.1 Bit Distortion

A signal consisting of five bits, 10101, was considered, each bit being 5 ms long. Delays were introduced at each antenna such that the leading edge of the first bit transmitted by each antenna arrived at Y at the same time. This is equivalent to introducing a phase shift at each antenna such that the main beam is steered to Y, but, depending on the relative path lengths from Y to antenna, the actual phase shift may be greater than 2π. In this

example, time delays of up to 4.32 ms had to be introduced at the individual transmitters.

Knowing the distance from the other locations to the antennas, and the delay at each antenna, it was then possible to calculate the relative times of arrival (t.o.a.) of the signals (that is, the leading edge of the first bit) at each location. Figure 9 shows the signals from the individual antennas, and the resultant, arriving at location D, 70 km NW of Y. (At Y all the bit edges would line up on the grid lines as the signal from antenna 9 does here.) Maximum time difference between t.o.a. of signal leading edges at D was 0.12 ms - this implies that a receiver at D could receive the message correctly.

The corresponding plot of t.o.a. at location Z is shown in Figure 10. Here the maximum difference in t.o.a. of bit leading edges is 7.03 ms - greater than one bit length. As can be seen, the resultant signal is totally distorted. Thus, for a receiving platform at Z to successfully receive the same message as at Y, the message would have to be repeated using a different set of time delays. And this would have to happen even if Z was well within the coverage area of the array.

8.2 Carrier Distortion

Signals transmitted by the distributed array would not, in fact, be a series of bits, but would be some form of Frequency Shift Keying (FSK). (This includes MSK (Minimum Shift Keying) which is FSK with a modulation index of 0.5 and is the current VLF modulation system.) In FSK two transmitting frequencies are used, F1 corresponding to a '1' and F2 to a '0'. When switching between the two frequencies, phase continuity is maintained. $F1 = F_c + F_o$ and $F2 = F_c - F_o$, where F_c is the carrier frequency (e.g. 20 kHz) and F_o is the offset frequency (typically 50 Hz). This has been modelled for Figures 11 and 12. The Figures show a 2 ms 'snapshot' of the individual and total signals received at locations Y and D respectively. (As for Figures 12 and 13, t=0 corresponds to the t.o.a. of the first antenna signal.)

It can be seen from the Figure 12 that, although the relative t.o.a. of signals at location D are only a small fraction of the bit length (5 ms), and hence do not appear to have a significant affect on the received bits (Figure 9), these delays correspond to a large fraction of the actual sine waves (20 kHz ± 50 Hz), so instead of adding up to give the maximum amplitude as at Y (Figure 11), a smaller amplitude (and hence power and SNR) is received.

8.3 Discussion

This section has attempted to illustrate graphically the effect on message reception of using a distributed array. Figure 10 shows that, if a receiving platform is located away from the main beam, even if it is not in a null and hence the SNR is sufficient for reception, the message information contained in the signal will be distorted, so message reception is actually only possible close to the main beam.

Figure 11 further shows that close to the location for which reception is optimised, although the message information may not be too severely distorted, the relative delays between the antenna signals may mean that the signals interfere with each other such that the total signal, and hence the received SNR, is reduced to such an extent that reception is difficult.

This brief assessment of distortion has made a number of simplifying assumptions:

(i) The amplitude of the signals from each antenna are equal at the receiving location - this is not necessarily true, as amplitude (field strength) is dependent on the distance of the receiver from the antenna.

(ii) The delays at each transmitter are specified to 0.01 ms, without any time/phase errors.

(iii) All assessment so far has been in the time domain. Although Figures 11 and 12 include the switch from F1 to F2, the difference between 20.05 kHz and 19.95 kHz cannot be distinguished on these graphs. Some frequency domain analysis would also be required.

Synthesising signals to simulate distortions is relatively straightforward, and would be necessary to assess the impact on differing designs of receivers.

9. CONCLUSIONS

The study has examined the relative effects of impairments on the performance of a large distributed antenna array operating at VLF and compared the performance with that obtained using a conventional antenna implementation.

1. There are a number of impairments which can be introduced at the individual transmitters - errors in phase, frequency and availability - which affect the coverage of the array, notably the positions of deep nulls restricting the coverage along some bearings.

The effect of these impairments could, in theory, be measured and used to calculate the coverage at any particular time. Since they are random, and in some cases continually varying, the transmitters would have to be monitored continuously, and data returned to some central processing point.

2. The problems with impairments could largely be overcome by steering the main beam to the receiving platform. Moreover, the work on signal distortion suggests that this would have to be done to ensure that a legible message was received. However, there are a number of disadvantages with beam steering:

(a) The narrow beamwidth means that the position of the platform needs to be known very accurately.

(b) The relative phase of the VLF signal at each antenna must be calculated, and implemented, precisely to steer the main beam with the necessary accuracy.

(c) It is only possible to communicate with one platform at a time. If the same message has to be sent to several platforms, the message must be repeated with the

main beam steered to several different directions. This increases the time taken to sent a message to several platforms, and means that there cannot be continuous communications to any single platform.

(d) The fact that the main beam is directed towards the platform may make it possible for the bearing of that platform to be deduced, thus defeating the principle of covert submarine operation.

3. It could be argued that in using a VLF distributed array, the risk from the vulnerability of a single site transmitter has been exchanged for that arising from the monitoring and control needed for the distributed transmitter system.

4. The system examined in this report is not considered to be suitable for use as a broadcast transmitter to a covert submarine requiring continuous and assured communications.

10. REFERENCES

1. Brookes, C. B., Jr. McCabe, J. H. Rhoads, F. J. "Theoretical VLF Multimode Propagation Predictions" NRL Report 6663, December 1967

2. Ferguson, J. A. Snyder, F. P. The NAVOCEANSYSCEN's Long Wave Propagation Capability Program, 1988

ACKNOWLEDGEMENT

This work has been carried out with the support of Procurement Executive Ministry of Defence.

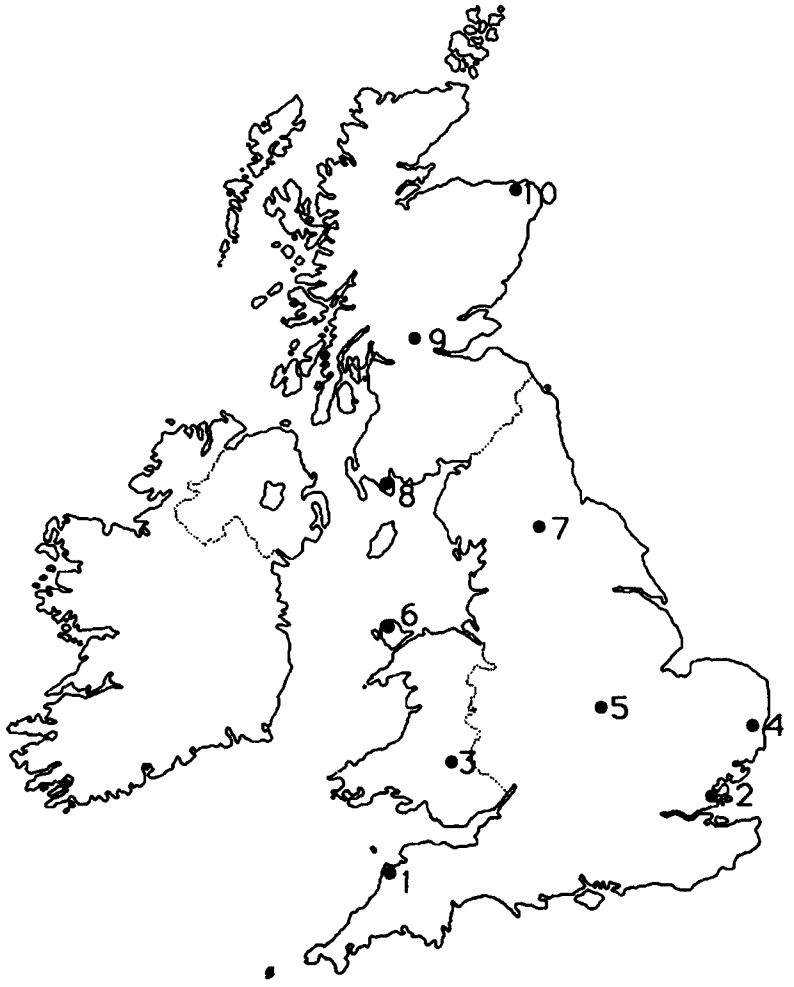

FIGURE 1: Positions of Antennas for Distributed Array Layout "FILEUK"

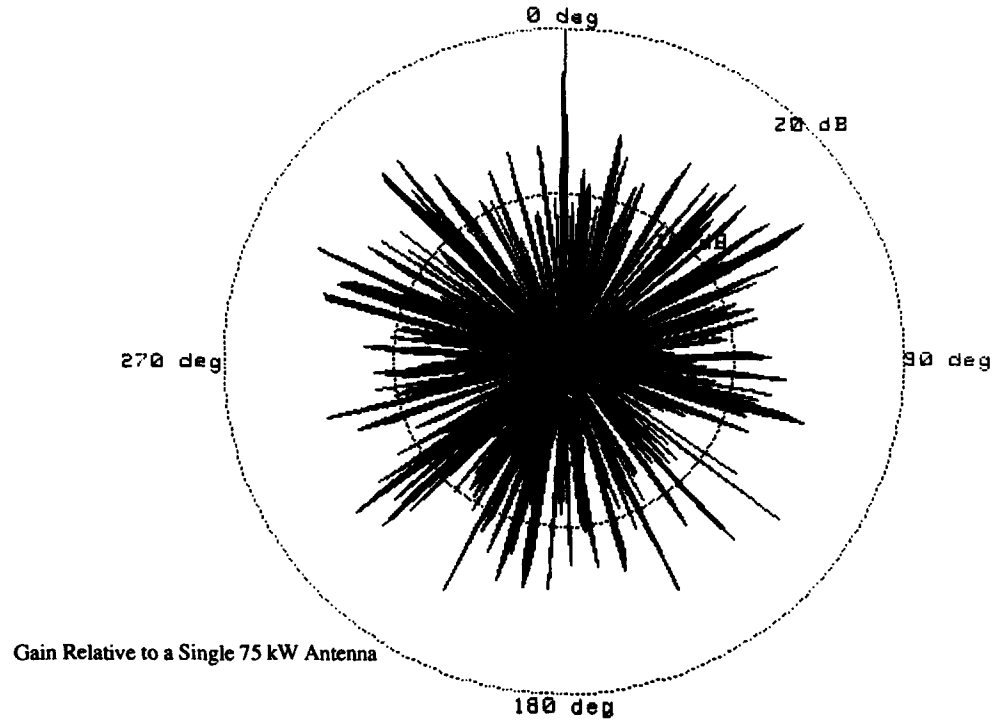

FIGURE 2: Radiation Pattern for Distributed Array "FILEUK", 20 kHz

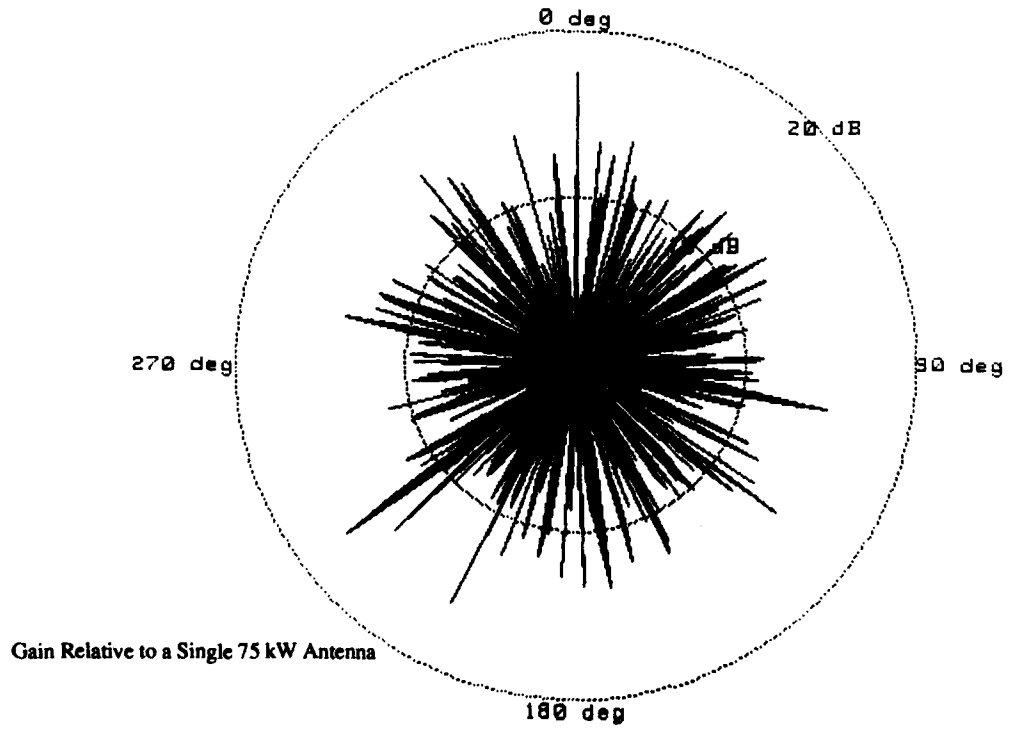

FIGURE 3: Radiation Pattern for Distributed Array "FILEUK", 20 kHz
Antenna Loss: Antennas 3 and 7 Off, Antenna 2 at Half Power

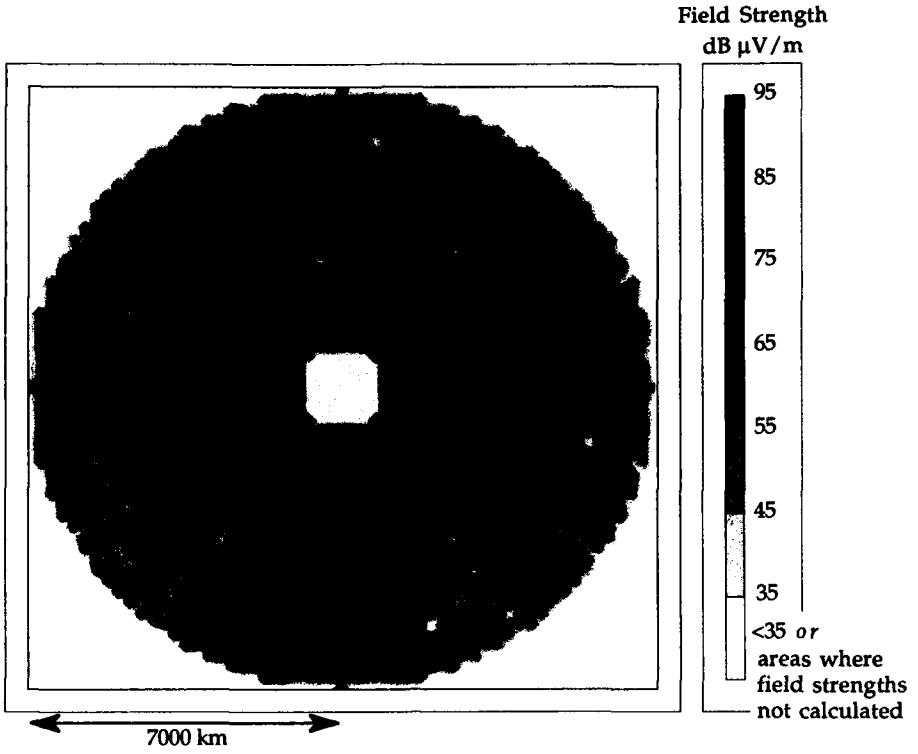

FIGURE 4a: Power Plot for Distributed Array "FILEUK", 20 kHz, Daytime

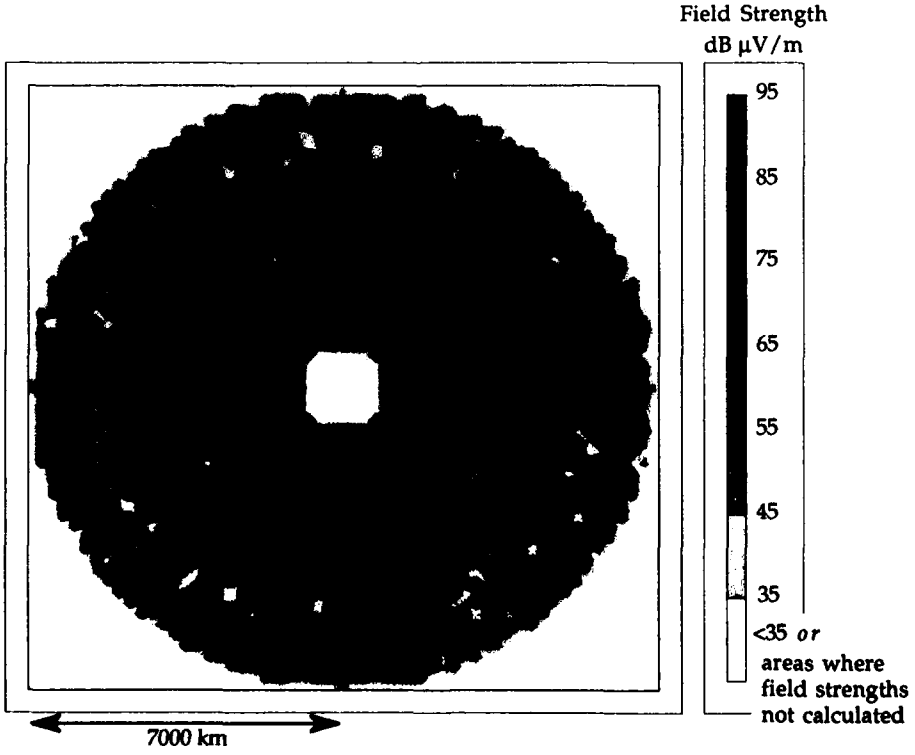

FIGURE 4b: Power Plot for Distributed Array "FILEUK", 20 kHz, Nighttime

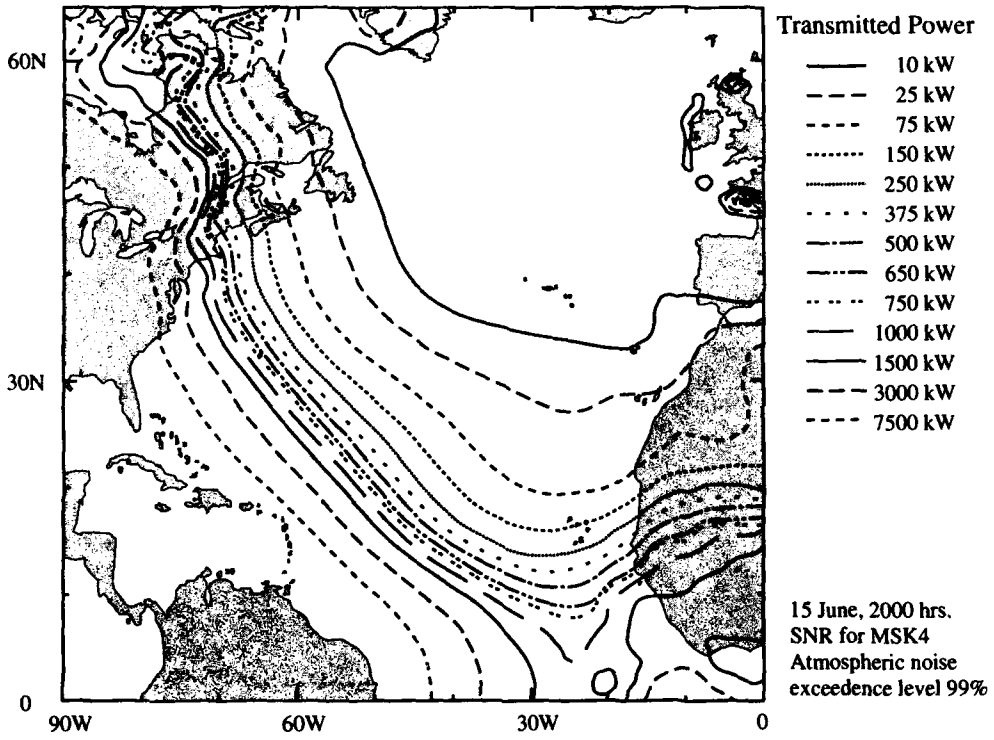

FIGURE 5: Coverage Limits for a Single Antenna Transmitting Various Powers, 20 kHz, Daytime

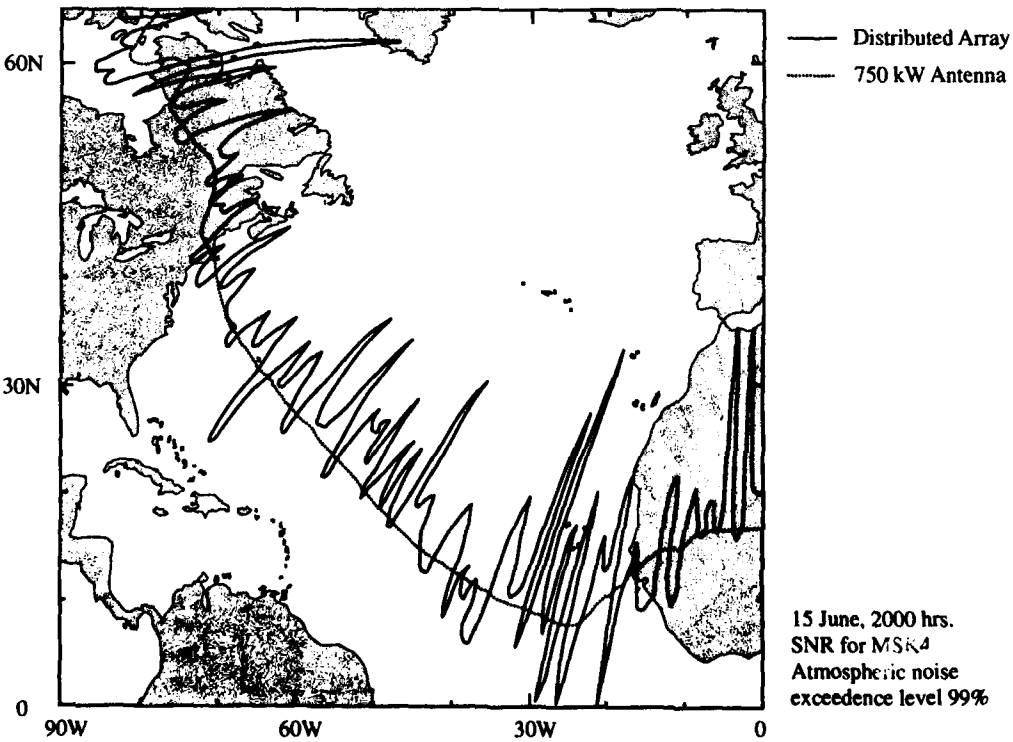

FIGURE 6: Coverage Limit for Distributed Array "FILEUK" and Single 750 kW Antenna, 20 kHz, Daytime

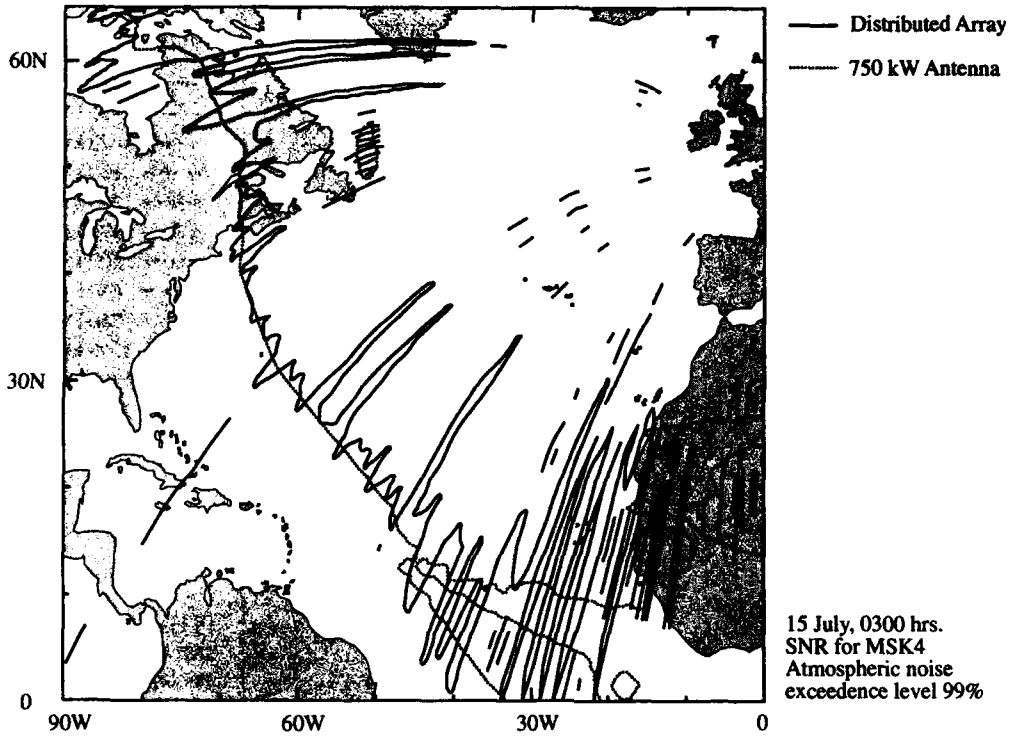

FIGURE 7: Coverage Limit for Distributed Array "FILEUK" and Single 750 kW Antenna, 20 kHz, Nighttime

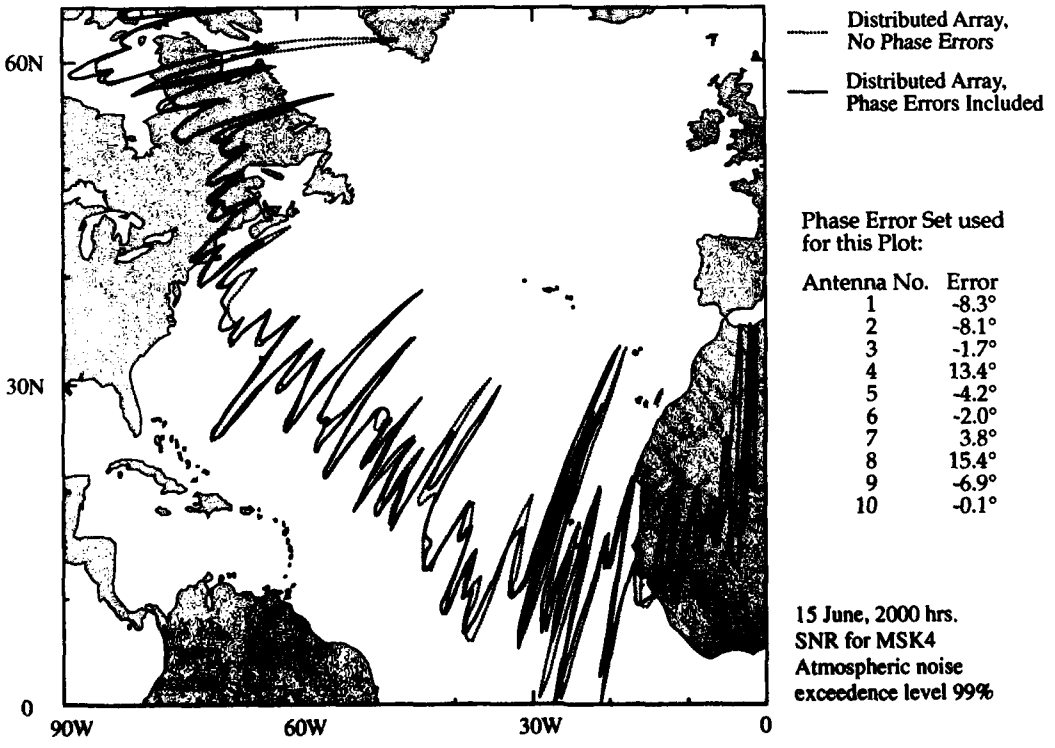

FIGURE 8: Coverage Limits for Distributed Array "FILEUK" With and Without Phase Errors, 20 kHz, Daytime

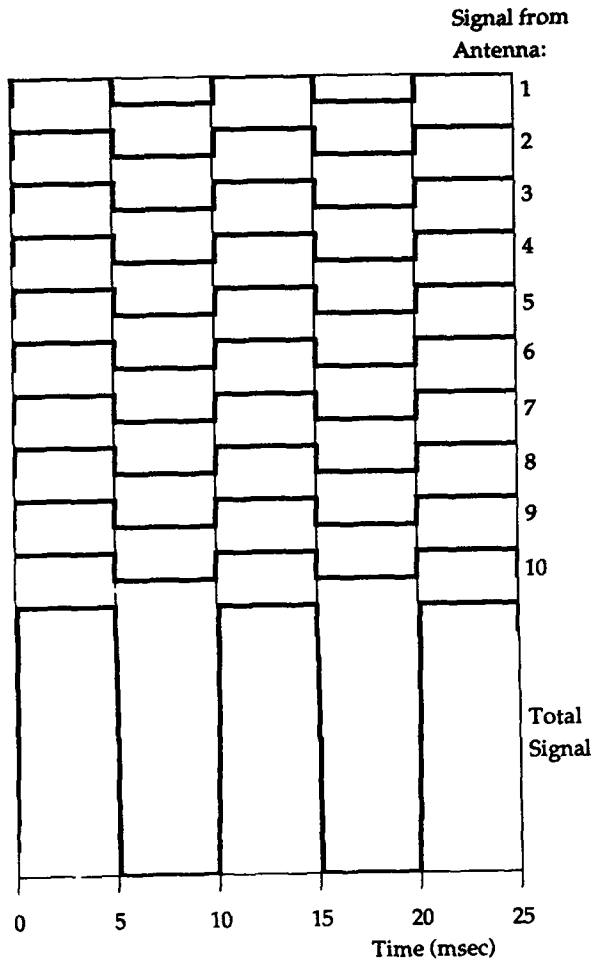

FIGURE 9: Individual and Total Signals (Bits) at Location D (Antenna Delays Optimised for Message Reception at Location Y)

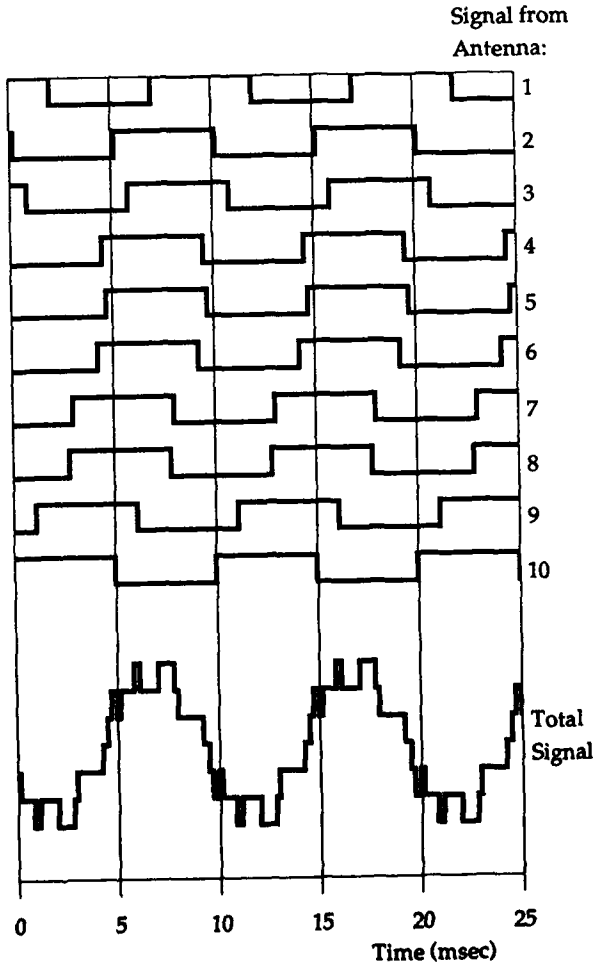

FIGURE 10: Individual and Total Signals (Bits) at Location Z (Antenna Delays Optimised for Message Reception at Location Y)

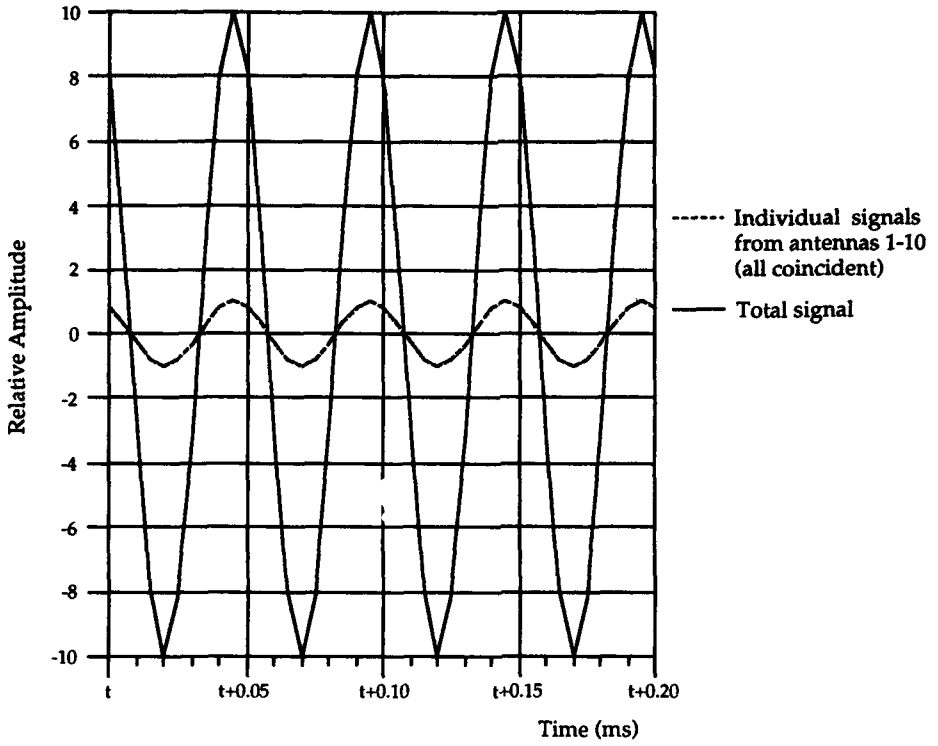

FIGURE 11: Relative Amplitudes of Individual and Total Signals (FSK) Received at Location Y (Antenna Delays Optimised for Message Reception at this Location)

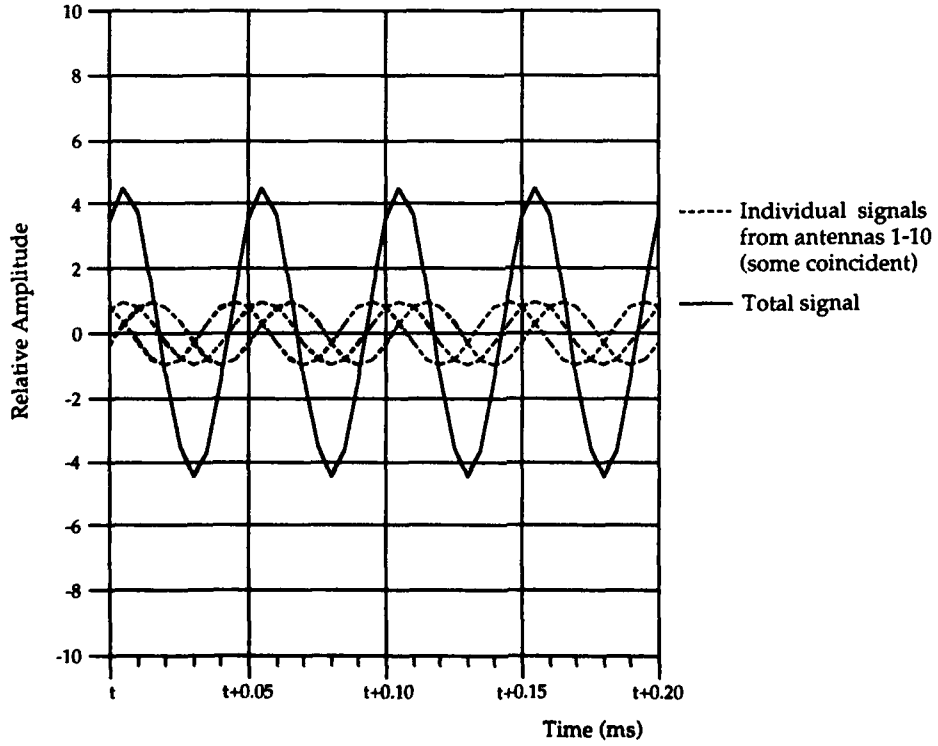

FIGURE 12: Relative Amplitudes of Individual and Total Signals (FSK) Received at Location D (Antenna Delays Optimised for Message Reception at Location Y)

Discussion

INAN

COMMENT. 1) I am surprised about the 1 ms phase error that you mentioned. I would think you can have quite better synchronization between sites, for example with GPS systems. 2) I wonder why you have not considered a linear array, for example with 1/2 spacing, which would have a clear main lobe which was to be steered using phase/beam diversity to transmit to multiple platforms.

AUTHOR'S REPLY

1) With GPS you can get inter-site sync h > 1 in 10^{-8}. But, you need to take into account the time delay involved in passing intersite control information over land lines, for example, Cornwall to Scotland time delay can be 200 msecs (= 40 bits for MSK). Also using GPS leads to system vulnerability-what do you do if the GPS satellites fail or are destroyed, or satcom links are broken? You also need to take into account the fact that a VLF transmitter cannot be adjusted instantly (because of the size of the tuning components, etc).

2) This study was initiated from a suggestion that an array of widely distributed antennas would be less vulnerable to destruction (either sabotage or aerial attack) because the antennas are so far apart. Half wavelength spacing would not satisfy this criteria. Having distributed the array antennas as widely as possible over the UK, the study then compared the array coverage to that of the optimun case - an omnidirectional transmitter. Having a distinct, steered main lobe is not optimal for the reasons given in the paper.

HILDEBRAND

COMMENT. Have you considered beam broadening methods? If you hide the main beam and use strong side lobes it should be easy to mask the bearing(s) for the communication path.

AUTHOR'S REPLY

No.

APPLICATION OF THE FOURIER TRANSFORM TO SHORT ANTENNAS

Prof. Francisco C.V. Grilo
Prof. António Manuel E.S. Casimiro
Faculdade de Engenharia da Universidade do Porto
Departamento de Engenharia Electrotécnica e de Computadores
Rua dos Bragas
4099 PORTO CODEX
PORTUGAL

Summary

As it is well known the far field pattern of an aperture is related to a distribution of radiating sources by the Fourier Transform [1].

In this paper we show that it is possible to use the Fourier Transform to make the analysis and synthesis of short antennas, too.

In this way we can easily have both the analytical and graphical representation of the antenna pattern and the errors that we make with the usual approximating models. It is also possible the use of the know how on the signal processing field to make the analysis and synthesis of the radiation pattern

All the theory is based on the Theorem of the Small Complex Translation [2] meaning that we can represent all the current distribution on the antenna by complex translations of an infinitesimal element of current.

The correspondent pattern can be found using an adequate spatial variable representation.

1.The small complex translation

In all this paper, both the sources an the produced fields are represented in the domain of the temporal Fourier Transform.

Let us suppose a source $I_1(x_o,y_o,z_o)$ that produces a field $E_1(x,y,z)$ that is linearly related with the source: $a\,e^{j\varphi}$ $I_1(x_o,y_o,z_o)$ produces the field $ae^{j\varphi}E_1(x,y,z)$.

We call a small complex translation of the source $I_1(x_o,y_o,z_o)$ made by the vector $d(x_d,y_d,z_d)$ the translation that creates the source $I_2(x,y,z)= a\,e^{j\varphi} I_1(x+x_d,y+y_d,z+z_d)$ (fig) where the produced far field E_2 that can be approximate in module and direction by

$$E_2 = a\,E_1 \qquad (1)$$

and the phase is given by

$$\text{phase } E_2 \equiv \text{phase } E_1\, e^{j\varphi} e^{j\,\vec{\beta}_o \mid \vec{d}} \qquad (2)$$

where

$\mid$ means inner product of vectors

$$\beta_o = \frac{2\pi}{\lambda}$$

λ is the wave length

Supposing that the sources are infinitesimal elements of current (fig 1):

Using the Maxwell equations the electric fields are (fig.2):

$$d\vec{E}_1 = j\beta_o z_o \frac{I_1\, dl}{4\pi r_1} \operatorname{sen}(\theta_1)\, e^{-j\beta_o r_1}\, \hat{\theta}_1 \qquad (3)$$

$$d\vec{E}_2 = j\beta_o z_o \frac{I_2\, dl}{4\pi r_2} \operatorname{sen}(\theta_2)\, e^{-j\beta_o r_2}\, \hat{\theta}_2 \qquad (4)$$

where $z_o = 120\pi$

Usually when we are dealing with arrays and antennas we are only interested in the far field pattern (fig.4)

In that case, the field E_2 can be approximate by field E_1 as shown in fig.4.

So

$$d\vec{E_2} \simeq d\,\vec{E_1} a e^{j\varphi} e^{j\,\vec{\beta}_o \mid \vec{d}} \qquad (5)$$

$$= d\,\vec{E}_{1\varepsilon}\, e^{j\,\vec{\beta}_o \mid \vec{d}} \qquad (6)$$

If all the sources can be obtained by small complex translations of one unitary source in the origin, the far field is related with the source distribution by the Fourier Transform [2] as resumed in next topic.

2.The use of the Fourier Relation

When the sources are distributed in one direction, the zz axis for instance,(1D) the far field can be represented with the variable θ_z (fig.3) because it is symmetrical around the zz axis

So if we have one linear and thin antenna with length "L" in the zz axis as shown in the fig.3 the infinitesimal electrical field $d\vec{E}(z)$ created by the infinitesimal element of current $I(z)$ is related with the infinitesimal electrical field $d\vec{E}(0)$ created by the infinitesimal element of current $I(0)$ by the small complex translation theorem:

$$d\vec{E}[I(z)] \simeq d\vec{E}_o(\theta_z)\frac{I(z)}{I(0)}e^{j\vec{\beta}_o\vec{z}}$$

$$= d\vec{E}_o(\beta)\frac{I(z)}{I(0)}e^{j\beta z} \qquad (7)$$

where $\beta=\beta_o\cos\theta_z$

The total field is obtained by integration of all the infinitesimal fields over the length "L"

$$\vec{E}_T(\beta) \simeq \frac{\vec{E}_o(\beta)}{I(0)}\int_{-\frac{L}{2}}^{\frac{L}{2}} I(z)e^{j\beta z}\,dz$$

$$= K\vec{E}_o(\beta)\ F^{-1}[I(z)] \qquad (8)$$

Where $K=\frac{2\pi}{I(0)}$

So, unless one constant, if the far field pattern is expressed in the variable β, it is related with the field produced by the unitary source placed in the origin, by one window $(-\beta_o,\beta_o)$ in the Inverse Fourier Transform of the current distribution.

Using a similar procedure we can see that for two dimensional (2D) or three dimensional (3D) distributions of sources the Fourier relation appears if we use the variables β_x,β_y and β_z as follows:

The far field produced by an infinitesimal element of current $I_o(x_o,y_o,z_o)$ in the space (fig.5) is

$$dE_o = j\beta_o Z_o\frac{\text{sen}(\theta)}{4\pi r}e^{j\vec{\beta}_o\vec{r}}I_o dl$$

$$= j\beta_o Z_o\frac{\text{sen}(\theta)}{4\pi r}e^{j\vec{\beta}_o\vec{r}}I_o d\tau \qquad (9)$$

where

$$d\tau = dx\,dy\,dz$$

I_o is the superficial density of current in the origin (0,0,0)

So, the electrical field produced by the infinitesimal element of current $I(x,y,z)$ is:

$$dE \simeq \frac{dE_o}{d\tau}\frac{I(x,y,z)}{I(0,0,0)}dxdydz\,e^{j\vec{\beta}_o\vec{d}}$$

$$= \frac{dE_o}{d\tau}f(x,y,z)\,dxdydz\,e^{j\vec{\beta}_o\vec{d}} \qquad (10)$$

The total electrical field, produced by the current distribution inside the small volume where we can use the small complex translations, is

$$E = \frac{dE_o}{d\tau}\int_V f(x,y,z)e^{j(\beta_x x+\beta_y y+\beta_z z)}dxdydz$$

with

$$\beta_x = \beta\cos(\hat{r}\hat{x})$$

$$\beta_y = \beta\cos(\hat{r}\hat{y})$$

$$\beta_z = \beta\cos(\hat{r}\hat{z})$$

So

$$E = \frac{dE_o}{d\tau}\int_x dx\,e^{j\beta_x x}\int_y dy\,e^{j\beta_y y}\int_z f(x,y,z)dz\,e^{j\beta_z z}$$

$$= \frac{dE_o}{d\tau}F_x^{-1}\left(F_y^{-1}\left(F_z^{-1}(f(x,y,z))\right)\right) \qquad (11)$$

Again the total field field is given by the product of the field produced by reference source and the three dimensional inverse Fourier Transform on the variable β, unless one constant.

3.The application to an small antenna with uniform distribution

Let's apply the developed theory to an antenna with an distribution of currents that can be considered uniform, supposing that has an length equal to "2a" and it is oriented on the zz direction (fig.8).

Let us consider as the reference source the infinitesimal dipole in the origin that has the well known field pattern $\text{sen}\theta$ (fig.6)

The factor that multiplies the field produced by the infinitesimal is easily found by the inverse Fourier transform (fig.7)

This factor depends on the length "2a" and the error that is made when it is assumed that the factor is constant can be seen in a graphical way.

So, when the antenna length is small compared with the wave length the factor is almost constant, but increasing if the factor is assumed to be constant the error increases, too.

4.Conclusions

The Fourier Transform can be used to make the analysis and synthesis of the radiation pattern in antennas with uniform distribution of current and which length is much small that the wave length, making possible the graphical visualisation of the error committed when it is assumed a constant array factor.

This procedure can be applied whenever we are dealing with a source distribution that can be obtained by small complex translations of a reference source in the origin.

In more complicated cases it is possible the use of Fourier Transform and Fast Fourier Transform procedures to make the analysis and synthesis in a computational way in, to simplify the calculus and to have a graphical idea about the errors involved in the model.

5.References

1 Silver, Samuel, James, Hubert M.,
Microwave Antenna Theory and Design,
McGraw-Hill Book Company, Inc.
1949

2 Grilo, Francisco. C.V., Casimiro, António. M. E. S.,
"The Basic Relation Between Point Sources and the Produced Fields",
PIERS (Progress In Electromagnetics Research Symposium),
MIT, Cambridge
USA, Julho 1991

3 Grilo, Francisco. C.V., Casimiro, António. M. E. S.,
"The Spatial Distribution of Sources and the Symmetry of the Far Field Pattern",
PIERS (Progress In Electromagnetics Research Symposium),
MIT, Cambridge
USA, Julho 1991

4 Schelkunoff S.A., Friis, H. T.,
Antennas Theory and Pratice,
John Wiley and Sons Inc.,
1966

5 Collin, R.E., Zucker, F.J.,
Antenna Theory, Mc Graw-Hill,
1969

6 Krauss,
J.D., Antennas,
McGraw-Hill,
1950

7 Jasic, H.
Antenna Engineering Handbook,
McGraw-Hill,
1961

8 Elliott, Robert S.,
Antenna Theory and Design, Prentice-Hall,
1981

9 Rusch, W.V.T., Potter, P.D.,
Analysis of Reflector Antennas,
Academic Press, New York,
1970

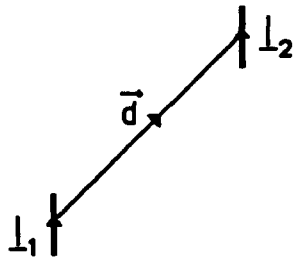

Fig. 1 The Complex Translation

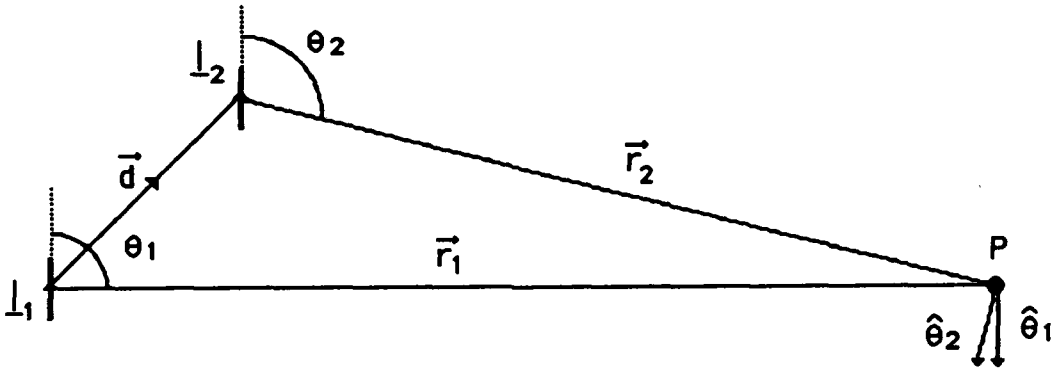

Fig. 2 The Parameters in the Translation

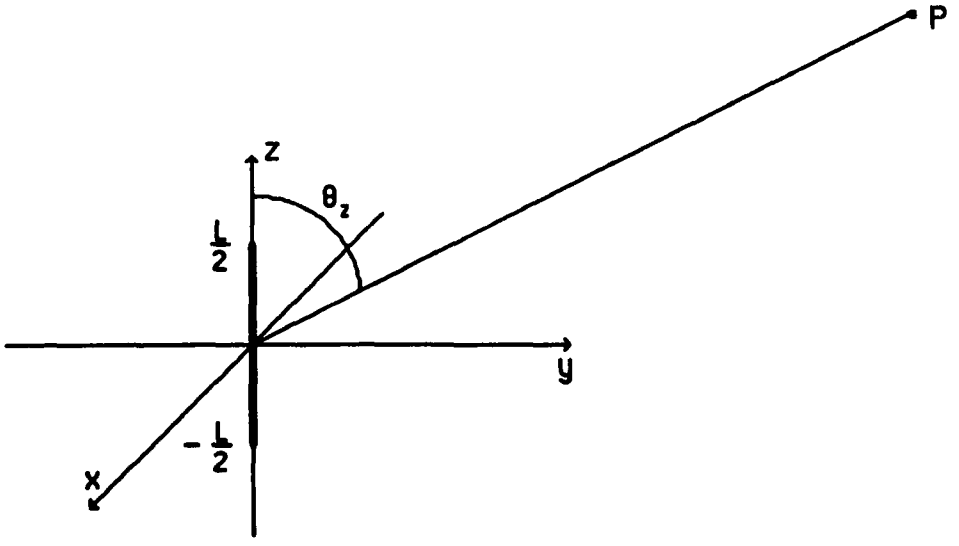

Fig. 3 The Linear Distribution of Sources

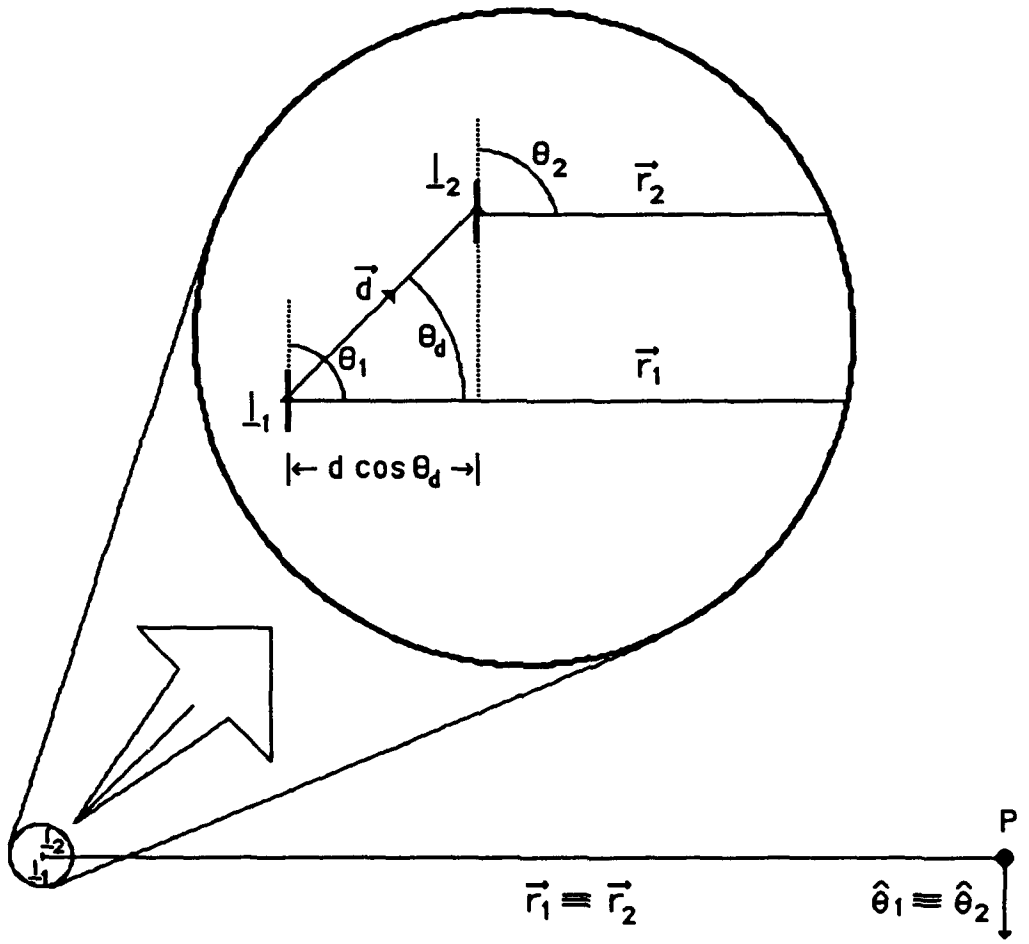

$$d\vec{E}_2 = j\beta_0 z_0 \frac{I_2\, dl}{4\pi(r_1 - d\cos\theta_d)} \operatorname{sen}(\theta_2)\, e^{-j\beta_0(r_1 - d\cos\theta_d)}\, \hat{\theta}_2$$

$$\simeq j\beta_0 z_0 \frac{I_1\, dl}{4\pi r_1} \operatorname{sen}(\theta)\, e^{-j\beta_0 r_1}\, \frac{I_2}{I_1}\, e^{j\beta_0 d\cos\theta_d}\, \hat{\theta}$$

$$= d\vec{E}_1\, \frac{I2}{I_1}\, e^{j\vec{\beta}_0 \vec{d}}$$

Fig. 4 The Far Field and the Small Complex Translation

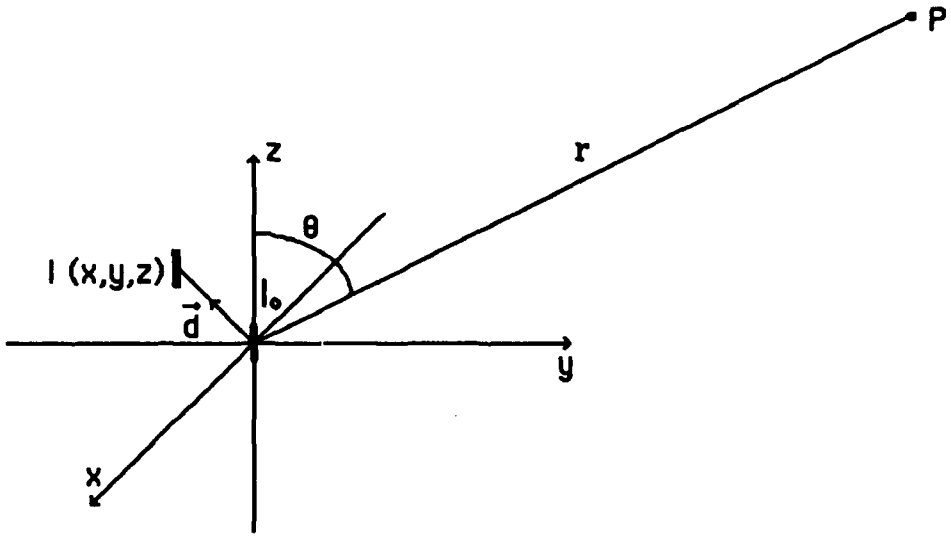

Fig. 5 The Three Dimensional Translation

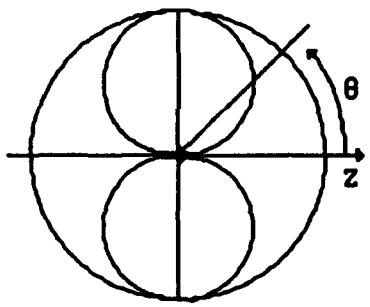

Fig. 6 The Field Pattern sen θ

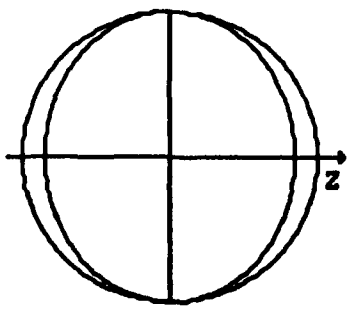

Fig. 7 The Factor of the Current Distribution

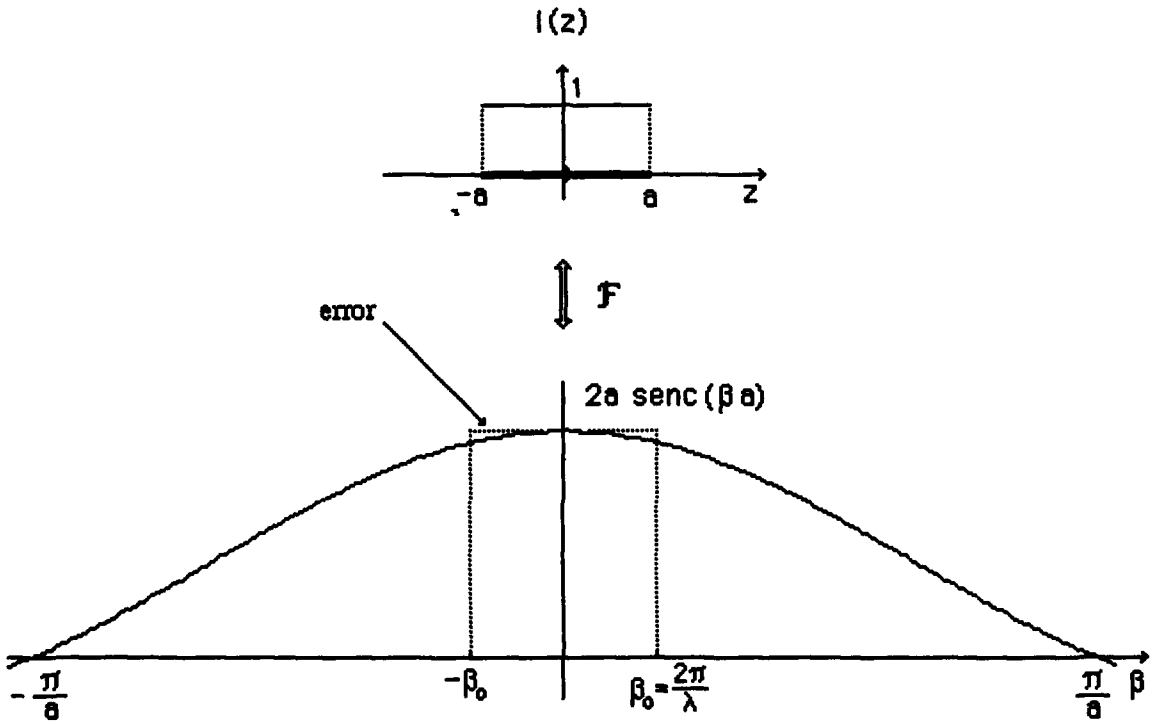

Fig.8 The small antenna with uniform distribution of current

ANTENNA MODELING AND ANALYSIS FOR ELF/VLF/LF APPLICATIONS

M. Bandinelli, S. Chiti, R. Cioni

IDS - Ingegneria Dei Sistemi, Pisa Via Roma 50, Italy

SUMMARY

This paper presents a numerical procedure which can be effectively used for the analysis/design of very-low frequency capacitive antenna system on complex platforms and for charge distribution computation. The "quasi-static" radiation problem has been solved by means of the corresponding electrostatic solution, by using a Method Of Moment (MOM) procedure. Pulse basis functions defined on surface-patch domains and point-matching test procedure are used, in conjunction with a powerful postprocessing numerical tool. Given the platform model, the postprocessing tool allows us to analyze all possible antenna configurations by running the Method of Moment computer code only once. The following parameters can be evaluated : i) Antenna Radiation Pattern, ii) Antenna Norton equivalent circuit (from which the effective voltage at the input of the receiver can be evaluated), iii) Induced charge distribution, iv) Scattered electric field distribution near the platform. The proposed solution is particularly useful for applications where the criticity of the structure requires a peculiar attention in defining structural elements that constitute the "electrical doublet" (conformal antenna).

INTRODUCTION

Based upon integral equations, a number of numerical techniques have been developed and investigated during last two decades, showing very interesting capabilities in many applications to real electromagnetic (e.m.) problems [12,14,15,17,18]. Their effectiveness in many engineering problems have also stated new guidelines for electromagnetic approach, both in the field of analysis and design.

Typical applications of numerical techniques are concerned with antenna siting problems and with the evaluation of current/charge distribution over complex objects; different numerical codes developed in the past are currently used and have been widely applied for the study of such problems and particularly in the field of antenna system performance, in real platform environments, over a wide frequency range frequently around resonant region of the platform/antenna system.

The present paper deals with the development of a numerical technique too, which can be applied both to antenna siting problem analysis and design and with charge distribution computation on complex objects; the numerical technique is based on a Method of Moment solution of the corresponding electrostatic problem, suitable for application in the quasi-static case. The procedure is based on a triangular surface patch representation of the body, in conjunction with pulse basis functions and point matching testing.

Regarding the case of charge distribution computation, the proposed technique can efficiently serve as a method of investigation about electrostatic charging of conductive bodies, which is a serious problem for many flying objects.

For antenna siting problems it can be pointed out that different antenna systems mounted on platform of limited size, such as flying object (aircraft, RPV), belongs to the category of capacitive quasi-static (due to the very small dimensions of the object with respect to the system operating wavelength) antennas as, for example, in the case of long range navigation aids (OMEGA, LORAN C and so on) sensors.

Antennas used for the mentioned applications have tipically very small size also with respect to platform ones, and their electromagnetic properties depends strongly both on the shape and dimensions of supporting platform; being essentially a kind of charge pick-up on the object, the antenna has to be well positioned in order to collect maximum charge quantity from the platform and maximize its efficiency.

These kind of antennas works in major cases on receiving operation, for which both antenna capacitance and collected charge from supporting structure can be determined by means of the proposed method, taking into account for interactions between conductive elements, antenna and structures, in their real geometrical configuration.

As discussed with better detail in the following, the method represent a very efficient and low cost analysis tool because, once fixed the geometry of the model and a canonical base of incident electric field, we need only one MOM evaluation in order to obtain the characteristic parameters of any sensor-platform configuration, for any excitation field source.

The paper is particularly devoted to the use of the procedure to the design problem of a receiving VLF antenna system. It contains a general description of the method, its theoretical development, the peculiarities of MOM formulation chosen, in terms of geometrical subdomain sections, basis and test functions, and the definition of parameters which can be evaluated by means of the method, such as radiation pattern, antenna equivalent circuit, charge distribution on the object, field distribution near scattering object.

LOW FREQUENCY E.M FIELDS

When the wavelength of an incident field is considerably greater than the typical dimensions of the scatterer, a "quasi-static" situation occurs. Such a situation is usually analyzed by means of the so-called Rayleigh series [1] of the e.m parameters such as "electric and magnetic fields", "induced current" and "induced charge". The Raylegh series is a power series in the frequency domain. The existence of this series has been proved and its radius of convergence has been found for smooth perfectly conducting objects [1]. The radius of convergence is equal to the absolute value of the lowest natural frequency of the object and hence under this value the Rayleigh series should converge to the exact solution. However the first few terms usually suffice for most of practical purposes.

Let $\vec{J}$ and ρ the current and charge densities induced on a conducting platform by an incident time-armonic e.m field $\vec{E}_i$, $\vec{H}_i$; they can be expressed in the following low-frequency (Rayleigh) expansion :

$$\vec{J} = \sum_{n=0}^{\infty} jk^n \vec{J}_n$$

$$\rho = \sum_{n=0}^{\infty} jk^n \rho_n$$

As it can be seen, the ratio of two consecutive terms is proportional to j ω (ω=angular frequency), so that only the first terms are important as the frequency approaches zero.

To find the Rayleigh series terms different procedures can be considered:

- following the approach of Stevenson [2,3], which expands the Maxwell equation in a low frequency series,and then solves for each term of it;
- by means of a procedure that uses a low frequency expansion of the Electric or Magnetic Field Integral Equation, (EFIE, MFIE) then solving a set of equations for the determination of $\vec{J}_0$, $\vec{J}_1$, ρ_0 and so on [4,5,6,7].

For the purpose of this paper, it is not of interest to examine the details of such procedures, but to analyze the properties of the first terms $\vec{J}_0$, $\vec{J}_1$ and ρ_0, that, as we will see, are related to the characteristic parameters of electrically short antennas. To this extent, it can be shown that:

$$\nabla_s \bullet \vec{J}_0 = 0$$

$$\nabla_s \bullet \vec{J}_1 = -j\omega\rho_0$$

These equations imply that the lines of $\vec{J}_0$ form closed loops on the surface S of the scatterer, whereas the lines of $\vec{J}_1$ terminate at charges ρ_0. $\vec{J}_0$ can be identified with the magnetostatic currents, and ρ_0 with the electrostatic charge induced on the body. It is worth noting that $\vec{J}_0$ has no relation with the total induced current flowing across any cross-section of the platform.

From the point of view of the e.m field radiated by these "low frequency" current distributions, it is however expected that $\vec{J}_0$ and $\vec{J}_1$ give rise to a magnetic and an electric dipole respectively.

CAPACITIVE ANTENNAS

Quasi-statically antennas correspond to very large wavelengths where it becomes difficult and costly (or sometimes impossible, especially when antennas have to be installed on moving platforms) to produce resonant aerials. On reception it is the signal-to-noise ratio that is of prime concern, rather than the absolute value of the received signal. We must therefore consider the dominant source of noise, and at these frequencies external noise is much more significant than internal noise.
Beyond the threshold where external noise starts to become dominant it proves therefore useless to improve the efficiency of the receiving aerial, since this will increase the noise in the same ratio as the effective signal. This means that the dimensions of receiving antennas operating at very low frequencies can be small comparing to wavelenght while giving satisfactory performances.

In this chapter a sintetic representation of a receiving capacitive antenna (or electric doublet) will be given, in order to introduce the implementation of the design procedure that will be described in the next chapter.

Although perhaps not pratically so important as in the "receiving case", also the transmitting capacitive antennas in the low frequency range will be analyzed, in order to identify the parameters by means of which it is possible to define an antenna siting procedure on a given platform.
Both problems can be analyzed referring to the Rayleigh series recalled in the previous chapter.

Synthetic Representation Of Receiving Capacitive Antenna

A capacitive antenna is schematically composed by a conducting object (with dimensions small compared to wavelenght) with one section insulated from the remaining part of the conductor. When excited by an incident e.m field, the two parts of the dipole (not necessarily geometrically symmetrical) present a potential difference that can be used as an input signal to a receiver. In the following we shall make reference to the smallest and the greatest of the two parts respectively as "sensor" and "platform". Intuitively, the sensor constitute the "hot pole", while the platform constitutes the 'ground reference'.

While the platform can be generally identified with the metallic structure on which the antenna is installed (as an example an aircraft or a ship), not necessarily the sensor must be a classical antenna structure as a monopole. Design considerations can suggest original solutions, obtained sectioning a part of the structure and using it as sensor.

We will represent the antenna, viewed from the feed terminals, by means of Norton Equivalent Circuit parameters I_{sc} (short-circuit current) and $\mathcal{Y}_{in}$ (input admittance) as shown in fig. 1 [8,9]. By means of such equivalent representation, it is immediate to obtain the voltage on the load Z_1 ($\mathcal{Y}_1$) connected to the antenna terminals.

Remembering the quasi-static nature of the problem under test we will refer to the Rayleigh series [1, 2] to evaluate these parameters. In particular we will solve for the electrostatic problem associated to the dinamic one (it means that the e.m incident field will be replaced by an equally polarized electrostatic field), by evaluating the charge distribution ρ_0 induced on the structure and the capacity C of the "sensor-platform" system. Through these parameters we can then entirely define the Norton equivalent circuit of the capacitive antenna. A detailed numerical analysis of the good performances obtainable in the low frequency range by means of this approach, in comparison with NEC [10] full-wave results, is also stated in [11] for a classical short dipole wire antenna.

short circuit current

Placing the antenna in an uniform electrostatic field would result in a redistribution of the charge density ρ_0 on the system so that charges +Q and -Q would appear on the two antenna elements. For the low-frequency dinamic problem, it follows that the current flowing through the short-circuited terminals of the antenna is well approximated as:

$$I_{sc} = j\omega Q \qquad (3)$$

It is obvious that the induced charge Q in the static problem depends upon the orientation of the antenna in the impressed field just as the short circuit terminal current in the dynamic problem depends upon the orientation of the antenna in accordance with its radiation pattern (it has to be noted that as a consequence of the quasi-static nature of the electrically small antenna problem, the radiation pattern will be that of an elementary dipole).

While dealing with capacitive antennas, the magnetic field solution ($\vec{J}_0$ in the induced current Rayleigh serie) need not be considered in evaluating the short circuit terminal current value, since all currents on the conducting surface which are accounted for in the magnetic field solution are solenoidal and contribute nothing to the net terminal current.
To deal with parameters which are independent from the incident field $\vec{E}_i$, it is convenient to define the "Equivalent Area" of the antenna :

$$\mathcal{A}_{eq} = Q/(\varepsilon_0 \, |\vec{E}_i|) \qquad (4)$$

where ε_0 is the permittivity of the homogeneous space surrounding the antenna. Using such a definition, it is possible to express the antenna short circuit current as:

$$I_{sc} = j\omega Q \; \varepsilon_0 \; \mathcal{A}_{eq} \; |\vec{E}_i| \qquad (5)$$

Recalling the well known "Effective lenght" $\mathcal{L}_e$, usually considered to define the receiving properties of wire antennas, it is seen that the equivalent area $\mathcal{A}_{eq}$ serves an analogue function in the Norton equivalent circuit : both are constants of the antenna and represent proportionality factors between the incident field amplitude and the level of excitation of a circuit connected to antenna terminals. While the "effective lenght" $\mathcal{L}_e$ is particularly convenient to use for thin wire antennas because of the simple relationship between $\mathcal{L}_e$ and the physical dimensions of such antennas, the Equivalent Area $\mathcal{A}_{eq}$ is well suited for the evaluation of many other forms of antenna elements.

Input impedance

Given the input impedance Z_{in} (or admittance $\mathcal{Y}_{in}$), in the frequency domain:

$$Z_{in} = 1/\mathcal{Y}_{in} = \mathcal{R}_{in} + j\,\mathcal{X}_{in} \qquad (6)$$

the resistive part $\mathcal{R}_{in}$ is in general subdivided into the sum :

$$\mathcal{R}_{in} = \mathcal{R}_{\mathcal{R}} + \mathcal{R}_{\varphi} \qquad (7)$$

($\mathcal{R}_{\mathcal{R}}$ = radiation resistance and $\mathcal{R}_{\varphi}$ = ohmic resistance, taking into account for the energy dissipation on the antenna, due to the material conductivity). The second term can normally be neglected with respect to other Z_{in} terms.
In the very low frequency problems it is customary to take Z_{in} as a pure capacitive reactance :

$$Z_{in} \sim 1/j\omega C \qquad (8)$$

where C is the "sensor-platform" capacity.

Once known the parameters $\mathcal{A}_{eq}$ and C, the equivalent circuit of fig. 1 characterizes suitably, from the point of view of the reception properties, the antenna configuration under test, allowing effective parametric evaluation varying the load impedance of the receiver.

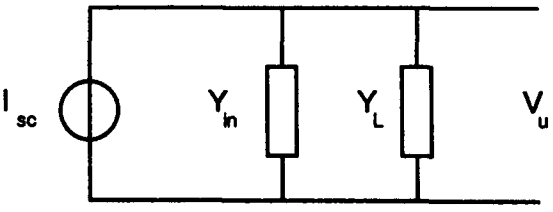

Fig. 1

TRANSMITTING CAPACITIVE ANTENNAS

Although most practical antennas installed on moving platforms, operating in the quasi-static domain are receiving antennas, it is worth noting that the same quantities used to

define the equivalent circuit of fig. 1 serve to evaluate the radiation characteristic of a capacitive antenna, such as the radiation pattern. The procedure to obtain this makes use of the reciprocity theorem.
The "sensor-platform" antenna is excited by means of an incident

electric field $\vec{E}_i$ as in the receiving problem, then the induced charge Q on the two parts of the antenna can be computed and presented in a polar diagram in corrispondence with the

incidence angles of the field $\vec{E}_i$.
Repeating this procedure for a number of incidence angles, for a fixed polarization, it is possible to obtain the directive gain pattern (supposing the ohmic losses on the structure be negligible) of the antenna for that polarization [8].

We should note that for this type of aerial the radiation pattern is always that of a simple dipole, however varying its orientation relative to the overall structure and the actual quantity of induced charge (e.g the gain G) [16].

DESCRIPTION OF THE DESIGN PROCEDURE

As described in the previous chapter, the design of an antenna configuration mainly requires the determination of the equivalent capacitance and the short circuit current.

The present analysis and design procedure is based on a MOM simulation code, followed by a suited data processing tool [19]. So, the whole procedure is mainly composed by the following steps:

♦ Definition of the e.m. model by a CAD tool;

♦ Run of the electrostatic method of moments computer code;

♦ Run of the postprocessor code by which the final results such as:

- Antenna equivalent area;
- Antenna equivalent capacitance;
- Antenna short circuit current;
- Charge distribution over the antenna and body structures;
- Field distribution around the structures and radiation patterns;

may be computed, displayed and stored on a memory mass device.

It is worth noting that:

♦ The determination of the equivalent capacitance requires the knowledge of the difference of potential between the sensor and the platform when:

- a charge (e.g. positive) is applied to the sensor;
- the same charge quantity, with opposite sign is applied to the platform;
- the sensor is open circuited, i.e. electrically separated from the platform.

♦ The determination of the short circuit current requires the knowledge of the total charge on the sensor when:

- an electric field vector, which has the same polarization of the field to be received, causes a charge redistribution on the e.m. model (platform+sensor);
- the sensor is short circuited, i.e. electrically connected to the platform.

So, in principle, two different models should be used and a lot of Method of Moment runs (one for every field polarization vector plus one for the equivalent capacitance determination) should be performed. Such a procedure should lead to a very time expensive and tedious activity. By modifying the procedure, only one e.m. model must be defined and the method of moment must be run only once, thus greatly increasing efficiency.

In order to have better understanding of the procedure, it is worth noting that our MOM computer code will output only an intermediate set of results, arising from a set of canonical eccitation sources linearly independent from each other (such sources may be charges or field vectors, along independent directions). The final solution will be computed by the postprocessor code, once the actual excitation has been stated.

Such a procedure is possible owing to the (quasi) static nature of the problem and cannot be applied when field propagation exists.

By running the method of moment computer code only once, the procedure is particularly optimized with respect to computer time, so a lot of situations may be efficiently taken into account. In the following sections each step of the procedure will be described.

The e.m model

The e.m. model is formed by triangular flat plates which allow the modeler to correctly simulate as well as single bended and double bended surfaces. A different attribute (group number) may be assigned to different blocks of the model, and is inherited by all the plates forming the block itself. We assume that blocks having different group number are electrically insulated each other; this is the case betwen a sensor and the remaining e.m. model (platform). The method of moment will consider the blocks electrically insulated and the connection may be forced at the post processing phase, in order to compute the short circuit current [19].

Method Of Moments Formulation For Electrostatics

The problem to be solved by method of moments is the determination of the charge density once fixed the eccitation source (the field vector or a net charge on the e.m. model or part of it) that is the solution of the Poisson equation [12]:

$$\nabla^2(\phi_{inc} + \phi_{scatt}) = -\frac{\rho}{\varepsilon} \qquad (9)$$

whose integral form is:

$$\phi_{tot}(\vec{r}) = \phi_{inc}(\vec{r}) + \phi_{scat}(\vec{r}) = \phi_{inc}(\vec{r}) + \iint_S \frac{\rho(\vec{r}_j)}{4\pi\varepsilon_0|\vec{r} - \vec{r}_j|} d\vec{r}_j \qquad (10)$$

Only ϕ_{inc} is known, while ϕ_{scatt} and ρ must be determined.
As known, the use of a Method of Moment formulation requires the solution of the above described integro/differential equation by a matrix formulation.

The expansion functions used in our procedure are step functions, each one different from zero only over a triangular element and zero otherwise: of course, each function has a domain different from all other functions. The weighting functions are dirac delta functions, centered on the centroid of each triangular element [13,14,15]. An additional equation needed in order to solve the problem is found by imposing the total charge value on each block of the e.m. model.

As a result, the number of equations is given by the number of plates plus the number of blocks electrically insulated each other.

The solutions are the induced charge density on each triangular element of the model and electrostatic potential of each block. Particular care has been devoted to the implementation of a well conditioned matrix in order to use a single precision arithmetics (32 bit).

The Canonical Set Of Excitations

The set of excitations is such that any other excitation, may be any field vector and/or any charge on the platform, may be described by a linear combination of the canonical excitations.

If the charge density is separately stored for each canonical eccitation, by applying the superposition theorem the charge density for any type of excitation may be computed.
Once fixed a cartesian reference system (0,X,Y,Z) the canonical set of excitation has been identified as:

- E field vector parallel to the X axis;
- E field vector parallel to the Y axis;
- E field vector parallel to the Z axis;
- A unit charge on each block of the e.m. model.

with a grandtotal of (3+number of blocks) excitations.
Note that most of CPU time is required to create and invert the matrix, while the number of solutions to be computed have a little impact on the total CPU time.

The Postprocessing Procedure

The postprocessing procedure mainly consists of the following steps:

- Computation of the antenna equivalent capacitance C by:
  - Forcing a unit positive charge Q on the sensor block;
  - Forcing a unit negative charge Q on the platform block;
  - Determining the difference of potential V between the two blocks;
  - Applying the formula C = Q/V.
- Computation of the short circuit current I_{sc} by:
  - Forcing the electrical connection

between the platform and the sensor blocks;
- Defining the E field vector of the e.s. field to be received;
- Computing the charge density over the whole e.s. model;
- Computing the total charge Q on the sensor block;
- Computing the short circuit current by the formula: $I_{sc} = j\omega Q$.

It must be stressed that the set of results computed by means of Method of Moments is given for the sensor electrically insulated from the platform, while the computation of the short circuit current I_{sc} needs the solution computed for an e.s. model with no electrical disconnections. The electrical connection required in the evaluation of I_{sc} is performed by the postprocessor and the resulting charge density distribution is computed in real time, starting from the canonical set of solutions. The whole procedure is therefore very efficient, thus allowing for the analysis of a large number of conformal antennas by creating a single e.m. model with a number of blocks equal to the number of antennas to be analyzed.

Use Of The Antenna Parameters In Real Applications

As reported in a previous chapter, antenna parameters above described may be used in order to analyze the receiver performances or to design the input amplifier, by means of the equivalent electrical circuit reported in fig. 1.
Given the input admittance of the receiver $\mathcal{Y}_L$, the load voltage is:

$$\mathcal{Y}_{in} = j\,\omega\,C$$

$$\mathcal{V}u = \frac{I_{sc}}{\mathcal{Y}_{in} + \mathcal{Y}_L} = \frac{j\,\omega\,\mathcal{A}eq\;\varepsilon_0\,\mathcal{E}_{inc}}{\mathcal{Y}_{in} + \mathcal{Y}_L} \qquad (11)$$

The transfer function has a zero at f=0 and, if $\mathcal{Y}_L$ is real, a pole at f = $\mathcal{Y}_L/(2\pi C)$, so it stems out that the input admittance of the receiver plays a very important role in terms of:

- The sensitivity of the whole system;
- A first rejection of low frequency man induced noise components.

DESIGN EXAMPLE

In order to show the characteristic and the performance of the capacitive antenna analysis and design procedure discussed in the previous chapters, it will be reported an example concerning the installation of an OMEGA receiver on a Remote-Piloting-Vehicle (RPV) METEOR MIRACH 100 aircraft.

In particular the problem can be stated as :
- e.m characterization of the OMEGA signal (10.2-13.6 kHz) exciting the receiving system;
- design of the optimum capacitive antenna, satysfing the mechanical and aerodynamic constraints; under this voice are as well as the siting problem of canonical probe (as monopole) and conformal antenna design, by using structural parts of the vehicle;
- analysis of the performance of the receiver supplied by the receiving antenna.

Within this paper the second and third items will be examined, while for simplicity it will be assumed OMEGA signal as a "plane-wave type" incident field. Fixed a cartesian reference system (O,X,Y,Z) with Z axis normal to the earth, we will assume the incident E-field polarized parallel to Z. A better e.m characterization of the OMEGA signal requires an analysis of VLF propagation phenomena in the low-altitude atmosphere that is beyond the scope of this work. It is however obvious that the design procedure can work for every type of field eccitation.

In fig. 2 a sketch of the aircraft and the Method of Moment patch model used in the design procedure are reported. Note that the dielectric part of the structure are not included in the model. This fact is justified since the low-frequency e.m field interact very weakly with non metallic materials.

The aircraft flighting trim has been assumed horizontal (parallel to ground), because this configuration is certainly the most operatively significative from the OMEGA radio-assistance point of view.

In fig. 3 the "antenna hypothesis" under test are specified . In particular, some of these are concerning a classical (monopole or "L-antenna") probe installed on the

aircraft, while other ones are concerning conformal antenna solutions, obtained by insulating a part of the structure (sensor) from the remaining of the platform (parachute box, vertical stabilizers...).
In the first case the problem is essentially an "antenna siting" one. In the second the designer had to choice the structural parts suitable to constitute the conformal antenna.
In the following we will refer to the hypothesis by means of "A%", as reported in the figure.

In fig. 4 the evaluated parameters $\mathcal{A}_{eq}$ (Equivalent Area), C (input capacity of the sensor-platform antenna), I_{sc} and $\mathcal{Y}_{in}$ (Short circuit current and input admittance of the Norton equivalent circuit of fig. 1), are reported. I_{sc} and $\mathcal{Y}_{in}$ are calculated at 10.2 Khz.

The parameters $\mathcal{A}_{eq}$ and I_{sc} give the designer an estimation of the receiving capability of the antenna, while by means of input admittance $\mathcal{Y}_{in}$ it is possible to evaluate the degree of antenna-load mismatching.

When fixed the receiver front-end, it is possible to evaluate the voltage induced on it by the incident field, simply resolving the Norton equivalent circuit of fig. 1.

In fig. 5 the voltage induced on three different receiver front-end impedance is reported, when feeded by each A1-A10 antenna. Once fixed any not-e.m constraints (structural constraints, cost constraints...), this table gives the designer the elements to guide the choice of the optimal capacitive antenna.

CONCLUSIONS

A numerical procedure has been presented which provides a low-cost design of receiving or transmitting capacitive antennas in the very low frequency range (when the typical dimensions of the antenna and the structure on which it is to be installed are very much smaller than the wavelenght).

The procedure, based on a non-usual application of the Method of Moment in the quasi-static approximation, can solve the electrostatic problem for each generic antenna configuration taking into account for the overall interaction between the different part ("sensor" and "platform") in their real geometrical configuration. The parameters of the Norton Equivalent Circuit are obtained for the receiving problem, so to easily calculate the actual voltage on the load representing the receiving equipment. The directive gain radiation pattern and the Equivalent Dipole Moment can be obtained for the transmitting problem.

Due to the quasi-static hypothesis valid for this type of problems, it has been possible to use in an effective way a Method Of Moment code. In fact, once modeled the overall metallic structure and fixed a canonical base of the incident electric field, we need only one MOM evaluation; then the results can easily and low-costly post-processed in order to obtain the characteristic parameters of any "sensor-platform" (antenna) configuration, for any excitation field configuration.
From the previous considerations comes that the proposed procedure can easily provide quantitative comparisons between several design solutions.

An example of design procedure of a capacitive OMEGA antenna to be installed on a small aircraft has been presented and discussed.

Although actually not implemented, a similar procedure can be developed for the analiysis and design of electrically short inductive antennas, such as small loops.

REFERENCES

[1] Ralph E. Kleinman, "The Rayleigh region", Proceedings of the IEEE, August 1965, pp 848-856
[2] A. F. Stevenson, "Solution of electromagnetic scattering problems as power series in the ratio (dimension of scatterer)/wavelenght", J. Appl. Phys., Vol. 24, Sept. 1953, pp. 1134-1142
[3] J. Van Bladel, "Electromagnetic fields", McGraw-Hill, New York, 1964
[4] B. Noble, "Integral equation perturbation methods in low frequency diffraction", Electromagnetic Waves, R. Langer ed., The University of Wisconsin Press, Madison 1962
[5] R. E. Kleinman, "Far field scattering at low frequencies", Appl. Sci. Res., Vol. 18, August 1967, pp. 1-8

[6] "EMP interaction : principle, techniques and reference data", Ed. by K.S.H. Lee, Hemisphere Publishing Corporation 1986
[7] C.H. Papas, "Theory of Electromagnetic Wave Propagation", McGraw-Hill, New York, 1965
[8] J.T. Bolljahn, R.F. Reese, "Electrically small antennas and the low-frequency aircraft antenna problem", IRE Transaction on Antennas and Propagation, October 1953
[9] S. Drabowitch, C. Ancona, "Antennas: Applications", North Oxford Academic Publisher Ltd, 1988
[10] G. J. Burke, A. J. Poggio, "Numerical Electromagnetic Code (NEC) - Method of Moments", Naval Ocean System Center, San Diego, CA 92152
[11] T.L. Simpson, J.C. Logan, J.W. Rockway, "Equivalent circuits for electrically small antennas using LS-decomposition with the Method of Moments", IEEE Trans. on Antennas and Propagations, Vol. AP-37, n.12, Dec. 1989
[12] R. F. Harrington, "Field computation by Moment Methods", N.Y., Mac Millan, 1968
[13] S.M. Rao, A.W. Glisson, D.R. Wilton, B.S. Vidula, "A simple numerical solution procedure for *static problems involving* arbitrary-shaped surfaces", IEEE Trans. on Antennas and Propagations, Vol. AP-27, n.5, Sept. 1979
[14] E. Arvas, R.F. Harrington, J.R. Mautz, "Radiation and scattering from electrically small conducting bodies of arbitrary shape", IEEE Trans. on Antennas and Propagation, Vol. AP-34, n.1, January 1986
[15] E. Arvas, R.F. Harrington, J.R. Mautz, "Radiation and scattering from electrically small conducting bodies of arbitrary shape above an infinite ground plane", IEEE Trans. on Antennas and Propagation, Vol. AP-34, n.1, January 1986
[16] R. E. Kleinman, "Dipole moments and near field potentials", Appl. Sci. Res., Vol. 27, April 1973, pp. 335-340
[17] J.R. Mautz, R.F. Harrington, "An E-field solution for a conducting surface small or comparable to the wavelenght", IEEE Trans. on Antennas and Propagation, Vol. AP-32, April 1984, pp. 330-339
[18] S.M Rao, D.R. Wilton, A.W. Glisson, "Electromagnetic scattering by surfaces of arbitrary shape", IEEE Trans. on Antennas and Propagation, Vol. AP-30, May 1982, pp 409-418
[19] R. Cioni, "Processing dei dati relativi al caso elettrostatico", IDS Tech. Rep. 89/014

ACNOWLEDGMENTS

Data relevant to the example presented *in this paper have been developed under* contract with Company METEOR CAE S.p.A - Ronchi dei Legionari (ITALY), and is presented here with its permission.

We wish to thank Dr. Eng. A. SBUELZ from METEOR CAE S.p.A for his support during the execution of the previously mentioned activity, and for his useful contributions during the preparation of this paper.

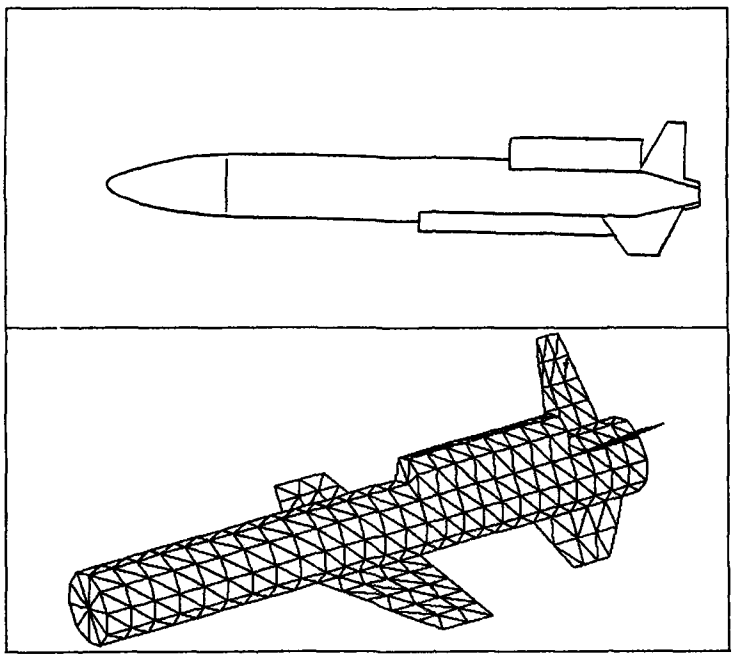

Fig. 2 RPV sketch and numerical model for MOM

DESIGN HYPOTHESES	SENSOR DESCRIPTION
A 1	Monopole on the upper side of the fuselage
A 2	Monopole on the lower side of the fuselage
A 3	Monopole on the parachute box
A 4	"L" probe on the upper side of the fuselage
A 5	"Blade antenna" on the parachute box
A 6	Parachute box
A 7	Vertical stabilizers (4/4)
A 8	Vertical stabilizers (3/4)
A 9	Vertical stabilizers (2/4)
A 10	Vertical stabilizers (1/4)

Fig. 3 Antenna design hypotheses under test

DESIGN HYPOTHESES	ANTENNA PARAMETERS (at 10.2 kHz)			
	Aeq [sm]	C [pF]	Isc [A]	Yin [mho]
A 1	0.051	2.94	$0.109\ 10^{-4}$	$j\ 1.88\ 10^{-7}$
A 2	0.046	2.94	$0.098\ 10^{-4}$	$j\ 1.88\ 10^{-7}$
A 3	0.067	2.96	$0.143\ 10^{-4}$	$j\ 1.89\ 10^{-7}$
A 4	0.090	8.70	$0.193\ 10^{-4}$	$j\ 5.60\ 10^{-7}$
A 5	0.179	10.30	$0.383\ 10^{-4}$	$j\ 6.60\ 10^{-7}$
A 6	1.007	74.20	$0.215\ 10^{-3}$	$j\ 4.75\ 10^{-6}$
A 7	0.853	40.10	$0.182\ 10^{-3}$	$j\ 2.56\ 10^{-6}$
A 8	0.727	23.70	$0.153\ 10^{-3}$	$j\ 1.52\ 10^{-6}$
A 9	0.561	17.50	$0.120\ 10^{-3}$	$j\ 1.12\ 10^{-6}$
A 10	0.343	11.00	$0.735\ 10^{-4}$	$j\ 7.05\ 10^{-7}$

Fig. 4 Antenna parameters

LOAD / DESIGN HYPOTHESES	R=20MOhm C = 5 pF	R=20MOhm C = 10 pF	R=20MOhm C = 25 pF
A 1	21.4	13.1	6.1
A 2	19.3	11.9	5.5
A 3	28.1	17.2	8.0
A 4	21.9	16.0	8.9
A 5	39.1	29.5	17.0
A 6	42.4	39.9	33.8
A 7	63.2	56.9	43.7
A 8	83.1	70.8	49.0
A 9	83.3	68.2	44.1
A 10	71.7	54.6	31.8

Fig. 5 Load voltage (Volt) for the A1-A10 design hypotheses

PATTERN MEASUREMENTS OF US NAVY ELF ANTENNAS

E. A. Wolkoff
W. A. Kraimer
Submarine Electromagnetic Systems Department
Naval Undersea Warfare Center Detachment
New London CT 06320, USA

SUMMARY

The radiation pattern of an ELF transmitting antenna can be determined from field components measured at a single point. Horizontal magnetic fields from the four US Navy ELF antennas in the north central United States were measured at three receiving locations. The three resulting pattern factors for each antenna are compared and shown to be in good agreement.

LIST OF SYMBOLS

ELF	Extremely low frequency
EW	East to west antenna
HED	Horizontal electric dipole
NRTF	Navy Radio Transmitter Facility
NS	North to south antenna
sdm	Standard deviation of the mean
SNR	Signal to noise ratio

INTRODUCTION

The United States Navy operates two ELF radio transmitter sites; NRTF Republic in the Michigan upper peninsula, and NRTF Clam Lake in northern Wisconsin. Each site has one north-south and one east-west antenna. The antenna elements are heavy aluminum cables 20 to 45km long suspended on wooden poles 3 to 5m above the surface of the earth. The cables are grounded at the ends with a single feed point between the grounds. Independent power amplifiers are used to excite the four antennas with modulated currents of 150A at NRTF Republic and 300A at NRTF Clam Lake. Generally all four antennas are operated as a single array to generate a strong signal over a large area. Transmitter coordinates are in table 1.

The coverage area of the ELF broadcast is the region on the earth's surface within which a receiver will correctly decode a message in a specified time with a specified probability of success. Given each antenna's radiation pattern and the magnitude and phase of the current driving it, the size and shape of the coverage area can be predicted. Conversely, antenna currents can be used to control the size and shape of the coverage area.

Patterns of all four antennas were measured in 1989. The purpose of this report is to describe the measurements and the resulting patterns, and show how to predict signal strengths from the combined antennas.

ANTENNA CHARACTERISTICS

The ELF antennas are less than 2 percent of a wavelength long and can be analyzed as horizontal electric dipole (HED) antennas. The efficiency of an HED near the earth is proportional to the square root of the effective earth resistivity. If the resistivity were homogeneous and isotropic the HED would have a cosine pattern in the horizontal plane, with maximum radiation off the ends, and with the radiated magnetic field phase-shifted 45° relative to the current.

The antenna sites are located on the Canadian Shield, a geologic region characterized by highly resistive, near-surface bedrock. Antenna efficiency here is some 20dB greater than for the usual conductive terrains found in most locations. It happens that the resistivity at these sites is inhomogeneous and anisotropic. This modifies the cosine pattern; the nulls are filled in, the radiation maxima are not off the ends of the HED, and the phase of the radiated magnetic field is not 45° with respect to the current. All four ELF antennas display these effects in various degree.

PROPAGATION MODEL

Field strengths of an HED antenna can be found by application of Bannister's ELF field strength equations [1]. These equations are valid at distances greater than a wavelength in the earth (about 30km at 76Hz at the Navy transmitter sites).

Bannister's equations have been modified here to permit the calculation of the phase as well as the magnitude of the field. The scalar earth conductivity has been replaced by antenna pattern factors to account for the anisotropy of the earth conductivity generally found at transmitter sites. Where Bannister simplified to obtain the magnitude only of field components, the complex form (Hankel and hyperbolic functions) has been restored. The antenna length has been absorbed into the antenna pattern factors. The azimuth to the field point previously defined as the angle counterclockwise from the electrical axis of the antenna is now defined as the angle clockwise from true north. Figure 1 shows the field components of an HED antenna at a location on the surface of the earth at a distance ϱ and azimuth ϕ relative to the location of the HED antenna.

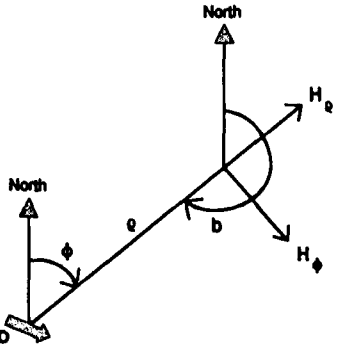

Figure 1. Fields at the Surface of the Earth of an HED Antenna

Constants:

j		$\sqrt{-1}$	
π		3.14159	
c	m/s	$3.0 \cdot 10^{8}$	speed of light
μ_0	H/m	$4\pi \cdot 10^{-7}$	free space permeability
a	m	$6.37 \cdot 10^{6}$	earth's radius

Variables:

ϕ		azimuth of field point clockwise from north
ϱ	m	great circle distance to field point from HED
H_ϕ	A/m	horizontal magnetic component in the transverse
H_ϱ	A/m	and radial directions at the point (ϕ, ϱ).

Parameters:

h	m	ionospheric height	
α	nepers/m	waveguide attenuation rate	
α_{dB}	dB/Mm	$\alpha \cdot 8.6859 \cdot 10^{6}$	
c/v		waveguide (inverse) relative phase velocity	
f	Hz	operating frequency	
ω	1/s	$2\pi f$	
I	A	antenna current	
k	1/m	ω/c	wave number
S_0		$c/v - j\alpha/k$	propagation constant
x		$kS_0\varrho$	
T_n	Ωm	antenna pattern factor north	
T_e	Ωm	antenna pattern factor east	

Functions:

$H_0^{(2)}$	Hankel fn of order 0, 2nd kind
$H_1^{(2)}$	Hankel fn of order 1, 2nd kind

The values of I, H_ϕ, H_ϱ, S_0, x, T_n, T_e, $H_0^{(2)}$ and $H_1^{(2)}$ are complex.

Correction functions for ionospheric reflections are now:

$u = \pi\varrho/2h,$

$t = u/S_0^2,$ note that S_0 and t are complex,

$G_h(t) = (2t/\pi)\coth t + (1-2/\pi)t^2\operatorname{csch}^2 t,$

$V_h(t) = t^3(\coth t)(\operatorname{csch}^2 t),$

$H_h(t) = G_h(t) + V_h(t).$

The modified field equations now become:

$$H_\phi \doteq \frac{IG_h(t)x}{4\omega\mu_0\varrho^3}[T_n\sin\phi - T_e\cos\phi][H_1^{(2)}(x) - xH_0^{(2)}(x)]\left[\frac{\varrho/a}{\sin(\varrho/a)}\right]^{1/2} \quad (1)$$

$$H_\varrho \doteq \frac{IH_h(t)x}{4\omega\mu_0\varrho^3}[T_n\cos\phi + T_e\sin\phi]\,H_1^{(2)}(x)\left[\frac{\varrho/a}{\sin(\varrho/a)}\right]^{3/2} \quad (2)$$

DETERMINATION OF ANTENNA PATTERN

The pattern factors may be found by substituting values of H_ϕ and H_ρ measured at a single receiver location into (1) and (2) then solving simultaneously for T_n and T_e.

Several conditions must be observed to assure that the model will provide accurate pattern factors.

1. Magnetic field measurements require high SNR and careful alignment of the loop antenna axes with respect to the direction to the transmitter.

2. Propagation parameters, (h, α, c/v), must be accurately known. The most certain values are for daylight paths, these paths are also the most stable. Values used are given in table 3. System variables, (I, ϕ, ρ), need to be accurately found. Distance and azimuth can be determined from a map. Antenna current magnitude can be obtained directly from the transmitter log, phase requires that accurate clock relations be maintained between the transmitters and receiver.

4. The field at the receiver is more strongly influenced by closer parts of the transmitting antenna. To avoid having a non-uniform conductivity under the transmitting antenna affect the field, the distance to the receiver should be large compared to the length of the transmitting antenna.

5. Conditions near the receiver must not distort the field. It is necessary to stay away from conductors that act as parasitic antenna elements, and avoid areas with strong contrasts in earth conductivity.

MEASUREMENT PLAN

To assure robust solutions of the pattern factors, horizontal orthogonal components of the magnetic field were measured at 3 receiver sites which met site selection criteria described later.

The receiving antennas were oriented in the north and east directions, H_ϕ and H_ρ were calculated for each particular transmitter. A magnetic compass adjusted for the magnetic declination was used to orient the loops. True north was verified by comparing the sun's magnetic azimuth (found with a transit) with the true azimuth (from an ephemeris).

Nine days with 8 hours a day of transmissions were scheduled for each receiver site to permit accurate estimates of the fields of all 4 transmitting antennas at 2 frequencies. Only daylight hours were used.

The first day was used for site selection and evaluation. The primary test was that the vertical magnetic field be at least 20dB down from the largest horizontal component. Measurements on the next four days were at 76Hz and the last four days at 44Hz. The schedule for each of the 4-day periods is shown in table 4. Each day is broken into 4 blocks of 2 hours.

Days 1 and 2 are designated as antenna alone (AA) days with transmissions from one antenna at a time. One antenna for each 2 hour block.

Day 3 is a single site (SS) day with the first 4 hours devoted to NRTF Republic and the second 4 hours to NRTF Clam Lake, note that the current phase in one antenna is shifted 180° during the second 2 hour block.

Day 4 is a dual site (DS) day with all 4 antennas transmitting in each block. Note that the phasing of different pairs of antennas is shifted in each 2 hour block.

The phase shifts on days 3 and 4 allow calculation of each antenna's contribution to the field. On an SS day, the fields measured in the second time block are added to those measured in the first block to obtain twice the contribution of the EW antenna, the second is subtracted from the first to obtain twice the contribution of the NS antenna. Similarly, on a DS day, the fields of all 4 blocks are added to obtain 4 times the contribution of the NRTF Republic EW antenna (appropriate sums and differences are used to find the contributions of the other 3 antennas). This is done to test for interactions between the antennas. A side benefit is an effective SNR improvement of 3dB on SS days and 6dB on DS days. The risk is that with substantial down time (of any transmitter or the receiver), the separate contributions can not be obtained.

The antenna currents were measured before any field measurements to find the relation of the actual to control room instrument readout. Transmitter clocks were adjusted to UTC using the GPS receiver clock. The clocks were checked and reset between measurement sites and after the final site was completed. A copy of each transmitter log was obtained showing start and stop times and antenna current readouts. Corrections for antenna current and timing were made during final data reduction. Late start or early stop times required rejection of the measured sample.

Individual data runs were 14 minutes long to allow 8 runs in a 2 hour block with 8 minutes left over. The extra time allocation was: 5 minutes for operators to switch transmitters at the end of a block; 1 minute grace period at the beginning of a block; 2 minutes distributed between the runs to store data, restart and make minor receiver adjustments.

SITE SELECTION

Sites were selected at azimuths that placed them approximately 45° off the ends of the transmitting antennas for strong H_ϕ and H_ρ components. Ranges greater than 10 times the length of the longest antenna element were chosen (ρ > 450km) to lessen the affect of different earth conductivities under different parts of the antenna. The search for electrically clean sites caused the range to be greater than the needed 450km.

Finding distortion-free sites is something of an art, long nearby conductors can act as parasitic antenna elements, and horizontal contrasts in earth conductivity can cause non-symmetrical currents in the earth. The following criteria guided site selection.

Clean-site criteria

Avoid railroads (3km), pipelines (2 to 16km), power lines (2 to 8km), telephone lines (2km), fences and other conductive structures (15 to 150m).

Choose areas with deep conductive overburden and free of faults or strong conductivity contrasts.

TRIP NARRATIVE

Measurements of the magnetic field generated by the ELF antennas were made at 3 receiver sites at distances of 500 to 1075km. Antenna current calibration and clock adjustments were made at the 2 transmitter sites. Locations of the centers of the ELF transmitting antennas, the center of the array, and the three receiver sites are in tables 1 and 2.

The measurement vehicle (van) departed from NUWC New London, Connecticut for NRTF Republic, Michigan where the station clocks were set to UTC using the GPS receiver, the magnitude and phase of the antenna currents were measured and compared to values shown in the control room, and the operators were briefed on the details of the transmission schedule and data logging requirements. The next stop was at NRTF Clam Lake, Wisconsin where the same tasks were repeated.

The first measurement site was at Pigeon River State Fish and Wildlife Area east of Mongo, Indiana. Measurements at both frequencies and all transmitter configurations were completed in 9 days.

The station clocks at Republic and Clam Lake were rechecked and found

to be within 9μs of UTC, and reset to zero offset.

The second measurement site was at Fort Niobrara National Wildlife Refuge northeast of Valentine, Nebraska. Measurements were completed with the loss of only 2 hours on the first day.

The third and last measurement site was at Roseau River Wildlife Area west of Ross, Minnesota. Measurements were completed in 9 days.

A final check of the station clocks showed errors of less than 19μs which would require phase adjustments of at most 0.5°.

DESCRIPTION OF MEASUREMENTS

At each receiver site, the horizontal magnetic field of the four transmitting antennas was measured in the north and east directions at both 44 and 76Hz.

Field measurements were made from a 12-passenger van equipped to operate at remote locations. The van carried a 2-channel digital ELF receiver incorporating air-core loop antennas, preamplifiers, tracking narrowband filters to attenuate power line interference, clippers to prevent saturation, lowpass antialiasing filters, analog-to-digital conversion, and a desktop computer to reduce and display data when collected, and to store results.

The loop antennas are contained in a plywood cube. A 464 turn winding of #18 aluminum wire is mounted on each inside face of the cube. Windings on opposite faces are connected in series to form 3 orthogonal antennas with turns-area products of $73m^2$, resistance of 51Ω, inductance of 270 mH, calculated equivalent H field noise of -116dB - 20Log f wrt 1A/m/√Hz.

Frequency stability and accuracy were provided by a rubidium frequency standard, timing traceable to UTC was provided by a GPS satellite receiver clock. A calibration and reference unit used the 1pps clock pulses and frequency standard to generate sampling pulses, tracking filter reference, and calibration signals.

A spectrum analyzer and portable 2-channel oscilloscope were used to set up the receiver and monitor the analog waveforms. Power was provided by a 1kW invertor operating off the test vehicle battery or alternator. Critical components operated through an uninterruptable power supply backed up by deep discharge batteries.

Loop antenna alignment

The cube containing the loop antennas was leveled with a bubble level mounted on the top, and oriented with a magnetic compass. The compass was adjusted for the local magnetic declination shown on an Aeronautical Chart. Magnetic declinations were checked by taking sunshots (azimuth and elevation) with a transit. A computer program, "Floppy Almanac 1989", from the US Naval Observatory, Nautical Almanac Office, was used to get the latitude and longitude of the subsolar point (declination and Greenwich hour angle) at the time of the sunshot. Actual azimuth and elevation were calculated as the great circle bearing and range from the receiver to the subsolar point.

Receiver operation

In each of the two receiver signal channels, a clipper after the interference filters removes voltage spikes, an antialiasing filter reduces high frequency components, an amplifier brings the peaks to between 8 and 10 volts at the input to the digitizer. The two measurement channels and a reference channel are sampled and digitized, (at 320 samples per second per channel), the digitized voltage samples are stored in the computer memory until 5 seconds of samples are acquired. A continuous calibration tone is injected into the channels to account for the reduction in the effective gain due to clipping. The tone is attenuated and injected in series with the loop antennas.

Data acquisition

At the end of every 5 seconds, the computer performed a digital version of quadrature demodulation on the stored samples. This was done for noise, signal and calibration frequencies (75, 76 and 77Hz, or 43, 44 and 45Hz) on the two signal channels, and at the calibration frequency on the reference channel. The gain of each signal channel was calculated as the ratio of the measured calibration voltages at the output of the signal channel (adjusted for attenuation used at the point of injection) and the reference channel. The gain was then calculated at the signal and noise frequencies using previously measured frequency responses. Finally, the signal and noise were referenced to the field using the previously calibrated antenna gain.

The running averages of the 5 second results were displayed graphically and numerically on the computer's color monitor along with system and diagnostic parameters. The cumulative coherent sums of signals and the noise power were saved in memory. At the end of a data run (usually 840s), the final average signal and noise were saved to the hard disk, along with all pertinent data.

Data reduction

A copy of each transmitter log was obtained and the individual data runs that had been saved on the hard disk were corrected for the recorded transmitter antenna current magnitude and phase. Generally the current was within 1A of the nominal magnitude (150 or 300A), and within 1° of the nominal phase (45 or -135°). Phase corrections also were made for clock differences from UTC.

Magnetic field

The measured and corrected H_x and H_y components for each data run were weighted and averaged over the 2 hour time block. The weight used was the inverse noise power in the bandwidth of the signal, (integration time divided by the measured 1Hz noise power).

The block averages for each day were used to calculate the contribution of each antenna to H_x and H_y (as described above in the Measurement Plan for SS and DS days). Each antenna's measured H_x and H_y fields were projected to obtain the signal and effective noise of H_ϕ and H_ρ.

The daily H_ϕ and H_ρ averages were weighted by their effective inverse noise powers and averaged to obtain a final single estimate for each combination of field component, receiver, transmitter, and frequency. The resulting 48 component estimates are complex numbers and have an associated effective noise or sdm. The daily and average values are summarized in tables 5, 6 and 7. It appears that the 76Hz signal from the Republic EW antenna to the Ft. Niobrara receiver on 5 Aug 89 is in error. Until the source of the error can be determined, all data will be retained and used in the pattern factor calculations. With this one exception, the daily values are not notably different whether transmissions are by multiple antennas (SS or DS days) or single antennas (AA days). This demonstrates that the field of the array is the superposition of the fields from the individual antennas.

Pattern Factors

The pattern factors, T_ρ, T_ϕ and associated sdm, were calculated separately for each of the 3 receiver sites using the range, azimuth and measured fields of the receiver (table 5, 6, or 7), the propagation parameters (table 3), and the propagation model (equations 1, 2). Finally, the weighted average over the 3 receiver sites was calculated. Pattern factors derived for each receiver site, and the weighted average for the 3 sites are in table 8.

FIELD STRENGTH PREDICTIONS

Field strength predictions based on the parameters in table 3 and the pat-

tern factors of table 8 should be fairly accurate. Error contribution of the pattern factors will be less than 0.5dB for all path conditions. For all-daylight paths at ranges less than 8Mm, fields should be predictable to within 1dB. Prediction errors for nighttime and mixed paths will be greater.

Field strengths for any one antenna can be calculated using the equations and parameters given here. The field strength for any combination of antennas transmitting can be found as the vector and phasor sum of the separate fields.

The procedure is to first solve the great circle from each transmitting antenna to the receiver location. Calculate H_ϕ and H_ρ for each source and rotate to common orthogonal directions to find H_x and H_y. Find the sums of the H_x and H_y components. Finally, calculate the direction of maximum H, and its magnitude.

REFERENCES

1. P. R. Bannister, "Simplified Formulas for ELF Propagation at Shorter Distances", *Radio Science*, vol. 21, no. 3, 1986, p. 529.

TRANSMITTER	LATITUDE	LONGITUDE
NRTF Republic NS	n46.24	w87.90
NRTF Republic EW	n46.33	w87.77
NRTF Clam Lake NS	n46.08	w90.90
NRTF Clam Lake EW	n46.10	w90.91
Full System	n46.19	w89.35

Table 1. Midpoints of Transmitting Antennas and Array

RECEIVER	LATITUDE	LONGITUDE
Pigeon River, Indiana	n41.6702	w85.2442
Ft. Niobrara, Nebraska	n42.8708	w100.4915
Roseau River, Minnesota	n48.9871	w96.0258

Table 2. Locations of Receiver Sites

f Hz	h km	c/v	α dB/Mm
44	48.2	1.26	1.03
76	55.5	1.23	1.25

Table 3. Daylight Propagation Parameters

		ANTENNA CURRENT PHASING (deg)			
type	GMT	NRTF Republic		NRTF Clam Lake	
		NS	EW	NS	EW
AA	1300 - 1455	45	---	---	---
	1500 - 1655	---	45	---	---
	1700 - 1855	---	---	45	---
	1900 - 2055	---	---	---	45
SS	1300 - 1455	45	45	---	---
	1500 - 1655	45	-135	---	---
	1700 - 1855	---	---	45	45
	1900 - 2055	---	---	45	-135
DS	1300 - 1455	45	45	45	45
	1500 - 1655	45	45	-135	-135
	1700 - 1855	45	-135	45	-135
	1900 - 2055	45	-135	-135	45

Table 4. Transmitter Schedule

freq	transmitter	type	date	H_ϕ			H_θ		
			Jul 1989	SNR dB	mag dBH	phase deg	SNR dB	mag dBH	phase deg
44Hz	Republic NS	AA	23	33.5	-137.6	16.8	32.3	-139.7	-18.6
	ϱ 551 km	AA	24	34.5	-137.3	16.9	32.7	-139.7	-17.1
	ϕ 156.4°	SS	25	37.0	-137.2	17.3	34.2	-140.4	-20.4
	b -21.8°	DS	26	41.2	-137.2	17.3	37.4	-140.3	-16.1
	I 150A @ 45°	avg		43.7	-137.3	17.2	40.7	-140.2	-17.6
	Republic EW	AA	23	28.0	-142.6	-158.9	39.4	-132.3	-22.5
	ϱ 556 km	AA	24	27.6	-143.6	-160.7	38.8	-132.7	-23.0
	ϕ 157.8°	SS	25	31.3	-142.9	-160.1	42.0	-132.7	-23.5
	b -20.4°	DS	26	34.9	-143.6	-159.7	45.1	-132.6	-24.1
	I 150A @ 45°	avg		37.5	-143.4	-159.8	48.1	-132.6	-23.6
	Clam Lake NS	AA	23	27.7	-142.2	0.9	32.1	-138.0	-27.5
	ϱ 667 km	AA	24	27.9	-141.6	-1.6	31.7	-137.9	-27.5
	ϕ 135.3°	SS	25	28.4	-140.9	3.0	31.2	-138.1	-27.4
	b -40.8°	DS	26	36.1	-142.0	3.5	39.6	-138.4	-29.2
	I 300A @ 45°	avg		37.8	-141.9	2.7	41.3	-138.3	-28.7
	Clam Lake EW	AA	23	29.2	-138.8	-166.0	19.8	-148.4	-6.0
	ϱ 670 km	AA	24	27.6	-138.5	-159.6	13.7	-152.7	-7.8
	ϕ 135.3°	SS	25	30.8	-138.5	-160.6	20.8	-148.4	-5.0
	b -40.7°	DS	26	38.8	-139.4	-161.3	29.7	-148.3	0.6
	I 300A @ 45°	avg		40.1	-139.2	-161.5	30.7	-148.5	-0.8
76Hz	Republic NS	AA	19	33.8	-136.6	19.4	32.2	-141.4	-39.7
	ϱ 551. km	AA	20	37.4	-136.8	17.3	34.7	-142.2	-39.2
	ϕ 156.4°	SS	21	41.2	-136.5	18.1	37.5	-142.1	-42.4
	b -21.8°	DS	22	42.6	-136.5	17.1	39.7	-141.7	-41.1
	I 150A @ 45°	avg		45.9	-136.5	17.6	42.9	-141.9	-41.1
	Republic EW	AA	19	30.5	-142.7	-156.4	40.8	-135.0	-40.5
	ϱ 556 km	AA	20	32.0	-142.7	-157.2	42.3	-135.0	-40.4
	ϕ 157.8°	SS	21	35.6	-142.1	-155.3	45.0	-134.8	-40.0
	b -20.4°	DS	22	36.5	-142.5	-157.3	46.5	-135.0	-40.9
	I 150A @ 45°	avg		40.3	-142.4	-156.6	50.2	-134.9	-40.5
	Clam Lake EW	AA	18	34.3	-141.4	4.9	35.7	-140.2	-44.3
	ϱ 667 km	AA	19	32.6	-140.9	5.5	34.4	-139.6	-45.0
	ϕ 135.3°	AA	20	34.1	-140.9	6.3	35.5	-140.0	-44.2
	b -40.8°	SS	21	34.0	-140.8	3.0	35.1	-140.2	-46.0
	I 300A @ 45°	DS	22	38.4	-141.5	2.9	40.1	-140.3	-45.8
		avg		42.2	-141.2	4.0	43.7	-140.1	-45.3
	Clam Lake EW	AA	18	35.1	-137.5	-160.0	22.5	-150.4	-18.2
	ϱ 670 km	AA	19	33.9	-137.3	-159.0	23.0	-148.7	-24.1
	ϕ 135.3°	AA	20	36.0	-137.0	-157.2	24.0	-149.4	-10.8
	b -40.7°	SS	21	37.4	-137.4	-158.4	26.8	-148.5	-22.2
	I 300A @ 45°	DS	22	42.5	-137.3	-158.7	31.2	-149.1	-21.5
		avg		45.2	-137.3	-158.6	33.8	-149.1	-20.4

Table 5. Measured Fields at Pigeon River.

freq	transmitter	type	date	H_ϕ			H_θ		
			Aug 1989	SNR dB	mag dBH	phase deg	SNR dB	mag dBH	phase deg
44Hz	Republic NS	AA	8	22.7	-149.5	15.6	26.1	-146.3	136.5
	Q 1064 km	AA	9	23.5	-148.8	19.2	27.2	-145.6	140.5
	ϕ -106.1°	SS	10	26.8	-149.4	14.6	31.2	-145.2	141.2
	b 65.1°	DS	11	30.8	-149.9	10.4	35.0	-145.5	142.8
	I 150A @ 45°	avg		33.2	-149.7	12.6	37.3	-145.5	141.7
	Republic EW	AA	8	32.0	-140.2	6.1	19.4	-153.7	-62.7
	Q 1077 km	AA	9	31.2	-140.9	4.8	20.5	-152.3	-43.2
	ϕ -106.3°	SS	10	35.6	-140.6	4.9	22.6	-153.7	-40.0
	b 64.7°	DS	11	40.3	-140.4	6.0	24.6	-155.9	-60.7
	I 150A @ 45°	avg		42.4	-140.5	5.7	28.0	-154.9	-53.6
	Clam Lake NS	AA	8	26.4	-144.6	24.0	29.9	-141.7	139.8
	Q 840 km	AA	9	24.8	-144.8	20.1	28.0	-142.0	136.0
	ϕ -111.7°	SS	10	30.5	-144.5	14.6	34.0	-141.3	139.6
	b 61.6°	DS	11	36.2	-144.5	20.2	39.1	-141.5	140.8
	I 300A @ 45°	avg		37.8	-144.5	19.4	40.8	-141.5	140.2
	Clam Lake EW	AA	8	25.7	-144.8	24.6	27.6	-143.4	-32.5
	Q 840 km	AA	9	25.5	-145.0	28.5	27.8	-142.8	-37.1
	ϕ -111.9°	SS	10	29.8	-145.1	25.3	31.7	-143.5	-31.2
	b 61.4°	DS	11	35.2	-145.5	19.8	36.8	-143.8	-35.4
	I 300A @ 45°	avg		37.0	-145.3	21.8	38.7	-143.6	-34.5
76Hz	Republic NS	AA	4	.	.	.	.	.	.
	Q 1064 km	AA	5	30.2	-146.8	-31.0	30.3	-148.0	86.6
	ϕ -106.1°	SS	6	29.3	-147.1	-23.6	30.0	-147.2	92.4
	b 65.1°	DS	7	33.6	-147.2	-20.8	34.2	-147.5	98.2
	I 150A @ 45°	avg		36.2	-147.1	-23.9	36.7	-147.6	94.2
	Republic EW	AA	3	40.0	-137.9	-25.3	23.2	-154.5	-109.5
	Q 1077 km	AA	4	36.9	-138.1	-27.8	18.7	-156.9	-105.6
	ϕ -106.3°	AA	5	36.5	-138.2	-26.8	24.4	-152.6	-58.8 ?
	b 64.7°	SS	6	38.4	-138.1	-29.5	20.9	-156.3	-124.0
	I 150A @ 45°	DS	7	42.8	-138.0	-26.9	27.4	-154.4	-117.7
		avg		46.6	-138.0	-27.0	30.1	-155.3	-106.2 ?
	Clam Lake NS	AA	3	35.0	-142.0	9.0	32.9	-143.9	116.1
	Q 840 km	AA	4	35.1	-142.4	3.9	33.3	-144.6	115.3
	ϕ -111.7°	AA	5	32.2	-141.7	0.5	31.2	-144.7	106.4
	b 61.6°	SS	6	32.4	-142.2	8.3	31.3	-143.6	116.4
	I 300A @ 45°	DS	7	38.7	-142.2	8.9	37.6	-144.0	119.8
		avg		42.3	-142.2	7.1	40.9	-144.2	116.6
	Clam Lake EW	AA	3	31.7	-142.3	14.1	27.8	-145.8	-57.3
	Q 840 km	AA	4	31.4	-141.8	14.9	28.9	-144.8	-62.2
	ϕ -111.9°	AA	5	30.1	-142.3	21.6	30.1	-144.3	-51.2
	b 61.4°	SS	6	32.8	-141.9	9.8	29.9	-145.0	-59.6
	I 300A @ 45°	DS	7	38.6	-142.3	13.3	36.4	-145.2	-63.4
		avg		41.2	-142.2	13.7	38.9	-145.1	-60.8

Table 6. Measured Fields at Fort Niobrara.

freq	transmitter	type	date	H_ϕ			H_θ		
			Aug 1989	SNR dB	mag dBH	phase deg	SNR dB	mag dBH	phase deg
44Hz	Republic NS	AA	23	24.9	-148.2	-155.0	33.5	-139.0	158.3
	ϱ 681 km	AA	24	24.2	-147.3	-162.5	32.1	-138.7	159.1
	ϕ -60.4°	SS	25	30.9	-146.2	-155.7	36.7	-140.3	147.7
	b 113.6°	DS	26	31.7	-147.9	-159.9	38.5	-139.2	159.6
	I 150A @ 45°	avg		35.1	-147.4	-158.2	41.9	-139.6	155.5
	Republic EW	AA	23	35.5	-137.6	14.2	32.2	-141.6	152.7
	ϱ 685 km	AA	24	35.0	-137.1	11.9	31.4	-140.8	151.7
	ϕ -61.5°	SS	25	39.0	-138.1	12.1	33.6	-143.4	143.7
	b 112.5°	DS	26	42.0	-137.7	13.9	35.6	-142.0	153.4
	I 150A @ 45°	avg		44.8	-137.7	13.3	39.5	-142.3	150.2
	Clam Lake NS	AA	23	31.8	-138.8	177.9	36.5	-133.7	162.3
	ϱ 502 km	AA	24	32.3	-138.6	177.8	36.9	-133.7	160.4
	ϕ -48.1°	SS	25	35.5	-139.1	174.6	39.6	-134.0	162.4
	b 128.1°	DS	26	40.1	-138.8	178.9	44.3	-134.0	161.2
	I 300A @ 45°	avg		42.3	-138.8	177.8	46.6	-133.9	161.5
	Clam Lake EW	AA	23	34.1	-135.1	14.6	23.7	-144.8	-159.8
	ϱ 500 km	AA	24	33.1	-135.4	16.5	21.2	-146.5	-159.5
	ϕ -48.2°	SS	25	38.7	-135.8	16.8	27.9	-145.7	-155.9
	b 128.0°	DS	26	43.3	-135.6	16.2	31.6	-146.6	-152.2
	I 300A @ 45°	avg		45.2	-135.6	16.2	33.8	-146.3	-154.1
76Hz	Republic NS	AA	19	30.4	-147.2	-165.5	34.4	-141.0	133.2
	ϱ 681 km	AA	20	31.3	-147.4	-163.9	35.0	-140.6	134.0
	ϕ -60.4°	SS	21	32.7	-147.7	-163.8	39.3	-140.6	133.8
	b 113.6°	DS	22	36.8	-146.8	-169.1	42.6	-140.8	131.5
	I 150A @ 45°	avg		39.6	-147.2	-166.7	45.2	-140.7	132.5
	Republic EW	AA	19	42.1	-136.3	8.7	32.6	-144.0	137.4
	ϱ 685 km	AA	20	42.4	-136.4	8.0	32.0	-144.3	136.2
	ϕ -61.5°	SS	21	44.3	-136.2	7.9	35.5	-144.3	139.2
	b 112.5°	DS	22	47.1	-136.4	9.2	39.1	-144.3	137.9
	I 150A @ 45°	avg		50.5	-136.3	8.6	41.8	-144.3	138.0
	Clam Lake NS	AA	18	33.0	-140.5	-169.6	37.0	-136.0	153.8
	ϱ 502 km	AA	19	36.3	-140.6	-174.4	40.0	-136.2	152.6
	ϕ -48.1°	AA	20	36.2	-140.7	-172.5	40.1	-136.1	151.8
	b 128.1°	SS	21	36.7	-140.3	-173.6	40.7	-136.0	153.4
	I 300A @ 45°	DS	22	43.1	-140.4	-174.4	47.3	-136.2	151.2
		avg		45.5	-140.4	-173.8	45.5	-136.1	151.8
	Clam Lake EW	AA	18	37.1	-134.9	29.4	25.4	-146.2	-160.5
	ϱ 500 km	AA	19	39.6	-135.0	28.8	28.1	-145.6	-163.7
	ϕ -48.2°	AA	20	39.2	-135.3	28.6	27.4	-146.1	-163.4
	b 128.0°	SS	21	42.1	-135.0	29.4	30.4	-146.3	-165.1
	I 300A @ 45°	DS	22	48.4	-135.1	28.5	37.2	-146.3	-166.8
		avg		50.3	-135.1	28.7	39.0	-146.2	-165.8

Table 7. Measured Fields at Roseau River.

freq	transmitter	receiver	pattern factor (Ωm)					
			T_n			T_e		
			Re	Im	sdm	Re	Im	sdm
44Hz	Republic NS	Pigeon River	8532	2705	1205	-40304	-29716	642
		Ft. Niobrara	7785	4904	1531	-42747	-31959	2721
		Roseau River	6516	233	3201	-40349	-25021	4885
		Average	8107	3280	1485	-40431	-29757	953
	Republic EW	Pigeon River	63334	32720	990	-8370	1720	911
		Ft. Niobrara	62249	32174	1918	-1731	-1834	4041
		Roseau River	55179	31573	2765	-3174	2085	3865
		Average	62376	32510	2358	-7805	1575	1904
	Clam Lake NS	Pigeon River	4904	3413	740	-26644	-11877	741
		Ft. Niobrara	3376	5612	879	-26647	-13231	783
		Roseau River	3697	4049	524	-25629	-12041	515
		Average	3961	4177	951	-26115	-12268	730
	Clam Lake EW	Pigeon River	16083	14024	970	9818	5423	973
		Ft. Niobrara	17241	12778	907	12018	5462	916
		Roseau River	13967	13866	444	10053	4823	442
		Average	14815	13709	1370	10337	5012	795
76Hz	Republic NS	Pigeon River	10802	2127	1255	-57255	-42531	983
		Ft. Niobrara	12692	4730	2754	-55775	-37400	5413
		Roseau River	10192	6097	1366	-52843	-38523	1413
		Average	10742	4023	2021	-55816	-41141	2819
	Republic EW	Pigeon River	77189	49572	1239	-7065	3733	1028
		Ft. Niobrara ?	83993	40375	3657	744	-5593	9331
		Roseau River	71010	51215	1057	2533	-3776	968
		Average	74093	50054	1333	-1962	-277	6082
	Clam Lake NS	Pigeon River	5362	6668	928	-31702	-21112	927
		Ft. Niobrara	7035	7856	1686	-29473	-21855	2494
		Roseau River	4703	7254	555	-28979	-19883	564
		Average	5036	7156	705	-29706	-20274	1339
	Clam Lake EW	Pigeon River	20230	24275	816	12704	10058	812
		Ft. Niobrara	22363	22391	1382	14079	9281	1976
		Roseau River	17102	24728	404	13177	9117	399
		Average	18018	24494	1756	13117	9300	445

Table 8. Antenna Pattern Factors, Measured and Weighted Averages

TETHERED AEROSTAT VLF/LF TRANSMITTER SYSTEM DESIGN CONSIDERATIONS

Richard L. Crawford
Thomas C. LaManna
SRI International
1611 N. Kent Street
Arlington, VA 22209, USA

Kenneth L. Jordan
Science Applications International Corporation
8619 Westwood Center Drive
Vienna, VA 22182, USA

1. SUMMARY

A tethered aerostat VLF/LF transmitter (TAVT) system is a cost-effective, survivable alternative for reconstituting VLF/LF communication connectivity to strategic forces in a post-attack environment. This paper describes the tradeoff design considerations that led to recommending a TAVT system with a 50,000-cubic-foot aerostat and a 5,000-foot tether used as the transmitting radio antenna. The major tradeoff factors considered in choosing this design were: survivability, transportability, coverage area, operating frequency range, maximum effective radiated power, cost, and corona avoidance.

2. INTRODUCTION

During the early part of the 1980s, considerable interest existed in providing survivable and enduring communication connectivity between the U.S. National Command Authority (NCA) and strategic forces during the trans- and post-attack periods. The large operational ground-based, fixed VLF transmitting facilities (e.g., Cutler, Maine) lacked survivability under nuclear attack while the endurance of aircraft-deployable VLF/LF systems (e.g., TACAMO) was questionable. The ability to maintain VLF/LF communication connectivity is highly desirable due to its inherent long range, relative insensitivity to a nuclear-disturbed environment and water penetration capabilities.

Therefore, the WWMCCS System Engineering Organization (WSEO) within the Defense Communications Agency (DCA) sponsored a study by General Electric[1] to develop a parametric technical data base for a tethered aerostat VLF/LF transmitter (TAVT) system. Following the parametric analysis, the WSEO and the U.S. Air Force Geophysics Laboratory (AFGL) contracted with Westinghouse to develop a proof-of-concept TAVT system using an existing 25,000-cubic foot aerostat design as shown in Figure 1. The TAVT system was designed, built and tested in operational exercises and electrical measurements were made on base impedance, bandwidth and efficiency of a 3,000-foot vertical antenna.[2]

The studies cited above involved major tradeoffs. The factors that were deemed important for both large and small aerostats are shown in Table 1. Since survivability was the most important factor in the design and was achieved by designing for transportability, the technical approach was to determine the minimum size that would meet the operational requirements of coverage area (i.e., range), operating frequency range and bandwidth required for anti-jam modes of modulation.

3. TECHNICAL APPROACH

With the proof-of-concept design experience as justification that the TAVT system was a viable concept for reconstituting submarine communications, a tradeoff analysis was made for three candidate TAVT system designs with antenna lengths of 3,000, 5,000 and 7,500 feet.[3] The study goals were to:

- Determine number, size and location of TAVT system nodes needed to meet coverage area requirements.
- Evaluate ability of candidate transport systems to move TAVT systems to required locations in a timely manner.
- Assess TAVT system vulnerability to jamming and physical destruction.

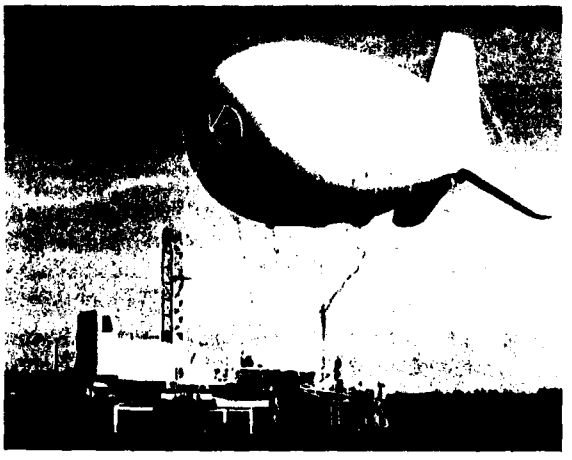

Figure 1. TAVT Aerostat and Mooring System

Table 1. Aerostat Design Parameters

Factors Favoring Large Aerostat	Factors Favoring Small Aerostat
Frequency Range	Helium Requirements
Bandwidth	Fuel Requirements
Operational Range	Personnel
Power	Transportability
Corona Avoidance	Survivability
Ground Plane Size	Cost
Tuning Coil Size	Logistics Support

- Evaluate technical risk areas to determine their impact on TAVT system configuration and performance.

Since the cost and logistics requirements are dependent upon post-attack communication requirements of endurance and frequency of transmissions, three communication missions were postulated to obtain a range of activities that would affect fuel and helium consumption. The transmission duty cycle determines the fuel consumption. Survivability obtained by moving determines the helium consumption due to the necessity of deflating the aerostat before moving to a new location. The three communication missions were designed to fully cover the potential operational cost for TAVT systems in a post-attack environment.

Since communication mission requirements and threat assessments are scenario-dependent, the major goal of this paper is to concentrate on the electrical performance factors and then summarize the results of the transportability and cost analyses.

3.1 PHYSICAL DESIGN

The seven major elements of a transportable TAVT system are shown in Figure 2. They are the aerostat, the mooring system, the metal-clad tether (antenna), transmitter and coupler trailer, power generator trailer, ground system and a helium supply truck.

3.1.1 Aerostat and Tether

The design of the aerostat is predicated on its lifting ability and is determined strictly by its volume. As the size of the aerostat increases, the volume increases as the cube of the linear dimension. However, the weight of the aerostat hull and system increases approximately as the square of the linear dimension. Thus, as aerostats become larger, they have a greater payload and altitude capability. For the TAVT system, the payload is the weight of the tether, the Faraday cage for lightning protection, and the blowers and valves needed to maintain the aerostat shape.

The lifting ability, and thus the size of the aerostat, is determined by the environmental factors of wind velocity, temperature, barometric pressure (pad elevation) and the positive lift required to overcome wind turbulence and icing.

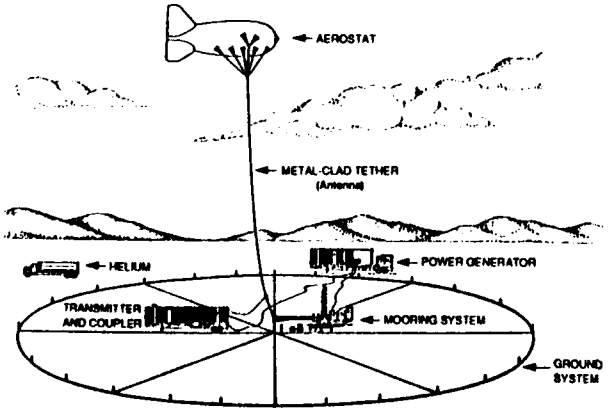

Figure 2. TAVT System Major Elements

Figure 3 shows the tradeoff curves for a TAVT system design at a 1,000-foot pad altitude and enough free lift to remain within a 30° line-of-sight measured from the base of the antenna to the zenith. This antenna displacement angle of 30° was chosen as the nominal design limit. This 30° displacement results in 1.25 dB loss in radiated power due to the reduced vertical height. The variation in base impedance is less than two percent. Curves similar to Figure 3 have been developed for pad elevations from sea level to 5,000 feet (for every 1,000 feet). With these curves and a selected location, the mean and maximum wind velocity at that location can be superimposed upon the graph to obtain the optimum size of the aerostat volume. For the three tether lengths, the aerostat volume, tether diameter and tether break strength are determined for the maximum wind velocity plus a safety factor.

The physical design parameters for the three tether lengths are shown in Table 2. The percent free lift and the wind velocity for the 30° displacement angle are approximately the same.

Table 2. Aerostat Design Parameters

Antenna Length (feet)	Aerostat Volume (cubic ft.)	Wind Velocity (knots)*	Free Lift (%)	Antenna Diameter (Inches)
3,000	25,000	44	32	0.578
5,000	50,000	45	32	0.630
7,500	100,000	47	30	0.680

*with 30° displacement

3.2 ELECTRICAL PERFORMANCE

Figure 4 shows the electrical pictorial schematic of the TAVT system. Careful attention was taken to avoid coronas by the use of a corona shield at the aerostat and corona ring near the base of the antenna. Radiated power is limited by

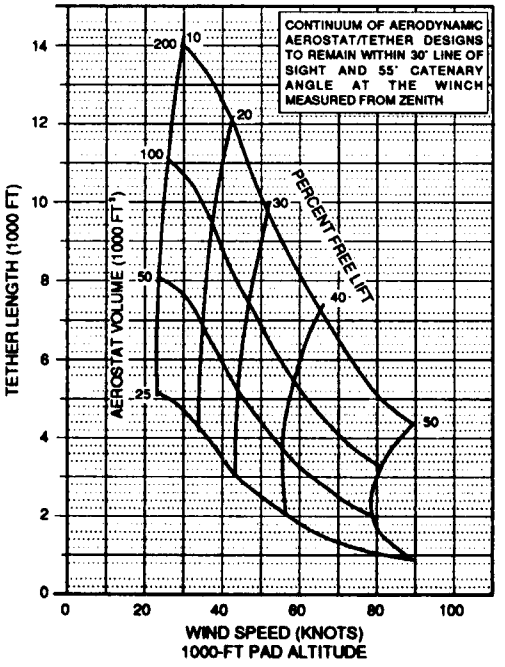

Figure 3. Continuum of Aerostat Designs

the inception of corona; thus, one of the major tradeoffs was to determine the optimum tether diameter. Figure 5 shows radiated power versus tether diameter for a 3,000-foot tether at 27 kHz. The corona onset voltage is inversely related to the tether wire diameter. The diameter of the tether wire is limited by the weight, volume, breaking strength and reeling problems. A tether diameter of 0.578 inches was selected with a weight of 119 pounds per 1,000 feet and breaking strength of 9,200 pounds.

At the antenna base, the voltage is a function of tether length (antenna height). Figure 6 shows the antenna base voltage as a function of tether length and frequency. The maximum base voltage is limited by corona at about 70 kV for a 0.5-inch-diameter antenna.

From the previous parametric curves, Figure 7 shows the estimated maximum radiated power without corona.

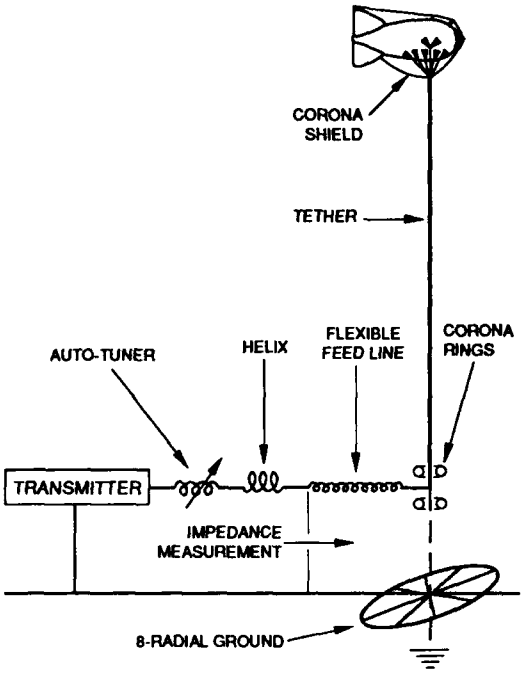

Figure 4. Electrical Pictorial Schematic of the TAVT System

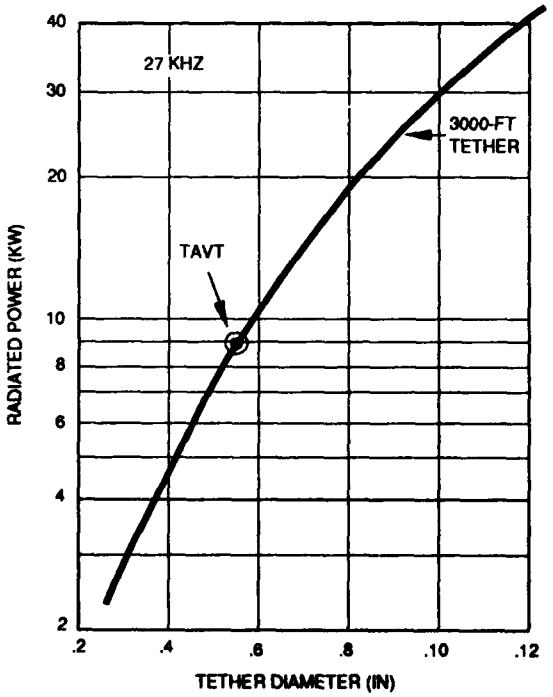

Figure 5. Effect of Antenna Wire Diameter on Radiated Power

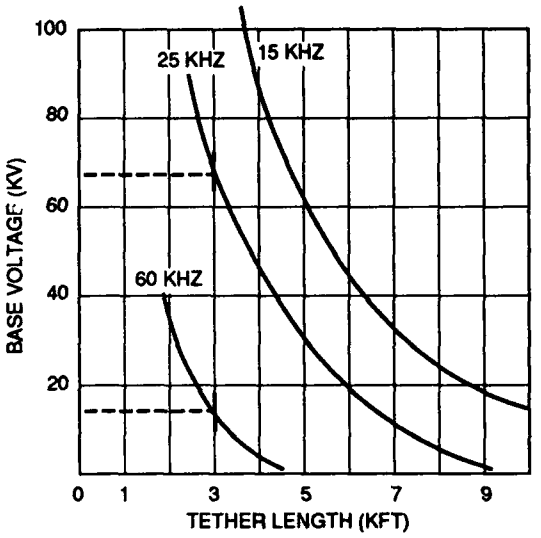

Figure 6. Antenna Base Voltage vs. Tether Length (Antenna Height) and Frequency

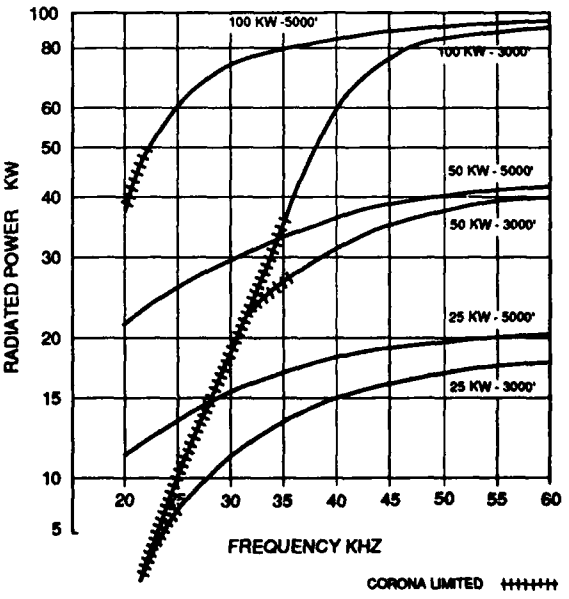

Figure 7. Estimated Maximum Radiated Power Without Corona

The tether design utilizes Kevlar as the strength member. Surrounding the Kevlar are the inner and outer metal coaxial braids insulated from one another electrically to allow transmission of 400 Hz aerostat power supplied in the coaxial mode for valves, blowers and all airborne power. The two metal braids, in parallel, also conduct the antenna VLF/LF current. Each braid is relatively loosely wound and they spiral in opposite directions so that half of the antenna current flows in each braid. Also included in the tether are two fiber optic cables for telemetering aerostat status information (e.g., pressure).

The radiation efficiency is equal to the radiation resistance divided by the sum of the radiation resistance, antenna wire resistance, tuning coil resistance and the ground system resistance. In selecting the design for the ground system, calculations were to determine the ground resistance as a function of radial distance and the number of radials. At a 160-foot radial distance, the ground system resistances are 2.2 ohms for 4 radials, 1.95 ohms for 8 radials, and 1.3 ohms for 16 radials with ground conductivity of 0.004 mho/meter, antenna height of 3,000 feet and a frequency of 27 kHz. Doubling the number of radials from 8 to 16 only increases the radiation efficiency by 3 percent. Thus, eight radials, each 160 feet in length, were selected as the ground system along with a 150 x 6 foot steel wire mesh ground screen underneath the mooring platform. The radials are connected by a circumference wire which has ground rods every 15 degrees and at the antenna base tying all radials and the ground screen together.

For the 3,000-foot antenna and the selected tether diameter and ground system, Figure 8 shows the base reactance and system bandwidth. Figure 9 shows the maximum radiated power for a 25 kW transmitter as a function of antenna height. Figure 10 shows the antenna bandwidth as a function of antenna height.

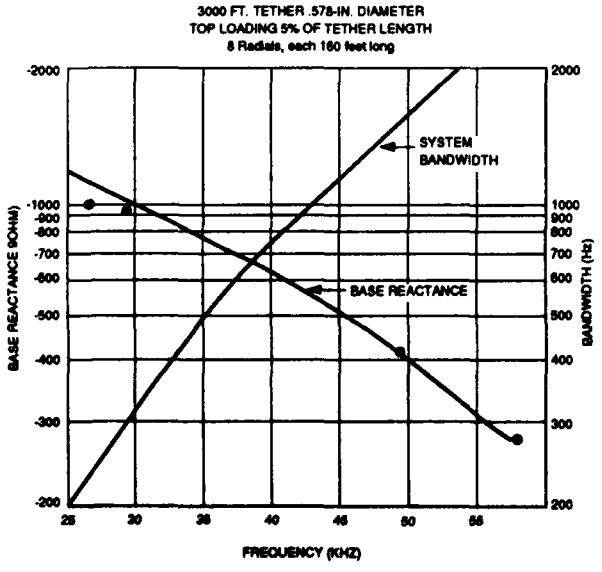

Figure 8. Base Reactance and System Bandwidt

3.3 PROPAGATION PERFORMANCE

For each TAVT system design, the radiation efficiency was calculated for the frequency range of 15-60 kHz. Then with transmitter powers of 25, 50, and 100 kW, the effective radiated power (ERP) was calculated. The ERP was then used in the Segmented Waveguide model[4] developed at the Naval Ocean Systems Center. Figure 11 shows typical range versus frequency curves for three of the potential nine combinations of antenna heights and transmitter power. These curves were generated for a typical submarine VLF receiver and with one of the MEECN modulation modes.

For connectivity to a submarine operating area, there are two major factors in propagation performance: sea water penetration and enough bandwidth to support the anti-jam modulations (MEECN Modes 8 and 9). Table 3 shows the operating frequency range for three antenna heights. The lower frequency for MEECN Mode 15 is determined by the corona limit. The lower frequency for MEECN Mode 9 is determined by the bandwidth requirement. The upper frequency for the 5,000-foot antenna is determined by the

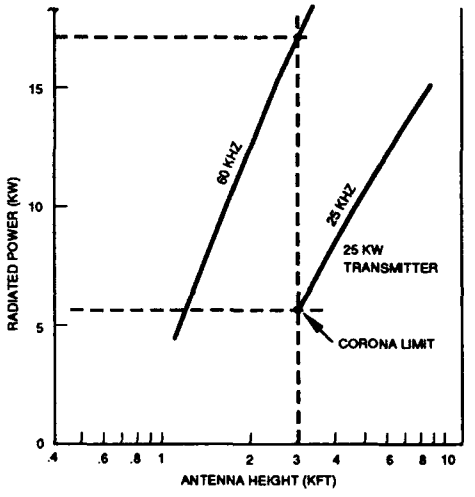

Figure 9. Antenna Heigfht vs. Maximum Radiated Power

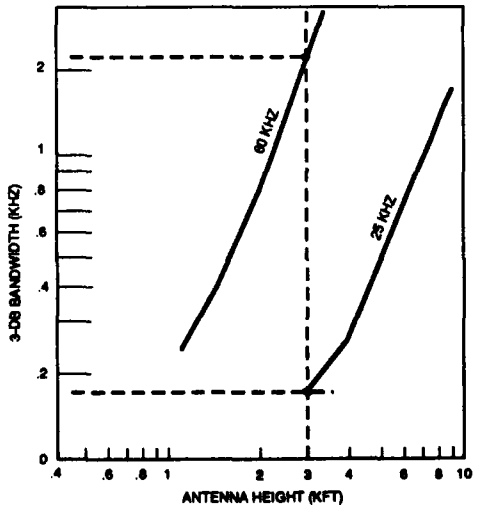

Figure 10. Antenna Height vs. Antenna Bandwidth

point where the antenna impedance transitions from capacitive to inductive (quarter wavelength).

Table 3. MEECN Modulation Mode Operating Frequency Ranges

Antenna Height (in feet)	MEECN Mode Frequency Ranges in kHz		
	15	8	9
3,000	25 - 82	25 - 82	35 - 82
4,000	20 - 61	20 - 61	29 - 61
5,000	15 - 49	15 - 49	24 - 49

3.4 OTHER FACTORS

Since survivability was the major design consideration and survivability is achieved by moving within the enemy's intelligence and targeting time, it was determined that the maximum aerostat size that could be designed for quick over-the-road transportability was 100,000 cubic feet. The upper bound on the aerostat size was thus established.

Based upon the actual procurement and operating costs of a 25,000-cubic-foot aerostat, the procurement cost, ten-year life cycle cost, fuel and helium cost, and personnel expenditures were determined for the three postulated missions and three aerostat sizes. Figure 12 shows the procurement cost for the most demanding mission using a 100-kW transmitter.

Figure 13 shows the required time for deploying a TAVT system after a move as a function of aerostat size.

In calculating the ten-year life cycle cost, the major differences in operating costs were the added logistics cost associated with extra personnel for handling a larger aerostat and the added extra cost of the helium and helium transport. For a 180-day mission that included 12 moves of 200 miles each, the relative increase in life cycle cost over the 3,000-foot TAVT system is 13 percent for the 5,000-foot TAVT system and 44 percent for the 7,500-foot TAVT system.

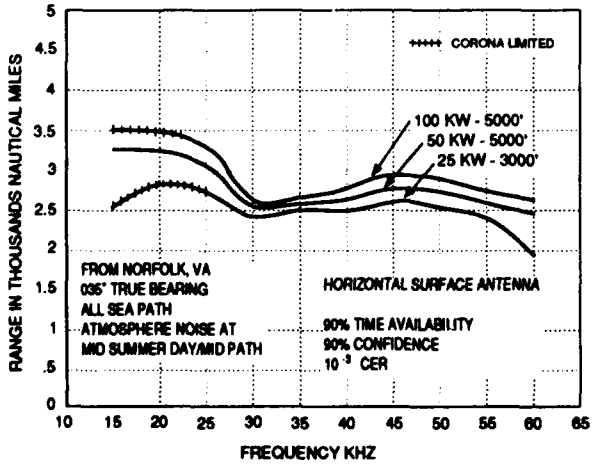

Figure 11. Estimated Range vs. Frequency Without Corona

4. CONCLUSIONS

The tradeoff analyses and the successful demonstration of a TAVT system with a 3,000-foot. antenna have shown that design, development and operational risks have been successfully addressed in pointing toward the optimum design for reconstituting VLF/LF communications to the submarines.

The recommended design was a 50,000-cubic foot aerostat with a 5,000-foot tether. The justification for the decision was based on the following rationale:

- 50,000-cubic foot aerostats have been built and flown in support of other missions. The modifications to the mooring system, tether and ground system over that demonstrated with the 3,000-foot TAVT would be small.
- The increase in bandwidth and the avoidance of corona at the lower frequencies allow the TAVT system to use anti-jam modulations for greater area coverage.
- The 13 percent increase in cost over the 3,000-foot TAVT is worth the added flexibility of using higher power transmitters and operating at lower frequencies.

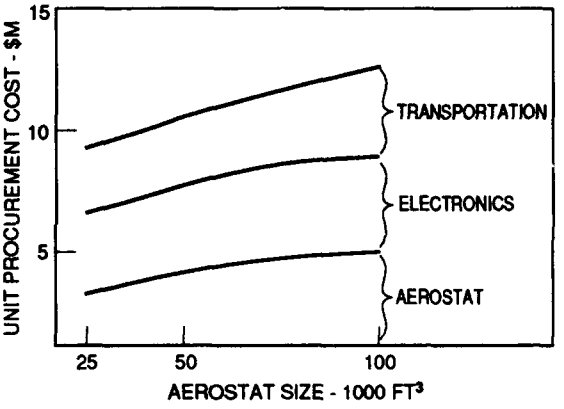

Figure 12. Unit Procurement Cost for A Typical Mission

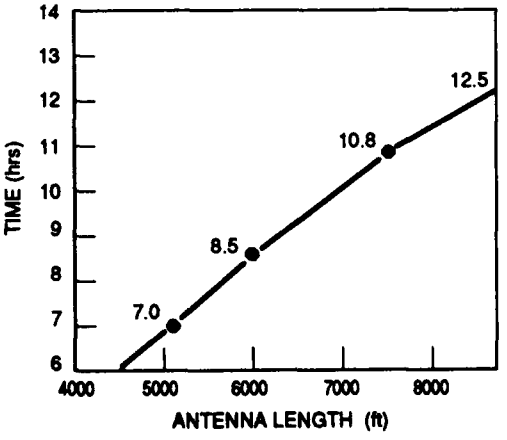

Figure 13. Required Time for Deployment

- No substantial difference exists in the vulnerability and operational concepts to increase survivability of a 5,000-foot TAVT system compared with a 3,000-foot system.
- The added gain of the 7,500-foot TAVT system in coverage area and flexibility (e.g., smaller grounding system) is not worth the added cost

5. REFERENCES

1. General Electric, "Reconstituted VLF Communications Program, Tethered Aerostat Parametric Analysis," 30 September 1981.

2. Westinghouse Electric Corporation, "Tethered Aerostat Antenna Program (TAAP) System Demonstration Model," AFGL-TR-88-0320, 31 October 1988.

3. Science Applications International Corporation, "Tethered Aerostat VLF/LF Transmitter (TAVT) System Analysis," September 1987.

4. Ferguson, J.A. and Snyder, F.P., "The Segmented Waveguide Program for Long Wavelength Propagation Calculations," NOSC TD 1071, April 1987.

VIABILITY ASSESSMENT FOR RELIABLE LONG-WAVE COMMUNICATION LINKS

T. S. Cory, P. E., Consultant
T. R. Holzheimer, Staff Engineer
E-Systems, Greenville Division
Greenville, Texas U.S.A.

SUMMARY

The success of Omega radionavigation suggests that highly reliable global communications are possible over diverse links to arbitrary receive locations at longwave frequencies. A model "TERNOISE" was generated and validated against existing models and with available noise data sets. The potential of such links, using the available TERNOISE model and available transmit assets, is confirmed by applying the accepted statistical methods of C.C.I.R Report 322-2 to several operational scenarios.[6] This investigation has generated the first known requirement for arbitrary land-based receive sites at extremely long distances. Emphasis is on inland ground-based receivers in low-latitude and equatorial regions which may be near noise (local storm) centers. Optimum frequencies for such inland links are expected to be about 7 kHz as opposed to greater than 20 kHz over seawater. Time availabilities of 90% for 50% of hours are expected out to ranges of 9000 km at a frequency of 24 kHz for the highest power stations, to 6000 km at 10 kHz for Omega stations, supporting data transfer rates of 25-50 bits per second at a bit error rate of 10^-3. This says that the frequency of operation must be judiciously picked and that there is a difference between a path purely over seawater and a path over land. Several available transmit sites were investigated. The existing high power transmit sites are called type 1 and the Omega radio-navigation transmit sites are called type 2 sites. The type 1 transmit sites have approximately 13 to 14 dB higher ERP than type 2 stations. However, the type 2 stations are spaced globally and can be picked up at essentially any point on the globe. This results in the possibility of coordinating type 2 station use and usage of multiple transmit sites (i.e. arraying). Data rates on the order of 50 baud are possible for type 1 sites and 5 to 25 baud for type 2 sites. This has to do with the fact that type 1 sites are typically 4 channel MSK having a large efficiency-bandwidth product while type 2 sites have a smaller efficiency-bandwidth product. The real limiting item is the antenna bandwidth which is typically no greater than 200 Hz for the various transmit sites. Predicted BER of 10^-6 are average with 10^-3 being the maximum. These availabilities convert to near-perfect receive S/No performance at lower 2.5-5 BPS rates while maintaining a 3 dB margin for forward error correction and a 6 dB contingency for noise uncertainty. The reference value for MSK for a non-fading signal is 14 dB. The available margin gained by processing, error correction, available bandwidths, etc. is approximately 21.6 dB. Analyses show that these numbers are conservative, resulting in estimates of error occurrence at 10^-3 BER having a period of at least 33.3 minutes.

LIST OF SYMBOLS

A	amplitude of incoherent wavehop sum
APD	amplitude probability distribution
BER	bit error rate
BPS	data transfer rate in bits/second
E_b/N_o	signal energy per bit/noise density
ERP	effective radiated power
Fa	received noise figure in dB above KT
FSK	frequency shift keying
KT	thermal noise power density; temperature in degrees Kelvin-Boltzmann's constant
FkHz	frequency in kilohertz
Ld	log deviation of received noise in dB below Fa
m	median received signal field derived from incoherent sum of wavehops
MSK	minimum-shift keying modulation
Ne	electron density
PSK	phase shift keying
S/No	signal-power/noise-power in bandwidth equalling the signalling rate
TE	transverse electric
TM	transverse magnetic
v	collision frequency
Vd	voltage deviation

INTRODUCTION

Traditional longwave VLF links have been characterized and designed for communication over seawater to ships at sea. Present Independent Research and Development

activities in the longwave community have emphasized high-latitude links, often to airborne platforms where both TE and TM modes are possible and of interest. The investigation underlying this paper is concerned with the viability of highly reliable long distance and geographically distributed ground-to-ground links to inland low-latitude regions. The concept is that of using frequencies in the ELF and/or VLF regions that exhibit low-loss, stable, non-fading signal propagation to extremely long ranges and that are relatively immune to man-made environmental disturbances; hence, very reliable. A requirement was to compute system link reliability on a statistical basis as a measure of viability. Because of the somewhat different geographic and operational emphasis involved, and the range of frequencies available from various transmit platforms, the initial objective was to characterize the propagation over a wide range of frequencies from ELF through VLF. This was done by combining the best available noise data and available signal propagation models so that signal-to-noise performance could be evaluated. Obtaining piecewise physical significance from the modeling process provided a necessary understanding of the communication link. The major deterrent to reliable communications is noise caused by propagation of lightning flash energy; thus, the noise uncertainty is due to storms and particularly the proximity of the receive site to major storm centers. The reliability goal was chosen to be a BER of 10^-4 90% of the time for 90% of the hours referred to maximum signalling rates of 25 or 50 Hz. The minimum predicted performance for which links are viable was chosen to be a BER of 10^-3 90% of the time for 50% of the hours. The minimum reliability criteria converts to essentially perfect reliability for data transfer rates of the order of 1 Hz.

Although airborne platforms operating into end-fed resonant antennas have the capability of handling raw data throughput exceeding 1000 Hz, ground station instantaneous bandwidths are limited to approximately 100 Hz. For a given transmitting antenna, the instantaneous bandwidth varies inversely with the fourth power of frequency(and the cubed power of height). Without considering more detail, the minimum 3-dB loaded bandwidth was initially chosen to be 20-25 Hz, so that a well-matched transmitter could support a minimum signalling rate of 10 Hz when employing a 1-chip/Hz modulation technique such as MSK or quaternary PSK.

DESCRIPTION OF RESOURCES

A skywave and groundwave model were developed. The groundwave model employed the rigorous residue series of Bremmer(underlying the C.C.I.R. Rec. 368 data) along with Millington's semi-empirical method for segmented mixed paths.[1, 7, 20] The skywave calculation employed a 44-term reflective wavehop model, after Bremmer, that was calibrated with measured layer heights from Brazil by Klemetti, and the ionospheric coefficients taken from the LF module of the Communication Assessment Program (CAP) which, in turn, were obtained from the Weapons Effects on D-Region Communications (WEDCOM) model.[3, 19] The ground conductivities were taken from C.C.I.R. Report 717 for frequencies below 30 KHz.[8] This model was selected for ease of personal computer (PC) implementation and the high degree of physical insight associated with the individual wave hops. Long range computations above waveguide cutoff employed the incoherent addition of hops. Below cutoff and/or at short range, computations were made as the sum of both coherent and incoherent hops, appropriate to the particular situation being evaluated. At long range, and appropriate to many hops, the method of Millington was again applied for mixed land-sea paths. The wavehop model is useable for hop-by-hop application of the geographic distribution of ground and ionospheric constituents.

The groundwave model was validated by comparison with C.C.I.R. Rec. 368, data which was computed using the same algorithm for homogeneous path conductivity. The skywave model was validated by comparison with NRL Report 6663 at a frequency of 12 KHz.[2] This comparison is illustrated in Figure 29-1, showing the "sawtooth" hop-by-hop ionospheric focusing given by this type of model over sea water. A wavehop range curve over soil is smooth.

The noise evaluation compared data taken from C.C.I.R. Report 322-2, low noise prediction (LNP) model, latest Stanford data, and a model, TERNOISE, developed by the authors. The TERNOISE model is based on Report 322-2 and augmented with NBS(now National Institute for Standards and Technology(NIST)) Monograph 23 APDs, using Report 322-2 statistical methods.[9] The predictions of TERNOISE below 10 Khz are linear extrapolations. The various noise data sets as applicable to Japan are illustrated in Figure 29-2.[16, 17] A particular link scenario application is illustrated in Figure 29-3.

The noise-only statistics were taken to represent the signal/noise process. The error introduced by this assumption is approximately one dB in the worst case; and therefore, the signal was taken to be deterministic.

TECHNICAL APPROACH

Evaluating the links of interest, the levels of signal and noise at the receive site were separately computed and then the energy density(S/No) was computed. This ratio was compared to the ratio required for BER's of either 10^-3 or 10^-4 for MSK, as shown in Figure 29-4. The margins were then used with the noise exceedance statistics to produce time availability. The median signal, determined at long range by the incoherent wavehop sum, is related to this sum by

median signal = m = 0.833A, where

m is the 50% value of the field as defined in the Madrid International Radio Conference in 1933.

The program TERNOISE was used to compute the noise levels and statistical variations of S/No. TERNOISE computes selected seasonal and diurnal average noise values in order to reduce the number of cases to consider to five; Seasonal Median, Seasonal Day, Seasonal Night, Winter Day, and Summer Night. In particular, the Seasonal Median is the arithmetic dB average of the C.C.I.R. Winter Day and Summer Night values.

The process used in Report 322-2 is invoked for reducing the four-hour block averages to hourly and short-term statistics. Upper decile deviations from the block median data are matched up with seasonal/diurnal measures, as shown in Figure 29-5. Using the lognormal graph, defined by median and upper decile values, the predicted hourly levels are found. For short-term noise, four particular APD's from Monograph 23 are used which are; Rayleigh, Vd = 4 and Ld = 10.5, Vd = 9 and Ld = 16, and Vd = 16 and Ld=25, as illustrated in Figure 29-6. Using these APD's and the variations of Vd and Ld with frequency for bounding winter day and summer night extremes, given in Figure 23 of Monograph 23, an algorithm computes the particular APD's and margins at particular frequencies for these bounding extremes. Then the margins appropriate for the five defined seasonal/diurnal conditions are determined in the same manner as the block averages. These margins are added to the median to give the expectation for the Instantaneous noise envelope. The margins used by the program to convert Fa into instantaneous noise figure are given in Figure 29-7. An example predicted curve set from TERNOISE for 50% of the time for 50% of the hours is given in Figure 29-8.

The predicted noise ignores the possible dip between two and four KHz due to waveguide cutoff. From a noise viewpoint, this dip may be very deep and sharp or it may be minimal, depending on proximity to, and the number of, noise sources involved. A single predominant source at long range produces the sharpest null. A close source propagating predominantly groundwave, or a number of uniformly distributed sources, minimize the null. Underground data taken by NIST from ELF through low LF frequencies shows a slight tendency at nulling, even in very quiet areas of coal mines. In fact, the median mine noise defined from these tests was taken as monotonically varying.

Of some engineering interest, sets of S/No curves were produced for homogeneous seawater and average soil for median and decile cases referred to seasonal median noise in Washington, D.C. These data sets, parametric in range and frequency, are given in Figures 29-9 through 29-12 for an assumed 1-kilowatt ERP.

RESULTS:

The propagation models were validated, depending on the areas of uncertainty of the data, and on the data available. The comparisons included the following:

- 12 kHz validation against data from NRL Report 6663
- 30 kHz validation against the CAP LF model
- ELF validation of the extrapolated TERNOISE data against LNP model at a 9000 km receive location
- ELF validation of the extrapolated TERNOISE data against LNP model and Stanford data at a receive location in Kochi, Japan

A comparison of wavehop calculations vs range with published data in NRL report 6663 for ground-based terminals over an otherwise undefined seawater path was performed at 12 kHz.

The 12 kHz validation was performed, with the values of 0.00045 mho/m at 69 km and 0.00035 mho/m at 86 km. These conductivity values were used in the model, but the physical heights were adjusted to the 70 km and 90 km respective day and night values used in the NRL 6663 report.

The agreement between the methods is excellent at a nominal range of 9000 km, especially during the day.

The wavehop-computed fieldstrength data over seawater exhibits a periodic shape. Each time the curve suddenly drops corresponds to another "hop" falling beyond line-of-sight. The cusp just before each drop is created by the convergence coefficient of the predominant hop-to-be-dropped which is at the lowest near-horizontal incident/takeoff angles, where the energy spreads out so much along the path direction that it is focused. Fieldstrength curves over land, calculated by the model, do not exhibit this periodic behavior.

Next, a comparison was made of wavehop fieldstrength computations versus range over the same path with the CAP LF module at it's limiting frequency of 30 kHz and out to it's limiting range of 8000 km. The wavehop computation employs a two-segment sea-land computation according to Millington's method, using an average ground conductivity of about 5 millimhos/meter.

The particular wavehop calculations comprising this data were made using an ionospheric conductivity of 0.000272 mho/m at a height of 68 km during the day, and a conductivity of 0.000136 mho/m during the night, which is appropriate for a height of 83 km. This data is representative of measurements made in Brazil prior to data reported by Klemetti.

The agreement between models is excellent at long range, converging as the range approaches 8000 km. The CAP data appears to have some nulls and/or periodic variations in range, that have not previously been observed by the authors. The agreement appears to be within about 2 dB at the ranges of interest.

The third comparison was of the output of the LNP noise prediction model versus TERNOISE. Only block averages of the noise are compared. The seasonal/diurnal noise values represented by the individual data sets is Summer Night, the noisiest case. The LNP model was cycled through January time blocks(summer in the southern hemisphere) until the highest level was found (which corresponded to 0841 local time) before making the frequency computation run. The validation phase consisted of confirming the continued rise of noise with decreasing frequency into the ELF region as predicted by the TERNOISE linear downward extrapolation. The TERNOISE model approximates the C.C.I.R. data down to 10 kHz, and is self-validating against the measured data available and

applicable in the low- and mid-latitude regions. Both of these data sets ignore the cutoff region.

The agreement is seen to be excellent at the extremes in frequency(low ELF and VLF above about 17 kHz). The agreement is excellent at all frequencies representing Type 1 transmit station operation. The biggest difference is the rising LNP-predicted noise levels as the frequency is decreased from about 17 kHz to the 8 kHz lower LNP VLF limit. In particular, at 10 kHz, the LNP-predicted level is 11 dB above the C.C.I.R.level, at about 38 dBuV/m*Hz^0.5 . At the average location, the time average Omega station signal level is expected to be in the 29 - 32 dBuV/m range which, suggests possible corruption in the noise data.

Lastly, data comparing TERNOISE and LNP models with measured Stanford University data at Kochi, Japan, taken again for the noisiest Summer Night noise values was investigated. The LNP search produced the highest block average value corresponding to July at 0848 local time.

Comparing data vs frequency given in Figure 29-2 shows agreement between all data sets above approximately 17 kHz, with the maximum delta being about 2 dB in this frequency region. The Stanford data bridges the cutoff region, showing different minimum frequencies for day and night. The low-ELF agreement between the model calculations is not exact, but it does show that we have adequate built-in conservatism in our model. The important comparison is at approximately 10 kHz, noting that one of the test frequencies is at 10.2 KHz which is the prime Omega frequency. Although it may be feasible (looking at tape recordings) to eliminate the effect of a strong local station like the one at Tsushima Japan, the signals from the remote Omega stations may appear like noise. The 10.2 kHz noise level happens to be about 29 dBuV/m*Hz^0.5, so that the measured noise level and the expected average remote Omega signal level are nearly the same. Additionally, the LNP-predicted noise level is 5 dB above the Stanford results, and roughly another 5 dB above the C.C.I.R.-based predicted value.

A brief outline of the link analysis calculation is given in Table 29-1

TABLE 29-1
LINK BUDGET FORMAT SUMMARY

- o Transmit Effective Radiated Power(ERP) dBk (with respect to 1 kw) (includes antenna pattern gain and RFD losses)
- o Signal/Noise-density(S/No), for 1 kw dB(1-Hz BW)
- o Noise Bandwidth (_____) dB
- o Signal/Noise Ratio(S/N) at receiver dB
  S/N required::
  14 dB for 10^-3 BER
  20 dB for 10^-4 BER
- o Binary Error Rate(BER) achieved

LINK ANALYSIS PARAMETERS

The day and night time layer heights of 69 and 86 km respectively are chosen based on data from Klemetti.

The atmospheric constituents of electron density and collision frequency taken from the CAP(i.e. WEDCOM) data base, are given in Figure 29-13.

Ionospheric conductivity data computed from the atmospheric constituents of Figure 29-13 are given in Figure 29-14.

Ground conductivity maps from C.C.I.R. Report 717 are used. There are no listed conductivities for land greater than 10 millimhos/meter, or less than 0.1 millimhos/meter. The majority minimum is about 1 millimho/meter. Other conductivity maps for Continental United States (CONUS) are available, and represent surface conductivities appropriate for higher frequencies where the skin depths are shallow, with surface conductivities approximately a factor of 3 greater than those shown in Report 717.

The modulation technique of choice at longwave frequencies is MSK, which is a essentially a four-phase one chip/bit modulation system having the most selective power spectral density, with sidebands falling off at the rate of 50 dB/decade. MSK is a coherent modulation type which is phase-continuous through the first derivative. It can be viewed either as FSK or PSK. MSK, for example, is FSK with a modulation index of 0.5. It is also two quadrature-combined binary PSK signals, with the same carrier frequency, but 90-degrees apart in phase. In the PSK analogy, the bits from the input data stream are alternated between the two channels, so each channel operates at half the total bit rate. Further signal processing such as using a Non-Return-to-Zero(NRZ) band-limited base-band signalling scheme, such as Manchester encoding, will further improve the actual bandwidth occupancy of the signal.

The performance of a modulation scheme depends on the noise statistics involved. There is a substantial difference between gaussian(white) noise and atmospheric noise which is impulsive. The actual Vd of the atmospheric noise makes only a second-order difference in the noise statistics. At higher frequencies, the dispersive effects of fading influence the modulation performance where the standard case is flat-flat fading(flat in both time and frequency). At VLF, the signal is essentially non-fading and the error rate curve is that of a non-fading signal in atmospheric noise.

TYPE 1 TRANSMISSION ANALYSIS

Analytical results are presented for two frequencies available at the type 1 transmit sites for median(50% hours, 50% time) and for decile (50% hours, 90% time) conditions representing average day(Seasonal Day noise values) and average night(Seasonal Night noise values) conditions. Additionally, the frequency constraint is removed and the performance is analyzed for a constant

transmit ERP of 24.8 dBk, for several seasonal/diurnal and statistical cases. The frequency analysis uses incoherent hop addition at all frequencies in the signal calculation, and ignores cutoff for both signal and noise phenomena. The fixed frequency link analysis is presented in Table 29-2.

TABLE 29-2
9000 km TYPE 1 DETAILED LINK ANALYSIS

o Transmit Carrier Power ref+33.0 dBk for 200 baud
Transmit ERP/Channel +24.8 dBk for 50 baud

o Median S/No for 1 kw +24.5 dB avg day @ 17.8 kHz
+23.0 dB avg night @ 17.8 kHz
+23.0 dB avg day @ 24.0 kHz
+20.8 dB avg night @ 24.0 kHz

o Noise Bandwidth -17.0 dB for 50 Hz

o Margin for 50% Hours, 90% Time
-13.8 dB avg day @ 17.8 kHz
-13.0 dB avg night @ 17.8 kHz
-13.4 dB avg day @ 24.0 kHz
-12.9 dB avg night @ 24.0 kHz

o S/N at Receiver 50% Hours, 90% Time

ref. median 32.3 dB	18.5 dB avg day @ 17.8 kHz
30.8 dB	18.8 dB avg night @ 17.8 kHz
30.8 dB	17.4 dB avg day @ 24.0 kHz
28.6 dB	15.6 dB avg night @ 24.0 kHz

o S/N Required (see Figure 27-4)
ref. 14.0 dB min for 10^-3 BER

o BER Achieved 50% hours, 90% Time

ref. median >10^-7	2.0*10^-4 avg day @ 17.8 kHz
2.0*10^-7	2.8*10^-4 avg night @ 17.8 kHz
2.0*10^-7	3.2*10^-4 avg day @ 24.0 kHz
1.2*10^-6	5.9*10^-4 avg night @ 24.0 kHz

BER's for an average day and average night are shown together with Summer Night data for decile time availability in Figure 29-15.

TYPE 2 TRANSMISSION ANALYSIS

The type 2 reception under Seasonal Median noise conditions is the most representative situation, world wide. A 25 Hz bandwidth (14 dBHz) and a minimum 10^-3 BER(14 dB S/N), require a margin above S/No of 28 dB. This performance level is achieved out to a range of 6000 to 7500 km for 50% of hours, 90% of time. These range profiles suggest possible reception from either 2 or 3 Type 2 sites at any location in the world. The exception to this is if one of the great circle paths does not have a majority of its path over seawater.

Analysis shows that five or six type 2 stations may be usable at any location for ranges out to 13,000 km over seawater. This analytical conclusion is in agreement with previous work.

The S/No curves for median and decile noise conditions, with a one-kilowatt ERP, referred to Seasonal Median, for mixed data link over a majority seawater and then over land, are presented in Figure 29-16. The decibel rate of fall-off on either side of the optimum frequency, of approximately 8 KHz, is significantly less than over a link having a long land segment terminating its path into the receive location.

Figure 29-17 shows the S/No prediction for a transpolar path with the majority of its path being over land(or ice) and passing over the north pole. There is a minimum occurring in the 6000 - 7000 km range that signifies the effect of the poor ground conductivity. The negative S/No dB's and the field strengths of less than a microvolt per meter above the minimum signify the unusability of the path for communications. As the wavehop propagation program sums the modes incoherently, the minimum is due to the reflection process on an individual mode basis. The minimum is due to the Brewster angle in which impinging waves are transmitted into the ground with minimal reflection.

RELATIONSHIP OF CALCULATED NOISE STATISTICS TO MESSAGE RELIABILTY

The link calculations have been made assuming data transfer at the maximum signalling rates for both broadcast and hypothetical Omega communications. The maximum rate of 50 Hz for broadcast is the modem per-channel clock rate, and the assumption is that the link would be assigned one such channel. The assumed maximum rate of 25 Hz for Omega communications is taken equal to the available antenna bandwidth. Such communications must be compatible with normal Omega reception. Use of a high clock rate for such communications may minimize interference with this normal narrow-band reception.

Actual data transfer rates for high reliability will be lower than 50 or 25 Hz. If transmission is at higher rates, then rate reduction must be accomplished with signal processing. The signal-to-noise ratio enhancement and forward error correction capability made possible by rate reduction (narrower bandwidth), is called processing gain. The forward error correction portion of the available processing gain, taken to be 3 dB, is that to correct a specified maximum BER, taken to be 10^-2, to essentially perfect copy. The remaining processing gain is applied as a margin to increase the time availability of the link.

The link data transfer rates were arbitrarily chosen to be of the order of one (1) Hz. These rates are assumed to be near the probable lower limit of acceptability for communications and are also, roughly the same as the equivalent bandwidth for normal Omega reception. Specified rates of 0.5 - 2.5 Hz for broadcast and 0.25 - 1.25 Hz for Omega were assumed, worst case. The 5:1 (or 7 dB) ranges for each type transmit site was assumed, as a margin, to accommodate uncertainty in short-term noise statistics in low-latitude geographic areas. The margin for uncertainty of the C.C.I.R. noise prediction is 6 dB. The additional 1-dB accommodated the error in using only the noise statistics for the signal-to-noise process.

The link data transfer rates correspond to nominal 20:1 bandwidth reduction plus an additional 5:1 bandwidth reduction to accommodate uncertainty, for a total worst case bandwidth reduction of 100:1. The corresponding reduction in mean-square power or rms voltage at the detector is greater than the bandwidth reduction because of the impulsive nature of the noise. The statistical margin above median (50% of the time for 50% of the hours) for high exceedence probabilities is proportional to the mean-square power. The reduction in rms voltage as a function of bandwidth change is given in Figure 26 of C.C.I.R. Report 322-2. For a TERNOISE assumed Vd of 12 dB in a bandwidth equal to the signalling rate and a 20:1 bandwidth reduction, this margin is reduced an additional 8.3 dB beyond the 13 dB linear bandwidth change. Allocating 1-dB to an imperfect detector (relative to ideal), the required margin will be reduced an additional 7.3 dB. For 100:1 bandwidth reduction, the margin is reduced an additional 9.6 dB beyond the 13 dB linear bandwidth change, or a net margin reduction of 8.6 dB.

Statistical communications systems performance estimates are often related to the way in which supporting link signal and noise data have historically been collected. Terms used include "time availability," "reliability," "service probability," "location variability," and "percent confidence." At VLF frequencies, these estimates are easier to understand because the signal is non-fading, there is essentially no location variability, and uncertainties are related only to the noise. The basis for measuring noise has been long-term averages, over several hours, of two or three statistics, rather than direct measurement of the amplitude probability distribution of the instantaneous noise envelope. As a result, separate long-term and short term margins must be applied. At VLF, hourly long-term averages equate to percent confidence that a short-term minute-by-minute time availability will be achieved.

The target link performance for this program is a BER of 10^-3 minimum 90% of the time for (with) 50% hours (confidence) referred to the maximum signalling (data clock) rates. This is approximately equal to perfect performance at the low rates, with excellent performance defined to be achieving a BER of 10^-3 or less 98.3% of the time for 99% of the hours, providing that a local lightning storm is not occurring at the time. Simply stated:

> If the computed BER is 10^-3 or better for 90% of the time for 50% of the hours at a data clock rate of 50 Hz (broadcast), of 25 Hz (Omega), this assures that the message will be received for a data transfer rate in the range of 0.5-to-2.5 Hz or 0.25-to-1.25 Hz respectively, providing that a lightning storm is not occurring at the time.

This results from the following:

The exclusion of 1% of the hours corresponds to an average of 1-hour/day of active lightning during an assumed three-month rainy season to represent the exclusion. The choice of 98.3% of the time is predicated on 1-minute per hour, the smallest unit of time for the minute-by-minute variations relative to the hourly variations. Thus, achieving the perfect reception condition must be possible using at least the slowest data transfer rate specified during the worst case seasonal and diurnal condition. Improved data transfer will be feasible during seasons and times of day other than Summer Night.

The comparison between high-rate and low-rate performance is illustrated in budget form as follows at a frequency of 10 kHz during the Summer Night referenced to the median 50% time during 50% hours condition:

(A) Required Margin for Near-Perfect Performance

98.3% time, 99% hour > median by	(+) 32.6 dB
90% time, 50% hours > median	(-) 12.6 dB
thus, 98.3% time, 99% hours > 90% time, 50% hours	20.0. dB

(B) Available Margin for Nominal 20:1 Rate Reduction

20:1 rate factor for processing gain	(+) 13.0 dB
allowance for imperfect detection	(-) 1.0 dB
excess margin for 20:1 rate reduction	(+) 8.3 dB
available margin for 20:1 bandwidth reduction	20.7 dB

(C) Available Margin for Maximum 100:1 Rate Reduction

100:1 rate factor for processing gain	(+) 20.0 dB
noise uncertainty	(-) 6.0 dB
error allowance for using only noise	(-) 1.0 dB
allowance for imperfect detection	(-) 1.0 dB
excess margin for 100:1 rate reduction	(+) 9.6 dB
available margin for 100:1: bandwidth reduction	21.6 dB

This is sufficient to accommodate the worst case over the low-rate range if error correction is not employed. Note that 10 kHz is the lowest frequency covered by the C.C.I.R. data base without extrapolation. These margins are referenced to an S/N of 14 dB, representing MSK for a non-fading signal in atmospheric noise in a bandwidth equal to the signalling rate (See figure 29-4).

These results are conservative for several reasons. At an uncorrected error rate of 10^-3 for the slowest broadcast data rate of 0.5 Hz, there is a predicted error every 2000 seconds, on average, which corresponds roughly to 250 message characters. This means that short messages could, in principle, be sent without error, however, good system design practice demands forward error correction. Using half-rate coding, the available margin above target would be reduced by 3 dB to 17 dB. The exclusion of local thunderstorms also reduces the required margins as well as protecting against the 1%-of-the-hours. In this situation, the use of the Seasonal Night noise measure is appropriate for the statistics relative to the median value, if the median noise delta of 8.1 dB between Summer Night and Seasonal Night is retained as representing worst case performance.

The Seasonal Night noise measure reduces the required margin form 20 to 18.6 dB.

Using the Seasonal Night variability above median, the available margin of 21.6 dB minus the required margin of 18.6 dB is 3 dB. This 3 dB is allocated for error detection and correction.

The results are still conservative because at a 10^-3 BER, the average period of error occurrence is 2000 seconds, or 33.3 minutes. However, there is still, 6 dB margin included in case the noise is up to 6 dB greater than the values used for calculation.

GENERAL CONSIDERATIONS

The process of signal reception in the VLF band is externally noise limited, with external noise figures greater than 140 dB below 30 kHz. Receive antennas may be pick-up probes rather than full-size antennas used for transmitting that are designed to optimize power gain or efficiency-bandwidth-product. The most important overall design consideration is sensitivity. Electrically small pickup probe antennas are required for portability, but must not be made too small or else the received noise will equal the internal noise of the receiver.

Because of the optimum frequency for S/No which is characteristic with land-based receive sites, there may not be much difference in performance between using frequencies ranging between 10 and 24 kHz. The 1/fourth-power-of-frequency is proportional to 1/height cubed which is proportional to n*BW for transmit antennas. Thus, operational considerations may govern the frequency selection, if resources over this large a frequency range are indeed available.

With respect to interference, the operating frequency should be as low as possible, consistent with an available ground-based station resource for transmitting. This makes deliberate interference very difficult, and renders interference virtually impossible because the interference installation would have to be fixed and could not be effectively implemented.

Signal processing, would not have to provide a margin for interference. Redundancy could be implemented for coding and to perform forward error detection and correction. At least 10 - 15 dB of processing gain may be achievable, and no more than 3 - 6 dB would be necessary for error detection and correction.

CONCLUSIONS

This paper illustrates the viability of reliable global communications at VLF as a consequence of the insight gained by performing link analyses vs frequency. The physical and economic reality of implementing these possibilities depends on the availability of transmit resources, possibly on a shared basis.

The low-latitude regions are those where the least VLF research and development has been applied, particularly in characterizing the noise. As noise is the most critical parameter in determining statistical communication performance at VLF, noise in typical low latitude and equatorial regions needs to be measured. Coincident with such noise measurements, communications performance over some link(s) terminating at the receive site should be measured. As low-latitude and equatorial regions are close to storm center "hot-spots", the rainy season (Summer Night) noise in such a location(s) should be measured as opportunities occur.

This investigation has predicted that the hypothesized VLF links will work, and that messages of prescribed quality will be received 90% of the time for 50% of the hours. These type of statistics in other frequency bands have a specific qualitative meaning. For example, a VHF/UHF link analysis predicting a given level of service 90% of the time for 90% of the hours means that the link is virtually certain to work all the time, and with some conservatism. The target design criteria for many such links is 90% of the time for 60% of the hours. When the propagation medium is even more variable, such as at HF, 90% of the hours is adequate for voice, but data circuits are often designed for 99%, or even 99.95%, of the hours. Thus, there is a question of just what these statistics mean at VLF. The authors' believe that at VLF, where location variability of signal is not a problem and signal stability itself is not a problem and the only statistical problem is noise, then 14 dB of margin above median may be viewed as either 99.9% of the hours and 50% of time or 50% of hours and 90% of time, but not both simultaneously. Also, when considering noise alone, the added S/No "delta" over gaussian of about 14 dB for a BER of 10^-4 provides additional margin. The incidence of instantaneous communication errors at VLF needs to be compared with statistical prediction measures, either by comparing measured communication link data with prediction analysis or by true link simulation.

Communication links have been investigated using existing transmit sites, and reliable links can be obtained over 6000 to 9000 km distances. This does require that the frequency of operation be judiciously picked. There is a difference between a path purely over sea water and/or over land. Analyses show that the choice of 24 KHz for sea water is appropriate, but that a path partially over land shows approximately 10 KHz as the optimum choice of frequency. This result occurs because of the altered propagation conditions caused by paths being over both sea water and land. However, it is also noted that a natural interference immunity exists at these frequencies and that the only noise that has major performance impacts are caused by lightning from localized storm centers.

This paper generates the first known requirements for arbitrary land-based receive sites at extremely long distances. The locations investigated included low-mid-latitude and equatorial receive sites. The continuous ELF/VLF frequency spectrum was evaluated for communications possibilities. Path characteristics were investigated which included combinations of sea water and land masses.

Recommended items for further investigation arise from the need for accurate minute-to-minute short term noise

statistics. These recommendations include complete link testing, making noise measurements near low latitude storm centers with the latest available hardware, performing VLF spectral characteristics, updating conductivity measurements.

Measurements of noise and existing signal levels for worst case in low latitude interior hotspots would help bound the VLF communication link performance.

REFERENCES

1. Bremmer, H., "Terrestrial Radio Waves, Theory of Propagation," Elsevier Publishing Company, Inc., 1949.

2. Brookes, C. Jr., "Theoretical VLF Multimode Propagation Predictions", NRL-6663, AD-663878, 1 December 1967.

3. "CAP Communications Assessment Program," Revisions 4.1, IBM Federal Systems Division, Arlington, VA, DCA Contract DDC100-84-C-0060, September 1986.

4. C.C.I.R. Rep 229-2, "Electrical Characteristics of the Surface of the Earth," C.C.I.R. XIII'th Plenary Assy, Vol.. V, Geneva 1974.

5. C.C.I.R. Rep 265-4, "Skywave Propagation at Frequencies Below 150 kHz With Particular Emphasis on Ionospheric Effects," C.C.I.R. XIV'th Plenary assy, 1978.

6. C.C.I.R. Rep 322-2, "Characteristics and Applications of Atmospheric Radio Noise Data, "International Telecommunications Union, Geneva 1983.

7. C.C.I.R. Rec. 368, "Ground Wave Propagation Curves for Frequencies Below 10 MHz," C.C.I.R. XIth Plenary Assembly, Geneva 1966.

8. C.C.I.R. Rep 717, "World Atlas of Ground Conductivities," C.C.I.R. XIV'th Plenary Assy, 1978.

9. Crichlow, W. G., et.al., "Amplitude Probability Distributions for Atmospheric Radio Noise," NBS Monograph 23, 4 November 1960.

10. Ferguson, J., "A Report on The NELC Integrated Prediction Program (PREDPROG)," NELC TN 1630, February 1970.

11. Ferguson, J. "Long Wave Propagation Model, " MILCOM Proc,. 1989, pp. 30.6.1-30.6.5.

12. Ferguson, J., "Integrated Propagation Prediction Simulator Software Base, NOSC TN 839, March 1980.

13. Ferguson, J., "The Segmented Waveguide Program for Long Wavelength Propagation Calculation," NOSC TD 1071, April 1987.

14. Ferguson, J., "WAVFLD: a Program to Compute Ionospheric Height Gain Functions and Field Strengths at VLF," NOSC TD 1192 November 1987.

15. Fine, H., "An effective Ground Conductivity Map for Continental United States," Proc. IRE 42, 1954, pg 1405.

16. Fraser-Smith, A. C., "Global Measurements of Low-Frequency Radio Noise," STAR Laboratory Stanford University, URSI, September 1989, Tokyo.

17. Fraser-Smith, A. C., "Measurements of ELF/VLF Radio Noise in Japan," STAR Laboratory, Stanford University, URSI September 1989, Tokyo.

18. Kirke, H. L., "Calculation of Ground-Wave Field Strength Over a Composite Land and Sea Path, Proc. IRE Vol. 96, May, 1949, pp 489-496.

19. Klemetti, W., "VLF/LF Reflection Properties of the Low Latitude Ionosphere," AFGL-TR-88-0034, February 1988.

20. Millington, G., "Ground-Wave Propagation Over an Inhomogeneous Smooth Earth," Proc. IEE (London) Part III, Vol. 96, January, 1949, pp. 53-64.

21. Spaulding, A. D., "Determination of Error Rates for Narrow-Band Communication of Binary-coded Messages in Atmospheric Radio Noise," communication, IEEE Trans. Comm. System 1963, p. 220.

22. Swanson, E. R., "Omega," Navigation, Vol. 18, No. 2,. Summer, 1971, pp 168-175.

23. Swanson, E. R., "VLF Timing: Conventional and Modern Techniques Including Omega," Proc. IEEE, Vol. 60, No. 5, May, 1972, pp. 540-551.

24. Ulander, H., "Technical Description of the Communications Assessment Program (CAP), Revision 3.0," IBM UD NC3-86-0003, Contract DCA100-84-C-0060 January 1986.

25. Wait, J. R. "Characteristics of the Earth-ionosphere Waveguide for VLF Radio Waves Nat. Bur. Stds. Tech. Note 300, 1964.

26. Warber, C, "Longwave Noise Prediction," Vol. 1, "Physical Basis of the Model," DNA-TR-90-224-V1, Contract DNA-001-87-C-0171, April 1991.

27. Warber, C., "Longwave Noise Prediction," Vol. 2, "User's Guide to the Computer Code LNP Version 1.1," DNA-TR-90-224-V1, Contract DNA-001-87-C-0171, September 1991.

28. Watt, A. D., "VLF Radio Engineering," Pergamon Press, New York 1967.

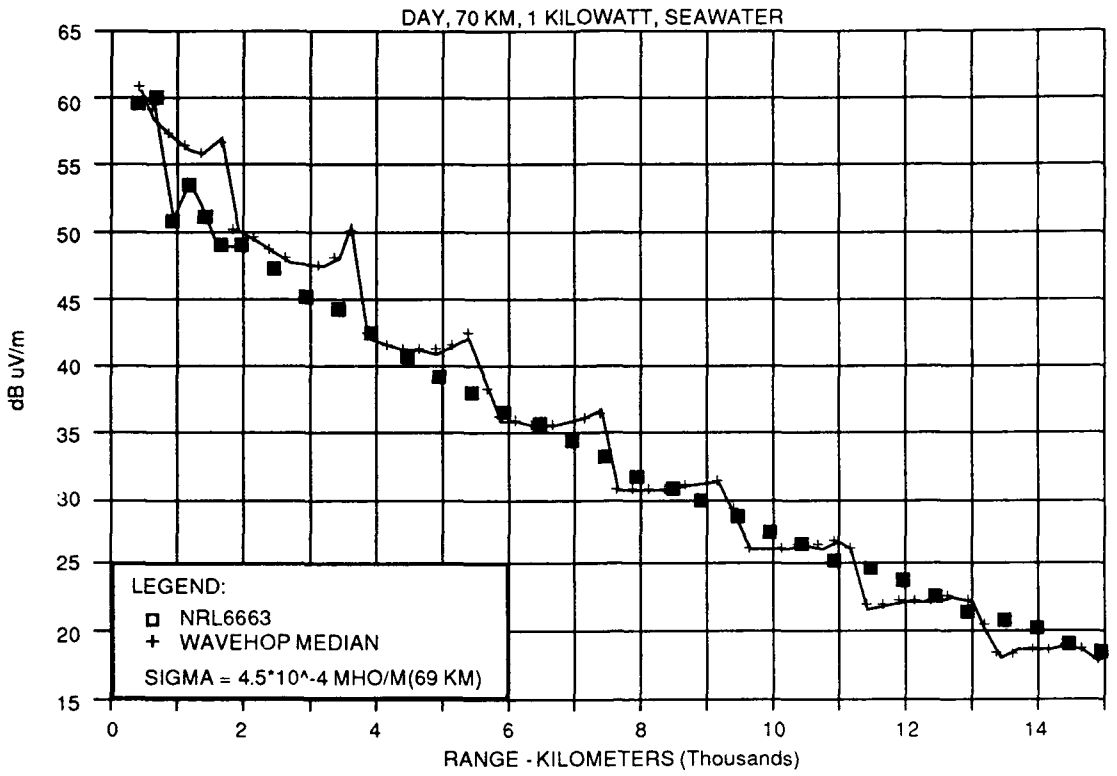

FIGURE 29-1. SKYWAVE FIELD STRENGTH AT 12 KHz

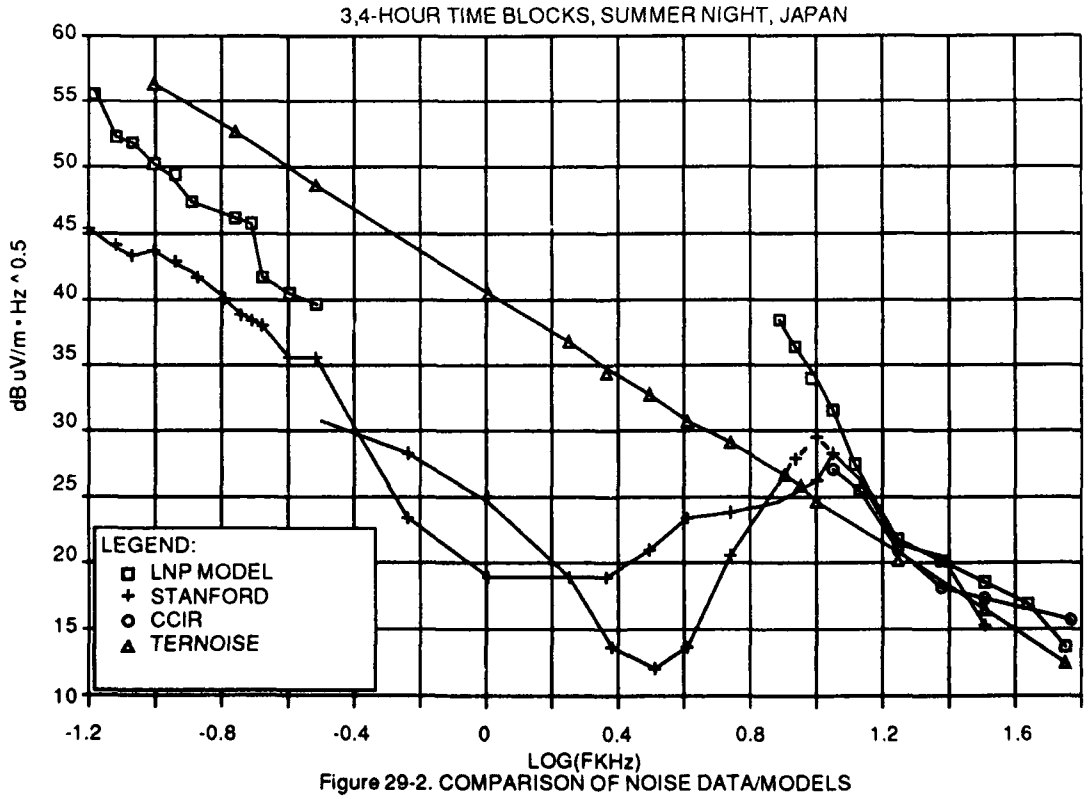

Figure 29-2. COMPARISON OF NOISE DATA/MODELS

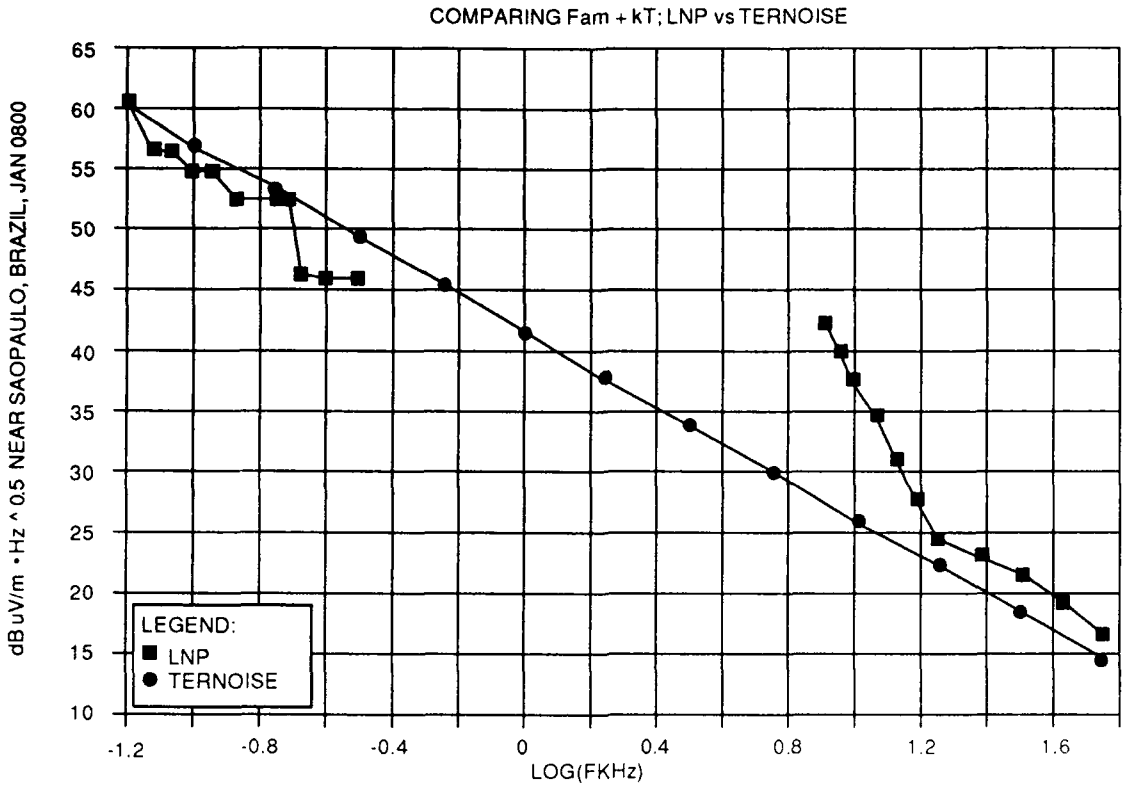

Figure 29-3. NOISE AVERAGED OVER 4-HOUR TIME BLOCKS

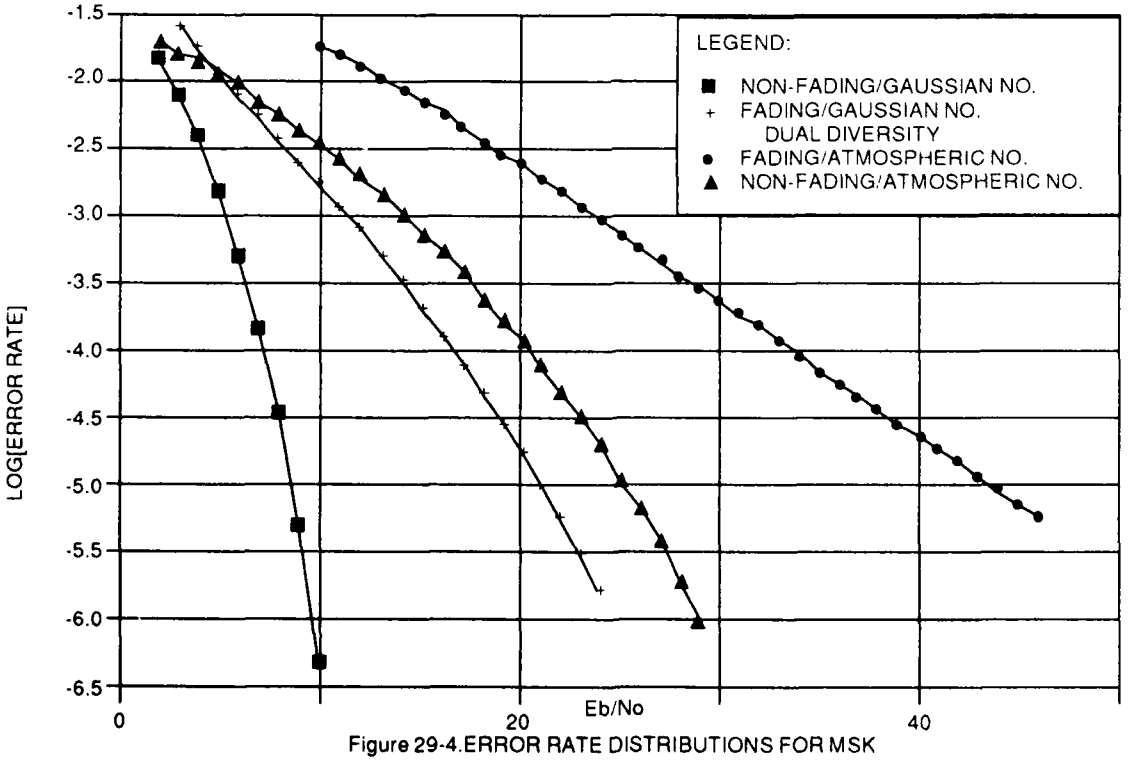

Figure 29-4.ERROR RATE DISTRIBUTIONS FOR MSK

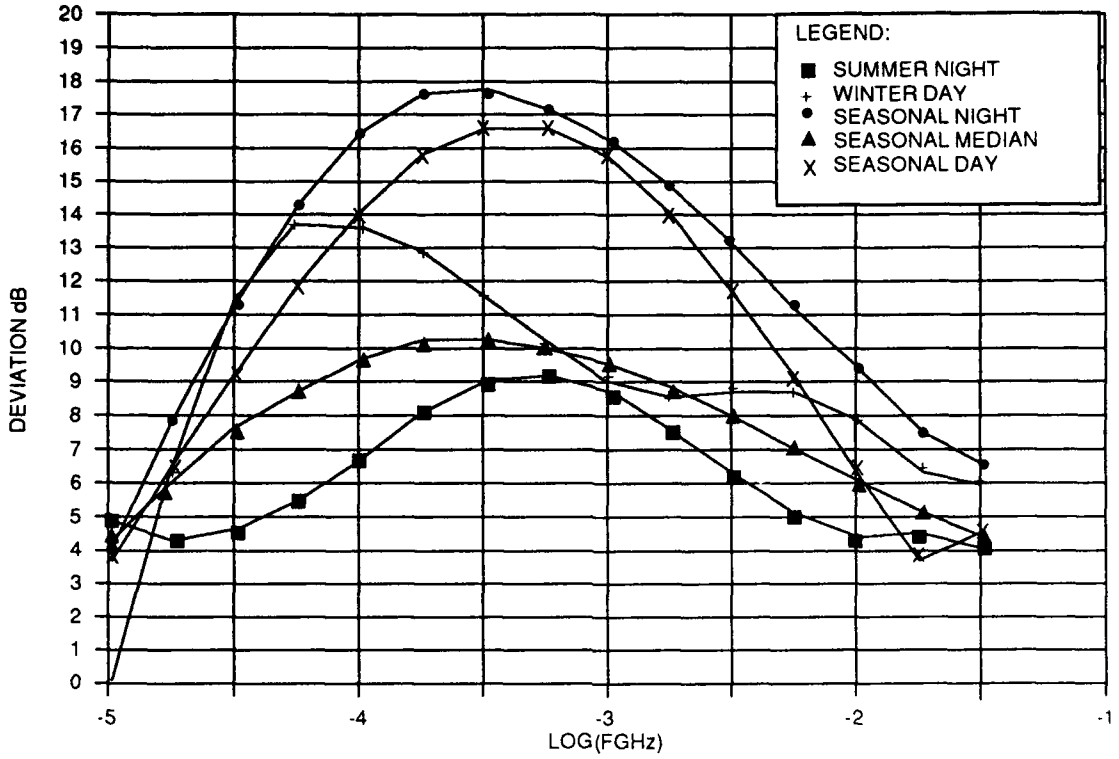

Figure 29-5.UPPER DECILE DEVIATION FROM FOUR-HOUR BLOCK MEDIAN, FAM

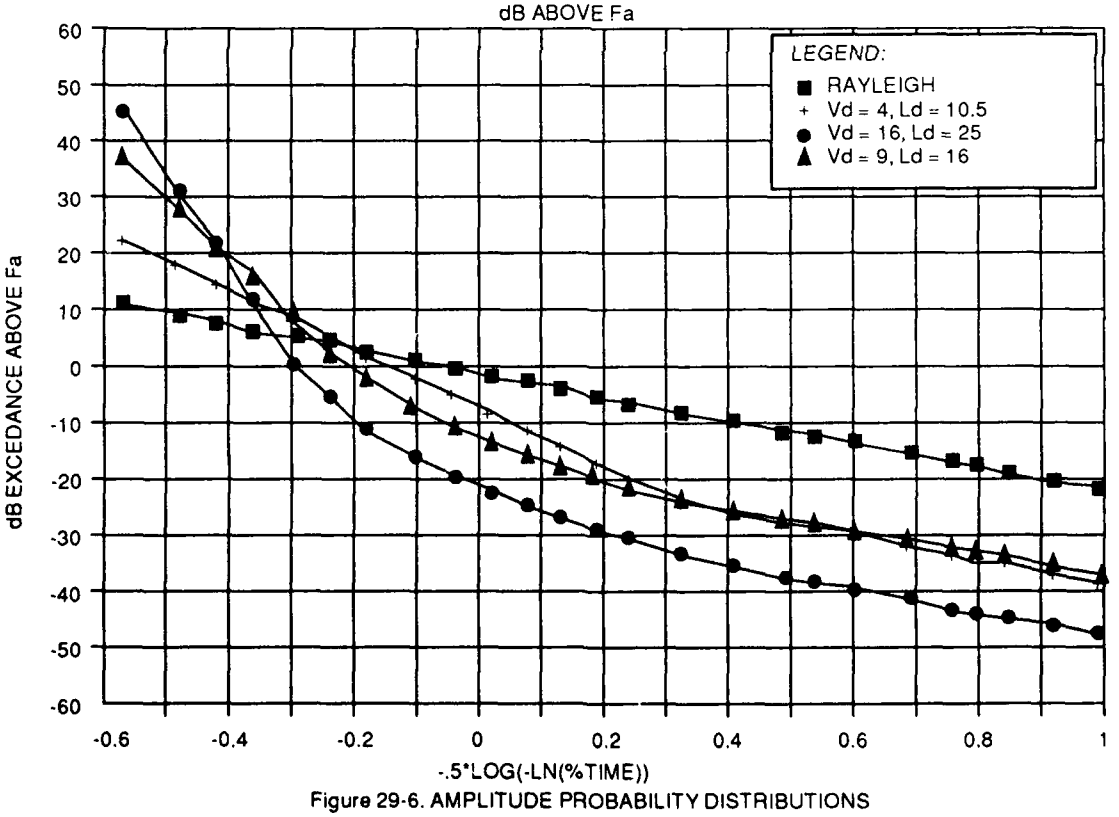

Figure 29-6. AMPLITUDE PROBABILITY DISTRIBUTIONS

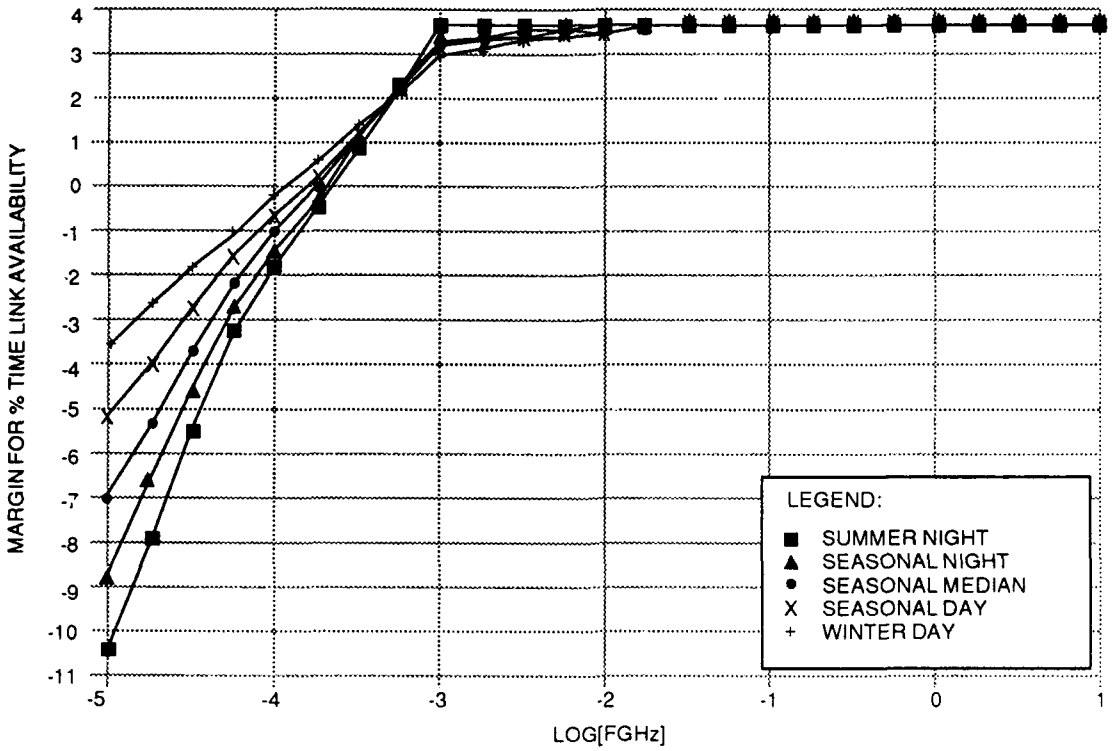

Figure 29-7. MARGIN REQUIRED TO CONVERT Fa TO INSTANTANEOUS NOISE FIGURE

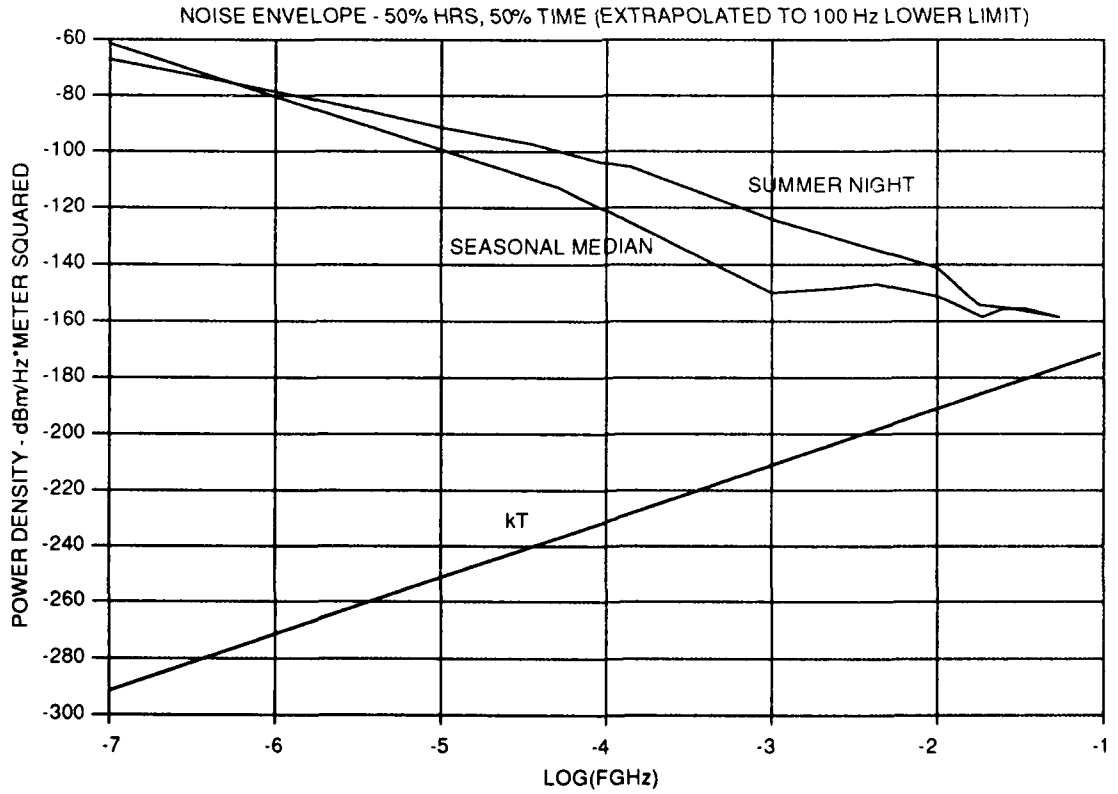

Figure 29-8. ATMOSPHERIC NOISE INSTANTANEOUS

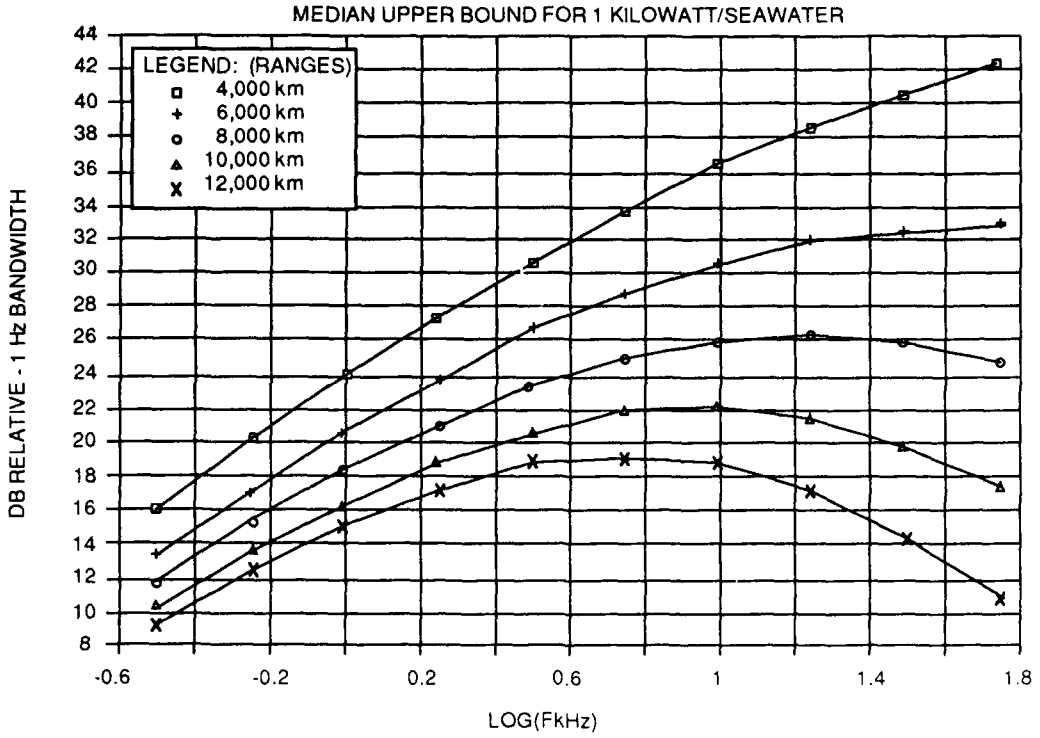

Figure 29-9. SIGNAL/NOISE DENSITY

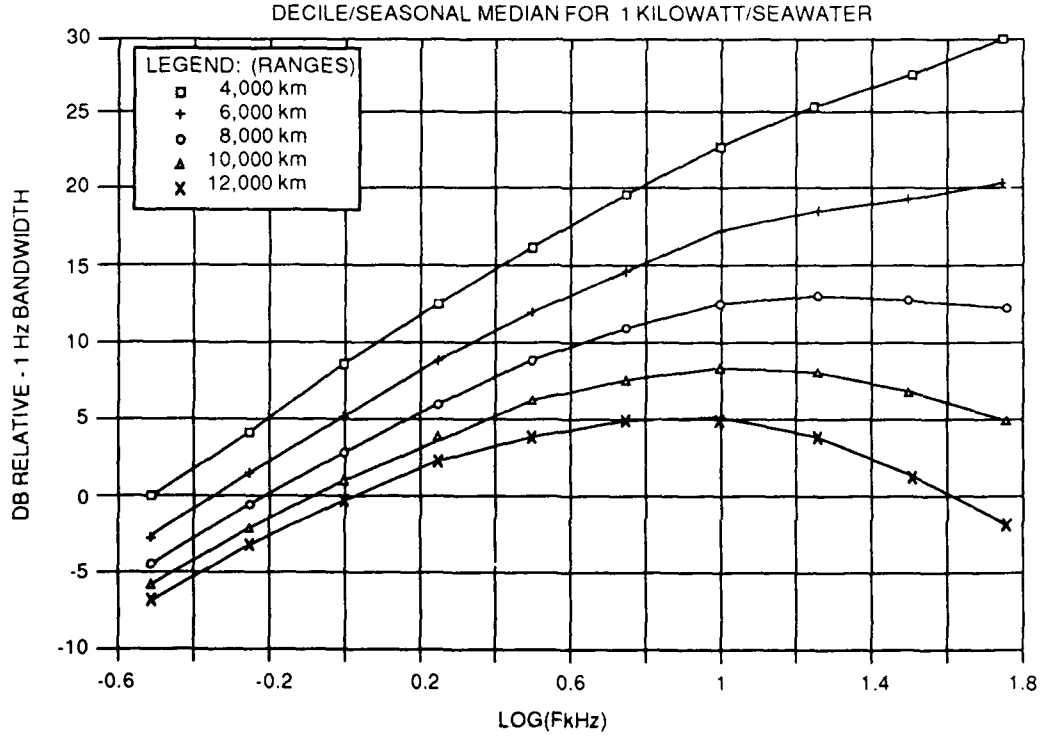

Figure 29-10. SIGNAL/NOISE DENSITY

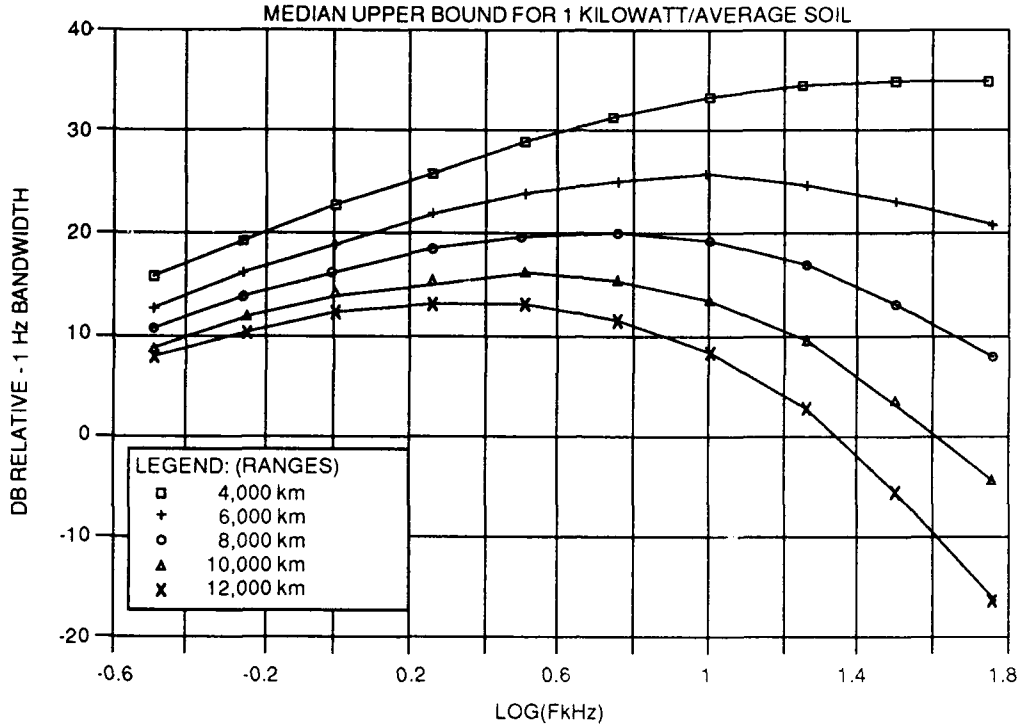

Figure 29-11. SIGNAL/NOISE DENSITY

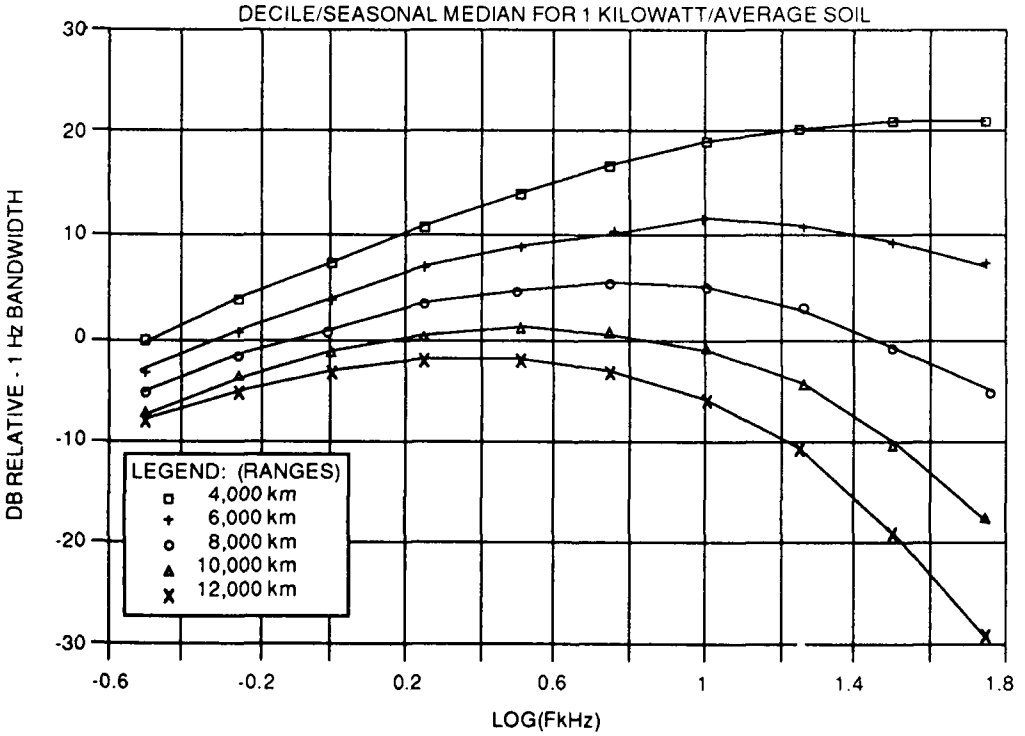

Figure 29-12. SIGNAL/NOISE DENSITY

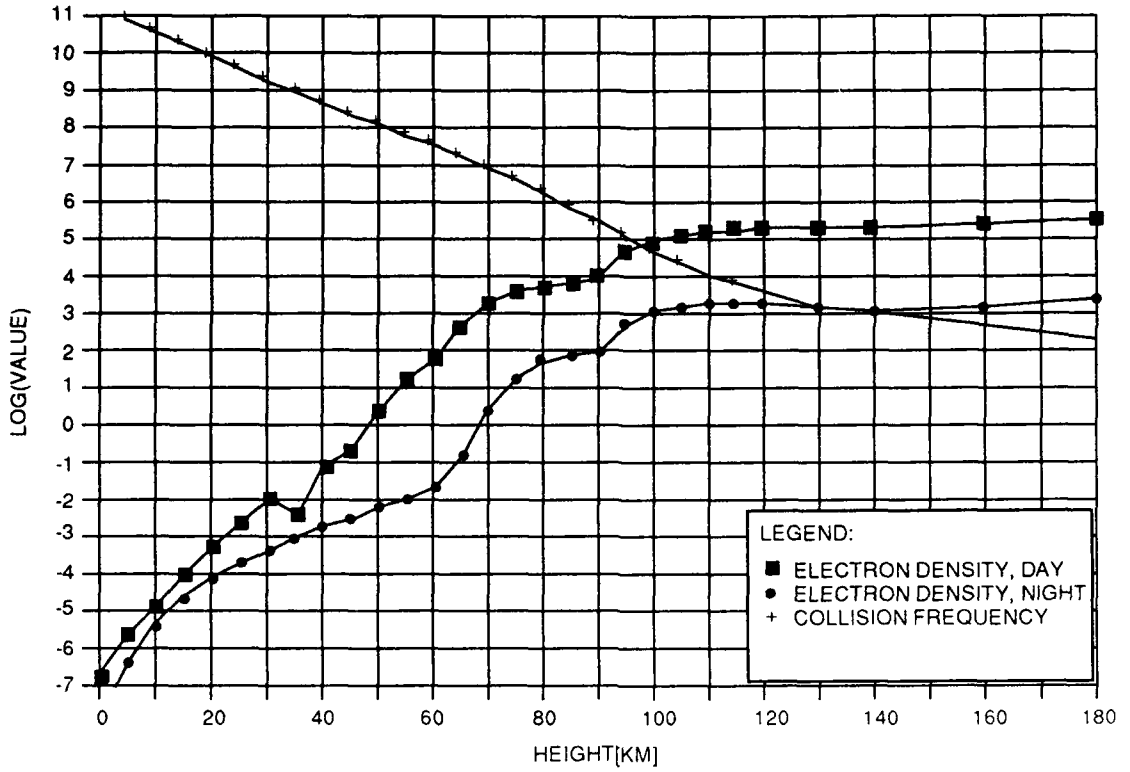

Figure 29-13. ATMOSPHERIC CONSTITUENTS FROM CAP ELECTRON DENSITY & COLLISION FREQUENCY

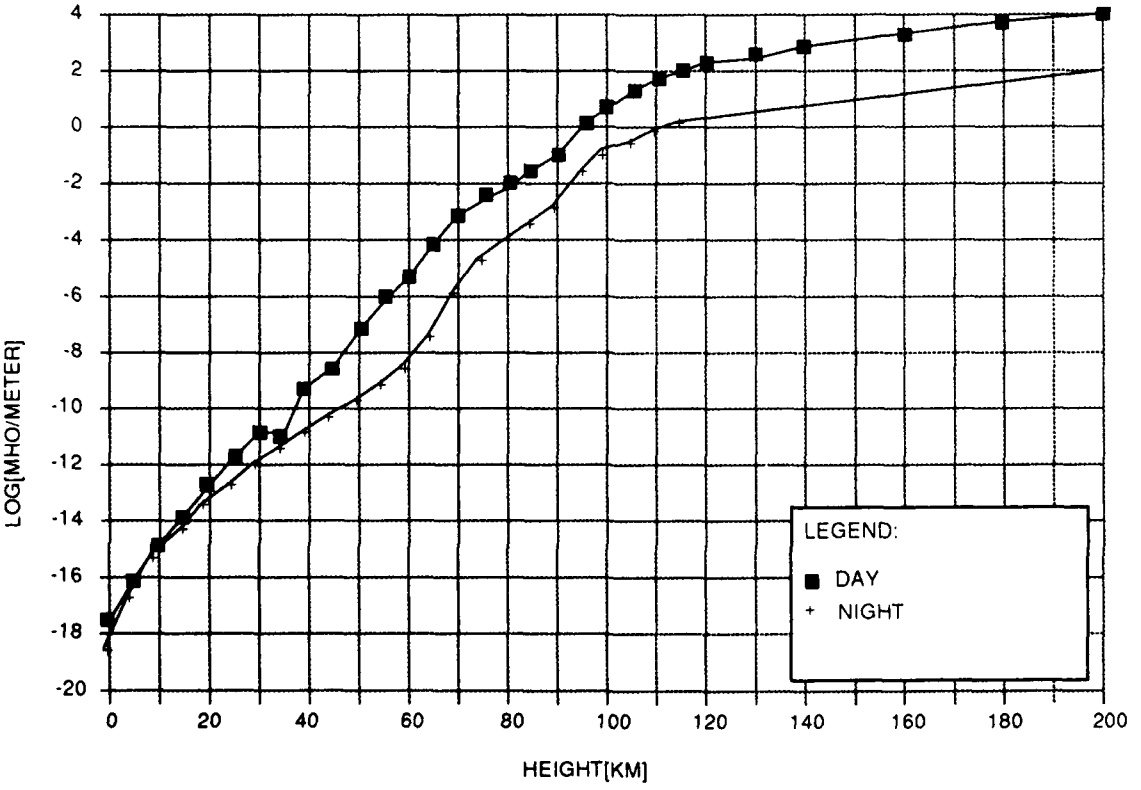

Figure 29-14. IONOSPHERIC CONDUCTIVITY DERIVED FROM CAP Ne & v DATA

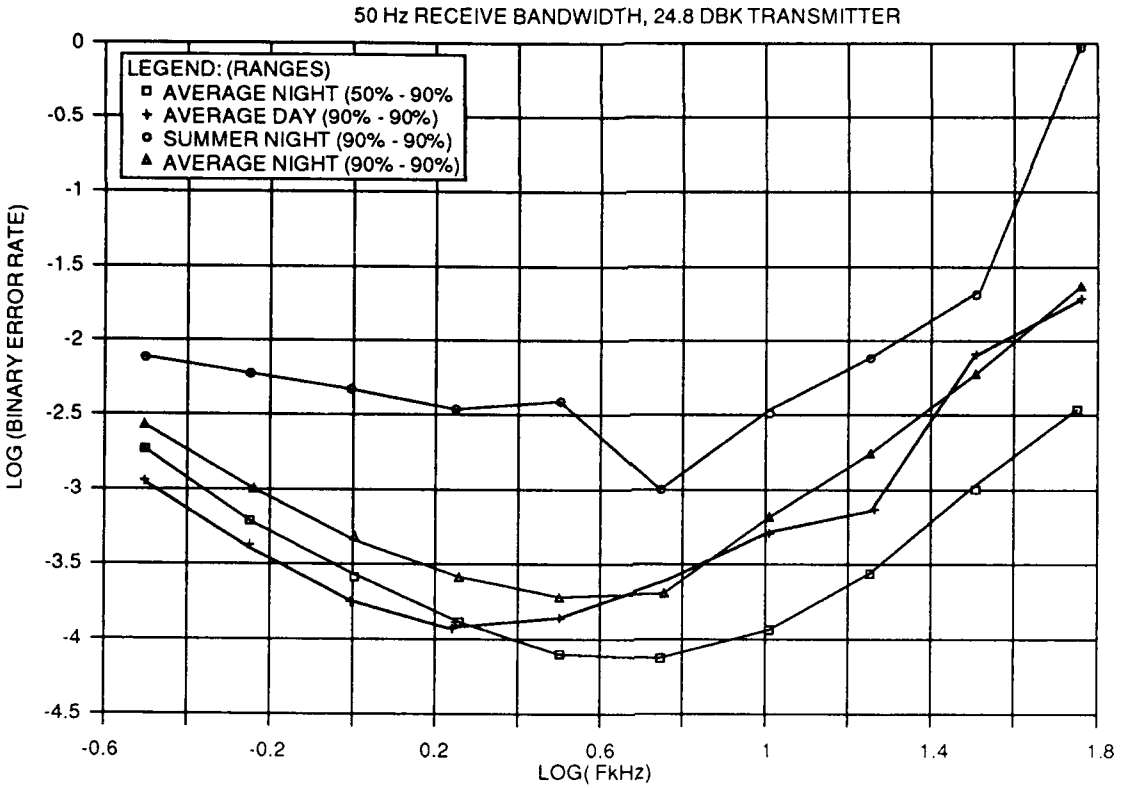

Figure 29-15. BINARY ERROR RATES

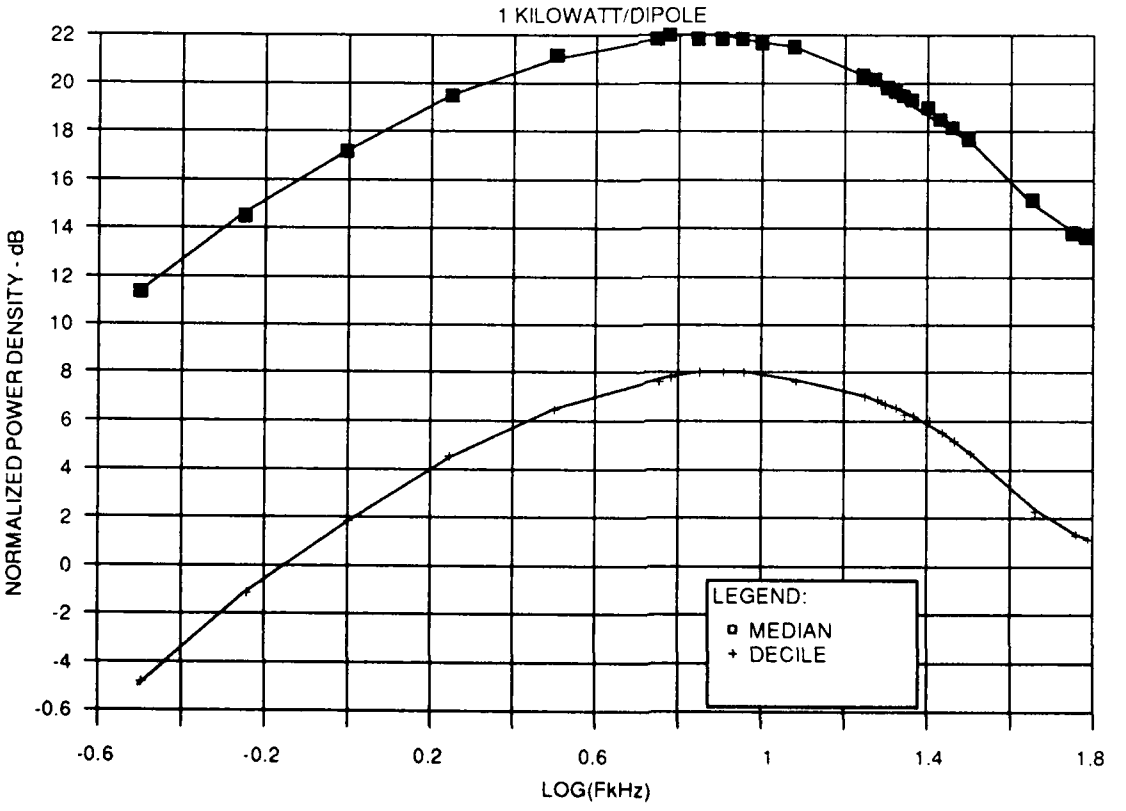

Figure 29-16. SIGNAL/NOISE DENSITY

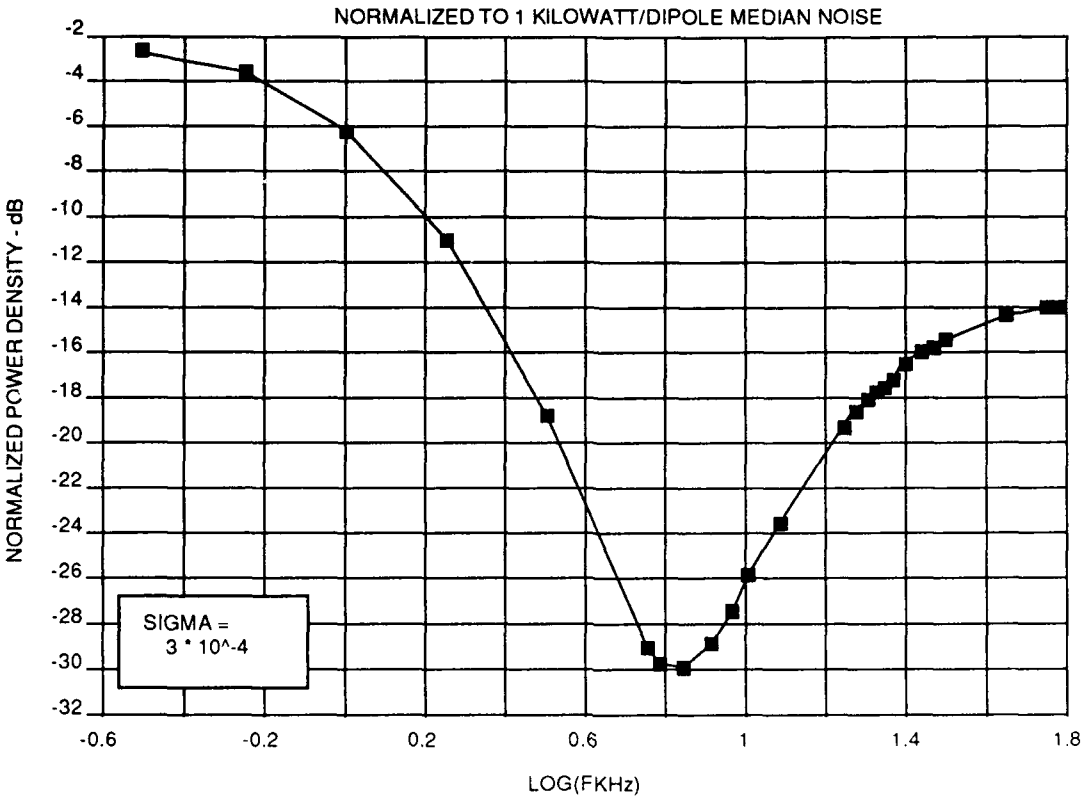

Figure 29-17. SIGNAL/NOISE FOR TRANSPOLAR PATH OVER NORTH POLE

Discussion

INAN

COMMENT. I am a little worried about your use of an "incoherent sun of ray hops" model. In this frequency range, the rays as they reflect will acquire substantial phase charges at the ionospheric reflection points. The reflection coefficients are sensitively dependent on angle of incidence and also the modes are excited (at the antenna) with a particular set of phases and amplitudes. The ray model is probably not appropriate for large distance (i.e. 9000 km), it should be much better to use a waveguide made approach, such as the LWPC.

AUTHOR'S REPLY

I agree that LWPC code is much more accurate and is the preferred approach. However, we needed method of visualization in a physical sense as required by our study. We did compare our results to those generated by the LNP (PSR) code for validation. We do not consider the wavehop model any more than a first order approximation with large contingency (i.e. deltas) included in the S/N estimates. We did compare, for first order approximation, coherent and incoherent suns beyond 6000 km which showed little change. For more detailed analysis and now that we have received LWPC we would use this for the next iteration, higher accuracy predicition.

ORBITING TRANSMITTER AND ANTENNA FOR SPACEBORNE COMMUNICATIONS AT ELF/VLF TO SUBMERGED SUBMARINES

by
P.R. Bannister
US Navy-NUWC, New London, CT 06320

J.K. Harrison, C.C. Rupp
NASA-MSFC, Huntsville, AL 35812

R.W.P. King
Harvard University, Gordon McKay Laboratory
Cambridge, MA 02138

M.L. Cosmo, and E.C. Lorenzini
Harvard-Smithsonian CFA, Cambridge, MA 02138

C.J. Dyer, M.D. Grossi
Raytheon Co., Submarine Signal Division
Portsmouth, RI 02871-1087

Abstract

An orbital emplacement for the transmitter and the antenna of a communications link at ELF (30 to 300 Hz) and VLF (3 kHz to 30 kHz) to submerged submarines, has been considered since the very inception of the space age. Only recently, however, space technology has reached sufficient maturity, for system designers to undertake serious studies of this link configuration.

The optimistic outlook stems from recent space technology developments, such as the design and construction by NASA of long orbiting tethers, and the testing, onboard Shuttle Orbiter ATLANTIS, scheduled for Summer 1992, of the first spaceborne 20 km metal wire. This is known as the Tethered Satellite System #1 (TSS-1, in short), a space mission that might be possibly followed by other flights, with tether lengths that could reach 100 km.

Once deployed at a height of, say, 300 km, from a Shuttle Orbiter, or from another suitable platform, a long, thin tether aligns itself along the local vertical by virtue of the gradient of the Earth gravity field. If made of metal, the tether can function as a VED (Vertical Electric Dipole) transmitting antenna at ELF and VLF.

1. INTRODUCTION TO SPACEBORNE TETHERS: AN EMERGING TECHNOLOGY FOR USE IN RADIOPHYSICS AND RADIOENGINEERING

Sometime in Summer 1992, a new structural element will make its appearance onboard the Shuttle Orbiter: a tether consisting of a very long, thin filament attached, at one end, to the Shuttle, and holding "by the leash," at the other end, a satellite. Hence the name "Tethered Satellite System," in short TSS, that has been given to this joint initiative by NASA and ASI (Italian Space Agency).

The Summer 1992 tether, a flexible thread with a diameter of a few millimeters, will have a length of 20 km. However, in later missions, tethers of 100 km length and even longer are a distinct possibility.

The tether aligns itself with the local vertical and stays so aligned, by virtue of the vertical gradient of the Earth gravity field. The tether's orientation, both for upward and downward deployment from the Shuttle, deviates only slightly from the local vertical, and its angular movements about that vertical resemble the angular movements of a pendulum attached to the Shuttle. While the Shuttle Orbiter moves in its orbital flight around the Earth, the tether stays roughly aligned with the center of the Earth.

In a few years, once that such basic operations as deployment and retrieval are thoroughly understood, the tether will find wide-spread use as a flexible structural element (capable of responding to traction) in large space structures of one, two, or three dimensions. This use is similar, in several respects, to the function of ropes in suspended bridges.

While two-dimensional and three-dimensional tethered structures belong to the long-term future, the attention of flexible-spacecraft designers will concentrate, in the short term, on the one-dimensional case. A single vertical tether, notwithstanding its simplicity, is capable of performing a variety of functions, among which, if the tether is made of metal, are the following:

(a) operating as a transmitting antenna (either resonant, or non-resonant, such as a travelling-wave radiator), for the effective radiation of electromagnetic waves. This specific use is the object of this paper. Tethers can be made of such a length that they radiate effectively e.m. waves at frequencies as low as ELF and VLF;

(b) operating as a receiving antenna, again either resonant or non-resonant;

(c) performing as a self-powered antenna, for radiation of e.m. waves at ULF (frequencies of 1 Hz or lower);

(d) generating DC electric energy, at the expenses of the platform's orbital energy. The electromotive force is $\underline{v} \times \underline{B} \cdot \underline{\ell}$, where $\underline{v}$ is the orbital velocity (about 7.7 km/sec for a height of 380 km), $\underline{B}$ is the Earth magnetic field (about 0.3 10^{-4} Weber/m^2), and ℓ is the length of the tether (20 km). The circuit closure is provided by the magneto-ionic plasma of the Earth ionosphere, while the contact between each end of the tether and the ionosphere is provided by a "plasma bridge" also known as a "plasma contactor."

As already told, NASA and ASI will launch in orbit, in Summer 1992 the TSS-1 mission, that uses a 20 km-long metal wire. This mission will verify, first of all, such dynamical issues as the feasibility of safe deployment and retrieval. In addition, it will perform experiments on the electrodynamic and electromagnetic mechanisms (c) and (d) above.

2. RADIATION OF E.M. WAVES FROM A TETHER IN THE IONOSPHERE TO THE SURFACE OF THE EARTH, AT ELF AND VLF FREQUENCIES.

2.1 Introductory Remarks

The possibility of transmitting electromagnetic waves from a Shuttle Orbiter to the surface of the earth is discussed in a paper by Grossi et al. (1991). The antenna generating the electromagnetic field consists of a vertical wire (the tether) which is driven with the Shuttle as ground. In this Section 2, the electromagnetic aspects of the problem are examined with available knowledge as the basis. Because the existing theory of the properties of the ionosphere and of antennas moving in it are approximate and complicated, quantitative results can be obtained only in terms of a relatively simple model.

2.2 The Model

The specific problem to be investigated is the electromagnetic field on the surface of the earth generated by currents in a vertical antenna moving in the F-layer of the ionosphere at a height of 400 km. The length of the antenna is 4 km. It is driven at its upper end by a generator voltage V_o against the space shuttle as a ground. A schematic diagram is in Fig. 2-1.

The ionosphere is assumed to extend from a height of 150 km to infinity as a homogeneous medium. It is given a sharp boundary with air as a simplification of the gradual layered boundary between 100 and 200 km. With the shuttle orbiting the earth along a great circle over the poles, the earth's magnetic field $B_o \sim 0.5 \times 10^{-4}$ Tesla is roughly parallel to the vertical antenna over the poles and perpendicular to it over the equator.

2.3 The Properties Of The Ionosphere

The ionosphere is a plasma consisting of electrons, protons, and neutral particles. In the F-layer, the electron and ion densities, η_e and η_i, have the following values:

$$\text{Daytime: } \eta_e = \eta_i = 1.4 \times 10^{12} \text{ per } m^3, \quad (1a)$$

$$\text{Nighttime: } \eta_e = \eta_i = 4 \times 10^{11} \text{ per } m^3. \quad (1b)$$

The electric charges are

$$q_e = -e = -1.6 \times 10^{-19} \text{ Coulombs} \quad (2a)$$

$$q_i = -q_e = 1.6 \times 10^{-19} \text{ Coulombs (for protons)} \quad (2b)$$

The masses are

$$m_e = 9.1 \times 10^{-31} \ kg, \quad (3a)$$

$$m_i = 1836.3 \times 19 \ m_e = 3.17 \times 10^{-26} \ kg \quad (3b)$$

The reason for including the factor 19 in (3b) is that the lower ionosphere consists of a mixture of ions including N^+, N_2^+, O_2^+, with a mean mass of 19 amu.

The plasma frequencies of the electrons and ions for daytime are

$$\omega_{pe}^2 = \frac{\eta_e e^2}{\epsilon_0 m_e} = 44.55 \times 10^{14}; \quad \omega_{pe} = 6.67 \times 10^7, \quad (4a)$$

$$\omega_{pi}^2 = \frac{\eta_i e^2}{\epsilon_0 m_i} = 1.2779 \times 10^{11}; \quad \omega_{pi} = 3.575 \times 10^5 \quad (4b)$$

With

$$B_0 = 0.5 \times 10^{-4} \text{ Tesla}, \quad (5)$$

the gyrofrequencies are

$$\omega_{ge} = \frac{eB_0}{m_e} = 8.8 \times 10^6, \quad (6a)$$

$$\omega_{gi} = \frac{eB_0}{m_i} = 2.53 \times 10^2 \quad (6b)$$

The effective collision frequencies – representing the sum of the electron – ion and electron – neutral collisions – are

$$\text{Daytime: } \nu \sim 10^3; \quad \text{Nighttime: } \nu \sim 4 \times 10^2 \quad (7)$$

2.4 Plasma Waves In The Ionosphere

The ionosphere is a complicated medium for the propagation of waves generated by oscillating currents at an angular frequency ω in an antenna. The frequencies of interest for the tether experiment are in the following ranges:

$$VLF: \quad 3\ kHz \leq f \leq 30\ kHz \quad or$$

$$1.88 \times 10^4 \leq \omega \leq 1.88 \times 10^5, \tag{8a}$$

$$ELF: \quad 30 \leq f \leq 300\ Hz \ or\ 188.5 \leq \omega \leq 1885 \tag{8b}$$

The specific frequencies to be investigated are

$$f = 9\ kHz\ and\ 30\ kHz; \quad f = 40\ Hz. \tag{9}$$

Three types of waves are examined as follows.

a) Electromagnetic Waves.

The condition for propagating waves of this type is

$$\omega \gg \omega_{pi} = 2.53 \times 10^2 \tag{10}$$

This is satisfied by the entire VLF range (8a), but not by the entire ELF range (8b). For frequencies that satisfy (10), the plasma behaves like a homogeneous medium with the relative effective permittivity and conductivity given by

$$\epsilon_{er} = 1 - \frac{\omega_p^2}{\omega^2 + \nu^2}; \quad \sigma_e = \frac{\nu\epsilon_0\omega_p^2}{\omega^2 + \nu^2}, \tag{11}$$

when the steady magnetic field B_0 is parallel to the electric field. These are modified when B_0 is in the direction of propagation, as shown in King and Harrison (1969) (Section 2.12). With (11), the wave number is

$$k_i = k_0 \left(\epsilon_{er} + \frac{i\sigma_e}{\omega\epsilon_0}\right)^{1/2} =$$

$$k_0 \left(1 - \frac{\omega_p^2}{\omega^2 + \nu^2}\right)^{1/2} (1 + ip)^{1/2} \tag{12}$$

where $k_0 = \omega/c$,

$$p = \frac{\sigma_e}{\omega\epsilon_0\epsilon_{er}} = \frac{\nu\omega_p^2}{\omega(\omega^2 + \nu^2 - \omega_p^2)} \tag{13}$$

and

$$(1 + ip)^{1/2} = f(p) + ig(p). \tag{14}$$

The quantities $f(p)$ and $g(p)$ are tabulated over a wide range in King and Prasad (1986).

When

$$\epsilon_{er} > 0 \ or\ \omega^2 + \nu^2 > \omega_p^2 \tag{15}$$

the wave number becomes

$$k_i = \beta_i + i\alpha_i; \ \beta_i = k_0\left(1 - \frac{\omega_p^2}{\omega^2 + \nu^2}\right)^{1/2} f(p), \tag{16}$$

$$\alpha_i = k_0 \left(1 - \frac{\omega_p^2}{\omega^2 + \nu^2}\right)^{1/2} g(p) < \beta_i, \tag{17}$$

so that propagation with low attenuation in the form

$$e^{ik_i r} = e^{-\alpha_i r} e^{i\beta_i r} \tag{18}$$

is possible. Alternatively, when

$$\epsilon_{er} < 0 \ or\ \omega^2 + \nu^2 < \omega_p^2, \tag{19}$$

$$k_i = \beta_i + i\alpha_i; \quad \beta_i = k_0\left(\frac{\omega_p^2}{\omega^2 + \nu^2} - 1\right)^{1/2} g(|p|) \tag{20}$$

$$\alpha_i = k_0\left(\frac{\omega_p^2}{\omega^2 + \nu^2} - 1\right)^{1/2} f(|p|) > \beta_i, \tag{21}$$

so that the high exponential attenuation makes propagation impossible.

With $\omega_p^2 = 44.55 \times 10^{14}$ and $\omega^2 + \nu^2 = (1.88 \times 10^4$ to $1.88 \times 10^5)^2 + 10^6 = 3.53 \times 10^8$ to 3.53×10^{10} for the VLF range, $\alpha_i > \beta_i$ and no propagation is possible. When the steady magnetic field B_0 is not parallel to the electric field, propagation is likewise generally not possible except in the Whistler mode considered in the next section.

b) The Whistler Mode

The existence of the steady earth's magnetic field B_0 makes propagation in other modes possible. Because the analytical formulation is extremely complicated, it is necessary to introduce the simplifying approximation of neglecting the losses due to collisions and treating the so-called cold plasma. This has been shown to be a good approximation of hot plasmas in its general description of the wave propagation.

A special range of propagation occurs when the parabolic branch of the dispersion curve is applicable. This is shown by Denisse and Delcroix (1963, page 95). The condition underlying propagation in this mode is

$$\omega < \omega_{ge} = 8.88 \times 10^6 \tag{22}$$

This follows from Fig. 8.7 in Denisse and Delcroix (1963). This is satisfied by the entire VLF range (8a).

The wave number k_i given by Denisse and Delcroix (1963, p. 98) with $\omega_{gi}^2 \ll \omega_{ge}^2$ is

$$k_i = \frac{k_0\omega_{pe}}{(\omega\omega_{ge})^{1/2}} = 2.37 \times 10^4 k_0 \omega^{-1/2} =$$

$$0.749 \times 10^{-4}\omega^{1/2} \tag{23}$$

For the two frequencies $\omega = 5.65 \times 10^4$ and $\omega = 1.88 \times 10^5$, this gives

$$\frac{k_i}{k_0} = \frac{\lambda_0}{\lambda_i} = \begin{cases} 100 & for\ f = 9\ kHz \\ 54.6 & for\ f = 30\ kHz \end{cases} \tag{24}$$

Specifically with

$$k_0 = \begin{Bmatrix} 1.88 \times 10^{-4}\ m^{-1} \\ 6.27 \times 10^{-4}\ m^{-1} \end{Bmatrix} \text{ or } \lambda_0 = \begin{cases} 33.4km \\ 10\ km \end{cases} \tag{25}$$

$$k_i = \begin{Bmatrix} 1.88 \times 10^{-2}\ m^{-1} \\ 3.42 \times 10^{-2}\ m^{-1} \end{Bmatrix} \text{ or } \lambda_i = \begin{cases} 334\ m \\ 184\ m \end{cases} \tag{26}$$

The effective permittivities are

$$\epsilon_{ir} = \frac{k_i^2}{k_0^2} = \begin{cases} 10^4 \\ 2975 \end{cases} \tag{27}$$

The antenna (tether) length is $h = 4$ km, so that

$$\frac{h}{\lambda_i} = \begin{cases} 12 & for\ f = 9\ kHz \\ 21.7 & for\ f = 30\ kHz \end{cases} \tag{28}$$

c) Alfven Waves

The ELF range (8b) does not satisfy the conditions for propagation with the Whistler mode. However, it does satisfy the conditions for propagation with Alfven waves. This condition is

$$\omega \ll \omega_{gi} = 2.53 \times 10^2 \tag{29}$$

For Alfven waves, the phase velocity is the so-called Alfven velocity given by

$$a = \frac{c\omega_{gi}}{\omega_{pi}} = 7.077 \times 10^{-4}c = 2.115 \times$$

$$10^5\ m/\sec = 211.5\ km/\sec \tag{30}$$

When $a/c \ll 1$, as in (30), the wave number is well approximated by

$$k_a = \beta_a + i\alpha_a \sim \frac{\omega}{a} + i\,\frac{\omega^2 c^2 \epsilon_0}{2\sigma_0 a^3}\ ;\quad \sigma_0 = \frac{m_e \nu}{\eta_e e^2} \tag{31}$$

For the frequency $f = 40$ Hz or $\omega = 251.3$ α_a is entirely negligible so that

$$k_a \sim \beta_a = \frac{\omega}{a} = 1.189 \times 10^{-3}\ m^{-1};\quad \alpha_a \sim 0. \tag{32}$$

and

$$\lambda_a = \frac{2\pi}{k_a} = 5.288\ km \tag{33}$$

The antenna length $h = 4$ km corresponds to

$$\frac{h}{\lambda_a} = 0.76 \tag{34}$$

2.5 The Air-Ionosphere Boundary

The electromagnetic field in the ionosphere generated by the current in the antenna travels outward with amplitudes at sufficient distances determined by the far-field pattern. The field incident on the ionosphere-air boundary is locally approximately a plane wave which is reflected and refracted according to Snell's law. Since the Whistler-mode field is incident from the ionosphere (Region i, wave number k_i) on the air (Region 0, wave number k_0) with $k_i/k_0 = 100$ when $f = 9$ kHz, it experiences total internal reflection when $\Theta > \Theta_{cr}$, where the critical angle is

$$\Theta_{cr} = \sin^{-1}\frac{k_0}{k_i} = \sin^{-1}(0.01) =$$

$$0.01 \text{ radian} = 0.57^o \tag{35}$$

This means that the only field that is transmitted into the air arrives at the boundary within a small cone with angle $\Theta = 0.57°$. This suffers reflection and refraction at the boundary. At normal incidence, $\Theta = 0$, the reflection and transmission coefficients for the electric field are

$$f_r = -\frac{k_i - k_0}{k_i + k_0} = -\frac{99}{101} = -0.980;$$

$$f_t = \frac{2k_0}{k_i + k_0} = \frac{2}{101} = 0.0198 \tag{36}$$

Thus, there is only a small circular window from the ionosphere into the air. It is directly below the antenna and, at the distance 250 km from the antenna to the boundary, it has the radius 2.5 km. Even in this window, the field incident from the ionosphere is largely reflected back upward with the reflection coefficient -0.98. The transmission coefficient is 0.0198 for propagation into the air.

In order to transmit a field through the window into the air and down to the earth, the field pattern of the antenna must have a significant amplitude within 0.57° of the perpendicular.

2.6 The Antenna

The properties of antennas in magnetoplasmas are very complicated. Analyses have been carried out by Seshadri (1965), (1968) and Bhat (1973) with the steady magnetic field parallel to the antenna and by Wunsch (1967) with the magnetic field perpendicular to the antenna. A detailed study of these investigations and application of their results to the present problem are beyond the scope of this preliminary study. For present purposes, the antenna will be treated as immersed in an infinite homogenous medium with the wave number k_i characteristic of the Whistler mode for the VLF rate (8a)

and k_a for the Alfven mode for the ELF range (8b).

There are two possibilities for the antenna with the length h = 4 km and the radius a = 1 mm. These are: (a) The antenna is coated with a layer of dielectric with the radius $b \sim 2$ mm. If the dielectric is teflon, ϵ_{dr} = 2.1. (b) The antenna is bare (or the insulation is so thin that $b/a \sim 1$). The properties of the antenna are very different in these two cases.

a) The Insulated Antenna

A conductor with radius a and a dielectric coating with radius b, relative permittivity ϵ_{dr}, and wave number $k_d = k_0\sqrt{\epsilon_{dr}}$ embedded in an infinite homogeneous ionosphere with the wave number k_i such that $|k_i|^2 \gg k_d^2$, has the properties of a transmission line. The wave number is

$$k_L = k_d\left\{1 + \frac{1}{\ln(b/a)}\left[i\left(\frac{2\pi r_0}{\omega\mu_0} + \frac{\pi}{2}\right) + \ln\frac{2}{|k_i b|} - 0.327\right]\right\}^{1/2} \quad (37)$$

The characteristic impedance is

$$Z_c = \frac{\omega\mu_0 k_L}{2\pi k_d^2}\ln\frac{b}{a} \quad (38)$$

In these formulas, r_0 is the resistance per unit length of the wire. For the Whistler mode at f = 9 kHz, it follows that

$$k_0 = 1.88 \times 10^{-4}\ m^{-1}, \quad k_d = 2.72\times10^{-4} m^{-1},$$
$$k_i = 1.88\times10^{-2} m^{-1} \quad (39)$$

With radius a = 1 mm, $r_0 = 2.2\times10^{-4}$ Ω/m so that $2\pi r_0/\omega\mu_0$ = 0.0195 Ω/m. This is negligible compared with $\pi/2$, which contributes the radiation resistance per unit length. With b = 2 mm,

$$k_L = \beta_L + i\alpha_L = (1.1 + i0.001)\times10^{-3} m^{-1} \quad (40)$$

so that

$$\beta_L = 1.1\times10^{-3} m^{-1}, \quad \lambda_L = 5.7\times10^3 m = 5.7\ km, \quad (41)$$

$$Z_c = 116.4\ \Omega \quad (42)$$

For a tether length of h = 4 km,

$$h/\lambda_L = 0.70 \quad (43)$$

The electrical length is sufficiently short so that, regardless of whether the antenna is terminated in its characteristic impedance so that a travelling wave of current is maintained or it is simply driven as a monopole against the space shuttle, the principal lobe of the field pattern is in the equatorial plane $\Theta = \pi/2$ and no significant field is maintained in the downward direction near Θ = 0. The insulated antenna is ideally suited for a horizontal orientation of the antenna and is essentially useless for the vertical orientation.

b) The Bare Antenna

At f = 9 kHz for the Whistler mode, the bare wire of length h = 4 km = 12 λ_i is electrically very long. If it is terminated to produce a travelling wave of current approximately given by $I_z = I_o e^{ik_i z}$, the electric field at large distances from the antenna is

$$E_\Theta^r = -\frac{i\omega\mu_0}{4\pi}\frac{e^{ik_i r}}{r}\int_0^h I_z(z')e^{-ik_i z'\cos\Theta}\sin\Theta\, dz' \quad (44)$$

with

$$I_z(z) = I_z(0)e^{ik_i z'}, \quad I_z(0) = -\frac{i2\pi V_0}{\zeta_i\Psi} \quad (45)$$

where

$$\Psi \sim 2\ln\frac{2h}{a} \quad (46)$$

Since $\omega\mu_0/k_i\zeta_i = 1$, the result is

$$E_\Theta^r = \frac{V_0}{\Psi}\frac{e^{ik_i r}}{r} f(\Theta) \quad (47)$$

$$|f(\Theta)| = \frac{\sin\Theta}{1-\cos\Theta}\sin\left[\frac{1}{2}k_i h\left(1-\cos\Theta\right)\right] \quad (48)$$

The far-field pattern given by $|f(\Theta)|$ is shown graphically in a polar plot in Fig. 2-2. It is seen that the principal lobe is downward-directed and rotationally symmetric with maximum at Θ_m = 14°.2. The field at Θ = 0° is, of course, zero. There are eleven minor maxima between the principal one and $\Theta = \pi/2$.

The field that enters the air from the ionosphere according to the field pattern in Fig. 2.2 is extremely small since the angle of incidence on the ionosphere-air boundary must be almost vertically down, specifically within 0.57° of the vertical. The magnitude of the field at Θ=0.01 rad = 0.57° is $f(\Theta)$ = 0.38, whereas it is $f_m(\Theta)$ = 7.34 at the maximum.

In order to direct the maximum of the field pattern vertically down continuously, the antenna must be tilted 14°.2 from the vertical and then made to rotate so that its lower end describes a circle. Since the tether normally oscillates through an angle near 14°.2, it is only necessary to impart a small transverse push to have it trace the edge of a cone. The rate of circulation is irrelevant so long as the tether continuously maintains an angle of 14°.2 with the vertical.

If the maximum of the field pattern in Fig. 2-2 is directed down, the full field intensity with $|f(\Theta)|$ = 7.34 is directed onto the circular window on the ionosphere-air boundary so that even with the small transmission

coefficient, the effective value of $|f(\Theta)|$ in the air is $|f(\Theta)|=0.15$.

With $h/a = 4\times10^3/10^{-3} = 4\times10^6$,

$$\Psi = 2\ln(2h/a) = 31.8, \tag{49}$$

and r = 400 km,

$$|E_\theta^r| = \frac{V_0}{\Psi}\frac{1}{r}\times0.15 = \frac{V_0}{31.8}\frac{1}{4\times10^5}\times0.15 =$$

$$V_0\times1.18\times10^{-8} \tag{50}$$

For an applied driving voltage to the antenna of $V_0 \sim 1kV$, the field incident on the surface of the earth is

$$|E_\theta^r| \sim 1.18\times10^{-5}V/m \tag{51}$$

This is easily measurable. The current at the driving point of the antenna is obtained from (45). It is

$$|I_z(0)| = \frac{2\pi\times10^3}{12\pi\times31.8} = 5.2 \text{ Amp} \tag{52}$$

Note that $\zeta_i = \zeta_0/\epsilon_{ir}^{1/2} = 120\pi/10 = 12\pi$.

2.7 Conclusion

There are several possible modes for the transmission of electromagnetic waves through the ionosphere to the earth surface. The Whistler mode appears to be the most promising for the VLF band when the source is a vertical traveiling-wave monopole erected on the lower side of the space shuttle. In order to maintain a continuously significant field on the surface of the earth or sea, it is necessary that the antenna be displaced from the vertical by an angle of 14°.2 for f = 9 kHz and rotated so that it traces the surface of a cone.

3. SMALL EXPENDABLE-TETHER DEPLOYMENT SYSTEM (SEDS-1)

3.1 General Description

The Small Expendable-Tether Deployer System (SEDS-1) is being built by NASA as a low-budget secondary payload for a March 1993 flight on a U.S. Air Force Delta II/GPS mission. SEDS will deploy a 23 kg endmass (or payload) at the end of a 20 km long tether. The experiment purpose is to test and demonstrate the feasibility of the design concept and to verify the computer models that have been built to predict tether dynamic behavior during this type of low tension deployment. The key features of SEDS are its simplicity, low tension deployment with minimum braking, non-retrievability of the tether (the tether is cut after it is fully deployed), and low cost. The 20-km deployment, which is initiated by spring ejection of the endmass at an initial speed of 1.5 meters per second, last about 90 minutes (one orbit).

3.2 Design Concept

SEDS consists of four parts: 1) the deployer (tether wound on a core, canister cover and base plate); 2) the brake/cutter assembly; 3) the electronics box; and 4) the endmass (or payload). A view of SEDS is show in Figure 3.1. The tether unwinds – about 46500 turns – from the outside periphery of a stationary core--there is no rotating reel. After unwinding the tether travels through a small opening in the top of the canister, to a friction brake, a tensiometer, then to the tether cutter, and finally attaches to the payload. The entire system weighs approximately 39 kg most of which is the 23 kg endmass.

The brake/cutter assembly contains a running-line tensiometer, stepper motor for turning the brake, the friction brake shaft and gearing, and tether cutter. The friction brake slows the deployment speed by wrapping several turns of the tether around a small shaft when approximately 19-km or 41026 turns of tether have been deployed. The tether is made from a polyethylene synthetic fiber called SPECTRA-1000. The 0.75 mm diameter is much larger than necessary for strength on this first flight but this size gives significant micrometeoroid protection (about a 0.1 percent risk for one orbit).

The endmass (or payload) weighs 23 kg and has an overall size of 20 × 33 × 41 cm. It contains a three-axis accelerometer, tensiometer, magnetometer, its own power, computer, telemetry system and supporting electronics. Two antennas are mounted on the sides for data transmission directly to the tracking stations during the experiment. The endmass and tether are cut, at the Delta II end, after deployment and burn-up on reentry into the atmosphere.

3.3 Electronics System

The SEDS electronics data and control system will record, store, and continuously downlink data over the Delta II S-band telemetry channel. It counts the turns as the tether unwinds from the spool, logs the time for each turn, serves as an event timer, responds to sequencer commands from the Delta II second stage, controls the stepper-motor/brake system, and activates the pyrotechnic charge for the tether cutter. Data stored, besides the turncounts, are tether tension, temperature, and supply voltage. The storage capacity is 160 kilobytes (approximately 115 kilobytes are required) and the downlink capacity ranges from 1 kilobit per second to 64 kilobits per second (requirement is 4.8 kilobits per second). The entire memory can be dumped in six minutes. The system weighs about 3 kg and has an overall size of 8 × 13 × 29 cm. A block diagram is shown in Figure 3.2.

3.4 Mission

The tether deployment begins 3780 seconds after Delta II lift-off at the apogee of a 204 × 704 km orbit. Full deployment of the 20 km tether is reached 5100 seconds later. After full deployment, the tether swings for ten minutes through an angle of approximately 50 degrees toward the local vertical. The tether is cut during the swing when it is near the local vertical position and over the Pacific Ocean at about 150 degrees east longitude. This occurs at 5800 seconds (slightly more than one orbit) after deployment begins. The reentry takes one-third of an orbit so the tether and payload should reenter over the Pacific Ocean near 100 degrees west longitude or just off the coast of Mexico. Table 3.I shows the Delta II/SEDS-1 sequence of events. Figure 3.3 gives the SEDS-1 ground track.

3.5 Tether Dynamics Calculations

A major goal of the first SEDS flight is to validate the extensive amount of computer modelling that has been done during the last several years to predict the dynamic behavior of a tether in space. The results of some recent calculations done by Control Dynamics are shown in Figure 3.3 for a 20 km deployment starting at the apogee of a 204 × 704 km orbit and lasting for 5800 seconds (1.6 hours or a little more than one SEDS orbit). Full deployment is reached at 5100 seconds followed by a 50 degree swing to the vertical that is completed at 5800 seconds when the tether is cut. During most of the deployment period the tether position is forward of vertical at an angle of about 50 degrees.

The tether length, deployment speed, and tension are shown in Figure 3.4. Deployment begins with spring ejection of the endmass at a speed of about 1.5 m/s. Tension forces initially are 0.03 to 0.04 n (3 to 4 g) with a slight increase beginning around 2700 seconds reaching a value of 3.0 n at full deployment (5100 seconds) and a maximum value of 4 n just before the tether is cut at 5800 seconds.

3.6 Measurements

The key measurements are the turns of the tether versus time as the tether unwinds. This is sensed optically and stored in the electronics system memory. The command times for operating the stepper-motor brake and the cutter are based on this measurement. Also, tether length and payout speed are determined from the turns data.

The time duration of each turn will be compared with similar laboratory test data to evaluate the accuracy of ground test results in predicting flight performance. A reasonably close comparison is important to succeed at developing future tether applications.

Other data collected will be temperature, tension (just before the final exit guide), and supply voltage. Radar data will be collected on the ground giving the Delta II and payload position.

4. FEASIBILITY EXPERIMENT

4.1 Science And Technology Objectives

There are several issues of feasibility concerning SEDS tethers that must be verified experimentally, before these tethers can be used as antennas in communication systems of practical relevance. First of all, we must verify that the dynamics of tether deployment and station-keeping is well understood, and fully controllable. NASA-MSFC has scheduled several flights of SEDS systems, as piggy-back payloads on board the Air Force Delta-II rocket, to test tether dynamics. There will be a SEDS-1 flight in March 1993, a SEDS-2 flight in March 1994, and a SEDSAT mission in July 1994 (this mission is under study but has not yet been approved). There will also be an electrodynamic mission called PMG in June 1993.

Once that the dynamics is well understood, we should start experimenting with the radiophysics and the radioengineering issues that are fundamental to the use of SEDS tethers as antennas, in communication links from orbit to Earth surface.

The most relevant of the scientific investigations to be carried out are the following:

(a) guidance of the e.m. waves radiated by the tether, along the lines of force of the Earth geomagnetic field, in the whistler regime, at VLF frequencies;

(b) Alfven wave guidance, also along the geomagnetic lines of force, at ELF frequencies, below the ion cyclotron frequency;

(c) investigation of non-linear effects in the ionosphere, due to the high level of radiated power. This involves determining the threshold of occurrence of non-linear effects, and establishing the analytical dependence of these effects upon the level of radiated power;

(d) determination of the angular aperture of the cone of capture of e.m. waves by the lines of force of the Earth magnetic field;

(e) determination of the transmission and of the reflection coefficients at the boundary between the bottom of the ionosphere and the top of the atmosphere, as a function of the angle of incidence (from above) of the e. m. waves radiated by the SEDS tether, when they reach this boundary in their descent toward the Earth surface;

(f) determination of the spatial extent of the illuminated area on the Earth surface. This is essential information, in order to establish the minimum number of satellites that are required to cover at all times a large

portion of the Earth surface (such as 60%, 80% or 100%).

The investigations listed above have an intrinsic scientific value within the realm of radiophysics. In addition, they represent essential steps that must be undertaken toward the goal of determining the feasibility of using SEDS tethers as antennas in space-to-ground communication links.

4.2 Application Goals

Because the ultimate use of the ELF/VLF propagation paths from orbit to Earth surface is in communications, we must characterize these paths as communication channels. The knowledge available on the applicable path properties is extremely limited, so that we must start from the fundamentals, and measure on the occasion of a first experiment, the following parameters:

(1) the response of the path to a "delta function" in the time domain. This will provide the measurement of the group delay, and of the time spread, inclusive of multipath spread;

(2) the response of the path to a "delta function" in the frequency domain. This will provide the measurement on the frequency spread, inclusive of Doppler shift and spread;

(3) the measurement of the path losses and of the noise;

(4) the measurement of the spatial and temporal variability of the channel properties;

(5) the distortion that affects specific communication waveforms, that are transmitted through the channel.

Once that the parameters above have been measured, it will be possible for communicators to select a waveform and to design a link that makes the best use of the available paths.

5. A SEDS/DELTA-II PAYLOAD FOR A FIRST FEASIBILITY EXPERIMENT

5.1 General

There are several factors that make it advisable to perform experiments on electrodynamic tethers by taking advantage of the availability of SEDS (Carroll 1987; Harrison et al., 1989) and of the Delta-II flight opportunities (Garvey and Marin, 1989). The most important factor is the low cost and the high frequency of flights of SEDS/Delta-II. In this paper we illustrate an experiment for inclusion in the SEDS/Delta-II demonstration program. The payload should be limited to radiation of e.m. waves in the VLF band (experimenting with ELF waves, a more difficult undertaking, should be considered for later times). The tether could be 4 km long, and should radiate a frequency of $\sim$ 9 kHz. A second tether, also 4 km long, could be used to generate DC electric power, with the objective of recharging the payload's batteries.

5.2 Description Of The Payload

The simplified block diagram of Figure 5-1 shows the principal elements of the proposed payload. They are:

(1) 2 conducting tethers, each 4 km long, each with its deployer; the electrical resistance of each 4-km tether is 88 ohm for the first mission (later-on, it could be lowered to 28 ohm); one tether teflon coated and one tether bare.

(2) 3 plasma contactors, complete with power supply and auxiliary units, each rated at 20 A, capable of providing a low-resistance bridge between each end of the tether and the ionosphere, and between the platform and the ionosphere;

(3) one solid-state VLF transmitter to feed one of the two tethers as a travelling-wave (TW) antenna at $\sim$ 9 kHz. To function as a TW radiator, the antenna requires the termination of the free end of the tether with a resistor equal to its equivalent-line characteristic impedance. Thus, the plasma contactor makes the "ground connection" to the ionospheric plasma;

(4) additional silver-zinc batteries on the Delta-II second stage;

(5) DC/AC static inverter (high voltage input);

(6) AC/DC converters (low voltage input).

Figure 5-2 shows a possible location for the payload on board the Delta-II. The required space is a fraction of the available toroidal volume (with mean radius 33", width 16" and height 20") all around the guidance section of the Delta-II. The SEDS deployer is accommodated in the shaded area of Figure 2.

As a DC electric power generator, the tether can draw from the ionosphere a current of 12 A DC, under the drive of a maximum electromotive force of 2.1 kV provided by the $V \times B \cdot \ell$ mechanism, where V is the orbital velocity, B the intensity of the Earth magnetic field, and ℓ is the tether's length.

As already indicated, while one of the two 4-km tethers is used to generate DC electric power, the other tether is used as a travelling wave transmitting antenna, at the frequency of 9 kHz.

This requires that the high-voltage emf due to the tether (1.05 kilovolt DC) be inverted by a static inverter into a low-voltage AC, that becomes easy to transform into the wanted values and converted ultimately into the

DC voltages required by the various power supplies. The tether DC electric power generator will supplement the batteries, will trickle charge them and stay connected with them, while feeding the on-board loads. We have worked out two cases for the DC generator:

(a) a 88 ohm tether, capable of feeding the payload with a 30% duty cycle.

(b) a 28 ohm tether, capable of feeding 100% of the time the same payload.

According to the SEDS deployer's manufacturer (Tether Applications, Inc.) a 4-km x 1-mm diameter tether with a resistance of 88 ohm can be accommodated into the deployer canister without any substantial modification to the hardware.

This tether will be used for the first mission. For future missions the tether resistance could be reduced to 28 ohm by using a 1.7 mm-diameter Copper wire. In this case the primary power generated by the upper tether would be 21 kW, 10 kW of which are delivered to the load (batteries or VLF transmitter) with a 100% duty cycle. In this latter case, the SEDS deployer must be enlarged.

The total mass of the payload is 360 kg ($\sim$ 794 lb). This includes the tether masses, three plasma contactors inclusive of their power supplies and auxiliary units, two Marman clamps, and two additional 250 Ah Silver-Zinc batteries on the Delta II which enable a mission duration of 4 days. Two of the three plasma contactors are installed on the end masses of the SEDS tether. One is attached to the platform itself. The primary power requirement for the payload is 28 volt DC, 10 kW at VLF. Use will be made of the Delta-II telemetry channels available to payloads. This use, however, will be very limited because the scientific data from our experiment are collected and recorded by the receiving stations on the Earth surface, and not onboard the platform.

The receiving terminals that were used during the flight of TSS-1 could be moved to new sites that are suitable for the SEDS-1 mission of March 1993.

5.3 Orbital Flight Parameters

The parameters for the orbital flight of the proposed electrodynamic/electromagnetic tether experiment could be taken to be similar to the parameters of the first SEDS/Delta-II flight (DeLoach et al., 1990), presently scheduled for March 1993, devoted to the measurement of the dynamic properties of the SEDS tether.

We estimate that by adding 260 lb of Silver-Zinc batteries (this figure is already included in the total mass of 790 lb) to the Delta's second stage, the mission can last as long as 4 days. The orbital decay will be approximately 2.5 km/orbit during electrodynamic operations.

A nominal inclination of 37° and an orbital altitude greater than 400 km with a circular or a low eccentricity orbit are acceptable. The prior knowledge of the orbital parameters is a particularly important factor in our case because we must establish the location of the receiving sites on the Earth surface as a function of the orbital parameters. We must make sure that the orbiting system flies as close as possible over each receiving site. In later flights, we could relax this specification and explore signal detectability at substantial distances from the ground track. For the first electrodynamic/electromagnetic mission, however, the receiving stations should be strictly located along the ground track.

5.4 Ground-Based Data Collection

Several instrumented sites at various locations on the Earth surface will be used for data collection and recording, equipped with the same instrumentation that has been developed for the TSS-1 electrodynamic mission. The existing instrumentation is mobile and can be relocated at sites that are on the ground track of the proposed SEDS/Delta-II mission. This instrumentation consists of the following equipment:

(a) Receiving/recording system developed for TSS-1 by Rice University under a subcontract from Smithsonian Astrophysical Observatory. This instrumentation, complete with data recorders, uses the following sensors:

- One set of 3-axis magnetic field sensor BF-4 (a coil magnetometer) for the band 0.3 Hz to 500 Hz;
- Two sets of 3-axis magnetic field sensor BF-6 (also a coil magnetometer) for the band 100 Hz to 100 kHz.

(b) Receiving/recording system developed for TSS-1 by University of Genova, Italy, using sensors that were loaned to University of Genova by US Navy, NUWC, New London, CT (NUWC sensors are encapsulated in Bentos glass spheres suitable for underwater deployment). The sensors are:

- Two sets of 3-axis induction coil magnetometer for the band 0.01 Hz to 100 Hz (Gritzke and Johnson, 1982);
- One set of Varian, optically pumped, cesium vapour magnetometer.

Another magnetometer has been added to the sensors that the University of Genova has borrowed from the US Navy: a SQUID, multi-axis system that was procured for the TSS-1 flight.

Given the planned orbital parameters, the schedule of data collection at each of the ground-based sites can be easily formulated with all necessary time accuracy. The number of channels that will be recorded at each site are

a function of the number of sensors and of the number of axial components for each sensor. In addition, a channel will be devoted to station's identification and time information consisting of Epoch and of 1-second time marks. Pertinent telemetry data from SEDS/Delta-II will be collected, processed, and formatted by the on-board computer (Rupp, 1988). These data will then be transmitted to the ground-based telemetry stations assigned to the flight, via the Second Stage telemetry link.

6. OPERATIONAL USES OF THE ORBITING TERMINAL FOR TACTICAL AND STRATEGIC COMMUNICATIONS TO SUBMERGED SUBMARINES

The orbital emplacement of the transmitting terminal brings with it the potentiality of covering, worldwide, all ocean areas, inclusive of the polar caps, should the orbit have a high-inclination. The waiting time, however, to have available the satellite, for any given location (should a single satellite be in orbit, with its transmitting terminal), would be too long. A constellation of several satellites would make it possible to cover, at any one time, a large portion of the Earth surface.

Figure 6.1 shows that less than ten satellites might be sufficient. A lot depends on the extent of the radius of the illuminated area, that is a quantity not reliably known from theory, and for which the final word will come from an experiment, such as the one illustrated in Section 5. Figure 6.1 shows that, assuming this radius to be somewhere between 3,500 km and 5,000 km, the required number of satellites would range between five and ten, to assure 80% coverage of the Earth surface.

With the constellation in place, assuming that transmissions take place at VLF, the system could be used to transmit EAM (Emergency Action Messages) to submerged submarines. The strategic communications link thus provided, would be a complement to "TACAMO," and would be characterized by a greatly enhanced geographical coverage. Should the ELF capability, then, be added to the satellite, the link would substantially augment the capabilities of the ground-based ELF facilities presently in use by US Navy.

With the present decrease in emphasis in strategic communications, due to the deep changes that have recently occurred in the world's geopolitical situation, tactical uses of the spaceborne transmitting terminal discussed in this paper, may be of greater interest. This system could be used by a Battle Group (Carrier, Destroyers, Submarines, etc.), deployed in remote ocean waters, to enable communications from a surface ship to a deeply submerged vessel.

7. CONCLUSIONS AND RECOMMENDATIONS

Since the early days of radio, long, thin-wire antennas have been a fundamental presence in transmission facilities at LF, VLF and lower frequencies. The orbiting tethers represent the latest addition to this family of long line radiators. It seems natural to perceive the spaceborne tethers as potentially useful to fulfill communications requirements that are world-wide in character, such as the strategic and tactical communications requirements of US Navy.

These authors hold the view that, notwithstanding the lack of pressing motivations to add, at this time, new operational systems to the communications arsenal, R&D activity on this and similar advanced subjects, should be vigorously pursued.

Especially in cases such as ours, in which a fully probative experiment on an entirely novel technological development can be performed at low cost, it is advisable to proceed with it, learn to the fullest what the new technology's capabilities are, and identify unrecognized potentials, possibly leading to even broader and unforeseen applications for this technology.

8. REFERENCES

Alford, A., 1936, A Discussion of Methods Employed in Calculations of E.M. Fields of Radiating Conductors, Electrical Communications, Vol. 16, pp. 70-88, July.

Barnett, A., and S. Olbert, 1986, Radiation of Plasma Waves by a Conducting Body Moving Through a Magnetized Plasma, JGR, Vol. 19, N.A9, pp. 10117-10135, September 1.

Bhat, B., Radio Science, 8(5), 483 (1973).

Carroll, J.A., 1987, The Small Expendable Deployment System (SEDS), Space Tethers for Science in the Space Station Era, Conference Proceedings, Vol. 14, Venice, Italy, October 4-8.

DeLoach, R., et al., 1990, End-Mass Instrumentation for the First SEDS/Delta-II Mission, 28th Aerospace Sciences Meeting, AIAA-90-0537, Reno, Nevada, January 8-11.

Denisse, J.F. and J.L. Delcroix, Plasma Waves, Interscience Publishers, New York, 1963.

Determan, W.R., 1988, SNAP-DYN: Concepts for Multikilowatt Space Power Applications, Proceedings 1988 IECEC Conference, Denver, Colorado, July 31-August 5, Volume 3, pp. 203-211.

Duff, B.M., 1964, "The Resistively-Loaded V-Antenna," NSG-579, Science Report No. 3, Harvard University.

Garvey, J.M. and D.R. Marin, 1989, Delta-II Secondary

Payload Opportunities for Tether Demonstration Experiments, Tether in Space-Toward Flight, AIAA, San Francisco, CA, May 17-19.

Gritzke, A.R. and R.H. Johnson II, 1982, Ocean Floor Geomagnetic Data Collection System, Naval Postgraduate School, Monterey, CA, December.

Grossi, M.D., 1973, A ULF Dipole Antenna on a Spaceborne Platform of the PPEPL Class, Letter Report to NASA/MSFC, Contract NAS8-28303, May 11.

Grossi, M.D., 1987, System Application Study, Section 3 of Final Report on NASA Grant NAG8-551, pp. 59-113, SAO, Cambridge, MA, February.

Grossi, M.D., 1987, Tether History and Historiography, Second International Conference on Tethers in Space, Venice, Italy, October 4-8.

Grossi, M.D., 1989, A New Class of Large-Size, Spaceborne Antennas Based on Tether Technology, NSF Workshop, PIERS, Boston, MA, 27 July.

Grossi, M.D., 1991, Investigation of the E.M. Properties of a Spaceborne Electrodynamic Tether as a Travelling Wave Antenna, SAO Proposal P2485 to NASA-OSSA, July.

Grossi, M.D., E.C. Lorenzini and M.L. Cosmo, 1991, SEDS/Delta-II Electrodynamic Tether Experiments on the Generation and Radiation of Electromagnetic Waves from ULF to VLF, SAO "White Paper," Rev. No. 3, June.

Harrison, J.K. et al., 1989, Small Expendable-Tether Deployer System (SEDS)- Development Status, Tether in Space-Toward Flight, AIAA, San Francisco, CA, May 17-19.

Iizuka, K., 1967, The Travelling-Wave V-Antenna and Related Antennas, IEEE Trans. AP, AP-15, No. 2, pp. 236-243, March.

Kelly, F.J. et al., 1976, Waveguide-Mode Power Budget for an ELF/VLF Transmitting Satellite, NRL Report 8032, September 17.

King, R.W.P. and C.W. Harrison, Jr., Antennas and Waves, MIT Press, Cambridge, MA, 1969.

King, R.W.P. and S. Prasad, Fundamental Electromagnetic Theory and Applications, Prentice-Hall, New York, 1986.

Myers, C.W., D.J. Kretzchmar, and M.D. Grossi, 1986, Spaceborne E.M. Wave Generation/Radiation Facility for the High-Power Illumination at ULF/ELF of Underwater Targets, DARPA/SPC, Arlington, VA, November 19.

Rupp, C.C., 1988, SEDS Computer System, NASA-MSFC Technical Document, Huntsville, Alabama, November.

Seshadri, S.R., Proc. of the IEE (London), 112(10), 1856 (1965).

Seshadri, S.R., J. Appl. Phys., 39(5), 2407 (1968).

Thompson, G.C., 1988, Design of an ELF/VLF Satellite for Under the Ice Submarine Communications, MS Thesis, Naval Postgraduate School, Monterey, California, September.

Wunsch, A.D., Can. Jour. Phys., 45, 1675 (1967).

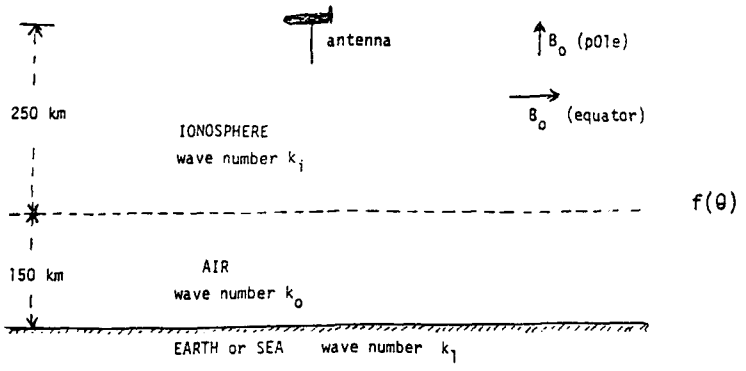

Figure 2-1 Schematic diagram of the Shuttle with a vertical tether antenna in the ionosphere over the Earth

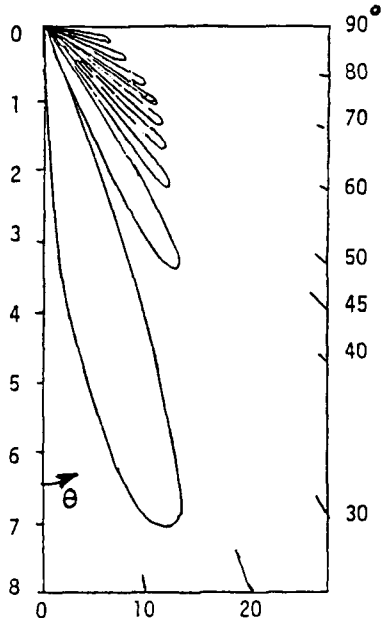

Figure 2-2 Far field of a Travelling-wave antenna in the ionosphere, using the whistler mode

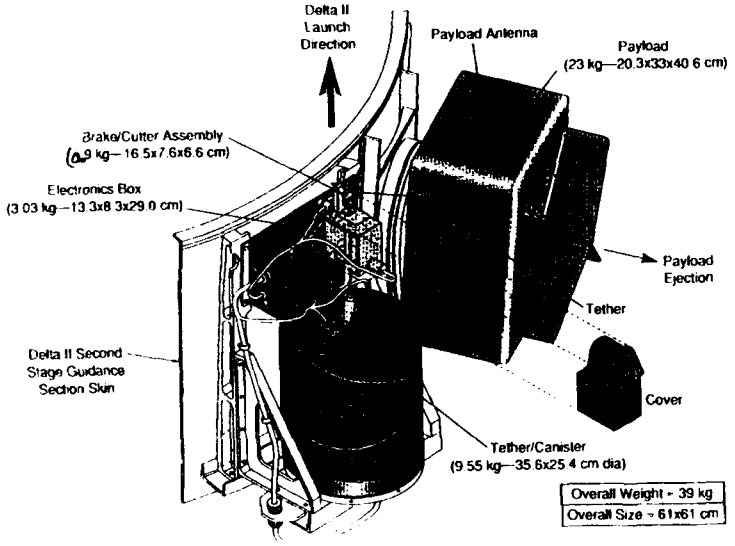

Figure 3-1 SEDS on Delta-II

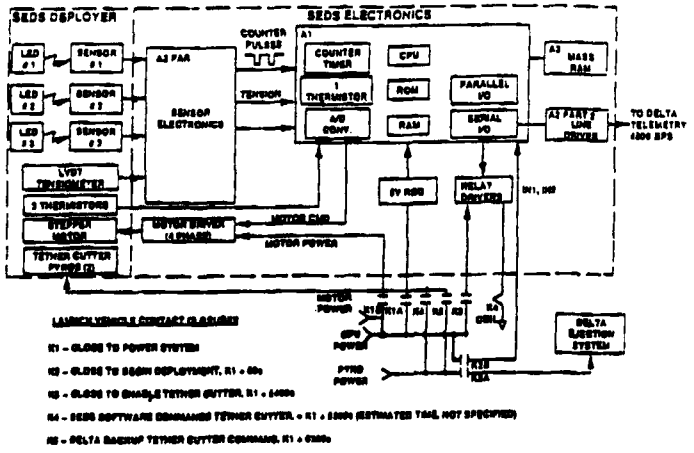

Figure 3-2 SEDS-1 Data System Block Diagram

Event	Delta II Time (sec)	SEDS-1 Time (sec)
Delta II Lift-off	0	
Stage II-III Separation	1262.8	
SEDS Power On	3720.0	0
Guam AOS	3729.4	
Deploy SEDS Endmass	3780.0	60
Begin Roll Maneuver to Tether Deploy Attitude	3785.0	
End Roll Maneuver to Tether Deploy attitude	3795.0	
Maintain Deploy Attitude	3830.0	
Guam LOS	4544.3	
Brake Initiation	8400.0	4680
Deployment Ends - Swing Begins	8570.0	4850
Guam AOS	9717.6	
SEDS Initiated Tether Cut Command	9949.0	6229
Delta Initiated Tether Cut Command (Back-Up)	10,080.0	6360
Guam LOS	10,475.4	
Hawaii AOS	10,777.3	

TABLE 3-I Delta II/SEDS-1 Sequence of Events

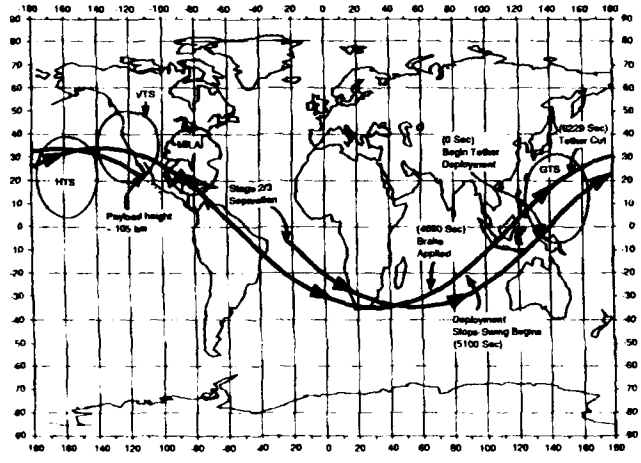

Figure 3-3 SEDS Ground Track

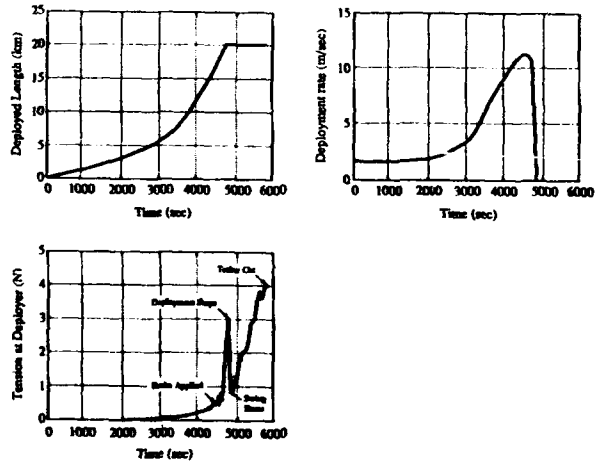

Figure 3-4 SEDS-1 Nominal Deployment Case

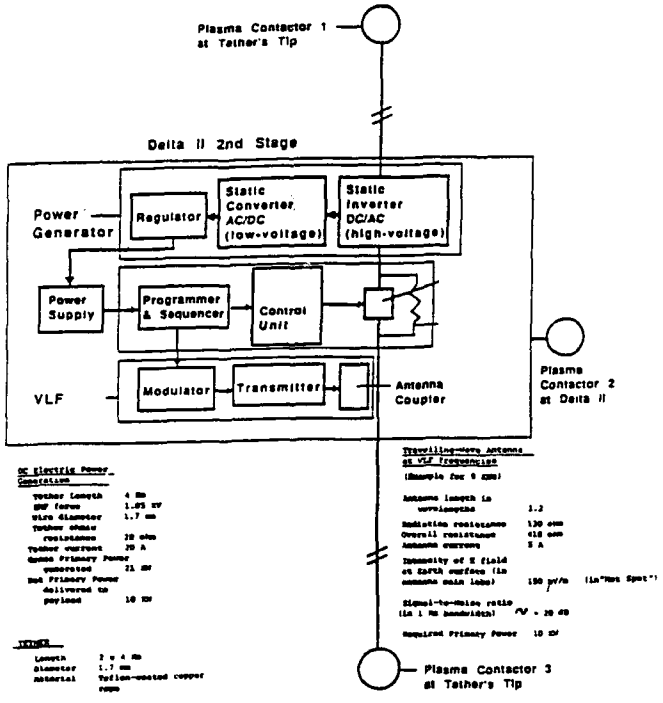

Figure 5-1
Simplified Block Diagram
of the payload

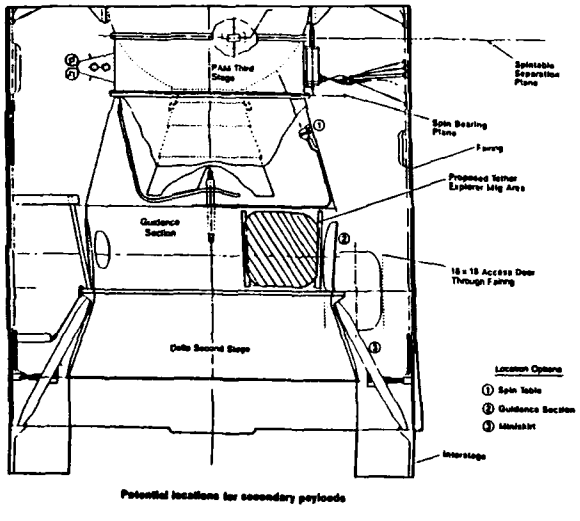

Potential locations for secondary payloads

Figure 5-2
SEDS Accomodation on Delta-II
Second Stage

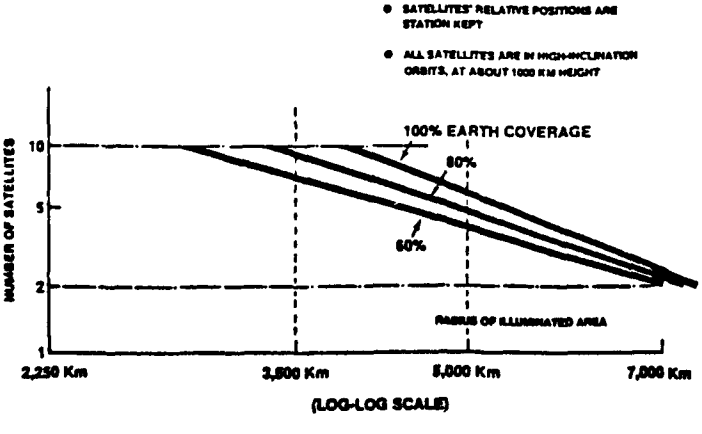

Figure 6-1
Number of satellites required
to cover the Earth surface

ROUND TABLE DISCUSSION

J.S. Belrose (CA) The purpose of the round table discussion is to summarize where we are in the field of the symposium, to make some comments on where we should be going and, if there are some controversial issues, although I have not heard too many at this meeting, to try and stimulate some discussion from the floor. We have seated at the table members of the program committee, two of the members are absent. I will give each of them an opportunity to say a few words, but we are not going to do all the talking -- the whole idea is to have a variety of views rather than only the views of those sitting at the table. So if anyone has anything to say, after we have said our piece, we would be very pleased to hear from you.

Since I am in the chair, I will begin. I'll make a few sketchy remarks about the meeting. I think it has been a successful meeting. We have with us some of the pioneers in the work, as well as some of the newer people doing work in recent years. We tried to have a balanced program starting with propagation aspects, radio environment (radio noise and interference), antenna considerations, system considerations, and ending with a discussion of the future for our work.

The session on Radio Propagation was I think a very good session. In the session on Radio Noise and Interference we learned about the new noise model, the Pacific Sierra model by Warber and Field; and we heard briefly about Tony Fraser-Smith's measurements of radio noise at a number of sites around the world, the STAR laboratory measurement program. So there are measurements going on, and an entirely different approach to coming up with a noise model is in the progress of being developed. The session on Antenna Considerations was interesting for me, and the topic was I think well covered in spite of the withdrawal of a few papers. I overviewed some general aspects of VLF/LF antennas myself, and spoke about a specific kind of antenna system, multiple tuned antennas, which has been neglected in recent years. We heard about measuring the dynamic bandwidth of antennas. That was an important paper because it related to a topic specifically mentioned in the theme of our meeting, viz. that the bandwidth of VLF antennas needs to be capable of handling 4 channel MSK. We heard about distributed antenna systems, which is certainly an entirely new concept for the VLF/LF part of the radio spectrum. We had a couple of very brief papers on different approaches to antenna modeling. The Systems Aspects, as you have already know was rather poorly covered, because of the withdrawal of 4 of the intended 5 papers. However, fortunately Mr. Holtzeimer did present his paper this morning so we did have the subject addressed in the view of that paper. Finally, concerning the session on the future, we had hoped for a more general coverage of this topic. We did have two good papers on orbiting antennas, in particular the TSS experiment, but we did not have any other papers on the future in other areas of the VLF/LF propagation and systems aspects.

So much for my introduction. Let us hear now form other members of the technical programme committee. We will start off with Jerry Ferguson, since he presented a paper and chaired Session 1. Jerry -

J.A. Ferguson (US) One of the things that plagues all of us, especially those that work at engineering oriented laboratories,

is the need to strike a balance between producing, or at least appearing to produce very good results and convincing the sponsor on how great we can do the job, while at the same time convincing the sponsor that job is not done yet. We in the VLF community, at least the part of the community that I represent, have done a very good job of convincing the sponsor that the job is done. In times of declining funding it gets harder and harder to convince the sponsor that they ought to spend some more money on continuing research. I have had more than one sponsor tell me that 30 years is enough.

When I did my PhD work under Henry Booker, the topic of my research was HF spread-F, and the most important reference I had for to this topic was the work that Prof. Booker himself had done more than 45 years ago. A sort of an ongoing mystery in my mind, even though I was actively pursuing the work, was why we were continuing to studying this topic after all these years, and why we did not already have all the answers. However, radio science makes a good career, so I didn't spend too much time worrying about this but I got on with the study, to see what new could be learned. I see in my VLF propagation research a similar decline. The computer models that we have struggled for so many years to improve and to make efficient, have finally matured. The effort in recent years has been to imbed our very elaborate computer code inside bigger systems. The bigger systems treat our propagation code, our physics of 30 years worth of effort, as a button The user specifies a receiver location, a transmitter location, and then presses a button to get an answer. Because the computers are so fast, and because we have done such a good job, the user will get that answer in a reasonable amount of time. The user will not ask a very complicated question. The fact that the computer model that he is employing to make these calculations is complicated will be lost on him. I see this happening with the noise models. But that is sort of what we are after anyway. The problem as I see it, because we are servicing engineering oriented customers, is that the research that is required to get these engineering answers tends to get glossed over. We are guilty of doing that our selves. In a sense we are shooting ourselves in the foot, to use an American idiom. I see also that there is a tremendous emphasis on the doable problem. We have seen that in some of the papers presented here. You saw this in my own work -- where we tend to confine ourselves to daytime propagation. Nighttime is more complicated. As a matter of fact our customers very rarely ask for a nighttime calculation, and they almost never ask for a calculation that involves a day/night terminator. These are the remaining difficult problems, but frankly I don't think that the sponsors of research are interested. The average daytime engineering answer is good enough for their purposes. Their purposes are how big of an antenna do I need to build? How much power do I have to generate? And where should I put this antenna? Once those questions are answered, they do not want to see us anymore, and maybe rightly so. Personally as a physicist I think that's bad. I want to continue to study interesting problems, but again in the military engineering environment, good enough is good enough. The 10% improvement that I might be able to offer with my physics and my geophysics background may not be of interest to the radio engineering community. That's all I have to say. That ought to stimulate some discussion.

J.S. Belrose (CA) Thank you Jerry. Next we will hear from Professor Bossy. The subject area of this particular meeting is

certainly not one in which he has been working, but the waves are reflected from the ionosphere and Professor Bossy, a long time member of the EPP panel, has been working on ionospheric problems for many years and so we'll ask an ionospheric expert to say a few comments. Professor Bossy-

L. Bossy (BE) I agree for the most part with what Dr. Ferguson has said. I will speak more form the theoretical point of view. Are the propagation details really independent of the structure of the D region? Could it not be useful to introduce something like the International Reference Ionosphere? In the IRI you find many details on the structure, and on the behaviour of the D-region with respect to the geographic and geomagnetic latitudes, that would be helpful for the computations you make for the needs which are put before you?

J.S. Belrose (CA) Thank you Professor Bossy. I agree, we do not see much reference to the IRI models. Nor do we hear about the very detailed electron density profiles measured by Prof. Reg Smith at Armidale, NSW Australia, by the method of cross modulation. The VLF community keeps referring back to the Deek's profiles, and to modifications made to those profiles by Dr. Bain. The Deck's profiles were based on a limited set of data, VLF/LF steep incidence data recorded at Cambridge many years ago. He sort of fiddled the profiles to obtain the best agreement with the experimental data. His approach was hands on one, manually making adjustments to get an agreement with the data, then you changing the profile a little bit and get a little bit better agreement with the data. Dr. Bain made further adjustments to the profiles to provide a better fit to the 16 kHz Hollingworth interference pattern measurements, signal versus distance measurements over distances of less that 1000 km. There has always been a concern about the validity of these profiles. Shellman, working at NOSC, which the lab was called when he was doing his work at that time, developed a direct inversion technique for converting propagation data to profiles. This technique in principle gives more confidence that the end result is right, but for this very elaborate inversion type of process to work he needed to have very high quality data, more or less noise free data.

Jerry Ferguson mentioned the Deek's profile and he showed one of his exponential profiles on top of a Deek's profile; and we heard reference to these profiles in the paper by Warrington and Jones.

So much for me, Professor Tacconi-

G. Tacconi (IT) I want to express some opinions on tethered satellite systems. I do not have much to add to what has been discussed this morning. After the presentations by Bannister and Bonifazi I think that it is clear as to the state of the (experimental) system. I only want to add that I have with me a copy of the future program for the TSS, which is foreseen up to 1998. This has been supplied by Professor Bonifazi. This document may be useful if there any questions to be answered about this technology and applications. Bannister spoke about the SEDS programme. We (my university) hope to participate in this programme. There are still some gaps concerning the modeling of the tethered antenna, which has to take into account all the surroundings of it so it is not a very simple task. In my opinion there is still a lack in modeling this global radiation system which is not as simple as a classical dipole. The complexity will depend mainly on the target that you have in mind: if it is to be a diagnostic tool for discovering properties of the ionosphere surrounding it; if the

properties of the tethered dipole itself are the prime interest; or if it is to be used for telecommunications purposes. There are many studies to do. Then there is the propagation modeling which is still to be considered. All the problems are the interfaces which hypothesize far field conditions, near field conditions or a mix of both of them. So some identification parameters, related to the operational targets which you can have in mind could be studied more precisely in the future. This is all I have to say.

J.S. Belrose (CA) Thank you Professor Tacconi. So much for the round table. Have we stimulated some discussion from the floor, would someone like to start off? Verne Hildebrand

V. Hildebrand (US) Jack, I would like to start with a question for you. On the D-region profiles you referred to, are you willing to put a density number on the peak of the nose that you have in the C layer? (Response: about 100 cm $^{-3}$). Most of the oblique reflection at VLF will take place at densities below that, so a lot of what is going on in the upper D region for many of our calculations isn't going to affect the propagation much, and as a result of that I think you added some confirmation to Jerry's use of the exponential profile. Second, do you have any error bars for those profiles? (Response: in most cases no, no error bars). My own experience is, and I have been out of this a while so I have to be very cautious, is that almost any remote measuring technique or in situ measurement of that part of the D region important to VLF propagation has very large error bars. The error bars are so great as to make it completely out of the range of any great use to us. That's why we have all gone back, I think, to use the VLF signal itself as a means of trying to probe the part of the D-region that is important to VLF propagation. At higher altitudes the error bars are quite small. But by the time you get down to the altitudes that are important to VLF its like a flag waving in the breeze, they are all over the place. Enough on these comments.

I would like to comment on something Jerry Ferguson said. We are preaching to the choir here. We all want to continue the kinds of work we are involved in. Its very difficult to establish communications between engineers that use our knowledge and those of us that are trying to generate knowledge. I think that the time lag tends to be in all almost walks of live about 10 to 14 years. My own experience as a systems engineer is that the systems have gotten way ahead of our knowledge. We are not really able to provide much of the information needed, and just to give an example of that, let me talk about the world of adaptive receiving equipment. I think I can do this in very general terms. The engineer today has quite a bit of technology that he can manipulate. He has filters with adjustable bandwidths. He has modulation schemes with all kinds of processing gain. He has nonlinear processing techniques, clipping is one that we are all familiar with, and there are others that can be used. Sophisticated computer techniques will buy you slight improvements. He has adaptive antennas. Signal processing is a part of modern system design. We don't have the foggiest notion of what the trade offs are, and how to process the signal to get the optimum receiver sensitivity. It is extremely important if you are going to use adaptive antennas to know how to apply these assets. If you process for a pattern to mitigate atmospheric noise, you have to know the geographic distribution of noise sources, if you are doing paper analysis. If you do a laboratory experiment with a receiver, you have no concept of what you are processing if

you don't know where the thunderstorm are. So we have to do scenario type analyses. If you process those receivers so that you get rid of the intense close in thunderstorm activity with an adaptive antenna, then your nonlinear processing is entirely different than you have used in the past. We just don't know what these mixes are. Furthermore, I'd say that 90% of the systems engineers don't have the foggiest notion of what they are dealing with. So we have two communities that don't know anything, about building systems. That's enough for that comment.

U.S. Inan (US) I would like to comment on Dr. Belrose's earlier comment. I think those of us who have experience in HF, and I don't, may have a misconception (it came out at least a couple of times in this meeting) that there is no D-region at night. Well from a VLF point of view, there is a D-region at night. because the VLF wave reflects at 1 to 10 electrons/cc as Verne Hildebrand also alluded to earlier. The D-region has simply elevated itself from 60 km reflection height to somewhere between 80 to 85 km reflection height. So there certainly is a nighttime D-region. Also the concept of a skywave and a groundwave has to reconsidered, because of the distance, 2000 km say, which is the distance from Washington to Newfoundland. The mode approach, I believe, is much more appropriate to think in terms of because the ray approach, would, if you quantitatively wanted to analyze the signal, would require a prohibitively large number of rays. So from a mode point of view, we believe what might happen in that experiment, is that the mode structure of the waves propagating from Washington to Newfoundland could be altered because of the collision frequency change overhead the Cutler transmitter. We have evidence that this can occur, because we did a similar experiment with the Puerto Rican transmitter in 1989. We had paths going from Cutler Maine to Palmer Station, Antarctica which passed over this station and the cross modulation was unquestionably there. It was small. We had to do processing to look for it, 0.07 dB to 0.1 dB type of changes, but it was quite measurable. So in this experiment, of course, we cannot know what we are going to see, that's why we do the experiment. We do it to learn the deficiencies of our models. I want to caution against the notion that there is no D region at night. and against the notion of carrying the skywave groundwave approach too far in VLF. I think that the proper approach really is the mode analysis at these distances and that's why we all extensively use Jerry's code.

J.S. Belrose (CA) I did not said there was no D region at night, in fact I showed in my introductory overview evidence for a nocturnal ionization process causing a change in the phase of a VLF signal steeply reflected from the D-region (the 16 kHz Rugby Cambridge path). I said that the absorption at night would be very small and transferred modulation is a function of absorption, mind you the absorption at VLF is small at either day or night, but it is less at night. Certainly your remarks about the magnitude of the effect you have measured/are looking for confirm this statement.

I was really not arguing in terms of wavehop versus waveguide mode propagation. If you plot field strength versus distance, both components are there no matter which method calculation you use. Concerning the distance of about 2000 km, while I did not comment on this in my introductory lecture, I have in the past -- look at Fig. 5. The diurnal variation of phase for the paths Rugby-Malta and Rugby-Idiris (at distances of 2200-2500 km) are sort of peculiar. The day time "phase height" and the "nighttime phase heights" are about the

same. There seems only to a mode change during the sunrise/sunset transitions. Notice I said "mode change", since I would agree with you that a propagation analysis by the waveguide mode would probably better explain the observed pattern.

J.H. Richter (US) All of us who are involved in defense research certainly recognize that we are in a period of intense restructuring and questioning of what is being done. In particular, in my present capacity of chairman of the EPP, I am being asked questions by AGARD and the military staff under which AGARD functions, to demonstrate that what we do is not only useful to NATO but that NATO is critically dependent upon what we are doing. That, of course, is a nearly impossible task but, what I would like to see discussed here is: What are the issues in the area of ELF/VLF? Where are the gaps in our knowledge that are still critical for military operations? There is no question that in the area of plasma physics you always will have a large number of very interesting problems. But, where are the gaps in knowledge that are really critical for military systems? Because only if we can identify these, can we justify future effort under the AGARD umbrella. There are other forums where you can participate, e.g. URSI. The discussion that we are having certainly would not need to be addressed to conduct work of interest to URSI. But AGARD asks these questions. Is it really, as Dr. Ferguson pointed out, that we have solved the problem, and so we can declare victory and move on to another area. I am purposely posing this a little bit provocative question, but I would like to get your feedback because I need that. What is it, that we can convince a military person, that is still critically missing in the design of ELF/VLF systems so that we can justify expending research in that area? I would very much appreciate some input in that area, because those are the questions being asked.

You may be aware that the future of NATO itself is not really sure. There are questions being asked of AGARD. Is AGARD needed? Or should it be combined with other R & D facilities under NATO? AGARD is, curiously enough, under the military part of NATO, while under the civilian part of NATO we have the Defence Research Group (DRG), and there may be some thoughts of combining those efforts. Anyway, we will be asked: What is it that we do in the EPP that is really critical for the future of NATO? And just to come back and say that there are some interesting scientific problems left that we would like to study, and that what we do contributes to some sort of military operations that are still being used is not enough. As was pointed out, even OMEGA, may not be around forever, because the trend is going more and more toward using satellites for both communication and navigation. With the present diminished threat of a global war, satellites are much more survivable. It is unlikely that the regional conflicts that are being anticipated would really result in an adversary taking out the satellite resources. That is obviously one of the arguments for depending more on satellites. In this respect I am really addressing not only ELF/VLF, I am addressing the entire question of ionospheric propagation and I would like to have some comments on that if possible.

J.A. Ferguson (US) To answer your question: In my opinion the single most important shortcoming in VLF propagation prediction is in the question of the day/night terminator. What happens while the ionosphere is undergoing that major transition? That question has been neglected largely because most VLF and LF propagation

prediction has been oriented towards an all out nuclear war. The questions of what's happening under ambient conditions was irrelevant. You had to be able to calculate or make predictions when the ionosphere was severely disturbed by manmade devices. So transition effects and even naturally occurring irregularities, which we know are there, were irrelevant as well. That has changed I hope. The naturally occurring disturbances, like the day/night terminator and all the irregular structures that are in the polar regions are what's left as far as prediction models are concerned. Not trying to make a pitch for the LWPC, the computer model has built into it the necessary mechanisms to calculate the signal strength under conditions when the ionosphere is changing, but we don't have good parameter values for these transition periods. Regarding the ionospheric profiles that Dr. Belrose mentioned, we have attempted to used profiles of that sort to model measured data, the problem is (to get back to Verne's point) that most of our measurements are over very long paths. A lot of the things you see in steep incidence sounding get averaged out and virtually disappear when you look at long path propagation. The challenge for the VLF community, I think, is to (and it's going to be hard) convince the user community that now, instead of looking at massive lay downs of nuclear weapons, there is a tactical role. So now there is a need to have short term prediction capabilities under ambient conditions, knowledge that we have or expect to obtain about the ionosphere and its effect on VLF longwave propagation, knowledge that can somehow be used to help communicators manage their communication resources. But then, to continue with my overall negative viewpoint, the primary user of VLF/LF communications is for maritime fleet broadcast, and for communications to submarines. I know that in my country, the whole question of whether a submarine fleet is a viable military option any more is under question. I do not know, even if we answer all these propagation questions at VLF, if we are ultimately going have a subscriber for all this knowledge. So I let some one else address that.

J.S. Belrose (CA) Before we lay down tools and stop doing propagation research we should at least give John Bickel time to analyze all his data!!

A.C. Fraser-Smith (US) I cannot attempt to answer all the questions being raised. I don't share your negative view Jerry, but I understand it very well. In response to Dr. Richter, I do believe that, although ELF/VLF is an old field, there are some dramatic events taking place in this field right now that may impact seriously upon AGARD's interest and what's going to happen to its military systems. We have seen a remarkable new transmitter going into operational use in Germany, and, if things loosen up in the old Soviet Union, we will learn more about what has been going on there. Maybe at a future AGARD meeting someone from Russia can talk about the Soviet efforts in VLF and ELF, which I think are probably dramatic, and which we didn't hear about in this meeting. In the United States, at the present time, there is this big HARP project planned for heating of the ionosphere which in my experience having made some measurements in connection with ionospheric heaters might turn out to be a fantastic new source of ELF and VLF signals for submarine communications, or at least a new source to generate them for use by the people. Unfortunately that wasn't discussed very much at this meeting. In my own experience I mentioned the Charge to Be Experiment, this was the rocket experiment in March. We were trying to use an electron beam in space to generate ELF and VLF signals. We

didn't succeed. That was in accord with theoretical papers being published. As the capability to generate high current electron beams in space develops, we will have a true wireless antenna capability up there to shoot out an electron beam and generate ELF and VLF signals on the ground. That has, from the NATO point of view, probably a very dramatic capability, because you might be able to jam VLF signals and ELF signals in certain regions of the world by using rockets or satellites. This is a new development taking place as well.

From the point of view of knowledge gaps, I mentioned my measurements at high latitudes. I was asked, not very long ago, to write a review on the particular kinds of noises you run into in the polar regions. These are auroral hiss, and polar chorus, which I don't really make a great deal of distinction between when I'm measuring with my systems. When I began trying to write that review I found that there wasn't enough information. The last really significant paper I ran into was by Tobin Jorgenson in Denmark, and that was about 25 years ago. I couldn't write a review on his observations of these signals. Yet I know that when big auroral hiss events occur they essentially blank out all other transmissions and other signals occurring in the polar regions. I am not sure of the statistical occurrences, and I am not really making an active attempt to measure auroral hiss. So there is still a lot of scope for measurements in the polar regions, just of noise. That's one of the gaps. I think I have covered my list. I am very enthusiastic about this meeting. I am just pointing things that are developing and which could have been presented.

One other thing that Bob Helliwell and I, at Stanford, have been interested in for a long time is applying more knowledge to the processing of signals for detecting transmissions in the presence of spheric noise. We feel that is a somewhat neglected area, but now with little computers now you can work hard to look at signals occurring between the spherics. I mention that most of the noise is impulsive and the US Navy at this current time gets around that by clipping the spherics before processing the data. We feel that there is a lot of information that could be derived about the statistics of spacing between the spherics, and looking in those quiet spaces between these impulsive signals for transmissions, hence gaining more sensitivity. I am pointing out areas where other studies could be made and new developments are occurring. I am enthusiastic about the future, from the scientific point of view. Whether or not there will be submarines is a bit outside my scope because I am not a systems engineer, but a physicist.

J.S. Belrose (CA) Tony, while you still have the microphone, could you comment from your point of view, what is going to happen to the noise measurement program that you have been involved with? Noise programs like the ones in CCIR were based on data. Now with the Pacific Sierra model we've taken an entirely new approach. Certainly they are comparing with your data, but are your data going to be summarized in some way and perhaps stored in a CCIR data base, or what will be the end result of your measurement program in so far as users are concerned who want noise data?

A.C. Faser-Smith (US) Assuming that my building doesn't collapse from the weight of all the magnetic tapes I have been acquiring over the years, my plan is to feed those data into CCIR, and I currently do have good links with the CCIR people within the United States, Don Spaulding for example. It is really a

question of turning the crank on the data. We have been turning out reports on the data. We are actually processing all the data that I have on tapes. That is every minute of data is being processed from the various stations. There is a lot of work required, and it is slow. We are still recording at certain locations around the world, predominately at high latitudes. I am hoping that we will have enough information to dramatically improve the CCIR model, particularly at the lower frequencies below 10 kHz where a lot of data are missing. (For the past 30 years the HF community has had to put up with an empirical noise model, now with the advent of the theoretical LNP model it would be exciting to see these concepts applied to HF -Ed)

E. Schweicher (BE) I have a very simple question. Is there really a future for ionospheric propagation? Except for submarine communications I think there is not much future for ionospheric studies and for LF and VLF studies of propagation in that frequency band. As you know we have a bright future using the satellites and using much higher frequencies where you can much achieve high antenna directivity and where the size of the system is much smaller. I would like to know if you really think that we should go on with long term studies in the field of ionospheric propagation? Personally, I think it would be wise for EPP to reduce the ionospheric activities.

J.S. Belrose (CA) That would be a very controversial point of discussion. I could make a comment myself but I see Dr. Richter -

J.H. Richter (US) Let me just answer. In the previous discussions I really think I got one fairly convincing point that I could make for continuing work in this area. First of all, your question of whether all ionospheric propagation should be abandoned in view of the satellite capabilities? There is no question that satellite communications is superior to anything you can do with the ionosphere. There is no question about that, if you look at bandwidth alone. The problem is that the military does want to have alternative methods that can be used if satellites are not available. Therefore, it is essential that they have an additional capability to satellites.

Now let me tell you what I picked up from the previous discussion with respect to justifying some additional work in this area. I want to try it out on you. The question asked is how do we change our effort in view of what we have learned from the Gulf War and the end of the Cold War? I think, if I understood it right, one could in a simplified way say the effort in the past has been geared towards a worst case scenario, high altitude nuclear bursts to disrupt communications, and potent jammers that only can be done by large countries. In view of the fact that it is unlikely that we will have high altitude nuclear bursts just to interrupt communications, in view of the fact that we probably won't have very potent jammers, we could make our fallback alternative ELF/VLF communications much more efficient by considering now the propagation phenomena that were mentioned, viz. considering in more detail nighttime propagation, and propagation across the terminator. Therefore, if you look at 1 MW radiated power, if you don't design a system that has to work in a highly disturbed environment and against jammers, you probably could make a much more efficient way of communicating. Therefore, it is time now to look at some of the physics that had been neglected in view of the fact that in the past we designed for worst case scenarios, which we don't have to do any more. I can see this as an argument that could be used to say

that some effort should be continued in ionospheric propagation. For the reason that the threat has changed it is time to address other questions that may result in (a selling point for the military) reduced power in the transmitting stations. I imagine if you can reduce your power from a megawatt to 10 kW you would save a lot of operating costs. Did I make myself clear? That was for me a sort of a convincing argument to maintain some effort in that area. There is no question, of course, and I have to agree with Professor Schweicher, that the attention of the military is in the high precision weapons area, in the electro-optics area, satellite communications, satellite navigation. There is no question that's where their attention is. But I think we can justify a continued effort in terrestrial systems by saying that you do not want to rely on satellite systems as a means of navigating or communicating solely, you have to have a fallback method. Now, since the whole question has changed, there is reduced threat of jamming, a reduced threat of high altitude nuclear detonations, and things like this, we can address the question of how can we make VLF communication more efficient. Is that a fair summary?

J.A. Ferguson (US) One of the things that I didn't say earlier concerning this focus on nuclear weapons effects, in many ways made the problem easier. Now that we are contending with the ambient environment, we are now dealing with a much tougher adversary. Because the sun, in its various cycles and its massive activity, introduces variables that we have no control over. I mean that the problem was simpler when you knew that the guy was going to throw a particular kind of weapon at you, it made the problem simpler. Now, it's a much, much more difficult problem requiring a lot more effort. If there is a need for VLF communications, then the problem, and the problems that are left are much tougher to solve. There is plenty of justification for continued effort, if not more justification for continued effort. When you get all excited about satellites you have to think again about this solar adversary, if you will, when the sun is very active even satellite systems are not immune. During the Gulf War GPS didn't work as well as it was supposed to because the sun was interfering. A lot of HF Coms didn't work as predicted because the sun was interfering. If we would have had that war at a minimum of the solar cycle (maybe we can schedule those things like that), everything would have worked better as planned and as predicted. We just happened to do it in a period when the sun was in one of its most active periods. A lot of expectations went by the board.

J.S. Belrose (CA) The provocative comment by Prof. Schweicher extends far outside the meeting here, as we just heard from comments by Jerry. Certainly the Canadian military have never given up with HF. The old expression that HF is dead but it won't lie down. In Canada we have many short period disturbances which are associated with the auroral belt, which extends to rather low latitudes in Canada, and these disturbances are very sporadic in both space and time. At CRC we have a number of people doing research in support of military HF communications -- we have an ongoing project in adaptive HF networking, for a system where you have a whole network of HF stations. If you have an ionospheric disturbance on one path you can find another path around it, with the store and forward techniques available in packet radio nowadays. In another area, communications engineers have been designing extremely sophisticated modems for digital voice and high data rate systems. However the young engineers, the people designing these new

modems, know little about HF propagation. Some of these modems won't work in the Canadian environment, because of the Doppler shift and frequency spread on the signal. Some of the modern modems are designed so that if the frequency spread is more than 1 Hz its performance is seriously degraded. A 1 Hz frequency spread is more or less quiet conditions in the Canadian Arctic. So some of the people that were previously ignoring HF propagation are busy planning and conducting HF propagation experiments, measuring in particular at least one parameter, Doppler spread. There is certainly a continuing need for High Frequency propagation in particular areas. I think that a major need is to ensure that radio engineers designing systems understand the need for our work.

A.S. Smith (UK) This is a comment on the point that Tony Fraser-Smith made about the high latitude ELF/VLF noise. It may not be a direct interest to this community, and the way we are proceeding now, but there are some interesting scientific questions which can be looked at. I would like to point out developments which are happening at high latitudes now, in the Antarctic, in the form of automatic geophysical observatories which are going to be placed in a network over the continent. These observatories will have a variety of instruments for geophysical studies including ELF and VLF receivers. There a lot of interesting questions about auroral phenomena which you can answer with this kind of experiment, having a network of receivers. Even if we come to a scenario where many VLF transmitters are scaled down in operations, it will still be very important to know about VLF propagation, to have these improved computer codes, to tell us about this for these purely scientific studies. I think that's an important point to bear in mind for the future.

R.F. Benson (US) I would like to respond. Several mentions were made of the Gulf War, but, if my memory serves me right, it was under President Ford that he had to rely on HF communications to get information when the ship the Miagez was hijacked. The only information that could get through, at that time, was due to HF because some of these other systems were not operational or failed or for some reason they were not suitable. From the multiplicity of communications, if we think in terms of, for example meteor burst communications, the aspects there are low cost, and the propagation path disappears so that would be very useful for military applications when some information has to be transmitted without interception. I think we have had many experiences of that in the past in this panel. The other thing, if the military ever needs reminding of why not to put all the eggs in one basket, they could use NASA as an example. I remember, that not too many years ago, the emphasis was to do everything on the shuttle. If you wanted to do any research at all you did it on the shuttle because we are going to do away with all our rockets, and the shuttle will be all things to all people and it will do everything. NASA has realized its mistake on that and now they are trying to go back into a multiplicity approach and have unmanned rockets as well as the shuttle program. I think that it is always a mistake to throw all your eggs into one basket.

J.S. Belrose (CA) The multiplicity approach to modern communications systems will be addressed at our meeting next fall where we are going to talk of multimedia. Is Paul Cannon here? Are you going to have ELF/VLF as one link in your multimedia?

P.S. Cannon (UK) I agree with the comment that you shouldn't put all your eggs

in one basket. There will be a meeting next fall on multimedia propagation and the basic theme of this meeting is: sometimes you may deliberately or sometimes you may accidentally have propagation by two paths. Sometimes that causes you problems, but on many occasions actually it gives you diversity in your system. I strongly support the idea that we should pursue various lines.

V Lammers (US) In response to Dr. Belrose's comments on Dr. Schweicher's proposal. It is true, there are HF systems that are troubled by propagation. In the US we constantly see the same thing, that after a system has been developed, it is found out that propagation hasn't really been taken into account. We use the same argument among ourselves. I work for the Rome laboratory which has the charter for propagation in the US Air Force. We are slowly being driven out of propagation. I am not an HF or VLF or ELF man I am a microwave man, but there is practically no more propagation research in our organization in the microwave region. Although it appeared that HF had a renaissance when the over-the-horizon radar was going to be improved beyond what's currently available, with the change in the political situation the HFDF community are struggling as well. We all have our arguments as to why our work is important. That doesn't necessarily mean that the people who control the purse strings agree to that. I guess that a lot of work has to be done to justify ELF or any other propagation work for that matter.

J.S. Belrose (CA) Thank you Mr. Lammers. Any other comments? Could we stimulate a comment from Dr. Albrecht about his interest in the land sea boundaries and propagation across the ground and interesting problems with respect to VLF/LF, that topic wasn't really discussed at this meeting. I am sure he could make some comments from his knowledge and points of view.

H.J. Albreicht (GE) Thank you, I wanted to stay out of the discussion. I am presently speaking with a rather strange accent, I apologize for my cold. The subject is of course very interesting and I guess the question concerned with the importance of propagation research seems to follow a cycle. In the defence research area some reorientation is necessary. I remember that towards the end of the sixties, HF was declared not applicable any more. There was no need to do any research because there will be satellites. Then HF was reborn as an important way to communicate. Then again it was declared superfluous. In the past this seemed to follow the sunspot cycle (an 11 year cycle) for some unknown reason. I don't know whether the sunspots have something to do with it. The ups and downs in HF being popular, and the older ones of us know this. I think it is most important that, in the whole field of electromagnetic wave propagation, a certain standard know how must be preserved,. so that we can respond to any particular specialized question. This also includes the subject that you asked me particularly to comment on, on the surface and near surface propagation. I think that a certain research areas should be followed, and we should be interested to do that. I know that there will be problems to justify such work at the present moment. It is very short sighted to declare this or any other area superfluous at this very point. We are in research and research means that it is a long termed development. That is about all I can contribute.

J.S. Belrose (CA) Thank you Dr. Albrecht. I think your comments are well taken. Would any body else like to say something? Dr. Bonifazi -

C. Bonifazi (IT) I don't want to make any comment on the present discussion. I think it is interesting. You have to not only to do the research but also to tell about your research.

I want to add something concerning the future, the near future. It could be useful to view the tethered system as an antenna application for ELF/VLF. And to move from the first scientific investigation to the application we need to do something more. And the SEDS program that Bannister was presenting is one of the key elements in this. To make clear that when I was making some comments in my presentation I was required to do it because the Italian Space Agency is formally working with NASA in this project. A few years ago we formed a joint (NASA, Italian Space Agency) working group. During the last two or three years, due to some miscommunications, something went wrong. We are informing NASA that the Italian Space Agency wants to collaborate with them in the SEDS program, for the simple reason that we have invested a lot of money in this new technology, and it is extremely important that this new technology be tested in flight. I think that what concerns the antenna application of the tether, it is extremely important that you have the new technology, especially the plasma contactor technology, which is essential for the simple reason that you will never get a current of 100 amps using an electron gun. In addition to having a high current and proper modulation you need a new device, and the plasma contactor is the proper one. The future is, in my opinion, with this new technology and this new system.

U.S. Inan (US) I want to thank Jerry for identifying the area of nighttime propagation and the day/night terminator type of issues which really have been neglected in the past. But to add a bit more extended vision to that. We have to realize that the mission of NATO now is in transformation and indeed the military aspect of the mission of NATO may not be as strongly emphasized in the future as it is now or has been in the past. What we have seen in this meeting is a bringing together people who have worked on the practical aspects of propagation, and those of us who are using VLF now to study the earth's environment. It is the environment, as Jerry mentioned, that we know very little about. In terms of the global change and the mission to planet Earth type of issues, VLF is going to be required to understand that region of the upper atmosphere which we call the ignorosphere. This community of experts that we have here have all things to contribute. Another side of it also is that any country or collection of countries, in this case, cannot afford to lose expertise in an area like this. The investigation of the issues, like the ones Jerry raised, is an excellent way to maintain that expertise and promote it and at the same time contribute to the educational charter of NATO, if it develops into a charter like that as it transforms itself. These are issues, electromagnetic propagation, scattering type of issues that manifest themselves rather uniquely in isotropic media which is the earth's ionosphere.

One of the concerns of us, as pioneers in the field of radio wave propagation, is the problem of having fresh blood coming in. Who are we to transfer our knowledge to if the fresh blood doesn't come in? I think all of you in all your organizations are concerned with that matter, in discussion with those that are providing the resources for the continuation of the research.

J.S. Belrose (CA) I think on that note, we need to end our round table

discussion. Is there anyone else who wants to make a final comment?

Well, let me thank you very much indeed for what I think was a useful and an enjoyable meeting; and this session has, I think, been a very useful discussion of the future for our work. The subject of the meeting, as I have already said, brought back nostalgic remembrances for me -- I enjoyed the opportunity to discuss this subject again in an AGARD forum, after 11 years. And, as I have also told you we (in our Laboratory) could make new contributions to the field, since during the past few years we reactivated research relevant to the subject matter of this conference. Let me close the technical part of the program and turn the meeting over to our panel chairman, Dr. Richter, who will conduct the closing ceremonies. Thank you gentlemen. Thank you ladies.

LIST OF PARTICIPANTS

ALBRECHT	Dr H.J. ALBRECHT, Germany FGAN - Neuemahrerstrasse 20 - W-5307 Wachtberg-Werthhoven
ALPERT	Prof Y.L. ALPERT, United States 1662 Commonwealth Avenue (Apt. 35) - Brighton - MA 02135
ANNAERT	Eng G. ANNAERT, Belgium Universite Libre de Bruxelles (Dept. Elec.) - Pleinlaan 2 - 1050 Brussels
ASHDOWN	Mrs G.A. ASHDOWN, United Kingdom DRA (Communications Dept) - Maritime Division - ARE Portsdown - Cosham - Hants PO6 4AA
BANNISTER	Mr P R BANNISTER, United States Naval Undersea Warfare Center - Code 3411 - New London - CT 06320
BARBERLO-CORSETTI	Dr P. BARBERLO-CORSETTI, The Netherlands SHAPE Technical Center - P O Box 174 - 2501 The Hague
BAREL	Prof Dr Ir A. BAREL, Belgium Free University of Brussels (Dept. Elec.) - Plainlaan 2 - 1050 Brussels
BEAHN	Dr T.J. BEAHN, United States Laboratory for Physical Sciences - 4928 College Avenue - College Park, MD 20740
BELROSE	Dr J.S. BELROSE, Canada Communications Research Center - Station H - P O Box 11490 - Ottawa ONK2H 8S2
BENSON	Dr R.F. BENSON, United States NASA/Goddard Space Flight Center - Code 692 - Greenbelt - MD 20771
BICKEL	Mr J.E. BICKEL, United States NCCOSC - RDT&E Division - Code 542 - San Diego - CA 92152-5000
BODET	Major Ir Ph. BODET, Belgium Coordonnateur AGARD - VSL - Etat-Major de la Force Aerienne - Quartier Reine Elisabeth - 1140 Brussels
BONIFAZI	Dr C. BONIFAZI, Italy Agenzia Spaziale Italiana - viale Regina Margherita 202 - 00198 Rome
BORGMANN	Mr D. BORGMANN, Germany Telefunken Systemtechnik - VR24 E2 - Sedanstrasse 10 - D-7900 Ulm
BOSSY	Prof L. BOSSY, Belgium UCCLE - 174 Avenue Winston Churchill - B1180 Brussels
BRIGHT	Dr K. BRIGHT, United Kingdom GEC Marconi Secure Systems - Browns Lane - The Airport - Portsmouth - Hants PO3 5PH
BURKE	Dr C.P. BURKE, United Kingdom Physics Dept. - Kings' College - Strand - London WC2R 2LS
CANNON	Dr P.S. CANNON - United Kingdom Radio Propagation Laboratory - Communications Dept - P161 Building - DRA - Farnborough - Hants GU146TD
CARIGLIA	Lt-Col. R. CARIGLIA, Italy AGARD - EPP Executive - 7 rue Ancelle - 92200 Neuilly sur Seine - France
CASIMIRO	Prof A.M.E.S. CASIMIRO, Portugal Faculdade de Engenharia da Universidade de Porto - Rua dos Bragas - 4099 Porto Codex
CASSARA'	Lt-Col. A. CASSARA', Italy Aeronautica Militare - DASR/RASA - 00040 Pratica di Mare
CHAPMAN	Mr P. S. CHAPMAN, United Kingdom DRA Portsdown - Cosham - Hants PO 6 4AA

CHASSAGNE	Mr F. CHASSAGNE, France Thomson - CSF/RGS - 66 rue du Fosse Blanc - 92231 Gennevilliers Cedex
CLEMENS	Ir C.H.M. CLEMENS, The Netherlands TNO-FEL - PO Box 96864 - NL-2509 JG The Hague
CRAWFORD	Dr R.L. CRAWFORD, United States SRI International - 1611 North Kent Street - Arlington - Virginia 22209
DE HAAN	Ir C.D. De HAAN, The Netherlands TNO-FEL - PO Box 96864 - NL 2509 JG The Hague
DECHAMPS	Adj Ph. DECHAMPS, Belgium Ecole Royale Militaire - Avenue de la Renaissance, 30 - B-1040 Brussels
DERMONT	Lt H. DERMONT, Belgium Ecole Royale Militaire - Avenue de la Renaissance, 30 - B-1040 Brussels
ELLIOTT	Mr M. ELLIOTT, Belgium ARFA - CIS Division - IMS, NATO HQ - B-1110 Evere
EVRARD	Gen-Maj. EVRARD, Belgium 119, Avenue de Val d'Or - B-1200 Brussels
FERGUSON	Dr J.A. FERGUSON, United States Head, Ionospheric Branch, NCCOSC - RDT&E Division - Code 542 - San Diego - CA 92152-5000
FLEURY	Dr R. FLEURY, France CNET LAB - BP 40 - 22301 Lannion
FLOOD	Dr W.A. FLOOD, United States Chief, Env.Sci.Branch, US Army Research Office PO Box 12211, Research Triangle Park, NC 27709-2211
FRASER-SMITH	Dr A.C. FRASER-SMITH, United States Standford Univesity, 202 Durand/STARLAB - Stanford - CA 94305-4055
FUERXER	L'Ing. En chef de l'Arm. FUERXER, France CNET - 38-40 rue du General Leclerc - 92131 Issy les Moulineaux
GHICOPOULOS	Dr B. GHICOPOULOS, Greece Hellenic Air Force - KETA - Post Office Terpsitheas - 16501 Glyfada - Athens
GUDEN	Mr S. GUDEN, Turkey 1 nci Hava Ikmal ve Bakim - Merkez K. Ligi - Eskisehir
HARRINGTON	Mr M. D. HARRINGTON, United Kingdom DRA, Communications Dept - Maritime Division - ARE Portsdown - Cosham - Hants PO6 4AA
HARTH	Prof Dr. W. HARTH, Germany Fachhochschule Koln - Betzdorferstrasse 2 - D-5000 Koln 21
HILDEBRAND	Mr V. E. HILDEBRAND, United States IWG Corporation - 1940 Fifth Avenue (Suite 200) - San Diego - CA 92101
HOHN	Dr D.H. HOHN, Germany FGAN - Forschungsinstitut fur Optik (FfO) - Schloss Kressbach - 7400 Tubingen
HOLZHEIMER	Mr T.R. HOLZHEIMER, United States E-Systems, Inc. - Greenville Division - P O Box 6056 - Greenville, TX 75403-6056
INAN	Prof U.S. INAN, United States Durand 321, STAR/EE Dept. - Stanford University - Stanford - CA 94305-4055
JODOGNE	Ing. Dr. J. C. JODOGNE, Belgium Institut Royal Meteorologique - 3 Avenue Circulaire - B-1180 Brussels
JORGE AFONSO	Major Eng. A. JORGE AFONSO, Portugal CLAFA, Direccao de Electrotecnica - Base de Alfragide - 2700 Amadora

KOSSEY	Dr P.A. KOSSEY, United States Ionospheric Effects Division - Phillips Laboratory - PL/GPI - Hanscom AFB, MA 01731-5000
LAFLIN	Mr M.G. LAFLIN, United States US DOC/NTIA/ITS - Mail Stop ITS.S2 - 325 Broadway - CO 80303
LAMMERS	Dr U. LAMMERS, United States Rome Laboratory (RL/ERCT) - Hanscom AFB - MA 01731-5000
LANUSSE	Dr A.F. LANUSSE, France DRET/SDR - Groupe 2 - 26 Boulevard Victor - 00460 Paris Armees
LASSUDRIE-DUCHESNE	Prof Dr P. LASSUDRIE-DUCHESNE, France CNET LAB - BP 40 - 22301 Lannion
LAUBER	Mr W. R. LAUBER, Canada Communications Research Center - Station H - Ottawa - ON K2H 8S2
LISEC	Mr E. LISEC, Belgium Allied Radio Frequency Agency - NATO HQ - 1110 Evere
LLANWYN JONES	Dr D. LLANWYN JONES, United Kingdom Physics Department - Kings' College - Strand - London WC2R 2LS
MARTIN	Lt Cdr C.W. MARTIN, United Kingdom AWWAG - COB II - H.M. Naval Base - Portsmouth PO1 3LE
MEAD	Mr J. D. MEAD, United Kingdom P O Box 87 - Farnborough - Hants GU14 6YU
MILBURN	Mr C. J. MILBURN, United Kingdom ARE Portsdown - CCM127 - Cosham - Hants PO6 4AA
NICHOLLS	Mrs D.M. NICHOLLS, United Kingdom DRA - Communications Department - Maritime Division - ARE Portsdown - Cosham - Hants PO6 4AA
PAPAPASCHALIS	Lt-Col. A. PAPAPASCHALIS, Greece Hellenic Air Force General Staff - Directorate C3 - Holargos - TGA 1010
PATRICIO	Eng. J.F. PATRICIO, Portugal Rua Alferes Barrilaro Ruas - No. 1, 8 Direito - 1800 Lisbon
PELT	Dr W. PELT, The Netherlands WC5/Ministry of Defence - PO Box 20702 - M-2500 ES Den Haag
PROHOROFF	Dr Ir S. PROHOROFF, Belgium ULB - Ecole Polytechnique - Av. F.D. Rossvelt 50 - B-1050 Brussels
RASMUSSEN	Mr J.E. RASMUSSEN, United States Chief, Ionospheric Applications Branch - PL/GPIA - Hanscom AFB - MA 01731-5000
RICHARD	Mr A. RICHARD, France Thomson - CSF/RGS - Service GPE/SAG - 66 rue du Fosse Blanc - 92231 Gennevilliers Cedex
RICHTER	Dr J.H. RICHTER, United States NCCOSC - RDT&E Division, Code 54 - San Diego - CA 92151-5000
ROGGE	Mr J. ROGGE, The Netherlands Konlinklijk Militaire Academie - Postbus 90.154 - 4800 RG Breda
SCHWEICHER	Prof Dr E. SCHWEICHER, Belgium Ecole Royale Militaire - Chaire OM - 30 Avenue de la Renaissance - B-1040 Bruxelles
SMITH	Dr A.J. SMITH, United Kingdom British Antarctic Survey - High Cross - Madingley Road - Cambridge - CB3 OET
TAAGHOLT	Mr J TAAGHOLT, Denmark Danish Polar Center - Hausergade 3 - DK-1128 Copenhagen K

TACCONI	Prof G. TACCONI, Italy Universita' di Genova - Dipt. Ingegnerai Biofisica (DIBE) - Via all'Opera Pia 11/A - 16145 Genoa
TULUNAY	Prof. Dr Y. TULUNAY, Turkey Dept. of Aeronautical Engineering - Middle East Technical University - O.D.T.U. - M.E.T.U. - Ankara 06531
VAN DER PERRE	Ir L. VAN DER PERRE, Belgium KUL Afd ESAT - Kardinaal Mercierlaan, 94 - B-3001 Heverlee
VAN DIEST	Maj-Gen. G. VAN DIEST, Belgium Deputy Chief of Staff for Logistics - Belgian Air Force - Quartier Reine Elisabeth - B-1140 Brussels
VAN HECKE	Lt-Gen. G. VAN HECKE, Belgium Aide to the King - Chief of Staff, Belgian Air Force - Quartier Reine Elisabeth - B-1140 Brussels
VICKERY	Mr W.K. VICKERY, United States Director, Ionospheric Effects Div. - Phillips Laboratory/GPI - Hanscom AFB - 01731-5000
VLOEBERGHS	Prof C. VLOEBERGHS, Belgium Ecole Royal Militare - 30 Avenue de la Renaissance - B-1040 Brussels
WARBER	Mr C.R. WARBER, United States Pacific-Sierra Research Corp. - 2901 28th Street - Santa Monica - CA 90405
WARRINGTON	Dr E.M. WARRINGTON, United Kingdom Dept. of Engineering - University of Leicester - Leicester LE1 7RH
WOLKOFF	Mr E.A. WOLKOFF, United States Naval Undersea Warfare Center - Code 341 - New London - CT 06320
WYMAN	Mr G. WYMAN, United Kingdom Chief Engineer EW - FPC 900 - British Aircraft Military Aircraft - PO Box 5 - Filton - Bristol BS12 7QW

REPORT DOCUMENTATION PAGE

1. Recipient's Reference	2. Originator's Reference	3. Further Reference	4. Security Classification of Document
	AGARD-CP-529	ISBN 92-835-0712-6	UNCLASSIFIED/ UNLIMITED

5. Originator Advisory Group for Aerospace Research and Development
North Atlantic Treaty Organization
7 Rue Ancelle, 92200 Neuilly sur Seine, France

6. Title ELF/VLF/LF RADIO PROPAGATION AND SYSTEMS ASPECTS

7. Presented at the Electromagnetic Wave Propagation Panel Symposium, held at the Quartier Reine Elisabeth, Brussels, Belgium, 28th September—2nd October 1992.

8. Author(s)/Editor(s)	9. Date
Various	May 1993
10. Author's/Editor's Address	**11. Pages**
Various	354

12. Distribution Statement There are no restrictions on the distribution of this document. Information about the availability of this and other AGARD unclassified publications is given on the back cover.

13. Keywords/Descriptors

Electromagnetic propagation
Radio noise and interference
Antenna considerations
Tethered ground based and satellite systems
Reliability of LW communication links

14. Abstract

This publication reports the papers presented to a specialists' meeting held by the Electromagnetic Wave Propagation Panel at its Fall 1992 meeting.

The topics covered on the occasion of that symposium include:

- Propagation aspects
  - Numerical modelling;
  - Propagation measurements; and
  - Propagation in sea water.
- Radio noise and interference
  - Long wave TE/TM Noise prediction model;
  - Measurements; and
  - ELF generated by auroral electrojet modulation.
- Antenna considerations
  - Antenna fundamentals;
  - Scale modelling;
  - Measurements of pattern and bandwidth; and
  - Tethered aerostat VLF/LF transmitting antennas.
- System aspects
  - Viability assessment for reliable LW communication links.
- Future satellite systems
  - Orbiting system for ELF/VLF strategic communications; and
  - Tethered satellite systems.

AGARD Conference Proceedings 529
Advisory Group for Aerospace Research and Development, NATO
ELF/VLF/LF RADIO PROPAGATION AND SYSTEMS ASPECTS
Published May 1993
354 pages

This publication reports the papers presented to a specialists' meeting held by the Electromagnetic Wave Propagation Panel at its Fall 1992 meeting.

The topics covered on the occasion of that symposium include:

- Propagation aspects
  - Numerical modelling;
  - Propagation measurements; and
  - Propagation in sea water.

P.T.O.

AGARD-CP-529

Electromagnetic propagation
Radio noise and interference
Antenna considerations
Tethered ground based and satellite systems
Reliability of LW communication links

AGARD Conference Proceedings 529
Advisory Group for Aerospace Research and Development, NATO
ELF/VLF/LF RADIO PROPAGATION AND SYSTEMS ASPECTS
Published May 1993
354 pages

This publication reports the papers presented to a specialists' meeting held by the Electromagnetic Wave Propagation Panel at its Fall 1992 meeting.

The topics covered on the occasion of that symposium include:

- Propagation aspects
  - Numerical modelling;
  - Propagation measurements; and
  - Propagation in sea water.

P.T.O.

AGARD-CP-529

Electromagnetic propagation
Radio noise and interference
Antenna considerations
Tethered ground based and satellite systems
Reliability of LW communication links

AGARD Conference Proceedings 529
Advisory Group for Aerospace Research and Development, NATO
ELF/VLF/LF RADIO PROPAGATION AND SYSTEMS ASPECTS
Published May 1993
354 pages

This publication reports the papers presented to a specialists' meeting held by the Electromagnetic Wave Propagation Panel at its Fall 1992 meeting.

The topics covered on the occasion of that symposium include:

- Propagation aspects
  - Numerical modelling;
  - Propagation measurements; and
  - Propagation in sea water.

P.T.O.

AGARD-CP-529

Electromagnetic propagation
Radio noise and interference
Antenna considerations
Tethered ground based and satellite systems
Reliability of LW communication links

AGARD Conference Proceedings 529
Advisory Group for Aerospace Research and Development, NATO
ELF/VLF/LF RADIO PROPAGATION AND SYSTEMS ASPECTS
Published May 1993
354 pages

This publication reports the papers presented to a specialists' meeting held by the Electromagnetic Wave Propagation Panel at its Fall 1992 meeting.

The topics covered on the occasion of that symposium include:

- Propagation aspects
  - Numerical modelling;
  - Propagation measurements; and
  - Propagation in sea water.

P.T.O.

AGARD-CP-529

Electromagnetic propagation
Radio noise and interference
Antenna considerations
Tethered ground based and satellite systems
Reliability of LW communication links

- Radio noise and interference
  - Long wave TE/TM Noise prediction model;
  - Measurements; and
  - ELF generated by auroral electrojet modulation.
- Antenna considerations
  - Antenna fundamentals;
  - Scale modelling;
  - Measurements of pattern and bandwidth; and
  - Tethered aerostat VLF/LF transmitting antennas.
- System aspects
  - Viability assessment for reliable LW communication links.
- Future satellite systems
  - Orbiting system for ELF/VLF strategic communications; and
  - Tethered satellite systems.

ISBN 92-835-0712-6

- Radio noise and interference
  - Long wave TE/TM Noise prediction model;
  - Measurements; and
  - ELF generated by auroral electrojet modulation.
- Antenna considerations
  - Antenna fundamentals;
  - Scale modelling;
  - Measurements of pattern and bandwidth; and
  - Tethered aerostat VLF/LF transmitting antennas.
- System aspects
  - Viability assessment for reliable LW communication links.
- Future satellite systems
  - Orbiting system for ELF/VLF strategic communications; and
  - Tethered satellite systems.

ISBN 92-835-0712-6

- Radio noise and interference
  - Long wave TE/TM Noise prediction model;
  - Measurements; and
  - ELF generated by auroral electrojet modulation.
- Antenna considerations
  - Antenna fundamentals;
  - Scale modelling;
  - Measurements of pattern and bandwidth; and
  - Tethered aerostat VLF/LF transmitting antennas.
- System aspects
  - Viability assessment for reliable LW communication links.
- Future satellite systems
  - Orbiting system for ELF/VLF strategic communications; and
  - Tethered satellite systems.

ISBN 92-835-0712-6

- Radio noise and interference
  - Long wave TE/TM Noise prediction model;
  - Measurements; and
  - ELF generated by auroral electrojet modulation.
- Antenna considerations
  - Antenna fundamentals;
  - Scale modelling;
  - Measurements of pattern and bandwidth; and
  - Tethered aerostat VLF/LF transmitting antennas.
- System aspects
  - Viability assessment for reliable LW communication links.
- Future satellite systems
  - Orbiting system for ELF/VLF strategic communications; and
  - Tethered satellite systems.

ISBN 92-835-0712-6

AGARD
NATO OTAN
7 RUE ANCELLE · 92200 NEUILLY-SUR-SEINE
FRANCE
Télécopie (1)47.38.57.99 · Télex 610 176

DIFFUSION DES PUBLICATIONS AGARD NON CLASSIFIEES

Aucun stock de publications n'a existé à AGARD. A partir de 1993, AGARD détiendra un stock limité des publications associées aux cycles de conférences et cours spéciaux ainsi que les AGARDographies et les rapports des groupes de travail, organisés et publiés à partir de 1993 inclus. Les demandes de renseignements doivent être adressées à AGARD par lettre ou par fax à l'adresse indiquée ci-dessus. *Veuillez ne pas téléphoner.* La diffusion initiale de toutes les publications de l'AGARD est effectuée auprès des pays membres de l'OTAN par l'intermédiaire des centres de distribution nationaux indiqués ci-dessous. Des exemplaires supplémentaires peuvent parfois être obtenus auprès de ces centres (à l'exception des Etats-Unis). Si vous souhaitez recevoir toutes les publications de l'AGARD, ou simplement celles qui concernent certains Panels, vous pouvez demander à être inclu sur la liste d'envoi de l'un de ces centres. Les publications de l'AGARD sont en vente auprès des agences indiquées ci-dessous, sous forme de photocopie ou de microfiche.

CENTRES DE DIFFUSION NATIONAUX

ALLEMAGNE
Fachinformationszentrum,
Karlsruhe
D-7514 Eggenstein-Leopoldshafen 2

BELGIQUE
Coordonnateur AGARD-VSL
Etat-Major de la Force Aérienne
Quartier Reine Elisabeth
Rue d'Evere, 1140 Bruxelles

CANADA
Directeur du Service des Renseignements Scientifiques
Ministère de la Défense Nationale
Ottawa, Ontario K1A 0K2

DANEMARK
Danish Defence Research Board
Ved Idraetsparken 4
2100 Copenhagen Ø

ESPAGNE
INTA (AGARD Publications)
Pintor Rosales 34
28008 Madrid

ETATS-UNIS
National Aeronautics and Space Administration
Langley Research Center
M/S 180
Hampton, Virginia 23665

FRANCE
O.N.E.R.A. (Direction)
29, Avenue de la Division Leclerc
92322 Châtillon Cedex

GRECE
Hellenic Air Force
Air War College
Scientific and Technical Library
Dekelia Air Force Base
Dekelia, Athens TGA 1010

ISLANDE
Director of Aviation
c/o Flugrad
Reykjavik

ITALIE
Aeronautica Militare
Ufficio del Delegato Nazionale all'AGARD
Aeroporto Pratica di Mare
00040 Pomezia (Roma)

LUXEMBOURG
Voir Belgique

NORVEGE
Norwegian Defence Research Establishment
Attn: Biblioteket
P.O. Box 25
N-2007 Kjeller

PAYS-BAS
Netherlands Delegation to AGARD
National Aerospace Laboratory NLR
P.O. Box 90502
1006 BM Amsterdam

PORTUGAL
Portuguese National Coordinator to AGARD
Gabinete de Estudos e Programas
CLAFA
Base de Alfragide
Alfragide
2700 Amadora

ROYAUME UNI
Defence Research Information Centre
Kentigern House
65 Brown Street
Glasgow G2 8EX

TURQUIE
Millî Savunma Başkanlığı (MSB)
ARGE Daire Başkanlığı (ARGE)
Ankara

Le centre de distribution national des Etats-Unis (NASA/Langley) ne détient PAS de stocks des publications de l'AGARD. D'éventuelles demandes de photocopies doivent être formulées directement auprès du NASA Center for Aerospace Information (CASI) à l'adresse suivante:

AGENCES DE VENTE

NASA Center for
Aerospace Information (CASI)
P.O. Box 8757
BWI Airport, Maryland 21240
United States

ESA/Information Retrieval Service
European Space Agency
10, rue Mario Nikis
75015 Paris
France

The British Library
Document Supply Division
Boston Spa, Wetherby
West Yorkshire LS23 7BQ
Royaume Uni

Les demandes de microfiches ou de photocopies de documents AGARD (y compris les demandes faites auprès du CASI) doivent comporter la dénomination AGARD, ainsi que le numéro de série d'AGARD (par exemple AGARD-AG-315). Des informations analogues, telles que le titre et la date de publication sont souhaitables. Veuiller noter qu'il y a lieu de spécifier AGARD-R-nnn et AGARD-AR-nnn lors de la commande des rapports AGARD et des rapports consultatifs AGARD respectivement. Des références bibliographiques complètes ainsi que des résumés des publications AGARD figurent dans les journaux suivants:

Scientifique and Technical Aerospace Reports (STAR)
publié par la NASA Scientific and Technical
Information Division
NASA Headquarters (NTT)
Washington D.C. 20546
Etats-Unis

Government Reports Announcements and Index (GRA&I)
publié par le National Technical Information Service
Springfield
Virginia 22161
Etats-Unis

(accessible également en mode interactif dans la base de données bibliographiques en ligne du NTIS, et sur CD-ROM)

Imprimé par Specialised Printing Services Limited
40 Chigwell Lane, Loughton, Essex IG10 3TZ

AGARD
NATO OTAN
7 RUE ANCELLE · 92200 NEUILLY-SUR-SEINE
FRANCE
Telefax (1)47.38.57.99 · Telex 610 176

DISTRIBUTION OF UNCLASSIFIED AGARD PUBLICATIONS

AGARD holds limited quantities of the publications that accompanied Lecture Series and Special Courses held in 1993 or later, and of AGARDographs and Working Group reports published from 1993 onward. For details, write or send a telefax to the address given above. *Please do not telephone.*

AGARD does not hold stocks of publications that accompanied earlier Lecture Series or Courses or of any other publications. Initial distribution of all AGARD publications is made to NATO nations through the National Distribution Centres listed below. Further copies are sometimes available from these centres (except in the United States). If you have a need to receive all AGARD publications, or just those relating to one or more specific AGARD Panels, they may be willing to include you (or your organisation) on their distribution list. AGARD publications may be purchased from the Sales Agencies listed below, in photocopy or microfiche form.

NATIONAL DISTRIBUTION CENTRES

BELGIUM
Coordonnateur AGARD — VSL
Etat-Major de la Force Aérienne
Quartier Reine Elisabeth
Rue d'Evere, 1140 Bruxelles

CANADA
Director Scientific Information Services
Dept of Nation
Ottawa, Ontari

DENMARK
Danish Defenc
Ved Idraetspar
2100 Copenha

FRANCE
O.N.E.R.A. (Di
29 Avenue de l
92322 Châtillo

GERMANY
Fachinformatic
Karlsruhe
D-7514 Eggen

GREECE
Hellenic Air Fc
Air War Colleg
Scientific and T
Dekelia Air Fo
Dekelia, Athen

ICELAND
Director of Avia
c/o Flugrad
Reykjavik

ITALY
Aeronautica Militare
Ufficio del Delegato Nazionale all'AGARD
Aeroporto Pratica di Mare
00040 Pomezia (Roma)

LUXEMBOURG
See Belgium

NETHERLANDS
Netherlands Delegation to AGARD
National Aerospace Laboratory, NLR
P.O. Box 90502
1006 BM Amsterdam

National Aeronautics and
Space Administration
Code JTT
Washington DC 20546
Official Business
Penalty for Private Use, $300

FOURTH CLASS

L4 001 AG-CP-529 930702S002672D
DEPT OF DEFENSE
DEFENSE TECHNICAL INFORMATION CENTER
ATTN : DTIC-OCP/JOYCE CHIRAS
CAMERON STATION BLDG 5
ALEXANDRIA VA 223046145

65 Brown Street
Glasgow G2 8EX

UNITED STATES
National Aeronautics and Space Administration (NASA)
Langley Research Center
M/S 180
Hampton, Virginia 23665

The United States National Distribution Centre (NASA/Langley) does NOT hold stocks of AGARD publications.
Applications for copies should be made direct to the NASA Center for Aerospace Information (CASI) at the address below.

SALES AGENCIES

NASA Center for
Aerospace Information (CASI)
P.O. Box 8757
BWI Airport, Maryland 21240
United States

ESA/Information Retrieval Service
European Space Agency
10, rue Mario Nikis
75015 Paris
France

The British Library
Document Supply Centre
Boston Spa, Wetherby
West Yorkshire LS23 7BQ
United Kingdom

Requests for microfiches or photocopies of AGARD documents (including requests to CASI) should include the word 'AGARD' and the AGARD serial number (for example AGARD-AG-315). Collateral information such as title and publication date is desirable. Note that AGARD Reports and Advisory Reports should be specified as AGARD-R-nnn and AGARD-AR-nnn, respectively. Full bibliographical references and abstracts of AGARD publications are given in the following journals:

Scientific and Technical Aerospace Reports (STAR)
published by NASA Scientific and Technical
Information Division
NASA Headquarters (NTT)
Washington D.C. 20546
United States

Government Reports Announcements and Index (GRA&I)
published by the National Technical Information Service
Springfield
Virginia 22161
United States
(also available online in the NTIS Bibliographic
Database or on CD-ROM)

Printed by Specialised Printing Services Limited
40 Chigwell Lane, Loughton, Essex IG10 3TZ

ISBN 92-835-0712-6